Department of Physics

University of Fribourg (Switzerland)

NONEQUILIBRIUM METHODS TO TREAT VERTEX CORRECTIONS IN CORRELATED ELECTRON SYSTEMS

THESIS

presented to the Faculty of Science and Medicine of the University of Fribourg (Switzerland)
in consideration for the award of the academic grade of
Doctor of Philosophy in Physics

by

OLIVIER SIMARD

from

SHERBROOKE, QUÉBEC, CANADA

Thesis No: 4553
Uniprint - Centre d'impression numérique
2023

Accepted by the Faculty of Science and Medecine of the University of Fribourg (Switzerland) upon the recommendation of

Co-examiner .... Prof. Roser Valentí,

Co-examiner .... Prof. Claude Monney,

President of the jury .... Prof. Guillermo Pedro Acuña,

Thesis supervisor .... Prof. Philipp Werner

Fribourg, April 19th 2023

Prof. Philipp Werner

Philipp Werner

Dean, Prof. Ulrich Ultes-Nitsche

© Olivier Simard, 2023

This work is published under a Creative Commons Attribution-NonCommercial-ShareAlike 4.0 International (CC BY-NC-SA 4.0) license: https://creativecommons.org/licenses/by-nc-sa/4.0/

https://doi.org/10.51363/unifr.sth.2023.007

À mes parents, Chantal et Yves

SUMMARY

In systems of indistinguishable particles, correlations between the quantum degrees of freedom can give rise to collective modes where particles behave coherently together over some correlation length and time, thereby forming *quasiparticles*. One example of such quasiparticle would be the π-ton [66], describing the binding of two particle-hole pairs via the exchange of momentum corresponding to the antiferromagnetic (AFM) wave vector. These quasiparticles would emerge in the vicinity of an AFM ordering instability [66, 119, 120] and nonlocal correlations are crucial to describe them. Especially, in systems out of equilibrium, nonlocality can give rise to prethermal states wherein the distribution function can be momentum-dependent [92, 119], and nonthermal exotic physics can be observed and manipulated [40, 68, 79, 84, 93, 132, 147, 157–159]. To be able to model and simulate systems out of equilibrium is a challenge. A few numerical methods such as nonequilibrium Dynamical Mean Field Theory (DMFT) [44] have been used extensively [5]. Nonequilibrium DMFT is designed to treat nonperturbatively the local time-dependent single-particle correlations. Since phenomena such as quantum criticality, high-T_c superconductivity or the creation of π-tons via light-matter coupling stem from nonlocal two-particle correlations, one needs to resort to diagrammatic extensions to DMFT [103] and other methods to effectively describe them, such as the post-processing DMFT treatment of vertex corrections, which will be introduced. The Two-Particle Self-Consistent approach (TPSC) and its variants figure among those methods that include nonlocal two-particle and single-particle correlations in a self-consistent way [121, 122]. TPSC and its variants have the ability to capture the effect of the growing spin fluctuations (paramagnons) in the self-energy when close to a magnetic phase transition leading to the breakdown of the Fermi-liquid quasiparticles at the Fermi level: this would mark the onset of a pseudo-gap [145, 152]. It fulfils the Mermin-Wagner theorem in two dimensions, the Pauli principle, and various two-particle local sum-rules [152]. In the works embodied in this thesis, numerical methods have been designed to access nonequilibrium regimes, by changing model parameters across time, allowing for nonlocal correlations to be properly included. With these new algorithms at hand, the π-tons were studied in the optical conductivity and magnetic response [119, 120] as well as spin and charge fluctuations in the 2D and 3D single-band Hubbard model [121, 122]. It is demonstrated by means of those methods that nonlocal two-particle vertex corrections can underpin prethermal states and could generate transient nonthermal states such as low-energy charge excitations associated with nonthermal negative temperatures. It is also shown that states lying close to the Fermi level control the thermalization timescale and that lattice hopping quenches changing the unit-cell dimensionality could allow one to play around with the charge and spin scattering channels.

SOMMAIRE

Dans les systèmes de particules indiscernables, les corrélations entre les différents degrés de liberté quantiques peuvent engendrer des modes collectifs en lesquels les particules se comportent de manière cohérente sur une certaine longueur de corrélation et sur un certain temps de corrélation, formant des *quasiparticules*. Un exemple de telles quasiparticules serait le π-ton [66], décrivant la liaison entre 2 paires particules-trous via l'échange de quantité de mouvement correspondant au vector d'onde antiferromagnétique (AFM). Ces quasiparticules se manifesteraient près d'une instabilité magnétique d'ordre AFM [66, 119, 120] et les corrélations non-locales joueraient un rôle incontournable. Dans les systèmes hors équilibre, la non-localité des corrélations peut générer des états pré-thermaux dans lesquels la statistique quantique n'est pas thermodynamique [92, 119] et des états quantiques exotiques de la matière émergent et peuvent être manipulés [40, 68, 79, 84, 93, 132, 147, 157–159]. Afin de modéliser et simuler les systèmes hors équilibre, on peut employer des méthodes numériques comme la théorie de champ moyen dynamique (*Dynamical Mean Field Theory* ou DMFT en anglais) [5, 44]. La DMFT hors équilibre est conçue pour traiter de manière non-perturbative les corrélations locales dépendantes du temps à une particule. Puisque les phénomènes tels que la criticalité quantique, la supraconductivité à haute-T_c ou la création de π-tons via le couplage lumière-matière émergent des corrélations non-locales à 2 particules, on doit se rapporter aux extensions diagrammatiques de la DMFT [103] et autres méthodes, comme le post-traitement DMFT des vertex. Parmi elles s'inscrivent les méthodes auto-cohérentes à 2 particules (*Two-Particle Self-Consistent approach* ou TPSC en anglais) ainsi que ses extensions, car elles incluent les corrélations non-locales à 1 et 2 particules dans la *self-énergie* de manière (auto-)cohérente. La TPSC et ses extensions comprennent l'effet grandissant des fluctuations de spin dans la *self-énergie* lorsque près d'une transition de phase magnétique et cela causerait le pseudogap [145, 152]. Ces méthodes satisfont le théorème de Mermin-Wagner en 2 dimensions, le principe de Pauli et des règles de somme locales à 2 particules [152]. Dans les travaux décrits par la présente thèse, des méthodes numériques spécifiques aux problèmes à plusieurs particules hors équilibre ont été conçues et implémentées afin d'inclure les fluctuations quantiques non-locales. Avec ces algorithmes à disposition, les π-tons ont été étudiées dans la réponse magnétique et la conductivité optique [119, 120], ainsi que le fluctuations de spin et de charge dans le modèle de Hubbard à une bande électronique en 1 et 2 dimensions [121, 122]. Il est notamment démontré dans cette thèse à l'aide de ces méthodes que les corrections de vertex non-locales à 2 particules influencent les états pré-thermaux et peuvent générer des états non-thermaux transitoires comme des excitations de charge à basse énergie associées à des températures effectives négatives. Il est aussi montré que les états près de la surface de Fermi contrôlent la thermalisation et que des rampes du terme de saut électronique changeant la dimension de la cellule-unité permettent de contrôler la diffusion dans les canaux de charge et de spin.

PUBLICATIONS

Some ideas and figures have appeared previously in the following publications:

1. **Diagrammatic study of optical excitations in correlated systems**, **O. Simard**, S. Takayoshi and P. Werner, *Phys. Rev. B* 103(10), 2021

2. **Nonequilibrium evolution of the optical conductivity of the weakly interacting Hubbard model: Drude response and π-ton type vertex corrections**, **O. Simard**, M. Eckstein and P. Werner, *Phys. Rev. B* 104(24), 2021
3. **Nonequilibrium two-particle self-consistent approach**, **O. Simard** and P. Werner, *Phys. Rev. B* 106, L241110, 2022
4. **Dynamical Mean Field Theory extension to the nonequilibrium Two-Particle Self-Consistent approach**, **O. Simard** and P. Werner, arXiv:2302.14134, 2023

Some content of this thesis is the object of other publications under preparation.

Dans la vie, il est avant tout utile de parfaire l'entendement,
autrement dit la Raison, autant que nous le pouvons,
et en cela seul consiste la souveraine félicité
ou béatitude de l'homme.

— Baruch Spinoza [124]

ACKNOWLEDGEMENTS

The past 3 $\frac{1}{2}$ years have been strewn with hurdles, with more than half of that period spent muddling through a worldwide pandemic crisis. They have nonetheless been extremely rewarding on both personal and professional bases, as I have met wonderful people, learnt and experienced so many things that have shaped me and that will live on for the rest of my life.

The first person I would like to thank is my supervisor Prof. Philipp Werner, whose support and wisdom have helped me pull out great scientific achievements. Your scientific intuition has always impressed me; most of the thinking process was carried out in your mind and was not expressed on media such as paper or a board. I will be forever grateful for what you have taught me in the course of my Ph.D, and I thank you for all the nice hikes in the Alps you have suggested. I would like to thank as well the examiners of my jury Prof. Claude Monney and Prof. Roser Valentí for their precious time.

I wish to also thank my colleagues, coming from all over the world, with whom I shared far more than just the office space, but fruitful and gratifying experiences, thoughts, and ideas. I really appreciated your openness on the very many different subjects of discussion we have talked over about. In particular, to mention them, I am thankful to Markus Lysne, Viktor Christiansson, Nikolaj Bittner, Aaram Kim, Changming Yue, Jiyu Chen, Francesco Petocchi, Sujay Ray, Jiawei Yan, Ruslan Mushkaev, Jiajun Li and Michael Schüler. I would also like to mention Pawel Bednarek, without whom the supercomputer I have used to launch calculations would be dysfunctional.

Je tiens maintenant à remercier mes amis, sans lesquels je n'aurais pas eu le support psychologique ni émotionnel pour aboutir avec confiance et sérénité cette période charnière de ma vie. Je désire en particulier remercier mes fidèles compagnons de ski Sergio Ruiz, Carlos Sanz Garcìa, Xavier Martinez et Matthieu Bogen. Je remercie également mes amis Alice Luisoni, Fatima Abdi, Marcin Kuczynski, Geoffroy Aubry, Enrico Fenoaltea, David Santos-Cottin, Aurélien Walter, Antoine Demont, Mathias Blaise, Charlotte Astaes et Lukas Schertel. Mes amis très précieux du Québec, qui m'ont beaucoup manqué, m'ont également assisté comme ils le pouvaient durant ce parcours. Je pense à Maxime Charlebois, Simon Verret et Karl Thibault avec lesquels les discussions sophistiquées m'ont beaucoup aidé à me ressourcer mentalement. Je pense aussi à mes irremplaçables amis avec lesquels je chérie parmi les meilleurs souvenirs, Etienne Auger, Sabine St-Jean, Laurent Bergeron, Camille Chartrand, Nathaniel Brochu et Simon-Gabriel Beauvais. Ceci n'est bien-sûr pas une liste exhaus-

tive des personnes ayant eu un grand impact sur moi, car elle serait bien trop longue.

Je clos les remerciements par les personnes les plus importantes dans ma vie; ma famille. Je remercie mes parents Chantal et Yves, les personnes qui m'ont incarné les valeurs m'ayant permis d'accomplir beaucoup dans la vie. Vous avez investi beaucoup de votre temps et énergie dans mon éducation afin de parfaire mon potentiel. Je remercie ma grand-maman Thérèse et mon grand-papa Gaétan aux côtés desquels j'ai eu la chance de grandir, ayant été très présents pour moi. Je remercie finalement mes petites soeurs Audrey, Mélanie et Marie-Eve, ainsi que mon petit frère Antoine, auxquels je pense souvent.

CONTENTS

I PREAMBLE 1
1 INTRODUCTION 3
- 1.1 Ultrafast time-resolved pump-probe techniques . . . 4
- 1.2 Light-induced nonthermal phenomena . . . 6

II MATHEMATICAL FRAMEWORK 9
2 NONEQUILIBRIUM QUANTUM MANY-BODY PHYSICS 11
- 2.1 Fundamental notions . . . 11
  - 2.1.1 Quantum statistics . . . 11
  - 2.1.2 Thermal statistics . . . 13
- 2.2 The contour idea . . . 13
  - 2.2.1 Langreth rules . . . 15
- 2.3 Correlation functions and equations of motion . . . 17
  - 2.3.1 One-particle Green's function . . . 18
  - 2.3.2 Two-particle Green's function . . . 20
  - 2.3.3 Equations of motion . . . 22
  - 2.3.4 Spectral functions . . . 24
- 2.4 Hedin's equations . . . 28
- 2.5 Fermionic path integrals in a nutshell . . . 31
  - 2.5.1 Grassmann algebra . . . 32
  - 2.5.2 Coherent states . . . 32
  - 2.5.3 Path integral of hybridized quantum systems . . . 34

III THEORETICAL METHODS 39
3 QUANTUM IMPURITY PROBLEM 41
- 3.1 Pathway to the Hubbard Model . . . 41
- 3.2 Anderson impurity model . . . 45
  - 3.2.1 DMFT . . . 46

4 RPA-TYPE POST-PROCESSING DMFT 59
- 4.1 General formalism . . . 59
- 4.2 Nonequilibrium calculation of the single-ladder vertex corrections 69

5 TPSC AND VARIANTS 71
- 5.1 General ideas . . . 71
- 5.2 TPSC . . . 72
  - 5.2.1 Spin and charge channels . . . 72
  - 5.2.2 TPSC ansatz . . . 77
  - 5.2.3 Equations of motion of the Hubbard model . . . 82
  - 5.2.4 Second-level approximation . . . 86
  - 5.2.5 Equations of motion of the multi-orbital Hubbard model 89
  - 5.2.6 Second-level approximation . . . 92
  - 5.2.7 Equations of motion of the Kanamori-Hubbard model . . 93
  - 5.2.8 Second-level approximation . . . 96
  - 5.2.9 DMFT+TPSC . . . 96

5.2.10 Summary of the different schemes 99
IV RESULTS 101
6 EQUILIBRIUM RESULTS 103
6.1 Post-processing DMFT 103
6.1.1 Phase diagram and renormalized couplings 104
6.1.2 Optical conductivity and $\mathbf{q} = \mathbf{0}$ spin susceptibility 107
6.1.3 Comparison to DMRG 117
6.2 TPSC and variants 119
6.2.1 TPSC and TPSC+GG 120
6.2.2 DMFT+TPSC 139
7 NONEQUILIBRIUM RESULTS 147
7.1 Post-processing DMFT 147
7.1.1 Single-particle spectrum 151
7.1.2 Optical conductivity 151
7.2 TPSC and variants 160
7.2.1 TPSC and TPSC+GG 160
7.2.2 DMFT+TPSC 174
V CONCLUSION 183
8 CONCLUSION 185
VI APPENDICE 189
A LANGRETH RULES 191
B GAUSSIAN INTEGRALS 193
C WEAK-COUPLING SELF-ENERGY EXPANSION 195
D CAUCHY INTEGRAL 199
E OPTICAL CONDUCTIVITY 201
F RECIPROCAL-SPACE LADDER-TYPE VERTEX CORRECTIONS 203
F.1 Odd number of ladders $\chi^{(\text{odd})}$ 204
F.2 Even number of ladders $\chi^{(\text{even})}$ 206
F.3 AL diagram 207
G KELDYSH DECOMPOSITION OF THE π-TON VERTEX CORRECTION 209
H NONEQUILIBRIUM APPROXIMATION TO THE TPSC IRREDUCIBLE VERTICES 215
I TEMPERATURE OF A THERMALIZED STATE 217
BIBLIOGRAPHY 219

LIST OF FIGURES

Figure 1.1 Left panel: sketch of the pump-probe X-ray techniques that can capture the photoinduced dynamics of the microscopic degrees of freedom. An incident pump pulse excites the array of atoms and after a certain delay Δt, an X-ray probe pulse is emitted to read out the underlying nonequilibrium physics by monitoring the changes in the Bragg peaks. Taken from Ref. [27]. Right panel: Sketch of the principles of an optical pump-probe set-up, wherein an incident tera-Hertz pump pulse with frequency ω_1 excites the sample surface, and then a probe pulse with frequency $\omega_2 \ll \omega_1$ measures the pump-induced changes that occurred after a certain time delay Δt. Taken from Ref. [10]. 5

Figure 1.2 Nonthermal pathways in the system's phase space by considering the tdGL formalism. The coordinate can represent some electronic order parameter or the lattice displacement. The subfigures are individually explained in the text. The figure is taken from Ref. [131]. 6

Figure 1.3 Three-temperature model applied in the context of ultrafast spin dynamics in ferromagnetic Nickel [16]. 8

Figure 1.4 Light-induced transient superconductivity in K_3C_{60} [26]. The resistivity transiently goes to zero upon driving the system with mid-infrared laser pulses. 8

Figure 1.5 Coherent lock-in of the phonon modes with the transient orbital-selective band energy renormalization near the Fermi level [47]. 8

Figure 2.1 Kadanoff-Baym contour with forward branch $\mathcal{C}_1$, backward branch $\mathcal{C}_2$, and the imaginary-time branch $\mathcal{C}_3$. The direction of the contour basically follows the ordering of the operators in Eq. (2.12) from right to left. 15

Figure 2.2 Diagrammatic representation of the one-particle Green's function (2.44). The thin line denotes the noninteracting one-particle Green's function $\mathcal{G}^0$. 21

Figure 2.3 Diagrammatic representation of the two-particle Green's function (2.46) in the particle-hole channel. The green box denotes χ and the pink box Γ. The bold arrows, representing interacting one-particle Green's functions, obey the Dyson's equation depicted by Fig. 2.2. 21

Figure 2.4 Diagrammatic representation of the self-energy (2.59). The wiggled line denotes a boson exchanged and the boxes have been defined in Fig. 2.3. 24

Figure 2.5 Diagrammatic representation of the $\mathcal{G}$-skeletonic two-particle irreducible vertex Γ. The last two terms make up $\tilde{\Gamma}$, denoted as a blue hatched box. 28

Figure 2.6 Diagrammatic representation of the Bethe-Salpeter equation (2.46) into which Γ has been substituted by Eq. (2.75). 29

Figure 2.7 Digrammatic representation of the self-energy (2.77) whose Γ has been split apart according to Eq. (2.75). The third term generates the class of *rainbow* diagrams by iterating through χ (see Eq. (2.77)). 29

Figure 2.8 Fully irreducible vertex Λ (orange box) illustrated in terms of diagrams. The blue box is defined in Fig. 2.75. 30

Figure 2.9 Diagrammatic representation of the screened potential (2.79). 30

Figure 2.10 $\mathcal{G}$- and W-skeletonic self-energy. 31

Figure 3.1 2nd-order self-energy Hartree diagram. The fermionic propagators represent the Weiss Green's functions $\mathcal{G}^0$. 50

Figure 3.2 2nd-order self-energy diagram 50

Figure 3.3 3rd-order diagram Σ_H^{3a} 51

Figure 3.4 3rd-order diagram Σ_H^{3b} 51

Figure 3.5 3rd-order diagram Σ_H^{3c} 51

Figure 3.6 3rd-order diagram Σ^{3a} 52

Figure 3.7 3rd-order diagram Σ^{3b} 52

Figure 3.8 3rd-order diagram Σ^{3c} 53

Figure 3.9 3rd-order diagram Σ^{3d} 53

Figure 3.10 3rd-order diagram Σ^{3e} 53

Figure 4.1 Diagrammatic representation of $\frac{\delta\Sigma}{\delta\mathcal{G}}$ when only keeping the first term of $\frac{\delta\mathcal{G}}{\delta\phi}$ (4.5). The first and last terms are those that will be retained in our approximation for $\frac{\delta\Sigma}{\delta\mathcal{G}}$. 62

Figure 4.2 General diagrammatic representation of susceptibilities (4.16). On the right-hand side, the first term is the particle-hole bubble and the second contains vertex corrections (χ_{corr}). 63

Figure 4.3 Diagrammatic representation of the terms of $\blacktriangleright^{(\text{even})}$ containing solely an even number of vertical ladders (pink boxes); the violet box is comprised of two pink boxes connected together by two Green's functions. The first term is the one that will be inputted in Eq. (4.17) to compute the single-ladder vertex corrections. 64

Figure 4.4 Diagrammatic representation of the terms of $\blacktriangleright^{(\text{odd})}$ containing solely an odd number of vertical ladders (pink box); again the violet box is comprised of two pink boxes connected together by two Green's functions. The first term is the one that will be retained to describe $\blacktriangleright$ in Eq. (4.17) to get the double-ladder vertex corrections. Note that in the case of the Hubbard model, for instantaneous interaction, $\bar{7} = \bar{3}$ and $\bar{8} = \bar{4}$ for the pink box. 65

Figure 4.5 Illustration of the single-ladder vertex corrections to the susceptibilities. All diagrams sharing this topology are summed up in Eq. (4.22). To represent $\chi_{j_ij_i}$, the vertices A and B are both set equal to the velocity v_i, while for $\chi_{S_zS_z}$ they are set to the Pauli matrices $\frac{\tau_z}{2}$. 66
Figure 4.6 Illustration of the double-ladder vertex correction to the susceptibilities. Similarly to Fig. 4.5, the vertices A and B equal v_i for $\chi_{j_ij_i}$ and $\frac{\tau_z}{2}$ for $\chi_{S_zS_z}$. 67
Figure 4.7 Diagrammatic representation of the AL-type vertex corrections considered. Also here, the vertices A and B equal v_i for $\chi_{j_ij_i}$, and $\frac{\tau_z}{2}$ for $\chi_{S_zS_z}$. 68
Figure 4.8 Vertex function for the AL-type diagram (cf. Fig. 4.7). The pink boxes represent particle-hole ladders (Eq. (4.23)). . . 68
Figure 5.1 Flow chart describing the self-consistent determination of $D(z)$, χ^{sp} and Γ^{sp} (alternative method). The green slot is replaced by the equation (5.69) in the implementation. . . 88
Figure 5.2 Flow chart describing the self-consistent determination of χ^{ch} and Γ^{ch}. Again, the green slot is replaced by the equation (5.69) in the implementation. 88
Figure 5.3 Flow chart describing the self-consistent DMFT+TPSC procedure. The yellow slot is replaced by the equation (5.69) in the implementation. 98
Figure 5.4 Flow graph showing the connections between the two first levels of TPSC, namely the first- (blue boxes) and second-level (green boxes) approximations. The red line shows that second-level irreducible vertices could in theory be worked out from the second-level self-energy $\Sigma^{(1)}$. The α renormalization of the vertices introduced via Eq. (5.71) aims to *update* the irreducible vertices such as to make the two-level approximations consistent. 100
Figure 6.1 Magnetization for various interaction parameters for the half-filled nearest-neighbor Hubbard model in 1D. 105
Figure 6.2 Magnetization for various interaction parameters for the half-filled nearest-neighbor Hubbard model in 2D. 106
Figure 6.3 AFM phase boundary (red line) obtained with the IPT solver in the space of U and T at half-filling. The black line indicates the temperatures corresponding to the largest single-ladder vertex corrections. The green dots denote the temperatures at which the susceptibilities will be computed. 107
Figure 6.4 AFM phase boundary (red line) obtained with the IPT solver in the space of U and T at half-filling. The black line indicates the temperatures corresponding to the largest single-ladder vertex corrections. Like in 1D, the green dots denote the temperatures at which the susceptibilities will be computed. 108

Figure 6.5 1D longitudinal optical conductivity for $U = 1$ (first column), $U = 2$ (second column) and $U = 3$ (third column) obtained using DMFT+IPT and (for the ladder corrections) appropriately renormalized interactions. First row: bare response. Second row: bare response plus single-ladder vertex corrections. Third row: bare response plus single-ladder and double-ladder vertex corrections. Fourth row: bare response plus single-ladder and AL vertex corrections. The temperatures considered for the different interactions are shown in the legends. 109

Figure 6.6 1D magnetic susceptibility for $U = 1$ (first column), $U = 2$ (second column) and $U = 3$ (third column) obtained using DMFT+IPT and (for the ladder corrections) appropriately renormalized interactions. First row: bare response. Second row: bare response plus single-ladder vertex corrections. Third row: bare response plus single-ladder and double-ladder vertex corrections. Fourth row: bare response plus single-ladder and AL vertex corrections. The temperatures considered for the different interactions are shown in the legends. 110

Figure 6.7 Longitudinal optical conductivity (top panel) and spin-spin response (bottom panel) in the 2D single-band Hubbard model at half-filling for $U = 2$. Only the single-ladder vertex corrections are shown for three distinct temperatures, in addition to the bare response. The temperatures are pointed out by the green dots figuring along the vertical grey line in Fig. 6.4. Top panel: imaginary part of the current-current correlation function for $T = 0.286, 0.222, 0.182$. Lower panel: imaginary part of the spin-spin response for the same temperatures as for optical conductivity. 112

Figure 6.8 Real part of Eq. (6.1) as a function of energy ω. The energies at which the real part approaches 1 correspond to the peaks observed near $\omega \simeq 0$ and $\omega \in [0.4, 0.9]$ in Figs. 6.5 and 6.6. 113

Figure 6.9 Analysis of different contributions to the π-ton spectrum in 1D. The different shades of red show the momentum dependence of the single-ladder vertex spectrum. Light, intermediate and dark colored lines show the contributions from momentum tuples with $\Delta\mathbf{k} = |\tilde{\mathbf{k}} - \bar{\mathbf{k}}| = 0, \frac{\pi}{2}$, and π, respectively. The shades of green show the momentum dependence of Im$\chi_{\mathrm{sl},j_ij_i}$, whereas the different shades of blue show that of Im$\chi_{\mathrm{sl},s_zs_z}$ (vertex corrections only). 115

Figure 6.10 Longitudinal optical conductivities separated into the bubble (blue shades) and the π-ton (red shades) contributions in equilibrium for different temperatures and $U = 2$. (The $U = 1$ results show the same qualitative trend, although the temperature scales are lower.) The vertical dotted lines indicate the energies for which we compute the time evolution of the spectral weight. The black dotted line portrays the π-ton at $U = 2$ and $T = 0.08$ using bare IPT instead of bold IPT. 116
Figure 6.11 Longitudinal optical conductivity for $U = 1,2,3$ and $T = 0$ obtained using DMRG. 117
Figure 6.12 Magnetic susceptibility for $U = 1,2,3$ and $T = 0$ obtained using DMRG. 118
Figure 6.13 Bandwidth-normalized spin and charge irreducible vertices as a function of normalized bare interaction for the nearest-neighbor square (2D) and cubic (3D) lattices for TPSC (bold lines) and TPSC+GG (dotted lines). The *dimensionless* temperature is $T/W = 0.05$ and the spin-density per site is $n = 0.5$. 121
Figure 6.14 Static spin susceptibility of the 2D model at momentum $\mathbf{k} = (\pi,\pi)$ as a function of temperature for interactions $U = 1,2,3$ and 4. The filling per spin is $n = 0.5$. The data points for TPSC+GG at $U = 4$ are not shown since the solution becomes unstable at high temperature ($T \approx 0.3$). The red curve can be compared with Fig. 3 of Ref. [144]. The interactions appearing in the legend are normalized by the bandwidth W to facilitate the comparison across dimensions; they are thus made *dimensionless*. The y-axis is upper-bounded to avoid squashing the data. 122
Figure 6.15 ξ_{sp} as a function of $1/T$ for $U = 2$ in the 2D half-filled nearest-neighbor Hubbard model. The y-axis uses a logarithmic scale. The methods compared are “OG TPSC” (green circles, called TPSC in Refs. [89, 110]), TPSC+GG (orange diamonds), DMFT+TPSC (cyan crosses), DΓA (blue circles), DiagMC (black triangles), TRILEX (red circles) and PA (green triangles). The data calculated using TRILEX, DiagMC, OG TPSC, DΓA and PA were taken from Ref. [110]. The 3^{rd}-order IPT impurity solver is used for DMFT+TPSC (see Section 3.2.1.3). 123
Figure 6.16 Γ^{ch} (top panel) and Γ^{sp} (bottom panel) as a function of T/W for $U = \{1,2,3\}$ in the 2D half-filled nearest-neighbor Hubbard model. The values of the vertices are normalized by U for compactness reasons and were obtained using TPSC+GG. 124

Figure 6.17 Γ^{ch} (top panel) and Γ^{sp} (bottom panel) as a function of T/W for $U = \{1,2,3\}$ in the 2D half-filled nearest-neighbor Hubbard model. The values of the vertices are normalized by U and were obtained using TPSC. The black vertical lines correspond to those drawn in Fig. 6.14. 125

Figure 6.18 TPSC (bold lines) and TPSC+GG (dotted lines) double occupancy extracted from the local ansatz (5.54) as a function of bandwidth-normalized temperature for various U. The 2D half-filled nearest-neighbor Hubbard model was used. 126

Figure 6.19 Top panel: TPSC electronic spectral density of the 2D model for spin-density $n = 0.5$ and the Fermi surface momentum $\mathbf{k}_F = (0, \pi)$. The bare interaction is $U = 4$ and the inverse temperature $\beta = 5.88$ ($T = 0.17$). Bottom panel: TPSC Matsubara Green's function for $n = 0.4375$ for the 2D model and the Fermi surface momentum $\mathbf{k}_{\mathrm{F}} = (0, \pi)$. The bare interaction is $U = 4$ and the inverse temperature $\beta = 4$. These results can be compared with Fig. 9 in Ref. [152] (top panel) and the left panel of Fig. 1 in Ref. [145] (bottom panel). Since the calculations are implemented on the Kadanoff-Baym contour, spectral functions can be calculated directly by Fourier transformation, *i.e.* without analytical continuation. 127

Figure 6.20 The imaginary parts of the *lesser* component of the charge (top panels) and spin (bottom panels) susceptibilities, obtained using TPSC in 2D. The left (right) panels show the equilibrium spectra for $U = 1$ ($U = 3$). The inverse temperature is $\beta = 3$. The time window used for the Fourier transform is $\Delta t = 5$. 128

Figure 6.21 Idem to Fig. 6.20 for TPSC+GG. 129

Figure 6.22 The imaginary parts of the *lesser* component of the second-level self-energy (top panels) and Green's function (bottom panels), obtained using TPSC. The left (right) panels show the equilibrium spectra for $U = 1$ ($U = 3$). The inverse temperature is $\beta = 3$. The time window used for the Fourier transform is $\Delta t = 5$. 130

Figure 6.23 Idem to Fig. 6.22 making use of TPSC+GG. 131

Figure 6.24 Spectra difference of various quantities Q between $Q(n = 1)$ and $Q(n = 1.15)$ at $T = 0.33$ and $U = 3$ in the nearest-neighbor Hubbard model calculated within TPSC. The *lesser* component is shown. The charge susceptibility is shown in the top left panel, the spin susceptibility in the bottom left panel, the second-level TPSC in the top right panel and the single-particle Green's function $\mathcal{G}^{(1)}$ in the bottom right panel. The time window $\Delta t = 5$. 132

Figure 6.25 Spectra difference of various quantities Q between $Q(t'_{\text{hop}} = 0)$ and $Q(t'_{\text{hop}} = -0.275)$ at $T = 0.33$ and $U = 3$ in the Hubbard model calculated within TPSC. The *lesser* component is shown once again. The quantities are placed in the same way as in Fig. 6.24. The time window $\Delta t = 5$. . . 133
Figure 6.26 Imaginary part of the Matsubara self-energy at the antinode ($\mathbf{k} = (0, \pi)$) for various methods (listed out in the legend) at $T = 0.33$ ($\beta = 3$) and $U = 2$ in the half-filled Hubbard model. The first several Matsubara frequencies are shown. This figure can be compared with the "TPSC" – which corresponds to OG TPSC in this thesis – panel in Fig. 10 of Ref. [110]. 134
Figure 6.27 Imaginary part of the Matsubara self-energy at the antinode ($\mathbf{k} = (0, \pi)$) for various methods (listed out in the legend) at $T = 0.1$ ($\beta = 10$) and $U = 2$ in the half-filled Hubbard model. This figure can also be partly found in Fig. 10 of Ref. [110]. 135
Figure 6.28 Dynamical renormalization parameter of the irreducible vertices α (5.70) as a function of normalized temperature for different interactions. The results are for the 3D single-band half-filled nearest-neighbor Hubbard model. The vertical lines mark the downturn of Γ^{sp} in Fig. 6.32. . 136
Figure 6.29 Static spin susceptibility of the 3D model at momentum $\mathbf{k}_\pi = (\pi, \pi, \pi)$ as a function of normalized temperature for interactions $U = 2, 3, 4$ and 5 using both TPSC (bold lines) and TPSC+GG (dotted lines). The filling per spin is $n = 0.5$. The interactions strengths in the legend are normalized by the bandwidth W. The vertical lines are identical as in Fig. 6.28. 137
Figure 6.30 Left panels: *lesser* charge (top panel) and spin (bottom panel) susceptibilities. Right panels: second-level TPSC self-energy (top panel) and single-particle Green's function ($\mathcal{G}^{(1)}$) (5.66) spectra (bottom panel). The calculations were performed using TPSC+GG at half-filling for the cubic lattice at $T = 0.2$ and $U = 3$. The wedge of the irreducible Brillouin zone cuts along $k_z = \pi$; the path runs along within that plane. The time window employed for the Fourier transforms is $\Delta t = 5$. 137
Figure 6.31 Γ^{ch} (top panel) and Γ^{sp} (bottom panel) as a function of T/W for $U = \{2, 3, 4, 5\}$ in the 3D half-filled nearest-neighbor Hubbard model. The values of the vertices are normalized by U for presentation reasons and were obtained using TPSC+GG. 139
Figure 6.32 Γ^{ch} (top panel) and Γ^{sp} (bottom panel) as a function of T for $U = \{2, 3, 4, 5\}$ in the 3D half-filled nearest-neighbor Hubbard model. The values of the vertices are normalized by U and were obtained using TPSC. The vertical lines are the same as in Fig. 6.29. 140

Figure 6.33 Bandwidth-normalized spin and charge irreducible vertices as a function of normalized bare interaction for the nearest-neighbor square (2D) and cubic (3D) lattices within DMFT+TPSC. The normalized inverse temperature is $\beta = 0.3125$ and the spin-density per site is $n = 0.5$. 141

Figure 6.34 Γ^{ch} (top panel) and Γ^{sp} (bottom panel) as a function of T/W for $U = \{1,2,3,4\}$ and $U = \{2,3,4,5\}$ in the 2D and 3D half-filled nearest-neighbor Hubbard model, respectively. The values of the vertices are normalized by U and were obtained using DMFT+TPSC. At $U/W = 0.5$, due to numerical difficulties to converge the solution at low temperatures, only few points are included. The black (green) vertical lines pin down the temperatures where Γ^{sp} deviates from a linear behavior in 3D (2D). 142

Figure 6.35 Static spin susceptibility of the 2D (3D) model at momentum $\mathbf{k}_\pi = (\pi,\pi)$ ($\mathbf{k}_\pi = (\pi,\pi,\pi)$) and half-filling as a function of normalized temperature for interactions $U = \{1,2,3,4\}$ ($U = \{2,3,4,5\}$) for DMFT+TPSC. The black and green vertical lines bear the same meaning and values as in Fig. 6.34. 142

Figure 6.36 Double occupancies D^{imp} (5.99) and D^{TPSC} (5.104) as a function of normalized temperature for several interactions U/W in the 2D (top panel) and 3D (bottom panel) nearest-neighbor Hubbard model. The annotated percentages denote the largest absolute variation relative to D^{imp}. 143

Figure 6.37 Left panels: *lesser* charge (top panel) and spin (bottom panel) susceptibilities. Right panels: second-level TPSC self-energy (top panel) and single-particle Green's function spectra (bottom panel). The calculations were performed using DMFT+TPSC at half-filling for the square lattice model at $T = 0.33$ and $U = 3$. The time window employed for the Fourier transforms is $\Delta t = 5$. 144

Figure 7.1 Energies as a function of time for an interaction ramp from $U = 1.5$ to 2.0 and initial temperature $T = 0.05$. Upper panel: change in the kinetic energy $\bar{E}_{\text{k}}$. Middle panel: change in the potential energy $\bar{E}_{\text{p}}(t)$. Lower panel: change in the total energy $\bar{E}_{\text{tot}}$. The black curves show the results for bold IPT, which conserves energy after the ramp, and the red curves show the results for bare IPT. A time step $\mathrm{d}t = 0.015$ is used on the real axis and 1200 imaginary time points on the Matsubara axis to ensure the stability of the solution at longer times. The shaded area indicates the duration of the interaction ramp. 149

Figure 7.2 Energies as a function of time for an interaction ramp from $U = 1.5$ to 1.0 and initial temperature $T = 0.05$. The plot has the same layout as in Fig. 7.1 and the same discretization of the KB contour was employed. The U-ramp used in this case corresponds to the mirror reflexion along the x-axis of that of Fig. 7.1. 149

Figure 7.3 Sketch of the interaction ramps and quenches discussed in the present section. The green dots (blue dots) show the temperatures of the thermalized systems after the U-ramps (U-quenches), while the red line shows the DMFT+IPT AFM phase boundary taken from Ref. [119]. The black cross represents the initial state ($U = 1.5, T = 0.05$). 150

Figure 7.4 Illustration of the time-dependent single-particle spectral function during and after the up ramp. The inset shows the profile of the interaction ramp. The inverse temperature of the initial state is $\beta = 20$ and the Fourier window is $\Delta t = 16$. 152

Figure 7.5 Real-time snapshots of the bubble contribution to the optical conductivity (blue) and the RPA π-ton vertex corrections (red) during and after the up ramp. The ramp shape is shown in the inset plot and the grey lines indicate the measurement times. The (dotted-)dashed black line shows the (bubble) π-ton contribution in the initial equilibrium state. 153

Figure 7.6 Real-time snapshots of the bubble contribution to the optical conductivity (blue) and the RPA π-ton vertex corrections (red) during and after the down ramp. The ramp shapes are shown in the inset plot and it corresponds to a mirror reflexion of the up-ramp along the x-axis. The grey lines indicate the measurement times which are the same as in Fig. 7.5. The black lines are the same as in Fig. 7.5 (same initial equilibrium state). 154

Figure 7.7 Time-dependent change in the bubble (left column) and π-ton (right panel) contributions to $\omega \mathrm{Re}\sigma_{jj}(\mathbf{q} = \mathbf{0}, \omega, t)$ at $\omega = 0.35$ (blue), 1.0 (orange) and 3.9 (green). The two upper rows of panels show the results for the ramps: upper (lower) panel for the ramp up (down). Likewise, the two lower rows of panels show the results for the quenches. The horizontal grey lines indicate the values reached in the thermalized state after the ramp. For a better visualization of the change in conductivity, the values at $t = 0$ are subtracted. Just like for Fig. 7.5, a time window $\Delta t = 7$ was used at all times t. 155

Figure 7.8 Spectral decompositions of the time traces (see Fig. 7.7) of the bubble contribution $\omega\mathrm{Re}\sigma_{jj}(\mathbf{q}=\mathbf{0},\omega,t)$ at the indicated energies. The plotted lines show the norms of the Fourier transformations, after subtracting a background proportional to the ramp shape. In the case of the quenches, the mean was subtracted. Dashed (solid) lines are for interaction ramps (quenches). 157

Figure 7.9 In the main plot, the grey curve depicts the Fermi distribution function for the thermalized state after the quench from $U = 1.5$ to $U = 2$ at $T = 0.05$. The other curves illustrate the non-equilibrium distributions $n_{\mathbf{k}}(t,\omega)$ at $\mathbf{k} = \frac{\pi}{2}$ (Fermi level) and for $t = \{10,20,30\}$. An exponential function was used to extrapolate the tails of both $\mathcal{A}^{<}(t,t+\Delta t')$ and $\mathcal{A}^{R}(t,t+\Delta t')$. A time window $\Delta t' = 4000$ was used in the Fourier transformation. In the inset plot, the time traces of the effective temperatures Eq. (7.5) of the $\mathbf{k}$-dependent distribution functions are plotted. 158

Figure 7.10 In the main plot, the time evolution of the lesser component of the dressed Green's function for the Fermi momentum $\mathbf{k} = \frac{\pi}{2}$ is plotted for the same quench. The inset shows the difference between the time traces of the quenched system and the thermalized system ($T = 0.085$ and $U = 2.0$). 159

Figure 7.11 Dynamics after interaction ramps from $U = 1$ to $U = 3$ using TPSC+GG. The dotted and dash-dotted lines show the ramp profiles in arbitrary units. The quantities plotted in light (dark) colors correspond to the slow (fast) ramp. Top panel: charge irreducible vertex $\Gamma^{\mathrm{ch}}(t)$. Middle panel: spin irreducible vertex $\Gamma^{\mathrm{sp}}(t)$. Bottom panel: Double occupancy $D(t)$. The arrows on the right indicate the thermalized values for the slow and fast ramps calculated from E_{tot} after the ramp. The ramp shapes are described by Eq. (7.3). 161

Figure 7.12 Top (Bottom) panels: Difference spectra of the lesser component of the charge (spin) susceptibility after the interaction ramp shown in the inset, using TPSC+GG. The inset black triangle illustrates the path in reciprocal space along which the spectra are displayed. The times t_i and t_f used in the calculation of the difference spectra are annotated in each panel. The time window used in the Fourier transformation is $\Delta t = 5$. Each row of panels uses the same colorscale. 162

Figure 7.13 Difference spectra analogous to Fig. 7.12, but calculated with TPSC. The corresponding initial and final times t_i and t_f are indicated in each panel. Top (Bottom) panels: The spectral difference of the *lesser* charge (spin) susceptibility after the interaction ramp shown in the inset (the vertical bars indicate the times t_i and t_f). The inset black triangle illustrates the path in reciprocal space along which the spectra are displayed, with the green coordinates corresponding to the initial **k**-point. The time window used for the Fourier transformation is $\Delta t = 5$. Each row of panels uses the same colorscale. 163

Figure 7.14 Results analogous to Fig. 7.11 using TPSC. The quantities plotted in light colors are associated with the smooth interaction ramp and those in dark colors with the sharp interaction ramp. The dotted lines represent the interaction ramps in arbitrary units. Top panel: charge irreducible vertex Γ^{ch}. Second panel: spin irreducible vertex Γ^{sp}. Third panel: Double occupancy $D(t)$. Bottom panel: α parameter enforcing the sum-rule Eq. (5.71). The thermal values for the two different ramps are almost indistinguishable. 164

Figure 7.15 Top (Bottom) panels: Difference spectra of the TPSC+GG lesser component of the charge (spin) susceptibility after the interaction ramp from $U = 1$ to $U = 3$ shown in the inset. The time window employed in the Fourier transformation is $\Delta t = 5$. Each row of panels uses the same colorscale. 165

Figure 7.16 Top (Bottom) panels: Difference spectra of the TPSC lesser component of the charge (spin) susceptibility after the interaction ramp from $U = 1$ to $U = 3$ shown in the inset. The time window employed in the Fourier transformation is $\Delta t = 5$. Each row of panels uses the same colorscale. 166

Figure 7.17 The imaginary parts of the *lesser* component of the spin (left panels) and charge (right panels) susceptibilities for momentum $\mathbf{k}_\pi$. The top (bottom) panels display the evolution of the susceptibilities upon ramping the interaction up (down). The initial temperature is $T = 0.33$. The insets show the profiles of the interaction ramps with the vertical bars representing the times for which the spectra are calculated. The time window for the Fourier transformation is $\Delta t = 5$. 167

Figure 7.18 Effective inverse temperatures $\beta_{\mathbf{k}}(t,\omega)$ for the Fermi momenta $\mathbf{k}=(0,\pi)$ (left panels) and $\mathbf{k}=(\frac{\pi}{2},\frac{\pi}{2})$ (see Eq. (7.6)). The gray curve plots the initial $\beta=3$, the blue curve $\beta_{\mathbf{k}}(t=0.2,\omega)$, the red curve $\beta_{\mathbf{k}}(t=1,\omega)$, the green curve $\beta_{\mathbf{k}}(t=2,\omega)$, and the black curve the thermalized value $\beta_{\text{th}}=2.35$. The top panels show the effective inverse temperature extracted from χ^{ch}, the middle panels for χ^{sp} and the bottom panels for $\mathcal{G}$. 168

Figure 7.19 Local TPSC (solid lines) and TPSC+GG (dashed lines) quantities in a dimensional ramp from a square lattice to a cubic translating into a ramp from $t_z^{\text{hop}}=0$ to $t_z^{\text{hop}}=1$ in the dispersion relation (6.3). The initial temperature is $T=0.2$ and the constant interaction is $U=2.5$. The charge irreducible vertex (top panel), spin irreducible vertex (second panel from top), D^{imp} (third panel from top) and α (bottom panel) are plotted for a time window of $\Delta t=7$. . 170

Figure 7.20 Evolution of the local electronic density of states when passing from a 2D square lattice to a 3D cubic lattice at half-filling. The equation describing this evolution is Eq. (6.3), with t_z^{hop} the perpendicular lattice hopping being changed. 171

Figure 7.21 The imaginary parts of the *lesser* component of the spin (top panel) and charge (bottom panel) susceptibilities for momentum $\mathbf{k}_\pi$ using TPSC. The initial temperature is $T=0.2$ and interaction $U=2.5$. The inset shows the profile of the perpendicular hopping ramps t_z^{hop} with the vertical bars representing the times at which the spectra are calculated. The time window for the Fourier transformation is $\Delta t=2.5$. 172

Figure 7.22 Top (Bottom) panels: Difference spectra of the lesser component of the charge (spin) susceptibility after the interaction ramp shown in the inset. The inset black triangle illustrates the path in reciprocal space along which the spectra are displayed, within the plane cut $k_z=\pi$. The times t_i and t_f used in the calculation of the difference spectra are annotated in each panel. The time window used in the Fourier transformation is $\Delta t=2.5$. Each row of panels uses the same colorscale. The method used here is TPSC. 173

Figure 7.23 Top (Bottom) panels: Difference spectra of the TPSC+GG lesser component of the charge (spin) susceptibility after the interaction ramp from $U=4$ to $U=2$ shown in the inset. The time window employed in the Fourier transformation is $\Delta t=5$. The 3D cubic lattice model is used and the initial temperature is $T=0.33$. Each row of panels uses the same colorscale. 174

Figure 7.24 Lattice-defined double occupancies calculated from Eq. (7.7) for lattice IPT, DMFT+IPT, OG TPSC, DMFT+TPSC and TPSC+GG. The interaction ramp travels from $U = 0$ to $U = 1$ (top panel) and from $U = 1$ to $U = 2$ (bottom panel) at initial inverse temperature $\beta = 5$. The grey shading indicates the time window over which the interaction changes. The model used is the 2D nearest-neighbor single-band Hubbard model (3.9). 176

Figure 7.25 Double occupancies calculated using the impurity quantities (5.99) in the case of DMFT+TPSC. In the case of TPSC, the double occupancy taken from Eq. (5.54) is shown. Nothing changes for lattice IPT, lattice $\Sigma^{(2)}$ and TPSC+GG. The same model and parameters as in Fig. 7.24 are employed and the top panel illustrates the ramp $U = 0 \to 1$ and the bottom panel shows $U = 1 \to 2$. Once more, the grey shading indicates the time range over which U changes. 177

Figure 7.26 Local DMFT+TPSC (dashed lines) and TPSC+GG (solid lines) quantities in the 2D single-band nearest-neighbor Hubbard model for the ramp $U = 1$ to $U = 3$ at initial temperature $T = 0.33$. The charge irreducible vertex (top panel), spin irreducible vertex (second panel from top), D^{imp} (third panel from top) and D^{TPSC} (bottom panel) are plotted for a time window of $\Delta t = 8$. 178

Figure 7.27 Top (Bottom) panels: Difference spectra of the TPSC lesser component of the charge (spin) susceptibility after the interaction ramp from $U = 1$ to $U = 3$ shown in the inset. The initial temperature is $T = 0.33$. The time window employed in the Fourier transformation is $\Delta t = 5$. Each row of panels uses the same colorscale. 179

Figure 7.28 Local DMFT+TPSC quantities in the dimensional ramp from $t_z^{\text{hop}} = 0$ to $t_z^{\text{hop}} = 1$ in the single-band nearest-neighbor Hubbard model for $U = 2.5$ at initial temperature $T = 0.2$. The charge irreducible vertex (top panel), spin irreducible vertex (second panel from top), D^{imp} (third panel from top) and D^{TPSC} (bottom panel) are plotted for a time window of $\Delta t = 8$. 180

Figure 7.29 Top (Bottom) panels: Difference spectra of the DMFT+TPSC lesser component of the charge (spin) susceptibility after the perpendicular lattice hopping ramp from $t_z^{\text{hop}} = 0$ to $t_z^{\text{hop}} = 1$ shown in the inset. The time window employed in the Fourier transformation is $\Delta t = 2.5$. Each row of panels uses the same colorscale. 181

Figure G.1 Kadanoff-Baym contour for $\chi^{>}_{\text{sl}}$ with $\bar{z} \succ \bar{z}'$, $\bar{z} \in \mathcal{C}_1$ and $\bar{z}' \in \mathcal{C}_1$. 209

Figure G.2 Kadanoff-Baym contour for $\chi^{>}_{\text{sl}}$ with $\bar{z} \succ \bar{z}'$, $\bar{z} \in \mathcal{C}_2$ and $\bar{z}' \in \mathcal{C}_2$. 211

Figure I.1 Total energy calculated in the 2D nearest-neighbor Hubbard model with TPSC+GG at $U = 3$ as a function of inverse temperature. 217
Figure I.2 Time-dependent energies calculated in the 2D nearest-neighbor Hubbard model with TPSC+GG for the up-ramp used in Fig. 7.15. Top panel: kinetic energy calculated from Eq. 7.1. Middle panel: potential energy calculated from Eq. 7.2. Bottom panel: Total energy calculated from the addition of $E_{\mathrm{p}} + E_{\mathrm{k}}$. 218

LIST OF TABLES

Table 2.1 Keldysh components of two-time contour-defined functions. A similar table is presented in Ref. [114]. 16

Table 5.1 Main characteristics of the methods at the second-level approximation. Checkmarks (✓) mean that a method is endowed with the characteristic, while the x-marks (X) mean the opposite. 100

ACRONYMES

AFM	Antiferromagnetic
AIM	Anderson Impurity Model
ARPES	Angle-resolved photoemission spectroscopy
CDMFT	Cellular Dynamical Mean Field Theory
CTQMC	Continuous-time quantum Monte Carlo
DFT	Density Functional Theory
DiagMC	Diagrammatic Monte Carlo method
DMFT	Dynamical Mean Field Theory
DMRG	Density Matrix Renormalization Group
FLEX	Self-consistent fluctuation exchange approximation
GL	Ginzburg-Landau
IPT	Iterated Perturbation Theory
KB	Kadanoff-Baym
KMS	Kubo-Martin-Schwinger
NCA	Noncrossing Approximation
PA	Parquet Approximation
PM	Paramagnetic
RPA	Random Phase Approximation
tdDFT	time-dependent Density Functional Theory
tdGL	time-dependent Ginzburg-Landau Theory
TPSC	Two-Particle Self-Consistent approach
trARPES	time- and angle-resolved photoemission spectroscopy
trXR	time-resolved X-ray
trXRD	time-resolved X-ray diffraction

Part I

PREAMBLE

A short introduction about various physical phenomena hinging on nonlocal electronic correlations is given. It will be discussed how nonlocal correlations can arise, setting out several experimental examples.

1

INTRODUCTION

Complex quantum materials consist of systems characterized by competing and correlated degrees of freedom whose interplay can give rise to symmetry-broken states. This competition involves spin, orbital, charge and lattice degrees of freedom relevant at comparable energy scales [79]. One way to separate them apart is via fine-tuned laser pulse excitation of correlated systems, which can reveal hidden states of distinct nature, in particular in strongly-correlated systems [159]. Moreover, dimensionality is an important aspect when it comes to describing the phases of matter. In low-dimensional correlated systems, close to phase instabilities and crossovers, nonlocal correlations become unavoidable to properly capture the underlying phase ordering mechanisms [66, 99, 103, 119, 157]. Up to hundreds of femtoseconds[1] after an impulsive excitation, the order parameter of a transient dynamical phase transition exhibits fluctuations with distinct nonthermal criticality [84, 132] and the electronic band structure can be strongly renormalized [14, 15, 20]. To access nonlocal correlations, single- and two-particle correlation functions need to be calculated consistently, and this is challenging for several reasons. There is a lack of methods out of equilibrium that include both local and nonlocal correlations while treating various degrees of freedom. Dynamical Mean Field Theory (DMFT) solely captures local correlations [6], GW+DMFT only charge fluctuations [8, 49], the phenomenological time-dependent Ginzburg-Landau theory (tdGL) only considers low-order microscopic electronic fluctuations [23] and time-dependent Density Functional Theory (tdDFT) doesn't capture inelastic scattering processes which are relevant for thermalization at long times [108].

Over the last three decades, tremendous advancements have been realized in the field of ultrafast quantum material science [131], notably in the development of pump-probe time-resolved X-ray (trXR) techniques [27] and femtosecond time- and angle-resolved photoemission spectroscopy (trARPES) [10]. In Section 1.1, the trXR techniques, which enable to probe the structural, electronic and magnetic degrees of freedom, as well as trARPES, which captures the band energy dynamics with orbital, space, and momentum resolution, will both be introduced in further details. Combinations of ultrafast time-resolved pump-probed techniques have been successfully used to disentangle the interplay of various interactions, such as the cooperative interplay between electron-electron and electron-phonon interactions in iron selenide and related pnictides [47]. Various experimental achievements making use of sophisticated ultrafast light-mediated pump-probe techniques are presented in Section 1.2 to introduce genuine nonthermal phenomena and concepts such as prethermalization [19, 92, 136], order parameter melting and revival [38, 50, 111, 157], photoinduced

Phonons are quasiparticles that represent quantized vibrations of the crystal lattice.

---

[1] Typically, in ultrafast pump-probe experiments, the photoinduced perturbations are probed from several hundreds of femtoseconds (10^{-15} second, denoted fs) to several nanoseconds (10^{-9} second, denoted ns) after the light pulses have *pumped* the system.

phase transitions [26, 84, 97, 157, 158] and degree-of-freedom-dependent relaxation timescales [16, 84, 98, 132].

Nonequilibrium TPSC and its variants are introduced in Chapter 5.

On the theoretical side, the design of reliable and computationally effective numerical methods is crucial to simulate nonthermal driven states up to experimentally relevant times of the order of picoseconds (10^{-12} second, denoted ps). Such methods would consequently allow one to study accurately on a theoretical basis the collapse and revival of nonthermal ordered phases triggered and controlled via impulsive excitations. With these enhanced methods, one could incidentally delve into more fundamental questions such as the role of competing long- and short-range correlations in hidden states and metastable states. One could also examine the role of order parameter fluctuations in nonthermal phase transitions beyond tdGL. Hence, there is a need to seek for nonequilibrium numerical many-body quantum methods treating nonlocal correlations that are computationally tractable and that do not trade off their predictive power for their *simplicity*. One such method, which combines diagrammatic techniques and DMFT, the so-called RPA-type post-processing DMFT method [119, 120], introduced in Chapter 4, has been used to calculate the growth of nonlocal particle-hole bound states emerging in the vicinity of a magnetic phase transition [66, 151], coined π-tons. Another method, which has recently been extended to nonequilibrium framework [121], is the so-called Two-Particle Self-Consistent approach (TPSC) [152]. TPSC correctly reproduces the pseudogap in cuprates [145] and the growth of antiferromagnetic (AFM) correlations approaching the renormalized classical regime [152]. It can also deal with superconducting phases in both the repulsive [77] and attractive [1] Hubbard models, as well as with two-particle vertex corrections [18], electronic screening [32] and multi-orbital systems [155, 156]. It has been used in conjunction with Density Functional Theory (DFT) at equilibrium to renormalize the bands of iron pnictides and chalcogenides [20]. The main caveat of TPSC is that is doesn't correctly capture strong local fluctuations and the original theory precludes one to study correlations deep in the renormalized classical regime. To correctly account for local fluctuations while at the same time account for the nonlocal correlations, a self-consistent combination of DMFT and TPSC is elaborated [122] in this thesis to tackle Hubbard-like models in the context of dimensional ramps of the unit-cell and interaction ramps, at various electron fillings (see Section 5.2.9).

1.1 ULTRAFAST TIME-RESOLVED PUMP-PROBE TECHNIQUES

Pump-probe spectroscopy figures as a mainspring for studying ultrafast dynamics of collective modes, order parameters and energy transfer processes in correlated electronic lattice systems. In this section, two salient ultrafast pump-probe experimental techniques will be presented, namely trARPES [10] and trXR [27]. Of course, since this is by no means an exhaustive review of all the ultrafast techniques utilizing the light-matter coupling, techniques like transient optical spectroscopy, ultrafast electron diffraction [157], and time-resolved scanning probes [39] will not be covered. Moreover, many ramifications of the methods that will be touched on won't even be skimmed over; the interested reader can refer to, *e.g.*, Ref. [27] for more details on trXR, to Ref. [10] for more details on trARPES, and to Ref. [131] for a broader overview of the state-of-the-art ultrafast light-mediated techniques.

Resolving temporally phenomena at the fundamental timescales can help unlock the manipulation of microscopic couplings [14, 28, 86, 87] and engineering of the energy band structure near the Fermi level [93, 153]. In Fig. 1.1, in the left panel, a sketch illustrating the basic principles of trXR is shown. trXR encompasses the techniques making use of X-ray diffraction, X-ray absorption spectroscopy and resonant X-ray diffraction. X-ray diffraction uses the constructive and destructive scatterings of X-rays by periodically-ordered atoms arranged in a crystal. trXR diffraction (trXRD) and absorption techniques can thereby deliver the atomic displacements in real-space with a sub-picometer resolution and a time resolution of ~ 10 fs [27]. The main asset of trXRD and electron diffraction is that it can track in time the displacement of the atomic cores in a photoexcited lattice. By carefully choosing the X-ray photon energy of the probe – in the soft or hard regimes – such that it is tuned to be in resonance with the atomic transitions, the magnetic moments of atoms and bond lengths can be transiently determined. The pump pulse produced in trXRD is typically photons in the near-infrared regime so as to resonantly produce large-amplitude lattice oscillations (of several picometers) that lead to nonlinear phonon couplings and disentangle competing orders. Notably, trXR scattering techniques have been used to study ultrafast ferroelectric switching [51], orbital and charge orders in photo-irradiated magnetite (Fe_3O_4) [115], charge density waves in materials with strong electron-phonon coupling [84], and light-induced superconductivity in the $YBa_2Cu_3O_{6.5}$ cuprates [86], to name but a few.

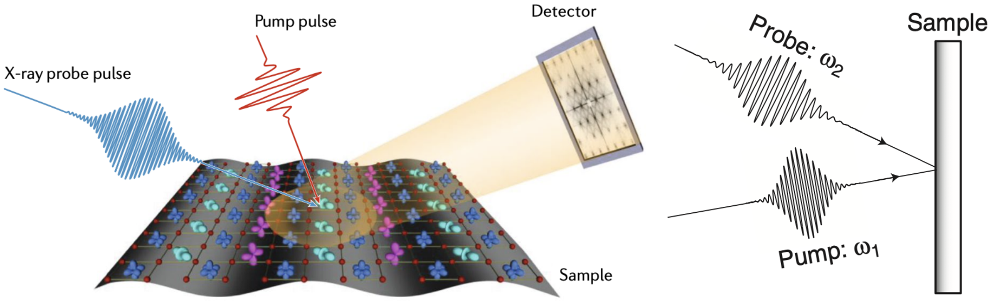

Figure 1.1: Left panel: sketch of the pump-probe X-ray techniques that can capture the photoinduced dynamics of the microscopic degrees of freedom. An incident pump pulse excites the array of atoms and after a certain delay Δt, an X-ray probe pulse is emitted to read out the underlying nonequilibrium physics by monitoring the changes in the Bragg peaks. Taken from Ref. [27]. Right panel: Sketch of the principles of an optical pump-probe set-up, wherein an incident tera-Hertz pump pulse with frequency ω_1 excites the sample surface, and then a probe pulse with frequency $\omega_2 \ll \omega_1$ measures the pump-induced changes that occurred after a certain time delay Δt. Taken from Ref. [10].

In Fig. 1.1, in the right-hand side panel, a dumbed down sketch of trARPES is shown. It shows a pump pulse, typically emitted from a free electron laser in the tera-Hertz regime, that hits the surface of a sample to be measured. Thereafter, a second wider pulse with frequency ω_2 probes the pump-induced changes, after a pump-probe delay Δt. The temporal evolution can be tracked by a successive emission of probe pulses. The pump/probe intensity ratio is usually larger than 20 so as to reduce the self-induced nonlinearities of the probe beam [10]. The changes in the probe's electric field (amplitude and phase) through reflectivity, transmission or polarization measurements can unveil different informations about the transient dynamics generated. trARPES allows one to access the changes in far-infrared optical conductivity by probing directly the (averaged) electronic structure over the Fermi surface. If the timescale over which the photoinduced dynamics occur is larger than the pump pulse duration, than most of the transient electronic energy transfer mechanisms can be captured.

1.2 LIGHT-INDUCED NONTHERMAL PHENOMENA

A selected amount of key experimental results in the field of ultrafast light-induced physics in quantum correlated systems will be flashed out and explained in a comprehensive manner. Prior to doing so, it will be argued that the light-induced nonequilibrium phenomena do not stem exclusively from the melting of thermal states by laser-heating. Due to the complex intertwining of a macroscopic number of quantum degrees of freedom resulting in competing or cooperating ordering mechanisms, nonthermal pathways can lead to the transient physics observed in experiments that share no equilibrium counterpart. The nonthermal effects can be partly attributed to the transient modification of the free energy landscape in the phase space of the interacting system. At equilibrium, the free energy potential describes phenomenologically, in the Ginzburg-Landau (GL) picture, the thermal and quantum fluctuations of the phase ordering parameter. To get the idea of nonthermal transient physics across, the GL free energy formalism will be employed in nonequilibrium settings to intuitively shed light on what hidden quantum states are.

In trARPES, the "coordinate" axis in Fig. 1.2 would be the electronic order parameter while for trXR it would be the lattice displacement.

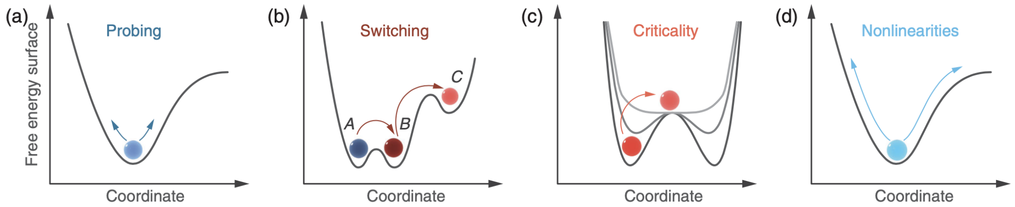

Figure 1.2: Nonthermal pathways in the system's phase space by considering the tdGL formalism. The coordinate can represent some electronic order parameter or the lattice displacement. The subfigures are individually explained in the text. The figure is taken from Ref. [131].

In Fig. 1.2 are shown four possible nonthermal pathways in the GL free energy landscape triggered by laser pulses, be it through trARPES or trXR techniques. The inset **(a)** of Fig. 1.2 shows the scenario where the system's order parameter ground state is located in a minimum and the photoinduced dynamics excite higher-energy collective modes inducing order parameter fluctuations that probe the synergy of the microscopic couplings. In this case, the nonthermal fluctuations in the GL free energy landscape "probe" the collective modes and transient coherent excitations. Next, in **(b)**, the possibility that the ground state of the system travels across hidden local minima in the free energy potential after the laser pulse is illustrated. Depending on the fluence of the laser pulse, the initial equilibrium state denoted by A can leap over to the nearest degenerate local minimum B, and if the laser pulse fluency, duration and frequency are tuned appropriately, the system's ground state can transiently move up to C and be *trapped* in this prethermal or metastable state. In **(c)** is shown the case where the photons transiently modify the critical behavior in the vicinity where a thermal phase transition can occur. Initially, the system lies in a local minimum ensuing a spontaneous quantum phase transition; the system's order parameter has been spontaneously selected through a second-order phase transition, and this could represent a transition from a metallic state to a superconducting one. Through the course of the application of the laser pulse, the GL free energy can be changed such that the thermal ordered state melts, *i.e.* a nonthermal phase transition transiently occurs. Nonthermal phase transitions feature a critical dynamical slowing-down of the nonlocal correlations close to a nonthermal critical point [157]. Finally, in the inset **(d)** of Fig. 1.2, the case where nonlinearities in the microscopic couplings are caused by the incident pulse photons is shown. The incident pulse can trigger nonlinear responses of, *e.g.*, the coupled electron-electron, electron-phonon, spin-spin and spin-phonon interactions, thereby instigating large transient fluctuations of the order parameter.

In the cluster of figures grouping Figs. 1.3, 1.4 and 1.5 are given several important examples of nonthermal phenomena accessible by ultrafast light-mediated experiments.

Firstly, discussing over Fig. 1.3, one can see an experimental plot (inset **(a)**) of the temperature reservoirs of the electron (T_e) and spin (T_s) degrees of freedom as a function of the probe-pulse delay Δt. The electronic temperature T_e is deduced from trARPES differential transmittance while that of the spin T_s is obtained from the time evolution of the magnetic hysteresis loops recorded for all probe-pulse delays Δt [16]. In **(b)** of Fig. 1.3, the experimental results are fitted to a three-temperature model showing remarkable qualitative agreement. The three-temperature (and two-temperature) model assumes that thermalized heat reservoirs associated to distinct quantum degrees of freedom communicate between one another and allows the calculation of the lattice nonthermal temperature T_l. Furthermore, through the knowledge of the specific heat of the relevant degrees of freedom, be it charge, lattice and spin, the coupling constants between those degrees of freedom can be deduced within this model [16]. This means that the evaluation of the dominating coupling constants in a quantum material can be carried out through trARPES experiments, since it enables the transient decoupling of quantum degrees of freedom.

Secondly, Fig. 1.4 shows the transient resistivity in photoexcited K_3C_{60} [26]. The resistivity ρ_0 is extracted from the complex optical conductivity σ measured through reflectivity or transmission measurements using trARPES, with the real part σ_1 representing the dynamics of the quasiparticles near the Fermi level and the imaginary part σ_2 representing the proportion of electrons in the Bose-Einstein condensate [10]. It was observed that a robust long-lived superconducting state, at a constant pulse duration, depends only very weakly on

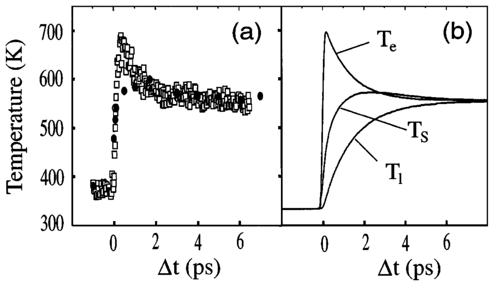

Figure 1.3: Three-temperature model applied in the context of ultrafast spin dynamics in ferromagnetic Nickel [16].

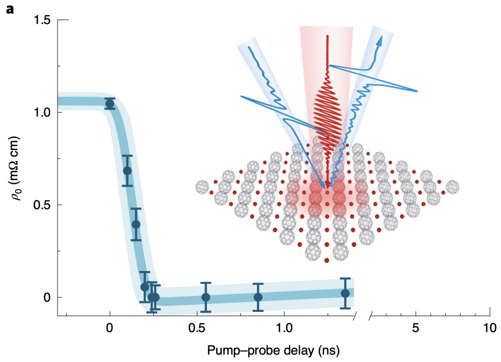

Figure 1.4: Light-induced transient superconductivity in K_3C_{60} [26]. The resistivity transiently goes to zero upon driving the system with mid-infrared laser pulses.

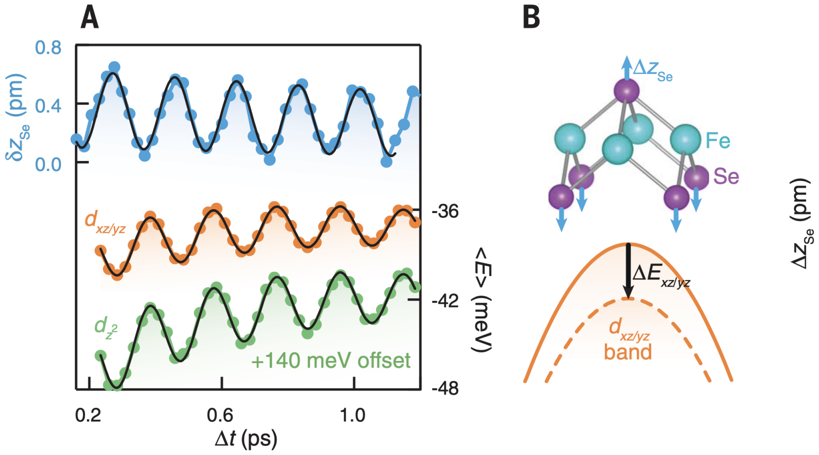

Figure 1.5: Coherent lock-in of the phonon modes with the transient orbital-selective band energy renormalization near the Fermi level [47].

the pump fluence: no qualitative difference in the transient dynamics is observed when using a fluence of 1.5 mJcm^{-2}, 10.0 mJcm^{-2} or 25.0 mJcm^{-2}. A schematic description of the pump and probe beams is depicted in the inset plot of Fig. 1.4, the likes of Fig. 1.1 (right panel).

Thirdly and lastly, in Fig. 1.5, in the inset **A**, are shown the amplitude oscillations of the band energies $d_{xz/yz}$ (orange curve) and d_{x^2} (green curve) crossing the Fermi level in FeSe along the $\Gamma - X$ direction in the first Brillouin zone, and the oscillations of the selenium displacement with respect to its equilibrium position (blue curve). This coherent in-phase behavior between the electronic band shift oscillations and the A_{1g} phonons shows that the electron-electron and electron-phonon interactions can have a cooperative interplay, paving the way to direct control of electron correlations via lattice distortions (and vice versa). The inset plot **B** puts together sketches of the lattice displacement of the selenium atom away from the iron planes and of the coherent lock-in shift of the bands around the Fermi level. The energy resolution of the band shifts is of the order of 1 meV (10^{-3} electron-volts) [47].

Part II

MATHEMATICAL FRAMEWORK

The mathematical framework to tackle nonequilibrium quantum many-body systems is presented. The knowledge and understanding of the concepts and tools covered in this part are crucial and it is recommended to brush up on them.

2

NONEQUILIBRIUM QUANTUM MANY-BODY PHYSICS

The theoretical framework to address nonequilibrium quantum many-body systems is a natural and straightforward generalization of the equilibrium counterpart. In this chapter, the nonequilibrium Green's function formalism will be introduced along with the various independent components – sometimes coined Keldysh components – the correlation functions can be broken down into. The essential notions are first set out in Section 2.1. The Langreth rules governing the handling of those components in key mathematical operations will be stated in Section 2.2.1. The generating functional technique will be the way to generate arbitrary correlation functions and to determine the equations of motion of Hamiltonian-based quantum systems (Section 2.3). The build-up of the aforementioned mathematical concepts and tools will ultimately lead to the Hedin's equations for nonequilibrium systems (Section 2.4). The Hedin's equations will prove to be extremely useful later on when it comes to derive the master equations of the Two-Particle Self-Consistent approach (TPSC) and its variants covered in Chapter 5 and the equations of the post-processing DMFT technique presented in Chapter 4. To conclude this chapter, the path integral formalism is presented in Section 2.5 to eventually introduce the quantum impurity problem and Dynamical Mean Field Theory (DMFT) in Chapter 3.

The mathematical steps follow up Refs. [127, 134]. Throughout this chapter and for the full extent of this thesis, unless advised otherwise, the fundamental physical constants $\hbar$ (Planck's constant), k_B (Boltzmann constant), e (electric charge) and the lattice constants will be set to 1. A dimension analysis allows one to restore them univocally.

2.1 FUNDAMENTAL NOTIONS

To treat quantum systems, one needs to describe quantum and thermal fluctuations. In Section 2.1.1, the time-evolution operator is introduced and in Section 2.1.2 the partition function is introduced.

2.1.1 *Quantum statistics*

The fundamental equation governing the time evolution of non-relativistic quantum states $|\Psi\rangle$ is the Schrödinger's equation

$$i\frac{\mathrm{d}\,|\Psi(t)\rangle}{\mathrm{d}t} = \hat{\mathcal{H}}(t)\,|\Psi(t)\rangle, \tag{2.1}$$

where $\hat{\mathcal{H}}$ is the time-dependent Hamiltonian describing an arbitrary system

The arbitrary system can be composed of fermions and bosons. The quantum statistics are encoded in the symmetries of the Green's functions.

$$\hat{\mathcal{H}}(t) = \hat{\mathcal{H}}_0(t) + \hat{\mathcal{H}}_{\text{int}}(t), \tag{2.2}$$

with $\hat{\mathcal{H}}_0$ the noninteracting part and $\hat{\mathcal{H}}_{\text{int}}$ the interacting part. Both components can have a time dependence. In general, the two components don't commute

$\left[\hat{\mathcal{H}}_0,\hat{\mathcal{H}}_{\text{int}}\right] \neq 0$, unless the noninteracting and interacting parts act on different irreducible subspaces of the Fock space $\mathfrak{F}$. The Fock space is the direct product of the single-particle, two-particle, $\cdots$, n-particle Hilbert space (n represents the number of particles)

$$\mathfrak{F} = \bigoplus_{n=0}^{\infty} \mathfrak{h}^{\otimes n}, \tag{2.3}$$

and it is the space one works with when using the grand-canonical ensemble. The single-particle Hilbert space is denoted by $\mathfrak{h}$. Furthermore, for arbitrary time-dependent Hamiltonian $\hat{\mathcal{H}}$, it could be that $\left[\hat{\mathcal{H}}(t),\hat{\mathcal{H}}(t')\right] \neq 0 \;\forall\; t \neq t'$.

Let's assume that Eq. (2.1) admits a solution to the many-body wave function of the form $|\Psi(t)\rangle = \hat{U}(t,t_0)\,|\Psi(t_0)\rangle$, where t_0 is some arbitrary initial time and $\hat{U}(t,t_0)$ represents the time evolution operator of quantum states. Eq. (2.1) represents a first-order differential equation whose solution needs to be unitary, *i.e.* $\hat{U}(t,t')^{-1} = \hat{U}^{\dagger}(t,t')$, since the quantum states remain normalized upon time evolution: $\langle\Psi(t_0)|\Psi(t_0)\rangle = \langle\Psi(t)|\Psi(t)\rangle = 1$. Also, to completely determine $\hat{U}$, one needs only one initial condition, namely $\hat{U}(t_0,t_0) = \hat{U}(t,t) = \hat{1}$. Insofar as the latter conditions are considered, Eq. (2.1) can be straightforwardly solved by iteration, leading to

$$\hat{U}(t,t_0) = \sum_{n=0}^{\infty}\left(\frac{1}{i}\right)^{n}\int_{t_0}^{t}\mathrm{d}t_1\int_{t_0}^{t_1}\mathrm{d}t_2\cdots\int_{t_0}^{t_{n-1}}\mathrm{d}t_n\;\hat{\mathcal{H}}(t_1)\hat{\mathcal{H}}(t_2)\cdots\hat{\mathcal{H}}(t_n). \tag{2.4}$$

The Hamiltonian $\hat{\mathcal{H}}$ is self-adjoint, *i.e.* $\hat{\mathcal{H}}(t) = \hat{\mathcal{H}}^{\dagger}(t)$, and therefore one can guess from Eq. (2.4) that for $\hat{U}$ to possess the properties of unitary operators, it should have the form of a complex exponential. Although, to achieve this, one needs to introduce a time-ordering super-operator $\mathcal{T}$ whose function is to organize in a chronological fashion the string of operators it acts upon:

$$\begin{aligned}\mathcal{T}\hat{\mathcal{H}}(t_1)\hat{\mathcal{H}}(t_2)\cdots\hat{\mathcal{H}}(t_n) &= \frac{1}{n!}\sum_{P\in S_n}\hat{\mathcal{H}}(t_{P(1)})\hat{\mathcal{H}}(t_{P(2)})\cdots\hat{\mathcal{H}}(t_{P(n)})\\ &\times\Theta(t_{P(1)}-t_{P(2)})\Theta(t_{P(2)}-t_{P(3)})\cdots\Theta(t_{P(n-1)}-t_{P(n)}),\end{aligned} \tag{2.5}$$

where S_n is the group of permutations over the set of n operators and P is one generator. The functions Θ are the Heaviside step functions. The time-ordering operator hence allows one to enlarge the integration domain over the hypercube at the expense of an extra factorial factor coming from the $n!$ identical terms this generates, thereby giving the desired exponential form for Eq. (2.4):

The group S_n is (anti)symmetric if the operators (anti)commute.

$$\begin{aligned}\hat{U}(t,t_0) &= \frac{1}{n!}\sum_{n=0}^{\infty}\left(\frac{1}{i}\right)^{n}\int_{t_0}^{t}\mathrm{d}t_1\int_{t_0}^{t}\mathrm{d}t_2\cdots\int_{t_0}^{t}\mathrm{d}t_n\mathcal{T}\hat{\mathcal{H}}(t_1)\hat{\mathcal{H}}(t_2)\cdots\hat{\mathcal{H}}(t_n)\\ &= \mathcal{T}e^{-i\int_{t_0}^{t}\mathrm{d}t'\hat{\mathcal{H}}(t')}.\end{aligned} \tag{2.6}$$

In Eq. (2.6), the infinite series corresponds to the Taylor expansion expression for the complex exponential. Eq. (2.6) represents the compact form of the operator describing the time evolution of the quantum states.

2.1.2 *Thermal statistics*

The quantum nature of elementary particles and excitations brings in a probabilistic aspect to their description. Albeit central, the quantum fluctuations don't suffice and the thermal fluctuations have to be taken into account. When dealing with a thermodynamic open system coupled to a heat reservoir and a particle reservoir, which means that the energy and the number of particle of the system can fluctuate, but not their average, one has to consider the grand-canonical ensemble with grand potential Ω reading

$$\Omega = U - TS - \mu N. \tag{2.7}$$

T and μ are intensive parameters representing the temperature and chemical potential, respectively, while U is the internal energy. The conjugate extensive variables S and N represent entropy and the number of particles, respectively. Maximizing the entropy minimizes the grand potential (2.7). Therefore, the physical density matrix operator $\hat{\rho}$ which weighs out the thermally favorable quantum states

$$\hat{\rho} = \sum_{\{|\Psi_i\rangle\}\in\mathfrak{F}} w_i \left|\Psi_i\right\rangle \left\langle\Psi_i\right| \tag{2.8}$$

should maximize the entropy

$$S[\hat{\rho}] = -\sum_{\{|\Psi_i\rangle\}\in\mathfrak{F}} \left\langle\Psi_i\right|\hat{\rho}\ln\hat{\rho}\left|\Psi_i\right\rangle. \tag{2.9}$$

Note that the weights in Eq. (2.8) $w_i \in \mathbb{R}^+$ are normalized over the Fock space (2.3), *i.e.* $\sum_{i\in\mathfrak{F}} w_i = 1$. Also, the set of Fock states $\{|\Psi_i\rangle\} = \{|\Psi(t_0)\rangle\}$. Eq. (2.9) is to be maximized to obtain an expression for the w_i's, while satisfying simultaneously a set of constraints, *i.e.* the facts that the thermal average of observables and the weights w_i are normalized. The expression for the density operator reads

Variational principle with the constraints as Lagrange multipliers is the way to derive an expression for $\hat{\rho}$.

$$\hat{\rho} = \frac{e^{-\beta\left(\hat{\mathcal{H}}^M - \mu\hat{N}\right)}}{\mathcal{Z}}, \tag{2.10}$$

where $\hat{\mathcal{H}}^M \equiv \hat{\mathcal{H}}(t=0^-)$ is the Matsubara component of Eq. (2.2) defining the system at equilibrium, *i.e.* just before the system is perturbed by external fields, $\beta = T^{-1}$ and

The density operator is self-adjoint, as can be easily seen from Eq. (2.8).

$$\mathcal{Z} \equiv \sum_{\{|\Psi_i\rangle\}\in\mathfrak{F}} \left\langle\Psi_i\right|\hat{\rho}\left|\Psi_i\right\rangle \tag{2.11}$$

is the partition function. Eq. (2.11) is the normalized Boltzmann distribution valid for thermodynamic systems.

2.2 THE CONTOUR IDEA

Time-dependent quantum averages of observables $\hat{\mathcal{O}}$ require the knowledge of the density matrix operator (2.10) describing the thermal statistics at equilibrium and the time-evolution operator (2.6) describing the time propagation of the quantum states. A simultaneous treatment of both operators will open on to the notion of contour. The contour will complement the mathematical framework to deal with nonequilibrium quantum systems.

The grand-canonical average of a time-dependent observable reads

$$\langle \hat{\mathcal{O}}(t) \rangle = \mathrm{Tr}\left[\hat{\rho}\hat{\mathcal{U}}(t_0,t)\hat{\mathcal{O}}(t)\hat{\mathcal{U}}(t,t_0)\right], \tag{2.12}$$

where $\mathrm{Tr}\left[\cdots\right] \equiv \sum_{\{|\Psi_i\rangle\}\in\mathfrak{F}} \langle \Psi_i | \cdots | \Psi_i \rangle$. The first step to defining the contour is to rewrite Eq. (2.12) in the following way

$$\langle \hat{\mathcal{O}}(t) \rangle = \mathrm{Tr}\Big[\underbrace{e^{-i\int_{t_0}^{t_0-i\beta}\mathrm{d}t'\hat{\mathcal{H}}^M}}_{\mathcal{C}_3}\underbrace{\bar{\mathcal{T}}e^{-i\int_{t}^{t_0}\mathrm{d}t'\hat{\mathcal{H}}(t')}}_{\mathcal{C}_2}\hat{\mathcal{O}}(t)\underbrace{\mathcal{T}e^{-i\int_{t_0}^{t}\mathrm{d}t'\hat{\mathcal{H}}(t')}}_{\mathcal{C}_1}\Big], \tag{2.13}$$

having noticed that $e^{-\beta\hat{\mathcal{H}}^M} = e^{-i\int_{t_0}^{t_0-i\beta}\mathrm{d}\tau\hat{\mathcal{H}}^M}$. Because the grand-canonical ensemble (2.10) will be used forth, the chemical potential μ is assumed to renormalize implicitely the Matsubara component of the Hamiltonian $\hat{\mathcal{H}}^M \to \hat{\mathcal{H}}^M - \mu\hat{N}$. In Eq. (2.13), the anti-chronological ordering operator $\bar{\mathcal{T}}$, ordering the operators in increasing time from left to right, was put to use. The real-time branch along which the operators are arranged from right to left in ascending time is denoted $\mathcal{C}_1$, whereas the one arranging the operators from right to left in decreasing time is denoted $\mathcal{C}_2$. The operators lying on the imaginary-time branch $\mathcal{C}_3$ are time-translational invariant, *i.e.* $\hat{\mathcal{O}}^M(\tau-\tau') = \hat{\mathcal{O}}^M(\tau'-\tau)$. It is important to stress that the time-evolution operator concerns $t \geq t_0$ while the density matrix operator is related to the system at equilibrium, *i.e.* just before the system is perturbed in time.

Since the observables commute under the action of the time-ordering super-operators $\mathcal{T}$ and $\bar{\mathcal{T}}$, the operators braced under $\mathcal{C}_1$, $\mathcal{C}_2$ and $\mathcal{C}_3$ in Eq. (2.13) can be combined, whereby a *contour-ordering* super-operator $\mathcal{T}_{\mathcal{C}}$ along the contour $\mathcal{C} \equiv \mathcal{C}_1 \oplus \mathcal{C}_2 \oplus \mathcal{C}_3$ that builds off of $\mathcal{T}$ and $\bar{\mathcal{T}}$ is brought about. Hence $\mathcal{T}_{\mathcal{C}}$, acts like $\mathcal{T}$ on $\mathcal{C}_1$ and like $\bar{\mathcal{T}}$ on $\mathcal{C}_2$. On $\mathcal{C}_3$, $\mathcal{T}_{\mathcal{C}}$ orders chronologically the operators within[1] $t \in [0, -i\beta]$. $\mathcal{T}_{\mathcal{C}}$ also places $\mathcal{C}_3$ *later* than $\mathcal{C}_2$ and $\mathcal{C}_2$ *later* than $\mathcal{C}_1$ in order to respect the right-to-left arrangement of the operators in Eq. (2.13). Moreover, if a contour-time argument z' lies *later* (*earlier*) on the contour than z, it means notation-wise that $z' \succ z$ ($z' \prec z$). The contour, as well called Kadanoff-Baym (KB) contour, is illustrated in Fig. 2.1.

Gathering all things up, Eq. (2.13) expressed on the KB contour becomes

$$\langle \hat{\mathcal{O}}(z) \rangle = \mathrm{Tr}\left[\mathcal{T}_{\mathcal{C}}e^{-i\int_{\mathcal{C}}\mathrm{d}z'\hat{\mathcal{H}}(z')}\hat{\mathcal{O}}(z)\right], \tag{2.14}$$

where the arguments $z \in \mathcal{C}$. From now on, the real-time arguments t will be reserved for the contour-time arguments $z \in \mathcal{C}_1 \oplus \mathcal{C}_2$, whereas the imaginary-time argument $\tau \equiv it$ will be reserved to denote contour-time arguments $z \in \mathcal{C}_3$. The integral along the contour $\int_{\mathcal{C}}$ of a contour-defined function $A(z)$ can be unpacked as follows

$$\begin{aligned}\int_{\mathcal{C}}\mathrm{d}z'A(z') &\equiv \int_{\mathcal{C}_1}\mathrm{d}t'A(t') + \int_{\mathcal{C}_2}\mathrm{d}t'A(t') + \int_{\mathcal{C}_3}\mathrm{d}\tau'A^M(\tau')\\ &= \int_{t_0}^{t}\mathrm{d}t'A(t') + \int_{t}^{t_0}\mathrm{d}t'A(t') - i\int_0^{\beta}\mathrm{d}\tau'A^M(\tau'),\end{aligned}$$

---

[1] On the vertical branch, t_0 is irrelevant due to translational invariance.

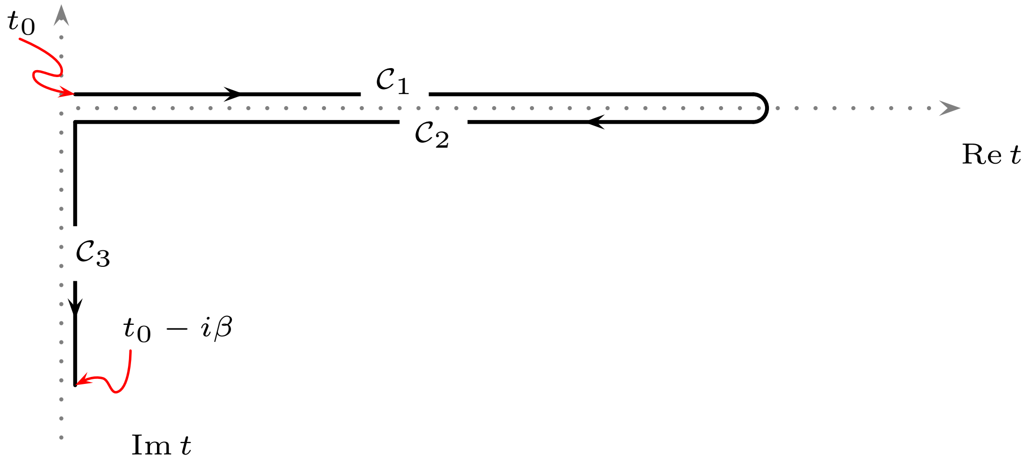

Figure 2.1: Kadanoff-Baym contour with forward branch $\mathcal{C}_1$, backward branch $\mathcal{C}_2$, and the imaginary-time branch $\mathcal{C}_3$. The direction of the contour basically follows the ordering of the operators in Eq. (2.12) from right to left.

where the boundary t corresponds to the maximal time reached along the real axis in Fig. 2.1, which can be stretched to infinity. Eq. (2.14) represents an important step in defining the correlation functions, because these will be related to observables such as the density of particles, current, optical conductivity, etc.

2.2.1 *Langreth rules*

Similarly to Eq. (2.5) for $\mathcal{T}$ on the forward branch, the contour-ordering superoperator $\mathcal{T}_c$ bestows the following structure on a general two-time contour-defined function B:

$$B(z,z') = B^{\delta}(z)\delta(z,z') + \Theta^{\mathcal{C}}(z,z')B^{>}(z,z') + \Theta^{\mathcal{C}}(z',z)B^{<}(z,z'), \tag{2.15}$$

where the Heaviside functions on the KB contour are defined such that $\Theta^{\mathcal{C}}(z,z') = 1$ if $z \succ z'$, and $\Theta^{\mathcal{C}}(z,z') = 0$ otherwise. In Eq. (2.15), the contour-time arguments z,z' can lie on any segment of the KB contour. B^{δ} is a one-time function that isn't comprised of correlations in time. The delta function $\delta^{\mathcal{C}}(z,z')$ is related to $\Theta^{\mathcal{C}}(z,z')$ via the partial derivative

$$\begin{aligned}
&\int_{z_i}^{z_f} \mathrm{d}z' B(z,z')\partial_{z'}\Theta^{\mathcal{C}}(z',z'') \\
&= \int_{z_i}^{z_f} \mathrm{d}z'\partial_{z'}\left(B(z,z')\Theta^{\mathcal{C}}(z',z'')\right) - \int_{z_i}^{z_f} \mathrm{d}z'\partial_{z'}B(z,z')\Theta^{\mathcal{C}}(z',z'') \\
&= B(z,z_f) - \left(B(z,z_f) - B(z,z'')\right) = B(z,z'').
\end{aligned} \tag{2.16}$$

A similar expression to Eq. (2.16) can be derived if the partial derivative had acted from the right onto the Heaviside function while integrating over z'', *i.e*,

$$\int_{z_i}^{z_f} \mathrm{d}z''\Theta^{\mathcal{C}}(z',z'')\overleftarrow{\partial}_{z''}B(z'',z');$$

although this would have produced an extra minus sign to the result. From Eq. (2.16), one can easily deduce that if the contour-time arguments lie on

i) $\mathcal{C}_1$, $\delta^{\mathcal{C}}(t,t') = \delta(t-t')$

ii) $\mathcal{C}_2$, $\delta^{\mathcal{C}}(t,t') = -\delta(t-t')$

iii) $\mathcal{C}_3$, $\delta^{\mathcal{C}}(t_0 - i\tau, t_0 - i\tau') = i\delta(\tau - \tau')$.

Now, because the contour-time arguments can be positioned on three different branches, the two-time objects such as B can be represented in terms of 3×3 matrices

$$B(z,z') = \begin{pmatrix} B_{11}(z,z') & B_{12}(z,z') & B_{13}(z,z') \\ B_{21}(z,z') & B_{22}(z,z') & B_{23}(z,z') \\ B_{31}(z,z') & B_{32}(z,z') & B_{33}(z,z') \end{pmatrix}, \tag{2.17}$$

and the space they span over is called the *Keldysh* space. In Eq. (2.17), all the possible combinations of contour-time arguments on $\mathcal{C}$ are shown. Employing the definition (2.15), one can express the elements of Eq. (2.17) into Keldysh components as displayed in Table 2.1.

	$\mathcal{C}_1$	$\mathcal{C}_2$	$\mathcal{C}_3$
$\mathcal{C}_1$	(causal) $B^\delta(t)\delta(t-t')+B^{\mathrm{T}}(t,t')$	(lesser) $B^<(t,t')$	(left-mixing) $B^\urcorner(t,\tau')$
$\mathcal{C}_2$	(greater) $B^>(t,t')$	(anti-causal) $-B^\delta(t)\delta(t-t')+B^{\bar{\mathrm{T}}}(t,t')$	(left-mixing) $B^\urcorner(t,\tau')$
$\mathcal{C}_3$	(right-mixing) $B^\ulcorner(\tau,t')$	(right-mixing) $B^\ulcorner(\tau,t')$	(Matsubara) $iB^\delta(\tau)\delta(\tau-\tau')+B^M(\tau,\tau')$

Table 2.1: Keldysh components of two-time contour-defined functions. A similar table is presented in Ref. [114].

The Langreth rules consist in a set of mathematical identities utilizing the Keldysh components in Table 2.1 that simplify convolutions

$$C(z,z') = \int_{\mathcal{C}} \mathrm{d}z'' A(z,z'')B(z'',z') \tag{2.18}$$

and products

$$\begin{cases} C(z,z') = A(z,z')B(z',z) \\ C(z,z') = A(z,z')B(z,z') \end{cases} \tag{2.19}$$

between contour-ordered functions like Eq. (2.15): it makes up the guidelines that translate these operations into analytical expressions that can be computed. The convolution is a group homomorphism, whereas products need special care if Eq. (2.15) is the general structure of contour functions (see Appendix A). A thorough summary of the Keldysh rules is given in Table 5.7 of Ref. [127]. Nevertheless, to introduce two other important Keldysh components, namely the retarded B^R

From Eqs. (2.20) *and* (2.21), $B^R(t,t') = B^A(t',t)^\dagger$.

$$B^R(t,t') = B^\delta(t)\delta(t-t') + \Theta(t-t')\left[B^>(t,t') - B^<(t,t')\right], \tag{2.20}$$

and the advanced B^A

$$B^A(t,t') = B^\delta(t)\delta(t-t') + \Theta(t'-t)\left[B^<(t,t') - B^>(t,t')\right], \tag{2.21}$$

and understand the mechanics behind the Langreth rules, the convolution (2.18) and products (2.19) are explicitly evaluated for the *lesser* Keldysh component $C^<$ in Appendix A. The *lesser* (*greater*) component of the convolution gives

$$C^{<(>)}(t,t') = \int_{t_0}^{t} \mathrm{d}\bar{t}\ A^R(t,\bar{t})B^{<(>)}(\bar{t},t') + \int_{t_0}^{t'} \mathrm{d}\bar{t}\ A^{<(>)}(t,\bar{t})B^A(\bar{t},t')$$
$$-\,i\int_0^\beta \mathrm{d}\bar{\tau}\ A^\rceil(t,\bar{\tau})B^\lceil(\bar{\tau},t'). \tag{2.22}$$

As for the products (2.19), the *lesser* (*greater*) components read

$$\begin{cases} C^{<(>)}(t,t') = A^{<(>)}(t,t')B^{>(<)}(t',t) \\ C^{<(>)}(t,t') = A^{<(>)}(t,t')B^{<(>)}(t,t'). \end{cases} \tag{2.23}$$

It is important to note that the Langreth rules carry over to expressions involving many convolutions and not just one like in Eq. (2.18). This will be particularly relevant in Chapter 4 and for that purpose Eqs. (2.22) and (2.23) serve as examples to get acquainted with the Langreth rules.

2.3 CORRELATION FUNCTIONS AND EQUATIONS OF MOTION

To start off, the nonequilibrium generating functional formalism is skimmed over [90]. That formalism will be used to define the one- and two-particle correlation functions, namely the one- and two-particle Green's functions, respectively. Later on, to calculate the equations of motion of Hamiltonian-based systems, one will need to resort to Green's functions.

The nonequilibrium Green's function can represent arbitrary order correlation functions between particles on the KB contour and these can be generated by the following functional $\mathcal{Z}$:

$$\mathcal{Z}[\phi] = \mathrm{Tr}\Big[\mathcal{T}_\mathcal{C} e^{-i\int_\mathcal{C}\mathrm{d}\bar{z}\ \hat{\mathcal{H}}(\bar{z})}\ \underbrace{e^{-i\iint_\mathcal{C}\mathrm{d}z_1\mathrm{d}z_2\ \hat{c}^\dagger_\alpha(z_1)\phi_{\alpha,\beta}(z_1,z_2)\hat{c}_\beta(z_2)}}_{\equiv S[\phi]}\Big], \tag{2.24}$$

where the KB contour corresponds to that illustrated in Fig. 2.1 and $\hat{c}^{(\dagger)}$ are fermionic annihilation (creation) operators. The fermionic ladder operators are elements of the anti-commuting algebra ($\delta_{\alpha,\beta} = 1$ if $\alpha = \beta$ and 0 otherwise)

As a reminder, the bosonic operators commute.

$$\{\hat{c}_\alpha(z_1), \hat{c}^\dagger_\beta(z_2)\} = \delta_{\alpha,\beta}\delta^\mathcal{C}(z_1,z_2), \quad \{\hat{c}_\alpha(z_1), \hat{c}_\beta(z_2)\} = 0.$$

$\mathcal{T}_\mathcal{C}$ is the time-ordering operator on $\mathcal{C}$ and ϕ is a source field defined on the contour. The greek indices represent arbitrary quantum degrees of freedom. $S[\phi]$ is a functional of a source field ϕ. The trace in Eq. (2.24) spans over the eigenstates in Fock space. The functional $\mathcal{Z}[\phi]$ is equal to Eq. (2.11) when $\phi \to 0$, since the time-evolution operator obeys $\hat{U}(t_0,t)\hat{U}(t,t_0) = \hat{1}$ and only the density matrix operator remains. The generated correlation functions become physically meaningful once the source field is turned off.

2.3.1 *One-particle Green's function*

Properly speaking, the correlation functions generated from $\ln\mathcal{Z}[\phi]$ *are the cumulants of the underlying distribution weighted by the Hamiltonian.*

According to Eq. (2.24), the contour Green's function reads

$$\mathcal{G}^{\phi}_{\epsilon,\zeta}(z_1,z_2) = -\frac{\delta \ln \mathcal{Z}[\phi]}{\delta \phi_{\zeta,\epsilon}(z_2,z_1)} = -i\langle \mathcal{T}_{\mathcal{C}}\hat{c}_{\epsilon}(z_1)\hat{c}^{\dagger}_{\zeta}(z_2)\rangle_{\phi}. \tag{2.25}$$

Since contour-defined functions are necessarily contour-ordered, Eq. (2.25) can be read off as

$$\mathcal{G}^{\phi}_{\epsilon,\zeta}(z_1,z_2) = -i\langle \hat{c}_{\epsilon}(z_1)\hat{c}^{\dagger}_{\zeta}(z_2)\rangle_{\phi}\Theta^{\mathcal{C}}(z_1,z_2) + i\langle \hat{c}^{\dagger}_{\zeta}(z_2)\hat{c}_{\epsilon}(z_1)\rangle_{\phi}\Theta^{\mathcal{C}}(z_2,z_1). \tag{2.26}$$

In Eq. (2.25), the grand-canonical ensemble average implies

$$\langle\cdots\rangle_{\phi} = \frac{1}{\mathcal{Z}[\phi]}\sum_i \langle \Psi_i|\, e^{-i\int_{\mathcal{C}}\mathrm{d}\bar{z}\hat{\mathcal{H}}(\bar{z})}S[\phi]\cdots|\Psi_i\rangle\,,$$

with the $\{|\Psi_i\rangle\}$ a set of eigenstates in Fock space. From Eq. (2.25), the Keldysh components laid out in Table 2.1 of the one-particle Green's function can be established. However, only four independent components suffice to fully specify a contour Green's function, namely the retarded $\mathcal{G}^R$, the Matsubara $\mathcal{G}^M$, the right-mixing $\mathcal{G}^{\urcorner}$ and the *lesser* $\mathcal{G}^<$. The other Keldysh components introduced in Section 2.2.1 can be related to the latter somehow. The *lesser* component, defined on the real-time axis, can be deduced easily from Eq. (2.26), giving

When unnecessary, the source field is left out.

$$\mathcal{G}^{<}_{\epsilon,\zeta}(t_1,t_2) = i\langle \hat{c}^{\dagger}_{\zeta}(t_2)\hat{c}_{\epsilon}(t_1)\rangle, \tag{2.27}$$

and its spectrum is defined as

$$\mathcal{A}^{<}_{\mathbf{k}}(\omega,t_2) = \frac{1}{2\pi}\operatorname{Im}\mathcal{G}^{<}_{\mathbf{k}}(\omega,t_2). \tag{2.28}$$

The retarded component defined in Eq. (2.20) is composed of Eq. (2.27):

$$\mathcal{G}^R(t_1,t_2) = \Theta(t_1-t_2)\left[\mathcal{G}^>(t_1,t_2) - \mathcal{G}^<(t_1,t_2)\right]. \tag{2.29}$$

Thereby, the retarded and advanced components lie on the real-time axis as well. Notice that the *greater* component $\mathcal{G}^>$ can be deduced from Eqs. (2.29) and (2.27). Both the retarded (2.29) and the lesser (2.27) Keldysh components of the single-particle Green's function are related via the Fermi-Dirac distribution function at equilibrium. However, it is not the case out of equilibrium. As will be demonstrated in Section 2.3.4, the retarded Keldysh component can be cast into a spectral representation via a partial forward Fourier transformation taking the form

$$\begin{aligned}\mathcal{G}^R(\omega,t_2) &= \lim_{\eta\to 0^+}\int_{t_2^+}^{\infty}\mathrm{d}t_1\; e^{i(\omega+i\eta)(t_1-t_2)}\mathcal{G}^R(t_1,t_2)\\ &= \lim_{\eta\to 0^+} i\int_{-\infty}^{\infty}\mathrm{d}\omega'\;\frac{[\mathcal{G}^>(\omega',t_2)-\mathcal{G}^<(\omega',t_2)]}{\omega-\omega'+i\eta},\end{aligned} \tag{2.30}$$

The forward Fourier transform is not equivalent to the Wigner transformation [6].

where $\mathrm{d}\omega^{(\prime)} \equiv 2\pi/\mathrm{d}t^{(\prime)}$ are infinitesimal differential frequencies. Eq. (2.30) is nothing else but a Hilbert transform and one naturally recovers the equilibrium case when $\mathcal{G}^R(\omega,t_2)$ doesn't depend on t_2, but rather on t_1-t_2. Eq. (2.30) implies that time-dependent retarded spectral functions can be extracted from the *lesser* and *greater* components, respectively denoted $\mathcal{A}^{<}$ and $\mathcal{A}^{>}$. From the *lesser* (*greater*) spectral function can be extracted the electron (hole) distribution function. The latter will be also covered in Section 2.3.4. From the retarded Green's function (2.30), as demonstrated in Appendix D, the time-dependent retarded spectral function $\mathcal{A}^R$ can be calculated as follows

$$\mathcal{A}^R(\omega,t_2) \equiv \mathcal{A}(\omega,t_2) = -\frac{1}{\pi}\mathrm{Im}\mathcal{G}^R(\omega,t_2). \tag{2.31}$$

The right-mixing component reads

$$\mathcal{G}^{\ulcorner}_{\epsilon,\zeta}(\tau_1,t_2) = -i\langle \hat{c}_\epsilon(\tau_1)\hat{c}^\dagger_\zeta(t_2)\rangle. \tag{2.32}$$

The left-mixing and right-mixing components are related via complex conjugation

$$\begin{aligned}
&\mathcal{G}^{\ulcorner}_{\epsilon,\zeta}(\tau_1,t_2)^\dagger \\
&= i\langle \hat{U}(t_0,t_2)\hat{c}_\zeta\hat{U}(t_2,t_0)\hat{U}(t_0,t_0-i\tau_1)\hat{c}^\dagger_\epsilon\hat{U}(t_0-i\tau_1,t_0-i\beta)\rangle \\
&= i\langle e^{-\hat{\mathcal{H}}^M\beta}e^{\hat{\mathcal{H}}^M(\beta-\tau_1)}\hat{c}^\dagger_\epsilon e^{-\hat{\mathcal{H}}^M(\beta-\tau_1)}\hat{U}(t_0,t_2)\hat{c}_\zeta\hat{U}(t_2,t_0)\rangle \\
&= \mathcal{G}^{\urcorner}_{\zeta,\epsilon}(t_2,\beta-\tau_1).
\end{aligned} \tag{2.33}$$

The latter is a consequence of the Kubo-Martin-Schwinger (KMS) boundary conditions for fermions and of the fact that the Matsubara components of the Hamiltonian mutually commute. The KMS boundary conditions also imply

The KMS boundary conditions are ascribed to the cyclic property of the trace and to the anticommuting algebra of fermionic field operators.

$$\begin{cases} \mathcal{G}^{\ulcorner}(\beta,t_2) = -\mathcal{G}^{\ulcorner}(0^+,t_2) = -\mathcal{G}^{>}(t_0,t_2) \\ \mathcal{G}^{\urcorner}(t_2,\beta) = -\mathcal{G}^{\urcorner}(t_2,0^+) = -\mathcal{G}^{<}(t_2,t_0). \end{cases} \tag{2.34}$$

The last independent Keldysh component $\mathcal{G}^M$ reads

$$\mathcal{G}^M_{\epsilon,\zeta}(\tau_1-\tau_2) = -\langle \mathcal{T}_\tau\hat{c}_\epsilon(\tau_1)\hat{c}^\dagger_\zeta(\tau_2)\rangle, \tag{2.35}$$

where the imaginary-time ordering super-operator $\mathcal{T}_\tau$ orders the imaginary time τ in ascending order from $\tau = 0$ to $\tau = \beta$, *i.e.*

$$\mathcal{T}_\tau\hat{c}(\tau_1)\hat{c}^\dagger(\tau_2) = \hat{c}(\tau_1)\hat{c}^\dagger(\tau_2)\Theta(\tau_1-\tau_2) - \hat{c}^\dagger(\tau_2)\hat{c}(\tau_1)\Theta(\tau_2-\tau_1).$$

Also, owing to the (anti)-periodicity of the Matsubara (fermionic) bosonic Green's function in imaginary time with period β

$$\mathcal{G}^M_{\epsilon,\zeta}(\tau) = \mp\mathcal{G}^M_{\epsilon,\zeta}(\tau-\beta) \qquad\qquad \forall\ \tau\in[0,\beta[, \tag{2.36}$$

one can respectively define fermionic and bosonic Matsubara frequencies as $i\omega_n \equiv \frac{(2n+1)\pi}{\beta}$ and $iq_n \equiv \frac{2n\pi}{\beta}$ with $n\in\mathbb{Z}$. Doing so, Fourier transforms can serve as a map transforming imaginary-time functions into Matsubara-frequency functions, and vice-versa

$$\begin{aligned}
\mathcal{G}^M_{\epsilon,\zeta}(i\omega_n) &= \int_0^\beta \mathrm{d}\tau\ e^{i\omega_n\tau}\mathcal{G}^M_{\epsilon,\zeta}(\tau) \\
\mathcal{G}^M_{\epsilon,\zeta}(\tau) &= \frac{1}{\beta}\sum_{n=-\infty}^{\infty} e^{-i\omega_n\tau}\mathcal{G}^M_{\epsilon,\zeta}(i\omega_n).
\end{aligned} \tag{2.37}$$

The transformations laid out in Eq. (2.37) apply to the bosonic frequencies as well: it suffices to replace $i\omega_n$ by iq_n. The Matsubara Green's function has also a spectral representation

$$\mathcal{G}(i\omega_n) = \int_{-\infty}^{\infty} \mathrm{d}\omega' \, \frac{\mathcal{A}^R(\omega')}{i\omega_n - \omega'}, \tag{2.38}$$

where $\mathcal{A}^R$ is the equilibrium retarded spectral function defined as

$$\mathcal{A}^R(\omega, t_2 = 0) = -\frac{1}{\pi}\mathrm{Im}\mathcal{G}^R(\omega). \tag{2.39}$$

As previously mentioned, the spectral function (2.39) as well as the spectral representation (2.38) are introduced in details in Section 2.3.4.

2.3.2 *Two-particle Green's function*

Returning back to Eq. (2.25), one can perform a second functional derivative

$$\frac{\delta \mathcal{G}^{\phi}_{\epsilon,\zeta}(z_1,z_2)}{\delta \phi_{\gamma,\delta}(z_4,z_3)} = \mathcal{G}^{\phi}_{\delta,\gamma}(z_3,z_4)\mathcal{G}^{\phi}_{\epsilon,\zeta}(z_1,z_2) - \langle \hat{c}^{\dagger}_{\gamma}(z_4)\hat{c}_{\delta}(z_3)\hat{c}_{\epsilon}(z_1)\hat{c}^{\dagger}_{\zeta}(z_2)\rangle_{\phi}, \tag{2.40}$$

which, defining the two-particle correlation function $\chi \equiv -i\frac{\delta\mathcal{G}}{\delta\phi}$ (*cf.* Eq. (12.18) in Ref. [127]), leads to

$$\begin{aligned}&\chi^{\phi}_{\epsilon,\zeta;\gamma,\delta}(z_1,z_2;z_4,z_3)\\ &= i\langle \mathcal{T}_{\mathcal{C}}\hat{c}^{\dagger}_{\gamma}(z_4)\hat{c}_{\delta}(z_3)\hat{c}_{\epsilon}(z_1)\hat{c}^{\dagger}_{\zeta}(z_2)\rangle_{\phi} - i\mathcal{G}^{\phi}_{\delta,\gamma}(z_3,z_4)\mathcal{G}^{\phi}_{\epsilon,\zeta}(z_1,z_2).\end{aligned} \tag{2.41}$$

Note that Eq. (2.40) corresponds to Eq. (15.11) in Ref. [127]. Eq. (2.41) corresponds to the two-particle correlation function.

Another important result about the two-particle correlation function (2.41) can be extracted from the "closure relation"

$$\frac{\delta\left(\mathcal{G}^{\phi}_{\epsilon,\bar{\alpha}}(z_1,\bar{z}_5)\mathcal{G}^{\phi}_{\bar{\alpha},\eta}(\bar{z}_5,z_2)^{-1}\right)}{\delta\phi_{\gamma,\delta}(z_4,z_3)} = 0, \tag{2.42}$$

where the continuous (discrete) variables dressed with a bar over are integrated (summed) over, allowing oneself to leave out the summation and integral symbols. The integrals are carried out along the KB contour according to Section 2.2 and the summations are done over discrete quantum degrees of freedom such as the spin, orbital, etc. Sometimes, even when summations or integrals are explicit, bars are used to emphasize their dummy character. Eq. (2.42) gives

$$\frac{\delta\mathcal{G}^{\phi}_{\epsilon,\zeta}(z_1,z_2)}{\delta\phi_{\gamma,\delta}(z_4,z_3)} = -\mathcal{G}^{\phi}_{\epsilon,\bar{\alpha}}(z_1,\bar{z}_5)\frac{\delta\mathcal{G}^{\phi}_{\bar{\alpha},\bar{\eta}}(\bar{z}_5,\bar{z}_6)^{-1}}{\delta\phi_{\gamma,\delta}(z_4,z_3)}\mathcal{G}^{\phi}_{\bar{\eta},\zeta}(\bar{z}_6,z_2), \tag{2.43}$$

and the modified Dyson's equation with the source field reads

$$\mathcal{G}^{\phi}_{\alpha,\eta}(z_5,z_6)^{-1} = \mathcal{G}^{0}_{\alpha,\eta}(z_5,z_6)^{-1} - \phi_{\alpha,\eta}(z_5,z_6) - \Sigma^{\phi}_{\alpha,\eta}(z_5,z_6). \tag{2.44}$$

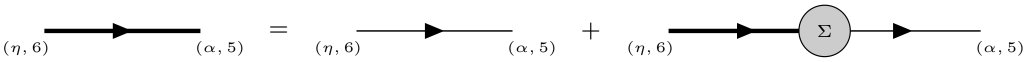

Figure 2.2: Diagrammatic representation of the one-particle Green's function (2.44). The thin line denotes the noninteracting one-particle Green's function $\mathcal{G}^0$.

Equation (2.44) appears naturally when deriving the equations of motion from Eq. (2.25), as will be shown later on in Section 2.3.3. Note that all the two-time objects introduced hitherto can be expressed in a 3×3 matrix form, as described in Ref. [6]. The Dyson's equation (2.44) can be inverted so as to single out the interacting one-particle Green's function $\mathcal{G}$, leading to the diagrammatic representation of $\mathcal{G}$ shown in Fig. 2.2.

Note that in Fig. 2.2 the source field was turned off.

Inserting Eq. (2.44) into Eq. (2.43), one gets

$$\begin{aligned}-i\frac{\delta\mathcal{G}^{\phi}_{\epsilon,\zeta}(z_1,z_2)}{\delta\phi_{\gamma,\delta}(z_4,z_3)} &= -i\mathcal{G}^{\phi}_{\epsilon,\gamma}(z_1,z_4)\mathcal{G}^{\phi}_{\delta,\zeta}(z_3,z_2)\\ &\quad - i\mathcal{G}^{\phi}_{\epsilon,\bar\alpha}(z_1,\bar z_5)\frac{\delta\Sigma^{\phi}_{\bar\alpha,\bar\eta}(\bar z_5,\bar z_6)}{\delta\mathcal{G}^{\phi}_{\bar\theta,\bar\varpi}(\bar z_7,\bar z_8)}\frac{\delta\mathcal{G}^{\phi}_{\bar\theta,\bar\varpi}(\bar z_7,\bar z_8)}{\delta\phi_{\gamma,\delta}(z_4,z_3)}\mathcal{G}^{\phi}_{\bar\eta,\zeta}(\bar z_6,z_2),\end{aligned}\tag{2.45}$$

where the chain rule for the self-energy $\Sigma[\mathcal{G}]$ was used. Defining the two-particle irreducible $\mathcal{G}$-skeletonic vertex function $\Gamma\equiv-\frac{\delta\Sigma}{\delta\mathcal{G}}$ (*cf.* Eq. (12.34) in Ref. [127]), one gets the Bethe-Salpeter equation (*cf.* Eq. (12.17) in Ref. [127])

$$\begin{aligned}\chi^{\phi}_{\epsilon,\zeta;\gamma,\delta}(z_1,z_2;z_4,z_3) &= -i\mathcal{G}^{\phi}_{\epsilon,\gamma}(z_1,z_4)\mathcal{G}^{\phi}_{\delta,\zeta}(z_3,z_2)\\ &\quad-\mathcal{G}^{\phi}_{\epsilon,\bar\alpha}(z_1,\bar z_5)\Gamma^{\phi}_{\bar\alpha,\bar\eta;\bar\theta,\bar\varpi}(\bar z_5,\bar z_6;\bar z_7,\bar z_8)\chi^{\phi}_{\bar\theta,\bar\varpi;\gamma,\delta}(\bar z_7,\bar z_8;z_4,z_3)\mathcal{G}^{\phi}_{\bar\eta,\zeta}(\bar z_6,z_2).\end{aligned}\tag{2.46}$$

The Bethe-Salpeter equation can be casted into Feynman diagrams, as shown in Fig. 2.3.

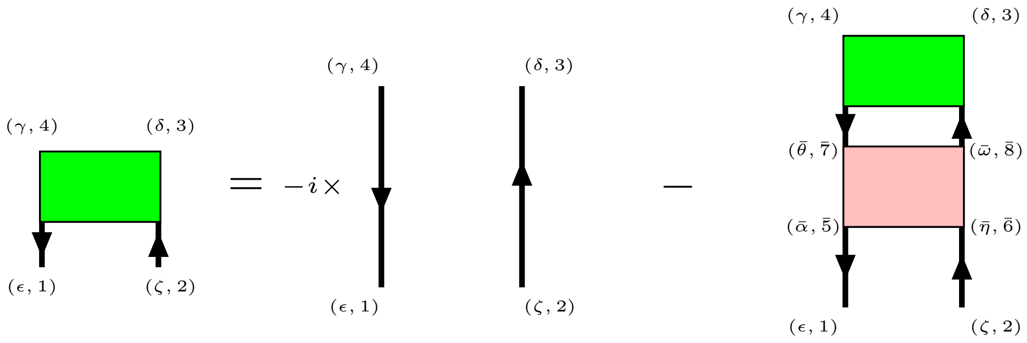

Figure 2.3: Diagrammatic representation of the two-particle Green's function (2.46) in the particle-hole channel. The green box denotes χ and the pink box Γ. The bold arrows, representing interacting one-particle Green's functions, obey the Dyson's equation depicted by Fig. 2.2.

Then, finally, Eqs. (2.41) and (2.46) can be combined to give

$$\begin{aligned}i\langle\mathcal{T}_{\mathcal{C}}\hat c^{\dagger}_{\gamma}(z_4)\hat c_{\delta}(z_3)\hat c_{\epsilon}(z_1)\hat c^{\dagger}_{\zeta}(z_2)\rangle_{\phi} &= i\mathcal{G}^{\phi}_{\delta,\gamma}(z_3,z_4)\mathcal{G}^{\phi}_{\epsilon,\zeta}(z_1,z_2)-i\mathcal{G}^{\phi}_{\epsilon,\gamma}(z_1,z_4)\mathcal{G}^{\phi}_{\delta,\zeta}(z_3,z_2)\\ &\quad-\mathcal{G}^{\phi}_{\epsilon,\bar\alpha}(z_1,\bar z_5)\Gamma^{\phi}_{\bar\alpha,\bar\eta;\bar\theta,\bar\varpi}(\bar z_5,\bar z_6;\bar z_7,\bar z_8)\chi^{\phi}_{\bar\theta,\bar\varpi;\gamma,\delta}(\bar z_7,\bar z_8;z_4,z_3)\mathcal{G}^{\phi}_{\bar\eta,\zeta}(\bar z_6,z_2).\end{aligned}\tag{2.47}$$

Eq. (2.47) will be used in Section 2.3.3 to re-express the four-point correlation function stemming from the equations of motion and isolate the self-energy.

2.3.3 *Equations of motion*

To derive the equations of motion of a system, one needs to first establish the Hamiltonian describing the system. In this section, a very general Hamiltonian is used, consisting in a bilinear term in field operators representing the kinetic energy and a quartic term in field operators representing the potential energy:

$$\hat{\mathcal{H}} = h_{\bar{\alpha}\bar{\beta}}(\bar{z}_1,\bar{z}_2)\hat{c}^{\dagger}_{\bar{\alpha}}(\bar{z}_1)\hat{c}_{\bar{\beta}}(\bar{z}_2) + \frac{1}{2}V^{\bar{\gamma}\bar{\delta}}_{\bar{\alpha}\bar{\beta}}(\bar{z}_1,\bar{z}_2,\bar{z}_3,\bar{z}_4)\hat{c}^{\dagger}_{\bar{\alpha}}(\bar{z}_1)\hat{c}^{\dagger}_{\bar{\gamma}}(\bar{z}_2)\hat{c}_{\bar{\delta}}(\bar{z}_3)\hat{c}_{\bar{\beta}}(\bar{z}_4), \tag{2.48}$$

where the tensor $h_{\alpha\beta}(z_1,z_2) = h_{\beta\alpha}(z_2,z_1)$ is symmetric and V is symmetric via the following variable permutations:

$$V^{\gamma\delta}_{\alpha\beta}(z_1,z_2,z_3,z_4) = V^{\alpha\beta}_{\gamma\delta}(z_2,z_1,z_4,z_3) = V^{\beta\alpha}_{\delta\gamma}(z_3,z_4,z_1,z_2). \tag{2.49}$$

To obtain the equations of motion, the contour one-body Green's function (2.25) is differentiated:

$$\begin{aligned} &i\partial_{z_1}\mathcal{G}^{\phi}_{\epsilon,\zeta}(z_1,z_2) = \partial_{z_1}\langle\mathcal{T}_{\mathcal{C}}\hat{c}_{\epsilon}(z_1)\hat{c}^{\dagger}_{\zeta}(z_2)\rangle_{\phi} \\ &= \delta^{\mathcal{C}}(z_1,z_2)\langle\{\hat{c}_{\epsilon},\hat{c}^{\dagger}_{\zeta}\}\rangle_{\phi} + \left\langle\mathcal{T}_{\mathcal{C}}\partial_{z_1}S[\phi]\hat{c}_{\epsilon}(z_1)\hat{c}^{\dagger}_{\zeta}(z_2)\right\rangle_{\phi} + i\left\langle\mathcal{T}_{\mathcal{C}}[\hat{\mathcal{H}},\hat{c}_{\epsilon}](z_1)\hat{c}^{\dagger}_{\zeta}(z_2)\right\rangle_{\phi}. \end{aligned} \tag{2.50}$$

Note that in Eq. (2.50), the partial derivative could be applied onto z_2 from the right, *i.e.* using $-i\overleftarrow{\partial}_{z_2}$. Bearing in mind that $[AB,C] = A\{B,C\} - \{A,C\}B = A[B,C] + [A,C]B$, the commutator in Eq. (2.50) is tackled by developing first the kinetic term:

$$\begin{aligned} \left[\hat{\mathcal{H}}_{\text{kin.}},\hat{c}_{\epsilon}\right](z_1) &= -h_{\bar{\alpha}\bar{\beta}}(\bar{z}_1,\bar{z}_2)\{\hat{c}^{\dagger}_{\bar{\alpha}}(\bar{z}_1),\hat{c}_{\epsilon}(z_1)\}\hat{c}_{\bar{\beta}}(\bar{z}_2) \\ &= -h_{\epsilon\bar{\beta}}(z_1,\bar{z}_2)\hat{c}_{\bar{\beta}}(\bar{z}_2). \end{aligned} \tag{2.51}$$

The second contribution to the commutator comes from the interaction term of Eq. (2.48):

$$\begin{aligned} \left[\hat{\mathcal{H}}_{\text{int.}},\hat{c}_{\epsilon}\right](z_1) &= \frac{1}{2}V^{\bar{\gamma}\bar{\delta}}_{\bar{\alpha}\bar{\beta}}(\bar{z}_1,\bar{z}_2,\bar{z}_3,\bar{z}_4)\left[\hat{c}^{\dagger}_{\bar{\alpha}}(\bar{z}_1)\hat{c}^{\dagger}_{\bar{\gamma}}(\bar{z}_2),\hat{c}_{\epsilon}(z_1)\right]\hat{c}_{\bar{\delta}}(\bar{z}_3)\hat{c}_{\bar{\beta}}(\bar{z}_4) \\ &= \frac{1}{2}V^{\epsilon\bar{\delta}}_{\bar{\alpha}\bar{\beta}}(\bar{z}_1,z_1,\bar{z}_3,\bar{z}_4)\hat{c}^{\dagger}_{\bar{\alpha}}(\bar{z}_1)\hat{c}_{\bar{\delta}}(\bar{z}_3)\hat{c}_{\bar{\beta}}(\bar{z}_4) \\ &\quad - \frac{1}{2}V^{\bar{\gamma}\bar{\delta}}_{\epsilon\bar{\beta}}(z_1,\bar{z}_2,\bar{z}_3,\bar{z}_4)\hat{c}^{\dagger}_{\bar{\gamma}}(\bar{z}_2)\hat{c}_{\bar{\delta}}(\bar{z}_3)\hat{c}_{\bar{\beta}}(\bar{z}_4). \end{aligned} \tag{2.52}$$

To simplify Eq. (2.52), the indices of the first term are exchanged in the following way: $(\bar{\delta},\bar{z}_3) \to (\bar{\beta},\bar{z}_4)$, $(\bar{\alpha},\bar{z}_1) \to (\bar{\gamma},\bar{z}_2)$ and $(\bar{\beta},\bar{z}_4) \to (\bar{\delta},\bar{z}_3)$. According to the symmetries of the interaction term (2.49), this substitution allows to merge the two terms, giving

$$\left[\hat{\mathcal{H}}_{\text{int.}},\hat{c}_{\epsilon}\right](z_1) = -V^{\bar{\gamma}\bar{\delta}}_{\epsilon\bar{\beta}}(z_1,\bar{z}_2,\bar{z}_3,\bar{z}_4)\hat{c}^{\dagger}_{\bar{\gamma}}(\bar{z}_2)\hat{c}_{\bar{\delta}}(\bar{z}_3)\hat{c}_{\bar{\beta}}(\bar{z}_4). \tag{2.53}$$

The second term of Eq. (2.50) remains to be differentiated and it involves the source field itself:

$$\begin{aligned}&\left\langle \mathcal{T}_{\mathcal{C}} \partial_{z_1} S[\phi] \hat{c}_{\epsilon}(z_1) \hat{c}^{\dagger}_{\zeta}(z_2) \right\rangle_{\phi} = \left\langle \mathcal{T}_{\mathcal{C}} \hat{c}_{\epsilon}(z_1) \partial_{z_1} e^{-i \int_{z_2}^{z_1} \mathrm{d}z_3 \int \mathrm{d}z_4 \hat{c}^{\dagger}_{\bar{\alpha}}(z_3) \phi_{\bar{\alpha},\bar{\beta}}(z_3,z_4) \hat{c}_{\bar{\beta}}(z_4)} \hat{c}^{\dagger}_{\zeta}(z_2) \right\rangle_{\phi} \\ &+ \left\langle \mathcal{T}_{\mathcal{C}} \partial_{z_1} e^{-i \int_{z_1}^{t_0 - i\beta} \mathrm{d}z_3 \int_{\mathcal{C}} \mathrm{d}z_4 \hat{c}^{\dagger}_{\bar{\alpha}}(z_3) \phi_{\bar{\alpha},\bar{\beta}}(z_3,z_4) \hat{c}_{\bar{\beta}}(z_4)} \hat{c}_{\epsilon}(z_1) \hat{c}^{\dagger}_{\zeta}(z_2) \right\rangle_{\phi} \\ &= i \left\langle \mathcal{T}_{\mathcal{C}} S[\phi] \int_{\mathcal{C}} \mathrm{d}z_4 \; \phi_{\bar{\alpha},\bar{\beta}}(z_1,z_4) \left[\hat{c}^{\dagger}_{\bar{\alpha}}(z_1) \hat{c}_{\bar{\beta}}(z_4), \hat{c}_{\epsilon}(z_1) \right] \hat{c}^{\dagger}_{\zeta}(z_2) \right\rangle_{\phi} \\ &= \int_{\mathcal{C}} \mathrm{d}z_4 \; \phi_{\epsilon,\bar{\beta}}(z_1,z_4) \mathcal{G}^{\phi}_{\bar{\beta},\zeta}(z_4,z_2). \end{aligned} \tag{2.54}$$

In Eq. (2.54), the fact that

$$\partial_x \int_x^{x'} \mathrm{d}x'' f'(x'') = \partial_x \left[f(x') - f(x) \right] = -f'(x)$$

was put to use. One can omit the annihilation operator in the exponential of $S[\phi]$, since it anticommutes with $\hat{c}_{\epsilon}(z_1)$ and it is taken care of by the contour-ordering operator. One can also not care about the global sign when carrying over parts of $S[\phi]$ within the thermal average, since its arguments consist of an even number of field operators. According to Eqs. (2.51), (2.53) and (2.54), the equations of motion (2.50) become

$$\begin{aligned} i\partial_{z_1} \mathcal{G}^{\phi}_{\epsilon,\zeta}(z_1,z_2) - h_{\epsilon\bar{\beta}}(z_1,\bar{z}_2) \mathcal{G}^{\phi}_{\bar{\beta}\zeta}(\bar{z}_2,z_2) - \phi_{\epsilon,\bar{\beta}}(z_1,\bar{z}_2) \mathcal{G}^{\phi}_{\bar{\beta},\zeta}(\bar{z}_2,z_2) = \delta^{\mathcal{C}}(z_1,z_2)\delta_{\epsilon,\zeta} \\ - iV^{\bar{\gamma}\bar{\delta}}_{\epsilon\bar{\beta}}(z_1,\bar{z}_2,\bar{z}_3,\bar{z}_4) \left\langle \mathcal{T}_{\mathcal{C}} \hat{c}^{\dagger}_{\bar{\gamma}}(\bar{z}_2) \hat{c}_{\bar{\delta}}(\bar{z}_3) \hat{c}_{\bar{\beta}}(\bar{z}_4) \hat{c}^{\dagger}_{\zeta}(z_2) \right\rangle_{\phi}. \end{aligned} \tag{2.55}$$

Since all averages are expressed in the grand-canonical ensemble, the Matsubara part of the one-body term $h^{M}_{\alpha\beta}$ in Eq. (2.55) is normalized by the chemical potential, as is done in Eq. (2.10). By defining the noninteracting Green's function $\mathcal{G}^0$ like

$$\left[i\partial_{z_1} \delta_{\epsilon,\bar{\beta}} \delta(z_1,\bar{z}_2) - h_{\epsilon\bar{\beta}}(z_1,\bar{z}_2) \right] \mathcal{G}^{0}_{\bar{\beta},\zeta}(\bar{z}_2,z_2) = \delta^{\mathcal{C}}(z_1,z_2)\delta_{\epsilon,\zeta}, \tag{2.56}$$

the equations of motion (2.55) become

$$\begin{aligned} \left[\mathcal{G}^{0}_{\epsilon,\bar{\beta}}(z_1,\bar{z}_2)^{-1} - \phi_{\epsilon,\bar{\beta}}(z_1,\bar{z}_2) \right] \mathcal{G}^{\phi}_{\bar{\beta},\zeta}(\bar{z}_2,z_2) = \delta^{\mathcal{C}}(z_1,z_2)\delta_{\epsilon,\zeta} \\ - iV^{\bar{\gamma}\bar{\delta}}_{\epsilon\bar{\beta}}(z_1,\bar{z}_2,\bar{z}_3,\bar{z}_4) \left\langle \mathcal{T}_{\mathcal{C}} \hat{c}^{\dagger}_{\bar{\gamma}}(\bar{z}_2) \hat{c}_{\bar{\delta}}(\bar{z}_3) \hat{c}_{\bar{\beta}}(\bar{z}_4) \hat{c}^{\dagger}_{\zeta}(z_2) \right\rangle_{\phi}. \end{aligned} \tag{2.57}$$

The Dyson's equation (2.44) can be seen encoded in the equations of motion (2.57). To map it to the Dyson's equation, the term containing the four-point correlation function must satisfy

$$\Sigma^{\phi}_{\epsilon,\bar{\beta}}(z_1,\bar{z}_2) \mathcal{G}^{\phi}_{\bar{\beta},\zeta}(\bar{z}_2,z_2) = -iV^{\bar{\gamma}\bar{\delta}}_{\epsilon\bar{\beta}}(z_1,\bar{z}_2,\bar{z}_3,\bar{z}_4) \left\langle \mathcal{T}_{\mathcal{C}} \hat{c}^{\dagger}_{\bar{\gamma}}(\bar{z}_2) \hat{c}_{\bar{\delta}}(\bar{z}_3) \hat{c}_{\bar{\beta}}(\bar{z}_4) \hat{c}^{\dagger}_{\zeta}(z_2) \right\rangle_{\phi}. \tag{2.58}$$

The Equation (2.58) relates the one-particle propagator $\mathcal{G}$ and the self-energy Σ to the two-particle correlation function expressed as a four-point correlation function. It also is a cornerstone of Hedin's equations, like will be seen in Section 2.4, because it holds all the microscopic details of the interactions acting in the physical system. The four-point correlation function (2.58) can be replaced with Eq. (2.47) provided that the variables in Eq. (2.47) be traded off like follows: $(\gamma,z_4) \to (\bar{\gamma},\bar{z}_2)$, $(\delta,z_3) \to (\bar{\delta},\bar{z}_3)$, $(\epsilon,z_1) \to (\bar{\beta},\bar{z}_4)$ and $(\zeta,z_2) \to (\zeta,z_2)$. Then, by multiplying from the right the resulting expression by $\mathcal{G}^{-1}$ to isolate the self-energy Σ, one gets

$$\begin{aligned}
&\Sigma^{\phi}_{\epsilon,\zeta}(z_1,z_2) \\
&= V^{\bar{\gamma}\bar{\delta}}_{\epsilon\bar{\beta}}(z_1,\bar{z}_2,\bar{z}_3,\bar{z}_4)\Big[-i\mathcal{G}^{\phi}_{\bar{\delta},\bar{\gamma}}(\bar{z}_3,\bar{z}_2)\delta_{\bar{\beta},\zeta}\delta(\bar{z}_4,z_2) + i\mathcal{G}^{\phi}_{\bar{\beta},\bar{\gamma}}(\bar{z}_4,\bar{z}_2)\delta_{\bar{\delta},\zeta}\delta(\bar{z}_3,z_2) \\
&+ \mathcal{G}^{\phi}_{\bar{\beta},\bar{\alpha}}(\bar{z}_4,\bar{z}_5)\Gamma^{\phi}_{\bar{\alpha},\zeta;\bar{\theta},\bar{\omega}}(\bar{z}_5,z_2;\bar{z}_7,\bar{z}_8)\chi^{\phi}_{\bar{\theta},\bar{\omega};\bar{\gamma},\bar{\delta}}(\bar{z}_7,\bar{z}_8;\bar{z}_2,\bar{z}_3)\Big]. \qquad (2.59)
\end{aligned}$$

The self-energy is fully described by Eq. (2.59) and it composes one of the Hedin's equations that will be covered in Section 2.4. The first term in Eq. (2.59) is often coined the Hartree term and the second the Fock term. The last term contains all the information about the dynamics of correlations.

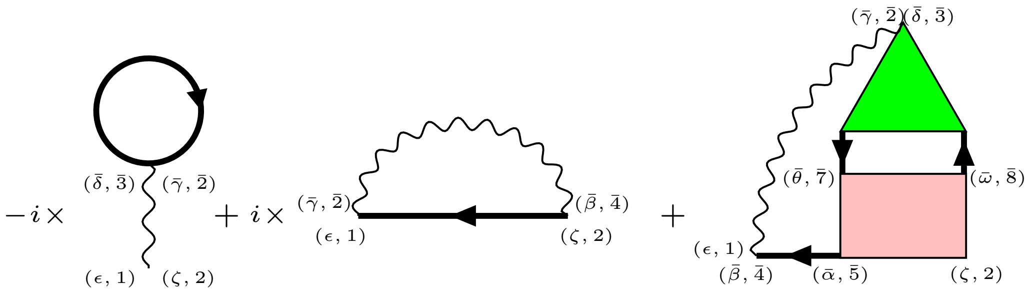

Figure 2.4: Diagrammatic representation of the self-energy (2.59). The wiggled line denotes a boson exchanged and the boxes have been defined in Fig. 2.3.

2.3.4 *Spectral functions*

The correlation functions Eqs. (2.25) and (2.46) contain information about the single-particle and two-particle excitation spectrum, respectively. The single-particle correlation function encapsulates the effect of the surrounding interacting particles onto a propagating particle as well as its feedback. On the other hand, the two-particle correlation function captures the collective modes of the system: it evaluates how two particles interact with each other in the course of their propagation through the interacting background.

To get the dynamical properties of a physical system, one must know how the system is initially prepared and how it evolves in time, *i.e* know the time-dependent Hamiltonian $\hat{\mathcal{H}}(t)$. As will be shown, the Lehmann representation of the correlation functions provides a transparent framework to calculate physical observables $\mathcal{O}$ and access spectral functions. It will motivate the spectral representation of Green's functions and clarify their purposes and properties. For instance, time-dependent observables can be expressed as

$$\mathcal{O}(t) = \mp i \sum_{\alpha,\beta} \mathcal{O}_{\alpha,\beta}\mathcal{G}^{<}_{\beta,\alpha}(t,t), \qquad (2.60)$$

with $\mathcal{G}^<(t_0,t_0) = \mathcal{G}^M(\tau-\tau^+)$. In general, the *lesser* component, which describes the propagation of electrons, reads

$$\mathcal{G}^<_{\alpha,\beta}(t,t') = \pm i \sum_k \rho_k \underbrace{\langle\Psi_k|\,\hat{\mathcal{U}}(t_0,t')\hat{c}^\dagger_\beta}_{\langle\Psi^L_k|}\underbrace{\hat{\mathcal{U}}(t',t)\hat{c}_\alpha\hat{\mathcal{U}}(t,t_0)\,|\Psi_k\rangle}_{|\Psi^R_k\rangle}, \tag{2.61}$$

Recall that the upper sign holds for fermions and the lower sign for bosons.

with the set $\{|\Psi_k\rangle\}$ representing the eigenstates of the equilibrium Hamiltonian $\hat{\mathcal{H}}^M$ with eigenvalues E_k. Thereof, the density matrix $\rho_k = e^{-\beta E_k}/\mathcal{Z}$. The evolution operators showing up in Eq. (2.61) are defined in Eq. (2.6). The *lesser* component (2.61) corresponds to the probability amplitude of finding a state that represents the annihilation of a particle with quantum number α in a state $\hat{\mathcal{U}}(t,t_0)\,|\Psi_k\rangle$ that has evolved from t_0 to t and then evolved from t to t' (described by the state $|\Psi^R_k\rangle$) resulting in a state that represents the annihilation of a particle with quantum number β in a state $\hat{\mathcal{U}}(t',t_0)\,|\Psi_k\rangle$ that has evolved from time t_0 to t' (described by the state $|\Psi^L_k\rangle$).

Another important Keldysh component, the *greater* component, which describes the propagation of holes, is defined as

$$\mathcal{G}^>_{\alpha,\beta}(t,t') = -i \sum_k \rho_k \underbrace{\langle\Psi_k|\,\hat{\mathcal{U}}(t_0,t)\hat{c}_\alpha}_{\langle\Psi^L_k|}\underbrace{\hat{\mathcal{U}}(t,t')\hat{c}^\dagger_\beta\hat{\mathcal{U}}(t',t_0)\,|\Psi_k\rangle}_{|\Psi^R_k\rangle}. \tag{2.62}$$

By breaking up the expectation value (2.62), it becomes clear that the *greater* component (2.62) bears a very similar meaning to the *lesser* component, although the annihilation operators $\hat{c}$ operating on the time-evolved equilibrium eigenstates $\{|\Psi_k\rangle\}$ are replaced with particle creation operators $\hat{c}^\dagger$. It is worthwhile pointing out that both the *lesser* (2.61) and *greater* (2.62) components obey the symmetry relation $\mathcal{G}^{>,<}_{\alpha,\beta}(t,t')^* = -\mathcal{G}^{>,<}_{\beta,\alpha}(t',t)$; this will allow, combined with the Heaviside function (Eq. (2.5)), to define a self-adjoint retarded spectral function the likes of Eq. (2.31). Let's now squeeze into Eq. (2.61) a closure relation over the set of eigenstates of $\hat{\mathcal{H}}^M$ $\{|\Psi_l\rangle\}$ and let's split up into two the unitary operator $\hat{\mathcal{U}}$ standing in the middle of the expectation values. This leads to

$$\begin{aligned}\mathcal{G}^<_{\alpha,\beta}(t,t') &= \pm i \sum_{kl} \rho_k \sum_{t''=t^+}^{t'} \langle\Psi_k|\,\hat{\mathcal{U}}(t_0,t')\hat{c}^\dagger_\beta\hat{\mathcal{U}}(t',t'')\,|\Psi_l\rangle\,\langle\Psi_l|\,\hat{\mathcal{U}}(t'',t)\hat{c}_\alpha\hat{\mathcal{U}}(t,t_0)\,|\Psi_k\rangle \\ &= \pm i \sum_{kl} \rho_k \sum_{t''=t^+}^{t'} \Psi^\beta_{kl}(t',t'')\Psi^\alpha_{kl}(t'',t)^*. \end{aligned} \tag{2.63}$$

The various elements are given some explanations to grasp their meaning. First, based off the equilibrium eigenstates, the expectation values $\Psi^{\beta(\alpha)}_{kl}$ evaluate the transition matrix elements between the state $|\Psi_l\rangle$ and a state characterized by the annihilation of a particle with quantum number $\beta(\alpha)$ after having evolved the state $|\Psi_k\rangle$ to time $t'(t)$, and then evolved with that one extra *hole* until time t''. Second, the expectation values Ψ can be considered as matrix elements in time and an effective partial matrix multiplication is carried out over time variable t'', ranging from t^+ to t', such as to ensure that all the intermediate times are accounted for. Third, since the boundaries of the time summation produce identical terms, one needs to start the summation at a time $t^+ = t + \delta t$ infinitesimally later than t ($\delta t \to 0^+$ here stands for the *smallest* time step). Finally, the

A hole describes the absence of an electron in the Fermi sea. It can be thought of as the antiparticle of the electron in condensed matter, to the extent that when it recombines with an electron, they both annihilate each other.

very same discussion easily carries over to $\mathcal{G}^{>}$ in Eq. (2.64), whose decomposition reads

$$\mathcal{G}^{>}_{\alpha,\beta}(t,t') = -i\sum_{kl}\rho_k \sum_{t''=t'^+}^{t} \Psi^{\alpha}_{kl}(t,t'')\Psi^{\beta}_{kl}(t'',t')^*. \tag{2.64}$$

Let's now tackle the forward partial Fourier representation of the retarded Green's function (2.30). Having in mind that the forward Fourier transform of $\Theta(t-t')$ gives

η is needed for the convergence of the integral.

$$\lim_{\eta\to 0^+}\int_{t'^+}^{\infty} \mathrm{d}t\; e^{i(\omega+i\eta)(t-t')}\Theta(t-t') = \lim_{\eta\to 0^+}\frac{i}{\omega+i\eta}, \tag{2.65}$$

the forward partial Fourier transformation

$$\mathcal{G}^{R}_{\alpha,\beta}(\omega,t') = \lim_{\eta\to 0^+}\int_{t'^+}^{\infty}\mathrm{d}t\; e^{i(\omega+i\eta)(t-t')}\Theta(t-t')\int_{-\infty}^{\infty}\mathrm{d}\omega'\; e^{-i\omega'(t-t')}\left[\mathcal{G}^{>}_{\alpha,\beta}(\omega',t') - \mathcal{G}^{<}_{\alpha,\beta}(\omega',t')\right] \tag{2.66}$$

leads to Eq. (2.30). One can infer the expressions of $\mathcal{G}^{<,>}(\omega',t')$ easily from Eq. (2.66)

$$\mathcal{G}^{>(<)}_{\alpha,\beta}(\omega',t') = \int_{t'^+(-\infty)}^{\infty(t'^+)}\mathrm{d}\bar{t}\; e^{i\omega'(\bar{t}-t')}\mathcal{G}^{>(<)}_{\alpha\beta}(\bar{t},t'), \tag{2.67}$$

and use Eqs. (2.63) and (2.64) to specify further Eq. (2.67). With the definition (2.29), the expression of $\mathcal{G}^R$ can be compressed down with the help of Eqs. (2.61) and (2.62) to give

$$\mathcal{G}^{R}_{\alpha,\beta}(t,t') = -i\theta(t-t')\langle\{\hat{c}_{\alpha}(t),\hat{c}^{\dagger}_{\beta}(t')\}\rangle, \tag{2.68}$$

with the angular brackets representing the thermodynamic ensemble average with respect to the equilibrium eigenstates $\{|\Psi_k\rangle\}$ and $\{\cdot,\cdot\}$ the anticommutator.

Further down below, the analytic properties of the numerator of Eq. (2.30) in the complex upper-half plane will allow one to systematically calculate spectral moments of the retarded Green's function. Specific details on how to carry out the contour integral in the complex plane are touched on in Appendix D.

SPECTRAL MOMENTS The focus here is turned to the expression delineating the forward Fourier transform of the retarded Green's function (2.30), from which the spectral moments can be generated systematically by integrating iteratively by parts. The leading terms of this development are

For conciseness, the limit over η has been dropped.

$$\begin{aligned}\mathcal{G}^R(\omega,t_2) &= \int_{t_2^+}^{\infty}\mathrm{d}t_1\; e^{i(\omega+i\eta)(t_1-t_2)}\mathcal{G}^R(t_1,t_2)\\ &= \frac{ie^{i(\omega+i\eta)0^+}\mathcal{G}^R(t_2^+,t_2)}{(\omega+i\eta)} - \frac{e^{i(\omega+i\eta)0^+}i\partial_{t_1}\mathcal{G}^R(t_1,t_2)\big|_{t_1=t_2^+}}{i\,(\omega+i\eta)^2}\\ &\quad - \frac{e^{i(\omega+i\eta)0^+}i^2\partial^2_{t_1}\mathcal{G}^R(t_1,t_2)\big|_{t_1=t_2^+}}{i\,(\omega+i\eta)^3} - \frac{1}{[i\,(\omega+i\eta)]^3}\int_{t_2^+}^{\infty}\mathrm{d}t_1\; e^{i(\omega+i\eta)(t_1-t_2)}\partial^3_{t_1}\mathcal{G}^R(t_1,t_2).\end{aligned} \tag{2.69}$$

The numerator of the first term in Eq. (2.69) simplifies to 1: that is the first moment of the retarded Green's functions and it is a direct consequence of the anti-commuting property of the fermionic field operators. The numerators of the succeeding terms comprising partial time derivative(s) can be expressed out in a more convenient form by employing once again Eq. (2.30):

$$\begin{aligned}
&i^n\partial^n_{t_1}\mathcal{G}^R(t_1,t_2)\big|_{t_1=t_2^+}\\
&=\lim_{\eta\to 0^+}\int_{-\infty}^{\infty}\mathrm{d}\omega\int_{-\infty}^{\infty}\mathrm{d}\omega'\; i^n\partial^n_{t_1}e^{-i(\omega+i\eta)(t_1-t_2)}\,\frac{i\left[\mathcal{G}^>(\omega',t_2)-\mathcal{G}^<(\omega',t_2)\right]}{\omega-\omega'+i\eta}\Bigg|_{t_1=t_2^+}\\
&=\lim_{\eta\to 0^+}\int_{-\infty}^{\infty}\mathrm{d}\omega\;(\omega+i\eta)^n\int_{-\infty}^{\infty}\mathrm{d}\omega'\;e^{-i(\omega+i\eta)0^+}\,\frac{i\left[\mathcal{G}^>(\omega',t_2)-\mathcal{G}^<(\omega',t_2)\right]}{\omega-\omega'+i\eta}\\
&=\pi\int_{-\infty}^{\infty}\mathrm{d}\omega\;\omega^n\left[\mathcal{G}^>(\omega,t_2)-\mathcal{G}^<(\omega,t_2)\right]. \qquad (2.70)
\end{aligned}$$

To get to the last line of Eq. (2.70), the Cauchy relation (D.9) derived in Appendix D was put to use – the numerator of the integrand was assumed to be holomorphic in the complex frequency upper half-plane. Results the likes of Eq. (2.70) that describe the spectral moments are derived in the Wigner representation in Ref. [139]. The imaginary number appearing in Eqs. (2.62) and (2.61) has not yet been canceled out in the numerator of the integrand of Eq. (2.70), thus the term within square brackets $[\cdots]$ has a $-i$ as factor (fermions). Finally, the retarded spectral moments μ^R are defined as, taking Eqs. (2.31) and (2.68) into account,

$$\begin{aligned}
\mu^R_n(t_2) &\equiv \int_{-\infty}^{\infty}\mathrm{d}\omega\;\omega^n\mathcal{A}^R(\omega,t_2)=i^n\partial^n_{t_1}\mathcal{A}^R(t_1,t_2)\big|_{t_1=t_2^+}\\
&=i^n\partial^n_{t_1}\langle\{\hat{c}(t_1),\hat{c}^\dagger(t_2)\}\rangle\big|_{t_1=t_2^+}. \qquad (2.71)
\end{aligned}$$

The *lesser* $\mu^<$ and *greater* $\mu^>$ spectral moments are obtained by simply replacing the retarded Keldysh component of the spectral function $\mathcal{A}$ in Eq. (2.71) with the corresponding Keldysh component. With Eq. (2.71) at hand, the spectral development (2.69) becomes

$$\mathcal{G}^R(\omega,t_2)=\sum_{n=0}^{\infty}\frac{\mu^R_n(t_2)}{(\omega+i\eta)^{n+1}}. \qquad (2.72)$$

Note that the retarded self-energy Σ^R shares the same analytical properties as the retarded Green's function in the complex frequency plane and it can therefore be represented as a series

$$\Sigma^R(\omega,t_2)=\sum_{n=0}^{\infty}\frac{\mu^{R'}_n(t_2)}{(\omega+i\eta)^n}, \qquad (2.73)$$

where this time the moments $\mu^{R'}$, defined just like Eq. (2.72) with $\mathcal{G}^R$ replaced by Σ^R, are those of the retarded self-energy. The self-energy (2.73) can have a contribution constant in frequency and it will be shown that it corresponds to the Hartree-Fock terms (see Eq. (2.59)). The combination of both Eqs. (2.72) and (2.73) enables oneself to deduce the moments $\mu^{R'}$. This will be done in Section 3.2.1.3 for the Hubbard model (3.9).

2.4 HEDIN'S EQUATIONS

The one-particle bosonic Green's function represents the interaction.

The Hedin's equations consist in a set of five coupled equations that builds off of the one-particle fermionic Green's function $\mathcal{G}$ (2.44), the self-energy Σ (2.59), the two-particle Green's function (susceptibility) χ (2.46), the one-particle bosonic Green's function W that needs yet to be defined, and finally the $\mathcal{G}$-skeletonic vertex function Γ. The Hedin's equations are a recasting of the latter equations that renders the self-energy $\mathcal{G}$- and W-skeletonic and the vertices two-particle irreducible and two-interaction line irreducible. The diagrammatic representation of the equations will facilitate the derivation of the full set of Hedin's equations.

To start off, the vertex Γ is computed from the self-energy (2.59), giving

$$\begin{aligned}\Gamma^{\phi}_{\epsilon,\zeta;\theta,\omega}(z_1,z_2;z_7,z_8) &= iV^{\bar{\gamma}\bar{\delta}}_{\epsilon\bar{\beta}}(z_1,\bar{z}_2,\bar{z}_3,\bar{z}_4)\delta_{\bar{\delta},\theta}\delta_{\bar{\gamma},\omega}\delta_{\bar{\beta},\zeta}\delta^{\mathcal{C}}(\bar{z}_4,z_2)\delta^{\mathcal{C}}(\bar{z}_3,z_7)\delta^{\mathcal{C}}(\bar{z}_2,z_8)\\
&- iV^{\bar{\gamma}\bar{\delta}}_{\epsilon\bar{\beta}}(z_1,\bar{z}_2,\bar{z}_3,\bar{z}_4)\delta_{\bar{\beta},\theta}\delta_{\bar{\gamma},\omega}\delta_{\bar{\delta},\zeta}\delta^{\mathcal{C}}(\bar{z}_3,z_2)\delta^{\mathcal{C}}(\bar{z}_4,z_7)\delta^{\mathcal{C}}(\bar{z}_2,z_8)\\
&- \frac{\delta\left(V^{\bar{\gamma}\bar{\delta}}_{\epsilon\bar{\beta}}(z_1,\bar{z}_2,\bar{z}_3,\bar{z}_4)\mathcal{G}^{\phi}_{\bar{\beta},\bar{\alpha}}(\bar{z}_4,\bar{z}_5)\Gamma^{\phi}_{\bar{\alpha},\zeta;\bar{\theta},\bar{\omega}}(\bar{z}_5,z_2;\bar{z}_7,\bar{z}_8)\chi^{\phi}_{\bar{\theta},\bar{\omega};\bar{\gamma},\bar{\delta}}(\bar{z}_7,\bar{z}_8;\bar{z}_2,\bar{z}_3)\right)}{\delta\mathcal{G}^{\phi}_{\theta,\omega}(z_7,z_8)},\end{aligned}\tag{2.74}$$

whose expression is diagrammatically illustrated by Fig. 2.5. The last two terms in Eq. (2.74) can be grouped together so as to give

$$\Gamma^{\phi}_{\epsilon,\zeta;\theta,\omega}(z_1,z_2;z_7,z_8) = iV^{\omega\theta}_{\epsilon\zeta}(z_1,z_8,z_7,z_2) + \tag{2.75}$$

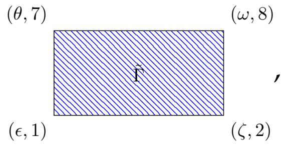

where the Hartree interaction line in Eq. (2.74) is singled out, having gathered the rest under the blue hatched box $\tilde{\Gamma}$.

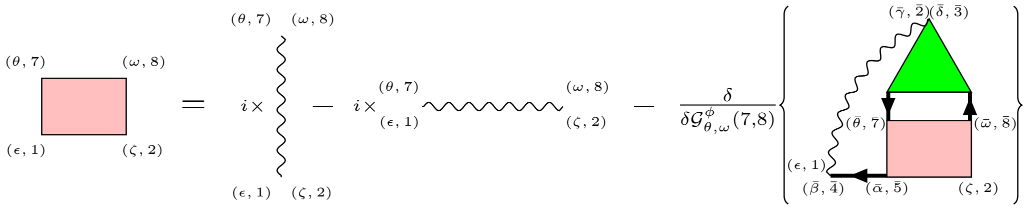

Figure 2.5: Diagrammatic representation of the $\mathcal{G}$-skeletonic two-particle irreducible vertex Γ. The last two terms make up $\tilde{\Gamma}$, denoted as a blue hatched box.

Due to the fact that Γ appears in the two-particle Green's function (2.46) (Fig. 2.3), the recasting of Γ (2.75) can be expanded within:

$$\begin{aligned}\chi^{\phi}_{\epsilon,\zeta;\gamma,\delta}(z_1,z_2;z_4,z_3) &= -i\mathcal{G}^{\phi}_{\epsilon,\gamma}(z_1,z_4)\mathcal{G}^{\phi}_{\delta,\zeta}(z_3,z_2)\\
&- i\mathcal{G}^{\phi}_{\epsilon,\bar{\alpha}}(z_1,\bar{z}_5)V^{\bar{\omega}\bar{\theta}}_{\bar{\alpha}\bar{\eta}}(\bar{z}_5,\bar{z}_8,\bar{z}_7,\bar{z}_6)\chi^{\phi}_{\bar{\theta},\bar{\omega};\gamma,\delta}(\bar{z}_7,\bar{z}_8;z_4,z_3)\mathcal{G}^{\phi}_{\bar{\eta},\zeta}(\bar{z}_6,z_2)\\
&- \mathcal{G}^{\phi}_{\epsilon,\bar{\alpha}}(z_1,\bar{z}_5)\tilde{\Gamma}^{\phi}_{\bar{\alpha},\bar{\eta};\bar{\theta},\bar{\omega}}(\bar{z}_5,\bar{z}_6;\bar{z}_7,\bar{z}_8)\chi^{\phi}_{\bar{\theta},\bar{\omega};\gamma,\delta}(\bar{z}_7,\bar{z}_8;z_4,z_3)\mathcal{G}^{\phi}_{\bar{\eta},\zeta}(\bar{z}_6,z_2).\end{aligned}\tag{2.76}$$

The equation (2.76) is diagrammatically represented by Fig. 2.6 and it will be useful later on to define the two-particle and two-interaction line irreducible vertex function Λ. Since the two-particle irreducible $\mathcal{G}$-skeletonic vertex function Γ appears also in the self-energy (2.59), the expression (2.75) can be developed in the self-energy to give

$$\begin{aligned}\Sigma^{\phi}_{\epsilon,\zeta}(z_1,z_2) &= -iV^{\bar{\gamma}\bar{\delta}}_{\epsilon\zeta}(z_1,\bar{z}_2,\bar{z}_3,z_2)\mathcal{G}^{\phi}_{\bar{\delta},\bar{\gamma}}(\bar{z}_3,\bar{z}_2) + iV^{\bar{\gamma}\zeta}_{\epsilon\bar{\beta}}(z_1,\bar{z}_2,z_2,\bar{z}_4)\mathcal{G}^{\phi}_{\bar{\beta},\bar{\gamma}}(\bar{z}_4,\bar{z}_2)\\ &+ iV^{\bar{\gamma}\bar{\delta}}_{\epsilon\bar{\beta}}(z_1,\bar{z}_2,\bar{z}_3,\bar{z}_4)\mathcal{G}^{\phi}_{\bar{\beta},\bar{\alpha}}(\bar{z}_4,\bar{z}_5)V^{\bar{\omega}\bar{\theta}}_{\bar{\alpha}\zeta}(\bar{z}_5,\bar{z}_8,\bar{z}_7,z_2)\chi^{\phi}_{\bar{\theta},\bar{\omega};\bar{\gamma},\bar{\delta}}(\bar{z}_7,\bar{z}_8;\bar{z}_2,\bar{z}_3)\\ &+ V^{\bar{\gamma}\bar{\delta}}_{\epsilon\bar{\beta}}(z_1,\bar{z}_2,\bar{z}_3,\bar{z}_4)\mathcal{G}^{\phi}_{\bar{\beta},\bar{\alpha}}(\bar{z}_4,\bar{z}_5)\tilde{\Gamma}^{\phi}_{\bar{\alpha},\zeta;\bar{\theta},\bar{\omega}}(\bar{z}_5,z_2;\bar{z}_7,\bar{z}_8)\chi^{\phi}_{\bar{\theta},\bar{\omega};\bar{\gamma},\bar{\delta}}(\bar{z}_7,\bar{z}_8;\bar{z}_2,\bar{z}_3). \end{aligned} \tag{2.77}$$

The equation (2.77) is shown in terms of Feynman diagrams in Fig. 2.7.

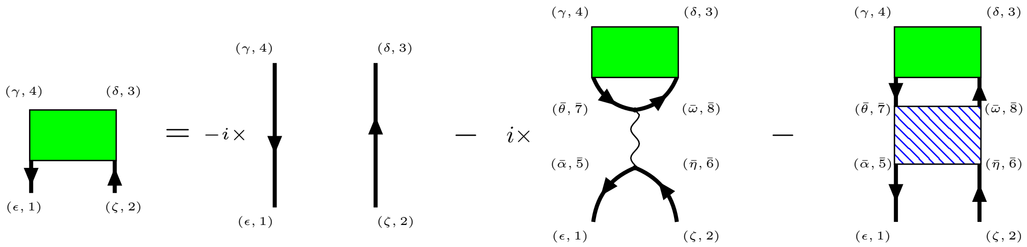
$(\gamma,4)$
$(\delta,3)$
$(\epsilon,1)$
$(\zeta,2)$
$= -i\times$
$(\gamma,4)$
$(\delta,3)$
$(\epsilon,1)$
$(\zeta,2)$
$- \quad i\times$
$(\gamma,4)$
$(\delta,3)$
$(\bar{\theta},\bar{7})$
$(\bar{\omega},\bar{8})$
$(\bar{\alpha},\bar{5})$
$(\bar{\eta},\bar{6})$
$(\epsilon,1)$
$(\zeta,2)$
$-$
$(\gamma,4)$
$(\delta,3)$
$(\bar{\theta},\bar{7})$
$(\bar{\omega},\bar{8})$
$(\bar{\alpha},\bar{5})$
$(\bar{\eta},\bar{6})$
$(\epsilon,1)$
$(\zeta,2)$

Figure 2.6: Diagrammatic representation of the Bethe-Salpeter equation (2.46) into which Γ has been substituted by Eq. (2.75).

In the expanded expression of the self-energy (2.77), the third term outlines how the screened interaction W should look like. The equation defining W will be laid out further down. It is important to recall that Eq. (2.75) states that the bare Fock term is included in $\tilde{\Gamma}$, and not the bare Hartree term – the bare Hartree term is inserted in Fig. 2.4 leading to the third term.

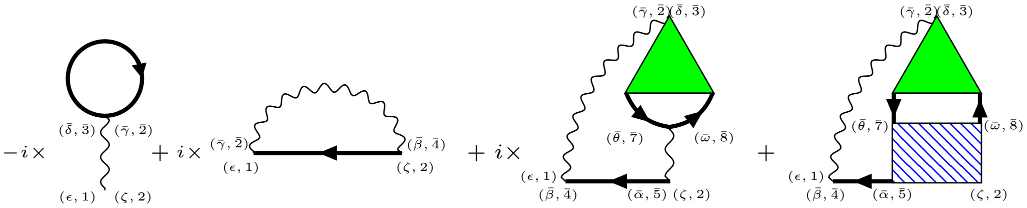
$-i\times$
$(\bar{\delta},\bar{3})$
$(\bar{\gamma},\bar{2})$
$(\epsilon,1)$
$(\zeta,2)$
$+\ i\times$
$(\bar{\gamma},\bar{2})$
$(\bar{\beta},\bar{4})$
$(\epsilon,1)$
$(\zeta,2)$
$+\ i\times$
$(\bar{\gamma},\bar{2})(\bar{\delta},\bar{3})$
$(\bar{\theta},\bar{7})$
$(\bar{\omega},\bar{8})$
$(\epsilon,1)$
$(\bar{\beta},\bar{4})$
$(\bar{\alpha},\bar{5})$
$(\zeta,2)$
$+$
$(\bar{\gamma},\bar{2})(\bar{\delta},\bar{3})$
$(\bar{\theta},\bar{7})$
$(\bar{\omega},\bar{8})$
$(\epsilon,1)$
$(\bar{\beta},\bar{4})$
$(\bar{\alpha},\bar{5})$
$(\zeta,2)$

Figure 2.7: Digrammatic representation of the self-energy (2.77) whose Γ has been split apart according to Eq. (2.75). The third term generates the class of *rainbow* diagrams by iterating through χ (see Eq. (2.77)).

Let's now consider Eq. (2.7) without the Hartree term (first term). If one removes the two Green's function lines at the bottom of all the diagrams in Fig. 2.6, then one would realise that each of the resulting terms appear as vertices at the right end of the last three terms in Fig. 2.7. The removal of those two $\mathcal{G}$-legs ushers in a new collection of terms, denoted $\tilde{\Lambda}$, and they read

$$\begin{aligned}&\tilde{\Lambda}^{\phi}_{\epsilon,\zeta;\gamma,\delta}(z_1,z_2;z_4,z_3)\\ &= \boxed{-i\delta^{\mathcal{C}}(z_1,z_4)\delta^{\mathcal{C}}(z_3,z_2)\delta_{\epsilon,\gamma}\delta_{\delta,\zeta}} - iV^{\bar{\omega}\bar{\theta}}_{\epsilon\zeta}(z_1,\bar{z}_8,\bar{z}_7,z_2)\chi^{\phi}_{\bar{\omega},\bar{\theta};\gamma,\delta}(\bar{z}_7,\bar{z}_8;z_4,z_3)\\ &- \boxed{\tilde{\Gamma}^{\phi}_{\epsilon,\zeta;\bar{\theta},\bar{\omega}}(z_1,z_2;\bar{z}_7,\bar{z}_8)\chi^{\phi}_{\bar{\theta},\bar{\omega};\gamma,\delta}(\bar{z}_7,\bar{z}_8;z_4,z_3)}. \end{aligned} \tag{2.78}$$

The boxed terms in Eq. (2.78) are the only fully irreducible terms upon iterating and they constitute the fully irreducible vertex Λ, shown in Fig. 2.8. The full irreducibility means that the set of equations are irreducible with respect to cutting two interacting Green's functions and two interaction lines, and this applies to the particle-hole and particle-particle channels.

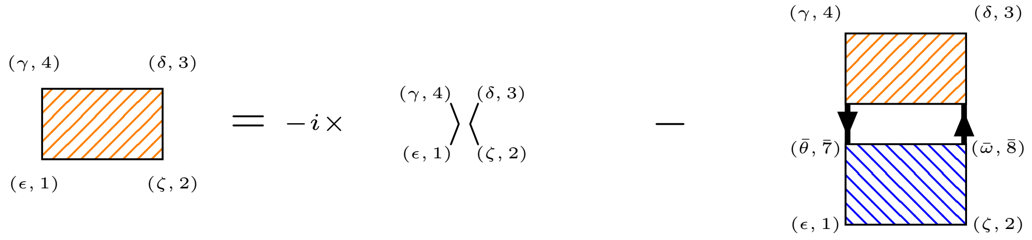
$(\gamma,4)$
$(\delta,3)$
$(\epsilon,1)$
$(\zeta,2)$
$= -i\times$
$(\gamma,4)$
$(\delta,3)$
$(\epsilon,1)$
$(\zeta,2)$
$-$
$(\gamma,4)$
$(\delta,3)$
$(\bar\theta,\bar 7)$
$(\bar\varpi,\bar 8)$
$(\epsilon,1)$
$(\zeta,2)$

Figure 2.8: Fully irreducible vertex Λ (orange box) illustrated in terms of diagrams. The blue box is defined in Fig. 2.75.

The attention is now turned to the sole term not boxed in Eq. (2.78), namely the class of rainbow diagrams. Looking back at Fig. 2.6, one can see that rainbow terms can be self-consistently generated by iterating through all the terms making up χ, *i.e.* by inserting self-consistently the content of χ (green box) into itself. Therein, by construction, the vertex of the set of rainbow diagrams boils down to this integral equation

$$\begin{aligned} & W^{\phi}_{\epsilon,\zeta;\gamma,\delta}(z_1,z_2;z_4,z_3) = iV^{\delta\gamma}_{\epsilon\zeta}(z_1,z_3;z_4,z_2) \\ & + V^{\bar\lambda\bar\iota}_{\epsilon\zeta}(z_1,\bar z_{11},\bar z_9,z_2)\mathcal{G}^{\phi}_{\bar\iota,\bar\nu}(\bar z_9,\bar z_{14})\mathcal{G}^{\phi}_{\bar\rho,\bar\lambda}(\bar z_{13},\bar z_{11})\Lambda^{\phi}_{\bar\nu,\bar\rho;\bar\kappa,\bar\mu}(\bar z_{14},\bar z_{13};\bar z_{10},\bar z_{12}) \\ & \times W^{\phi}_{\bar\kappa,\bar\mu;\gamma,\delta}(\bar z_{10},\bar z_{12};z_4,z_3), \end{aligned} \tag{2.79}$$

corresponding to the aforementioned interacting one-particle bosonic Green's function. The screened potential (2.79), shown in Fig. 2.9, is comprised of the fully irreducible vertex function Λ represented in Fig. 2.8.

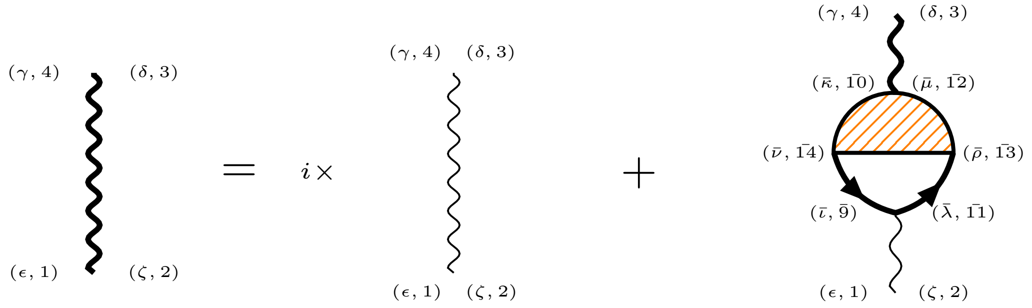
$(\gamma,4)$
$(\delta,3)$
$(\epsilon,1)$
$(\zeta,2)$
$=$
$i\times$
$(\gamma,4)$
$(\delta,3)$
$(\epsilon,1)$
$(\zeta,2)$
$+$
$(\gamma,4)$
$(\delta,3)$
$(\bar\kappa,\bar{10})$
$(\bar\mu,\bar{12})$
$(\bar\nu,\bar{14})$
$(\bar\rho,\bar{13})$
$(\bar\iota,\bar 9)$
$(\bar\lambda,\bar{11})$
$(\epsilon,1)$
$(\zeta,2)$

Figure 2.9: Diagrammatic representation of the screened potential (2.79).

From Eq. (2.79) can be defined the polarization Π:

$$\Pi^{\phi}_{\epsilon,\zeta;\gamma,\delta}(z_1,z_2;z_4,z_3) = \mathcal{G}^{\phi}_{\epsilon,\bar\nu}(z_1,\bar z_{14})\mathcal{G}^{\phi}_{\bar\rho,\zeta}(\bar z_{13},z_2)\Lambda^{\phi}_{\bar\nu,\bar\rho;\gamma,\delta}(\bar z_{14},\bar z_{13};z_4,z_3). \tag{2.80}$$

To sum up, the screened potential W defined in Eq. (2.79) takes care of the rainbow-type vertices in the self-energy[2] (2.77) and the fully irreducible vertex Λ defined in Eq. (2.78) (boxed terms) takes care of the remaining terms. The three last terms composing the self-energy (2.77) can be merged to give an expression of the self-energy that is skeletonic in both $\mathcal{G}$ and W, disregarding the Hartree term:

---

[2] See the third term in Fig. 2.7.

$$\begin{aligned}\Sigma^{\phi}_{\epsilon,\zeta}(z_1,z_2) &= -iV^{\bar{\gamma}\bar{\delta}}_{\epsilon\zeta}(z_1,\bar{z}_2,\bar{z}_3,z_2)\mathcal{G}^{\phi}_{\bar{\delta},\bar{\gamma}}(\bar{z}_3,\bar{z}_2)\\ &+ iW^{\phi}_{\epsilon,\bar{\beta};\bar{\gamma},\bar{\delta}}(z_1,\bar{z}_4;\bar{z}_2,\bar{z}_3)\mathcal{G}^{\phi}_{\bar{\beta},\bar{\alpha}}(\bar{z}_4,\bar{z}_5)\Lambda^{\phi}_{\bar{\alpha},\zeta;\bar{\gamma},\bar{\delta}}(\bar{z}_5,z_2;\bar{z}_2,\bar{z}_3). \qquad (2.81)\end{aligned}$$

The equation (2.81) is illustrated in Fig. 2.10. For instance, the Fock term can be easily generated from Eq. (2.81) by using the first-order terms of both Λ and W.

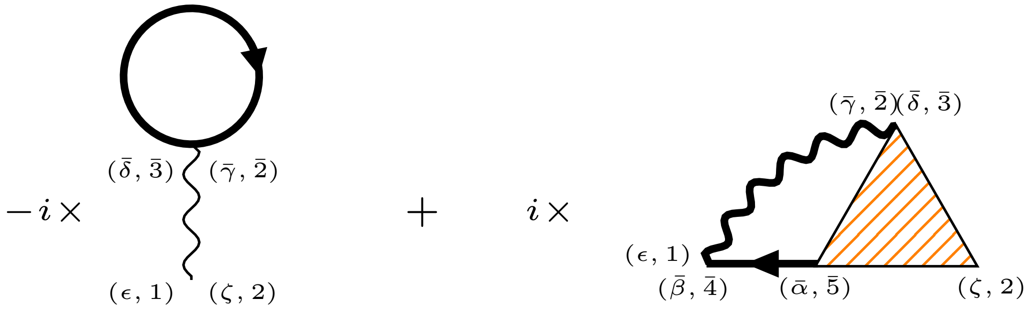

Figure 2.10: $\mathcal{G}$- and W-skeletonic self-energy.

The set of Eqs. (2.81), (2.79), (2.78) (boxed terms), (2.80) and (2.44) altogether constitute the Hedin's equations, which will be used later on. The Hedin's equation will provide the systematic guideline to express the class of relevant diagrams that embody the physical processes in the neighbourhood of a anti-ferromagnetic phase instability, and this will be done in Chapter 4. The irreducible vertices that will appear in TPSC (and variants) in Section 5.1 are only $\mathcal{G}$-skeletonic, and will therefore be denoted by Γ.

2.5 FERMIONIC PATH INTEGRALS IN A NUTSHELL

The path integral formalism is designed to deal with fermionic systems containing an *infinite* number of identical particles. It harnesses the algebra of anticommuting generators, called Grassmann algebra, and the properties of Gaussian integrals to recast the partition function (2.24) ($\phi \to 0$). The Grassmann fields (generators) are homomorphic to the ladder operators introduced in Section 2.1 and obey the anti-periodic boundary conditions in imaginary time (2.34). Within this formalism, the equations of motion describing the dynamics of the system are obtained via the stationary phase principle.

The path integral formalism will be mainly useful to derive the DMFT equations in Section 3.2. The properties of interest of the Grassmann algebra are first set out in Section 2.5.1 and Section 2.5.2. The goal is then to represent the path integral of a generic system hybridizing two disjoint Hilbert spaces; one depicting the local finite degrees of freedom of the fields and the other the continuum to which it is coupled. This is done in Section 2.5.3. This is crucial in the formulation of DMFT [43, 44] and its extensions that capture the nonlocal correlations [103].

2.5.1 *Grassmann algebra*

The Grassmann algebra is introduced in the context of coherent fermion states and a detailed and comprehensive review is given in Ref. [95]. A Grassmann algebra consists of a set of generators $\{\eta_i, \eta_i^*\}$, $i \in \mathbb{Z}$, that anticommutes with each other

$$\begin{cases} \eta_i^{(*)}\eta_j^{(*)} + \eta_j^{(*)}\eta_i^{(*)} = 0 \\ \eta_i^{(*)}\eta_j + \eta_j^{(*)}\eta_i = 0, \end{cases} \tag{2.82}$$

$\forall\, i, j = 1, \cdots, n$. The unit (identity) generator is denoted 1. The generators η and η^* are conjugate from one another,

The operation of conjugation $(*)$ is linear and involutive.

$$(\lambda \eta_i \eta_j^*)^* = \lambda^* \eta_j \eta_i^*, \quad \forall\, \lambda \in \mathbb{C}.$$

Under multiplication, the *element* $1 + \eta_i^{(*)}$ is the inverse of $1 - \eta_i^{(*)}$. The integral and differential calculus is also defined over the field of Grassmann operators. The partial derivatives obey

$$\begin{cases} \frac{\partial}{\partial \eta_i}\frac{\partial}{\partial \eta_j} + \frac{\partial}{\partial \eta_j}\frac{\partial}{\partial \eta_i} = 0 \\ \eta_i \frac{\partial}{\partial \eta_j} + \frac{\partial}{\partial \eta_j}\eta_i = \delta_{i,j}. \end{cases} \tag{2.83}$$

Eq. (2.83) is valid for any combination of generators in the set $\{\eta_k, \eta_k^*\}$. The differential operator is therefore nilpotent just like the generators $\eta_i^{(*)}$, *i.e.* $\left(\eta_i^{(*)}\right)^2 = 0$ according to relations (2.82). The identities (2.83) can be easily verified when acting them upon general functions

$$f(\eta_i, \eta_j; \{\eta\}) = 1 + \eta_i \lambda(\{\eta\}) + \eta_j \gamma(\{\eta\}) + \eta_i \eta_j \omega(\{\eta\}), \tag{2.84}$$

with λ, γ and ω general functions of generators $\eta_{k \neq i,j}$. For closedness of the algebra, the integral operator is defined to be the *same* as the differential one (equivalent for any combination of η_i and η_i^*):

$$\begin{cases} \frac{\partial}{\partial \eta_i}\eta_j^* \eta_i = \int \mathrm{d}\eta_i \; \eta_j^* \eta_i = -\eta_j^* \\ \frac{\partial}{\partial \eta_i} 1 = \int \mathrm{d}\eta_i \; 1 = 0. \end{cases} \tag{2.85}$$

There is therefore no metric in Grassmann algebra.

2.5.2 *Coherent states*

The fermionic coherent states consist in an over-complete set of Grassmann vectors $\{|\eta\rangle\}$ that spans over the Fock space, meaning that any many-particle state $|\Psi\rangle$ can be expanded over the former set, with Grassmann generators η as coefficients. These coefficients η turn out to be the eigenvalues to the ladder operator $\hat{c}$, with $|\eta\rangle$ the eigenvectors

$$\hat{c}_\alpha |\eta\rangle = \eta_\alpha |\eta\rangle, \tag{2.86}$$

if the eigenvectors read

$$|\eta\rangle = e^{-\sum_\alpha \eta_\alpha \hat{c}^\dagger_\alpha} |0\rangle = \prod_\alpha (1 - \eta_\alpha \hat{c}^\dagger_\alpha) |0\rangle , \tag{2.87}$$

where $|0\rangle$ denotes the void and α arbitrary degrees of freedom characterizing the fields. Note that the ladder operators $\hat{c}^{(\dagger)}$ anticommute with the Grassmann generators η in the same way Grassmann generators anticommute (Eq. (2.82)). The adjoint of Eq. (2.87) simply gives

$$\langle\eta| = \langle 0| e^{-\sum_\alpha \hat{c}_\alpha \eta^*_\alpha} = \langle 0| \prod_\alpha (1 - \hat{c}_\alpha \eta^*_\alpha) , \tag{2.88}$$

such that the overlap $\langle\eta|\eta\rangle$ gives, taking into account that $\eta_\alpha \hat{c}_\alpha$ commutes with $\eta_\beta \hat{c}^\dagger_\beta$, $\forall\, \alpha \neq \beta$,

$$\begin{aligned}\langle\eta|\eta\rangle &= \langle 0| \prod_\alpha (1 + \eta^*_\alpha \hat{c}_\alpha) \prod_\beta (1 - \eta_\beta \hat{c}^\dagger_\beta) |0\rangle = \langle 0| \prod_\alpha (1 + \eta^*_\alpha \hat{c}_\alpha)(1 - \eta_\alpha \hat{c}^\dagger_\alpha) |0\rangle \\ &= \prod_\alpha \langle 0| 1 + \eta^*_\alpha \eta_\alpha \hat{c}_\alpha \hat{c}^\dagger_\alpha |0\rangle = e^{\sum_\alpha \eta^*_\alpha \eta_\alpha} . \end{aligned} \tag{2.89}$$

The eigenvalue problem (2.86) can be straightforwardly verified using the algebraic properties laid out in Section 2.5.1:

$$\begin{aligned}\hat{c}_{\alpha'} |\eta\rangle &= \prod_{\alpha\neq\alpha'} (1 - \eta_\alpha \hat{c}^\dagger_\alpha) \hat{c}_{\alpha'} (1 - \eta_{\alpha'} \hat{c}^\dagger_{\alpha'}) |0\rangle = \prod_{\alpha\neq\alpha'} (1 - \eta_\alpha \hat{c}^\dagger_\alpha) \eta_{\alpha'} (1 - \hat{c}^\dagger_{\alpha'} \hat{c}_{\alpha'}) |0\rangle \\ &= \prod_{\alpha\neq\alpha'} (1 - \eta_\alpha \hat{c}^\dagger_\alpha) \eta_{\alpha'} (1 - \eta_{\alpha'} \hat{c}^\dagger_{\alpha'}) |0\rangle = \eta_{\alpha'} |\eta\rangle , \end{aligned} \tag{2.90}$$

where the anticommutation relations $\{\hat{c}^\dagger_{\alpha'}, \hat{c}_{\alpha'}\} = \delta_{\alpha,\alpha'}$ have been used. From Eq. (2.88) it is easy to show the adjoint relation $\langle\eta| \hat{c}^\dagger_{\alpha'} = \langle\eta| \eta^*_{\alpha'}$. Also, by applying $\hat{c}^\dagger_{\alpha'}$ onto the coherent state (2.87), one can verify that $\hat{c}^\dagger_{\alpha'} |\eta\rangle = -\frac{\partial}{\partial \eta_{\alpha'}} |\eta\rangle$ and, therefore, $\langle\eta| \hat{c}_{\alpha'} = -\langle\eta| \frac{\overleftarrow{\partial}}{\partial \eta^*_{\alpha'}}$. To conclude, according to the inner product (2.89), the closure relation onto the coherent states of the Fock space reads

$$\int \prod_\alpha \mathrm{d}\eta^*_\alpha \mathrm{d}\eta_\alpha e^{-\sum_\alpha \eta^*_\alpha \eta_\alpha} |\eta\rangle \langle\eta| = \hat{1} . \tag{2.91}$$

As a consequence, the inner product between two functions g and f of the form (2.84) together with partial integration leads to

$$\begin{aligned} f \cdot \frac{\partial g}{\partial \eta} &= \int \prod_\alpha \mathrm{d}\eta^*_\alpha \mathrm{d}\eta_\alpha e^{-\sum_\alpha \eta^*_\alpha \eta_\alpha} f(\{\eta_\alpha\})^* \frac{\partial g(\{\eta_\alpha\})}{\partial \eta_{\alpha'}} \\ &= \int \prod_\alpha \mathrm{d}\eta^*_\alpha \mathrm{d}\eta_\alpha e^{-\sum_\alpha \eta^*_\alpha \eta_\alpha} f(\{\eta_\alpha\})^* \eta^*_{\alpha'} g(\{\eta_\alpha\}) = (\eta f) \cdot g , \end{aligned} \tag{2.92}$$

where the fact that

$$\frac{\partial}{\partial \eta} e^{-\eta^* \eta} g(\{\eta\}) = e^{-\eta^* \eta} \left(\frac{\partial g(\{\eta\})}{\partial \eta} + \eta^* g(\{\eta\}) \right)$$

was put to use. Eq. (2.92) means that in the Grassmann algebras the generators η_α are hermitian conjugates to the derivatives $\frac{\partial}{\partial \eta_\alpha}$. This dual relation replaces that between the canonical momentum and position operators and it will be clearer in Section 2.5.3.

2.5.3 *Path integral of hybridized quantum systems*

The path integral expression for a system coupling two distinct Fock spaces $\{|\eta\rangle\}$ and $\{|\xi\rangle\}$ is derived. The general Hamiltonian describing this set-up is

$$\hat{\mathcal{H}}(t) = \\ \hat{\mathcal{H}}_{\text{loc}}[\hat{c}_\sigma^\dagger,\hat{c}_\sigma](t) + \sum_{\alpha,\sigma}\iint \text{d}t\text{d}t' \left(\Theta_{\sigma,\alpha}(t,t')\hat{c}_\sigma^\dagger(t)\hat{b}_\alpha(t') + \text{H.c.}\right) + \sum_\alpha \epsilon_\alpha \hat{b}_\alpha^\dagger\hat{b}_\alpha, \quad (2.93)$$

where the ladder operators $\hat{c}_\sigma^{(\dagger)}$ annihilate (create) a fermion of quantum numbers σ in the Fock space $\mathfrak{F}(\{|\eta\rangle\})$ and the ladder operators $\hat{b}^{(\dagger)}$ annihilate (create) a fermion with quantum numbers α in $\mathfrak{F}(\{|\xi\rangle\})$. The term Θ is a complex number that couples the two disjoint Fock spaces: it represents the transition probability whereby a particle is removed at time t' from $\mathfrak{F}(\{|\xi\rangle\})$ to be created at time t in $\mathfrak{F}(\{|\eta\rangle\})$. The hermitian conjugate, denoted "H.c." in Eq. (2.93), denotes the reverse process. The Hamiltonian $\hat{\mathcal{H}}_{\text{loc}}$ describes the physics taking place in $\mathfrak{F}(\{|\eta\rangle\})$ whereas the last term in Eq. (2.93) sets forth the energy spectrum ϵ_α of the noninteracting particles existing in $\mathfrak{F}(\{|\xi\rangle\})$. The Hamiltonian component acting in $\mathfrak{F}(\{|\xi\rangle\})$ is static and can be seen as the environment embedding $\mathfrak{F}(\{|\eta\rangle\})$. The complete Fock space of the physical system delineated by the Hamiltonian (2.93) is a direct product of the two disjoint Fock spaces: $\{|\eta,\xi\rangle\} = \{|\eta\rangle \otimes |\xi\rangle\}$.

Let's now turn to the contour-time evolution operators (2.14). Since they make up a semi-group, closure relations the likes of (2.91) can be squeezed in to ramify their matrix elements:

$$\left\langle \eta_{\sigma',f},\xi_{\alpha',f}\right| \hat{U}(t_0 - i\beta, t_0) \left|\eta_{\sigma,0},\xi_{\alpha,0}\right\rangle = \\ \lim_{n\to\infty}\int \prod_{k=1}^{n-1}\prod_{\alpha,\sigma} \text{d}\eta_{\sigma,k}^*\text{d}\eta_{\sigma,k}\text{d}\xi_{\alpha,k}^*\text{d}\xi_{\alpha,k} e^{-\sum_{k=1}^{n-1}\sum_\sigma \eta_{\sigma,k}^*\eta_{\sigma,k}} e^{-\sum_{k=1}^{n-1}\sum_\alpha \xi_{\alpha,k}^*\xi_{\alpha,k}} \\ \times \left\langle \eta_{\sigma',f},\xi_{\alpha',f}\right| \hat{U}(z_f, z_{n-1}) \left|\eta_{\sigma,n-1},\xi_{\alpha,n-1}\right\rangle \left\langle \eta_{\sigma,n-1},\xi_{\alpha,n-1}\right| \hat{U}(z_{n-1},z_{n-2}) \cdots \left|\eta_1,\xi_1\right\rangle \\ \times \left\langle \eta_{\sigma,1},\xi_{\alpha,1}\right| \hat{U}(z_1,z_0) \left|\eta_{\sigma,0},\xi_{\alpha,0}\right\rangle, \quad (2.94)$$

where the initial state is denoted $|\eta_{\sigma,0},\xi_{\alpha,0}\rangle$ and the final state $\left|\eta_{\sigma,f},\xi_{\alpha,f}\right\rangle$. The contour-times $z_f = t_0 - i\beta$ and $z_0 = t_0$. In Eq. (2.94), the Trotter-Suzuki decomposition was used to split up into $n-1$ parts the integral domain in the argument of the complex exponential defining $\hat{U}$. Among these $n-1$ parts, N_τ lie along the imaginary-time axis and N lie along the real axis. Indeed, according to the Baker-Hausdorff formula, when $N \to \infty$, the error ensuing this decomposition vanishes, since it scales like $\mathcal{O}\left(\frac{t_f - t_0}{N^2}\right)$ – on the imaginary-time axis the Hamiltonian is time-translational invariant and therefore commutes at any time τ, but it doesn't necessarily hold on the real-axis for (2.93) at different times, *i.e.* $[\hat{\mathcal{H}}(t),\hat{\mathcal{H}}(t')] \neq 0, \forall\, t \neq t'$. The matrix element can be simplified further by substituting $\hat{U}$ and by utilizing the result (2.89). It gives

The contour-time integral subscript $\mathcal{C}$ has been dropped out to enlighten the equations.

$$\begin{aligned}&\left\langle \eta_{\sigma',f},\xi_{\alpha',f}\right|\hat{U}(z_f,z_0)\left|\eta_{\sigma,0},\xi_{\alpha,0}\right\rangle = \\ &\lim_{n\to\infty}\int\prod_{k=1}^{n-1}\prod_{\alpha,\sigma}\mathrm{d}\eta^*_{\sigma,k}\mathrm{d}\eta_{\sigma,k}\mathrm{d}\xi^*_{\alpha,k}\mathrm{d}\xi_{\alpha,k}\boxed{e^{-\sum_{k=1}^{n-1}\sum_\sigma\eta^*_{\sigma,k}\eta_{\sigma,k}}}\boxed{e^{-\sum_{k=1}^{n-1}\sum_\alpha\xi^*_{\alpha,k}\xi_{\alpha,k}}} \\ &\times e^{-i\int\mathrm{d}z\hat{\mathcal{H}}_{\mathrm{loc}}[\eta^*,\eta](z)-i\sum_{\alpha,\sigma}\iint\mathrm{d}z\mathrm{d}z'(\Theta_{\sigma,\alpha}(z,z')\eta^*_\sigma(z)\xi_\alpha(z')+\mathrm{H.c.})-i\sum_\alpha\int\mathrm{d}z\epsilon_\alpha\xi^*_\alpha(z)\xi_\alpha(z)} \\ &\times\boxed{e^{\sum_{k=1}^{n}\sum_\sigma\eta^*_{\sigma,k}\eta_{\sigma,k-1}}}\boxed{e^{\sum_{k=1}^{n}\sum_\alpha\xi^*_{\alpha,k}\xi_{\alpha,k-1}}}.\end{aligned} \tag{2.95}$$

The subscript k represents a particular subdivision of the contour. The Grassmann fields obey the KMS boundary conditions, stating that $\eta^{(*)}(z_f)=-\eta^{(*)}(z_i)$ and $\xi^{(*)}(z_f)=-\xi^{(*)}(z_i)$. The terms encircled in blue and red can be combined together. Doing so, due to the fact that $n\to\infty$, the argument of the combination results in an integral over the contour where the differential element $\mathrm{d}z=-i\mathrm{d}\tau=-i\lim_{N_\tau\to\infty}\frac{\beta}{N_\tau}$ on $\mathcal{C}_3$, $\mathrm{d}z=-\mathrm{d}t=-\lim_{N\to\infty}\frac{t_f}{N}$ on $\mathcal{C}_2$ and $\mathrm{d}z=\mathrm{d}t$ on $\mathcal{C}_1$.[3] Furthermore, the combination makes derivatives appear, since, for instance, $\lim_{n\to\infty}\frac{\eta_{\sigma,k}-\eta_{\sigma,k-1}}{\mathrm{d}z}=\frac{\partial\eta_\sigma(z)}{\partial z}$. Thus, the matrix element (2.95) becomes

$$\begin{aligned}&\left\langle \eta_{\sigma',f},\xi_{\alpha',f}\right|\hat{U}(t_f,t_0)\left|\eta_{\sigma,0},\xi_{\alpha,0}\right\rangle = \\ &\int\mathcal{D}[\eta^*_\sigma,\eta_\sigma]\mathcal{D}[\xi^*_\alpha,\xi_\alpha]e^{i\sum_\sigma\int\mathrm{d}z\eta^*_\sigma(z)i\frac{\partial\eta_\sigma(z)}{\partial z}}e^{i\sum_\alpha\int\mathrm{d}z\xi^*_\alpha(z)i\frac{\partial\xi_\alpha(z)}{\partial z}} \\ &\times e^{-i\int\mathrm{d}z\mathcal{H}_{\mathrm{loc}}[\eta^*,\eta](z)-i\sum_{\alpha,\sigma}\iint\mathrm{d}z\mathrm{d}z'(\Theta_{\sigma,\alpha}(z,z')\eta^*_\sigma(z)\xi_\alpha(z')+\mathrm{H.c.})-i\sum_\alpha\int\mathrm{d}z\epsilon_\alpha\xi^*_\alpha(z)\xi_\alpha(z)} \\ &\times e^{\sum_\sigma\eta^*_\sigma(z_f)\eta_\sigma(z_f)}e^{\sum_\alpha\xi^*_\alpha(z_f)\xi_\alpha(z_f)}.\end{aligned} \tag{2.96}$$

The *measure* $\mathcal{D}$ was defined in Eq. (2.96), for instance, as follows

$$\mathcal{D}[\eta^*_\sigma,\eta_\sigma]\equiv\lim_{n\to\infty}\prod_{k=1}^{n-1}\prod_\sigma\mathrm{d}\eta^*_{\sigma,k}\mathrm{d}\eta_{\sigma,k}.$$

The lagrangian density $\mathcal{L}$ of the system (2.93) can be identified in Eq. (2.96):

$$\begin{aligned}&\mathcal{L}[\eta^*_\sigma,\eta_\sigma;\xi^*_\alpha,\xi_\alpha](z)= \\ &\sum_\sigma\eta^*_\sigma(z)i\frac{\partial\eta_\sigma(z)}{\partial z}+\sum_\alpha\xi^*_\alpha(z)i\frac{\partial\xi_\alpha(z)}{\partial z}-\mathcal{H}[\eta^*_\sigma,\eta_\sigma;\xi^*_\alpha,\xi_\alpha](z).\end{aligned}$$

Now, instead of computing a single matrix element such as in Eq. (2.96), it would be convenient to compute the trace of the contour-time evolution operator to get the partition function (2.24) ($\phi\to 0$). Since it was chosen that $z_f=t_0-i\beta$ and $z_i=t_0$, it turns out that the trace over the contour is directly obtained from Eq. (2.96) because of the KMS boundary conditions

$$\left\langle \eta_{\sigma,f},\xi_{\alpha,f}\right|\hat{U}(z_f,z_0)\left|\eta_{\sigma,0},\xi_{\alpha,0}\right\rangle=\left\langle \eta_{\sigma,f},\xi_{\alpha,f}\right|\hat{U}(z_f,z_0)\left|-\eta_{\sigma,f},-\xi_{\alpha,f}\right\rangle. \tag{2.97}$$

Hence, due to Eq. (2.89), the exponential terms in the last line of Eq. (2.96) get cancelled out, because

$$\left\langle \eta_{\sigma,f},\xi_{\alpha,f}\right|\hat{U}(z_f,z_0)\left|-\eta_{\sigma,f},-\xi_{\alpha,f}\right\rangle=U(z_f,z_0)e^{-\sum_\sigma\eta^*_\sigma(z_f)\eta_\sigma(z_f)}e^{-\sum_\alpha\xi^*_\alpha(z_f)\xi_\alpha(z_f)}.$$

This leaves one with the following compact expression describing the partition function in terms of the contour-time Grassmann fields

---

[3] See Section 2.2 for a reminder of the structure of the contour.

$$\mathcal{Z}[\eta_\sigma^*,\eta_\sigma;\xi_\alpha^*,\xi_\alpha] = \int \mathcal{D}[\eta_\sigma^*,\eta_\sigma]\mathcal{D}[\xi_\alpha^*,\xi_\alpha]e^{iS[\eta_\sigma^*,\eta_\sigma;\xi_\alpha^*,\xi_\alpha]}, \tag{2.98}$$

where the action S was defined as

$$S[\eta_\sigma^*,\eta_\sigma;\xi_\alpha^*,\xi_\alpha] \equiv \int \mathrm{d}z\mathcal{L}[\eta_\sigma^*,\eta_\sigma;\xi_\alpha^*,\xi_\alpha](z). \tag{2.99}$$

Although the partition function (2.98) seems to have been stripped down to its simplest form, one can resort to Gaussian integral properties to integrate out the Grassmann fields ξ related to the *surrounding* environment. First off, let's expand the action (2.99) in Eq. (2.98) and reorganize the exponential argument

$$\begin{aligned}&\mathcal{Z}[\eta_\sigma^*,\eta_\sigma;\xi_\alpha^*,\xi_\alpha] = \\ &\int \mathcal{D}[\eta_\sigma^*,\eta_\sigma]\mathcal{D}[\xi_\alpha^*,\xi_\alpha]e^{i\sum_\sigma\int\mathrm{d}z\eta_\sigma^*(z)i\frac{\partial\eta_\sigma(z)}{\partial z}-i\int\mathrm{d}z\mathcal{H}_{\mathrm{loc}}[\eta_\sigma^*,\eta_\sigma](z)} \\ &\times e^{i\sum_\alpha\int\mathrm{d}z\xi_\alpha^*(z)\left[i\frac{\partial}{\partial z}-\epsilon_\alpha\right]\xi_\alpha(z)-i\sum_{\alpha,\sigma}\iint\mathrm{d}z\mathrm{d}z'(\Theta_{\sigma,\alpha}(z,z')\eta_\sigma^*(z)\xi_\alpha(z')+\mathrm{H.c.})},\end{aligned} \tag{2.100}$$

All the terms in the exponential argument of Eq. (2.100) are either bilinear or quartic in Grassmann fields, therefore they can be moved around without changing sign. The focus is now turned to the last line of Eq. (2.100) containing the fields ξ. If the term in square brackets is defined as $\left[i\frac{\partial}{\partial z}-\epsilon_\alpha\right]\delta_{\alpha,\beta} \equiv H_{\alpha,\beta}$ and the fields ξ are substituted according to the following

Recall that the bars over the contour-time variables implicitely represent an integral on the contour (see Section 2.3.2).

$$\begin{cases}\xi_\alpha(z) \to \rho_\alpha(z) + \sum\limits_{\omega,\gamma} H_{\alpha,\omega}^{-1}(z,\bar{z})\Theta_{\omega,\gamma}^*(\bar{z},\bar{z}')\eta_\gamma(\bar{z}') \\ \xi_\alpha^*(z) \to \rho_\alpha^*(z) + \sum\limits_{\gamma,\omega} \eta_\gamma^*(\bar{z}')\Theta_{\gamma,\omega}(\bar{z}',\bar{z})H_{\alpha,\omega}^{-1}(z,\bar{z})^*,\end{cases} \tag{2.101}$$

then this leads to the argument below

$$\begin{aligned}&\sum_{\alpha,\beta}\rho_\alpha(\bar{z})^*H_{\alpha,\beta}(\bar{z},\bar{z}')\rho_\beta(\bar{z}') \\ &-\sum_{\gamma,\gamma'}\eta_\gamma^*(\bar{z}')\underbrace{\sum_{\omega,\omega'}\Theta_{\gamma,\omega}(\bar{z}',\bar{z})H_{\omega,\omega'}^{-1}(\bar{z},\bar{z}'')\Theta_{\omega',\gamma'}^*(\bar{z}'',\bar{z}''')}_{\equiv\Delta_{\gamma,\gamma'}(\bar{z}',\bar{z}''')}\eta_{\gamma'}(\bar{z}''').\end{aligned} \tag{2.102}$$

The hybridization function Δ has been defined in Eq. (2.102): it couples the disjoint Fock spaces $\mathfrak{F}(\{|\eta\rangle\})$ and $\mathfrak{F}(\{|\xi\rangle\})$. The change of variables (2.101) changes the measure $\mathcal{D}[\xi_\alpha^*,\xi_\alpha] \to \mathcal{D}[\rho_\sigma^*,\rho_\sigma]$, although as shown in Appendix B, the Jacobian of this transformation is the identity, since it is an isomorphism. The Hermitian matrix $H_{\alpha,\beta}$ is diagonal, such that it can easily be integrated out, as demonstrated in Appendix B. However, it is useful to note that even if $H_{\alpha,\beta}$ were to not be diagonal, a unitary transformation U could be chosen such as to diagonalize $H_{\alpha,\beta}$. After the integration over the fields ρ, the partition function (2.100) depends solely on the fields η, and one gets

A unitary transformation leaves the Jacobian unchanged.

$$\begin{aligned}&\mathcal{Z}[\eta_\sigma^*,\eta_\sigma] = \det[H] \\ &\times\int\mathcal{D}[\eta_\sigma^*,\eta_\sigma]e^{i\sum_\sigma\int\mathrm{d}z\eta_\sigma^*(z)i\frac{\partial\eta_\sigma(z)}{\partial z}-i\int\mathrm{d}z\mathcal{H}_{\mathrm{loc}}[\eta_\sigma^*,\eta_\sigma](z)-i\sum_{\gamma,\gamma'}\eta_\gamma^*(\bar{z}')\Delta_{\gamma,\gamma'}(\bar{z}',\bar{z}'')\eta_{\gamma'}(\bar{z}'')}.\end{aligned} \tag{2.103}$$

In light of the expression of the noninteracting Green's function $\mathcal{G}^0$ (2.56), the first and last terms in the exponential argument of Eq. (2.103) can be combined to give

$$\mathcal{Z}[\eta^*_\sigma,\eta_\sigma] = \det[H]\int \mathcal{D}[\eta^*_\sigma,\eta_\sigma]e^{i\sum_{\gamma,\gamma'}\eta^*_\gamma(\bar{z}')\mathcal{G}^0_{\gamma,\gamma'}(\bar{z}',\bar{z}'')^{-1}\eta_{\gamma'}(\bar{z}'')-i\int \mathrm{d}z\mathcal{H}_{\mathrm{loc}}[\eta^*_\sigma,\eta_\sigma](z)}, \tag{2.104}$$

where $\mathcal{G}^0$ is explicitely

$$\left[i\partial_z\delta_{\gamma,\bar{\gamma}'}\delta^{\mathcal{C}}(z,\bar{z}') - \Delta_{\gamma,\bar{\gamma}'}(z,\bar{z}')\right]\mathcal{G}^0_{\bar{\gamma}',\gamma'}(\bar{z}',z') = \delta^{\mathcal{C}}(z,z')\delta_{\gamma,\gamma'}.$$

The partition function (2.104) is the effective impurity partition function of the Anderson model which will be discussed in Section 3.2. Note that the argument of the exponential in Eq. (2.104) is the effective action of the impurity system, having integrated out the fermionic degrees of freedom of the environment

$$S[\eta^*_\sigma,\eta_\sigma] = \sum_{\gamma,\gamma'}\eta^*_\gamma(\bar{z}')\mathcal{G}^0_{\gamma,\gamma'}(\bar{z}',\bar{z}'')^{-1}\eta_{\gamma'}(\bar{z}'') - \int \mathrm{d}z\mathcal{H}_{\mathrm{loc}}[\eta^*_\sigma,\eta_\sigma](z). \tag{2.105}$$

Part III

THEORETICAL METHODS

> *The many, the most vulgar, would seem to conceive the good and happiness as pleasure, and hence they also like the life of gratification. Here they appear completely slavish, since the life they decide on is a life for grazing animals.*
>
> — Aristotle, Nicomachean Ethics

In this part of the thesis, the theoretical methods employed to capture the local and nonlocal quantum correlations are introduced. Namely, the nonequilibrium Dynamical Mean Field Theory (DMFT), the Two-Particle Self-Consistent approach (TPSC) and its variants (TPSC+GG) are derived and discussed. The Random Phase Approximation (RPA)-type DMFT post-processing method to treat two-particle vertex corrections is detailed. The hybrid between DMFT and TPSC, so-called DMFT+TPSC method, is covered as well. Finally, various technicalities whose knowledge is required for the success of their implementations are broached.

3

QUANTUM IMPURITY PROBLEM

In systems of correlated electrons, the interplay between the kinetic energy and potential energy is where lies the crux of the matter, since the latter is bound to the interplay of local and spatial quantum correlations. In intermediately-to-strongly coupled systems, the electron-electron interaction is comparable to or larger than the kinetic energy. In this regime, phenomena of great interest arise such as the high-temperature superconductivity in cuprates where non-local spin fluctuations would pair up electrons and holes [7, 17, 30], heavy-fermion compounds which consist in metals doped with local magnetic moments whereby the effective electronic mass can be several orders of magnitude larger than its bare value [4], or the Mott metal-insulating transition where transition metal oxides become insulating due to strong Coulomb interactions in valence orbitals [45], to name but a few.

Since quantum correlations in low-energy physics are often nonperturbative in nature, one cannot simply resort to perturbation theory. One way to go about this is to split up the infinite degrees of freedom embedded in the quantum field theory into two distinct categories: one which is dealt with *exactly* consisting in the *quantum impurity* and the other enclosing the rest of the degrees of freedom of the system approximated as an external mean field [2]. Dynamical Mean-Field Theory (DMFT) [43, 44] maps the lattice system onto a quantum impurity that is embedded self-consistently within an auxiliary mean field representing the effective impurity environment. The auxiliary field is the so-called hybridization function, which will be introduced using the nonequilibrium formalism developed in Chapter 2, and it can be calculated by requiring that the local electronic propagator (lattice-averaged) be equal to the propagator on the quantum impurity. Hence, DMFT allows to treat local correlations approximatively in finite dimensional lattice systems [44].

However, DMFT takes exactly into account only the local correlations and it averages out the rest of the lattice assuming translational invariance over the full lattice. Doing so, DMFT leaves out the nonlocal quantum fluctuations and therefore it could not provide information about instabilities associated with a particular wave vector – long-range spin-ordered states and superconductivity with delocalized gap symmetries are examples of states of matter not detectable within DMFT.

3.1 PATHWAY TO THE HUBBARD MODEL

The Hubbard model is an approximation introduced to describe transition metals and rare-earth metals [58]. Those metallic systems share a significant property, *i.e.* the fact that they are compounds whose outer electronic (valence) orbitals are very localized in space. Let's see now how the assumption of highly localized valence electrons affect the general Hamiltonian (2.48). In Eq. (2.48), the greek letter subscripts denote arbitrary discrete quantum degrees of freedom and the only continuous variable introduced was the contour-time variable z. Such arbitrary discrete degrees of freedom could be the electronic orbital η, the spin σ, the lattice site j, etc. However, to properly describe electronic correlations in materials, one must consider the spatial expansion of the single-particle wave functions. To do this, the spin-orbital basis $|\eta,\sigma\rangle$ is introduced along with the position-spin basis $|\mathbf{x},\sigma'\rangle$

$$\langle\eta,\sigma|\mathbf{x},\sigma'\rangle = \phi_{\eta,\sigma}(\mathbf{x})\delta_{\sigma,\sigma'}, \tag{3.1}$$

where the function $\phi_{\eta,\sigma}(\mathbf{x})$ is the single-particle wave function in the position representation. If $\hat{\psi}_{\sigma}^{(\dagger)}(\mathbf{x})$ denotes the annihilation (creation) operator of a delocalized electron with spin σ, then the corresponding ladder operators in spin-orbital basis read

$$\begin{aligned}&|\eta,\sigma\rangle = \\ &\hat{c}^{\dagger}_{\eta,\sigma}|0\rangle = \int \mathrm{d}\mathbf{x}\,|\mathbf{x}\rangle\,\langle\mathbf{x}|\eta,\sigma\rangle = \int \mathrm{d}\mathbf{x}\;\phi_{\eta,\sigma}(\mathbf{x})\,|\mathbf{x},\sigma\rangle = \int \mathrm{d}\mathbf{x}\;\phi_{\eta,\sigma}(\mathbf{x})\hat{\psi}^{\dagger}_{\sigma}(\mathbf{x})\,|0\rangle\,,\end{aligned}$$

where the closure relation over the position basis was employed. It is then easy to affirm that

$$\begin{cases}\hat{c}^{\dagger}_{\eta,\sigma} = \displaystyle\int \mathrm{d}\mathbf{x}\;\phi_{\eta,\sigma}(\mathbf{x})\hat{\psi}^{\dagger}_{\sigma}(\mathbf{x}) \\ \hat{c}_{\eta,\sigma} = \displaystyle\int \mathrm{d}\mathbf{x}\;\phi^{*}_{\eta,\sigma}(\mathbf{x})\hat{\psi}_{\sigma}(\mathbf{x}).\end{cases} \tag{3.2}$$

The single-particle basis functions form an orthonormal basis, *i.e.*

$$\int \mathrm{d}\mathbf{x}\;\phi^{*}_{\eta,\sigma}(\mathbf{x})\phi_{\nu,\sigma'}(\mathbf{x}) = \delta_{\eta,\nu}\delta_{\sigma,\sigma'}.$$

From Eq. (3.2), the tensor elements $h_{\alpha,\beta}$ and $V^{\gamma,\delta}_{\alpha,\beta}$ of Eq. (2.48) can be easily casted into spin-orbital space

$$h_{\alpha,\beta}(z_1,z_2) \to h_{(\eta,\sigma);(\nu,\sigma')}(z) = \int \mathrm{d}\mathbf{x}\;\phi^{*}_{\eta,\sigma}(\mathbf{x},z)h_{\sigma,\sigma'}(\mathbf{x},z)\phi_{\nu,\sigma'}(\mathbf{x},z), \tag{3.3}$$

and

$$\begin{aligned}&V^{\gamma,\delta}_{\alpha,\beta}(z_1,z_2,z_3,z_4) \to V^{(\kappa,\sigma');(\iota,\sigma')}_{(\eta,\sigma);(\nu,\sigma)}(\mathbf{x},\mathbf{x}';z,z') = \\ &\int \mathrm{d}\mathbf{x}\mathrm{d}\mathbf{x}'\;\phi^{*}_{\eta,\sigma}(\mathbf{x})\phi^{*}_{\kappa,\sigma'}(\mathbf{x}')V_{\sigma,\sigma'}(\mathbf{x},\mathbf{x}';z,z')\phi_{\iota,\sigma'}(\mathbf{x}')\phi_{\nu,\sigma}(\mathbf{x}).\end{aligned} \tag{3.4}$$

In Eq. (3.3), the single-particle Hamiltonian will be considered diagonal in spin space, *i.e.* the spin doesn't flip when electrons hop from one orbital to another ($\sigma = \sigma'$). The interaction term in Eq. (3.4) is a two-body interaction and this explains why it depends only on two variables. In transition metals and rare-earth materials, the valence orbitals close to the Fermi level are well energetically separated from the core electronic shells, and therefore the approximation whereby the orbitals $\kappa = \iota$ and $\eta = \nu$ can be carried out in Eq. (3.4). Furthermore, since the Coulomb interaction varies slowly around the nucleus as $\frac{1}{|\mathbf{x}-\mathbf{x}'|}$ and the electrons in the valence shells of these materials are very localized around the atomic nucleus, the local electronic interaction is the dominant one and it can be approximated as a constant in real space

$$\begin{aligned}&V^{(\kappa,\sigma');(\iota,\sigma')}_{(\eta,\sigma);(\nu,\sigma)}(\mathbf{x},\mathbf{x}';z,z') \to U^{\sigma,\sigma'}_{\eta,\kappa}(z)\delta_{\eta,\nu}\delta_{\kappa,\iota}\delta(\mathbf{x}-\mathbf{x}')\delta^{\mathcal{C}}(z,z')\\ &= \int \mathrm{d}\mathbf{x}\mathrm{d}\mathbf{x}' \; \left|\phi_{\eta,\sigma}(\mathbf{x})\right|^2 V_{\sigma,\sigma'}(\mathbf{x},\mathbf{x}';z,z')\left|\phi_{\kappa,\sigma'}(\mathbf{x}')\right|^2. \end{aligned} \tag{3.5}$$

The orbital-dependent on-site electronic potential U acts on electrons with opposite spins when both are on the same orbital, *i.e.* $U^{\sigma,\sigma'}_{\eta,\nu} \to U^{\sigma}_{\eta,\eta}\delta_{\sigma',-\sigma}$. The Coulomb interaction $U^{\sigma,\sigma'}_{\eta,\nu}$ acting on electrons across different orbitals $\eta \neq \nu$ is smaller than that of the on-site Coulomb repulsion ($\eta = \nu$ and $\sigma' = -\sigma$). Fundamentally, intra-atomic correlations play a crucial role even in itinerant systems with relatively broad bands and moderate Hubbard repulsion, such as transition metals or iron pnictides and chalcogenides. If the wave functions are chosen real, *i.e.* $\phi^* = \phi$, then a lot of the matrix elements generated by the Coulomb integrals (3.4) of the from $V^{\nu,\nu}_{\eta,\nu}$ vanish by symmetry. Nevertheless, there is yet another important set of Coulomb integrals missing that doesn't zero out due to symmetry considerations. Indeed, since the electronic orbitals can hybridize, there is a matrix element characterizing the Coulomb integrals (3.4) which takes into account the orbital mixing in real space

$$\begin{aligned}&V^{(\kappa,\sigma');(\iota,\sigma')}_{(\eta,\sigma);(\nu,\sigma)}(\mathbf{x},\mathbf{x}';z,z') \to J^{\sigma,\sigma'}_{\eta,\kappa}(z)\delta_{\eta,\nu}\delta_{\kappa,\iota}\delta(\mathbf{x}-\mathbf{x}')\delta^{\mathcal{C}}(z,z')\\ &= \int \mathrm{d}\mathbf{x}\mathrm{d}\mathbf{x}' \; \phi^*_{\eta,\sigma}(\mathbf{x})\phi^*_{\kappa,\sigma'}(\mathbf{x}')V_{\sigma,\sigma'}(\mathbf{x},\mathbf{x}';z,z')\phi_{\eta,\sigma'}(\mathbf{x}')\phi_{\kappa,\sigma}(\mathbf{x}). \end{aligned} \tag{3.6}$$

Setting the wave functions real in Eq. (3.6) means that the spin-exchange energy is the same as the pair-hopping energy. The term denoted J in Eq. (3.6) is the on-site inter-orbital Hund's coupling that reflects the rule stating that the groundstate of a system composed of many-electron atomic shells should maximize the total spin angular momentum quantum number S [46, 63]. This means that the spins tend to align each other when located on different orbitals. Because the orbital mixing might affect the spin degrees of freedom, it is convenient to denote in Eq. (3.6) a Hund's term which is spin-diagonal $J_\sigma\delta_{\sigma,\sigma'}$ and one which is spin off-diagonal $J'_\sigma\delta_{\sigma',-\sigma}$. The spin-diagonal Hund's term J represents the pair-hopping energy related to orbital mixing whereas the spin off-diagonal term J' denotes the spin-exchange energy. In the case considered where the wave functions are real functions, like the case considered later on, $J = J'$.

The total spin S and orbital angular moment L both feature as one of the four quantum numbers that specify the atom's electron wave functions.

In the realm of condensed-matter physics, the various interactions discussed so far govern to a large extent the equations of motion of electrons moving on an atomic lattice. There needs now a model Hamiltonian to be able to harness the many-body quantum field theoretical tools developed in Chapter 2 and calculate the propagation of electrons on an atomic lattice along with numerous correlation functions that describe how electrons correlate to each other. In the grand-canonical ensemble, the Hamiltonian describing interacting atomic electrons on a multi-orbital lattice with Hund's coupling, so-called the Kanamori-Hubbard model [63], reads

$$\begin{aligned}\hat{\mathcal{H}}(t) = &\sum_{\substack{ij,\sigma\\ \eta\nu}} \left[h^{\sigma}_{\eta,\nu}(\mathbf{R}_i - \mathbf{R}_j;t) - \mu\delta_{i,j}\delta_{\eta,\nu}\right] \hat{c}^{\dagger}_{\eta,\sigma}(\mathbf{R}_i)\hat{c}_{\nu,\sigma}(\mathbf{R}_j)\\ &+ \frac{1}{2}\sum_{\substack{ij,\eta\nu\\ \sigma\sigma'}} \left[U^{\sigma,\sigma'}_{\eta,\nu}(\mathbf{R}_i;t) - J^{\sigma}_{\eta,\nu}(\mathbf{R}_i;t)\delta_{\sigma,\sigma'}(\mathbb{1} - \delta_{\eta,\nu})\right] \hat{n}_{\eta,\sigma}(\mathbf{R}_i)\hat{n}_{\nu,\sigma'}(\mathbf{R}_j)\\ &+ \frac{1}{2}\sum_{\substack{\eta\nu,ij,\sigma\\ \eta\neq\nu}} \Big[J^{\sigma}_{\eta,\nu}(\mathbf{R}_i;t)\hat{c}^{\dagger}_{\eta,\sigma}(\mathbf{R}_i)\hat{c}_{\eta,-\sigma}(\mathbf{R}_i)\hat{c}_{\nu,\sigma}(\mathbf{R}_j)\hat{c}^{\dagger}_{\nu,-\sigma}(\mathbf{R}_j)\\ &\qquad - J'^{\sigma}_{\eta,\nu}(\mathbf{R}_i;t)\hat{c}^{\dagger}_{\eta,\sigma}(\mathbf{R}_i)\hat{c}_{\nu,-\sigma}(\mathbf{R}_j)\hat{c}_{\nu,\sigma}(\mathbf{R}_j)\hat{c}^{\dagger}_{\eta,-\sigma}(\mathbf{R}_i)\Big]. \end{aligned} \tag{3.7}$$

In Eq. (3.7), the lattice vector $\mathbf{R}$ locates atomic sites and $h_{\eta,\nu}$ describes the electrons hopping from orbital η to orbital ν, respectively located at $\mathbf{R}_i$ and $\mathbf{R}_j$. The Hund's terms vanish when $\eta = \nu$. It is clear from the second term of the Kanamori-Hubbard model that the configuration where electrons on different orbitals have their spins align is favorable in energy, thereby satisfying the second Hund's rule. The Kanamori model would be the key model capturing the exotic physics of ruthenates [71], such as the unconventional superconductivity and the anomalous optical conductivity at low temperatures. It would also capture the physics underlying the high-temperature superconductivity in iron pnictides [146] and chalcogenides [128]. In the scenario where the Hund's coupling $J^{(\prime)}$ is much smaller than the Coulomb interaction U, *i.e.* $|J^{(\prime)}|/|U| \ll 1$, one recovers the multi-orbital Hubbard model

$$\begin{aligned}\hat{\mathcal{H}}(t) = &\sum_{\substack{ij,\sigma\\ \eta\nu}} \left[h^{\sigma}_{\eta,\nu}(\mathbf{R}_i - \mathbf{R}_j;t) - \mu\delta_{i,j}\delta_{\eta,\nu}\right] \hat{c}^{\dagger}_{\eta,\sigma}(\mathbf{R}_i)\hat{c}_{\nu,\sigma}(\mathbf{R}_j)\\ &+ \frac{1}{2}\sum_{\substack{i,\eta\nu\\ \sigma\sigma'}} U^{\sigma,\sigma'}_{\eta,\nu}(\mathbf{R}_i;t)\hat{n}_{\eta,\sigma}(\mathbf{R}_i)\hat{n}_{\nu,\sigma'}(\mathbf{R}_i), \end{aligned} \tag{3.8}$$

where the subscripts i,j denote the lattice atomic sites, η,ν the orbitals, the spin $\sigma \in \{\uparrow,\downarrow\}$ and the particle number $\hat{n}_{\eta,\sigma} = \hat{c}^{\dagger}_{\eta,\sigma}\hat{c}_{\eta,\sigma}$. The one-body Hamiltonian is hermitian: $h^{\sigma}_{\eta,\nu}(t) = h^{\sigma}_{\nu,\eta}(t)^{*}$. Based on the approximations done so far, when the localized orbitals are energetically separated apart such that the electronic potential can be considered diagonal in orbital space and the number of bands crossing the Fermi energy can be boiled down to one, the Hamiltonian describing electrons on a translational invariant lattice reads

$$\begin{aligned}\hat{\mathcal{H}}(t) = &\sum_{\substack{ij,\sigma\\ \eta\nu}} \left[h^{\sigma}_{\eta,\nu}(\mathbf{R}_i - \mathbf{R}_j;t) - \mu\delta_{i,j}\delta_{\eta,\nu}\right] \hat{c}^{\dagger}_{\eta,\sigma}(\mathbf{R}_i)\hat{c}_{\nu,\sigma}(\mathbf{R}_j)\\ &+ \frac{1}{2}\sum_{i,\sigma,\nu} U_{\nu,\nu}(\mathbf{R}_i;t)\hat{n}_{\nu,\sigma}(\mathbf{R}_i)\hat{n}_{\nu,-\sigma}(\mathbf{R}_i). \end{aligned} \tag{3.9}$$

Eq. (3.9) is the so-called Hubbard model and it is a special case of the multi-orbital Hubbard model (3.8). The local single-orbital Coulomb interaction is denoted $U_{\nu,\nu}$ and is usually normalized to the nearest-neighbor hopping energy t^{hop}.

The Hubbard model is probably the most studied Hamiltonian model to describe strongly correlated systems. Among many of its applications, the model

(3.9) would embody the fundamental physics taking place in the high-T_c superconducting cuprates [118], *i.e.* the Mott insulating regime [3, 45, 102], long-range antiferromagnetism [85, 110] and d-wave superconductivity [41, 78, 117]. The hopping term $h_{i,j}$ is limited to the stacked CuO_2 planes which are weakly coupled along the c principal axis, and U is the local interaction on the Cu d-shell valence orbital [52]. The intra-plane lattice parameters a along x-axis and b along y-axis are similar [60], therefore the CuO_2 planes can be approximated as a square lattice.

3.2 ANDERSON IMPURITY MODEL

The Hubbard model (3.9) can be mapped to the AIM to define the local (impurity) part in the hybridized system (2.93), *i.e.* $\hat{\mathcal{H}}_{\text{loc}}$ would be replaced by the Hubbard local interaction

$$\begin{aligned}\hat{\mathcal{H}}_{\text{AIM}}(t) &= \frac{1}{2}U(t)\sum_{i,\sigma}\hat{n}_{i,\sigma}\hat{n}_{i,-\sigma}\\ &+\sum_{\alpha,\sigma}\iint \mathrm{d}t\mathrm{d}t'\,\left(\Theta_{\sigma,\alpha}(t,t')\hat{c}^{\dagger}_{\sigma}(t)\hat{b}_{\alpha}(t') + \text{H.c.}\right) + \sum_{\alpha}(\epsilon_{\alpha}-\mu)\,\hat{b}^{\dagger}_{\alpha}\hat{b}_{\alpha},\end{aligned} \tag{3.10}$$

where μ is the chemical potential on the impurity, renormalizing the energy spectrum of electronic states in the embedding environment. In the Hubbard model (3.9), the Coulomb potential U is constrained to a single orbital around the Fermi level, therefore the local Hamiltonian of the impurity model (3.10) has been stripped off of its orbital-related indices. Also, the lattice site index i of Eq. (3.9) has been demoted to subscript. The ladder operators $\hat{b}^{(\dagger)}$ annihilate (create) electrons in some auxiliary bath. The Hamiltonian (3.10) is that of the Anderson impurity model (AIM). This model Hamiltonian was originally introduced to describe the physics of localized magnetic moments in metals, coined Kondo systems [2]. In such Kondo systems, the localized magnetic moment sitting on valence electronic d or f-shell represents the impurity and the free-electron environment stands for the metallic background to which the impurity is coupled via the transition matrix elements Θ.

The effective impurity action (2.105) of the AIM (3.10) explicitly reads

$$S[\eta^{*}_{\sigma},\eta_{\sigma}] = \sum_{\substack{\alpha,\alpha'\\ \sigma,\sigma'}}\eta^{*}_{\alpha,\sigma}(\bar{z}')\mathcal{G}^{0}_{\alpha,\sigma;\alpha',\sigma'}(\bar{z}',\bar{z}'')^{-1}\eta_{\alpha',\sigma'}(\bar{z}'') - \frac{1}{2}\sum_{i,\sigma}\int \mathrm{d}z\; U(z)n_{i,\sigma}n_{i,-\sigma}, \tag{3.11}$$

where the Weiss Green's function is

$$\left[(i\partial_z+\mu)\,\delta_{\sigma,\bar{\sigma}}\delta_{\alpha,\bar{\alpha}}\delta(z,\bar{z}) - \Delta_{\sigma,\alpha;\bar{\sigma},\bar{\alpha}}(z,\bar{z})\right]\mathcal{G}^{0}_{\bar{\sigma},\bar{\alpha};\sigma',\alpha'}(\bar{z},z') = \delta^{\mathcal{C}}(z,z')\delta_{\alpha,\alpha'}\delta_{\sigma,\sigma'}, \tag{3.12}$$

where the hybridization function is expressed as

$$\begin{aligned}&\Delta_{\sigma,\alpha;\sigma',\alpha'}(z,z') =\\ &\sum_{\substack{\tilde{\alpha},\tilde{\alpha}'\\ \tilde{\sigma},\tilde{\sigma}'}}\Theta_{\alpha,\sigma;\tilde{\alpha},\tilde{\sigma}}(z,\bar{z})\left[(i\partial_{\bar{z}}-\epsilon_{\tilde{\alpha}}+\mu)\,\delta_{\tilde{\alpha},\tilde{\alpha}'}\delta_{\tilde{\sigma},\tilde{\sigma}'}\delta^{\mathcal{C}}(\bar{z},\bar{z}')\right]^{-1}\Theta_{\tilde{\alpha}',\tilde{\sigma}';\alpha',\sigma'}(\bar{z}',z').\end{aligned} \tag{3.13}$$

The hybridization function (3.13) is spin-diagonal and spin-independent, but, in general, it could be off-diagonal in spin and spin-dependent. In fact, a simple way to break the spin symmetry on the impurity would be, without allowing for spin flip, to have that $\Delta_{\uparrow,\alpha;\uparrow,\alpha'} \neq \Delta_{\downarrow,\alpha;\downarrow,\alpha'}$. Having nailed down the effective action of the AIM, the distribution describing the contributions of the different configurations of the system in phase space – often represented by means of Feynman diagrams – can be calculated via the partition function (2.104). This distribution is used to access expectation values of observables, such as the energy, the density of states, the optical conductivity, etc. The AIM can be generalized to accommodate for multiple orbitals on the impurity, by means of replacing the potential term of $\hat{\mathcal{H}}_{\text{loc}}$ by that of either Eq. (3.7) or (3.8).

3.2.1 *DMFT*

DMFT maps self-consistently correlated electron lattice systems onto a local quantum impurity that is described by the Anderson impurity Hamiltonian (3.10), so as to effectively capture the effect of the lattice environment onto the interacting local (orbital) electrons [44]. To achieve the latter, the electronic self-energy is approximated as fully local. The feedback of environment onto the impurity electrons is encapsulated in the hybridization function Δ. It adds up to the self-energy stemming from the electronic correlations on the orbital impurity associated with the local degrees of freedom of the original lattice, denoted Σ^{imp}. DMFT is exact in infinite dimensions where the coordination number is infinite [43, 91, 94] and it has been extended to the nonequilibrium Kadanoff-Baym-Keldysh formalism [5, 42].

The DMFT procedure will be presented sequentially, *i.e.* the algorithmic description will be walked through step by step. To initiate the DMFT procedure, one needs to first guess an expression for Δ, and it can be guided by the asymptotic expression of Δ that can be calculated analytically [69]. Then, for a given Δ, Σ^{imp} can be isolated from the impurity Green's function $\mathcal{G}^{\text{imp}}$ calculated by sampling stochastically the configuration distribution of the effective action (3.11). Various stochastic methods tackle the solution of the impurity self-energy, like the class of Continuous-time Quantum Monte Carlo Methods [53, 54, 106, 148]. Those stochastic methods solve exactly for Σ^{imp}, insofar as the statistical error is considered. There exist other classes of methods that approximate Σ^{imp}, some of which are reliable at weak-coupling strength and some at strong-coupling strength. The weak-coupling approximations hinge on perturbation theory and will be introduced in Section 3.2.1.3. The strong-coupling impurity solvers such as the Noncrossing Approximation and its generalizations [21, 37, 56] sum up leading-order diagrams contributing to the infinite-U Anderson partition function (2.104). These strong-coupling solvers are reliable when the local electronic interaction (U) significantly exceeds the electronic bandwidth (W), whereas the weak-coupling solvers allow one to properly describe physics whenever $U \lesssim W/2$ [137].

3.2.1.1 *Paramagnetic state*

In the paramagnetic (PM) phase, for the DMFT self-consistency to hold, the impurity self-energy $\Sigma^{\text{imp}}(z,z') \equiv \Sigma(z,z')\delta_{i,j}$ is approximated to be the same on all lattice sites i,j, meaning that $\Sigma_{i,j}(z,z') \simeq \Sigma(z,z')\delta_{i,j}$. As a consequence, the electrons on the lattice propagate according to the lattice Green's function $\mathcal{G}_{\mathbf{k}}$, reading

The way DMFT is formulated in Section 3.2.1.1 for the PM state could also apply to a ferromagnetic state where there are no staggered fields.

$$[i\partial_z + \mu - \epsilon(\mathbf{k})]\,\mathcal{G}_{\sigma,\mathbf{k}}(z,z') - \int_{\mathcal{C}} \mathrm{d}z''\, \Sigma^{\text{imp}}_{\sigma}(z,z'')\mathcal{G}_{\sigma,\mathbf{k}}(z'',z') = \delta^{\mathcal{C}}(z,z'), \tag{3.14}$$

with the electronic dispersion relation denoted $\epsilon(\mathbf{k})$. The impurity Green's function $\mathcal{G}^{\text{imp}}$ relates to both the impurity self-energy Σ^{imp} and the Weiss Green's function (3.12), which acts as a dynamical mean field, through the Dyson's equation

$$\mathcal{G}^{\text{imp}}_{\sigma}(z,z') = \mathcal{G}^{0}_{\sigma}(z,z') + \mathcal{G}^{0}_{\sigma}(z,\bar{z})\Sigma^{\text{imp}}_{\sigma}(\bar{z},\bar{z}')\mathcal{G}^{\text{imp}}_{\sigma}(\bar{z}',z'). \tag{3.15}$$

Next, to close the DMFT scheme, the lattice Green's function (3.14) is averaged over the Brillouin zone, whereby one obtains the local Green's function defined as

$$\frac{1}{N_k}\sum_{\mathbf{k}} \mathcal{G}_{\sigma,\mathbf{k}}(z,z') \equiv \mathcal{G}^{\text{loc}}_{\sigma}(z,z'). \tag{3.16}$$

The local Green's function (3.16) is then set equal to the impurity Green's function $\mathcal{G}^{\text{imp}}$ obtained by solving the AIM (Section 3.2), such that the Dyson's equation (3.15) can be employed to update the Weiss Green's function $\mathcal{G}^0$:

$$\mathcal{G}^{0}_{\sigma}(z,\bar{z})\left[\delta^{\mathcal{C}}(\bar{z},z') + F_{\sigma}(\bar{z},z')\right] = \mathcal{G}^{\text{loc}}_{\sigma}(z,z'), \tag{3.17}$$

where the contour function $F_{\sigma}(z,z') \equiv \Sigma^{\text{imp}}_{\sigma}(z,\bar{z})\mathcal{G}^{\text{loc}}_{\sigma}(\bar{z},z')$. Eq. (3.17) is a Volterra integral equation of the 2nd kind. Given that $\mathcal{G}^0[\Delta]$ is a functional of the hybridization function, it contains relevant information to sample the partition distribution function as is done in the impurity solver (see Section 2.5.3).

3.2.1.2 *Antiferromagnetic state*

In the case where spin rotational symmetry is broken, two sublattices $a \in \{A,B\}$ associated with opposite spin projections $\sigma \in \{\uparrow,\downarrow\}$ come about due to the fact that the original Brillouin zone gets split into two halves: it requires dealing with a bipartite lattice. To deal with a bipartite lattice system within DMFT, it entails a generalization of the DMFT equations to accommodate for the enlargement of the impurity Hilbert space. The various Green's functions now bear a matrix form in sublattice space and the locality of the self-energy translates into the statement that $\Sigma_{i,j,\sigma}(z,z') = \Sigma^{a}_{\sigma}(z,z')\delta_{i,j}$. Moreover, the bipartite lattice Green's function becomes

The unit-cell size doubles in a bipartite lattice.

$$\mathcal{G}^{ab}_{\mathbf{k},\sigma}(z,z') =$$
$$\begin{pmatrix} (i\partial_z + \mu + h\sigma)\delta^{\mathcal{C}}(z,\bar{z}) - \Sigma^{AA}_{\sigma}(z,\bar{z}) & -\epsilon_{\mathbf{k}}(z)\delta^{\mathcal{C}}(z,\bar{z}) \\ -\epsilon_{\mathbf{k}}(z)\delta^{\mathcal{C}}(z,\bar{z}) & (i\partial_z + \mu - h\sigma)\delta^{\mathcal{C}}(z,\bar{z}) - \Sigma^{BB}_{\sigma}(z,\bar{z}) \end{pmatrix}$$
$$\times \begin{pmatrix} \mathcal{G}^{AA}_{\mathbf{k},\sigma}(\bar{z},z') & \mathcal{G}^{AB}_{\mathbf{k},\sigma}(\bar{z},z') \\ \mathcal{G}^{BA}_{\mathbf{k},\sigma}(\bar{z},z') & \mathcal{G}^{BB}_{\mathbf{k},\sigma}(\bar{z},z') \end{pmatrix} = \begin{pmatrix} \delta^{\mathcal{C}}(z,z') & 0 \\ 0 & \delta^{\mathcal{C}}(z,z') \end{pmatrix}, \tag{3.18}$$

where the momentum $\mathbf{k}$ spans over the original Brillouin zone and the staggered magnetization breaking the spin symmetry is denoted h. The staggered magnetization effectively produces a chemical potential shift on the two sublattices triggering an anti-alignment of the spin projection between the sublattices. The sublattice matrix elements of the Green's function in Eq. (3.18) can be easily singled out, since Eq. (3.18) maps to

$$\begin{pmatrix} A & B \\ C & D \end{pmatrix} \begin{pmatrix} A' & B' \\ C' & D' \end{pmatrix} = \begin{pmatrix} 1 & 0 \\ 0 & 1 \end{pmatrix}. \tag{3.19}$$

Upon multiplying out the matrices in Eq. (3.19), one obtains the following set of coupled equations

$$\begin{cases} AA' + BC' = 1 \\ AB' + BD' = 0 \\ CA' + DC' = 0 \\ CB' + DD' = 1 \end{cases}$$

which can be worked out further to lay out the elements of the sublattice Green's function $\mathcal{G}^{ab}_{\mathbf{k},\sigma}$ as such

$$\begin{cases} A' = (A - BD^{-1}C)^{-1} \\ B' = -A^{-1}BD' \\ C' = -D^{-1}CA' \\ D' = (D - CA^{-1}B)^{-1}. \end{cases} \tag{3.20}$$

By substituting the definitions of A, B, C, D fetched from Eq. (3.18) into Eq. (3.20) and by defining the diagonal elements A and B of Eq. (3.18) by g^{AA}_{σ} and g^{BB}_{σ}, respectively, one gets

$$\begin{cases} \mathcal{G}^{AA}_{\mathbf{k},\sigma}(z,z') = \left(\delta^{\mathcal{C}}(z,\bar{z}') - g^{AA}_{\sigma}(z,\bar{z})\epsilon_{\mathbf{k}}(\bar{z})g^{BB}_{\sigma}(\bar{z},\bar{z}')\epsilon_{\mathbf{k}}(\bar{z}')\right)^{-1} g^{AA}_{\sigma}(\bar{z}',z') \\ \mathcal{G}^{AB}_{\mathbf{k},\sigma}(z,z') = g^{BB}_{\sigma}(z,\bar{z})\epsilon_{\mathbf{k}}(\bar{z})\mathcal{G}^{AA}_{\mathbf{k},\sigma}(\bar{z},z') \\ \mathcal{G}^{BA}_{\mathbf{k},\sigma}(z,z') = g^{AA}_{\sigma}(z,\bar{z})\epsilon_{\mathbf{k}}(\bar{z})\mathcal{G}^{BB}_{\mathbf{k},\sigma}(\bar{z},z') \\ \mathcal{G}^{BB}_{\mathbf{k},\sigma}(z,z') = \left(\delta^{\mathcal{C}}(z,\bar{z}') - g^{BB}_{\sigma}(z,\bar{z})\epsilon_{\mathbf{k}}(\bar{z})g^{AA}_{\sigma}(\bar{z},\bar{z}')\epsilon_{\mathbf{k}}(\bar{z}')\right)^{-1} g^{BB}_{\sigma}(\bar{z}',z'). \end{cases} \tag{3.21}$$

Just like for the paramagnetic case, the closedness of the DMFT equations prescribes that the local part of the lattice Green's function coincide with the impurity Green's function

$$\frac{1}{N_k}\sum_{\mathbf{k}} \mathcal{G}^{ab}_{\sigma,\mathbf{k}}(z,z') \equiv \mathcal{G}^{a,\text{loc}}_{\sigma}(z,z')\delta_{ab} = \mathcal{G}^{a,\text{imp}}_{\sigma}(z,z')\delta_{ab}, \tag{3.22}$$

where the local sublattice component is diagonal under lattice inversion symmetry. Similarly to Eq. (3.15), the Dyson's equation links both the impurity self-energy and Green's function to the Weiss Green's function, although in this case at the sublattice level:

$$\mathcal{G}^{a,\mathrm{imp}}_{\sigma}(z,z') = \mathcal{G}^{0,a}_{\sigma}(z,z') + \mathcal{G}^{0,a}_{\sigma}(z,\bar{z})\Sigma^{a,\mathrm{imp}}_{\sigma}(\bar{z},\bar{z}')\mathcal{G}^{a,\mathrm{imp}}_{\sigma}(\bar{z}',z'). \tag{3.23}$$

The Weiss Green's function then fed back into the impurity solver can be determined using the straightforward equivalent of Eq. (3.17) on each sublattice:

$$\mathcal{G}^{a,0}_{\sigma}(z,\bar{z})\left[\delta^{\mathcal{C}}(\bar{z},z') + F^{a}_{\sigma}(\bar{z},z')\right] = \mathcal{G}^{a,\mathrm{loc}}_{\sigma}(z,z'). \tag{3.24}$$

Hinging on the facts that the nature of the broken symmetry is spontaneous and that a different sublattice imply a different spin projection in the antiferromagnetic (AFM) phase, there is a redundancy in the labelling of the degrees of freedom when using both a and σ in Eqs. (3.23), (3.22), (3.21) and (3.24). One can identify that, for instance, $\Sigma^{-a}_{\sigma} = \Sigma^{a}_{-\sigma}$, with the superscript "$-a$" simply referring to the opposite sublattice – this relation holds for any contour-defined functions.

3.2.1.3 *Iterated Perturbation Theory*

By making use of Hedin's equations introduced in Section 2.4, one can generate systematically in a perturbative fashion, order by order, the Feynman diagrams that characterize single- and two-particle correlation functions. This, however, cannot be done for arbitrary high expansion order in the interaction U, since it would churn out a quantity of diagrams too great to be manageable. To sum up all the relevant diagrams, or at least a subset of it, one needs to resort to nonperturbative methods among which stand DMFT and its cluster extensions [81], or TPSC and its variants, which will be covered further down below in Chapter 5.

As far as the Hubbard model is concerned, the Fock interaction term vanishes (see Fig. 2.7) and this leads to two self-energy diagrams of order $\mathcal{O}(U^2)$ and eight diagrams of order $\mathcal{O}(U^3)$. These leading diagrams are derived step by step in Appendix C. In this section, the diagrams are written down along with their diagrammatic representation.

Going to order $\mathcal{O}(U^4)$, the number of diagrams dramatically increases and it is expensive to evaluate them all, even in the particle-hole scenario where odd diagrams cancel out.

To second order, the Hartree contribution $\Sigma^{(2)}_{H}$ reads

$$\Sigma^{(2)}_{H,\sigma}(z,z') = (-i)^2 U(z)\int_{\mathcal{C}}\mathrm{d}\bar{z}\ \mathcal{G}^{0}_{-\sigma}(z,\bar{z})U(\bar{z})\mathcal{G}^{0}_{\sigma}(\bar{z},\bar{z}^{+})\mathcal{G}^{0}_{-\sigma}(\bar{z},z^{+})\delta^{\mathcal{C}}(z,z'). \tag{3.25}$$

The diagram expressed in Eq. (3.25) is shown in Fig. 3.1. The diagram described by Eq. (3.25), along with the first-order Hartree diagram shown in Fig. 2.10, is necessary to spontaneously break the spin SU(2) symmetry within DMFT, since it confers different chemical potentials to the different spin projections. The particle densities $n_{\downarrow}$ and $n_{\uparrow}$ would then differ and their sum would give the initial impurity particle density n before the spontaneous symmetry breaking: $n_{\downarrow} + n_{\uparrow} = n$. The remaining second-order diagram comprises one bubble diagram, as depicted in Fig. 3.2, and reads

$$\Sigma^{(2)}_{\sigma}(z,z') = U(z)\mathcal{G}^{0}_{\sigma}(z,z')U(z')\mathcal{G}^{0}_{-\sigma}(z',z^{+})\mathcal{G}^{0}_{-\sigma}(z,z'^{+}). \tag{3.26}$$

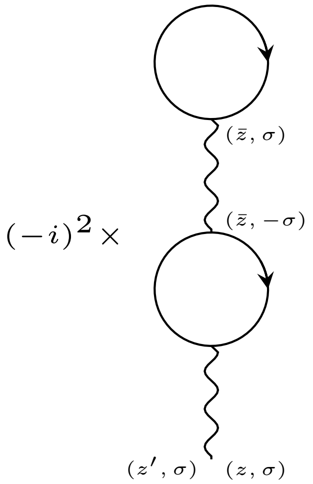

Figure 3.1: 2^{nd}-order self-energy Hartree diagram. The fermionic propagators represent the Weiss Green's functions $\mathcal{G}^0$.

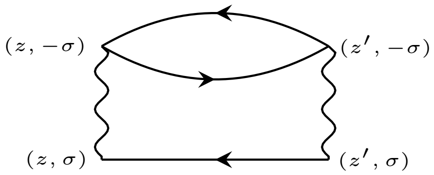

Figure 3.2: 2^{nd}-order self-energy diagram

Check out Section 2.3.1 for a refresher on Matsubara frequencies.

The self-energy (3.26) expressed as a functional of the Weiss Green's function $\Sigma^{(2)}[\mathcal{G}^0]$ captures the Mott-insulating crossover because Eq. (3.26) correctly reproduces the high-frequency limit of the Hubbard model (3.9)[1], which coincides with the atomic limit at half-filling, but violates energy conservation at longer times. On the other hand, the self-energy expressed in terms of the boldified Green's function $\Sigma^{(2)}[\mathcal{G}]$ leads to a conserving scheme at the expense of scrapping the Mott metal-to-insulator transition. This is due to the fact that, even though the perturbation theory expressed in terms of the interacting Green's functions leads to the correct asymptotics at half-filling, it doesn't set in at $i\omega_n \sim W$, but rather at $i\omega_n \gg U$, which is at too large energy and contradicts the Pauli exclusion principle. In order to carry out the perturbation theory using the dressed Green's functions, one would need to consider the frequency dependent two-particle vertex corrections as well to get physically sound results. In the weak-coupling regime $U \lesssim W/2$, both schemes lead to similar results on short times [119].

Let's turn now to the determination of the 3^{rd}-order self-energy diagrams. The set of diagrams contributing to the time-singular component of the self-energy (one-time contribution) counts to three. The first element of the set is obtained by inserting a Hartree diagram into the outer-most propagator of the 2^{nd}-order diagram (3.25). This produces the following diagram

---

[1] See the discussion further down below under the paragraph "Asymptotic limits of the hubbard model self-energy" to understand this in more depth.

$$\Sigma^{3a}_{H,\sigma}(z,z') = (-i)^3 U(z)\mathcal{G}^0_{-\sigma}(z,\bar{z})U(\bar{z})\mathcal{G}^0_{\sigma}(\bar{z},\bar{z}')U(\bar{z}')\mathcal{G}^0_{-\sigma}(\bar{z}',\bar{z}'^{+})\mathcal{G}^0_{\sigma}(\bar{z}',\bar{z}^{+})\mathcal{G}^0_{-\sigma}(\bar{z},z^{+})\delta^{\mathcal{C}}(z,z'). \tag{3.27}$$

The next time-singular 3rd-order self-energy diagram stems from the insertion of a propagator featuring two Hartree self-energies into the Hartree term. This gives

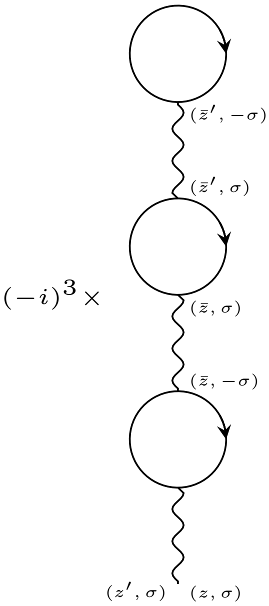
$(\bar{z}', -\sigma)$
$(\bar{z}', \sigma)$
$(-i)^3 \times$
$(\bar{z}, \sigma)$
$(\bar{z}, -\sigma)$
(z', σ)
(z, σ)

Figure 3.3: 3rd-order diagram Σ^{3a}_{H}

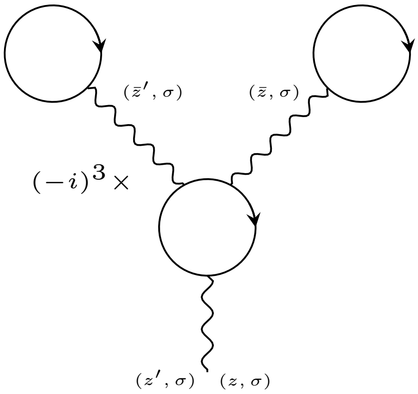
$(\bar{z}', \sigma)$
$(\bar{z}, \sigma)$
$(-i)^3 \times$
(z', σ)
(z, σ)

Figure 3.4: 3rd-order diagram Σ^{3b}_{H}

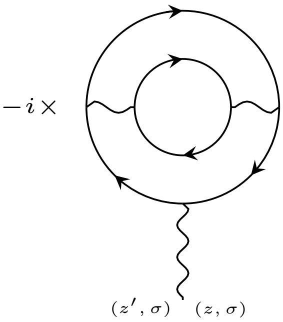
$-i \times$
(z', σ)
(z, σ)

Figure 3.5: 3rd-order diagram Σ^{3c}_{H}

$$\Sigma^{3b}_{H,\sigma}(z,z') = (-i)^3 U(z)\mathcal{G}^0_{-\sigma}(z,\bar{z})U(\bar{z})\mathcal{G}^0_{\sigma}(\bar{z},\bar{z}^{+})\mathcal{G}^0_{-\sigma}(\bar{z},\bar{z}')U(\bar{z}')\mathcal{G}^0_{\sigma}(\bar{z}',\bar{z}'^{+})\mathcal{G}^0_{-\sigma}(\bar{z}',z^{+})\delta^{\mathcal{C}}(z,z'). \tag{3.28}$$

The last time-singular contribution comes from the insertion of the bare 2nd-order self-energy diagram (3.26) into the Hartree propagator, giving

$$\Sigma^{3c}_{H,\sigma}(z,z') = -iU(z)\mathcal{G}^0_{-\sigma}(z,\bar{z})U(\bar{z})\mathcal{G}^0_{\sigma}(\bar{z},\bar{z}')U(\bar{z}')\mathcal{G}^0_{-\sigma}(\bar{z}',\bar{z}^{+})\mathcal{G}^0_{-\sigma}(\bar{z},\bar{z}')\mathcal{G}^0_{\sigma}(\bar{z}',z^{+})\delta^{\mathcal{C}}(z,z'). \tag{3.29}$$

The set of diagrams consisting of Eqs. (3.27), (3.28) and (3.29) renormalizes to 3$^{\text{rd}}$-order the chemical potential and are illustrated in Figs. 3.3, 3.4 and 3.5, respectively.

Another category of diagrams originates from the consideration of the second-order self-energy diagram (3.26) in the vertex function Γ of Eq. (2.59). This gives three distinct vertex terms out of which two lead to a nonzero contribution. Furthermore, to obtain those diagrams, the lowest-order diagram in the Bethe-Salpeter equation (2.46) is used in Eq. (2.59). The first of those diagrams reads

$$\Sigma^{3a}_{\sigma}(z,z') = iU(z)U(z')\mathcal{G}^0_{-\sigma}(z,z')\mathcal{G}^0_{\sigma}(z,\bar{z})\mathcal{G}^0_{\sigma}(\bar{z},z')U(\bar{z})\mathcal{G}^0_{-\sigma}(z',\bar{z})\mathcal{G}^0_{-\sigma}(\bar{z},z^+), \tag{3.30}$$

and the second diagram of this category reads

$$\Sigma^{3b}_{\sigma}(z,z') = iU(z)U(z')\mathcal{G}^0_{-\sigma}(z',z^+)\mathcal{G}^0_{-\sigma}(z,\bar{z}^+)\mathcal{G}^0_{\sigma}(z,\bar{z})U(\bar{z})\mathcal{G}^0_{\sigma}(\bar{z},z')\mathcal{G}^0_{-\sigma}(\bar{z},z'^+). \tag{3.31}$$

The diagram representing Eq. (3.30) is shown in Fig. 3.6 and the one representing Eq. (3.31) is shown in Fig. 3.7.

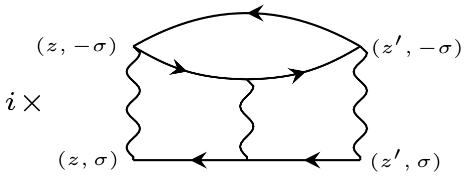

Figure 3.6: 3$^{\text{rd}}$-order diagram Σ^{3a}

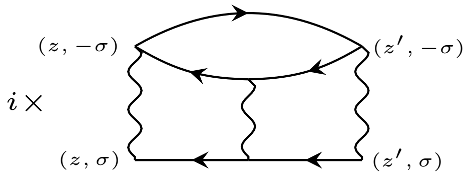

Figure 3.7: 3$^{\text{rd}}$-order diagram Σ^{3b}

The next series of 3$^{\text{rd}}$-order Feynman diagrams comes from the insertion of one Green's function into the second-order self-energy (3.26) whose self-energy is the Hartree term (2.81). This category of 3$^{\text{rd}}$-order self-energy diagrams is composed of three diagrams. The series of diagrams has as first diagram (Fig. 3.8)

$$\Sigma^{3c}_{\sigma}(z,z') = -iU(z)U(z')\mathcal{G}^0_{\sigma}(z,z')\mathcal{G}^0_{-\sigma}(z',z^+)\mathcal{G}^0_{-\sigma}(z,\bar{z})U(\bar{z})\mathcal{G}^0_{\sigma}(\bar{z},\bar{z}^+)\mathcal{G}^0_{-\sigma}(\bar{z},z'), \tag{3.32}$$

as second (Fig. 3.9)

$$\Sigma^{3d}_{\sigma}(z,z') = -iU(z)U(z')\mathcal{G}^0_{\sigma}(z,z')\mathcal{G}^0_{-\sigma}(z',\bar{z})U(\bar{z})\mathcal{G}^0_{\sigma}(\bar{z},\bar{z}^+)\mathcal{G}^0_{-\sigma}(\bar{z},z^+)\mathcal{G}^0_{-\sigma}(z,z') \tag{3.33}$$

and as third (Fig. 3.10)

$$\Sigma^{3e}_{\sigma}(z,z') = -iU(z)U(z')\mathcal{G}^0_{\sigma}(z,\bar{z})U(\bar{z})\mathcal{G}^0_{-\sigma}(\bar{z},\bar{z}^+)\mathcal{G}^0_{\sigma}(\bar{z},z')\mathcal{G}^0_{-\sigma}(z',z^+)\mathcal{G}^0_{-\sigma}(z,z'^+). \tag{3.34}$$

As argued in Ref. [138], the addition of the third-order self-energy diagrams within Iterated Perturbation Theory (IPT) allows one to access higher values of U/W and to dope the systems in electrons or holes away from half-filling. The inclusion of these extra self-energy diagrams however does not improve the IPT impurity solver in the strong-coupling regime ($U > W$) and at half-filling, although it does in the weak-coupling regime.

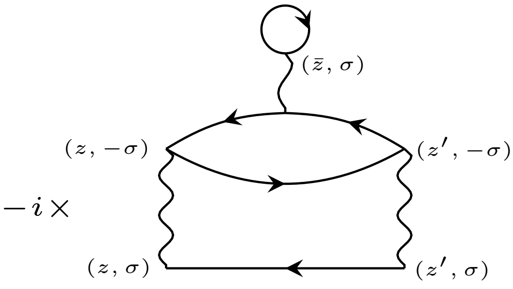

Figure 3.8: 3^{rd}-order diagram Σ^{3c}

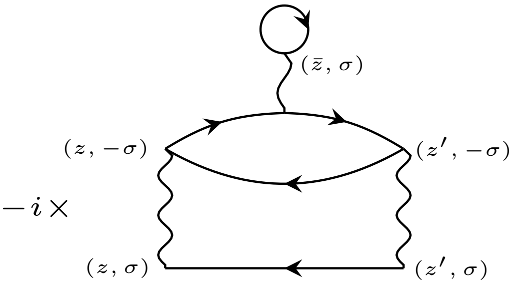

Figure 3.9: 3^{rd}-order diagram Σ^{3d}

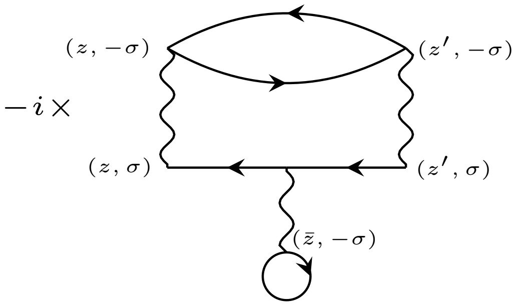

Figure 3.10: 3^{rd}-order diagram Σ^{3e}

ASYMPTOTIC LIMITS OF THE HUBBARD MODEL SELF-ENERGY In this section, the high-frequency and atomic limits of the retarded Green's functions are derived and shown to coincide in the half-filled case in the PM phase. This, as a consequence, means that perturbation theory to second order can capture the lower and upper Hubbard bands that are otherwise of nonperturbative nature. That explains why second-order IPT (see Section 3.2.1.3) is only reliable in the half-filled regime and why third-order IPT is reliable away from half-filling as long as $|\mu - {\mu^{R}}'_{0}(t')|$ and $|\mu - U(t')(1-n_{-\sigma})|$ are much smaller than W [152].

To calculate the high-frequency regime, the development (2.72) comprising the retarded spectral moments (2.71) is used, wherein only the first few terms contribute significantly. The three dominant moments of the retarded spectral function in the Hubbard model (3.9) will be determined in this regime, from which the first two moments of the retarded self-energy (2.73) can be deduced. Looking back at Eq. (2.71), it is easy to note that the first spectral moment of the retarded Green's function ($n=0$) reads

$$\left[\mu_0^R(t')\right]_{l,m}^{\sigma',\sigma''} = \langle\{\hat{c}_{l,\sigma'}(t),\hat{c}^{\dagger}_{m,\sigma''}(t')\}\rangle\big|_{t=t'^{+}} = \mathbb{1}\delta_{\sigma',\sigma''}\delta_{l,m}. \tag{3.35}$$

The spin and lattice orbitals are now considered, since these degrees of freedom are crucial to the Hubbard model.

The moments are functions of the degrees of freedom of the system. The retarded spectral moment that follows up ($n=1$) is determined from

$$\begin{aligned}\left[\mu_1^R(t')\right]_{l,m}^{\sigma',\sigma''} &= i\partial_t\langle\{\hat{c}_{l,\sigma'}(t),\hat{c}^{\dagger}_{m,\sigma''}(t')\}\rangle\big|_{t=t'^{+}}\\ &= (i)^2\langle\{\left[\hat{\mathcal{H}},\hat{c}_{l,\sigma'}\right](t),\hat{c}^{\dagger}_{m,\sigma''}(t')\}\rangle\big|_{t=t'^{+}}.\end{aligned} \tag{3.36}$$

This entails the calculation of a commutator and an anticommutator. Let's work out first the commutator. Following up on Eqs. (2.51) and (2.52), it is easy to get that for the Hubbard model (3.9)

$$
\begin{aligned}
\left[\hat{\mathcal{H}},\hat{c}_{l,\sigma'}\right](t) &= \sum_{ij,\sigma}\left(h^{\sigma}_{i,j}(t)-\mu\delta_{i,j}\right)\left[\hat{c}^{\dagger}_{i,\sigma}\hat{c}_{j,\sigma},\hat{c}_{l,\sigma'}\right]+\frac{1}{2}U(t)\sum_{i,\sigma}\left[\hat{n}_{i,\sigma}\hat{n}_{i,-\sigma},\hat{c}_{l,\sigma'}\right] \\
&= -\sum_{j}\left(h^{\sigma'}_{l,j}(t)-\mu\delta_{l,j}\right)\hat{c}_{j,\sigma'}-U(t)\hat{n}_{i,-\sigma'}\hat{c}_{i,\sigma'}\delta_{l,i}.
\end{aligned}
\tag{3.37}
$$

As a reminder, the one-body operator h is assumed hermitian just like in Eq. (2.48). Then, evaluating the anticommutator with Eq. (3.37), one finally gets

$$
\left[\mu^{R}_{1}(t')\right]^{\sigma',\sigma''}_{l,m}=\left(h^{\sigma'}_{l,m}(t')-\mu\delta_{l,m}\right)\delta_{\sigma',\sigma''}+U(t')\langle\hat{n}_{l,-\sigma'}\rangle\delta_{\sigma',\sigma''}\delta_{l,m}.
\tag{3.38}
$$

The trace of the one-body Hamiltonian, consisting of the hopping energies between the lattice sites – this includes orbitals in the case of the multi-orbital Hubbard model (3.8) – is zeroed out if all the matrix elements lie off the diagonal. Although, if the one-body Hamiltonian is comprised of time-dependent on-site energy terms (lying on the diagonal), the trace doesn't cancel out. Next, the third retarded spectral moment is ($n=2$)

The trace is invariant under similarity transformations, which means that for invertible matrices A and D, $TrA = TrD^{-1}AD$.

$$
\begin{aligned}
\left[\mu^{R}_{2}(t')\right]^{\sigma',\sigma''}_{l,m} &= (i)^2\partial^2_t\langle\{\hat{c}_{l,\sigma'}(t),\hat{c}^{\dagger}_{m,\sigma''}(t')\}\rangle\big|_{t=t'^{+}} \\
&= (i)^4\langle\{\left[\hat{\mathcal{H}},\left[\hat{\mathcal{H}},\hat{c}_{l,\sigma'}\right]\right](t),\hat{c}^{\dagger}_{m,\sigma''}(t')\}\rangle\big|_{t=t'^{+}}.
\end{aligned}
\tag{3.39}
$$

The nested commutator can be computed based on Eq. (3.37). Doing so, this gives four terms

$$
\begin{aligned}
\left[\hat{\mathcal{H}},\left[\hat{\mathcal{H}},\hat{c}_{l,\sigma'}\right]\right](t) &= -\sum_{i'j',\sigma}\sum_{j}\left(h^{\sigma'}_{l,j}(t)-\mu\delta_{l,j}\right)\left(h^{\sigma}_{i',j'}(t)-\mu\delta_{i',j'}\right)\left[\hat{c}^{\dagger}_{i',\sigma}\hat{c}_{j',\sigma},\hat{c}_{j,\sigma'}\right] \\
&\quad -U(t)\hat{n}_{l,-\sigma'}\sum_{i'j',\sigma}\left(h^{\sigma}_{i',j'}(t)-\mu\delta_{i',j'}\right)\left[\hat{c}^{\dagger}_{i',\sigma}\hat{c}_{j',\sigma},\hat{c}_{l,\sigma'}\right] \\
&\quad -\frac{U(t)}{2}\sum_{i'j,\sigma}\left(h^{\sigma'}_{l,j}(t)-\mu\delta_{l,j}\right)\left[\hat{n}_{i',\sigma}\hat{n}_{i',-\sigma},\hat{c}_{j,\sigma'}\right]-\frac{U(t)^2}{2}\hat{n}_{l,-\sigma'}\sum_{i',\sigma}\left[\hat{n}_{i',\sigma}\hat{n}_{i',-\sigma},\hat{c}_{l,\sigma'}\right] \\
&= \sum_{jj'}\left(h^{\sigma'}_{l,j}(t)-\mu\delta_{l,j}\right)\left(h^{\sigma'}_{j,j'}(t)-\mu\delta_{j,j'}\right)\hat{c}_{j',\sigma'}+U(t)\hat{n}_{l,-\sigma'}\sum_{j'}\left(h^{\sigma'}_{l,j'}(t)-\mu\delta_{l,j'}\right)\hat{c}_{j',\sigma'} \\
&\quad +U(t)\sum_{j}\left(h^{\sigma'}_{l,j}(t)-\mu\delta_{l,j}\right)\hat{n}_{j,-\sigma'}\hat{c}_{j,\sigma'}+U(t)^2\hat{n}_{l,-\sigma'}\hat{c}_{l,\sigma'},
\end{aligned}
\tag{3.40}
$$

where the Pauli principle was put to use to get the last term on the last line of Eq. (3.40), namely that $\hat{n}^2_{l,-\sigma'}=\hat{n}_{l,-\sigma'}$. Evaluating the anticommutator in Eq. (3.39) with the result of the nested commutator (3.40) and assuming that the densities on different lattice sites are the same on average in the PM phase $\langle\hat{n}_{l,-\sigma'}\rangle=\langle\hat{n}_{m,-\sigma'}\rangle$, one obtains finally as third moment

$$
\begin{aligned}
\left[\mu^{R}_{2}(t')\right]^{\sigma',\sigma''}_{l,m} &= \sum_{j}\left(h^{\sigma'}_{l,j}(t')-\mu\delta_{l,j}\right)\left(h^{\sigma'}_{j,m}(t')-\mu\delta_{j,m}\right)\delta_{\sigma',\sigma''} \\
&\quad +2U(t)\langle\hat{n}_{l,-\sigma'}\rangle\left(h^{\sigma'}_{l,m}(t)-\mu\delta_{l,m}\right)\delta_{\sigma',\sigma''}+U(t')^2\langle\hat{n}_{l,-\sigma'}\rangle\delta_{l,m}\delta_{\sigma',\sigma''}.
\end{aligned}
\tag{3.41}
$$

So what can be fleshed out of the moments (3.38) and (3.41) just calculated? By using the Langreth rules (see Section 2.2.1) to determine the Dyson's equation (2.44) that expresses the retarded Green's function in terms of the retarded self-energy Σ^R, one can relate the spectral moments $\mu^{R'}$ (2.73) to those μ^R (2.72) already known. The retarded Dyson's equation reads

$$\underbrace{\left[\left((i\partial_t+\mu)\delta_{l,m}-h^{\sigma}_{l,m}(t)\right)\delta(t-t')\right]}_{\mathcal{G}^0_{lm,\sigma}(t,t')^{-1}}\mathcal{G}^R_{lm,\sigma}(t,t')-\int_{t'}^{t}\mathrm{d}\bar{t}\,\Sigma^R_{l\bar{j},\sigma}(t,\bar{t})\mathcal{G}^R_{\bar{j}m,\sigma}(\bar{t},t')=\delta(t-t'),$$

whose Fourier transform yields

$$\mathcal{G}^R_{lm,\sigma}(\omega,t')=\left[\mathcal{G}^0_{lm,\sigma}(\omega,t')^{-1}-\Sigma^R_{lm,\sigma}(\omega,t')\right]^{-1}.$$

It is important to bring up to attention that the noninteracting Green's function $\mathcal{G}^0$ is not retarded *per se*, since it is a δ-function in frequency (not in time). Using the development (2.73) to express Σ^R, the leading terms at infinite frequency (shortest times after t') read

$$\begin{aligned}
\mathcal{G}^R_{lm,\sigma}(\omega,t')&=\left[(\omega+i\eta)\delta_{l,m}+\mu\delta_{l,m}-h^{\sigma}_{l,m}(t')-[\mu^{R'}_0(t')]^{\sigma}_{l,m}-\frac{[\mu^{R'}_1(t')]^{\sigma}_{l,m}}{\omega+i\eta}-\cdots\right]^{-1}\\
&=(\omega+i\eta)^{-1}\left[\delta_{l,m}-\frac{h^{\sigma}_{l,m}(t')+[\mu^{R'}_0(t')]^{\sigma}_{l,m}-\mu\delta_{l,m}}{\omega+i\eta}-\frac{[\mu^{R'}_1(t')]^{\sigma}_{l,m}}{(\omega+i\eta)^2}-\cdots\right]^{-1}\\
&\simeq(\omega+i\eta)^{-1}\Bigg[\delta_{l,m}+\frac{h^{\sigma}_{l,m}(t')+[\mu^{R'}_0(t')]^{\sigma}_{l,m}-\mu\delta_{l,m}}{\omega+i\eta}+\frac{[\mu^{R'}_1(t')]^{\sigma}_{l,m}}{(\omega+i\eta)^2}\\
&+\frac{\sum_n\left(h^{\sigma}_{l,n}(t')-\mu\delta_{l,n}+[\mu^{R'}_0(t')]^{\sigma}_{l,n}\right)\left(h^{\sigma}_{n,m}(t')-\mu\delta_{n,m}+[\mu^{R'}_0(t')]^{\sigma}_{n,m}\right)}{(\omega+i\eta)^2}\\
&+\mathcal{O}\left(\frac{1}{\omega^3}\right)\Bigg],
\end{aligned}\tag{3.42}$$

having utilized the Taylor expansion around $x=0$ of $\frac{1}{1-x}=\sum_{n=0}^{\infty}x^n$ for $x\ll 1$. Therefore, according to Eq. (3.42), the moments of the retarded Green's function and retarded self-energy to order $\mathcal{O}(1/\omega^2)$ are related as follows

$$\left[\mu^R_1(t')\right]^{\sigma}_{l,m}=h^{\sigma}_{l,m}(t')-\mu\delta_{l,m}+\left[\mu^{R'}_0(t')\right]^{\sigma}_{l,m}.\tag{3.43}$$

From Eq. (3.43), one can identify the leading two moments of the retarded self-energy in the Hubbard model. Based on Eq. (3.38) describing μ^R_1, the moment

$$\left[\mu^{R'}_0(t')\right]^{\sigma}_{l,m}=U(t')\langle\hat{n}_{l,-\sigma}\rangle\delta_{l,m}.\tag{3.44}$$

In Eq. (3.42), considering Eq. (3.44), the terms of order $\mathcal{O}(1/\omega^3)$ when gathered give

$$\begin{aligned}
[\mu^R_2(t')]^{\sigma}_{l,m}&=[\mu^{R'}_1(t')]^{\sigma}_{l,m}+\sum_n\left(h^{\sigma}_{l,n}(t')-\mu\delta_{l,n}\right)\left(h^{\sigma}_{n,m}(t')-\mu\delta_{n,m}\right)\\
&+2U(t')\langle\hat{n}_{l,-\sigma}\rangle\left(h^{\sigma}_{l,m}(t')-\mu\delta_{l,m}\right)+U(t')^2\langle\hat{n}_{l,-\sigma}\rangle^2\delta_{l,m}.
\end{aligned}\tag{3.45}$$

By substituting the equation describing μ^R_2 (3.41) into Eq. (3.45), the second retarded self-energy moment becomes

$$\left[\mu_1^{R'}(t')\right]^{\sigma}_{l,m} = U(t')^2\langle \hat{n}_{l,-\sigma}\rangle(1-\langle \hat{n}_{l,-\sigma}\rangle)\delta_{l,m}. \tag{3.46}$$

Hence, combining the retarded moments of the self-energy (3.44) and (3.46), the leading terms of the Hubbard self-energy expanded from infinity yield

$$\Sigma^R_{lm,\sigma}(\omega,t') \simeq U(t')\langle \hat{n}_{l,-\sigma}\rangle\delta_{l,m} + \frac{U(t')^2\langle \hat{n}_{l,-\sigma}\rangle(1-\langle \hat{n}_{l,-\sigma}\rangle)\delta_{l,m}}{\omega+i\eta}. \tag{3.47}$$

To justify the usage of perturbation theory in the impurity solver in the case of the half-filled Hubbard model ($\langle \hat{n}_{l,-\sigma}\rangle = 1/2$), the self-energy expansion for very large frequency (3.47) will be compared with that of the atomic limit.

Let's move on now to determine the single-particle spectral weight of the impurity electrons in the atomic limit ($U \gg W$). In the limit of a local interaction much larger than the bandwidth (hopping energy), the Hubbard model Hamiltonian (3.9) simplifies down to

$$\hat{\mathcal{H}}(t) = \frac{1}{2}U(t)\sum_{\sigma}\hat{n}_{\sigma}\hat{n}_{-\sigma}. \tag{3.48}$$

The equations of motion of the single-particle retarded Green's function in the grand-canonical ensemble (2.10) reads

$$i\partial_t \mathcal{G}^R_{\sigma'}(t,t') = \delta(t-t') + i\Theta(t-t')\langle\{\left[\hat{\mathcal{H}},\hat{c}_{\sigma'}\right](t),\hat{c}^{\dagger}_{\sigma'}(t')\}\rangle, \tag{3.49}$$

such that plugging the result (3.37) (last term) into (3.49) gives

$$\begin{aligned}
i\partial_t \mathcal{G}^R_{\sigma'}(t,t') &= \delta(t-t') + i\Theta(t-t')\mu\langle\{\hat{c}_{\sigma'}(t),\hat{c}^{\dagger}_{\sigma'}(t')\}\rangle \\
&- iU(t)\Theta(t-t')\langle\{\hat{n}_{-\sigma'}(t)\hat{c}_{\sigma'}(t),\hat{c}^{\dagger}_{\sigma'}(t')\}\rangle \\
&= \delta(t-t') - \mu\mathcal{G}^R_{\sigma'}(t,t') + U(t)\mathcal{G}^R_{2,\sigma'}(t,t'),
\end{aligned} \tag{3.50}$$

where the two-particle retarded Green's function was defined as

$$\mathcal{G}^R_{2,\sigma'}(t,t') \equiv -i\Theta(t-t')\langle\{\hat{n}_{-\sigma'}(t)\hat{c}_{\sigma'}(t),\hat{c}^{\dagger}_{\sigma'}(t')\}\rangle.$$

Fourier transforming Eq. (3.50) leads to

$$\begin{aligned}
&i\int_{-\infty}^{\infty}\mathrm{d}t\; e^{i(\omega+i\eta)(t-t')}\partial_t\mathcal{G}^R_{\sigma'}(t,t') = (\omega+i\eta)\mathcal{G}^R_{\sigma'}(t,t') \\
&= 1 - \mu\mathcal{G}^R_{\sigma'}(\omega,t') + U(t')\mathcal{G}^R_{2,\sigma'}(\omega,t').
\end{aligned} \tag{3.51}$$

The Fourier transform of the partial time derivative requires that the boundaries of the integral run from $-\infty$ to ∞, because it is not bounded like the retarded Green's function, *i.e.* $i\partial_t$ is defined and nonzero for all times t before t'. The domain of integration upon which the retarded Green's functions are nonzero automatically spans from t' to ∞. Let's carry on by calculating the equations of motion of $\mathcal{G}_2$ in hope that it reduces itself down to a closed set of intertwined equations with Eq. (3.51):

$$\begin{aligned}
&i\partial_t\mathcal{G}^R_{2,\sigma'}(t,t') \\
&= \delta(t-t')\langle\{\hat{n}_{-\sigma'}(t)\hat{c}_{\sigma'}(t),\hat{c}^{\dagger}_{\sigma'}(t')\}\rangle + \Theta(t-t')\langle\{\partial_t\hat{n}_{-\sigma'}(t)\hat{c}_{\sigma'}(t),\hat{c}^{\dagger}_{\sigma'}(t')\}\rangle \\
&= \delta(t-t')\langle\hat{n}_{-\sigma'}(t)\rangle + i\Theta(t-t')\langle\{[\hat{\mathcal{H}},\hat{n}_{-\sigma'}\hat{c}_{\sigma'}](t),\hat{c}^{\dagger}_{\sigma'}(t')\}\rangle.
\end{aligned} \tag{3.52}$$

The interaction (3.48) preserves the number of particles, therefore any particle number operator commutes with other fermionic operators. The commutator in Eq. (3.52) gives

$$[\hat{\mathcal{H}},\hat{n}_{-\sigma'}\hat{c}_{\sigma'}](t) = -U(t)\hat{n}_{-\sigma'}(t)^2\hat{c}_{\sigma'}(t) = -U(t)\hat{n}_{-\sigma'}(t)\hat{c}_{\sigma'}(t), \tag{3.53}$$

making use of the Pauli principle. Inserting the result of the commutator (3.53) back into Eq. (3.52) and Fourier transforming just like in Eq. (3.51), one obtains

$$(\omega + i\eta)\mathcal{G}^R_{2,\sigma'}(\omega,t') = \langle\hat{n}_{-\sigma'}(t')\rangle - \mu\mathcal{G}^R_{2,\sigma'}(\omega,t') + U(t')\mathcal{G}^R_{2,\sigma'}(\omega,t'). \tag{3.54}$$

Combining Eqs. (3.51) and (3.54), one comes across

$$\mathcal{G}^R_{\sigma'}(\omega,t') = \frac{1-\langle\hat{n}_{-\sigma'}\rangle}{\omega+i\eta+\mu} + \frac{\langle\hat{n}_{-\sigma'}\rangle}{\omega+i\eta+\mu-U(t')}. \tag{3.55}$$

The Hubbard model preserves the particle number, hence the particle density doesn't depend on time. The retarded Green's function (3.55) describes a system where spin up electrons must pay an energy cost of $-\mu + U(t')$ to occupy the fraction of sites $\langle\hat{n}_{-\sigma'}\rangle$ with spin down, and an energy cost $-\mu$ for the other fraction of sites without spin down electrons. At half-filling, the Hubbard model is particle-hole symmetric, and the chemical potential $\mu = U(t'=0)/2$ effectively shifts the energy scale such that the Mott insulator gap appears at $\omega = 0$. Thereof, the single-particle Green's function can be re-expressed as

$$\begin{aligned}\mathcal{G}^R_{\sigma'}(\omega,t') &= \frac{1/2}{\omega+i\eta+\frac{U(t')}{2}} + \frac{1/2}{\omega+i\eta-\frac{U(t')}{2}}\\ &= \frac{1}{\omega+i\eta-\frac{U(t')^2}{4(\omega+i\eta)}}.\end{aligned} \tag{3.56}$$

The fact that the half-filled high-frequency limit of the Hubbard retarded self-energy (3.47) coincides with the retarded self-energy in the atomic limit has a nontrivial consequence. The leading term in the large-U limit of the second-order IPT self-energy (3.26) is the same as set out in Eq. (3.47), since the fictitious densities $n_0(t)$ extracted from the Weiss Green's functions $n_0(t) = -\frac{1}{\pi}\mathrm{Im}\mathcal{G}^0(t,t^+)$ are equal to $n(t) = -\frac{1}{\pi}\mathrm{Im}\mathcal{G}^R(t,t^+)$ at half-filling [105]. The latter automatically ensures that the atomic limit is respected by the second-order self-energy (3.26). In Ref. [62], the second-order IPT self-energy is interpolated between the high-frequency limit, the atomic limit and the low-frequency behavior to allow to wander away from half-filling while respecting the asymptotics.

4

RPA-TYPE POST-PROCESSING DMFT

In this section, the general formalism for computing the optical conductivity and related susceptibilities is explained. The Hedin's equations [127, 134] derived in Section 2.4 are used to derive the π-ton ladder-type vertex corrections to the current-current and spin-spin correlation functions. In Section 4.2, the nonequilibrium formula to calculate the single-ladder π-ton vertex corrections is introduced and discussed. These ladder-type corrections are two-particle vertex corrections treated in a DMFT post-processing fashion, as opposed to the spin and charge irreducible $\mathcal{G}$-skeletonic two-particle vertices that are treated self-consistently in DMFT+TPSC (see Section 5.2.9). This means that the lattice Green's functions (3.14) are inputted directly in the expressions describing two-particle vertex corrections that have been analytically derived before hand. Albeit the scheme's reliability relies strongly on the physical intuition of the underlying physical processes governing phenomena in the system of study, it proves to provide a good and computationally cheap qualitative scheme to calculate two-particle vertex corrections that involve momentum and energy dependence, in and out of equilibrium [119, 120]. Arguably, this method is reliable in the limit where the features of the electronic density of states impact more the signature of the collective modes than the collective modes influence the single-particle properties – like would be the case in systems at weak coupling.

The specific expressions delineating the two-particle vertex corrections lie in the attempt to describe the π-ton bound state [66] that would take place in the normal state of high-T$_c$ layered copper-oxide superconductors [13, 140], in the vicinity of the AFM phase boundary where it admits strong fluctuations at momentum $\mathbf{k}_{\pi} = (\pi, \pi, \cdots)$. These π-tons would dominate the vertex corrections in the longitudinal optical conductivity in the Hubbard model and these would come in through momentum scattering $\tilde{\mathbf{k}} - \bar{\mathbf{k}} \simeq \mathbf{k}_{\pi}$ of particle-hole pairs. These π-ton instabilities would kick in when the charges couple to light (photons). They would manifest themselves through the high sensitivity of the optical gap to an applied magnetic field [66].

4.1 GENERAL FORMALISM

The vertex corrections to various response functions can be computed using the Schwinger formalism and linear response theory [127, 134]. Specifically, the response functions of interest are the charge and spin response functions for the Hubbard model (3.9) characterized by local density-density interactions. The equations will be derived first at equilibrium, since only one of them has been tested in nonequilibrium settings [119]. For the sake of an efficient notation,

As a reminder, $\mathbf{x}$ *represents real-space coordinates and* τ *imaginary time.*

numbers encapsulating space-time variables are introduced, *i.e.* $1 \equiv (\mathbf{x}_1, \tau_1)$, and bars over the numbers are used to indicate a space-time integration:

$$A(\bar{1}) \equiv \int_0^{\beta} \mathrm{d}\tau_1 \int \cdots \int_{-\infty}^{\infty} \mathrm{d}^D x_1 \; A(\mathbf{x}_1, \tau_1),$$

with D the spatial dimension(s) of the system. Like mentioned previously, Greek letters represent discrete electronic degrees of freedom such as spin and orbitals and when they feature bars over they are implicitly summed over. Furthermore, some of the expressions that will be encountered were derived in Chapter 2 and are narrowed down to deal solely with the equilibrium case.

In the Schwinger formalism [90], the Martin-Schwinger hierarchy of quantum-field correlators can be generated from the simple functional $\mathcal{Z}$ of a source field

$$\mathcal{Z}[\phi] = \mathrm{Tr}\left[e^{-\beta\hat{\mathcal{H}}^M}\mathcal{T}_{\tau}e^{-\hat{c}^{\dagger}_{\bar{\alpha}}(\bar{1})\phi_{\bar{\alpha},\bar{\beta}}(\bar{1},\bar{2})\hat{c}_{\bar{\beta}}(\bar{2})}\right], \tag{4.1}$$

where ϕ is the same source field as in Section 2.3, whose value has to be set to zero when computing physical quantities. Note that this source field is not defined on the Kadanoff-Baym contour Fig. 2.1. The trace Tr spans over the Fock eigenstates of $\hat{\mathcal{H}}^M$. The imaginary-time ordering super-operator $\mathcal{T}_{\tau}$ appearing in Eq. (4.1) is defined in Eq. (2.35). To get Eq. (4.1) from Eq. (2.24), the fact that $z = -i\tau$ on $\mathcal{C}_3$ was used (see Section 2.2). The system is connected to both temperature and particle baths, so the grand-canonical ensemble is used and it is implied that $\hat{\mathcal{H}}^M \to \hat{\mathcal{H}}^M - \mu\hat{N}$, with μ the chemical potential and N the total number of particles. The corresponding imaginary-time single-particle Green's function is given by (*cf.* Eq. (2.35))

$$-\frac{\delta \ln \mathcal{Z}[\phi]}{\delta\phi_{\alpha,\beta}(2,1)} = -\langle\mathcal{T}_{\tau}\hat{c}_{\alpha}(1)\hat{c}^{\dagger}_{\beta}(2)\rangle_{\phi} = \mathcal{G}^{\phi}_{\alpha,\beta}(1,2), \tag{4.2}$$

where the average value means

$$\langle\cdots\rangle_{\phi} \triangleq \mathrm{Tr}\left[\frac{e^{-\beta\hat{\mathcal{H}}^M}}{\mathcal{Z}[\phi]}e^{-\hat{c}^{\dagger}_{\bar{\alpha}}(\bar{1})\phi_{\bar{\alpha},\bar{\beta}}(\bar{1},\bar{2})\hat{c}_{\bar{\beta}}(\bar{2})}\cdots\right]. \tag{4.3}$$

By taking one more derivative with respect to the source field one can generate the four-point correlation function linked to the self-energy via the equations of motion and Dyson's equation

$$\begin{aligned}\frac{\delta\mathcal{G}^{\phi}_{\alpha,\beta}(1,3)}{\delta\phi_{\gamma,\delta}(2^+,2)} =& \mathcal{G}^{\phi}_{\delta,\gamma}(2,2^+)\mathcal{G}^{\phi}_{\alpha,\beta}(1,3)\\ &+ \langle\mathcal{T}_{\tau}\hat{c}_{\alpha}(1)\hat{c}^{\dagger}_{\beta}(3)\hat{c}^{\dagger}_{\gamma}(2^+)\hat{c}_{\delta}(2)\rangle_{\phi}.\end{aligned} \tag{4.4}$$

Another important ingredient is the identity relation (2.42) which simply gives at equilibrium

$$\begin{aligned}\frac{\delta\mathcal{G}^{\phi}_{\eta,\xi}(1,3)}{\delta\phi_{\gamma,\delta}(2^+,2)} =& \mathcal{G}^{\phi}_{\eta,\gamma}(1,2^+)\mathcal{G}^{\phi}_{\delta,\xi}(2,3)\delta_{\eta,\gamma}\delta_{\xi,\delta}\\ &+ \mathcal{G}^{\phi}_{\eta,\bar{\beta}}(1,\bar{4})\frac{\delta\Sigma^{\phi}_{\bar{\beta},\bar{\theta}}(\bar{4},\bar{\bar{5}})}{\delta\mathcal{G}^{\phi}_{\bar{\iota},\bar{\kappa}}(\bar{6},\bar{7})}\frac{\delta\mathcal{G}^{\phi}_{\bar{\iota},\bar{\kappa}}(\bar{6},\bar{7})}{\delta\phi_{\gamma,\delta}(2^+,2)}\mathcal{G}^{\phi}_{\bar{\theta},\xi}(\bar{\bar{5}},3).\end{aligned} \tag{4.5}$$

Starting from now, to close in on the diagrammatic representation the terms of Eq. (4.5) will hold, the following notations will be employed

$$\begin{cases} \dfrac{\delta\Sigma^{\phi}_{\sigma}(4,5)}{\delta\mathcal{G}^{\phi}_{\sigma'}(6,7)} \to \square^{\phi}_{\sigma\sigma'}\left(\dfrac{4,5}{6,7}\right) \\ \dfrac{\delta\mathcal{G}^{\phi}_{\sigma}(6,7)}{\delta\phi_{\sigma'}(2^{+},2)} \to \blacktriangleright^{\phi}_{\sigma\sigma'}(6,7,2). \end{cases} \tag{4.6}$$

Indeed, the first term of Eq. (4.6) will account for the ladder-type vertex corrections, whereas the second term will seal off the top of the susceptibility/polarization bubbles (see the last term of Fig. 2.9). Since the Hubbard model enters the equations of motion, the Greek subscripts have been traded off for spin indices, and the various propagators are now spin diagonal (a single spin index). One can think of the term $\square$ as the pink box shown in Fig. 2.5 and it will simplify down to $\square^{\phi}_{\sigma\sigma'}(4-5)\delta(4-6)\delta(5-7)\delta_{\sigma',-\sigma}$ so as to depend only on momentum differences between the particle-hole bubbles wrapping around the vertex. Ultimately, the vertex $\square$ represents a single vertical infinite ladder and it can be duplicated through iterating Eq (2.46). Since the $\square$ term is a central element to the two-particle vertex corrections, its expression is worked out first by returning back to the equations of motion in D dimension(s)

$$\begin{aligned} -\partial_{\tau_1}\langle\mathcal{T}_{\tau}\hat{c}_{\sigma}(1)\hat{c}^{\dagger}_{\sigma}(\bar{2})\rangle_{\phi} = -\delta^{D}(x_1-x_2)\delta(\tau_1-\tau_2) - \left\langle\mathcal{T}_{\tau}\partial_{\tau_1}S[\phi]\hat{c}_{\sigma}(1)\hat{c}^{\dagger}_{\sigma}(2)\right\rangle_{\phi} \\ - \left\langle\mathcal{T}_{\tau}\left[\hat{\mathcal{H}}^{M},\hat{c}_{\sigma}(1)\right]\hat{c}^{\dagger}_{\sigma}(2)\right\rangle_{\phi}, \end{aligned} \tag{4.7}$$

which, using the Dyson equation (2.44), yields

$$\Sigma^{\phi}_{\sigma}(1,\bar{2})\mathcal{G}^{\phi}_{\sigma}(\bar{2},2) = -\sum_{\sigma_2}U\delta_{\sigma_2,-\sigma}\delta(1-\bar{2})\left\langle\mathcal{T}_{\tau}\hat{c}_{\sigma}(1)\hat{c}^{\dagger}_{\sigma}(2)\hat{c}^{\dagger}_{\sigma_2}(\bar{2}^{+})\hat{c}_{\sigma_2}(\bar{2})\right\rangle_{\phi}. \tag{4.8}$$

Making use of Eqs. (4.4) and (4.5), one may re-express the right-hand side of Eq. (4.8) as

$$\begin{aligned} \Sigma^{\phi}_{\sigma}(1,\bar{2})\mathcal{G}^{\phi}_{\sigma}(\bar{2},2) = -\sum_{\sigma_2}U\delta_{\sigma_2,-\sigma}\delta(1-\bar{2})\Big[\mathcal{G}^{\phi}_{\sigma}(1,\bar{2}^{+})\mathcal{G}^{\phi}_{\sigma}(\bar{2},2)\delta_{\sigma,\sigma_2} - \\ \mathcal{G}^{\phi}_{\sigma_2}(\bar{2},\bar{2}^{+})\mathcal{G}^{\phi}_{\sigma}(1,2) + \sum_{\sigma'}\mathcal{G}^{\phi}_{\sigma}(1,\bar{4})\frac{\delta\Sigma^{\phi}_{\sigma}(\bar{4},\bar{3})}{\delta\mathcal{G}^{\phi}_{\sigma'}(\bar{5},\bar{6})}\frac{\delta\mathcal{G}^{\phi}_{\sigma'}(\bar{5},\bar{6})}{\delta\phi_{\sigma_2}(\bar{2}^{+},\bar{2})}\mathcal{G}^{\phi}_{\sigma}(\bar{3},2)\Big]. \end{aligned} \tag{4.9}$$

In this section, the equilibrium vertex function $\Gamma \equiv \frac{\delta\Sigma}{\delta\mathcal{G}}$ *is defined without a "-" sign, as opposed to the nonequilibrium case Section 2.4.*

After some manipulations, one obtains the expression for the self-energy

$$\begin{aligned} \Sigma^{\phi}_{\sigma}(1,3) = U\mathcal{G}^{\phi}_{-\sigma}(1,1^{+})\delta(1-3) \\ - U\sum_{\sigma'}\mathcal{G}^{\phi}_{\sigma}(1,\bar{4})\frac{\delta\Sigma^{\phi}_{\sigma}(\bar{4},3)}{\delta\mathcal{G}^{\phi}_{\sigma'}(\bar{5},\bar{6})}\frac{\delta\mathcal{G}^{\phi}_{\sigma'}(\bar{5},\bar{6})}{\delta\phi_{-\sigma}(1^{+},1)}, \end{aligned} \tag{4.10}$$

which is important to determine the vertex function corresponding to the functional derivative of the self-energy with respect to the interacting Green's function. To get an expression for the vertex, one must work out $\frac{\delta\Sigma}{\delta\mathcal{G}}$ from Eq. (4.10).

Carrying out the functional derivative defining the vertex function and keeping exclusively the first terms, one gets

$$\begin{aligned}\frac{\delta\Sigma^{\phi}_{\sigma}(1,3)}{\delta\mathcal{G}^{\phi}_{\sigma'}(4,5)} &= U\delta_{\sigma',-\sigma}\delta(4-5)\delta(1-3)\delta(1-4)\\ &\quad - U\delta(1-4)\delta_{\sigma,\sigma'}\frac{\delta\Sigma^{\phi}_{\sigma}(5,3)}{\delta\mathcal{G}^{\phi}_{-\sigma}(\bar{7},\bar{8})}\mathcal{G}^{\phi}_{-\sigma}(\bar{7},1^{+})\mathcal{G}^{\phi}_{-\sigma}(1,\bar{8})\\ &\quad - U\delta_{\sigma',-\sigma}\delta(1-5)\mathcal{G}^{\phi}_{\sigma}(1,\bar{7})\frac{\delta\Sigma^{\phi}_{\sigma}(\bar{7},3)}{\delta\mathcal{G}^{\phi}_{\sigma'}(4,\bar{8})}\mathcal{G}^{\phi}_{\sigma'}(5,\bar{8})\\ &\quad - U\delta_{\sigma',-\sigma}\delta(1-4)\mathcal{G}^{\phi}_{\sigma}(1,\bar{7})\frac{\delta\Sigma^{\phi}_{\sigma}(\bar{7},3)}{\delta\mathcal{G}^{\phi}_{\sigma'}(\bar{8},5)}\mathcal{G}^{\phi}_{\sigma'}(\bar{8},4^{+}) - \cdots,\end{aligned} \tag{4.11}$$

which is shown diagrammatically in Fig. 4.1. The expression for a single vertical ladder is obtained when keeping the first and last terms in Eq. (4.11). Isolating $\frac{\delta\Sigma}{\delta\mathcal{G}}$ from those two terms yields

$$\frac{\delta\Sigma_{\sigma}(1,3)}{\delta\mathcal{G}_{\sigma'}(4,5)} = \frac{U\delta_{\sigma',-\sigma}\delta(3-5)}{\delta(1-3)\delta(4-5)+U\delta(1-4)\mathcal{G}_{\sigma}(1,3)\mathcal{G}_{\sigma'}(5,4^{+})}. \tag{4.12}$$

This relation is an approximation that sets the □ term showing up in Eq. (4.6). The source field is set to 0 ($\phi \to 0$) in Eq. (4.12) since this is the final form sought. The vertex function (4.12) clearly leads to a nonzero value only if the Green's function attached to it on one side have opposite spins to those attached on the other side (see Fig. 4.5): one □ flips the spin. Furthermore, to distinguish ladder-type vertex corrections whose right extremity terminates with a spin flip from those that don't, the term ▶ will be split up into an even contribution containing an even number of vertical ladders (pink boxes) terminating with the same spin, denoted $\blacktriangleright^{(\text{even})}$ (see Fig. 4.3), and an odd contribution containing an odd number of vertical ladders $\blacktriangleright^{(\text{odd})}$ terminating with a spin flip (see Fig. 4.4). Both $\blacktriangleright^{(\text{even})}$ and $\blacktriangleright^{(\text{odd})}$ are discussed further down.

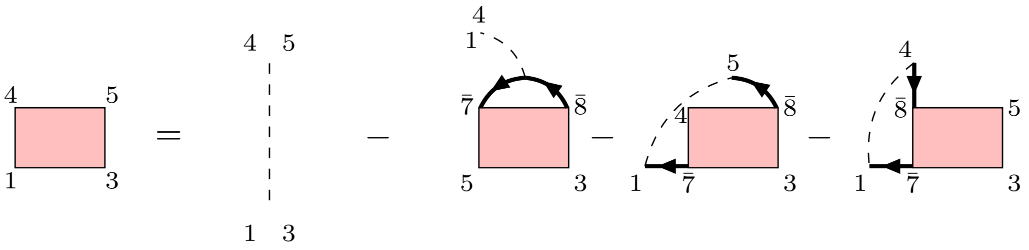

Figure 4.1: Diagrammatic representation of $\frac{\delta\Sigma}{\delta\mathcal{G}}$ when only keeping the first term of $\frac{\delta\mathcal{G}}{\delta\phi}$ (4.5). The first and last terms are those that will be retained in our approximation for $\frac{\delta\Sigma}{\delta\mathcal{G}}$.

Next, the susceptibilities, whose vertex corrections are to be computed, need to be defined. To that effect, Eqs. (4.4) and (4.5) are combined to derive the expressions for the density-density response, and based on this, the current-

current response along direction $i \in \{x,y\}$ $\chi_{j_ij_i}$ and the spin-spin response $\chi_{S_zS_z}$. From Eq. (4.4), the most general expression to the susceptibilities read

$$\begin{aligned}\chi^{\sigma\sigma'}(1,1^+;2^+,2) &= -\left.\frac{\delta\mathcal{G}^{\phi}_{\sigma}(1,1^+)}{\delta\phi_{\sigma'}(2^+,2)}\right|_{\phi=0}\\ &= \langle\mathcal{T}_\tau\hat{n}_{\sigma'}(2)\hat{n}_{\sigma}(1)\rangle - \langle\hat{n}_{\sigma'}(2)\rangle\langle\hat{n}_{\sigma}(1)\rangle\\ &= \langle\mathcal{T}_\tau\left(\hat{n}_{\sigma'}(2) - \langle\hat{n}_{\sigma'}(2)\rangle\right)\left(\hat{n}_{\sigma}(1) - \langle\hat{n}_{\sigma}(1)\rangle\right)\rangle, \qquad (4.13)\end{aligned}$$

from which the charge susceptibility is defined as

$$\chi_{\text{ch}}(1,1^+;2^+,2) \triangleq \sum_{\sigma\sigma'}\chi^{\sigma\sigma'}(1,1^+;2^+,2) \qquad (4.14)$$

and the spin susceptibility

$$\begin{aligned}\chi_{\text{sp}}(1,1^+;2^+,2) = \chi_{S_zS_z}(1,1^+;2^+,2) &\triangleq \sum_{\sigma\sigma'}\tau_z^{\sigma\sigma}\chi^{\sigma\sigma'}(1,1^+;2^+,2)\tau_z^{\sigma'\sigma'}\\ &= \langle\mathcal{T}_\tau\left(\hat{M}_{\sigma'}(2) - \langle\hat{M}_{\sigma'}(2)\rangle\right)\left(\hat{M}_{\sigma}(1) - \langle\hat{M}_{\sigma}(1)\rangle\right)\rangle, \qquad (4.15)\end{aligned}$$

with $\tau_z \equiv \text{diag}\{1,-1\}$ the diagonal Pauli matrix and $\hat{M}_\sigma \equiv \hat{n}_\sigma - \hat{n}_{-\sigma}$. Alternatively, one can express $\chi^{\sigma\sigma'}$ (4.13) using Eq. (4.5) and the Hubbard model selection rules to get

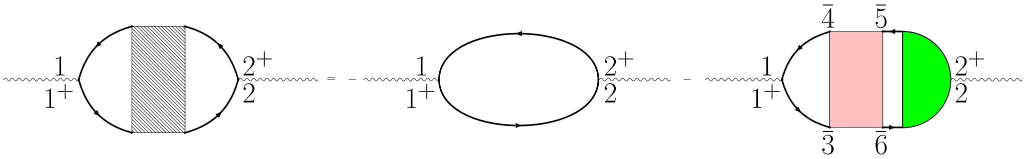

Figure 4.2: General diagrammatic representation of susceptibilities (4.16). On the right-hand side, the first term is the particle-hole bubble and the second contains vertex corrections (χ_{corr}).

$$\begin{aligned}\chi^{\sigma\sigma'}(1,1^+;2^+,2) &= -\mathcal{G}_\sigma(1,2^+)\mathcal{G}_\sigma(2,1^+)\delta_{\sigma,\sigma'}\\ &\quad - \boxed{\sum_{\sigma''}\mathcal{G}^{\phi}_{\sigma}(1,\bar{4})\frac{\delta\Sigma^{\phi}_{\sigma}(\bar{4},\bar{3})}{\delta\mathcal{G}^{\phi}_{\sigma''}(\bar{5},\bar{6})}\frac{\delta\mathcal{G}^{\phi}_{\sigma''}(\bar{5},\bar{6})}{\delta\phi_{\sigma'}(2^+,2)}\mathcal{G}^{\phi}_{\sigma}(\bar{3},1^+)\bigg|_{\phi=0}}, \qquad (4.16)\end{aligned}$$

whose second term (encircled), abbreviated χ_{corr}, corresponds to vertex corrections and can be re-expressed with the notation (4.6) so far adopted as

$$\begin{aligned}&\chi^{\sigma\sigma'}_{\text{corr}}(1,1^+;2^+,2) =\\ &\quad -\sum_{\sigma''}\mathcal{G}^{\phi}_{\sigma}(1,\bar{4})\mathcal{G}^{\phi}_{\sigma}(\bar{3},1^+)\square^{\phi}_{\sigma\sigma''}(\bar{4}-\bar{3})\blacktriangleright^{\phi}_{\sigma''\sigma'}(\bar{4},\bar{3},2)\bigg|_{\phi=0}. \qquad (4.17)\end{aligned}$$

The susceptibility (4.16) is expressed diagrammatically in Fig. 4.2 and its first term will be sometimes referred to as the bare response. Eq. (4.16) will provide the groundwork to put up the formulae that represent the ladder-type vertex corrections for the different susceptibilities $\chi_{j_ij_i}$ (current-current response function) and $\chi_{S_zS_z}$ (spin-spin response function). In the case of the density-density correlation function, the vertices A and B in the diagrams 4.5 and 4.6 (as well as the particle-hole bubble) are identity operators, in the case of $\chi_{S_zS_z}$ they are

Pauli operators $\frac{1}{2}\tau_z$ and in the case of $\chi_{j_i j_i}$ the velocities $v_i(k) = \partial_{k_i}\epsilon(k)$ (since the charge is set to unity). The longitudinal optical conductivity σ_{ii} can be deduced from the imaginary component of the current-current correlation function (see Appendix E) as

$$\mathrm{Re}\,\sigma_{ii}(q_i,\omega) = \frac{\mathrm{Im}\,\chi_{j_i j_i}(q_i,\omega)}{\omega}. \tag{4.18}$$

Since RPA-ladder-type vertex corrections are supposed to dominate the vertex corrections to the optical conductivity [66], three types of contributions are considered, two of which involve vertical ladder diagrams, while the third is of Aslamazov-Larkin (AL) type with two horizontal ladders.

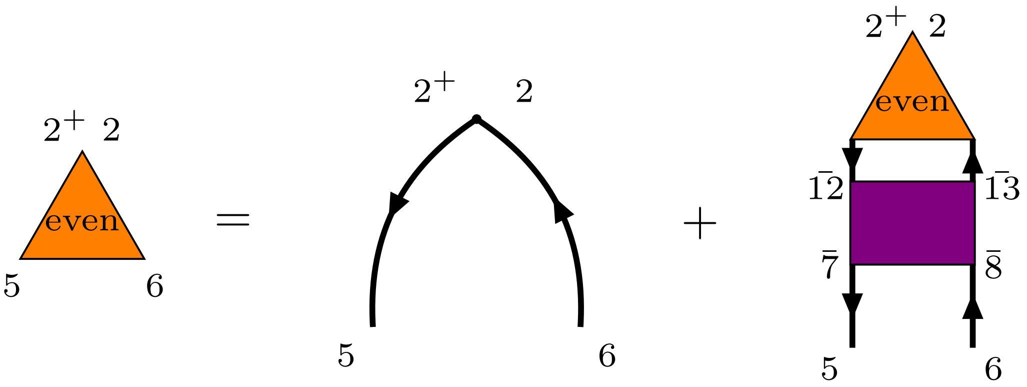

Figure 4.3: Diagrammatic representation of the terms of $\blacktriangleright^{(\text{even})}$ containing solely an even number of vertical ladders (pink boxes); the violet box is comprised of two pink boxes connected together by two Green's functions. The first term is the one that will be inputted in Eq. (4.17) to compute the single-ladder vertex corrections.

Like pointed out before, the $\blacktriangleright$ term consists of terms with even ($\blacktriangleright^{(\text{even})}$) number of ladder diagrams ($\square$ term) that do not flip the spin as result of the interaction with the photon, and terms with odd ($\blacktriangleright^{(\text{odd})}$) number of ladder diagrams that flips the spin. The expression for $\blacktriangleright^{(\text{even})}$, which sums up all even-ladder corrections to the triangle vertex, reads

$$\begin{aligned}
&\frac{\delta\mathcal{G}^{\phi,(\text{even})}_{\sigma''}(5,6)}{\delta\phi_{\sigma'}(2^+,2)} = \mathcal{G}^{\phi}_{\sigma''}(5,2^+)\mathcal{G}^{\phi}_{\sigma''}(2,6)\delta_{\sigma'',\sigma'} \\
&\qquad + \sum_{\tilde{\sigma}',\tilde{\sigma}''} \mathcal{G}^{\phi}_{\sigma''}(5,\bar{1})\mathcal{G}^{\phi}_{\sigma''}(\bar{3},6)\frac{\delta\Sigma^{\phi}_{\sigma''}(\bar{1},\bar{3})}{\delta\mathcal{G}^{\phi}_{\tilde{\sigma}'}(\bar{7},\bar{8})}\mathcal{G}^{\phi}_{\tilde{\sigma}'}(\bar{7},\bar{10})\mathcal{G}^{\phi}_{\tilde{\sigma}'}(\bar{11},\bar{8})\frac{\delta\Sigma^{\phi}_{\tilde{\sigma}'}(\bar{10},\bar{11})}{\delta\mathcal{G}^{\phi}_{\tilde{\sigma}''}(\bar{12},\bar{13})} \\
&\qquad \times \frac{\delta\mathcal{G}^{\phi,(\text{even})}_{\tilde{\sigma}''}(\bar{12},\bar{13})}{\delta\phi_{\sigma'}(2^+,2)} \\
&\Leftrightarrow \\
&\blacktriangleright^{\phi,(\text{even})}_{\sigma''\sigma'}(5,6,2) = \mathcal{G}^{\phi}_{\sigma''}(5,2^+)\mathcal{G}^{\phi}_{\sigma''}(2,6)\delta_{\sigma'',\sigma'} \\
&\qquad + \sum_{\tilde{\sigma}',\tilde{\sigma}''} \mathcal{G}^{\phi}_{\sigma''}(5,\bar{7})\mathcal{G}^{\phi}_{\sigma''}(\bar{8},6)\square^{\phi}_{\sigma''\tilde{\sigma}'}(\bar{7}-\bar{8})\mathcal{G}^{\phi}_{\tilde{\sigma}'}(\bar{7},\bar{10})\mathcal{G}^{\phi}_{\tilde{\sigma}'}(\bar{11},\bar{8})\square^{\phi}_{\tilde{\sigma}'\tilde{\sigma}''}(\bar{10}-\bar{11}) \\
&\qquad \times \blacktriangleright^{\phi,(\text{even})}_{\tilde{\sigma}''\sigma'}(\bar{10},\bar{11},2).
\end{aligned} \tag{4.19}$$

Eq. (4.19) is illustrated diagrammatically in Fig. 4.3. The last term of Eq. (4.19) is denoted as $\blacktriangleright^{\phi,(\mathrm{even}),\mathrm{corr}}_{\sigma''\sigma'}$. Note that self-consistently substituting $\blacktriangleright^{(\mathrm{even})}$ into the right hand side will generate a ladder containing an even number of vertical ladders ($\square$). $\blacktriangleright^{(\mathrm{even}),\mathrm{corr}}$ corresponds to the last term in Fig. 4.3, where the two ladders are represented by a violet box.

Similarly to $\blacktriangleright^{(\mathrm{even})}$, one can come up with an expression for $\blacktriangleright^{(\mathrm{odd})}$ to calculate the double-ladder (χ_{dl}) and higher-order even-ladder corrections. The only difference between $\blacktriangleright^{(\mathrm{odd})}$ and $\blacktriangleright^{(\mathrm{even})}$ is the first term with which the diagrams are generated self-consistently. Therefore, considering the notation introduced and the symmetries inherited from the Hubbard model, one gets

$$
\begin{aligned}
&\frac{\delta \mathcal{G}^{\phi,(\mathrm{odd})}_{\sigma''}(5,6)}{\delta \phi_{\sigma'}(2^+,2)} = \mathcal{G}^{\phi}_{\sigma''}(5,\bar{1})\mathcal{G}^{\phi}_{\sigma''}(\bar{3},6)\frac{\delta \Sigma^{\phi}_{\sigma''}(\bar{1},\bar{3})}{\delta \mathcal{G}^{\phi}_{\sigma'}(\bar{7},\bar{8})}\mathcal{G}^{\phi}_{\sigma'}(\bar{7},2^+)\mathcal{G}^{\phi}_{\sigma'}(2,\bar{8}) \\
&\qquad + \sum_{\tilde{\sigma}',\tilde{\sigma}''} \mathcal{G}^{\phi}_{\sigma''}(5,\bar{1})\mathcal{G}^{\phi}_{\sigma''}(\bar{3},6)\frac{\delta \Sigma^{\phi}_{\sigma''}(\bar{1},\bar{3})}{\delta \mathcal{G}^{\phi}_{\tilde{\sigma}'}(\bar{7},\bar{8})}\mathcal{G}^{\phi}_{\tilde{\sigma}'}(\bar{7},\bar{10})\mathcal{G}^{\phi}_{\tilde{\sigma}'}(\bar{11},\bar{8})\frac{\delta \Sigma^{\phi}_{\tilde{\sigma}'}(\bar{10},\bar{11})}{\delta \mathcal{G}^{\phi}_{\tilde{\sigma}''}(\bar{12},\bar{13})} \\
&\qquad \times \frac{\delta \mathcal{G}^{\phi,(\mathrm{odd})}_{\tilde{\sigma}''}(\bar{12},\bar{13})}{\delta \phi_{\sigma'}(2^+,2)} \\
&\Leftrightarrow \\
&\blacktriangleright^{\phi,(\mathrm{odd})}_{\sigma''\sigma'}(5,6,2) \\
&= \mathcal{G}^{\phi}_{\sigma''}(5,\bar{7})\mathcal{G}^{\phi}_{\sigma''}(\bar{8},6)\square^{\phi}_{\sigma''\sigma'}(\bar{7}-\bar{8})\mathcal{G}^{\phi}_{\sigma'}(\bar{7},2^+)\mathcal{G}^{\phi}_{\sigma'}(2,\bar{8}) + \blacktriangleright^{\phi,(\mathrm{odd}),\mathrm{corr}}_{\sigma''\sigma'}(5,6,2). \quad (4.20)
\end{aligned}
$$

Eq. (4.20) has the diagrammatic representation shown in Fig. 4.4. This time, Eq. (4.20) generates iteratively terms consisting of a ladder containing an odd number of vertical ladders. In Appendix F, a detailed derivation of the momentum-space expressions of Eqs. (4.19) and (4.20) is presented.

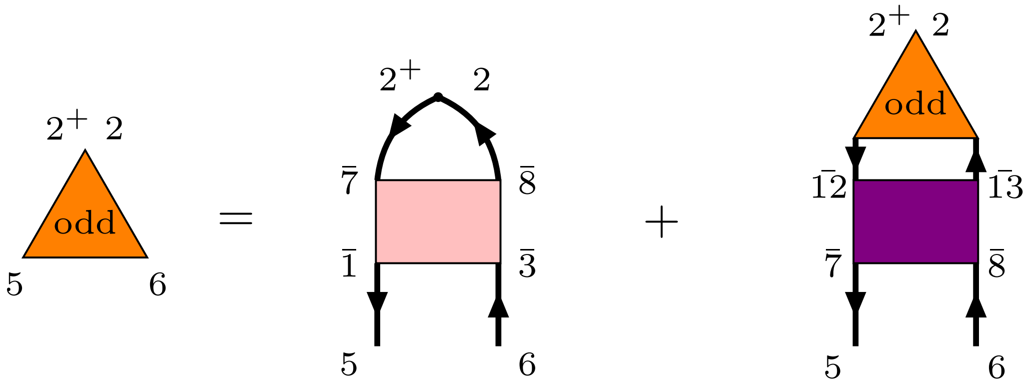

Figure 4.4: Diagrammatic representation of the terms of $\blacktriangleright^{(\mathrm{odd})}$ containing solely an odd number of vertical ladders (pink box); again the violet box is comprised of two pink boxes connected together by two Green's functions. The first term is the one that will be retained to describe $\blacktriangleright$ in Eq. (4.17) to get the double-ladder vertex corrections. Note that in the case of the Hubbard model, for instantaneous interaction, $\bar{7}=\bar{3}$ and $\bar{8}=\bar{4}$ for the pink box.

SINGLE-LADDER VERTEX CORRECTIONS The single-ladder vertex corrections make up the lowest order vertex corrections comprising an odd number of vertical ladders, therefore leading to a spin flip once the photon is reemitted. They correspond to setting $\chi^{\sigma\sigma'}_{\text{corr}} \to \chi^{\sigma\sigma'}_{\text{sl}}$ in Eq. (4.17), for which a generic diagram is shown in Fig. 4.5. Therefore, the first term of $\blacktriangleright^{(\text{even})}$ in Eq. (4.19) is used, since Eq. (4.17) already has one vertical ladder ($\square$). Thus, retaining only the first term on the right hand side of (4.19), one obtains the real-space expression for the single-ladder vertex corrections, corresponding to the lowest-order vertex corrections consisting of an odd number of vertical ladders:

$$\chi^{\sigma\sigma'}_{\text{sl}}(1,2) = -\frac{U\delta_{\sigma',-\sigma}\mathcal{G}_{\sigma}(1,\bar{5})\mathcal{G}_{\sigma'}(\bar{6},2^{+})\mathcal{G}_{\sigma'}(2,\bar{3})\mathcal{G}_{\sigma}(\bar{3},1^{+})}{\delta(\bar{5}-\bar{3})\delta(\bar{6}-\bar{3}) + U\delta(\bar{5}-\bar{6})\mathcal{G}_{\sigma}(\bar{5},\bar{3})\mathcal{G}_{\sigma'}(\bar{3},\bar{6})}, \tag{4.21}$$

with $\phi \to 0$. Fourier transformed to reciprocal space, Eq. (4.21) gives:

$$\begin{aligned}\chi^{\sigma-\sigma}_{\text{sl}}(q) &= -\frac{U}{(\beta V)^{2}}\sum_{\tilde{k},\bar{k}}\frac{\mathcal{G}_{\sigma}(\tilde{k})\mathcal{G}_{\sigma}(\tilde{k}-q)\mathcal{G}_{-\sigma}\left(\bar{k}-q\right)\mathcal{G}_{-\sigma}(\bar{k})}{1+\underbrace{\frac{U}{\beta V}\sum_{\tilde{q}}\mathcal{G}_{\sigma}(\tilde{k}-\tilde{q})\mathcal{G}_{-\sigma}(\bar{k}-\tilde{q})}_{\equiv\chi^{\sigma-\sigma}_{d}(\tilde{k}-\bar{k})}}\\ &= -\frac{1}{(V\beta)^{2}}\sum_{\tilde{k},\bar{k}}\mathcal{G}_{\sigma}(\tilde{k})\mathcal{G}_{\sigma}(\tilde{k}-q)\square_{\sigma-\sigma}(\tilde{k}-\bar{k})\mathcal{G}_{-\sigma}(\bar{k})\mathcal{G}_{-\sigma}(\bar{k}-q).\end{aligned} \tag{4.22}$$

In Eq. (4.22), the 4-vector notation was employed, meaning $k = (\mathbf{k}, i\omega_n)$. The second term in the denominator of Eq. (4.22) was defined by χ_d for conciseness and later purposes. In reciprocal space, after Fourier transforming Eq. (4.12), the $\square$ term reads

$$\square_{\sigma-\sigma}(\tilde{k}-\bar{k}) = \frac{U}{1+\chi^{\sigma-\sigma}_{d}(\tilde{k}-\bar{k})}. \tag{4.23}$$

Close to some AFM phase instability, the single-ladder vertex corrections are the dominant ones in the both the longitudinal optical conductivity and the spin-spin response function [120].

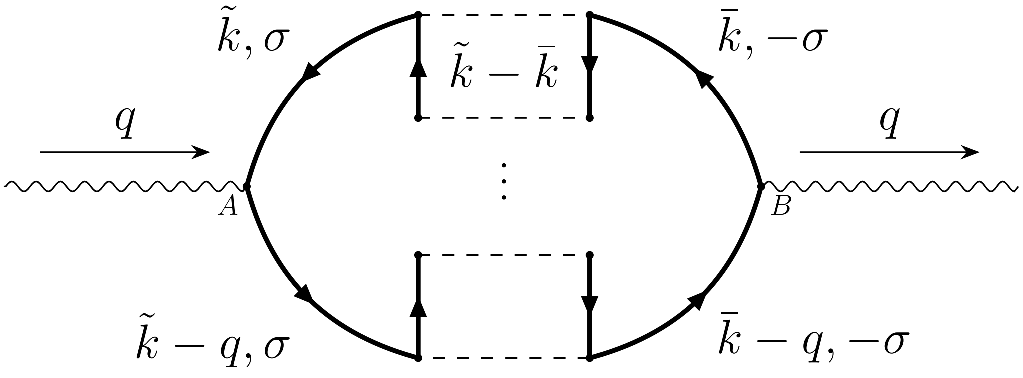

Figure 4.5: Illustration of the single-ladder vertex corrections to the susceptibilities. All diagrams sharing this topology are summed up in Eq. (4.22). To represent $\chi_{j_i j_i}$, the vertices A and B are both set equal to the velocity v_i, while for $\chi_{S_z S_z}$ they are set to the Pauli matrices $\frac{\tau_z}{2}$.

DOUBLE-LADDER VERTEX CORRECTIONS The double-ladder case where the set of diagrams representing the vertex correction includes terms with two vertical ladders stacked together sideways is also considered ($\chi^{\sigma\sigma'}_{\text{corr}} \rightarrow \chi^{\sigma\sigma'}_{\text{dl}}$), as depicted in Fig. 4.6. That set of diagrams sums up the lowest-order vertex corrections comprising an even number of vertical ladders and they are generated keeping only the first-order term of Eq. (4.20) and inserting it into Eq. (4.17) ($\phi \rightarrow 0$):

$$\chi^{\sigma\sigma'}_{\text{dl}}(1,2) = -\sum_{\sigma''} \mathcal{G}_{\sigma}(1,\bar{4})\mathcal{G}_{\sigma}(\bar{3},1^{+})\Box_{\sigma\sigma''}(\bar{4}-\bar{3})\mathcal{G}_{\sigma''}(\bar{4},\bar{7})\mathcal{G}_{\sigma''}(\bar{8},\bar{3})\Box_{\sigma''\sigma'}(\bar{7}-\bar{8}) \times \mathcal{G}_{\sigma'}(\bar{7},2^{+})\mathcal{G}_{\sigma'}(2,\bar{8}). \tag{4.24}$$

Carrying out the Fourier transformation of Eq. (4.24) into reciprocal space $(\mathbf{k},\omega_n)$ yields:

$$\chi^{\sigma\sigma}_{\text{dl}}(q) = -\frac{1}{(\beta V)^3} \sum_{\substack{\tilde{k},\bar{k} \\ \bar{q}}} \mathcal{G}_{\sigma}(\tilde{k})\mathcal{G}_{\sigma}(\tilde{k}-q)\Box_{\sigma-\sigma}(\tilde{k}-\bar{k})\mathcal{G}_{-\sigma}(\bar{k}) \times \mathcal{G}_{-\sigma}(\bar{k}-q)\Box_{-\sigma\sigma}(\bar{q})\mathcal{G}_{\sigma}(\bar{k}-\bar{q})\mathcal{G}_{\sigma}(\bar{k}-q-\bar{q}). \tag{4.25}$$

As opposed to Eq. (4.22), the double-ladder vertex corrections are less relevant in the vicinity of a magnetic phase transition [120].

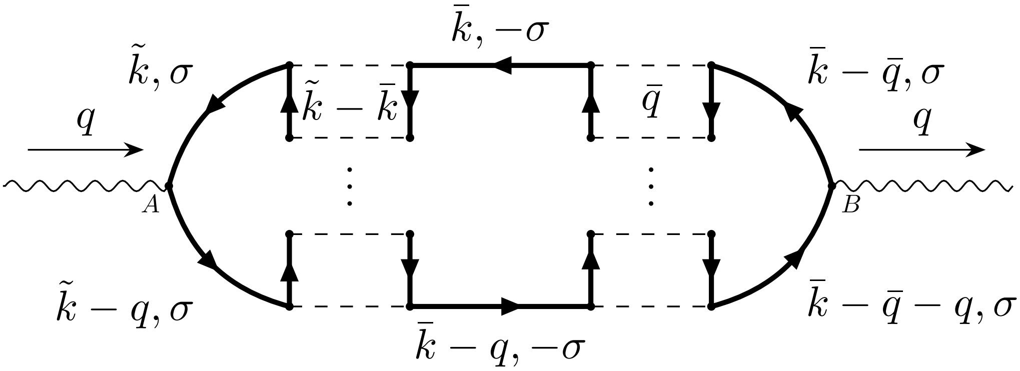

Figure 4.6: Illustration of the double-ladder vertex correction to the susceptibilities. Similarly to Fig. 4.5, the vertices A and B equal v_i for $\chi_{j_i j_i}$ and $\frac{\tau_z}{2}$ for $\chi_{S_z S_z}$.

ASLAMAZOV-LARKIN VERTEX CORRECTIONS As a third class of diagrams, the Aslamazov-Larkin-type [9] vertex corrections ($\chi^{\sigma\sigma'}_{\text{corr}} \rightarrow \chi^{\sigma\sigma'}_{\text{AL}}$), where two ladders are inserted horizontally instead of vertically, are considered. It can be expressed in real space in the form

$$\chi^{\sigma\sigma'}_{\text{AL}}(1,1^{+};2^{+},2) = \mathcal{G}_{\sigma}(1,1\bar{2})\mathcal{G}_{\sigma}(1\bar{6},1^{+})\Box_{\sigma-\sigma}(1\bar{2}-1\bar{3})\mathcal{G}_{-\sigma}(1\bar{8},1\bar{3})\mathcal{G}_{-\sigma}(1\bar{2},1\bar{6}) \times \Box_{-\sigma\sigma}(1\bar{8}-1\bar{6})\delta_{\sigma',\sigma}\mathcal{G}_{\sigma'}(1\bar{3},2^{+})\mathcal{G}_{\sigma'}(2,1\bar{8}), \tag{4.26}$$

from which the vertex function can be isolated as:

$$\Gamma^{\sigma\sigma'}_{\text{AL}}(12,13;11,14) = \frac{\delta\Sigma_{\sigma}(12,13)}{\delta\mathcal{G}_{-\sigma}(1\bar{5},1\bar{7})}\mathcal{G}_{-\sigma}(1\bar{8},1\bar{5})\mathcal{G}_{-\sigma}(1\bar{7},1\bar{6})\frac{\delta\Sigma_{-\sigma}(1\bar{6},1\bar{8})}{\delta\mathcal{G}_{\sigma}(11,14)}\delta_{\sigma',\sigma}. \tag{4.27}$$

The vertex function (4.27) entering the AL-type vertex corrections (4.26) is off-diagonal in spins, just like Eq. (4.23). Eq. (4.27) is illustrated diagrammatically in Fig. 4.8. The expression for the ladders $\Box$ is the same as in Eq. (4.23). Fourier transforming Eq. (4.26), one obtains

$$\chi^{\sigma\sigma'}_{\mathrm{AL}}(q) = \frac{1}{(V\beta)^3} \sum_{\substack{\tilde{k},\bar{k}\\ q'}} \mathcal{G}_\sigma(\tilde{k})\mathcal{G}_\sigma(\tilde{k}-q)\Box_{\sigma-\sigma}(q')\mathcal{G}_{-\sigma}(\bar{k}-q') \\ \times \mathcal{G}_{-\sigma}(\tilde{k}-q')\Box_{-\sigma\sigma}(q'-q)\mathcal{G}_\sigma(\bar{k})\mathcal{G}_\sigma(\bar{k}-q). \tag{4.28}$$

Equation (4.28) is illustrated diagrammatically in Fig. 4.7. Similarly to Eq. (4.25), the AL-type vertex corrections seem to play a less important role in the vicinity of a magnetic phase transition than the single-ladder vertex corrections [120]. For that reason, in Section 4.2, only the single-ladder vertex corrections are calculated in the nonequilibrium regime.

In the nonequilibrium regime, Eqs. (4.28) and (4.25) would be too computationally expensive to compute (more than a week).

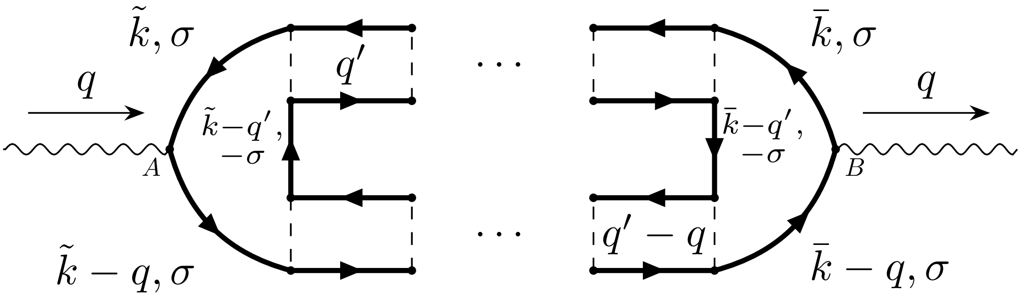

Figure 4.7: Diagrammatic representation of the AL-type vertex corrections considered. Also here, the vertices A and B equal v_i for $\chi_{j_i j_i}$, and $\frac{\tau_z}{2}$ for $\chi_{S_z S_z}$.

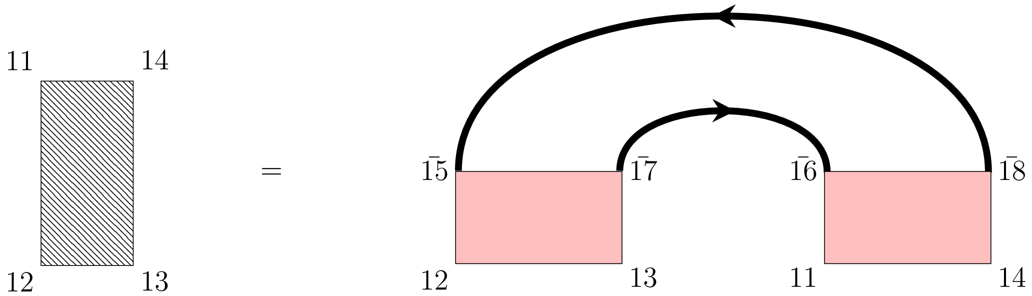

Figure 4.8: Vertex function for the AL-type diagram (cf. Fig. 4.7). The pink boxes represent particle-hole ladders (Eq. (4.23)).

In the context of superconductivity, the vertex corrections analogous to the single-ladder diagrams (Figs. 4.5 and 4.6) are known as the Maki-Thompson (MT) diagrams [83, 130]. The significance of the MT and other diagrams has been extensively discussed, and it is known that the Aslamazov-Larkin (AL) diagram [9] , with horizontal ladders instead of vertical ladders (Fig. 4.8), plays an important role in the normal state of superconductors. Hence, also in the present context of optical and spin responses near an AFM phase, it may be important to consider non-π-ton diagram topologies, including AL-type vertex corrections.

4.2 NONEQUILIBRIUM CALCULATION OF THE SINGLE-LADDER VERTEX CORRECTIONS

In the Kadanoff-Baym space, the general expression of the single-ladder vertex corrections (4.22) to the charge susceptibility reads

$$\begin{aligned}\chi_{\mathrm{sl}}^{\sigma-\sigma}(\mathbf{q};z,z') = &-\int\frac{\mathrm{d}^D\tilde{k}}{(2\pi)^D}\int\frac{\mathrm{d}^D\bar{k}}{(2\pi)^D}\int_{\mathcal{C}}\mathrm{d}\bar{z}\int_{\mathcal{C}}\mathrm{d}\bar{z}'\;\mathcal{G}^{\sigma}_{\tilde{\mathbf{k}}}(z,\bar{z})\mathcal{G}^{\sigma}_{\tilde{\mathbf{k}}-\mathbf{q}}(\bar{z}',z)\\ &\times\square^{\sigma-\sigma}_{\tilde{\mathbf{k}}-\bar{\mathbf{k}}}(\bar{z},\bar{z}')\mathcal{G}^{-\sigma}_{\bar{\mathbf{k}}}(\bar{z},z')\mathcal{G}^{-\sigma}_{\bar{\mathbf{k}}-\mathbf{q}}(z',\bar{z}').\end{aligned} \tag{4.29}$$

Only the case where $\mathbf{q}=\mathbf{0}$ is considered, because exciton-like polaritons can hardly couple to light at wavelengths $\mathbf{q}\neq\mathbf{0}$ due to the steepness of the dispersion relation of light. The vertical ladder denoted by a "$\square$" encapsulates a singular 2$^{\text{nd}}$ kind Volterra integral equation that needs to be solved before attaching the four outer Green's functions. It can be broken down as such: $\square^{\delta}(z)\delta^{\mathcal{C}}(z,z')+\square^{<}(z,z')\theta^{\mathcal{C}}(z',z)+\square^{>}(z,z')\theta^{\mathcal{C}}(z,z')$, where $\square^{\delta}(z)\to U(z)$ (*cf.* Eq. (2.15)). The latter reads

$$\begin{aligned}&\square^{\sigma-\sigma}_{\tilde{\mathbf{k}}-\bar{\mathbf{k}}}(z,z') = U(z)\delta^{\mathcal{C}}(z,z') - U(z)\int\frac{\mathrm{d}^Dk}{(2\pi)^D}\int_{\mathcal{C}}\mathrm{d}\bar{z}\;\mathcal{G}^{\sigma}_{\mathbf{k}}(z,\bar{z})\mathcal{G}^{-\sigma}_{\mathbf{k}-\tilde{\mathbf{k}}+\bar{\mathbf{k}}}(\bar{z},z)\square^{\sigma-\sigma}_{\tilde{\mathbf{k}}-\bar{\mathbf{k}}}(\bar{z},z')\\ &\Leftrightarrow\\ &\int_{\mathcal{C}}\mathrm{d}\bar{z}\left[\delta^{\mathcal{C}}(z,\bar{z})+U(z)\int\frac{\mathrm{d}^Dk}{(2\pi)^D}\mathcal{G}^{\sigma}_{\mathbf{k}}(z,\bar{z})\mathcal{G}^{-\sigma}_{\mathbf{k}-\tilde{\mathbf{k}}+\bar{\mathbf{k}}}(\bar{z},z)\right]\square^{\sigma-\sigma}_{\tilde{\mathbf{k}}-\bar{\mathbf{k}}}(\bar{z},z') = U(z)\delta^{\mathcal{C}}(z,z').\end{aligned} \tag{4.30}$$

The Volterra integral equation (4.30) is singular on the Kadanoff-Baym contour. Once the $\square$ term has been solved for, it is inserted into Eq. (4.29) to solve for the single-ladder vertex corrections. From Eq. (4.29), both the lesser and greater components are aimed for, denoted $\chi^{>}_{\mathrm{sl}}$ and $\chi^{<}_{\mathrm{sl}}$, respectively. The domain of integration can be broken down into nine distinct contributions. These nine contributions are laid out in Appendix G and some colour coding is used to help follow through. The contour-time variable z will be set to be the upper bound in time (in absolute value) throughout this section and in Appendix G, without loss of generality. If one solves for $\square$ in Eq. (4.30) and plugs it into Eq. (4.29), one gets

$$\begin{aligned}&\chi_{\mathrm{sl}}^{\sigma-\sigma}(\mathbf{q};z,z')\\ &=-\int\frac{\mathrm{d}^D\tilde{k}}{(2\pi)^D}\int\frac{\mathrm{d}^D\bar{k}}{(2\pi)^D}\int_{\mathcal{C}}\mathrm{d}\bar{z}\;\mathcal{G}^{\sigma}_{\tilde{\mathbf{k}}}(z,\bar{z})\mathcal{G}^{\sigma}_{\tilde{\mathbf{k}}-\mathbf{q}}(\bar{z},z)U(\bar{z})\mathcal{G}^{-\sigma}_{\bar{\mathbf{k}}}(\bar{z},z')\mathcal{G}^{-\sigma}_{\bar{\mathbf{k}}-\mathbf{q}}(z',\bar{z})\\ &-\int\frac{\mathrm{d}^D\tilde{k}}{(2\pi)^D}\int\frac{\mathrm{d}^D\bar{k}}{(2\pi)^D}\int_{\mathcal{C}}\mathrm{d}\bar{z}\int_{\mathcal{C}}\mathrm{d}\bar{z}'\;\mathcal{G}^{\sigma}_{\tilde{\mathbf{k}}}(z,\bar{z})\mathcal{G}^{\sigma}_{\tilde{\mathbf{k}}-\mathbf{q}}(\bar{z}',z)\\ &\qquad\times\left[\square^{<}_{\tilde{\mathbf{k}}-\bar{\mathbf{k}}}(\bar{z},\bar{z}')\theta^{\mathcal{C}}(\bar{z}',\bar{z})+\square^{>}_{\tilde{\mathbf{k}}-\bar{\mathbf{k}}}(\bar{z},\bar{z}')\theta^{\mathcal{C}}(\bar{z},\bar{z}')\right]\mathcal{G}^{-\sigma}_{\bar{\mathbf{k}}}(\bar{z},z')\mathcal{G}^{-\sigma}_{\bar{\mathbf{k}}-\mathbf{q}}(z',\bar{z}').\end{aligned} \tag{4.31}$$

The first term of Eq. (4.31) counts as a local contribution of the vertex corrections since $\square$ only depends on one time argument, whereas the second term depends on two different times and accounts for the retarded effects of the vertex corrections. In the end, one needs to sum over the spin projections and a factor of 2 pops out. The last term of Eq. (4.31) dominates the other.

5

TPSC AND VARIANTS

In this chapter, the general ideas that the Two-Particle Self-Consistent approach (TPSC) embodies are outlined. The theoretical framework forming the groundwork of TPSC is set out and the master equations are subsequently derived. A few extensions and variants to the original TPSC algorithm [152], such as TPSC+GG and DMFT+TPSC are presented and detailed. This chapter will be wrapped up by a walk-through of the core aspects of the algorithms, backed up by the formalism hitherto developed.

5.1 GENERAL IDEAS

TPSC originally builds off an approximation to the equations of motion (2.58) of the repulsive single-band Hubbard model (3.9) that consequently provides an expression to the nonlocal PM self-energy, with a paramagnon-like structure [144, 145, 152]. The approximation hinges on the local field approximation [123, 126] justifying the Hartree-Fock decomposition of higher-order correlation functions to close the Martin-Schwinger hierarchy [90]. The crossing-symmetric version of the TPSC self-energy corresponds to the average of the transversal and longitudinal channels, in turn expressed in terms of the spin and charge channels. It assumes furthermore that the two-particle $\mathcal{G}$-skeletonic irreducible vertices in the spin and charge channels (see Eq. (2.81)) are fully local, *i.e.* the full momentum and frequency dependences are left out. These irreducible vertices are set so as to respect various local two-particle sum-rules.

In Ref. [110], another variant of TPSC, called TPSC+, was proposed and it essentially uses a mixture of the noninteracting (5.28) and interacting (5.66) Green's functions in the bubble χ^0 (5.65).

TPSC has been extensively used to study two-dimensional lattice systems [110], although it is applicable to systems of higher dimensionality as well. It captures the pseudogap physics in superconducting cuprates [76] and the growth of antiferromagnetic correlations in the renormalized classical regime, where the antiferromagnetic correlation length becomes larger than the de Broglie wave length beyond a crossover temperature T_x [152]. In the renormalized classical regime, the growth of the spin fluctuations leads to a precursor of an AFM gap, where the spin fluctuations destroy the Fermi-liquid quasiparticles below T_x and above the zero-temperature phase transition in 2D (TPSC fulfils the Mermin-Wagner theorem) [145]. The shadow AFM bands can be observed in the spectral function at the Fermi level when the nonlocal propagator is dressed with the TPSC self-energy. TPSC also satisfies the Kanamori-Brueckner screening [63], which states that the screening of the spin correlation in the renormalized classical regime saturates with increasing U – the spin irreducible vertex therefore saturates. It can also be extended to treat symmetry-broken states [77], two-particle vertex corrections [18], multi-orbital [155, 156] and multi-orbital Hubbard-like systems [32]. TPSC has been successfully used in conjunction with Density Functional Theory [20] and DMFT [75, 89].

5.2 TPSC

The formalism and the steps in the derivation somewhat follow Refs. [121], [152], [127] and [156]. The theory lies within the nonequilibrium generating functional formalism developed to deal with many-particle quantum systems [90]. Parts of that formalism have been covered in Chapter 2 in the context of nonequilibrium quantum many-particle systems.

5.2.1 *Spin and charge channels*

In the particle-hole channel, the PM self-energy can generally be broken down into two significant channels, especially in systems with dominant density-density correlations: the spin (sp) and charge (ch) channels. These two channels respectively account for the spin and charge correlations. Thus, in the PM state, the two-particle correlation functions (2.46) and vertices (2.74) can be casted into separate spin and a charge contributions.

SPIN CHANNEL The general spin susceptibility χ^{sp} reads

$$\begin{aligned}\chi^{\mathrm{sp}}_{\epsilon,\zeta;\gamma,\delta}(1,1^+;2^+,2) &\triangleq -2i\left(\frac{\delta\mathcal{G}^{\phi,\uparrow}_{\epsilon,\zeta}(1,1^+)}{\delta\phi^{\uparrow}_{\gamma,\delta}(2^+,2)}-\frac{\delta\mathcal{G}^{\phi,\uparrow}_{\epsilon,\zeta}(1,1^+)}{\delta\phi^{\downarrow}_{\gamma,\delta}(2^+,2)}\right)\Bigg|_{\phi\to0}\\ &=\sum_{\sigma\sigma'}\tau_z^{\sigma\sigma}\chi^{\sigma\sigma'}_{\epsilon,\zeta;\gamma,\delta}(1,2)\tau_z^{\sigma'\sigma'}\end{aligned} \tag{5.1}$$

and the spin irreducible vertex Γ^{sp} reads

$$\Gamma^{\mathrm{sp}}_{\epsilon,\zeta;\gamma,\delta}(1,2;3,4)\triangleq-\sum_{\sigma}\tau_z^{\sigma\sigma}\frac{\delta\Sigma^{\sigma}_{\epsilon,\zeta}(1,2)}{\delta\mathcal{G}^{\downarrow}_{\gamma,\delta}(3,4)}, \tag{5.2}$$

where the numerals introduced in Eqs. (5.1) and (5.2) represent both the lattice atomic sites and contour-time variables, *i.e.* $1\equiv(\mathbf{R}_i,z_1)$ and $2\equiv(\mathbf{R}_j,z_2)$, and the spin rotational SU(2) invariance has been invoked. Hence, the contour functions showing up in Eqs. (5.1) and (5.2) use compressed notation that would otherwise look like, had it been unpacked,

$$\mathcal{G}^{\sigma}_{\alpha,\beta}(1,1^+):=\mathcal{G}^{\sigma}_{\alpha,\beta}(\mathbf{R}_i-\mathbf{R}_j;z_1,z_1^+). \tag{5.3}$$

The difference in lattice vectors $\mathbf{R}$ implies lattice translational invariance, which is assumed throughout this thesis. The matrix τ_z is the diagonal Pauli matrix $\tau_z\equiv\mathrm{diag}\{1,-1\}$. In Eq. (5.1), the spin superscript σ (σ') is tied up with the subscripts lying on the left(right)-hand of the semicolon. The susceptibility (5.1) can be specified further using Eq. (2.41):

SU(2) is a double-cover of SO(3) and locally, in the neighborhood of the identity, they are isomorphic groups.

$$\begin{aligned}\chi^{\mathrm{sp}}_{\epsilon,\zeta;\gamma,\delta}(1,2)=\sum_{\sigma\sigma'}\tau_z^{\sigma\sigma}\Big[&i\langle\mathcal{T}_{\mathcal{C}}\hat{c}^{\dagger}_{\gamma,\sigma'}(2^+)\hat{c}_{\delta,\sigma'}(2)\hat{c}_{\epsilon,\sigma}(1)\hat{c}^{\dagger}_{\zeta,\sigma}(1^+)\rangle\\ &-i\mathcal{G}^{\sigma'}_{\delta,\gamma}(2,2^+)\mathcal{G}^{\sigma}_{\epsilon,\zeta}(1,1^+)\Big]\tau_z^{\sigma'\sigma'}.\end{aligned} \tag{5.4}$$

In Eq. (5.4), owing to the spin rotational invariance, $\mathcal{G}^{\uparrow}_{\alpha,\beta}=\mathcal{G}^{\downarrow}_{\alpha,\beta}$ and therefore they cancel each other out, leaving out only the four-point correlation functions.

To re-express χ^{sp} (5.4), the orbital-dependent SU(2) spin operators defined on the Bloch sphere are put to use

$$\hat{S}^{i}_{\zeta,\epsilon}(1) \triangleq \left(\hat{c}^{\dagger}_{\zeta,\uparrow}(1),\hat{c}^{\dagger}_{\zeta,\downarrow}(1)\right)\tau_i\left(\hat{c}_{\epsilon,\uparrow}(1),\hat{c}_{\epsilon,\downarrow}(z_1)\right)^{\intercal}, \tag{5.5}$$

where the superscript runs over $i \in \{x,y,z\}$. One can travel across the irreducible representations $\hat{S}^i$ of SU(2) via the Casimir (ladder) operators $\hat{S}^{\pm}$ defined as

$$\begin{aligned}\hat{S}^{\pm}_{\zeta,\epsilon}(1) &\equiv \frac{1}{2}\left(\hat{S}^{x}_{\zeta,\epsilon}(1) \pm i\hat{S}^{y}_{\zeta,\epsilon}(1)\right)\\ &= \begin{cases}\hat{c}^{\dagger}_{\zeta,\uparrow}(1)\hat{c}_{\epsilon,\downarrow}(1) & (+)\\ \hat{c}^{\dagger}_{\zeta,\downarrow}(1)\hat{c}_{\epsilon,\uparrow}(1) & (-).\end{cases}\end{aligned} \tag{5.6}$$

In the PM state, the expectation values of all the $\hat{S}^i$ operators are the same. The Casimir operators (5.6) will be utilized later on when working out the PM self-energy in the transversal channel and the two-particle local sum-rules. Now, according to Eq. (5.6), the spin susceptibility (5.4) can hold a different representation, using the $\hat{S}^z$ operators

$$\begin{aligned}\chi^{\text{sp}}_{\epsilon,\zeta;\gamma,\delta}(1,2) &= -i\langle\mathcal{T}_{\mathcal{C}}\hat{S}^{z}_{\gamma,\delta}(2)\hat{S}^{z}_{\zeta,\epsilon}(1)\rangle + i\langle\hat{S}^{z}_{\delta,\gamma}(2)\rangle\langle\hat{S}^{z}_{\zeta,\epsilon}(1)\rangle\\ &= 2i\langle\mathcal{T}_{\mathcal{C}}\hat{c}^{\dagger}_{\gamma,\uparrow}(2^{+})\hat{c}_{\delta,\uparrow}(2)\hat{c}_{\epsilon,\uparrow}(1^{-})\hat{c}^{\dagger}_{\zeta,\uparrow}(1)\rangle\\ &\quad - 2i\langle\mathcal{T}_{\mathcal{C}}\hat{c}^{\dagger}_{\gamma,\uparrow}(2^{+})\hat{c}_{\delta,\uparrow}(2)\hat{c}_{\epsilon,\downarrow}(1^{-})\hat{c}^{\dagger}_{\zeta,\downarrow}(1)\rangle.\end{aligned} \tag{5.7}$$

The result (5.7) can be compared to that obtained at equilibrium (4.15).

Eq. (5.7) clearly states that the spin correlations are put forth, since the Hartree-Fock background $\langle\cdot\rangle\langle\cdot\rangle$ is pulled out from the two-particle correlation function – however, the Hartree-Fock term doesn't contribute in the PM state. To calculate the PM self-energy that will embody the TPSC assumptions, a slightly more convenient way of writing down the spin susceptibility (5.7) will be employed. To figure that out, the formula (2.46) is reformulated to fit the definitions laid out in Eqs. (5.1) and (5.2). To start with, reframing Eq. (2.46) to reflect Eq. (5.1), one realizes that

$$\begin{aligned}\chi^{\text{sp}}_{\epsilon,\zeta;\gamma,\delta}(1,2) &= -2i\mathcal{G}^{\uparrow}_{\epsilon,\gamma}(1,2^{+})\mathcal{G}^{\uparrow}_{\delta,\zeta}(2,1^{+}) - 2\mathcal{G}^{\uparrow}_{\epsilon\bar{\alpha}}(1,\bar{3})\\ &\times\Big[\Gamma^{\uparrow\uparrow\bar{\sigma}'\bar{\sigma}''}_{\bar{\alpha},\bar{\eta};\bar{\theta},\bar{\omega}}(\bar{3},\bar{5};\bar{6},\bar{7})\chi^{\bar{\sigma}'\bar{\sigma}''\uparrow\uparrow}_{\bar{\theta},\bar{\omega};\gamma,\delta}(\bar{6},\bar{7};2) -\\ &\qquad\Gamma^{\uparrow\uparrow\bar{\sigma}'\bar{\sigma}''}_{\bar{\alpha},\bar{\eta};\bar{\theta}\bar{\omega}}(\bar{3},\bar{5};\bar{6},\bar{7})\chi^{\bar{\sigma}'\bar{\sigma}''\downarrow\downarrow}_{\bar{\theta},\bar{\omega};\gamma,\delta}(\bar{6},\bar{7};2)\Big]\mathcal{G}^{\uparrow}_{\bar{\eta},\zeta}(\bar{5},1^{+}).\end{aligned} \tag{5.8}$$

The factor of 2 pops out after tracing over the spin degrees of freedom. The spin indices σ' and σ'' summed over must take on the same spin projection in order to lead to nonzero values[1], *i.e.* $\chi^{\sigma'\sigma''\sigma\sigma} = 0\ \forall\ \sigma' \neq \sigma''$. This allows one to conveniently collapse into one label the two spin labels sitting on each side of the semicolon, *i.e.* $\Gamma^{\text{sp}} \equiv \Gamma_{\uparrow\uparrow;\uparrow\uparrow} - \Gamma_{\uparrow\uparrow;\downarrow\downarrow} \equiv \Gamma_{\uparrow\uparrow} - \Gamma_{\uparrow\downarrow}$. In Eq. (5.1), only the functional derivative with all the same spin projections gives a nonzero Hartree-Fock term and therefore only one bubble term lives on in Eq. (5.8). Using the noninteracting susceptibility

---

[1] The Hubbard model conserves spin as well, not just particle number.

$$\chi^{0}_{\epsilon,\zeta;\gamma,\delta}(1,2) = -2i\mathcal{G}^{\sigma}_{\epsilon,\gamma}(1,2)\mathcal{G}^{\sigma}_{\delta,\zeta}(2,1), \tag{5.9}$$

the spin susceptibility in the PM state reads

$$\begin{aligned}\chi^{\text{sp}}_{\epsilon,\zeta;\gamma,\delta}(1,2) &= -2i\mathcal{G}^{\uparrow}_{\epsilon,\gamma}(1,2^{+})\mathcal{G}^{\uparrow}_{\delta,\zeta}(2,1^{+}) + 2\mathcal{G}^{\uparrow}_{\epsilon,\bar{\alpha}}(1,\bar{3})\\ &\quad\times \left[-\Gamma^{\uparrow\uparrow}_{\bar{\alpha},\bar{\eta};\bar{\theta}\bar{\omega}}(\bar{3},\bar{5};\bar{6},\bar{7}) + \Gamma^{\uparrow\downarrow}_{\bar{\alpha},\bar{\eta};\bar{\theta},\bar{\omega}}(\bar{3},\bar{5};\bar{6},\bar{7})\right]\\ &\quad\times \left[\chi^{\uparrow\uparrow}_{\bar{\theta},\bar{\omega};\gamma,\delta}(\bar{6},\bar{7};2) - \chi^{\downarrow\uparrow}_{\bar{\theta},\bar{\omega};\gamma,\delta}(\bar{6},\bar{7};2)\right]\mathcal{G}^{\uparrow}_{\bar{\eta},\zeta}(\bar{5},1^{+})\\ &= \chi^{0}_{\epsilon,\zeta;\gamma,\delta}(1,2) - \frac{i}{2}\chi^{0}_{\epsilon,\zeta;\bar{\alpha},\bar{\eta}}(1;\bar{3},\bar{5})\Gamma^{\text{sp}}_{\bar{\alpha},\bar{\eta};\bar{\theta},\bar{\omega}}(\bar{3},\bar{5};\bar{6},\bar{7})\chi^{\text{sp}}_{\bar{\theta},\bar{\omega};\gamma,\delta}(\bar{6},\bar{7};2).\end{aligned} \tag{5.10}$$

In Eq. (5.10), the spin rotational invariance enabled the factorization of χ and Γ into their spin components and two factors of 2 were absorbed in the definitions of χ^{0} and χ^{sp}.

TPSC relies on local two-particle sum-rules to determine the irreducible vertices in both the spin and charge channels. The most general model Hamiltonian treated so far within TPSC is the Kanamori-Hubbard model (3.7) [156]. In the spin (charge) channel, these sum-rules take their origin from the Pauli exclusion principle and the evaluation of the spin (charge) susceptibility when local in space-time ($2 \to 1^{+}$). Moreover, since the Kanamori-Hubbard model is comprised exclusively of interactions of density-density nature $\langle \hat{n}_{\alpha,\beta}\hat{n}_{\delta,\gamma}\rangle$ and spin-spin nature $\langle \hat{S}^{+}_{\alpha,\beta}\hat{S}^{-}_{\delta,\gamma}\rangle$, only three collections of orbital subscripts of Eq. (5.7) will lead to definite sum-rules. The latter statement hinges on the fact that the Kanamori-Hubbard model – and related models – conserve the total number of particles and the total spin. The first local two-particle sum-rule for the spin channel is obtained when setting $\epsilon \to \zeta \to \gamma \to \delta$ and it is connected to single-orbital spin correlations. This gives

Once the contour-time ordering operator has ordered the field operators in the ensemble average according to their time argument, it can be dropped out along with the superscripts "+" and "-".

$$\begin{aligned}\chi^{\text{sp}}_{\epsilon,\epsilon;\epsilon,\epsilon}(1,1^{+}) &= -2i\langle \mathcal{T}_{\mathcal{C}}\overbrace{\hat{c}^{\dagger}_{\epsilon,\uparrow}(1^{++})\hat{c}_{\epsilon,\uparrow}(1^{+})}^{\equiv\hat{n}_{\epsilon,\uparrow}(1^{+})}\hat{c}^{\dagger}_{\epsilon,\uparrow}(1)\hat{c}_{\epsilon,\uparrow}(1^{-})\rangle\\ &\quad + 2i\langle \mathcal{T}_{\mathcal{C}}\hat{c}^{\dagger}_{\epsilon,\uparrow}(1^{++})\hat{c}_{\epsilon,\uparrow}(1^{+})\hat{c}^{\dagger}_{\epsilon,\downarrow}(1)\hat{c}_{\epsilon,\downarrow}(1^{-})\rangle\\ &= -2i\langle \hat{n}^{\uparrow}_{\epsilon}(1)\rangle + 2i\langle \hat{n}^{\uparrow}_{\epsilon}(1)\hat{n}^{\downarrow}_{\epsilon}(1)\rangle.\end{aligned} \tag{5.11}$$

The spin sum-rule (5.11) is the one used in the original formulation of TPSC for the single-band Hubbard model. The Pauli principle was used to get to the last line of Eq. (5.11). In Eq. (5.11), the time-ordering operator has sorted the string of field operators in ascending order going from right to left. The second local two-particle spin sum-rule involves spin correlations across two distinct orbitals. This case comes down to substituting $\zeta \to \epsilon$, $\delta \to \gamma$ and $2 \to 1^{+}$ in Eq. (5.7):

$$\begin{aligned}\chi^{\text{sp}}_{\epsilon,\epsilon;\gamma,\gamma}(1,1^{+}) &= -2i\langle \mathcal{T}_{\mathcal{C}}\hat{c}^{\dagger}_{\gamma,\uparrow}(1^{++})\hat{c}_{\gamma,\uparrow}(1^{+})\hat{c}^{\dagger}_{\epsilon,\uparrow}(1)\hat{c}_{\epsilon,\uparrow}(1^{-})\rangle\\ &\quad + 2i\langle \mathcal{T}_{\mathcal{C}}\hat{c}^{\dagger}_{\gamma,\uparrow}(1^{++})\hat{c}_{\gamma,\uparrow}(1^{+})\hat{c}^{\dagger}_{\epsilon,\downarrow}(1)\hat{c}_{\epsilon,\downarrow}(1^{-})\rangle\\ &= -2i\langle \hat{n}^{\uparrow}_{\epsilon}(1)\hat{n}^{\uparrow}_{\gamma}(1)\rangle + 2i\langle \hat{n}^{\uparrow}_{\epsilon}(1)\hat{n}^{\downarrow}_{\gamma}(1)\rangle.\end{aligned} \tag{5.12}$$

The sum-rule (5.12) would have to be supplemented to Eq. (5.11) when dealing with the multi-orbital Hubbard model (3.8). The last two-particle sum-rule fixes the Hund's term appearing in the Kanamori-Hubbard model (3.8) on the last line ($J^{(\prime)}$ term) and it is obtained setting $\gamma \to \epsilon$, $\zeta \to \delta$ and $2 \to 1^{+}$ in Eq. (5.7):

$$\begin{aligned}\chi^{\mathrm{sp}}_{\epsilon,\delta;\epsilon,\delta}(1,1^+) &= -2i\langle \hat{c}^\dagger_{\epsilon,\uparrow}(1)(\mathbb{1} - \hat{c}^\dagger_{\delta,\uparrow}(1)\hat{c}_{\delta,\uparrow}(1))\hat{c}_{\epsilon,\uparrow}(1)\rangle \\ &\quad + 2i\langle \hat{c}^\dagger_{\epsilon,\uparrow}(1)(\delta_{\epsilon,\delta} - \hat{c}_{\epsilon,\downarrow}(1)\hat{c}^\dagger_{\delta,\downarrow}(1))\hat{c}_{\delta,\uparrow}(1)\rangle \\ &= -2i\langle \hat{n}^\uparrow_\epsilon(1)\rangle + 2i\langle \hat{c}^\dagger_{\epsilon,\uparrow}(1)\hat{c}^\dagger_{\delta,\uparrow}(1)\hat{c}_{\delta,\uparrow}(1)\hat{c}_{\epsilon,\uparrow}(1)\rangle \\ &\quad + 2i\langle \hat{n}^\uparrow_{\epsilon,\delta}(1)\rangle\delta_{\epsilon,\delta} - 2i\langle \hat{c}^\dagger_{\epsilon,\uparrow}(1)\hat{c}_{\epsilon,\downarrow}(1)\hat{c}^\dagger_{\delta,\downarrow}(1)\hat{c}_{\delta,\uparrow}(1)\rangle \\ &= 2i\langle \hat{n}^\uparrow_{\epsilon,\delta}(1)\rangle\delta_{\epsilon,\delta} - 2i\langle \hat{n}^\uparrow_{\epsilon,\delta}(1)\rangle\delta_{\epsilon,\delta} - 2i\langle \hat{n}^\uparrow_\epsilon(1)\rangle \\ &\quad + 2i\langle \hat{n}^\uparrow_\epsilon(1)\hat{n}^\uparrow_\delta(1)\rangle - 2i\langle \underbrace{\hat{c}^\dagger_{\epsilon,\uparrow}(1)\hat{c}_{\epsilon,\downarrow}(1)}_{=\hat{S}^+_{\epsilon,\epsilon}(1)}\underbrace{\hat{c}^\dagger_{\delta,\downarrow}(1)\hat{c}_{\delta,\uparrow}(1)}_{=\hat{S}^-_{\delta,\delta}(1)}\rangle. \end{aligned} \tag{5.13}$$

From looking at the first line of Eq. (5.13), the first two terms with the Kronecker delta function cancel each other out. Then, the last term figuring in Eq. (5.13) needs to be taken care of using Eq. (5.6):

Eq. (5.14) assumes spin rotational symmetry.

$$\begin{aligned}&-2i\langle \hat{S}^+_{\epsilon,\epsilon}(1)\hat{S}^-_{\delta,\delta}(1)\rangle = -\frac{i}{2}\langle \hat{S}^x_{\epsilon,\epsilon}(1)\hat{S}^x_{\delta,\delta}(1)\rangle - \frac{i}{2}\langle \hat{S}^y_{\epsilon,\epsilon}(1)\hat{S}^y_{\delta,\delta}(1)\rangle \\ &= -i\langle \hat{S}^z_{\epsilon,\epsilon}(1)\hat{S}^z_{\delta,\delta}(1)\rangle. \end{aligned} \tag{5.14}$$

The result (5.14) is an important result that will also be used when calculating the self-energy in the transversal channel. The spin-spin correlation function (5.14) has already been evaluated in Eq. (5.7), so the final form of the 3rd local sum-rule relevant to the Kanamori-Hubbard model reads

$$\chi^{\mathrm{sp}}_{\epsilon,\delta;\epsilon,\delta}(1,1^+) = \underline{-i\langle \hat{n}^\uparrow_\epsilon(1)\rangle - i\langle \hat{n}^\uparrow_\delta(1)\rangle} + 2i\langle \hat{n}^\uparrow_\epsilon(1)\hat{n}^\downarrow_\delta(1)\rangle. \tag{5.15}$$

Since by symmetry $\chi^{\mathrm{sp}}_{\epsilon,\delta;\epsilon,\delta} = \chi^{\mathrm{sp}}_{\delta,\epsilon;\delta,\epsilon}$, Eq. (5.15) is an average of the latter sum-rule expressions that thereby enforces the symmetry relation to hold. For that reason, the terms underlined in Eq. (5.15) appear. The three expressions (5.11), (5.12) and (5.15) are utilized to determine their respective local irreducible vertex that appears in the Bethe-Salpeter equation (5.10), respectively denoted[2] $\Gamma^{\mathrm{sp}}_{\epsilon,\epsilon;\epsilon,\epsilon}$, $\Gamma^{\mathrm{sp}}_{\epsilon,\epsilon;\gamma,\gamma}$ and $\Gamma^{\mathrm{sp}}_{\epsilon,\delta;\epsilon,\delta}$. One can easily check that Eq. (5.15) falls back on the single-orbital sum-rule (5.11) when all orbital indices are the same.

The local two-particle spin sum-rule for $\chi^{sp}_{\delta,\epsilon;\delta,\epsilon}$ can be easily obtained by permuting the orbital indices $\epsilon \rightleftharpoons \delta$ in Eq. (5.13).

CHARGE CHANNEL To get the various relevant quantities that describe the charge correlations, similar steps to those undertaken in the paragraph of the spin channel just above are followed through. The notation introduced to deal with the spin channel carries over to the charge channel. Thus, the general charge susceptibility χ^{ch} reads

$$\begin{aligned}\chi^{\mathrm{ch}}_{\epsilon,\zeta;\gamma,\delta}(1,1^+;2^+,2) &\triangleq -2i\left(\frac{\delta\mathcal{G}^{\phi,\uparrow}_{\epsilon,\zeta}(1,1^+)}{\delta\phi^\uparrow_{\gamma,\delta}(2^+,2)} + \frac{\delta\mathcal{G}^{\phi,\uparrow}_{\epsilon,\zeta}(1,1^+)}{\delta\phi^\downarrow_{\gamma,\delta}(2^+,2)}\right)\Bigg|_{\phi\to 0} \\ &= \sum_{\sigma\sigma'}\chi^{\sigma\sigma'}_{\epsilon,\zeta;\gamma,\delta}(1,2) \end{aligned} \tag{5.16}$$

and the charge irreducible vertex Γ^{ch} reads

$$\Gamma^{\mathrm{ch}}_{\epsilon,\zeta;\gamma,\delta}(1,2;3,4) \triangleq -\sum_\sigma \frac{\delta\Sigma^\sigma_{\epsilon,\zeta}(1,2)}{\delta\mathcal{G}^\downarrow_{\gamma,\delta}(3,4)}, \tag{5.17}$$

---

[2] The spin vertices will also eventually be local in orbital, as part of the TPSC assumptions.

where the difference with the spin vertex and spin susceptibility lies in the disappearance of the τ_z Pauli matrices. Developing Eq. (5.16), the charge susceptibility can be expressed as

The result (5.18) can be compared to that obtained at equilibrium (4.13).

$$\begin{aligned}\chi^{\text{ch}}_{\epsilon,\zeta;\gamma,\delta}(1,2) &= -i\langle\mathcal{T}_{\mathcal{C}}\hat{n}_{\gamma,\delta}(2)\hat{n}_{\zeta,\epsilon}(1)\rangle + i\langle\hat{n}_{\gamma,\delta}(2)\rangle\langle\hat{n}_{\zeta,\epsilon}(1)\rangle\\ &= -2i\langle\mathcal{T}_{\mathcal{C}}\hat{n}^{\uparrow}_{\gamma,\delta}(2)\hat{n}^{\uparrow}_{\zeta,\epsilon}(1)\rangle - 2i\langle\mathcal{T}_{\mathcal{C}}\hat{n}^{\uparrow}_{\gamma,\delta}(2)\hat{n}^{\downarrow}_{\zeta,\epsilon}(1)\rangle\\ &\quad + i\langle\hat{n}_{\gamma,\delta}(2)\rangle\langle\hat{n}_{\zeta,\epsilon}(1)\rangle, \end{aligned}\tag{5.18}$$

where $\hat{n}_{\alpha,\beta}(1) = \hat{n}^{\uparrow}_{\alpha,\beta}(1) + \hat{n}^{\downarrow}_{\alpha,\beta}(1)$. Now, just like Eq. (5.8), an expression of the charge susceptibility more suitable to extract the PM self-energy can be drawn out of Eqs. (2.46) and (5.1):

$$\begin{aligned}\chi^{\text{ch}}_{\epsilon,\zeta;\gamma,\delta}(1,2) &= -2i\mathcal{G}^{\uparrow}_{\epsilon,\gamma}(1,2^{+})\mathcal{G}^{\uparrow}_{\delta,\zeta}(2,1^{+}) - 2\mathcal{G}^{\uparrow}_{\epsilon\bar{\alpha}}(1,\bar{3})\\ &\quad\times\Big[\Gamma^{\uparrow\uparrow\bar{\sigma}'\bar{\sigma}''}_{\bar{\alpha},\bar{\eta};\bar{\theta},\bar{\omega}}(\bar{3},\bar{5};\bar{6},\bar{7})\chi^{\bar{\sigma}'\bar{\sigma}''\uparrow\uparrow}_{\bar{\theta},\bar{\omega};\gamma,\delta}(\bar{6},\bar{7};2)+\\ &\qquad\quad\Gamma^{\uparrow\uparrow\bar{\sigma}'\bar{\sigma}''}_{\bar{\alpha},\bar{\eta};\bar{\theta},\bar{\omega}}(\bar{3},\bar{5};\bar{6},\bar{7})\chi^{\bar{\sigma}'\bar{\sigma}''\downarrow\downarrow}_{\bar{\theta},\bar{\omega};\gamma,\delta}(\bar{6},\bar{7};2)\Big]\mathcal{G}^{\uparrow}_{\bar{\eta},\zeta}(\bar{5},1^{+}).\end{aligned}\tag{5.19}$$

The only difference between Eq. (5.8) and Eq. (5.19) is the "-" sign squeezed in the square brackets $[\cdots]$. The definition $\Gamma^{\text{ch}} := \Gamma_{\uparrow\uparrow} + \Gamma_{\uparrow\downarrow}$ is yet to be introduced in Eq. (5.19). Using the noninteracting bubble expression (5.9), the charge susceptibility in the PM state simply boils down to

$$\begin{aligned}\chi^{\text{ch}}_{\epsilon,\zeta;\gamma,\delta}(1,2) &= -2i\mathcal{G}^{\uparrow}_{\epsilon,\gamma}(1,2^{+})\mathcal{G}^{\uparrow}_{\delta,\zeta}(2,1^{+}) - 2\mathcal{G}^{\uparrow}_{\epsilon,\bar{\alpha}}(1,\bar{3})\\ &\quad\times\left[\Gamma^{\uparrow\uparrow}_{\bar{\alpha},\bar{\eta};\bar{\theta},\bar{\omega}}(\bar{3},\bar{5};\bar{6},\bar{7}) + \Gamma^{\uparrow\downarrow}_{\bar{\alpha},\bar{\eta};\bar{\theta},\bar{\omega}}(\bar{3},\bar{5};\bar{6},\bar{7})\right]\\ &\quad\times\left[\chi^{\uparrow\uparrow}_{\bar{\theta},\bar{\omega};\gamma,\delta}(\bar{6},\bar{7};2) + \chi^{\downarrow\uparrow}_{\bar{\theta},\bar{\omega};\gamma,\delta}(\bar{6},\bar{7};2)\right]\mathcal{G}^{\uparrow}_{\bar{\eta},\zeta}(\bar{5},1^{+})\\ &= \chi^{0}_{\epsilon,\zeta;\gamma,\delta}(1,2) + \frac{i}{2}\chi^{0}_{\epsilon,\zeta;\bar{\alpha},\bar{\eta}}(1;\bar{3},\bar{5})\Gamma^{\text{ch}}_{\bar{\alpha},\bar{\eta};\bar{\theta},\bar{\omega}}(\bar{3},\bar{5};\bar{6},\bar{7})\chi^{\text{ch}}_{\bar{\theta},\bar{\omega};\gamma,\delta}(\bar{6},\bar{7};2).\end{aligned}\tag{5.20}$$

As will be seen when deriving the TPSC self-energy expressions describing the Hamiltonian models (3.7), (3.8) and (3.9), the combination of Eqs. (5.10) and (5.20) will prove to be very useful. Indeed, if one writes out $\Gamma^{\text{ch}}\chi^{\text{ch}} \pm \Gamma^{\text{sp}}\chi^{\text{sp}}$, one symbolically gets

$$\begin{aligned}\Gamma^{\text{ch}}\chi^{\text{ch}} \pm \Gamma^{\text{sp}}\chi^{\text{sp}} &= 2\left[\Gamma_{\uparrow\uparrow} + \Gamma_{\uparrow\downarrow}\right]\left[\chi_{\uparrow\uparrow} + \chi_{\uparrow\downarrow}\right] \pm 2\left[\Gamma_{\uparrow\downarrow} - \Gamma_{\uparrow\uparrow}\right]\left[\chi_{\uparrow\uparrow} - \chi_{\uparrow\downarrow}\right]\\ &= \begin{cases}4\Gamma_{\uparrow\uparrow}\chi_{\uparrow\downarrow} + 4\Gamma_{\uparrow\downarrow}\chi_{\uparrow\uparrow} & (+)\\ 4\Gamma_{\uparrow\uparrow}\chi_{\uparrow\uparrow} + 4\Gamma_{\uparrow\downarrow}\chi_{\downarrow\uparrow} & (-),\end{cases}\end{aligned}\tag{5.21}$$

which is a generic result that can be substituted into the longitudinal and transversal expressions for the TPSC self-energy.

Moving on to the local two-particle charge sum-rules needed to set the charge irreducible vertices, the same reasoning as for the spin channel is applied. The first local two-particle sum-rule ($\epsilon \to \zeta \to \gamma \to \delta$ in Eq. (5.18)) reads

$$\chi^{\text{ch}}_{\epsilon,\epsilon;\epsilon,\epsilon}(1,1^{+}) = -2i\langle\hat{n}^{\uparrow}_{\epsilon}(1)\rangle - 2i\langle\hat{n}^{\uparrow}_{\epsilon}(1)\hat{n}^{\downarrow}_{\epsilon}(1)\rangle + i\langle\hat{n}_{\epsilon}(1)\rangle^{2}.\tag{5.22}$$

The sum-rule (5.22) is used to set $\Gamma^{\text{ch}}_{\epsilon,\epsilon;\epsilon,\epsilon}$ in Eq. (5.20). The second sum-rule comes from substituting $\zeta \to \epsilon$, $\delta \to \gamma$ and $2 \to 1^{+}$ in Eq. (5.18):

$$\chi^{\mathrm{ch}}_{\epsilon,\epsilon;\gamma,\gamma}(1,1^+) = -2i\langle \hat{n}^{\uparrow}_{\gamma}(1)\hat{n}^{\uparrow}_{\epsilon}(1)\rangle - 2i\langle \hat{n}^{\uparrow}_{\gamma}(1)\hat{n}^{\downarrow}_{\epsilon}(1)\rangle \\ + i\langle \hat{n}_{\gamma}(1)\rangle\langle \hat{n}_{\epsilon}(1)\rangle. \tag{5.23}$$

The sum-rule (5.23) is used to calculate $\Gamma^{\mathrm{ch}}_{\epsilon,\epsilon;\gamma,\gamma}$ in Eq. (5.20). Finally, the last sum-rule is obtained setting $\gamma \to \epsilon$, $\zeta \to \delta$ and $2 \to 1^+$ in Eq. (5.18):

$$\begin{aligned}
\chi^{\mathrm{ch}}_{\epsilon,\delta;\epsilon,\delta}(1,1^+) &= -2i\langle \hat{c}^{\dagger}_{\epsilon,\uparrow}(1)\hat{c}_{\delta,\uparrow}(1)\hat{c}^{\dagger}_{\delta,\uparrow}(1)\hat{c}_{\epsilon,\uparrow}(1)\rangle \\
&\quad - 2i\langle \hat{c}^{\dagger}_{\epsilon,\uparrow}(1)\hat{c}_{\delta,\uparrow}(1)\hat{c}^{\dagger}_{\delta,\downarrow}(1)\hat{c}_{\epsilon,\downarrow}(1)\rangle + i\langle \hat{n}_{\delta,\epsilon}(1)\rangle\langle \hat{n}_{\epsilon,\delta}(1)\rangle \\
&= -2i\langle \hat{c}^{\dagger}_{\epsilon,\uparrow}(1)(\mathbb{1} - \hat{c}^{\dagger}_{\delta,\uparrow}(1)\hat{c}_{\delta,\uparrow}(1))\hat{c}_{\epsilon,\uparrow}(1)\rangle \\
&\quad - 2i\langle \hat{c}^{\dagger}_{\epsilon,\uparrow}(1)(\delta_{\delta,\epsilon} - \hat{c}_{\epsilon,\downarrow}(1)\hat{c}^{\dagger}_{\delta,\downarrow}(1))\hat{c}_{\delta,\uparrow}(1)\rangle + i\langle \hat{n}_{\delta,\epsilon}(1)\rangle\langle \hat{n}_{\epsilon,\delta}(1)\rangle \\
&= -2i\langle \hat{n}^{\uparrow}_{\epsilon}(1)\rangle - 4i\langle \hat{n}^{\uparrow}_{\epsilon,\delta}(1)\rangle\delta_{\delta,\epsilon} + 2i\langle \hat{n}^{\uparrow}_{\epsilon}(1)\hat{n}^{\uparrow}_{\delta}(1)\rangle \\
&\quad + 2i\langle \underbrace{\hat{c}^{\dagger}_{\epsilon,\uparrow}(1)\hat{c}_{\epsilon,\downarrow}(1)}_{=\hat{S}^{+}_{\epsilon,\epsilon}(1)}\underbrace{\hat{c}^{\dagger}_{\delta,\downarrow}(1)\hat{c}_{\delta,\uparrow}(1)}_{=\hat{S}^{-}_{\delta,\delta}(1)}\rangle + i\langle \hat{n}_{\delta,\epsilon}(1)\rangle\langle \hat{n}_{\epsilon,\delta}(1)\rangle,
\end{aligned}$$

which, using the result of Eq. (5.14), yields

$$\chi^{\mathrm{ch}}_{\epsilon,\delta;\epsilon,\delta}(1,1^+) = \underline{-i\langle \hat{n}^{\uparrow}_{\epsilon}(1)\rangle - i\langle \hat{n}^{\uparrow}_{\delta}(1)\rangle} - 4i\delta_{\delta,\epsilon}\langle \hat{n}^{\uparrow}_{\epsilon,\delta}(1)\rangle + 4i\langle \hat{n}^{\uparrow}_{\epsilon}(1)\hat{n}^{\uparrow}_{\delta}(1)\rangle \\ - 2i\langle \hat{n}^{\uparrow}_{\epsilon}(1)\hat{n}^{\downarrow}_{\delta}(1)\rangle + i\langle \hat{n}_{\delta,\epsilon}(1)\rangle\langle \hat{n}_{\epsilon,\delta}(1)\rangle. \tag{5.24}$$

To once again enforce the symmetry $\chi^{\mathrm{ch}}_{\epsilon,\delta;\epsilon,\delta} = \chi^{\mathrm{ch}}_{\delta,\epsilon;\delta,\epsilon}$, Eq. (5.24) is actually the average of these two expressions, explaining why two density terms show up (terms underlined with a dotted line). The three expressions (5.22), (5.23) and (5.24), along with the Bethe-Salpeter equation (5.20), are used to determine the local irreducible vertex they associate with, respectively denoted $\Gamma^{\mathrm{ch}}_{\epsilon,\epsilon;\epsilon,\epsilon}$, $\Gamma^{\mathrm{ch}}_{\epsilon,\epsilon;\gamma,\gamma}$ and $\Gamma^{\mathrm{ch}}_{\epsilon,\delta;\epsilon,\delta}$. One can verify that the charge sum-rule for the single-orbital model (5.22) can be recovered from Eq. (5.24).

In the sections coming up, in light of Section 5.2.1, the PM TPSC self-energy expressions for the models covered in Section 3.1 will be derived from the equations of motion and, as will be explained in Section 5.2.2, they will serve as an approximation to the nonlocal self-energy in their respective Hamiltonian model.

5.2.2 *TPSC ansatz*

To calculate the single- and two-particle correlation functions, TPSC puts forward an ansatz for the Luttinger-Ward functional [80] Φ that approximates the local irreducible vertices in the particle-hole channel (transversal and longitudinal), namely the vertices expressed in terms of the charge (Γ^{ch}) and spin (Γ^{sp}) degrees of freedom. The starting point is the following Luttinger-Ward functional, established in Ref. [152],

$$\Phi[\mathcal{G}] = \frac{1}{2}\sum_i \int_{\mathcal{C}} \mathrm{d}z \, \sum_{\sigma} \mathcal{G}^{\sigma}_{\bar{\alpha},\bar{\beta}}(\mathbf{R}_i;z,z^+)\Gamma^{\sigma\sigma}_{\bar{\alpha},\bar{\beta};\bar{\delta},\bar{\gamma}}(\mathbf{R}_i;z)\mathcal{G}^{\sigma}_{\bar{\delta},\bar{\gamma}}(\mathbf{R}_i;z,z^+) \\ + \frac{1}{2}\int_{\mathcal{C}} \mathrm{d}z \, \sum_{\sigma} \mathcal{G}^{\sigma}_{\bar{\alpha},\bar{\beta}}(\mathbf{R}_i;z,z^+)\Gamma^{\sigma-\sigma}_{\bar{\alpha},\bar{\beta};\bar{\delta},\bar{\gamma}}(\mathbf{R}_i;z)\mathcal{G}^{-\sigma}_{\bar{\delta},\bar{\gamma}}(\mathbf{R}_i;z,z^+), \tag{5.25}$$

Recall that the variables with bars over are dummy variables that are summed/integrated over.

where the quantities are defined on the Kadanoff-Baym contour, with arguments $z \in \mathcal{C}$. The Greek subscripts summed over hold atomic quantum degrees of freedom, such as orbitals and atomic sites, and therefore the contour functions are dressed up as shown in Eq. (5.3). The spin is represented by the superscript σ. The Green's functions in Eq. (5.25) are technically interacting ones. The integral breaks down into contour components according to the Langreth rules presented in Section 2.2.1. From Eq. (5.25), both the self-energy and the $\mathcal{G}$-skeletonic two-particle irreducible vertices can be obtained. According to Eq. (5.25), a conserving first-level approximation TPSC self-energy $\Sigma^{(0)}$ obeys

$$\Sigma^{\sigma,(0)}_{\alpha,\beta}(2,3) = \frac{\delta\Phi[\mathcal{G}]}{\delta\mathcal{G}^{\sigma}_{\beta,\alpha}(3,2)}, \tag{5.26}$$

which yields

$$\begin{aligned}&\Sigma^{\sigma,(0)}_{\alpha,\beta}(2,3)\\ &= \Gamma^{\sigma\sigma}_{\beta,\alpha;\bar{\delta},\bar{\gamma}}(3)\mathcal{G}^{\sigma}_{\bar{\delta},\bar{\gamma}}(3,3^+)\delta^{\mathcal{C}}(3^+,2) + \Gamma^{\sigma-\sigma}_{\beta,\alpha;\bar{\delta},\bar{\gamma}}(3)\mathcal{G}^{-\sigma}_{\bar{\delta},\bar{\gamma}}(3,3^+)\delta(3^+,2),\end{aligned} \tag{5.27}$$

in which the rotational spin symmetry $\Gamma^{\sigma-\sigma} = \Gamma^{-\sigma\sigma}$ was used. Since the Γ's are simply scalar functions, the self-energy (5.27) can be absorbed with the chemical potential μ_0 when defining the lattice Green's function at the first level of approximation:

$$\begin{aligned}&\sum_j \left(i\partial_z + \mu_0 - h^{\sigma}_{\alpha,\beta}(\mathbf{R}_i - \mathbf{R}_j;z) - \Sigma^{\sigma,(0)}_{\alpha,\beta}(\mathbf{R}_i;z)\delta_{i,j}\right)\mathcal{G}^{\sigma,(0)}_{\alpha,\beta}(\mathbf{R}_j;z,z')\\ &= \delta^{\mathcal{C}}(z,z')\delta_{i,j}\delta_{\alpha,\beta}.\end{aligned} \tag{5.28}$$

In essence, the Green's function $\mathcal{G}^{(0)}$ is noninteracting.

From now on, the channels A are denoted by L and T for the longitudinal and transversal channels, respectively. At first level approximation, TPSC is initiated with an approximation to Eq. (2.58) that boils down to some Hartree-Fock factorization [126]:

$$\begin{aligned}\Sigma^{\phi,(0)}_{\epsilon,\bar{\beta};\sigma\bar{\sigma}'}(1,\bar{2})\mathcal{G}^{\phi,(0)}_{\bar{\beta},\zeta;\bar{\sigma}'\sigma}(\bar{2},2) \simeq I^{\phi,\sigma\bar{\sigma}'}_{\epsilon,\zeta;\bar{\gamma}}(A;1)\Big(&\mathcal{G}^{\phi,(0)}_{\bar{\gamma};\bar{\sigma}'}(1,1^+)\mathcal{G}^{\phi,(0)}_{\epsilon,\zeta;\sigma}(1,2)\delta_{A,L}\\ &- \mathcal{G}^{\phi,(0)}_{\bar{\gamma};\sigma\bar{\sigma}'}(1,1^+)\mathcal{G}^{\phi,(0)}_{\epsilon,\zeta;\bar{\sigma}'\sigma}(1,2)\delta_{A,T}\Big),\end{aligned} \tag{5.29}$$

where the tensor I embodies the local irreducible vertices in both the longitudinal and transversal channels – it might take on a different form depending on the channel. Equation (5.29) will provide an expression to the local two-particle irreducible vertices appearing in the first-level approximation (5.27) that is specific to the model Hamiltonian in consideration. The first term is associated with the longitudinal channel while the second term is associated with the transversal one. The kernel I is comprised of the four-point correlation function (2.58) and the interaction term V (hidden in I) in Eq. (5.29) has been specialized to deal with all the Hamiltonian models discussed in Section 3.1, requiring that the indices $\bar{\gamma} \to \bar{\delta}$ and $\bar{\beta} \to \zeta$ be traded off, then that the tuples $\epsilon \to (\epsilon,\sigma)$, $\zeta \to (\zeta,\sigma)$ and $\bar{\gamma} \to (\bar{\gamma},\bar{\sigma}')$ be substituted into Eq. (2.58):

The "-" in front of the transversal term in Eq. (5.29) stems from a reshuffling of the fermionic field operators to recover the same I in both channels.

$$V^{\bar{\gamma},\bar{\delta}}_{\epsilon,\bar{\beta}}(1,\bar{2},\bar{3},\bar{4}) \to V^{\sigma\sigma'}_{\epsilon,\zeta;\bar{\gamma}}(1)\delta(1^{++},\bar{2})\delta(1^{+},\bar{3})\delta(1^{-},\bar{4})\delta_{\bar{\beta},\zeta}\delta_{\bar{\gamma},\bar{\delta}} \tag{5.30}$$

The spin degrees of freedom were split up from the remaining ones in the tuples and a single-time dependence of the interaction was assumed. The kernel I is built such that Eq. (5.29) becomes exact in the local case whereby the contour-time variable $z_2 \to z_1$; one would then recover the local counterpart of Eq. (2.58) having substituted the interaction (5.30). Computed in the longitudinal channel $\phi_{\sigma\sigma}$, the general kernel I, which makes up the TPSC ansatz, takes the form

$$I^{\phi,\sigma\bar{\sigma}'}_{\epsilon,\zeta;\bar{\gamma}}(L;1) = -iV^{\sigma\bar{\sigma}'}_{\epsilon,\zeta;\bar{\gamma}}(1)\frac{\left\langle \hat{n}_{\bar{\gamma},\bar{\sigma}'}(1)\hat{n}_{\epsilon,\sigma}(1)\right\rangle_{\phi}}{\left\langle \hat{n}_{\bar{\gamma},\bar{\sigma}'}(1)\right\rangle_{\phi}\left\langle \hat{n}_{\epsilon,\sigma}(1)\right\rangle_{\phi}}. \tag{5.31}$$

By inserting the irreducible vertex tensor I (5.31) back into the first-level self-energy (5.29), then setting off the source field ϕ, one gets back the local-in-time and local-in-space version of Eq. (2.58) with the appropriate interaction term (5.30). Note that since $\mathcal{G}^{\phi}_{\sigma-\sigma} = 0$ when $\phi \to 0$ in Eq. (5.29), the spin irreducible vertex is the only physical byproduct of the transversal channel. The bars over the indices designate those that are summed over in Eq. (5.29).

In the case of the Hubbard model (3.9), $V^{\sigma\bar{\sigma}'}_{\epsilon,\zeta;\bar{\gamma}}(1) \to U_{\epsilon,\epsilon}(1)\delta_{\bar{\gamma},\epsilon}\delta_{\epsilon,\zeta}\delta_{\bar{\sigma}',-\sigma}$ becomes fully local in Eq. (5.31), giving

$$I^{\mathrm{H},\phi,\sigma\bar{\sigma}'}_{\epsilon,\zeta;\bar{\gamma}}(L;1) = -iU_{\epsilon,\epsilon}(1)\frac{\langle \hat{n}_{\epsilon,-\sigma}(1)\hat{n}_{\epsilon,\sigma}(1)\rangle_{\phi}}{\left\langle \hat{n}_{\epsilon,-\sigma}(1)\right\rangle_{\phi}\left\langle \hat{n}_{\epsilon,\sigma}(1)\right\rangle_{\phi}}\delta_{\bar{\gamma},\epsilon}\delta_{\zeta,\epsilon}\delta_{\bar{\sigma}',-\sigma}. \tag{5.32}$$

The superscript "H" stands for "Hubbard". The suitable interaction for the multi-orbital Hubbard model (3.8) in Eq. (5.31) would be $V^{\sigma\bar{\sigma}'}_{\epsilon,\zeta;\bar{\gamma}}(1) \to U^{\sigma\bar{\sigma}'}_{\epsilon,\zeta}(1)\delta_{\bar{\gamma},\zeta}$, with $U^{\sigma\sigma'}_{\epsilon,\epsilon} = 0$ when $\sigma' = \sigma$, where now inter-orbital Coulomb repulsion is allowed:

$$I^{\mathrm{MH},\phi,\sigma\bar{\sigma}'}_{\epsilon,\zeta;\bar{\gamma}}(L;1) = -iU^{\sigma\bar{\sigma}'}_{\epsilon,\zeta}(1)\frac{\left\langle \hat{n}_{\zeta,\bar{\sigma}'}(1)\hat{n}_{\epsilon,\sigma}(1)\right\rangle_{\phi}}{\left\langle \hat{n}_{\zeta,\bar{\sigma}'}(1)\right\rangle_{\phi}\left\langle \hat{n}_{\epsilon,\sigma}(1)\right\rangle_{\phi}}\delta_{\bar{\gamma},\zeta}, \tag{5.33}$$

where the superscript "MH" stands for "Multi-orbital Hubbard". Finally, in the case of the Kanamori-Hubbard model (3.7) where spin-exchange energy is considered, the kernel I is some combination of Eq. (5.32) and Eq. (5.33) where the Hund's coupling comes in:

$$\begin{aligned} &I^{\mathrm{KH},\phi,\sigma\bar{\sigma}'}_{\epsilon,\zeta;\bar{\gamma}}(L;1) \\ &= -i(U^{\sigma\bar{\sigma}'}_{\epsilon,\zeta}(1) - J^{\sigma}_{\epsilon,\zeta}(1)\delta_{\sigma,\bar{\sigma}'})\frac{\left\langle \hat{n}_{\zeta,\bar{\sigma}'}(1)\hat{n}_{\epsilon,\sigma}(1)\right\rangle_{\phi}}{\left\langle \hat{n}_{\zeta,\bar{\sigma}'}(1)\right\rangle_{\phi}\left\langle \hat{n}_{\epsilon,\sigma}(1)\right\rangle_{\phi}}\delta_{\bar{\gamma},\zeta}, \end{aligned} \tag{5.34}$$

where the superscript "KH" means "Kanamori-Hubbard". Depending on the value that the dummy variables $\bar{\sigma}'$ and $\bar{\gamma}$ take on in Eq. (5.34), some terms will zero out. Overall, one needs to resort to Eqs. (5.32), (5.33) or (5.34) to get the vertices that are then used in the second-level approximation of their respective model. The connection between the first- and second-level approximation is illustrated further down by means of a graph (Fig. 5.4).

Now, the sign difference in Eq. (5.29) is traced back to its source. Had the kernel I (5.31) been calculated in the transversal channel, one would have gotten

Eq. (5.35) is homogeneous to $\left.\frac{\delta\mathcal{G}^{\phi,-\sigma\sigma}_{\bar{\gamma},\zeta}(1^{+},2)}{\delta\phi^{-\sigma\sigma}_{\bar{\gamma},\epsilon}(1^{++},1^{-})}\right|_{\zeta\to\epsilon,2\to1}$.

$$I^{\phi,\sigma\bar{\sigma}'}_{\epsilon,\zeta;\bar{\gamma}}(T;1) = -iV^{\sigma\bar{\sigma}'}_{\epsilon,\zeta;\bar{\gamma}}(1)\frac{\left\langle \mathcal{T}_{\mathcal{C}}\hat{c}^{\dagger}_{\bar{\gamma},\bar{\sigma}'}(1^{++})\hat{c}_{\epsilon,\sigma}(1^{-})\hat{c}^{\dagger}_{\epsilon,\sigma}(1)\hat{c}_{\bar{\gamma},\bar{\sigma}'}(1^{+})\right\rangle_{\phi}}{\left\langle \hat{n}_{\bar{\gamma},\bar{\sigma}'}(1)\right\rangle_{\phi}\left\langle \hat{n}_{\epsilon,\sigma}(1)\right\rangle_{\phi}}\delta_{\bar{\sigma}',-\sigma}. \tag{5.35}$$

The density operator $\hat{n}^{\sigma\bar{\sigma}'}_{\epsilon,\zeta}$ turns into a spin ladder operator $\hat{S}^{\pm}_{\epsilon,\zeta}$ (5.6) when $\sigma' = -\sigma$.

The four-point correlation function appearing in Eq. (5.35) is obtained generating the single-particle (2.25) and two-particle (2.47) Green's functions by employing a transversal source field in spin space $\phi_{-\sigma\sigma}$. As will be seen, not all distinct interaction components associated to the Kanamori-Hubbard model feature a transversal irreducible vertex, just like was the case for the longitudinal channel where the last term of Eq. (3.7) did not have any expression for the irreducible vertex. For the first-level transversal vertex to the Hubbard model, the same interaction expression as that utilized in Eq. (5.32) is repurposed in Eq. (5.35), leading to

$$I^{\mathrm{H},\phi,\sigma\bar{\sigma}'}_{\epsilon,\zeta;\bar{\gamma}}(T;1) = iU_{\epsilon,\epsilon}(1)\frac{\left\langle \hat{n}_{\epsilon,-\sigma}(1)\hat{c}^{\dagger}_{\epsilon,\sigma}(1)\hat{c}_{\epsilon,\sigma}(1)\right\rangle_{\phi}}{\left\langle \hat{n}_{\epsilon,-\sigma}(1)\right\rangle_{\phi}\left\langle \hat{n}_{\epsilon,\sigma}(1)\right\rangle_{\phi}}\delta_{\bar{\gamma},\epsilon}\delta_{\zeta,\epsilon}\delta_{\bar{\sigma}',-\sigma}. \tag{5.36}$$

Solely a minus sign separates the transversal spin vertex ansatz $I^{\mathrm{H}}(T)$ (5.36) from the longitudinal one $I^{\mathrm{H}}(L)$ (5.32). However, the relation between $I^{\mathrm{MH}}(T)$ and $I^{\mathrm{MH}}(L)$ is slightly more complicated in the case of the multi-orbital Hubbard model. Indeed, the two-particle correlation function stemming from the equations of motion cannot be reproduced by substituting $V^{\sigma\bar{\sigma}'}_{\epsilon,\zeta;\bar{\gamma}}(1) \to U^{\sigma\bar{\sigma}'}_{\epsilon,\zeta}(1)\delta_{\bar{\gamma},\zeta}$ into Eq. (5.35), unless $\sigma' = -\sigma$. In other words, the four-point correlation function $\langle \mathcal{T}_{\mathcal{C}}\hat{c}^{\dagger}_{\zeta,\sigma}(1^{++})\hat{c}_{\epsilon,\sigma}(1^{+})\hat{c}^{\dagger}_{\epsilon,\sigma}(1)\hat{c}_{\zeta,\sigma}(1^{-})\rangle_{\phi}$ cannot be produced from Eq. (5.35). Henceforth, the interaction $V^{\sigma\bar{\sigma}'}_{\epsilon,\zeta;\bar{\gamma}}(1) \to U^{\sigma\bar{\sigma}'}_{\epsilon,\zeta}(1)\delta_{\bar{\gamma},\zeta}\delta_{\bar{\sigma}',-\sigma}$ is the only component of the multi-orbital Hubbard model that remains in the transversal channel and this gives

$$I^{\mathrm{MH},\phi,\sigma\bar{\sigma}'}_{\epsilon,\zeta;\bar{\gamma}}(T;1) = iU^{\sigma-\sigma}_{\epsilon,\zeta}(1)\frac{\left\langle \hat{n}_{\zeta,-\sigma}(1)\hat{c}^{\dagger}_{\epsilon,\sigma}(1)\hat{c}_{\epsilon,\sigma}(1)\right\rangle_{\phi}}{\left\langle \hat{n}_{\zeta,-\sigma}(1)\right\rangle_{\phi}\left\langle \hat{n}_{\epsilon,\sigma}(1)\right\rangle_{\phi}}\delta_{\bar{\gamma},\zeta}\delta_{\bar{\sigma}',-\sigma}. \tag{5.37}$$

It is straightforward to notice that $I^{\mathrm{MH},\sigma-\sigma}(L)$ (5.33) and $I^{\mathrm{MH},\sigma-\sigma}(T)$ (5.37) differ only by a global minus sign. Next, turning to the Kanamori-Hubbard model, two terms are needed to set two distinct spin irreducible vertices – one associated to the multi-orbital Hubbard model and one associated with the Hund's term –

$$I^{\mathrm{KH},\phi,\sigma\bar{\sigma}'}_{\epsilon,\zeta;\bar{\gamma}}(T;1) = I^{\mathrm{MH},\phi,\sigma\bar{\sigma}'}_{\epsilon,\zeta;\bar{\gamma}}(T;1) + \text{corrections}. \tag{5.38}$$

The "corrections" of Eq. (5.38) will be detailed in Section 5.2.7.2, since they cannot be obtained from Eq. (5.35). The expressions of the irreducible vertices I are tensors and for convenience some specific elements will be separated apart when writing down the second-level self-energy approximations later on (see, *e.g.* Eq. (5.80) which shows two distinct elements of Eq. (5.33)).

From Eq. (5.29), the first-level longitudinal self-energy approximation reads

$$\begin{aligned}\Sigma^{\mathrm{L},\phi,(0)}_{\epsilon,\zeta;\sigma}(1,2) &= I^{\phi,\sigma\bar{\sigma}'}_{\epsilon,\zeta;\bar{\gamma}}(A;1)\mathcal{G}^{\phi,(0)}_{\bar{\gamma};\bar{\sigma}'}(1,1^{+})\delta(1,2)\delta_{A,L}\\ &= iI^{\phi,\sigma\bar{\sigma}'}_{\epsilon,\zeta;\bar{\gamma}}(L;1)n_{\bar{\gamma},\bar{\sigma}'}(1)\delta(1,2),\end{aligned} \tag{5.39}$$

such that

$$\frac{\delta\Sigma^{\mathrm{L},\phi,(0)}_{\epsilon,\zeta;\sigma}(1,2)}{\delta\mathcal{G}^{\phi,(0)}_{\gamma,\delta;\sigma'}(4,3)} = I^{\phi,\sigma\sigma'}_{\epsilon,\zeta;(\gamma,\delta)}(L;1)\delta(1,4)\delta(1^+,3)\delta(1,2)$$
$$+\, i\frac{\delta I^{\phi,\sigma\bar{\sigma}'}_{\epsilon,\zeta;\bar{\gamma}}(L;1)}{\delta\mathcal{G}^{\phi,(0)}_{\gamma,\delta;\sigma'}(4,3)} n_{\bar{\gamma},\bar{\sigma}'}(1)\delta(1,2). \tag{5.40}$$

Owing to the spin rotational invariance, $I^{\sigma\sigma} = I^{-\sigma-\sigma}$ and $I^{-\sigma\sigma} = I^{\sigma-\sigma}$. Similar symmetries apply to the functional derivatives: $\frac{\delta I^{\sigma\sigma'}}{\delta\mathcal{G}^{(0)}_{\sigma}} = \frac{\delta I^{\sigma\sigma'}}{\delta\mathcal{G}^{(0)}_{-\sigma}}$. Now, since the irreducible vertex in the longitudinal spin channel for the first-level approximation reads (*cf.* (5.2))

$$-\,\Gamma^{\mathrm{sp}}_{\epsilon,\zeta;\gamma,\delta}(1,2;4,3) \triangleq \left.\frac{\delta\Sigma^{\mathrm{L},\phi,(0)}_{\epsilon,\zeta;\sigma}(1,2)}{\delta\mathcal{G}^{\phi,(0)}_{\gamma,\delta;-\sigma}(4,3)}\right|_{\phi\to0} - \left.\frac{\delta\Sigma^{\mathrm{L},\phi,(0)}_{\epsilon,\zeta;\sigma}(1,2)}{\delta\mathcal{G}^{\phi,(0)}_{\gamma,\delta;\sigma}(4,3)}\right|_{\phi\to0}$$
$$\approx \left(I^{\phi,\sigma\sigma}_{\epsilon,\zeta;(\gamma,\delta)}(L;1) - I^{\phi,\sigma-\sigma}_{\epsilon,\zeta;(\gamma,\delta)}(L;1)\right)\delta(1,4)\delta(1^+,3)\delta(1,2), \tag{5.41}$$

the latter will serve to connect the kernels $I(L)$ to the local longitudinal irreducible spin vertices. Likewise, the local longitudinal charge irreducible vertex is approximated as

$$-\,\Gamma^{\mathrm{ch}}_{\epsilon,\zeta;\gamma,\delta}(1,2;4,3) \triangleq \left.\frac{\delta\Sigma^{\mathrm{L},\phi,(0)}_{\epsilon,\zeta;\sigma}(1,2)}{\delta\mathcal{G}^{\phi,(0)}_{\gamma,\delta;-\sigma}(4,3)}\right|_{\phi\to0} + \left.\frac{\delta\Sigma^{\mathrm{L},\phi,(0)}_{\epsilon,\zeta;\sigma}(1,2)}{\delta\mathcal{G}^{\phi,(0)}_{\gamma,\delta;\sigma}(4,3)}\right|_{\phi\to0}$$
$$\approx \Gamma^{\mathrm{ch}}_{\epsilon,\zeta;\gamma,\delta}(1)\delta(1,4)\delta(1^+,3)\delta(1,2), \tag{5.42}$$

where Γ^{ch} has a different analytical expression from Γ^{sp} and can be calculated from our knowledge of Γ^{sp} by using the local two-particle charge sum-rules (5.22), (5.23) and (5.24).

A transversal spin vertex $\Gamma^{\sigma-\sigma\sigma-\sigma}$ can be worked out from the first-level self-energy ansatz (5.29). To achieve this, one refers to the identity

$$\Gamma^{\sigma-\sigma\sigma-\sigma}_{\epsilon,\zeta;\gamma,\delta}(1,2;3,4) \triangleq -\left.\frac{\delta\Sigma^{\phi,(0)}_{\epsilon,\zeta;\sigma-\sigma}(1,2)}{\delta\mathcal{G}^{\phi,(0)}_{\gamma,\delta;\sigma-\sigma}(3,4)}\right|_{\phi\to0},$$

where $\Sigma^{\phi,(0)}_{\sigma-\sigma}$ can be extracted from Eq. (5.29),

$$\Sigma^{\phi,(0)}_{\epsilon,\zeta;\sigma-\sigma}(1,2) = -I^{\phi,\sigma-\sigma}_{\epsilon,\zeta;\bar{\gamma}}(T;1)\mathcal{G}^{\phi,(0)}_{\bar{\gamma},\sigma-\sigma}(1,1^+)\delta(1,2). \tag{5.43}$$

Hence,

$$\Gamma^{\sigma-\sigma\sigma-\sigma}_{\epsilon,\zeta;\gamma,\delta}(1,2;3,4) = I^{\sigma-\sigma}_{\epsilon,\zeta;(\gamma,\delta)}(T;1)\delta(1,3)\delta(1^+,4)\delta(1,2). \tag{5.44}$$

As already mentioned, it will be possible to relate some transversal irreducible vertices to their longitudinal counterparts: this is the subject of the next few sections where the ansatz to the spin vertex are lifted to the second-level approximation of TPSC.

5.2.3 *Equations of motion of the Hubbard model*

The TPSC second-level approximation to the Hubbard self-energy is sought for in this section. This second-level approximation is obtained from the calculation of the equations of motion (2.50), where $\hat{\mathcal{H}}$ is the model Hamiltonian (3.9). It makes use of the ansatz worked out at first level in Section 5.2.2 to set the vertices. A general single-particle Green's function that describes the propagation of electrons governed by the Kanamori-Hubbard model (3.7), to which the Hubbard model is a special case, can be represented by Eq. (5.3). The last term of Eq. (2.50) is focused upon and the commutator it contains gives

$$\begin{aligned}[\hat{\mathcal{H}},\hat{c}_{\epsilon,\sigma}(\mathbf{R}_i)](z_1) = -\sum_{\beta,k}\left[h^{\sigma}_{\epsilon,\beta}(\mathbf{R}_i-\mathbf{R}_k;z_1)-\mu\delta_{i,k}\delta_{\epsilon,\beta}\right]\hat{c}_{\beta,\sigma}(\mathbf{R}_k;z_1)\\ - U_{\epsilon,\epsilon}(\mathbf{R}_i;z_1)\hat{n}_{\epsilon,-\sigma}(\mathbf{R}_i;z_1)\hat{c}_{\epsilon,\sigma}(\mathbf{R}_i;z_1).\end{aligned} \tag{5.45}$$

Developing the last term of Eq. (2.50) results in the equations of motion

$$\begin{aligned}&i\partial_{z_1}\mathcal{G}^{\phi,\sigma}_{\epsilon,\zeta}(\mathbf{R}_i-\mathbf{R}_j;z_1,z_2)-h^{\sigma}_{\epsilon,\bar{\beta}}(\mathbf{R}_i-\mathbf{R}_{\bar{k}};z_1)\mathcal{G}^{\phi,\sigma}_{\bar{\beta},\zeta}(\mathbf{R}_{\bar{k}}-\mathbf{R}_j;z_1,z_2)\\ &-\phi^{\sigma\bar{\sigma}'}_{\epsilon,\bar{\beta}}(\mathbf{R}_i-\mathbf{R}_{\bar{k}};z_1,\bar{z}_4)\mathcal{G}^{\phi,\bar{\sigma}'\sigma}_{\bar{\beta},\zeta}(\mathbf{R}_{\bar{k}}-\mathbf{R}_j;\bar{z}_4,z_2)=\delta^{\mathcal{C}}(z_1,z_2)\delta_{\epsilon,\zeta}\delta_{i,j}\\ &-iU_{\epsilon,\epsilon}(z_1)\left\langle\mathcal{T}_{\mathcal{C}}\hat{n}_{\epsilon,-\sigma}(\mathbf{R}_i;z_1)\hat{c}_{\epsilon,\sigma}(\mathbf{R}_i;z_1)\hat{c}^{\dagger}_{\zeta,\sigma}(\mathbf{R}_i;z_2)\right\rangle_{\phi}.\end{aligned} \tag{5.46}$$

Note that the adjoint can be obtained in a similar fashion by acting from the right with the complex conjugate operator $-i\overleftarrow{\partial}_{z_2}$ on the single-particle Green's function. However, acting on whichever side does not really matter, since the interacting Green's function and TPSC self-energy obtained from Eq. (5.46) obey $\mathrm{Tr}\left[\Sigma*\mathcal{G}\right](z,z')=\mathrm{Tr}\left[\mathcal{G}*\Sigma\right](z,z')$. From Eq. (5.46) one can recognize the modified Dyson's equation (2.44). Indeed, one has

$$\begin{aligned}&\left[\mathcal{G}^{\phi,0,\sigma\bar{\sigma}'}_{\epsilon,\bar{\beta}}(\mathbf{R}_i-\mathbf{R}_{\bar{k}};z_1,\bar{z}_2)^{-1}-\phi^{\sigma\bar{\sigma}'}_{\epsilon,\bar{\beta}}(\mathbf{R}_i-\mathbf{R}_{\bar{k}};z_1,\bar{z}_2)\right]\mathcal{G}^{\bar{\sigma}'\sigma}_{\bar{\beta},\zeta}(\mathbf{R}_{\bar{k}}-\mathbf{R}_j;\bar{z}_2,z_2)\\ &\quad=\delta^{\mathcal{C}}(z_1,z_2)\delta_{\epsilon,\zeta}\delta_{i,j}+\Sigma^{\phi,\sigma\bar{\sigma}'}_{\epsilon,\bar{\beta}}(\mathbf{R}_i-\mathbf{R}_{\bar{k}};z_1,\bar{z}_2)\mathcal{G}^{\phi,\bar{\sigma}'\sigma}_{\bar{\beta},\zeta}(\mathbf{R}_{\bar{k}}-\mathbf{R}_j;\bar{z}_2,z_2),\end{aligned}$$

such that the four-point correlation function relates to the self-energy and Green's function via

$$\begin{aligned}&\Sigma^{\phi,\sigma\bar{\sigma}'}_{\epsilon,\bar{\beta}}(\mathbf{R}_i-\mathbf{R}_{\bar{k}};z_1,\bar{z}_2)\mathcal{G}^{\phi,\bar{\sigma}'\sigma}_{\bar{\beta},\zeta}(\mathbf{R}_{\bar{k}}-\mathbf{R}_j;\bar{z}_2,z_2)\equiv\left[\Sigma^{\phi}*\mathcal{G}^{\phi}\right]^{\sigma}_{\epsilon,\zeta}(\overbrace{\mathbf{R}_i-\mathbf{R}_j}^{\equiv\mathbf{R}_{ij}};z_1,z_2)\\ &\quad=-iU_{\epsilon,\epsilon}(z_1)\left\langle\mathcal{T}_{\mathcal{C}}\hat{n}_{\epsilon,-\sigma}(\mathbf{R}_i;z_1)\hat{c}_{\epsilon,\sigma}(\mathbf{R}_i;z_1)\hat{c}^{\dagger}_{\zeta,\sigma}(\mathbf{R}_j;z_2)\right\rangle_{\phi}.\end{aligned} \tag{5.47}$$

The result of Eq. (5.47) provides an expression for the self-energy of the model Hamiltonian. The operator "$*$" in Eq. (5.47) denotes a convolution on the contour $\mathcal{C}$, in real space, in orbital space and in spin space. Once the desired correlation functions have been generated, the physical results are obtained by setting the source field to zero. When deemed convenient, to lighten the notation, the lattice site index will be merged with the contour-time variable, like was done in Section 5.2.1. It will be shown below that the very same four-point correlation function (5.47) can be calculated in both the longitudinal (Section 5.2.3.1) and transversal (Section 5.2.3.2) channels, that is by using a source field to generate Eqs. (2.41) and (2.46) which does not induce a spin-flip ($\phi_{\sigma\sigma}$) and one inducing a spin-flip ($\phi_{\sigma-\sigma}$), respectively. The two expressions of the self-energy will then be averaged to restore the crossing symmetry, giving the second-level approximation of the theory $\Sigma^{\text{TPSC},(1)}$.

5.2.3.1 *Longitudinal expression of the self-energy*

To get the second-level longitudinal self-energy, several variable substitutions are performed in Eq. (2.47) to adapt the labelling of the quantum numbers to the Hubbard model and retrieve the four-point correlation function of Eq. (5.47): $\gamma \to (\epsilon,-\sigma)$, $\delta \to (\epsilon,-\sigma)$, $\epsilon \to (\epsilon,\sigma)$ and $\zeta \to (\zeta,\sigma)$. At the same time, for the contour-time variables, one has to make the following substitutions: $z_4 \to z_1^{++}$, $z_3 \to z_1^{+}$, $z_2 \to z_2$ and $z_1 \to z_1$. Then, inserting the resulting four-point correlation function back into Eq. (5.47), one ends up with the relation

$$\begin{aligned}\left[\Sigma^{\mathrm{L},\phi} * \mathcal{G}^{\phi}\right]^{\sigma\sigma}_{\epsilon,\zeta}(1,2) &= -iU_{\epsilon,\epsilon}(1)\mathcal{G}^{\phi,-\sigma-\sigma}_{\epsilon,\epsilon}(1^+,1^{++})\mathcal{G}^{\phi,\sigma\sigma}_{\epsilon,\zeta}(1,2)\\ &+ iU_{\epsilon,\epsilon}(1)\mathcal{G}^{\phi,\sigma-\sigma}_{\epsilon,\epsilon}(1,1^{++})\mathcal{G}^{\phi,-\sigma\sigma}_{\epsilon,\zeta}(1^+,2) + U_{\epsilon,\epsilon}(1)\mathcal{G}^{\phi}_{(\epsilon,\sigma),\bar{\alpha}}(1,\bar{3})\\ &\times \Gamma^{\phi}_{\bar{\alpha},\bar{\eta};\bar{\theta},\bar{\omega}}(\bar{3},\bar{5};\bar{6},\bar{7})\chi^{\phi}_{\bar{\theta},\bar{\omega};(\epsilon,-\sigma),(\epsilon,-\sigma)}(\bar{6},\bar{7};1^{++},1^{+})\mathcal{G}^{\phi}_{\bar{\eta},(\zeta,\sigma)}(\bar{5},2). \qquad (5.48)\end{aligned}$$

The second term of Eq. (5.48) cancels out for the Hubbard model, namely $\mathcal{G}^{\phi}_{\sigma-\sigma} = 0$ when $\phi \to 0$. The longitudinal component to the second-level TPSC self-energy can then be straightforwardly isolated by multiplying by $\mathcal{G}^{-1}_{\sigma}$ from the right:

$$\begin{aligned}\Sigma^{\mathrm{L},\phi}_{\epsilon,\zeta;\sigma}(1,2) &= -iU_{\epsilon}(1)\mathcal{G}^{\phi}_{\epsilon,-\sigma}(1^+,1^{++})\delta(1,2)\delta_{\epsilon,\zeta}\\ &+ U_{\epsilon}(1)\mathcal{G}^{\phi}_{(\epsilon,\sigma),\bar{\alpha}}(1,\bar{3})\Gamma^{\phi}_{\bar{\alpha},(\zeta,\sigma);\bar{\theta},\bar{\omega}}(\bar{3},2;\bar{6},\bar{7})\chi^{\phi}_{\bar{\theta},\bar{\omega};(\epsilon,-\sigma)}(\bar{6},\bar{7};1). \qquad (5.49)\end{aligned}$$

A diagrammatic representation of the longitudinal self-energy would correspond to the last term figuring in Fig. 2.4. In Eq. (5.49), for the sake of conciseness, tuples of repeated indices denoting the same degree of freedom have collapsed into one single index without ambiguity, *i.e.*

$$\chi^{\sigma\sigma-\sigma-\sigma}_{\theta,\omega;\epsilon,\epsilon}(6,7;1^{++},1^{+}) \to \chi^{\sigma-\sigma}_{\theta,\omega;\epsilon}(6,7;1).$$

So far, the dummy subscripts in Eq. (5.49) still combine spin, orbital and lattice site labels. However, in order to distinguish the spin and charge channels from each other, the spin σ will be split apart from the other degrees of freedom in order to be summed up separately. Doing so, by expanding the implicitly summed quantities in Eq. (5.49) and canceling the source field ϕ, one obtains

$$\begin{aligned}\Sigma^{\mathrm{L},\sigma}_{\epsilon,\zeta}(1,2) &= -iU_{\epsilon}(1)\mathcal{G}_{\epsilon,-\sigma}(1,1^{+})\delta(1,2)\delta_{\epsilon,\zeta}\\ &+ U_{\epsilon}(1)\mathcal{G}^{\sigma}_{\epsilon,\bar{\alpha}}(1,\bar{3})\Big[\Gamma^{\sigma\sigma}_{\bar{\alpha},\zeta;\bar{\theta},\bar{\omega}}(\bar{3},2;\bar{6},\bar{7})\chi^{\sigma-\sigma}_{\bar{\theta},\bar{\omega};\epsilon}(\bar{6},\bar{7};1)\\ &\qquad + \Gamma^{\sigma-\sigma}_{\bar{\alpha},\zeta;\bar{\theta},\bar{\omega}}(\bar{3},2;\bar{6},\bar{7})\chi^{-\sigma-\sigma}_{\bar{\theta},\bar{\omega};\epsilon}(\bar{6},\bar{7};1)\Big]. \qquad (5.50)\end{aligned}$$

In Eq. (5.50), θ and ω had to have the same spin projections since $\Gamma^{\sigma'\sigma''\sigma\sigma} = 0$ and $\chi^{\sigma'\sigma''\sigma\sigma} = 0 \;\forall\; \sigma' \neq \sigma''$. The longitudinal self-energy (5.50) can be expressed in terms of the charge χ^{ch} (5.16) and spin χ^{sp} (5.1) susceptibilities, and of the two corresponding $\mathcal{G}$-skeletonic irreducible vertices, *i.e.* the charge Γ^{ch} (5.17) and spin Γ^{sp} (5.2) vertices. These irreducible vertices are momentum-averaged quantities fixed through the two-particle sum-rules described in Section 5.2.1. The result (5.21) can be substituted into the self-energy (5.50). Doing so, the physical longitudinal self-energy can be expressed as

$$\begin{aligned}\Sigma^{\mathrm{L}}_{\epsilon,\zeta;\sigma}(1,2) &= U_{\epsilon}(1)n^{-\sigma}_{\epsilon}(1)\delta(1,2)\delta_{\epsilon,\zeta}\\ &+ \frac{U_{\epsilon}(1)}{4}\mathcal{G}^{\sigma}_{\epsilon,\bar{\alpha}}(1,\bar{3})\Big[\Gamma^{\mathrm{ch}}_{\bar{\alpha},\zeta;\bar{\theta},\bar{\omega}}(\bar{3},2;\bar{6},\bar{\bar{7}})\chi^{\mathrm{ch}}_{\bar{\theta},\bar{\omega};\epsilon}(\bar{6},\bar{\bar{7}};1)\\ &\qquad\qquad + \Gamma^{\mathrm{sp}}_{\bar{\alpha},\zeta;\bar{\theta},\bar{\epsilon}}(\bar{3},2;\bar{6},\bar{\bar{7}})\chi^{\mathrm{sp}}_{\bar{\theta},\bar{\omega};\epsilon}(\bar{6},\bar{\bar{7}};1)\Big].\end{aligned} \tag{5.51}$$

If one replaces the irreducible vertices in Eq. (5.51) with fully local ones (in orbital, real-space and contour-time), namely (*cf.* Eq. (2.78))

$$\Gamma^{\mathrm{ch/sp}}_{\epsilon,\zeta;\theta,\omega}(3,2;6,7) \approx \Gamma^{\mathrm{ch/sp}}_{\zeta}(2)\delta(2,6)\delta(2^{+},7)\delta(2,3)\delta_{\zeta,\theta}\delta_{\zeta,\omega}\delta_{\zeta,\epsilon}, \tag{5.52}$$

one finds [18, 152]

$$\begin{aligned}\Sigma^{\mathrm{L},\sigma}_{\epsilon,\zeta}(1,2) &= U_{\epsilon}(1)n^{-\sigma}_{\epsilon}(1)\delta(1,2)\delta_{\epsilon,\zeta} + \frac{U_{\epsilon}(1)}{4}\mathcal{G}^{\sigma}_{\epsilon,\zeta}(1,2)\\ &\times\Big[\Gamma^{\mathrm{ch}}_{\zeta}(2)\chi^{\mathrm{ch}}_{\zeta,\epsilon}(2,1) + \Gamma^{\mathrm{sp}}_{\zeta}(2)\chi^{\mathrm{sp}}_{\zeta,\epsilon}(2,1)\Big].\end{aligned} \tag{5.53}$$

In the spin longitudinal channel, a correspondence established at the first-level approximation between the double-occupancy $\langle\hat{n}_{\sigma}\hat{n}_{-\sigma}\rangle$ and the spin irreducible vertex Γ^{sp} can be drawn from Eqs. (5.41) and (5.32):

$$\Gamma^{\mathrm{sp}}_{\zeta}(1) = -iU_{\zeta}(1)\frac{\big\langle\hat{n}_{\zeta,-\sigma}(1)\hat{n}_{\zeta,\sigma}(1)\big\rangle_{\phi}}{\big\langle\hat{n}_{\zeta,-\sigma}(1)\big\rangle_{\phi}\big\langle\hat{n}_{\zeta,\sigma}(1)\big\rangle_{\phi}}. \tag{5.54}$$

5.2.3.2 *Transversal expression of the self-energy*

The four-point correlation function appearing in Eq. (5.47) can also be obtained by employing a transversal field [129]. To see that, it is worthwhile to first work out Eq. (2.41) using a transversal source field $\phi_{\sigma-\sigma}$:

$$\begin{aligned}&\chi^{\phi,\sigma-\sigma\sigma-\sigma}_{ab;dc}(1,2;4,3)\\ &= i\langle\mathcal{T}_{\mathcal{C}}\hat{c}^{\dagger}_{d,\sigma}(4)\hat{c}_{c,-\sigma}(3)\hat{c}_{a,\sigma}(1)\hat{c}^{\dagger}_{b,-\sigma}(2)\rangle_{\phi} - i\mathcal{G}^{\phi}_{cd,-\sigma\sigma}(3,4)\mathcal{G}^{\phi}_{ab,\sigma-\sigma}(1,2).\end{aligned} \tag{5.55}$$

To get Eq. (5.55), one can perform the following substitutions into Eq. (2.41): $\epsilon \to (a,\sigma)$, $\zeta \to (b,-\sigma)$, $\gamma \to (d,\sigma)$ and $\delta \to (c,-\sigma)$. To match the four-point correlation function appearing in Eq. (5.47), one needs to execute one last variable substitutions in Eq. (5.55): $(a,z_1) \to (\epsilon,z_1^{+})$, $(b,z_2) \to (\zeta,z_2)$, $(c,z_3) \to (\epsilon,z_1)$ and $(d,z_4) \to (\epsilon,z_1^{++})$. Doing so, the last term of Eq. (5.55) vanishes when the source field is turned off. Making the same variable substitutions in Eq. (2.46) as done hitherto in Eq. (2.41), one obtains

$$\begin{aligned}&\chi^{\phi,\sigma-\sigma\sigma-\sigma}_{\epsilon,\zeta;\epsilon,\epsilon}(1^{+},2;1^{++},1) = -i\mathcal{G}^{\phi,\sigma}_{\epsilon,\epsilon}(1^{+},1^{++})\mathcal{G}^{\phi,-\sigma}_{\epsilon,\zeta}(1,2)\\ &- \mathcal{G}^{\phi,\sigma}_{\epsilon,\bar{a}}(1^{+},\bar{3})\Gamma^{\phi,\sigma-\sigma\bar{\sigma}'\bar{\sigma}''}_{\bar{a}\bar{b}\bar{c}\bar{d}}(\bar{3},\bar{\bar{5}};\bar{6},\bar{\bar{7}})\chi^{\phi,\bar{\sigma}'\bar{\sigma}''\sigma-\sigma}_{\bar{c},\bar{d};\epsilon,\epsilon}(\bar{6},\bar{\bar{7}};1^{++},1)\mathcal{G}^{\phi,-\sigma}_{\bar{b},\zeta}(\bar{\bar{5}},2).\end{aligned} \tag{5.56}$$

In Eq. (5.56), the spin selection rule forbidding antiparallel spins in Green's functions once $\phi \to 0$ was used in advance. Next, the result (5.56) is inserted into Eq. (5.55) to isolate the four-point correlation function which is then multiplied by $U_\epsilon(z_1)$ to recover something the likes of Eq. (5.47), but now in the case of the transversal channel. This yields

$$\begin{aligned}
&\Sigma^{\mathrm{T},\phi,-\sigma\bar{\sigma}'}_{\epsilon,\bar{b}}(1,\bar{2})\mathcal{G}^{\phi,\bar{\sigma}'-\sigma}_{\bar{b},\zeta}(\bar{2},2)\\
&= iU_\epsilon(1)\mathcal{G}^{\phi,-\sigma\sigma}_{\epsilon}(1,1^+)\mathcal{G}^{\phi,\sigma-\sigma}_{\epsilon,\zeta}(1,2) - iU_\epsilon(1)\mathcal{G}^{\phi,\sigma}_{\epsilon}(1,1^+)\mathcal{G}^{\phi,-\sigma}_{\epsilon,\zeta}(1,2)\\
&- U_\epsilon(1)\mathcal{G}^{\phi,\sigma}_{\epsilon,\bar{a}}(1,\bar{3})\Gamma^{\phi,\sigma-\sigma\bar{\sigma}'\bar{\sigma}''}_{\bar{a},\bar{b};\bar{c},\bar{d}}(\bar{3},\bar{5};\bar{6},\bar{7})\chi^{\phi,\bar{\sigma}'\bar{\sigma}''\sigma-\sigma}_{\bar{c},\bar{d};\epsilon}(\bar{6},\bar{7};1)\mathcal{G}^{\phi,-\sigma}_{\bar{b},\zeta}(\bar{5},2).
\end{aligned} \tag{5.57}$$

From Eq. (5.57), the physical transversal component to the second-level TPSC self-energy reads

$$\begin{aligned}
\Sigma^{\mathrm{T},-\sigma}_{\epsilon,\zeta}(1,2) &= U_\epsilon(1)n^{\sigma}_{\epsilon}(1)\delta(1,2)\delta_{\epsilon,\zeta}\\
&- U_\epsilon(1)\mathcal{G}^{\sigma}_{\epsilon,\bar{a}}(1,\bar{3})\Gamma^{\sigma-\sigma\sigma-\sigma}_{\bar{a},\zeta;\bar{c},\bar{d}}(\bar{3},2;\bar{6},\bar{7})\chi^{\sigma-\sigma\sigma-\sigma}_{\bar{c},\bar{d};\epsilon}(\bar{6},\bar{7};1),
\end{aligned} \tag{5.58}$$

since $\chi^{\sigma\sigma-\sigma\sigma} = \chi^{\sigma-\sigma-\sigma\sigma} = 0$. The fact that $\chi^{\sigma-\sigma-\sigma\sigma} = 0$ can be easily checked out by referring to Eqs. (5.6) and (5.55):

$$\begin{aligned}
\chi^{\sigma-\sigma-\sigma\sigma}_{\alpha,\beta}(1,2) &= i\langle\mathcal{T}_{\mathcal{C}}\hat{c}^{\dagger}_{\beta,-\sigma}(1^+)\hat{c}_{\beta,\sigma}(1)\hat{c}_{\alpha,\sigma}(2)\hat{c}^{\dagger}_{\alpha,-\sigma}(2^+)\rangle\\
&= -i\langle\mathcal{T}_{\mathcal{C}}\hat{S}^{\mp}_{\alpha}(1)\hat{S}^{\mp}_{\beta}(2)\rangle.
\end{aligned} \tag{5.59}$$

In Eq. (5.59), it becomes $\hat{S}^-$ if $\sigma =\uparrow$ and $\hat{S}^+$ if $\sigma =\downarrow$. Because in all the model Hamiltonians considered the total spin is conserved, expectation values like Eq. (5.59) drop out. Moreover, the vertex function appearing in Eq. (5.58) is assumed to be fully local, as done in Sec. 5.2.3.1 for the longitudinal component (Eq. (5.52)). Utilizing both Eqs. (5.7) and (5.14), the transversal component $\chi^{\sigma-\sigma\sigma-\sigma} = \frac{1}{2}\chi^{\mathrm{sp}}$. Furthermore, the transversal irreducible vertex $\Gamma^{\sigma-\sigma\sigma-\sigma} = -\Gamma^{\mathrm{sp}}$ according to Eq. (5.44) when substituting the Hubbard interaction $V^{\sigma\bar{\sigma}'}_{\epsilon,\zeta,\bar{\gamma}}(1) \to U_\epsilon(1)\delta_{\bar{\gamma},\epsilon}\delta_{\epsilon,\zeta}\delta_{\bar{\sigma}',-\sigma}$:

$$\begin{aligned}
\Gamma^{\sigma-\sigma\sigma-\sigma}_{\epsilon,\zeta;\gamma,\delta}(1,2;4,3) &\approx iU_\epsilon(1)\frac{\langle\mathcal{T}_{\mathcal{C}}\hat{n}_{\epsilon,-\sigma}(1)\hat{n}_{\epsilon,\sigma}(1)\rangle}{\langle\hat{n}_{\epsilon,-\sigma}(1)\rangle\,\langle\hat{n}_{\epsilon,\sigma}(1)\rangle}\\
&\qquad\times\delta(1,4)\delta(1^+,3)\delta(1,2)\delta_{\epsilon,\zeta}\delta_{\epsilon,\gamma}\delta_{\epsilon,\delta}\\
&= -\Gamma^{\mathrm{sp}}_{\zeta}(1).
\end{aligned} \tag{5.60}$$

All things considered, Eq. (5.58) becomes [129]

$$\begin{aligned}
\Sigma^{\mathrm{T},\sigma}_{\epsilon,\zeta}(1,2) &= U_\epsilon(1)n^{-\sigma}_{\epsilon}(1)\delta(1,2)\delta_{\epsilon,\zeta}\\
&\quad + \frac{U_\epsilon(1)}{2}\mathcal{G}^{-\sigma}_{\epsilon,\zeta}(1,2)\Gamma^{\mathrm{sp}}_{\zeta}(2)\chi^{\mathrm{sp}}_{\zeta,\epsilon}(2,1).
\end{aligned} \tag{5.61}$$

Indeed, by construction, there are no charge transversal contributions.

5.2.4 *Second-level approximation*

Gathering all the results stemming from the TPSC ansatz, the total self-energy for the second-level approximation, which is an average of the longitudinal (5.53) and the transversal (5.61) components, can be written down as:

$$\Sigma^{\text{TPSC},(1)}_{\epsilon,\zeta;\sigma}(1,2) = U_{\epsilon}(1)n^{-\sigma}_{\epsilon}(1)\delta(1,2)\delta_{\epsilon,\zeta} + \frac{U_{\epsilon}(1)}{8}\mathcal{G}^{(0)}_{\epsilon,\zeta;\sigma}(1,2) \times \left[\Gamma^{\text{ch}}_{\zeta}(2)\chi^{\text{ch}}_{\zeta,\epsilon}(2,1) + 3\Gamma^{\text{sp}}_{\zeta}(2)\chi^{\text{sp}}_{\zeta,\epsilon}(2,1)\right]. \tag{5.62}$$

Because the irreducible vertices were derived within the first-level approximation where the self-energy is defined by Eq. (5.43), the Green's function in Eq. (5.62) is dressed with $\Sigma^{(0)}$ for consistency, justifying the usage of $\mathcal{G}^{(0)}$. If the Fourier transform of Eq. (5.62) is performed, one easily obtains [18]

$$\int \mathrm{d}^D(\mathbf{R}_i - \mathbf{R}_j)\; e^{-i\mathbf{k}\cdot(\mathbf{R}_i-\mathbf{R}_j)}\Sigma^{\phi,(1)}_{\sigma}(\mathbf{R}_i - \mathbf{R}_j;z_1,z_2) = \Sigma^{\text{TPSC},(1)}_{\mathbf{k},\sigma}(z_1,z_2)$$
$$= U(z_1)n_{-\sigma}(z_1)\delta^{\mathcal{C}}(z_1,z_2) + \frac{U(z_1)}{8}\int \frac{\mathrm{d}^D\mathbf{q}}{(2\pi)^D}\,\mathcal{G}^{(0)}_{\mathbf{k}+\mathbf{q},\sigma}(z_1,z_2) \times \left[\Gamma^{\text{ch}}(z_2)\chi^{\text{ch}}_{\mathbf{q}}(z_2,z_1) + 3\Gamma^{\text{sp}}(z_2)\chi^{\text{sp}}_{\mathbf{q}}(z_2,z_1)\right]. \tag{5.63}$$

In Eq. (5.63), the numerals that bulked both the lattice and contour-time degrees of freedom have been unwrapped. Also, because the Hubbard model (3.9) is a single-band model, the orbital indices have been dropped out. In the original formulation of TPSC [152], the susceptibilities χ^{ch} (5.20) and χ^{sp} (5.10) are functionals of $\mathcal{G}^0$ (5.28)

$$\chi^{\text{sp/ch}}_{\mathbf{q}}(z_1,z_2) = \chi^0_{\mathbf{q}}(z_1,z_2) + (-1)^{l+1}\frac{i}{2}\chi^0_{\mathbf{q}}(z_1,\bar{z})\Gamma^{\text{sp/ch}}(\bar{z})\chi^{\text{sp/ch}}_{\mathbf{q}}(\bar{z},z_2), \tag{5.64}$$

where χ^0 is the noninteracting susceptibility in reciprocal space

$$\chi^0_{\mathbf{q}}(z_1,z_2) = -2i\int_{-\pi}^{\pi}\frac{\mathrm{d}^Dk}{(2\pi)^D}\,\mathcal{G}^{(0)}_{\mathbf{k}}(z_1,z_2)\mathcal{G}^{(0)}_{\mathbf{k}+\mathbf{q}}(z_2,z_1). \tag{5.65}$$

In the Bethe-Salpeter equation (5.64), $l = 0$ for charge (ch) and $l = 1$ for spin (sp). The second-level TPSC Green's function $\mathcal{G}^{(1)}$ is built from Eq. (5.63):

$$[i\partial_{z_1} + \mu - \epsilon(\mathbf{k})]\,\mathcal{G}^{(1)}_{\sigma,\mathbf{k}}(z_1,z_2) - \int_{\mathcal{C}}\mathrm{d}z''\;\Sigma^{\text{TPSC},(1)}_{\mathbf{k},\sigma}(z_1,z'')\mathcal{G}^{(1)}_{\sigma,\mathbf{k}}(z'',z_2) = \delta^{\mathcal{C}}(z_1,z_2), \tag{5.66}$$

where μ is the second-level chemical potential. The step from which ones leaps from the first-level approximation to the self-energy $\Sigma^{(0)}$ (5.27) to the second-level approximation $\Sigma^{(1)}$ (5.63) isn't strictly conserving in the Kadanoff-Baym sense, as was already pointed out in Ref. [156]. Although, it is conserving to a good approximation for a large range of bare interactions U and dopings n, especially in the weak-coupling regime since Eq. (5.63) (longitudinal component) becomes the second-order lattice IPT self-energy in the limit $U \to 0$ [109]

$$\Sigma^{(2)}_{\mathbf{k},\sigma}(z_1,z_2) = U(z_1)U(z_2) \times \int \frac{\mathrm{d}^D q \mathrm{d}^D k'}{(2\pi)^{2D}} \mathcal{G}_{\mathbf{k}+\mathbf{q},\sigma}(z_1,z_2)\mathcal{G}_{\mathbf{k}'+\mathbf{q},-\sigma}(z_2,z_1^+)\mathcal{G}_{\mathbf{k}'+\mathbf{q},-\sigma}(z_1,z_2{}^+), \tag{5.67}$$

which has a well-defined Luttinger-Ward functional. Moreover, the fact that the second-level approximation to the TPSC self-energy (5.63) develops into the second-order lattice IPT self-energy (5.67) in the limit where $U \to 0$ makes it appealing to conceive a method that harnesses both TPSC and DMFT self-consistently. This scheme should work particularly well when using a weak coupling impurity solver as the IPT described in Section 3.2.1.3. This asymptotical behavior of $\Sigma^{\text{TPSC},(1)}$ alleviates the double-counting problem since in the limit where U/W is small, the second-level Luttinger-Ward functional that would generate $\Sigma^{\text{TPSC},(1)}$ can be approximated by that of the lattice second-order $\Sigma^{(2)}_{\mathbf{k}}$ self-energy. This nonequilibrium DMFT+TPSC scheme is explained in Section 5.2.9.

ALGORITHM The algorithm for TPSC goes as follows. First, compute the noninteracting Green's function $\mathcal{G}^{(0)}$ (5.28) that makes up the noninteraction two-particle Green's function $\chi^0 \equiv -2i\mathcal{G}^{(0)}\mathcal{G}^{(0)}$ (5.65) and guess the time-dependent double occupancy $D(z) = \langle \hat{n}_\sigma(z)\hat{n}_{-\sigma}(z)\rangle$. Then, self-consistently solve for χ^{sp} and Γ^{sp} following the flow chart of Fig. 5.1 until $D(z)$ has converged using as a constraint the local spin two-particle sum-rule (5.11):

$$i\int \frac{\mathrm{d}^D q}{(2\pi)^D}\, \chi^{\text{sp/ch}}_{\mathbf{q}}(z,z^+) = \langle \hat{n}(z)\rangle + 2(-1)^l \langle \hat{n}_{-\sigma}(z)\hat{n}_\sigma(z)\rangle - (1-l)\langle \hat{n}(z)\rangle^2, \tag{5.68}$$

where $\langle \hat{n}\rangle = \langle \hat{n}_\uparrow + \hat{n}_\downarrow\rangle$ is the total density of particles. In Eq. (5.68), when $l = 0$, one does recover the charge sum-rule (5.22). In the actual implementation of TPSC and its variants, to solve for the spin-related quantities, a multidimensional root-finding method for nonlinear systems of equations is employed, since the alternative method depicted in Fig. 5.1 is a bit less efficient, especially close to T_x. As explained in Appendix H, the form of the Bethe-Salpeter equations (5.64) needs to be changed so as to satisfy the local two-particle sum-rules (5.68). The approximated Bethe-Salpeter equations read

As a reminder, $l = 0$ for charge (ch) and $l = 1$ for spin (sp).

$$\chi^{\text{sp/ch}}_{\mathbf{q}}(z,z') = \chi^0_{\mathbf{q}}(z,z') + (-1)^{l+1}\frac{i}{2}\Gamma^{\text{sp/ch}}(z)\chi^0_{\mathbf{q}}(z,\bar{z})\chi^{\text{sp/ch}}_{\mathbf{q}}(\bar{z},z'). \tag{5.69}$$

If the Bethe-Salpeter equations (5.64) were to be used instead of Eq. (5.69), then varying the vertices $\Gamma^{\text{sp/ch}}(t)$ so as to satisfy the two-particle sum-rules (5.68) at time step t wouldn't change the expression, whatever the value of the vertices (see Appendix H).

The next step is to solve for the charge quantities χ^{ch} and Γ^{ch}. This is done using a multidimensional root-finding method for non-linear system of equations at each time step[3]. The two equations which must be simultaneously solved are displayed in Fig. 5.2 and it involves the charge two-particle sum-rule ($l = 0$) (5.68). As far as TPSC is concerned, the algorithm terminates once all the

---

[3] The spin quantities are solved using the same multidimensional root-finding algorithm.

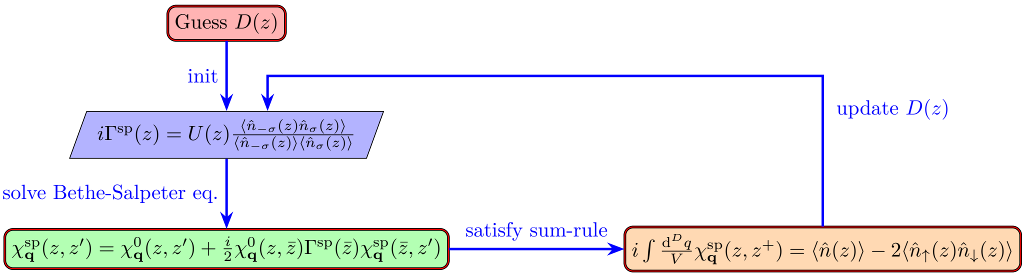
Guess $D(z)$
init
$i\Gamma^{\mathrm{sp}}(z) = U(z)\frac{\langle\hat{n}_{-\sigma}(z)\hat{n}_{\sigma}(z)\rangle}{\langle\hat{n}_{-\sigma}(z)\rangle\langle\hat{n}_{\sigma}(z)\rangle}$
update $D(z)$
solve Bethe-Salpeter eq.
$\chi^{\mathrm{sp}}_{\mathbf{q}}(z,z') = \chi^{0}_{\mathbf{q}}(z,z') + \frac{i}{2}\chi^{0}_{\mathbf{q}}(z,\bar{z})\Gamma^{\mathrm{sp}}(\bar{z})\chi^{\mathrm{sp}}_{\mathbf{q}}(\bar{z},z')$
satisfy sum-rule
$i\int\frac{\mathrm{d}^Dq}{V}\chi^{\mathrm{sp}}_{\mathbf{q}}(z,z^+) = \langle\hat{n}(z)\rangle - 2\langle\hat{n}_{\uparrow}(z)\hat{n}_{\downarrow}(z)\rangle$

Figure 5.1: Flow chart describing the self-consistent determination of $D(z)$, χ^{sp} and Γ^{sp} (alternative method). The green slot is replaced by the equation (5.69) in the implementation.

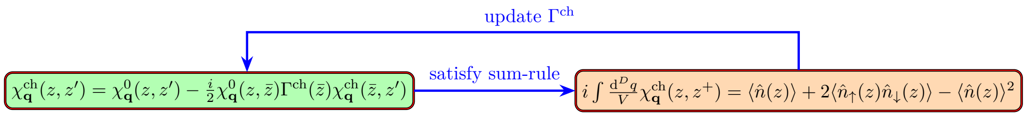
update Γ^{ch}
$\chi^{\mathrm{ch}}_{\mathbf{q}}(z,z') = \chi^{0}_{\mathbf{q}}(z,z') - \frac{i}{2}\chi^{0}_{\mathbf{q}}(z,\bar{z})\Gamma^{\mathrm{ch}}(\bar{z})\chi^{\mathrm{ch}}_{\mathbf{q}}(\bar{z},z')$
satisfy sum-rule
$i\int\frac{\mathrm{d}^Dq}{V}\chi^{\mathrm{ch}}_{\mathbf{q}}(z,z^+) = \langle\hat{n}(z)\rangle + 2\langle\hat{n}_{\uparrow}(z)\hat{n}_{\downarrow}(z)\rangle - \langle\hat{n}(z)\rangle^2$

Figure 5.2: Flow chart describing the self-consistent determination of χ^{ch} and Γ^{ch}. Again, the green slot is replaced by the equation (5.69) in the implementation.

quantities in each channel have been solved and the second-level self-energy

$$\Sigma^{\mathrm{TPSC},(1)}_{\mathbf{k},\sigma}[\alpha](z_1,z_2) = U(z_1)n_{-\sigma}(z_1)\delta_{\mathcal{C}}(z_1,z_2) + \frac{U(z_1)}{8}\int\frac{\mathrm{d}^Dq}{(2\pi)^D}\alpha(z_2)$$
$$\times\left[3\Gamma^{\mathrm{sp}}(z_2)\chi^{\mathrm{sp}}_{\mathbf{q}}(z_2,z_1) + \Gamma^{\mathrm{ch}}(z_2)\chi^{\mathrm{ch}}_{\mathbf{q}}(z_2,z_1)\right]\mathcal{G}^{(0)}_{\mathbf{k}+\mathbf{q},\sigma}(z_1,z_2) \tag{5.70}$$

has been computed. In Eq. (5.70), the one-time variable α has been inserted into Eq. (5.63) such as to satisfy the sum-rule involving the double occupancy appearing in Eq. (5.54) obtained for solving the spin quantities (see Fig. 5.1):

$$\frac{-i}{2}\int\frac{\mathrm{d}^Dk}{(2\pi)^D}\left[\Sigma^{\mathrm{TPSC},(1)}_{\mathbf{k},\bar{\sigma}}[\alpha](z_1,\bar{z})\mathcal{G}^{(1)}_{\mathbf{k},\bar{\sigma}}[\Sigma^{\mathrm{TPSC},(1)}](\bar{z},z_1^+)\right]$$
$$= U(z_1)\langle\hat{n}_{-\sigma}(z_1)\hat{n}_{\sigma}(z_1)\rangle. \tag{5.71}$$

This further renormalization of the irreducible vertices is necessary in order to get physically sound results upon quenching parameters in the Hubbard model (3.9). In the original formulation of TPSC [152], coined "OG TPSC" in Chapter 6 and Chapter 7, the algorithm does not make use of the sum-rule (5.71). Since this renormalization of the vertices involves a convolution over the contour $\mathcal{C}$, it can be thought of as a "dynamical" renormalization as opposed to how $\Gamma^{\mathrm{ch/sp}}$ are determined in the first place (see Eq. (5.68)), which consists rather in a reciprocal-space average. The variant TPSC+GG reintroduces the Green's function $\mathcal{G}^{(1)}[\Sigma^{\mathrm{TPSC},(1)}]$ computed with Eq. (5.70) into the noninteracting bubble χ^0 and repeats the subroutines described in Figures 5.1 and 5.2 until overall convergence. The electron filling is set with the chemical potential μ_0 appearing in the definition of $\mathcal{G}^{(0)}$, and should be close to the chemical potential μ of the second-level Green's function $\mathcal{G}^{(1)}$ (5.66) since the difference $\mu-\mu_0$ is compensated by the change of the real part of the retarded self-energy at the Fermi surface $\mathrm{Re}\Sigma^{\mathrm{TPSC},(1),\mathrm{R}}(\mathbf{k}_F,\omega=\mu)$ [152]: this can serve as an internal accuracy check.

TPSC+GG turns out to be more stable at longer times and it conserves better energy than TPSC. Although, TPSC+GG is limited to smaller interaction values and time windows (large computational cost).

5.2.5 *Equations of motion of the multi-orbital Hubbard model*

In the case of the multi-orbital Hubbard model, the Hamiltonian (3.8) is evaluated in the commutator in the last term of Eq. (2.50). It yields

$$
\begin{aligned}
[\hat{\mathcal{H}},\hat{c}_{\epsilon,\sigma}(\mathbf{R}_i)](z_1) = &-\sum_{\beta,k}\left[h^{\sigma}_{\epsilon,\beta}(\mathbf{R}_{ik};z_1)-\mu\delta_{i,k}\delta_{\epsilon,\beta}\right]\hat{c}_{\beta,\sigma}(\mathbf{R}_k;z_1)\\
&-\sum_{\beta,\sigma'}U^{\sigma\sigma'}_{\epsilon,\beta}(\mathbf{R}_i;z_1)\hat{n}_{\beta,\sigma'}(\mathbf{R}_i;z_1)\hat{c}_{\epsilon,\sigma}(\mathbf{R}_i;z_1).
\end{aligned}
\tag{5.72}
$$

In Eq. (5.72), the fact that the interaction tensor is symmetric $U_{\epsilon,\beta} = U_{\beta,\epsilon}$ was put forth. Given Eq. (5.72), the equations of motion become

$$
\begin{aligned}
&i\partial_{z_1}\mathcal{G}^{\phi,\sigma}_{\epsilon,\zeta}(\mathbf{R}_{ij};z_1,z_2)-h^{\sigma}_{\epsilon,\bar{\beta}}(\mathbf{R}_{i\bar{k}};z_1)\mathcal{G}^{\phi,\sigma}_{\bar{\beta},\zeta}(\mathbf{R}_{\bar{k}j};z_1,z_2)\\
&\qquad-\phi^{\sigma\bar{\sigma}'}_{\epsilon,\bar{\beta}}(\mathbf{R}_{i\bar{k}};z_1,\bar{z}_4)\mathcal{G}^{\phi,\bar{\sigma}'\sigma}_{\bar{\beta},\zeta}(\mathbf{R}_{\bar{k}j};\bar{z}_4,z_2)\\
&=\delta^{\mathcal{C}}(z_1,z_2)\delta_{\epsilon,\zeta}\delta_{i,j}-iU^{\sigma\bar{\sigma}'}_{\epsilon,\bar{\beta}}(z_1)\left\langle\mathcal{T}_{\mathcal{C}}\hat{n}_{\bar{\beta},\bar{\sigma}'}(\mathbf{R}_i;z_1)\hat{c}_{\epsilon,\sigma}(\mathbf{R}_i;z_1)\hat{c}^{\dagger}_{\zeta,\sigma}(\mathbf{R}_j;z_2)\right\rangle_{\phi}.
\end{aligned}
\tag{5.73}
$$

Notice that only the four-point correlation function in Eq. (5.73) is different from Eq. (5.46); it acts as a fingerprint of the lattice model Hamiltonian and only this difference will trigger substantial differences in the two-particle sum-rules and the second-level TPSC self-energies. Again resorting to the Dyson's equation (2.44), one can reshuffle Eq. (5.73) so as to realize that the four-point correlation function relates to the self-energy and Green's function via

$$
\begin{aligned}
&\left[\Sigma^{\phi}*\mathcal{G}^{\phi}\right]^{\sigma}_{\epsilon,\zeta}(\mathbf{R}_{ij};z_1,z_2)\\
&\qquad=-iU^{\sigma\bar{\sigma}'}_{\epsilon,\bar{\beta}}(z_1)\left\langle\mathcal{T}_{\mathcal{C}}\hat{n}_{\bar{\beta},\bar{\sigma}'}(\mathbf{R}_i;z_1)\hat{c}_{\epsilon,\sigma}(\mathbf{R}_i;z_1)\hat{c}^{\dagger}_{\zeta,\sigma}(\mathbf{R}_j;z_2)\right\rangle_{\phi}.
\end{aligned}
\tag{5.74}
$$

The main difference between Eq. (5.47) and Eq. (5.74) revolves around the inter-orbital Coulomb interaction included through $U_{\epsilon,\beta}$. The operator "$*$" was defined in Eq. (5.47). Again, to ease off on the notation, the lattice site index will be combined with the contour-time. The four-point correlation function appearing in Eq. (5.74) can only be calculated in the longitudinal (Section 5.2.5.1) channel when $\bar{\sigma}' = \sigma$, since using a source field $\phi_{\sigma-\sigma}$ to generate Eqs. (2.41) and (2.46) will not produce the expression sought after. However, there exists a transversal expression to Eq. (5.74) when the spin $\bar{\sigma}' = -\sigma$. The latter can be verified trying it out with Eqs. (5.55) and (5.56).

5.2.5.1 *Longitudinal expression of the self-energy*

To formalize the second-level longitudinal self-energy to the multi-orbital Hubbard model, the necessary variable substitutions need to be carried out in Eq. (2.47) to match the labelling of the quantum numbers with the four-point correlation function of Eq. (5.74): $\gamma \to (\bar{\beta},\bar{\sigma}')$, $\delta \to (\bar{\beta},\bar{\sigma}')$, $\epsilon \to (\epsilon,\sigma)$ and $\zeta \to (\zeta,\sigma)$. Regarding the contour-time variables, one has to make the same substitutions as in Section 5.2.3.1: $z_4 \to z_1^{++}$, $z_3 \to z_1^{+}$, $z_2 \to z_2$ and $z_1 \to z_1$. Then, multiplying the result by $-U^{\sigma\sigma'}_{\epsilon,\beta}$, one gets

$$\begin{aligned}\left[\Sigma^{\mathrm{L},\phi} * \mathcal{G}^{\phi}\right]^{\sigma}_{\epsilon,\zeta}(1,2) &= -iU^{\sigma\bar{\sigma}'}_{\epsilon,\bar{\beta}}(1)\mathcal{G}^{\phi}_{\bar{\beta};\bar{\sigma}'}(1^{+},1^{++})\mathcal{G}^{\phi,\sigma}_{\epsilon,\zeta}(1,2)\\ &+ iU^{\sigma\bar{\sigma}'}_{\epsilon,\bar{\beta}}(1)\mathcal{G}^{\phi,\sigma\bar{\sigma}'}_{\epsilon,\bar{\beta}}(1,1^{++})\mathcal{G}^{\phi,\bar{\sigma}'\sigma}_{\bar{\beta},\zeta}(1^{+},2) + U^{\sigma\bar{\sigma}'}_{\epsilon,\bar{\beta}}(1)\mathcal{G}^{\phi}_{(\epsilon,\sigma),\bar{\alpha}}(1,\bar{3})\\ &\times \Gamma^{\phi}_{\bar{\alpha},\bar{\eta};\bar{\theta},\bar{\omega}}(\bar{3},\bar{5};\bar{6},\bar{7})\chi^{\phi}_{\bar{\theta},\bar{\omega};(\bar{\beta},\bar{\sigma}')}(\bar{6},\bar{7};1^{++},1^{+})\mathcal{G}^{\phi}_{\bar{\eta},(\zeta,\sigma)}(\bar{5},2). \end{aligned} \tag{5.75}$$

This time, the second term of Eq. (5.75) does not vanish. The second-level TPSC self-energy for the multi-orbital Hubbard model then reads:

$$\begin{aligned}\Sigma^{\mathrm{L},\phi}_{\epsilon,\zeta;\sigma}(1,2) &= -iU^{\sigma\bar{\sigma}'}_{\epsilon,\bar{\beta}}(1)\mathcal{G}^{\phi}_{\bar{\beta},\bar{\sigma}'}(1^{+},1^{++})\delta(1,2)\delta_{\epsilon,\zeta}\\ &+ iU^{\sigma}_{\epsilon,\zeta}(1)\mathcal{G}^{\phi,\sigma}_{\epsilon,\zeta}(1,1^{++})\delta(1,2) + U^{\sigma\bar{\sigma}'}_{\epsilon,\bar{\beta}}(1)\mathcal{G}^{\phi}_{(\epsilon,\sigma),\bar{\alpha}}(1,\bar{3})\\ &\times \Gamma^{\phi}_{\bar{\alpha},(\zeta,\sigma);\bar{\theta},\bar{\omega}}(\bar{3},2;\bar{6},\bar{7})\chi^{\phi}_{\bar{\theta},\bar{\omega};(\bar{\beta},\bar{\sigma}')}(\bar{6},\bar{7};1). \end{aligned} \tag{5.76}$$

From now on, the spin indices are reinstated to better spot out the spin and charge quantities. Developing the spin summation in Eq. (5.76) and canceling the source field ϕ, one obtains

$$\begin{aligned}\Sigma^{\mathrm{L},\sigma}_{\epsilon,\zeta}(1,2) &= U^{\sigma\bar{\sigma}'}_{\epsilon,\bar{\beta}}(1)n_{\bar{\beta},\bar{\sigma}'}(1)\delta(1,2)\delta_{\epsilon,\zeta} - U^{\sigma}_{\epsilon,\zeta}(1)n^{\sigma}_{\epsilon,\zeta}(1)\delta(1,2)\\ &+ U^{\sigma\bar{\sigma}'}_{\epsilon,\bar{\beta}}(1)\mathcal{G}^{\sigma}_{\epsilon,\bar{\alpha}}(1,\bar{3})\Big[\Gamma^{\sigma\sigma}_{\bar{\alpha},\zeta;\bar{\theta},\bar{\omega}}(\bar{3},2;\bar{6},\bar{7})\chi^{\sigma\bar{\sigma}'}_{\bar{\theta},\bar{\omega};\bar{\beta}}(\bar{6},\bar{7};1)\\ &\qquad + \Gamma^{\sigma-\sigma}_{\bar{\alpha},\zeta;\bar{\theta},\bar{\omega}}(\bar{3},2;\bar{6},\bar{7})\chi^{-\sigma\bar{\sigma}'}_{\bar{\theta},\bar{\omega};\bar{\beta}}(\bar{6},\bar{7};1)\Big]. \end{aligned} \tag{5.77}$$

Due to the fact that the multi-orbital Hubbard model preserves total spin projection, terms like $\Gamma^{\sigma'\sigma''\sigma\sigma} = 0$ and $\chi^{\sigma'\sigma''\sigma\sigma} = 0 \ \forall \ \sigma' \neq \sigma''$. It should be clear that the second term of Eq. (5.77) is nonzero only if the orbitals $\epsilon \neq \zeta$, since the Pauli exclusion principle prohibits two spins with same projection to sit on the same orbital (single energy level). Then, developing the sum over σ' and putting Eq. (5.21) to use, the physical longitudinal self-energy can be expressed as

Keep in mind that $U^{\sigma\sigma}_{\epsilon,\zeta} = 0$ if $\epsilon = \zeta$.

$$\begin{aligned}\Sigma^{\mathrm{L},\sigma}_{\epsilon,\zeta}(1,2) &= U^{\sigma\bar{\sigma}'}_{\epsilon,\bar{\beta}}(1)n_{\bar{\beta},\bar{\sigma}'}(1)\delta(1,2)\delta_{\epsilon,\zeta} - U^{\sigma}_{\epsilon,\zeta}(1)n^{\sigma}_{\epsilon,\zeta}(1)\delta(1,2)\\ &+ \frac{U^{\sigma}_{\epsilon,\bar{\beta}}(1)}{4}\mathcal{G}^{\sigma}_{\epsilon,\bar{\alpha}}(1,\bar{3})\Big[\Gamma^{\mathrm{ch}}_{\bar{\alpha},\zeta;\bar{\theta},\bar{\omega}}(\bar{3},2;\bar{6},\bar{7})\chi^{\mathrm{ch}}_{\bar{\theta},\bar{\omega};\bar{\beta}}(\bar{6},\bar{7};1)\\ &\qquad - \Gamma^{\mathrm{sp},0}_{\bar{\alpha},\zeta;\bar{\theta},\bar{\omega}}(\bar{3},2;\bar{6},\bar{7})\chi^{\mathrm{sp}}_{\bar{\theta},\bar{\omega};\bar{\beta}}(\bar{6},\bar{7};1)\Big]\\ &+ \frac{U^{\sigma-\sigma}_{\epsilon,\bar{\beta}}(1)}{4}\mathcal{G}^{\sigma}_{\epsilon,\bar{\alpha}}(1,\bar{3})\Big[\Gamma^{\mathrm{ch}}_{\bar{\alpha},\zeta;\bar{\theta},\bar{\omega}}(\bar{3},2;\bar{6},\bar{7})\chi^{\mathrm{ch}}_{\bar{\theta},\bar{\omega};\bar{\beta}}(\bar{6},\bar{7};1)\\ &\qquad + \Gamma^{\mathrm{sp},1}_{\bar{\alpha},\zeta;\bar{\theta},\bar{\omega}}(\bar{3},2;\bar{6},\bar{7})\chi^{\mathrm{sp}}_{\bar{\theta},\bar{\omega};\bar{\beta}}(\bar{6},\bar{7};1)\Big]. \end{aligned} \tag{5.78}$$

The spin irreducible vertices have been separated out according to the interaction term they associate with because the TPSC ansatz that determine their value differ. If one replaces the irreducible vertices in Eq. (5.78) with fully local ones (5.52), one retrieves

$$\begin{aligned}\Sigma^{\mathrm{L},\sigma}_{\epsilon,\zeta}(1,2) &= U^{\sigma\bar{\sigma}'}_{\epsilon,\bar{\beta}}(1)n_{\bar{\beta},\bar{\sigma}'}(1)\delta(1,2)\delta_{\epsilon,\zeta} - U^{\sigma}_{\epsilon,\zeta}(1)n^{\sigma}_{\epsilon,\zeta}(1)\delta(1,2)\\ &+ \frac{U^{\sigma}_{\epsilon,\bar{\beta}}(1)}{4}\mathcal{G}^{\sigma}_{\epsilon,\bar{\alpha}}(1,2)\left[\Gamma^{\mathrm{ch}}_{\bar{\alpha},\zeta}(2)\chi^{\mathrm{ch}}_{\zeta;\bar{\beta}}(2,1) - \Gamma^{\mathrm{MH,sp,0}}_{\bar{\alpha},\zeta}(2)\chi^{\mathrm{sp}}_{\zeta;\bar{\beta}}(2,1)\right]\\ &+ \frac{U^{\sigma-\sigma}_{\epsilon,\bar{\beta}}(1)}{4}\mathcal{G}^{\sigma}_{\epsilon,\bar{\alpha}}(1,2)\left[\Gamma^{\mathrm{ch}}_{\bar{\alpha},\zeta}(2)\chi^{\mathrm{ch}}_{\zeta;\bar{\beta}}(2,1) + \Gamma^{\mathrm{MH,sp,1}}_{\bar{\alpha},\zeta}(2)\chi^{\mathrm{sp}}_{\zeta;\bar{\beta}}(2,1)\right]. \qquad (5.79)\end{aligned}$$

As far as the multi-orbital Hubbard model is concerned, the TPSC ansatz to the longitudinal spin irreducible vertex are calculated using both Eqs. (5.41) and (5.33):

$$\begin{cases}\Gamma^{\mathrm{MH,sp,0}}_{\alpha,\zeta}(1) = -iU^{\sigma}_{\alpha,\zeta}(1)\dfrac{\langle\hat{n}_{\zeta,\sigma}(1)\hat{n}_{\alpha,\sigma}(1)\rangle_{\phi}}{\langle\hat{n}_{\zeta,\sigma}(1)\rangle_{\phi}\langle\hat{n}_{\alpha,\sigma}(1)\rangle_{\phi}} & (\alpha \neq \zeta)\\ \Gamma^{\mathrm{MH,sp,1}}_{\alpha,\zeta}(1) = -iU^{\sigma-\sigma}_{\alpha,\zeta}(1)\dfrac{\langle\hat{n}_{\zeta,-\sigma}(1)\hat{n}_{\alpha,\sigma}(1)\rangle_{\phi}}{\langle\hat{n}_{\zeta,-\sigma}(1)\rangle_{\phi}\langle\hat{n}_{\alpha,\sigma}(1)\rangle_{\phi}}. & \end{cases} \qquad (5.80)$$

The charge vertices Γ^{ch} in Eq. (5.79) are set using the sum-rule (5.23) in conjunction with the Bethe-Salpeter equation (5.64) with some extra approximation (see Appendix H).

5.2.5.2 *Transversal expression of the self-energy*

To derive a transversal expression to the self-energy, one can drop the terms in Eq. (5.74) that are multiplied by interaction terms of the form $U^{\sigma\sigma}_{\alpha,\beta}$, since the resulting four-point correlation function cannot be obtained in the transversal channel. This means that the derivation is very similar to that of the Hubbard model done in Section 5.2.3.2, although $U^{\sigma-\sigma}_{\alpha,\beta}$ is now depending on the orbitals under consideration. For that reason, some steps of the derivation will be skipped. The susceptibility $\chi^{-\sigma\sigma-\sigma\sigma}_{\beta,\zeta;\beta,\epsilon}(1^{+},2;1^{++},1^{-})$ has to be computed from both Eqs. (2.41) and (2.46) to get the transversal self-energy and this entails making the following substitutions: $\epsilon \to (\beta,-\sigma)$, $\zeta \to (\zeta,\sigma)$, $\gamma \to (\beta,-\sigma)$ and $\delta \to (\epsilon,\sigma)$. The contour-time substitutions that need to be made are: $z_4 \to z_1^{++}$, $z_3 \to z_1^{-}$, $z_2 \to z_2$ and $z_1 \to z_1^{+}$. Gathering the two respective expressions coming out of Eqs. (2.41) and (2.46), then multiplying by $U^{\sigma-\sigma}_{\epsilon,\beta}$ and summing over β, produces the relation required to extract the transversal self-energy

$$\begin{aligned}&\Sigma^{\mathrm{T},\phi,\sigma\bar{\sigma}'}_{\epsilon,\bar{\beta}}(1,\bar{2})\mathcal{G}^{\phi,\bar{\sigma}'\sigma}_{\bar{\beta},\zeta}(\bar{2},2)\\ &= iU^{\sigma-\sigma}_{\epsilon,\bar{\beta}}(1)\mathcal{G}^{\phi,\sigma-\sigma}_{\epsilon,\bar{\beta}}(1,1^{++})\mathcal{G}^{\phi,-\sigma\sigma}_{\bar{\beta},\zeta}(1^{+},2) - iU^{\sigma-\sigma}_{\epsilon,\bar{\beta}}(1)\mathcal{G}^{\phi,-\sigma}_{\bar{\beta}}(1^{+},1^{++})\mathcal{G}^{\phi,\sigma}_{\epsilon,\zeta}(1,2)\\ &- U^{\sigma-\sigma}_{\epsilon,\bar{\beta}}(1)\mathcal{G}^{\phi,-\sigma}_{\bar{\beta},\bar{\alpha}}(1,\bar{3})\Gamma^{\phi,-\sigma\sigma\bar{\sigma}'\bar{\sigma}''}_{\bar{\alpha},\bar{\eta};\bar{\theta},\bar{\omega}}(\bar{3},\bar{5};\bar{6},\bar{7})\chi^{\phi,\bar{\sigma}'\bar{\sigma}''-\sigma\sigma}_{\bar{\theta},\bar{\omega};\bar{\beta},\epsilon}(\bar{6},\bar{7};1)\mathcal{G}^{\phi,\sigma}_{\bar{\eta},\zeta}(\bar{5},2). \qquad (5.81)\end{aligned}$$

In light of Eq. (5.81), the physical transversal component to the second-level TPSC self-energy reads

$$\begin{aligned}\Sigma^{\mathrm{T},-\sigma}_{\epsilon,\zeta}(1,2) &= U^{\sigma-\sigma}_{\epsilon,\bar{\beta}}(1)n^{-\sigma}_{\bar{\beta}}(1)\delta(1,2)\delta_{\epsilon,\zeta}\\ &- U^{\sigma-\sigma}_{\epsilon,\bar{\beta}}(1)\mathcal{G}^{-\sigma}_{\bar{\beta},\bar{\alpha}}(1,\bar{3})\Gamma^{-\sigma\sigma-\sigma\sigma}_{\bar{\alpha},\zeta}(\bar{3},2;\bar{6},\bar{7})\chi^{-\sigma\sigma-\sigma\sigma}_{\zeta;\bar{\beta},\epsilon}(\bar{6},\bar{7};1), \qquad (5.82)\end{aligned}$$

since $\chi^{\sigma\sigma-\sigma\sigma} = \chi^{\sigma-\sigma-\sigma\sigma} = 0$ in the multi-orbital Hubbard model and the first term in Eq. (5.81) vanishes after multiplying from the right by $\mathcal{G}_{\sigma}^{-1}$. The vertex function appearing in Eq. (5.82) is approximated as fully local (see Sec. 5.2.3.1). Moreover, it was argued in Section 5.2.3.2 that the transversal susceptibility component $\chi^{\sigma-\sigma\sigma-\sigma} = \frac{1}{2}\chi^{\mathrm{sp}}$: it is clear in this case that the same equivalence applies. The susceptibility is also nonzero only if[4] $\beta \to \epsilon$. Although, for the transversal spin irreducible vertex, one has to be careful. For that reason, Eq. (5.44) is used once more with the proper substitution of the multi-orbital Hubbard interaction leading to a nonzero transversal component $V^{\sigma\bar{\sigma}'}_{\epsilon,\zeta;\bar{\gamma}}(1) \to U^{\sigma\bar{\sigma}'}_{\epsilon,\zeta}(1)\delta_{\bar{\gamma},\zeta}\delta_{\bar{\sigma}',-\sigma}$:

$$\begin{aligned}
\Gamma^{\sigma-\sigma\sigma-\sigma}_{\epsilon,\zeta;\gamma,\delta}(1,2;4,3) &\approx iU^{\sigma-\sigma}_{\epsilon,\zeta}(1)\frac{\left\langle \mathcal{T}_{\mathcal{C}}\hat{n}_{\zeta,-\sigma}(1)\hat{n}_{\epsilon,\sigma}(1)\right\rangle}{\left\langle \hat{n}_{\zeta,-\sigma}(1)\right\rangle\left\langle \hat{n}_{\epsilon,\sigma}(1)\right\rangle} \\
&\quad \times \delta(1,3)\delta(1^{+},4)\delta(1,2)\delta_{\delta,\gamma}\delta_{\gamma,\zeta} \\
&= -\Gamma^{\mathrm{MH,sp,1}}_{\epsilon,\zeta}(1).
\end{aligned} \tag{5.83}$$

Then, following on Eq. (5.83), the self-energy (5.82) is finally

$$\begin{aligned}
\Sigma^{\mathrm{T},\sigma}_{\epsilon,\zeta}(1,2) &= U^{\sigma-\sigma}_{\epsilon,\bar{\beta}}(1)n^{-\sigma}_{\bar{\beta}}(1)\delta(1,2)\delta_{\epsilon,\zeta} \\
&\quad + \frac{U^{\sigma-\sigma}_{\epsilon}(1)}{2}\mathcal{G}^{-\sigma}_{\epsilon,\bar{\alpha}}(1,2)\Gamma^{\mathrm{MH,sp,1}}_{\bar{\alpha},\zeta}(2)\chi^{\mathrm{sp}}_{\zeta,\epsilon}(2,1).
\end{aligned} \tag{5.84}$$

Thus, the irreducible vertex $\Gamma^{\mathrm{sp},0}$ (5.80) is only appearing in the longitudinal channel.

5.2.6 *Second-level approximation*

The crossing-symmetric second-level TPSC self-energy approximation to the multi-orbital Hubbard model is drawn from the average of Σ^{L} (5.79) and Σ^{T} (5.84), giving:

$$\begin{aligned}
\Sigma^{\mathrm{TPSC},(1)}_{\epsilon,\zeta;\sigma}(1,2) &= \sum_{\beta} U^{\sigma-\sigma}_{\epsilon,\beta}(1)n^{-\sigma}_{\beta}(1)\delta(1,2)\delta_{\epsilon,\zeta} \\
&+ \frac{1}{2}\sum_{\beta\neq\zeta} U^{\sigma}_{\epsilon,\beta}(1)n^{\sigma}_{\beta}(1)\delta(1,2)\delta_{\epsilon,\zeta} - \frac{1}{2}U^{\sigma}_{\epsilon,\zeta}(1)n^{\sigma}_{\epsilon,\zeta}(1)\delta(1,2) \\
&+ \sum_{\alpha,\beta\neq\epsilon}\frac{U^{\sigma}_{\epsilon,\beta}(1)}{8}\mathcal{G}^{\sigma}_{\epsilon,\alpha}(1,2)\left[\Gamma^{\mathrm{ch}}_{\alpha,\zeta}(2)\chi^{\mathrm{ch}}_{\zeta;\beta}(2,1) - \Gamma^{\mathrm{MH,sp,0}}_{\alpha,\zeta}(2)\chi^{\mathrm{sp}}_{\zeta;\beta}(2,1)\right] \\
&+ \sum_{\alpha,\beta}\frac{U^{\sigma-\sigma}_{\epsilon,\beta}(1)}{8}\mathcal{G}^{\sigma}_{\epsilon,\alpha}(1,2)\left[\Gamma^{\mathrm{ch}}_{\alpha,\zeta}(2)\chi^{\mathrm{ch}}_{\zeta;\beta}(2,1) + 3\Gamma^{\mathrm{MH,sp,1}}_{\alpha,\zeta}(2)\chi^{\mathrm{sp}}_{\zeta;\beta}(2,1)\right],
\end{aligned} \tag{5.85}$$

---

[4] Refer to Eq. (5.14) and verify that when one of the operators $\hat{S}^{\pm}$ is not diagonal in orbital index, it gives zero.

which Fourier transformed leads to

$$\Sigma^{\text{TPSC},(1)}_{\epsilon,\zeta;\sigma}(\mathbf{k};z_1,z_2) = \Sigma^{\text{HF,TPSC},(1)}_{\epsilon,\zeta;\sigma}(z_1) + \sum_{\alpha,\beta\neq\epsilon} \frac{U^{\sigma}_{\epsilon,\beta}(z_1)}{8} \int \frac{\mathrm{d}^D\mathbf{q}}{(2\pi)^D}\, \mathcal{G}^{(0),\sigma}_{\epsilon,\alpha}(\mathbf{k}+\mathbf{q};z_1,z_2)$$
$$\times \left[\Gamma^{\text{ch}}_{\alpha,\zeta}(z_2)\chi^{\text{ch}}_{\zeta;\beta}(\mathbf{q};z_2,z_1) - \Gamma^{\text{MH,sp},0}_{\alpha,\zeta}(z_2)\chi^{\text{sp}}_{\zeta;\beta}(\mathbf{q};z_2,z_1)\right] + \sum_{\alpha,\beta} \frac{U^{\sigma-\sigma}_{\epsilon,\beta}(z_1)}{8} \int \frac{\mathrm{d}^D\mathbf{q}}{(2\pi)^D}$$
$$\times \mathcal{G}^{(0),\sigma}_{\epsilon,\alpha}(\mathbf{k}+\mathbf{q};z_1,z_2)\left[\Gamma^{\text{ch}}_{\alpha,\zeta}(z_2)\chi^{\text{ch}}_{\zeta;\beta}(\mathbf{q};z_2,z_1) + 3\Gamma^{\text{MH,sp},1}_{\alpha,\zeta}(z_2)\chi^{\text{sp}}_{\zeta;\beta}(\mathbf{q};z_2,z_1)\right]. \tag{5.86}$$

The various summations are explicated in Eqs. (5.85) and (5.86). The term Σ^{HF} is a short-hand notation that regroups all the Hartree-Fock terms featuring in Eq. (5.85) (to the count of 3).

5.2.7 *Equations of motion of the Kanamori-Hubbard model*

In this section, the equations of motion of the Kanamori-Hubbard model (3.7) are developed in the same fashion as done in Section 5.2.3 and Section 5.2.5. Hence, referring to Eq. (2.50), one computes first the commutator

$$\begin{aligned}[\hat{\mathcal{H}},\hat{c}_{\epsilon,\sigma}(\mathbf{R}_i)](z_1) = &-\sum_{\beta,k}\left[h^{\sigma}_{\epsilon,\beta}(\mathbf{R}_{ik};z_1) - \mu\delta_{i,k}\delta_{\epsilon,\beta}\right]\hat{c}_{\beta,\sigma}(\mathbf{R}_k;z_1)\\
&-\sum_{\beta,\sigma'}\left(U^{\sigma\sigma'}_{\epsilon,\beta}(\mathbf{R}_i;z_1) - J^{\sigma}_{\epsilon,\beta}(\mathbf{R}_i;z_1)\delta_{\sigma,\sigma'}\right)\hat{n}_{\beta,\sigma'}(\mathbf{R}_i;z_1)\hat{c}_{\epsilon,\sigma}(\mathbf{R}_i;z_1)\\
+\sum_{\beta\neq\epsilon} J^{\sigma}_{\epsilon,\beta}(\mathbf{R}_i;z_1)&\Big(\hat{c}^{\dagger}_{\beta,-\sigma}(\mathbf{R}_i;z_1)\hat{c}_{\beta,\sigma}(\mathbf{R}_i;z_1)\hat{c}_{\epsilon,-\sigma}(\mathbf{R}_i;z_1)\\
&+\hat{c}^{\dagger}_{\epsilon,-\sigma}(\mathbf{R}_i;z_1)\hat{c}_{\beta,\sigma}(\mathbf{R}_i;z_1)\hat{c}_{\beta,-\sigma}(\mathbf{R}_i;z_1)\Big).\end{aligned} \tag{5.87}$$

The spin exchange energy J' is assumed the same as the pair-hopping one J, implying that the electronic single-particle wave functions are real-valued and the Hund's coupling is real symmetric $J_{\epsilon,\beta} = J_{\beta,\epsilon}$. In Eq. (5.72), the fact that $U_{\epsilon,\beta} = U_{\beta,\epsilon}$ was used. Furthermore, it is implicitly understood that the interaction $U^{\sigma\sigma}_{\epsilon,\epsilon} = 0$ due to Pauli spin exclusion principle. Also, the Hund's coupling is a genuine multi-orbital interaction, implying that the diagonal terms vanish $J_{\epsilon,\epsilon} = 0$. The commutator (5.87) leads to

$$\begin{aligned}&\left[\Sigma^{\phi} * \mathcal{G}^{\phi}\right]^{\sigma}_{\epsilon,\zeta}(\mathbf{R}_{ij};z_1,z_2)\\
&= -i\left(U^{\sigma\bar{\sigma}'}_{\epsilon,\bar{\beta}}(\mathbf{R}_i;z_1) - J^{\sigma}_{\epsilon,\bar{\beta}}(\mathbf{R}_i;z_1)\delta_{\sigma,\bar{\sigma}'}\right)\left\langle\mathcal{T}_{\mathcal{C}}\hat{n}_{\bar{\beta},\bar{\sigma}'}(\mathbf{R}_i;z_1)\hat{c}_{\epsilon,\sigma}(\mathbf{R}_i;z_1)\hat{c}^{\dagger}_{\zeta,\sigma}(\mathbf{R}_j;z_2)\right\rangle_{\phi}\\
&+iJ^{\sigma}_{\epsilon,\bar{\beta}}(\mathbf{R}_i;z_1)\Big(\langle\mathcal{T}_{\mathcal{C}}\hat{c}^{\dagger}_{\bar{\beta},-\sigma}(\mathbf{R}_i;z_1^{++})\hat{c}_{\bar{\beta},\sigma}(\mathbf{R}_i;z_1^{+})\hat{c}_{\epsilon,-\sigma}(\mathbf{R}_i;z_1)\hat{c}^{\dagger}_{\zeta,\sigma}(\mathbf{R}_j;z_2)\rangle_{\phi}\\
&\qquad+\langle\mathcal{T}_{\mathcal{C}}\hat{c}^{\dagger}_{\epsilon,-\sigma}(\mathbf{R}_i;z_1^{++})\hat{c}_{\bar{\beta},\sigma}(\mathbf{R}_i;z_1^{+})\hat{c}_{\bar{\beta},-\sigma}(\mathbf{R}_i;z_1)\hat{c}^{\dagger}_{\zeta,\sigma}(\mathbf{R}_j;z_2)\rangle_{\phi}\Big),\end{aligned} \tag{5.88}$$

binding together the self-energy and Green's function. The Eq. (5.88) shares many similarities with the Eqs. (5.74) and (5.47) due to the fact that both the

Hubbard and multi-orbital Hubbard models are special cases of the Kanamori-Hubbard model. Although, now the interaction $U^{\sigma\sigma'}_{\epsilon,\beta}$ in the second term is *renormalized* by the Hund's coupling favouring high-spin states across different orbitals. An additional term only involving the Hund's coupling also makes its appearance, although it can only be generated in the transversal channel with appropriate source fields. In the longitudinal channel, the last term of the equations of motion (5.88), with J as prefactor, contributes only in an Hartree-Fock term (see Eq. (5.89)).

5.2.7.1 *Longitudinal expression of the self-energy*

The major addition here lies in the last term of the equations of motion (5.88). The first correlation function leads to the same expressions to the self-energy developed for the multi-orbital Hubbard model in Section 5.2.5, to the exception that Eq. (5.75) is multiplied by the interaction $-(U^{\sigma\sigma'}_{\epsilon,\beta} - J^{\sigma}_{\epsilon,\beta}\delta_{\sigma,\sigma'})$. It gives

$$\begin{aligned}
\Sigma^{\mathrm{L},\sigma}_{\epsilon,\zeta}(1,2) &= \left(U^{\sigma\bar{\sigma}'}_{\epsilon,\bar{\beta}}(1) - J^{\sigma}_{\epsilon,\bar{\beta}}(1)\delta_{\sigma,\bar{\sigma}'}\right) n_{\bar{\beta},\bar{\sigma}'}(1)\delta(1,2)\delta_{\epsilon,\zeta} \\
&- \left(U^{\sigma}_{\epsilon,\zeta}(1) - J^{\sigma}_{\epsilon,\zeta}(1)\right) n^{\sigma}_{\epsilon,\zeta}(1)\delta(1,2) + J^{\sigma}_{\epsilon,\zeta}(1)\left(n^{-\sigma}_{\epsilon,\zeta}(1) + n^{-\sigma}_{\zeta,\epsilon}(1)\right)\delta(1,2) \\
&+ \frac{\left(U^{\sigma}_{\epsilon,\bar{\beta}}(1) - J^{\sigma}_{\epsilon,\bar{\beta}}(1)\right)}{4}\mathcal{G}^{\sigma}_{\epsilon,\bar{\alpha}}(1,2)\left[\Gamma^{\mathrm{ch}}_{\bar{\alpha},\zeta}(2)\chi^{\mathrm{ch}}_{\zeta;\bar{\beta}}(2,1) - \Gamma^{\mathrm{KH,sp,0}}_{\bar{\alpha},\zeta}(2)\chi^{\mathrm{sp}}_{\zeta;\bar{\beta}}(2,1)\right] \\
&+ \frac{U^{\sigma-\sigma}_{\epsilon,\bar{\beta}}(1)}{4}\mathcal{G}^{\sigma}_{\epsilon,\bar{\alpha}}(1,2)\left[\Gamma^{\mathrm{ch}}_{\bar{\alpha},\zeta}(2)\chi^{\mathrm{ch}}_{\zeta;\bar{\beta}}(2,1) + \Gamma^{\mathrm{MH,sp,1}}_{\bar{\alpha},\zeta}(2)\chi^{\mathrm{sp}}_{\zeta;\bar{\beta}}(2,1)\right]. \qquad (5.89)
\end{aligned}$$

The longitudinal spin irreducible vertex $\Gamma^{\mathrm{KH,sp,0}}$ in Eq. (5.89) has a slightly different form when compared to that of the multi-orbital Hubbard model (5.80). It is now expressed as

$$\Gamma^{\mathrm{KH,sp,0}}_{\alpha,\zeta}(z_1) = -i\left(U^{\sigma}_{\alpha,\zeta}(z_1) - J^{\sigma}_{\alpha,\zeta}(z_1)\right)\frac{\left\langle \hat{n}_{\zeta,\sigma}(z_1)\hat{n}_{\alpha,\sigma}(z_1)\right\rangle_{\phi}}{\left\langle \hat{n}_{\zeta,\sigma}(z_1)\right\rangle_{\phi}\left\langle \hat{n}_{\alpha,\sigma}(z_1)\right\rangle_{\phi}} \qquad (\alpha \neq \zeta). \qquad (5.90)$$

The Eq. (5.89) depicts the complete Kanamori-Hubbard longitudinal self-energy. The last term of Eq. (5.88) contains correlation functions whose expression can't be derived in the longitudinal channel, but only in the transversal one – they will be the subject of Section 5.2.7.2.

5.2.7.2 *Transversal expression of the self-energy*

In this section, the new contributions to the transversal self-energy (5.82) introduced via the extra Hund's coupling will be tackled. The first correlation function of the last term of Eq. (5.88) can be obtained exchanging the following indices in Eq. (2.47): $\gamma \to (\bar{\beta},-\sigma)$, $\delta \to (\bar{\beta},\sigma)$, $\epsilon \to (\epsilon,-\sigma)$ and $\zeta \to (\zeta,\sigma)$. The exchange in contour-time variables goes as follows: $z_4 \to z_1^{++}$, $z_3 \to z_1^{+}$, $z_2 \to z_2$ and $z_1 \to z_1$. Then, multiplying the four-point correlation function by $J_{\epsilon,\bar{\beta}}$ and multiplying from the right by $\mathcal{G}^{-1}$, this results in

The notation Σ^1 and Γ^1 in Eq. (5.91) is meant to insist on the fact that this is only part of the complete transversal expression.

$$\begin{aligned}\Sigma^{1,\mathrm{T},\sigma}_{\epsilon,\zeta}(1,2) &= J^{\sigma}_{\epsilon,\zeta}(1)n^{-\sigma}_{\epsilon,\zeta}(1)\delta(1,2)\\ &\quad - J^{\sigma}_{\epsilon,\bar{\beta}}(1)\mathcal{G}^{-\sigma}_{\epsilon,\bar{\alpha}}(1,\bar{3})\Gamma^{1,-\sigma\sigma-\sigma\sigma}_{\bar{\alpha},\zeta;\bar{\theta},\bar{\omega}}(\bar{3},2;\bar{6},\bar{7})\chi^{-\sigma\sigma-\sigma\sigma}_{\bar{\theta},\bar{\omega};\bar{\beta}}(\bar{6},\bar{7};1),\end{aligned} \tag{5.91}$$

since $\chi^{\sigma\sigma-\sigma\sigma} = \chi^{\sigma-\sigma-\sigma\sigma} = 0$ for the same reasons evoked in Eq. (5.59). The ansatz for the local transversal spin irreducible vertex in this case is homogenous to

$$\begin{aligned}\chi^{-\sigma\sigma-\sigma\sigma}_{\epsilon,\zeta;\beta}(1^-,1;1^{++},1^+) &= -i\frac{\delta\mathcal{G}^{\phi,-\sigma\sigma}_{\epsilon,\zeta}(1^-,2)}{\delta\phi^{-\sigma\sigma}_{\beta}(1^{++},1^+)}\bigg|_{\zeta\to\epsilon,2\to1,\phi\to0}\\ &= -i\langle\mathcal{T}_{\mathcal{C}}\hat{c}^{\dagger}_{\zeta,-\sigma}(1^{++})\hat{c}_{\zeta,\sigma}(1^+)\hat{c}^{\dagger}_{\epsilon,\sigma}(1)\hat{c}_{\epsilon,-\sigma}(1^-)\rangle\\ &= -i\langle\hat{S}^{\mp}_{\zeta}(1)\hat{S}^{\pm}_{\epsilon}(1)\rangle,\end{aligned} \tag{5.92}$$

which can't be, by any manipulation, obtained from $I^{-\sigma\sigma}(T)$ as detailed in Eq. (5.35) – it has to be dealt with separately. Glancing at Eq. (5.14), one can come up with the equivalence

$$-i\langle\hat{S}^{\mp}_{\zeta}(1)\hat{S}^{\pm}_{\epsilon}(1)\rangle = -i\langle\hat{n}_{\zeta,\sigma}(1)\hat{n}_{\epsilon,\sigma}(1)\rangle + i\langle\hat{n}_{\zeta,\sigma}(1)\hat{n}_{\epsilon,-\sigma}(1)\rangle. \tag{5.93}$$

Again, to match with the first correlation function of the last term in Eq. (5.88) in the local limit, one would need to multiply Eq. (5.93) by the Hund's coupling and divide each term by its Hartree-Fock decomposition:

$$\begin{aligned}&-i\langle\hat{S}^{\mp}_{\zeta}(1)\hat{S}^{\pm}_{\epsilon}(1)\rangle = -iJ^{\sigma}_{\epsilon,\zeta}(1)\left(\frac{\langle\hat{n}_{\zeta,\sigma}(1)\hat{n}_{\epsilon,\sigma}(1)\rangle}{\langle\hat{n}_{\zeta,\sigma}(1)\rangle\langle\hat{n}_{\epsilon,\sigma}(1)\rangle} - \frac{\langle\hat{n}_{\zeta,\sigma}(1)\hat{n}_{\epsilon,-\sigma}(1)\rangle}{\langle\hat{n}_{\zeta,\sigma}(1)\rangle\langle\hat{n}_{\epsilon,-\sigma}(1)\rangle}\right)\\ &= \Gamma^{1,-\sigma\sigma-\sigma\sigma}_{\epsilon,\zeta}(1).\end{aligned} \tag{5.94}$$

In Eqs. (5.92), (5.93) and (5.94), the upper (lower) superscript characterizing $\hat{S}$ is selected if $\sigma =\uparrow$ ($\sigma =\downarrow$); this arrangement applies as well for what's coming up next.

As for the second correlation function of the last term of Eq. (5.88), the variable substitutions required in Eq. (2.47) read out like $\gamma \to (\epsilon,-\sigma)$, $\delta \to (\bar{\beta},\sigma)$, $\epsilon \to (\bar{\beta},-\sigma)$ and $\zeta \to (\zeta,\sigma)$, and $z_4 \to z_1^{++}$, $z_3 \to z_1^{+}$, $z_2 \to z_2$ and $z_1 \to z_1$. These substitutions produce the same result as Eq. (5.91), to the exception that the vertex is now denoted $\Gamma^{2,-\sigma\sigma-\sigma\sigma}$, since the ansatz differs from that of Eq. (5.94):

$$\begin{aligned}\chi^{-\sigma\sigma-\sigma\sigma}_{\beta,\zeta;\epsilon,\beta}(1^-,1;1^{++},1^+) &= -i\frac{\delta\mathcal{G}^{\phi,-\sigma\sigma}_{\beta,\zeta}(1^-,2)}{\delta\phi^{-\sigma\sigma}_{\epsilon,\beta}(1^{++},1^+)}\bigg|_{\zeta\to\epsilon,2\to1,\phi\to0}\\ &= -i\langle\mathcal{T}_{\mathcal{C}}\hat{c}^{\dagger}_{\epsilon,-\sigma}(1^{++})\hat{c}_{\zeta,\sigma}(1^+)\hat{c}^{\dagger}_{\epsilon,\sigma}(1)\hat{c}_{\zeta,-\sigma}(1^-)\rangle\\ &= -i\langle\hat{S}^{\mp}_{\epsilon,\zeta}(1)\hat{S}^{\pm}_{\epsilon,\zeta}(1)\rangle.\end{aligned} \tag{5.95}$$

This time, Eq. (5.95) mixes up the orbitals

$$-i\langle\hat{S}^{\mp}_{\epsilon,\zeta}(1)\hat{S}^{\pm}_{\epsilon,\zeta}(1)\rangle = -i\langle\hat{n}^{\sigma}_{\epsilon,\zeta}(1)\hat{n}^{\sigma}_{\epsilon,\zeta}(1)\rangle + i\langle\hat{n}^{\sigma}_{\epsilon,\zeta}(1)\hat{n}^{-\sigma}_{\epsilon,\zeta}(1)\rangle. \tag{5.96}$$

Eq. (5.96) should theoretically be nonzero. Nevertheless, because the correlation functions in Eq. (5.96) do not appear in any two-particle sum-rules (see Section 5.2.1) nor in any other irreducible spin vertex ansatz so far established, they are left dangling without sufficient number of contraints. Therefore, one approximates $\Gamma^{2,-\sigma\sigma-\sigma\sigma}=0$. The Hartree-Fock term from $\Sigma^{2,\mathrm{T}}$ however adds up to that of $\Sigma^{1,\mathrm{T}}$ and reads

$$\Sigma^{2,\mathrm{T},\sigma}_{\epsilon,\zeta}(1,2) = J^{\sigma}_{\epsilon,\zeta}(1)n^{-\sigma}_{\zeta,\epsilon}(1)\delta(1,2).$$

Invoking the locality of the vertex function appearing in Eq. (5.91), as well as using the fact that $\chi^{-\sigma\sigma-\sigma\sigma}=\frac{1}{2}\chi^{\mathrm{sp}}$, the total transversal component to the Kanamori-Hubbard TPSC self-energy comes down to the addition of Eqs. (5.84) and (5.91)

$$\begin{aligned}\Sigma^{\mathrm{T},\sigma}_{\epsilon,\zeta}(1,2) &= U^{\sigma-\sigma}_{\epsilon,\bar{\beta}}(1)n^{-\sigma}_{\bar{\beta}}(1)\delta(1,2)\delta_{\epsilon,\zeta} + J^{\sigma}_{\epsilon,\zeta}(1)\left(n^{-\sigma}_{\epsilon,\zeta}(1)+n^{-\sigma}_{\zeta,\epsilon}(1)\right)\delta(1,2)\\ &+\frac{U^{\sigma-\sigma}_{\epsilon}(1)}{2}\mathcal{G}^{-\sigma}_{\epsilon,\bar{\alpha}}(1,2)\Gamma^{\mathrm{MH,sp,1}}_{\bar{\alpha},\zeta}(2)\chi^{\mathrm{sp}}_{\zeta,\epsilon}(2,1)+\frac{J^{\sigma}_{\epsilon,\bar{\beta}}(1)}{2}\mathcal{G}^{-\sigma}_{\epsilon,\bar{\alpha}}(1,2)\Gamma^{\mathrm{KH,sp,1}}_{\bar{\alpha},\zeta}(2)\chi^{\mathrm{sp}}_{\zeta,\bar{\beta}}(2,1),\end{aligned} \tag{5.97}$$

where $\Gamma^{\mathrm{MH,sp,1}}$ is laid out in Eq. (5.83) and the spin irreducible vertex $\Gamma^{\mathrm{KH,sp,1}}$ is the same as Eq. (5.94).

5.2.8 *Second-level approximation*

The average of Σ^{L} (5.89) and Σ^{T} (5.97) gives the second-level approximation to the Kanamori-Hubbard model

$$\begin{aligned}&\Sigma^{\mathrm{TPSC},(1)}_{\epsilon,\zeta;\sigma}(1,2)\\ &=\sum_{\beta}U^{\sigma-\sigma}_{\epsilon,\beta}(1)n^{-\sigma}_{\beta}(1)\delta(1,2)\delta_{\epsilon,\zeta}+\frac{1}{2}\sum_{\beta\neq\zeta}\left(U^{\sigma}_{\epsilon,\beta}(1)-J^{\sigma}_{\epsilon,\beta}(1)\right)n^{\sigma}_{\beta}(1)\delta(1,2)\delta_{\epsilon,\zeta}\\ &-\frac{1}{2}\left(U^{\sigma}_{\epsilon,\zeta}(1)-J^{\sigma}_{\epsilon,\zeta}(1)\right)n^{\sigma}_{\epsilon,\zeta}(1)\delta(1,2)+J^{\sigma}_{\epsilon,\zeta}(1)\left(n^{-\sigma}_{\epsilon,\zeta}(1)+n^{-\sigma}_{\zeta,\epsilon}(1)\right)\delta(1,2)\\ &+\sum_{\alpha,\beta\neq\epsilon}\frac{\left(U^{\sigma}_{\epsilon,\beta}(1)-J^{\sigma}_{\epsilon,\beta}(1)\right)}{8}\mathcal{G}^{\sigma}_{\epsilon,\alpha}(1,2)\left[\Gamma^{\mathrm{ch}}_{\alpha,\zeta}(2)\chi^{\mathrm{ch}}_{\zeta,\beta}(2,1)-\Gamma^{\mathrm{KH,sp,0}}_{\alpha,\zeta}(2)\chi^{\mathrm{sp}}_{\zeta,\beta}(2,1)\right]\\ &+\sum_{\alpha,\beta}\frac{U^{\sigma-\sigma}_{\epsilon,\beta}(1)}{8}\mathcal{G}^{\sigma}_{\epsilon,\alpha}(1,2)\left[\Gamma^{\mathrm{ch}}_{\alpha,\zeta}(2)\chi^{\mathrm{ch}}_{\zeta,\beta}(2,1)+3\Gamma^{\mathrm{MH,sp,1}}_{\alpha,\zeta}(2)\chi^{\mathrm{sp}}_{\zeta,\beta}(2,1)\right]\\ &+\sum_{\alpha,\beta\neq\epsilon}\frac{J^{\sigma}_{\epsilon,\beta}(1)}{4}\mathcal{G}^{-\sigma}_{\epsilon,\alpha}(1,2)\Gamma^{\mathrm{KH,sp,1}}_{\alpha,\zeta}(2)\chi^{\mathrm{sp}}_{\zeta,\beta}(2,1).\end{aligned} \tag{5.98}$$

The Fourier transform of Eq. (5.98) is easy to carry out.

5.2.9 *DMFT+TPSC*

The combination of DMFT introduced in Section 3.2.1 and TPSC introduced in Section 5.2 aims to replace the local TPSC self-energy component with the DMFT one in a self-consistent manner in order to better capture the strong local fluctuations [122]. Methods that have combined DMFT and TPSC in a *single-shot* fashion – the local correlations are directly replaced with the DMFT ones without self-consistency – have been recently explored [89, 155]. In the Hubbard model, the TPSC self-energy (5.63) would embody self-consistently in the DMFT procedure the effects of the lattice environment onto spin and charge degrees of freedom. In this section, the algorithmic procedure that defines nonequilibrium self-consistent DMFT+TPSC is laid out. This scheme can be straightforwardly generalized to multi-orbital systems such as the multi-orbital Hubbard model (3.8) and the Kanamori-Hubbard model (3.7). The full scheme is summarized by the flow chart in Fig. 5.3.

ALGORITHM To start out the DMFT+TPSC procedure, one must initially guess a Weiss Green's function (3.12) that will enter the impurity solver described in Section 3.2.1.3. The impurity solver computes an impurity self-energy, denoted $\Sigma_{\text{imp}}[\mathcal{G}_0]$, that renormalizes the energy spectrum of the impurity interacting electrons embedded in the lattice environment. Then, the impurity double occupancy D^{imp}

$$D^{\text{imp}}(z) = \frac{-i}{2U(z)} \int_{\mathcal{C}} \mathrm{d}z' \; \mathrm{Tr} \left[\Sigma^{\text{imp}}_{\sigma}(z,z') \mathcal{G}^{\text{imp}}_{\sigma}(z',z) \right]^{<} + \frac{1}{4} \sum_{\sigma} n_{\sigma}(z) n_{-\sigma}(z), \quad (5.99)$$

is used instead of the one extracted from the ansatz (5.54) as is the case for TPSC and TPSC+GG. D^{imp} is employed to set both the spin and charge irreducible vertices according to Figs. 5.1 and 5.2, respectively, making use of the respective local sum-rules (5.68). This time, the susceptibilities defined through the Bethe-Salpeter equation (5.64) are slightly different from TPSC, in that the noninteracting two-particle Green's function χ^0 is defined as

$$\chi^0_{\mathbf{q}}(z,z') = -2i \int \frac{\mathrm{d}^D k}{(2\pi)^D} \; \mathcal{G}_{\mathbf{k}}(z,z') \mathcal{G}_{\mathbf{k}+\mathbf{q}}(z',z), \quad (5.100)$$

where the lattice Green's function $\mathcal{G}_{\mathbf{k}}$ is defined in Eq. (3.14) and contains the local impurity self-energy. Then, the nonlocal TPSC self-energy can be calculated using Eq. (5.63). The TPSC self-energy (5.63) is improved by subtracting out the local self-energy component of $\Sigma^{\text{TPSC},(1)}_{\mathbf{k}}$, defined as

$$\Sigma^{\text{TPSC},(1)}_{\text{loc},\sigma}(z,z') \equiv \frac{1}{N_k} \sum_{\mathbf{k}} \Sigma^{\text{TPSC},(1)}_{\mathbf{k},\sigma}(z,z'),$$

to replace it with the impurity self-energy $\Sigma^{\sigma}_{\text{imp}}$. The TPSC self-energy with improved local correlations then reads

$$\Sigma^{(1)}_{\mathbf{k},\sigma}(z,z') \equiv \Sigma^{\text{TPSC},(1)}_{\mathbf{k},\sigma}(z,z') - \Sigma^{\text{TPSC},(1)}_{\text{loc},\sigma}(z,z') + \Sigma^{\sigma}_{\text{imp}}(z,z'), \quad (5.101)$$

and the improved TPSC lattice Green's function $\mathcal{G}^{\text{lat},(1)}_{\mathbf{k}}$ dressed with $\Sigma^{(1)}_{\mathbf{k}}$ (5.101) is defined as

$$\begin{aligned} &\left[i\partial_z + \mu - \epsilon(\mathbf{k}) - \Sigma^{\delta,\sigma}_{\text{imp}}(z) \right] \mathcal{G}^{\text{lat},(1)}_{\mathbf{k},\sigma}(z,z') \\ &\qquad - \int_{\mathcal{C}} \mathrm{d}z'' \; \Sigma^{(1)}_{\mathbf{k},\sigma}(z,z'') \mathcal{G}^{\text{lat},(1)}_{\mathbf{k},\sigma}(z'',z') = \delta^{\mathcal{C}}(z,z'). \end{aligned} \quad (5.102)$$

Once the improved TPSC lattice Green's function (5.102) is known, the lattice average

$$\mathcal{G}^{\sigma}_{\text{loc}}(z,z') \equiv \frac{1}{N_k} \sum_{\mathbf{k}} \mathcal{G}^{\text{lat},(1)}_{\mathbf{k},\sigma}(z,z') \quad (5.103)$$

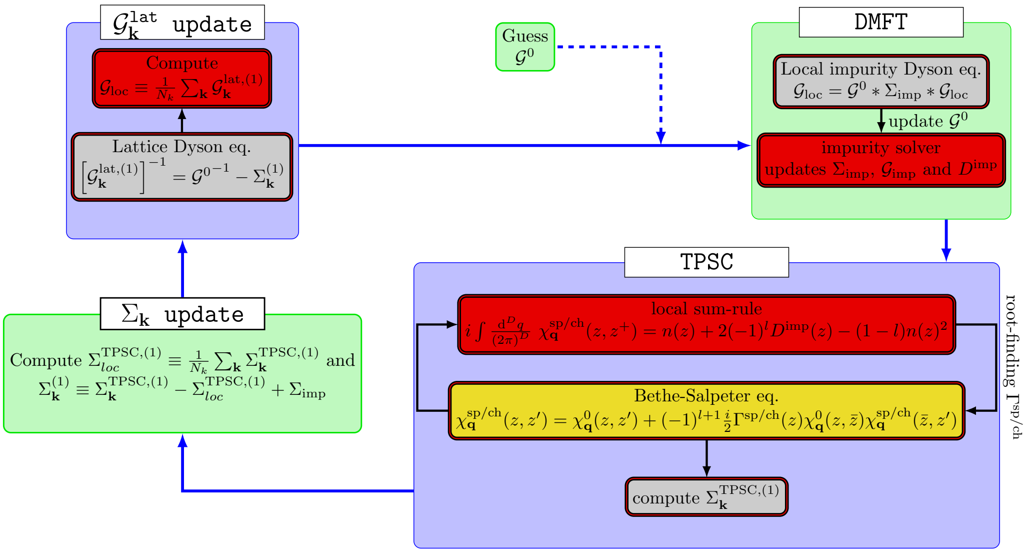
$\mathcal{G}^{\text{lat}}_{\mathbf{k}}$ update
Compute $\mathcal{G}_{\text{loc}} = \frac{1}{N_k}\sum_{\mathbf{k}} \mathcal{G}^{\text{lat},(1)}_{\mathbf{k}}$
Lattice Dyson eq. $\left[\mathcal{G}^{\text{lat},(1)}_{\mathbf{k}}\right]^{-1} = \mathcal{G}^{0^{-1}} - \Sigma^{(1)}_{\mathbf{k}}$
Guess $\mathcal{G}^0$
DMFT
Local impurity Dyson eq. $\mathcal{G}_{\text{loc}} = \mathcal{G}^0 * \Sigma_{\text{imp}} * \mathcal{G}_{\text{loc}}$
update $\mathcal{G}^0$
impurity solver updates Σ_{imp}, $\mathcal{G}_{\text{imp}}$ and D^{imp}
$\Sigma_{\mathbf{k}}$ update
Compute $\Sigma^{\text{TPSC},(1)}_{loc} \equiv \frac{1}{N_k}\sum_{\mathbf{k}} \Sigma^{\text{TPSC},(1)}_{\mathbf{k}}$ and $\Sigma^{(1)}_{\mathbf{k}} \equiv \Sigma^{\text{TPSC},(1)}_{\mathbf{k}} - \Sigma^{\text{TPSC},(1)}_{loc} + \Sigma_{\text{imp}}$
TPSC
local sum-rule $i\int \frac{d^D q}{(2\pi)^D}\, \chi^{\text{sp/ch}}_{\mathbf{q}}(z,z^+) = n(z) + 2(-1)^l D^{\text{imp}}(z) - (1-l)n(z)^2$
Bethe-Salpeter eq. $\chi^{\text{sp/ch}}_{\mathbf{q}}(z,z') = \chi^0_{\mathbf{q}}(z,z') + (-1)^{l+1}\frac{i}{2}\Gamma^{\text{sp/ch}}(z)\chi^0_{\mathbf{q}}(z,\bar{z})\chi^{\text{sp/ch}}_{\mathbf{q}}(\bar{z},z')$
root-finding $\Gamma^{\text{sp/ch}}$
compute $\Sigma^{\text{TPSC},(1)}_{\mathbf{k}}$

Figure 5.3: Flow chart describing the self-consistent DMFT+TPSC procedure. The yellow slot is replaced by the equation (5.69) in the implementation.

is calculated. Finally, by solving the Volterra equation (3.17) with $\mathcal{G}_{\text{loc}}$ (5.103) and Σ_{imp} at hand, the Weiss Green's function can be updated and reinserted into the impurity solver. The whole process is therafter repeated until the scheme converges.

Apart from looking at the energy conservation across the time propagation of the DMFT+TPSC solution, the comparison between the DMFT double occupancy D^{imp} (5.99) and that extracted from the lattice quantities

$$D^{\text{TPSC},(1)}(z) = \frac{-i}{2U(z)}\int_{\mathcal{C}} \mathrm{d}z'\ \mathrm{Tr}\left[\Sigma^{(1)}_{\mathbf{k},\sigma}(z,z')\mathcal{G}^{\text{lat},(1)}_{\mathbf{k},\sigma}(z',z)\right]^{<} + \frac{1}{4}\sum_{\sigma} n_{\sigma}(z)n_{-\sigma}(z), \tag{5.104}$$

with $\Sigma^{(1)}_{\mathbf{k}}$ defined in Eq. (5.101) and $\mathcal{G}^{\text{lat},(1)}_{\mathbf{k}}$ defined in Eq. (5.102), reveals to be a good internal accuracy check for the method. Thus, if the difference between $D^{\text{imp}}(z)$ and $D^{\text{TPSC},(1)}(z)$ is relatively small, the method should be reliable. However, this small difference leads to some ambiguity in the determination of the total energy to compute the thermalized values, as discussed in Section 7.2.2, since the lattice environment would have a different energy from the impurity. To cure for this discrepancy, a renormalization parameter the likes of α in Eq. (5.71) can be introduced in Eq. (5.104) and tweaked so as to make Eqs. (5.104) and (5.99) equal; this variation is coined DMFT+TPSCα and is detailed further down. Note that the formula (5.104) can be derived by Fourier transforming Eq. (5.47) and its present form is only valid in the single-orbital case, *i.e.* when $j \to i$ and $\zeta \to \epsilon$ in Eq. (5.47). Hence, the fact that the impurity electrons – associated to the local degrees of freedom – and the lattice electrons can have different temperatures in DMFT+TPSC means that different temperature reservoirs and relaxation timescales are associated to the electrons living in those disjoint of the Fock subspaces. This temperature discrepancy would be a consequence of the lack of internal consistency between the DMFT and TPSC levels.

As shown in Section 6.2.2 (Fig. 6.36), the comparison between the DMFT double occupancy D^{imp} (5.99) and the one extracted from the lattice quantities (5.104) – using $\Sigma^{(1)}_{\mathbf{k}}$ defined in Eq. (5.101) and $\mathcal{G}^{\mathrm{lat},(1)}_{\mathbf{k}}$ defined in Eq. (5.102) – turns out to be a good internal accuracy check for the method. If the difference between $D^{\mathrm{imp}}(z)$ and $D^{\mathrm{TPSC},(1)}(z)$ becomes too large, the results become unreliable.

Similarly to TPSC and TPSC+GG employing the sum-rule (5.71) to improve the consistency between the TPSC and DMFT approximations, DMFT+TPSC can be endowed with "D consistency" by enforcing that the impurity double occupancy D^{imp} (5.99) be equal to that computed from the TPSC lattice-defined quantities (5.104):

$$\mathrm{Tr}\left[\Sigma^{(1)}_{\mathbf{k},\sigma}[\alpha](z,\bar{z})\mathcal{G}^{\mathrm{lat},(1)}_{\mathbf{k},\sigma}(\bar{z},z)\right]^{<} = \mathrm{Tr}\left[\Sigma^{\mathrm{imp}}_{\sigma}(z,\bar{z})\mathcal{G}^{\mathrm{imp}}_{\sigma}(\bar{z},z)\right]^{<}, \tag{5.105}$$

with

$$\Sigma^{(1)}_{\mathbf{k},\sigma}[\alpha](z,z') \equiv \Sigma^{\mathrm{TPSC},(1)}_{\mathbf{k},\sigma}[\alpha](z,z') - \Sigma^{\mathrm{TPSC},(1)}_{\mathrm{loc},\sigma}[\alpha](z,z') + \Sigma^{\mathrm{imp}}_{\sigma}(z,z'), \tag{5.106}$$

or, alternatively,

$$\Sigma^{(1)}_{\mathbf{k},\sigma}[\alpha](z,z') \equiv \Sigma^{\mathrm{TPSC},(1)}_{\mathbf{k},\sigma}(z,z') - \alpha(z)\Sigma^{\mathrm{TPSC},(1)}_{\mathrm{loc},\sigma}(z,z') + \Sigma^{\mathrm{imp}}_{\sigma}(z,z'), \tag{5.107}$$

where α, in the case of Eq. (5.106), serves a similar purpose as in Eq. (5.71), in that it renormalizes further the irreducible vertices in Eq. (5.70) so as to fulfil Eq. (5.105). In Eq. (5.107), the parameter α can be seen as a time-dependent correction to the hybridization function appearing in the DMFT self-consistency (Eq. (3.12)). These *modified* DMFT+TPSC methods are coined DMFT+TPSCα. It turns out however that none of the lattice self-energies (5.106) and (5.107) lead to stable nonequilibrium solutions. Thus, DMFT+TPSCα will only be shown in equilibrium set-ups and using Eq. (5.106) in the self-consistency procedure.

5.2.10 *Summary of the different schemes*

In order to clarify the differences between the methods covered in this thesis, Table 5.1 sets them out so as to summarize the salient characteristics describing each of them. Moreover, a graph shows the connection between the first- and second-level approximations in Fig. 5.4.

A similar summary of the methods can be found in Ref. [122].

The first column of Table 5.1 titled "Self-consistent" specifies which of the methods are self-consistent, *i.e.* iterates over the quantities defined in the method until the solution has converged. Hence, the methods that do not check out this characteristic compute the self-energy and related quantities in a "one-shot" fashion. The next column titled "D consistency" identifies which methods make use of a parameter α to even out the local and lattice double occupancies. For example, in the case of TPSC and TPSC+GG, the sum-rule (5.71) ensures that the double occupancy obtained at first-level approximation from Eq. (5.54) be equal (consistent) to that calculated from the second-level quantities $\Sigma^{(1)}_{\mathbf{k}}$ (5.70) and $\mathcal{G}^{(1)}$ (5.66). Indeed, in a fully conserving scheme, the double occupancy appearing in Eq. (5.54), which is ultimately extracted from the first-level approximation self-energy $\Sigma^{(0)}_{\mathbf{k}}$ (5.43), should be equal to that obtained

	Self-consistent	D consistency	$\Sigma^{(1)}_{\mathbf{k}}$
OG TPSC	X	X	Eq. (5.63)
TPSC	X	✓	Eqs. (5.70) & (5.71)
TPSC+GG	✓	✓	Eqs. (5.70) & (5.71)
DMFT+TPSC	✓	X	Eqs. (5.101)
DMFT+TPSCα	✓	✓	Eqs. (5.106)/(5.107) & (5.105)

Table 5.1: Main characteristics of the methods at the second-level approximation. Checkmarks (✓) mean that a method is endowed with the characteristic, while the x-marks (X) mean the opposite.

from the second-level single-particle quantities $\Sigma^{(1)}_{\mathbf{k}}$ and $\mathcal{G}^{(1)}$; this is what the sum-rule (5.71) ensures. In the case of DMFT+TPSCα, which is a "D-consistent" method, the sum-rule Eq. (5.105) relates both Eqs. (5.99) and (5.104) by tuning α. Finally, the last column of Table 5.1 refers to the second-level self-energies featuring in each method along with the extra sum-rule they need to satisfy if the method is "D-consistent".

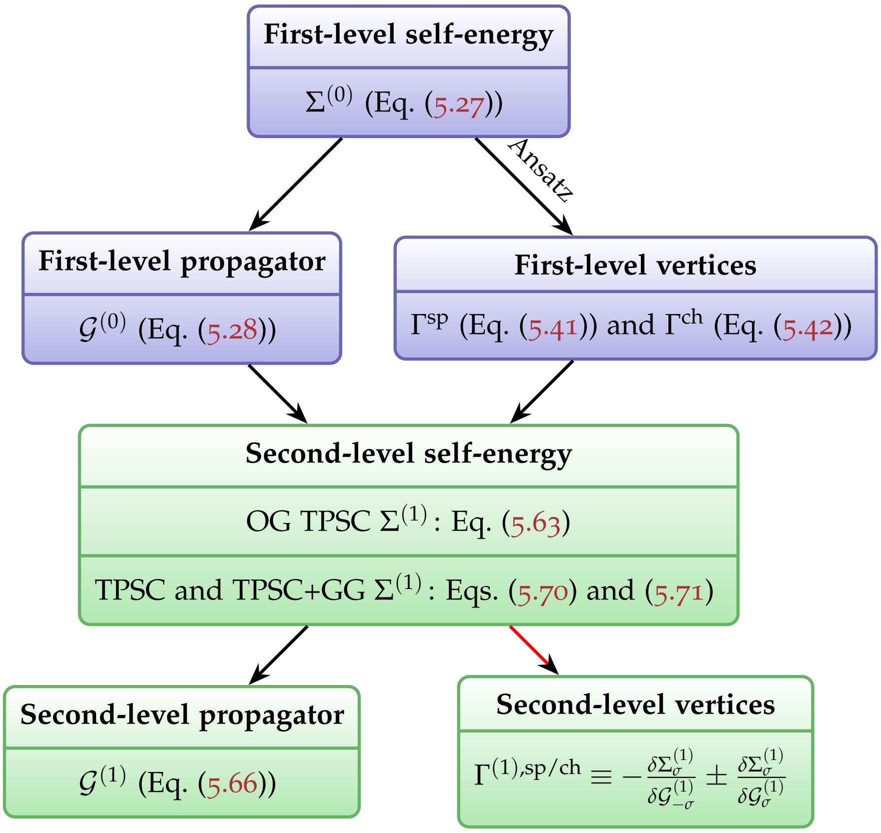
First-level self-energy
$\Sigma^{(0)}$ (Eq. (5.27))
Ansatz
First-level propagator
$\mathcal{G}^{(0)}$ (Eq. (5.28))
First-level vertices
Γ^{sp} (Eq. (5.41)) and Γ^{ch} (Eq. (5.42))
Second-level self-energy
OG TPSC $\Sigma^{(1)}$: Eq. (5.63)
TPSC and TPSC+GG $\Sigma^{(1)}$: Eqs. (5.70) and (5.71)
Second-level propagator
$\mathcal{G}^{(1)}$ (Eq. (5.66))
Second-level vertices
$\Gamma^{(1),\text{sp/ch}} \equiv -\frac{\delta\Sigma^{(1)}_{\sigma}}{\delta\mathcal{G}^{(1)}_{-\sigma}} \pm \frac{\delta\Sigma^{(1)}_{\sigma}}{\delta\mathcal{G}^{(1)}_{\sigma}}$

Figure 5.4: Flow graph showing the connections between the two first levels of TPSC, namely the first- (blue boxes) and second-level (green boxes) approximations. The red line shows that second-level irreducible vertices could in theory be worked out from the second-level self-energy $\Sigma^{(1)}$. The α renormalization of the vertices introduced via Eq. (5.71) aims to *update* the irreducible vertices such as to make the two-level approximations consistent.

Part IV

RESULTS

La beauté est la forme de la finalité d'un objet, en tant qu'elle est perçue dans cet objet sans représentation d'une fin.

— Emmanuel Kant [64]

In this part of the thesis, the main results carried out using the numerical methods developed, namely post-processing RPA-DMFT, and TPSC and its variants, are presented and discussed. The calculations shown in this thesis were performed under both equilibrium and nonequilibrium conditions. The systems are driven out of equilibrium by either varying the local Coulomb interaction or changing the hopping between lattice sites.

6

EQUILIBRIUM RESULTS

In this section, the equilibrium results of the post-processing RPA-type DMFT method to treat two-particle vertex corrections, introduced in Chapter 4, will be presented and discussed in Section 6.1. The Section 6.1 will set the stage to carry on with the nonequilibrium results, presented further down in Section 7.1. Then, the equilibrium results of TPSC and its variants will be exposed in Section 6.2. The Section 6.2 breaks down into a section dedicated to TPSC and TPSC+GG introduced in Section 5.2, namely Section 6.2.1, and a section dedicated to the DMFT+TPSC schemes introduced in Section 5.2.9, namely Section 6.2.2. The nonequilibrium results of TPSC and related methods are shown and discussed in Section 7.2.

The totality of the results presented below cover the Hubbard model described by Eq. (3.9). Even though it has been shown that TPSC can be generalized to treat multi-orbital systems in Section 5.2 and Ref. [156], the other models, namely the Kanamori-Hubbard and multi-orbital Hubbard models, are currently under implementation on the KB contour and therefore no results are yet available. Since all the formalism leading up to TPSC has been set out in the nonequilibrium Keldysh-Schwinger formalism developed in Chapter 2, the equations derived have to be narrowed down to the vertical imaginary-time axis $\mathcal{C}_3$ (see Fig. 2.1) in equilibrium. This can be easily carried out performing the transformation $z \to t_0 - i\tau$, τ being the imaginary time (see Table 2.1).

6.1 POST-PROCESSING DMFT

The RPA-type post-processing DMFT method discussed and introduced in Chapter 4 is tried out on the weakly interacting half-filled single-band Hubbard model (3.9) in dimensions $D = 1$ and $D = 2$ using the DMFT Green's functions obtained with second-order IPT (Section 3.2.1.3) in order to capture the bound particle-hole excitations, coined π-ton, in both the longitudinal optical conductivity and the magnetic susceptibility. Note that for the equilibrium calculations, bare IPT was employed, unless mentioned otherwise (see discussion underneath Eq. (3.26)). Since DMFT produces results representative of high-dimensional systems, irrespective of the dimension D, the choices of $D = 1$ and $D = 2$ are meant to reduce greatly the computational cost of the momentum summations as well as the memory load. Hence, as will be seen, qualitatively similar results have been obtained for $D = 2$ and $D = 1$. Moreover, due to the Mermin-Wagner theorem, the existence of AFM long-range order at Néel temperature $T_N > 0$ in the DMFT solution for dimensions $D < 3$ is representative of $D \geq 3$ and one should thus interpret the diagrammatic results that will be presented as characteristic properties of high-dimensional Hubbard models close to the AFM phase boundary.

The π-ton-type vertex corrections in the strongly correlated (Mott) regime have also been computed using Noncrossing Approximation (NCA) as impurity solver [21, 37]. NCA is a reliable impurity solver only when the on-site interaction U is much larger than the bandwidth W of the lattice model. Although, for all the interactions and dimensions considered, the RPA-type vertex corrections drawn from NCA are not physically meaningful, since they yield large values at high temperatures, far away from the AFM phase boundary. Besides, it is well established that the diagrammatic extensions of DMFT [104], even though more accurate, suffer convergence problems at intermediate to strong coupling, related to the multivaluedness of the Luttinger-Ward functional, or the occurrence of divergences in the two-particle irreducible vertex functions [29, 55]. Then, the fact that NCA is tailored for strongly interacting systems makes it dubious to use along with the post-processing RPA-type treatment. The focus is therefore restricted to the weakly-correlated region of the phase diagram, where the poles in the π-ton expressions can be shifted to the actual AFM boundary via modest corrections of the bare interaction.

As mentioned, the RPA-type post-processing method has been fed with DMFT lattice Green's functions calculated using both the NCA and IPT impurity solvers. Because IPT and NCA are self-consistent methods that capture local correlations, the bare susceptibility results should fulfil conservation laws discussed in details in Appendix E. All the bare longitudinal optical conductivities shown in this section obey the sum rule Eq. (E.7) to a very good accuracy (3^{rd} digit).

6.1.1 *Phase diagram and renormalized couplings*

To map out the magnetic phase diagram of the Hubbard model at half-filling, DMFT needs to allow for spin rotational symmetry to break as explained in Section 3.2.1.2. This is done by using a bipartite lattice effectively introducing two quantum impurities per unit-cell with a potentially spin-specific chemical potential. For that matter, for the DMFT solutions to converge in the symmetry-broken state when using second-order IPT, one has to minimally consider the second-order Hartree self-energy contribution (Fig. 3.1). To *spontaneously* break the spin symmetry, the staggered magnetization h appearing in Eq. (3.18) is turned on in the first few DMFT iterations of the equilibrium simulation, then turned off for the rest of the simulation. The DMFT solution will thereafter stabilize in the most energetically favorable magnetic state. To identify the parameter regions with strong AFM fluctuations expected to enhance the π-ton-type vertex corrections, one first seeks to map the AFM phase boundary at half-filling as a function of interaction U and temperature T. One of the observables indicating that one is located in the AFM phase is a nonzero magnetization denoting the difference in spin-density per site $\langle \hat{n}_{\sigma} - \hat{n}_{-\sigma} \rangle$. The magnetizations of the 1D (Fig. 6.1) and 2D (Fig. 6.2) Hubbard model are illustrated for a wide array of interactions.

The impurity solver used in the DMFT procedure is second-order IPT Section 3.2.1.3 so the results should be reliable mostly for $U \lesssim W$. In the 1D case, the bandwidth $W = 4t_{\text{hop}}$ and consequently a lot of interaction values displayed

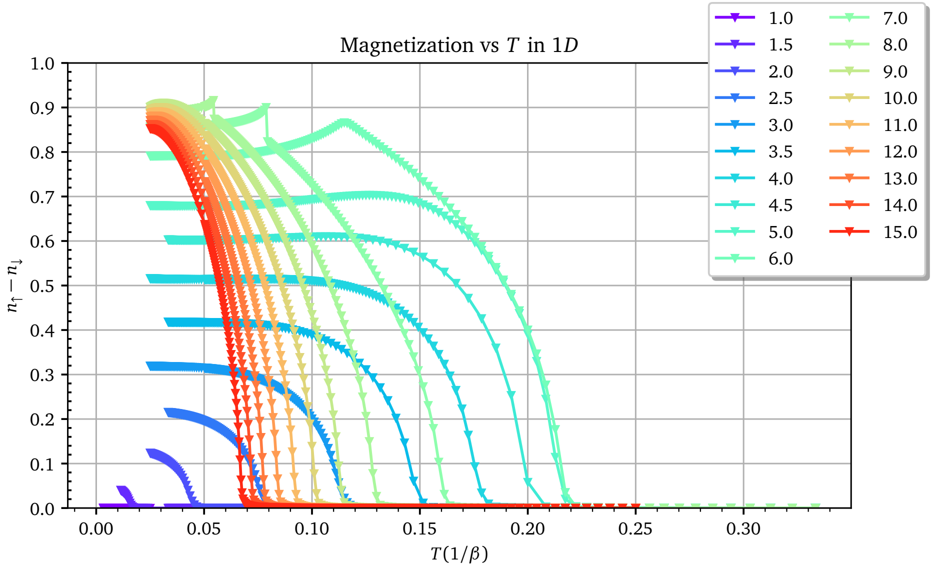

Figure 6.1: Magnetization for various interaction parameters for the half-filled nearest-neighbor Hubbard model in 1D.

in Fig. 6.1 exceed W. The magnetization values are particularly dubious when they feature discontinuous jumps or when they curve back down at low temperature – the magnetization should remain stable at a fixed value after some temperature. Looking back at Fig. 6.1, the magnetizations above $U \simeq 5$ start showing spurious humps and discontinuities whereas in 2D it starts around $U \simeq 8$ according to Fig. 6.2. The phase boundary is set where, in temperature, the magnetization becomes nonzero, *i.e.* larger than 2.5×10^{-2}. Therefore, from Figs. 6.1 and 6.2, one can already observe that the Néel temperature T_N increases upon increasing U up to $U = 5 - 6$ in 1D or $U = 7 - 8$ in 2D, where it shows the highest T_N, and then falls back down at a slower rate. The magnetization value it stabilizes to at lower temperature also increases in interaction until it starts saturating around $U = 10$ in both 1D and 2D. Furthermore, the magnetization amplitude at lower interaction values in 1D are much lower than those in 2D for the same interactions. The resulting magnetic phase boundaries are traced out in red in Fig. 6.3 for the 1D case and in Fig. 6.4 for the 2D case.

To ensure that the computed lattice susceptibilities (4.15) and (4.18) diverge at the DMFT phase boundary, one would have to calculate a local two-particle vertex from the impurity model and use it as a local approximation for the vertex of the lattice model in the solution of a Bethe-Salpeter equation like Eq. (2.46) [57, 59]. Making use of the DMFT Green's functions in RPA-type ladder vertices like Fig. 4.2 does not guarantee that the corresponding susceptibility will diverge, or become large, in the vicinity of the magnetic phase boundary. To find out the interaction regime wherein the RPA-π-ton approach produces physically meaningful results, the (U,T) parameters' region in which the denominator of the single-ladder diagram (4.22) at $\tilde{\mathbf{k}} - \bar{\mathbf{k}} = \pi$ – or $\tilde{\mathbf{k}} - \bar{\mathbf{k}} = (\pi, \pi)$ in 2D – and $\omega_{n=0}$ vanishes (black line) is plotted and compared to the DMFT magnetic phase boundary (red line) in Fig. 6.3 for 1D and Fig. 6.4 for 2D. At small U, the black line remains close to the AFM phase boundary both in 1D and 2D and it essentially follows the Hartree phase boundary [138]. Although,

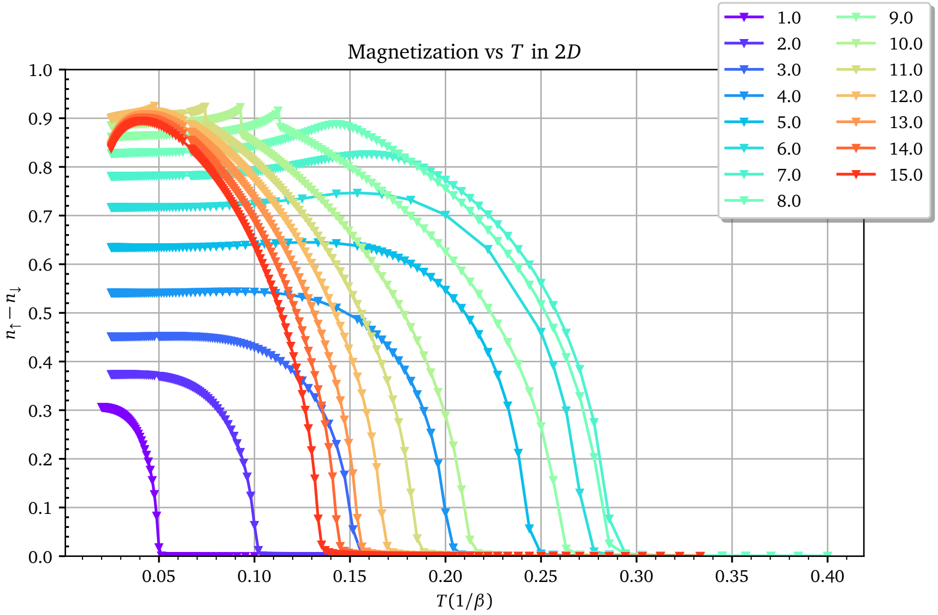

Figure 6.2: Magnetization for various interaction parameters for the half-filled nearest-neighbor Hubbard model in 2D.

at higher interaction values, the black and red lines drift away from each other. In 1D, the single-ladder vertex divergence at $U \approx 4$ reaches a maximum of $T \approx 0.35$, which is almost 50% higher than T_N, and then drops to small values faster than the AFM boundary. In the case of 2D, the single-ladder vertex features a divergence about 30% larger in temperature that the DMFT T_N at $U \approx 5$, before dropping back down in temperature. The drops of the black lines seen in Figs. 6.3 and 6.4 qualitatively follow the shape of the phase boundary and it is not found in DMFT+NCA, even though it should provide a more accurate description of the single-particle quantities on the "Mott insulating" side of the AFM dome. In DMFT+NCA, the temperature associated with the dominant ladder contribution increases with increasing U and it does not qualitatively follow the DMFT phase boundary (not shown). Hence, the RPA-π-ton corrections to DMFT susceptibilities will only be calculated in the weak-coupling regime ($U \lesssim 3$) employing DMFT+IPT Green's functions.

Because the dominant vertex corrections from the single-ladder (4.22), double-ladder (4.25) and AL-type (4.28) diagrams set in at temperatures which may be quite far from the Néel temperature calculated within DMFT, renormalized interactions U^{ren} are introduced. These renormalized couplings depend on U and displace the pole in the single-ladder expression to match T_N at the given U. With increasing U, the poles of the ladder-type vertex corrections move away from the DMFT phase boundary by moving up in temperature on the weak-coupling side. It is important to mention that the DMFT Green's functions entering the susceptibility calculations are computed with the unrenormalized U; only the U's appearing in the denominator and numerator of the vertex expressions (4.22), (4.25) and (4.28) are renormalized. In 1D, at $U = 3$, one finds $U^{\mathrm{ren}} = U/1.4$, while at $U = 2$, one finds $U^{\mathrm{ren}} = U/1.33$. Still in 1D, at $U = 1$, U^{ren} is close enough to T_N to not need to consider a renormalized coupling. In 2D, to show that one finds signatures of the vertex corrections in

The same renormalized interactions will be used in the nonequilibrium calculations (Section 7.1).

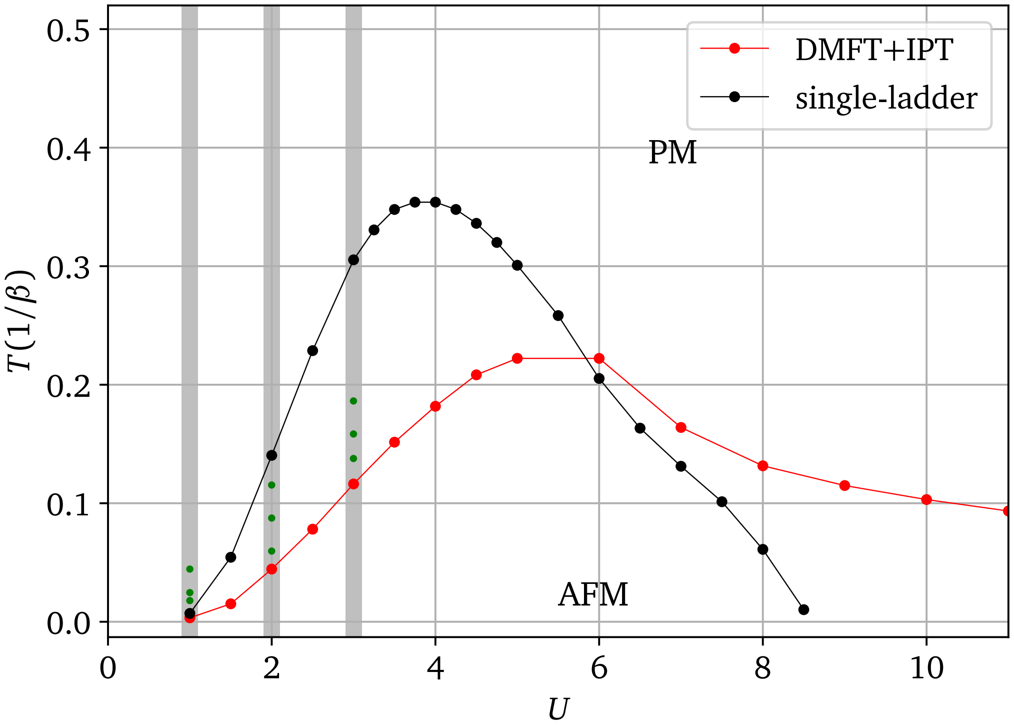

Figure 6.3: AFM phase boundary (red line) obtained with the IPT solver in the space of U and T at half-filling. The black line indicates the temperatures corresponding to the largest single-ladder vertex corrections. The green dots denote the temperatures at which the susceptibilities will be computed.

the spectra of the susceptibilities that are similar to 1D, the single-ladder vertex corrections are shown only at $U = 2$ and the renormalization factor used is $U^{\text{ren}} = U/1.05$. The fact that one needs interaction renormalization U^{ren} in the vertex expressions of Section 4.1 indicates that the contribution from other diagram topologies becomes significant and one can't simply brush them aside by considering only vertical ladder-type vertex corrections (Eqs. (4.22) and (4.25)) – they do not account for all the relevant physics.[1] These renormalizations of the bare interaction U probably stem from the fact that the π-ton diagrams discussed in Ref. [66, 120] are not limited to RPA-type ladders, but involve contributions to the vertex coming from various crossing-symmetric channels. This procedure so far described where U^{ren} renormalizes the vertex to match the DMFT phase boundary is similar to the Kanamori theory for itinerant ferromagnetism in which a renormalized interaction is used in the mean field Stoner condition [63].

In dimensions $D \leq 2$ at finite temperatures, no second-order phase transitions can occur. The fact that an AFM phase boundary can be traced is an artefact of higher dimensions where DMFT performs particularly well.

6.1.2 *Optical conductivity and* $\mathbf{q} = \mathbf{0}$ *spin susceptibility*

For the 1D results, like indicated by the grey vertical lines of Fig. 6.3, the focus will be put on $U = 1, 2$ and 3 where IPT is reliable and the post-processing DMFT method produces meaningful results. The two-particle vertex corrections

---

[1] In the case of the double-ladder and AL corrections, even though the largest contribution may be shifted, the same U^{ren} as that calculated for the single-ladder corrections is used. This allows one to make meaningful comparison.

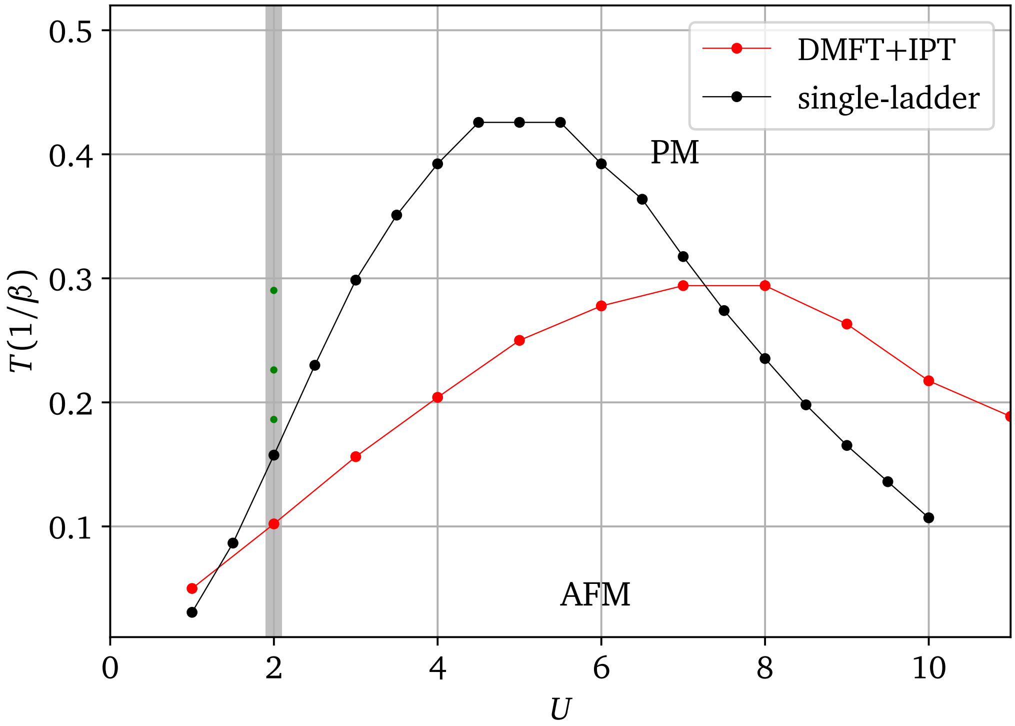

Figure 6.4: AFM phase boundary (red line) obtained with the IPT solver in the space of U and T at half-filling. The black line indicates the temperatures corresponding to the largest single-ladder vertex corrections. Like in 1D, the green dots denote the temperatures at which the susceptibilities will be computed.

to the optical conductivity and magnetic susceptibility are computed for three temperatures approaching the phase boundary (see green dots in Fig. 6.3). The Green's functions entering the bubble and π-ton diagrams are DMFT Green's functions for the corresponding U, while the interactions appearing in the ladder vertex corrections are renormalized as discussed in Section 6.1.1. The real-frequency spectra of the susceptibilities below are obtained using the Maximum Entropy method [25]. However, the positivity of the spectral weight is not a priori guaranteed. Strong non-causal features should be detectable by Padé analytical continuation [143] and they would already be signalled by a non-monotonic ω_n-dependence of the data [96]. Since neither are observed for $U \leq 3$, it is valid to use maximum entropy analytical continuation [25], which enforces the positivity of the spectra.

To start with, the optical conductivity $\langle j_x j_x \rangle$ is shown in Fig 6.5 for $U = 1$ and $T = 0.04, 0.02, 0.014$, $U = 2$ and $T = 0.111, 0.083, 0.056$, and $U = 3$ and $T = 0.182, 0.154, 0.133$, while the spin-spin response $\langle S_z S_z \rangle$ spectra are shown in Fig. 6.6 for the same parameter sets. The layout of both Figs. 6.5 and 6.6 are the same: each column shows for the indicated value of U starting from the top panel and going down: i) the bare response (4.16), ii) the single-ladder (4.22) vertex corrections in addition to the bare response, iii) the single-ladder and double-ladder (4.25) vertex corrections in addition to the bare response, and iv) the single-ladder and AL-type (4.28) vertex corrections plus the bare response.

In the top panels, at small energies ω, the bubble contributions to the susceptibilities exhibit a peak which is the so-called Drude peak, as well as a weak

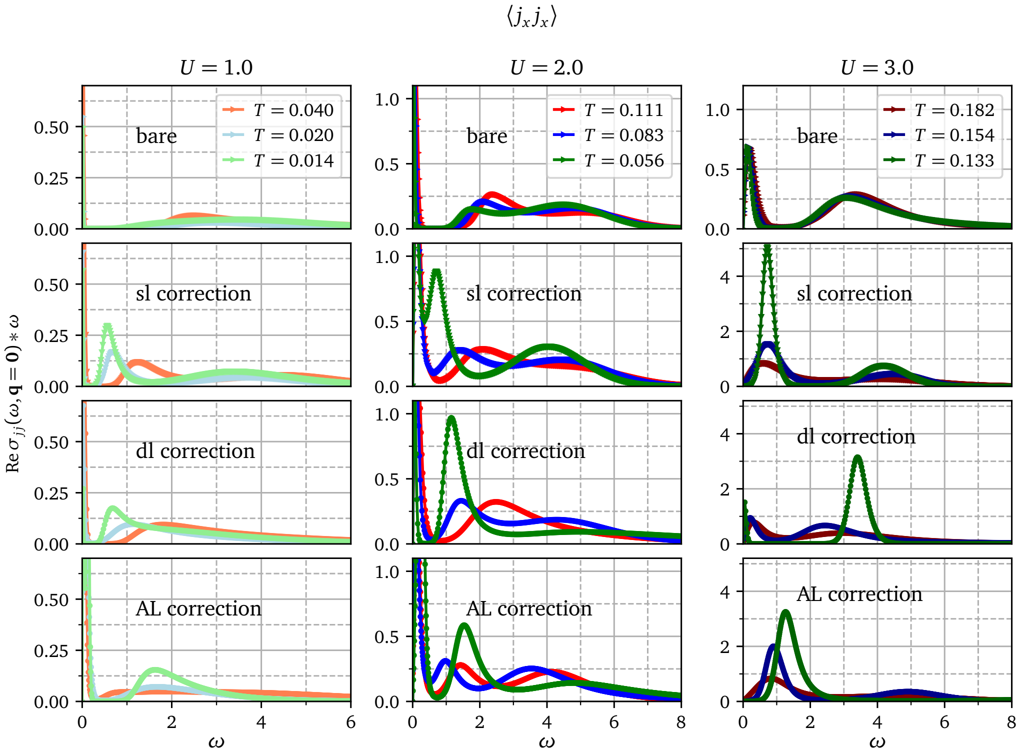

Figure 6.5: 1D longitudinal optical conductivity for $U = 1$ (first column), $U = 2$ (second column) and $U = 3$ (third column) obtained using DMFT+IPT and (for the ladder corrections) appropriately renormalized interactions. First row: bare response. Second row: bare response plus single-ladder vertex corrections. Third row: bare response plus single-ladder and double-ladder vertex corrections. Fourth row: bare response plus single-ladder and AL vertex corrections. The temperatures considered for the different interactions are shown in the legends.

hump near $\omega \approx 4$, which originates from the peaks located at the edges of the 1D density of states. As U gets larger, the electron scattering rate increases, and the Drude peak widens. For $U = 2$ and 3, there is also spectral weight around $\omega \approx U$, coming from Hubbard satellites in the density of states, and this feature becomes more prominent with the increase in U. As the temperature is lowered, the Drude peak of the optical conductivity becomes very narrow and sharp. As pointed out in Ref. [120], in a Fermi liquid, the Drude weight $\sigma_{\mathrm{Drude}}(\omega) \propto \gamma/[\pi(\gamma^2 + \omega^2)]$ with $\gamma \sim T^2$ the scattering rate. Hence, at $U = 1$ and low T, there is an almost δ-function-like peak in the conductivity at $\omega = 0$. To prevent that the Drude peak outweighs the structures in the susceptibility spectra at higher energies that are worth highlighting, the optical conductivity is multiplied by the frequency $\mathrm{Re}\sigma_{jj}(q = 0, \omega) * \omega = \mathrm{Im}\chi_{jj}(q = 0, \omega)$. In the case of the spin susceptibility, $\mathrm{Im}\chi_{S_z S_z}(q = 0, \omega)$ is plotted in Fig. 6.6.

Then, in the second row of panel from top, the effects of the single-ladder vertex corrections on the optical conductivity are illustrated in Fig. 6.5. From these vertex corrections arises a peak at $\omega \approx 0.6$, which grows as T_N is approached. In terms of energy, this peak associated with the π-ton vertex corrections lies in between the Drude peak, secluded at $\omega \approx 0$, and the spectral features at larger energies related to Hubbard sub-bands and the sharp density of states at

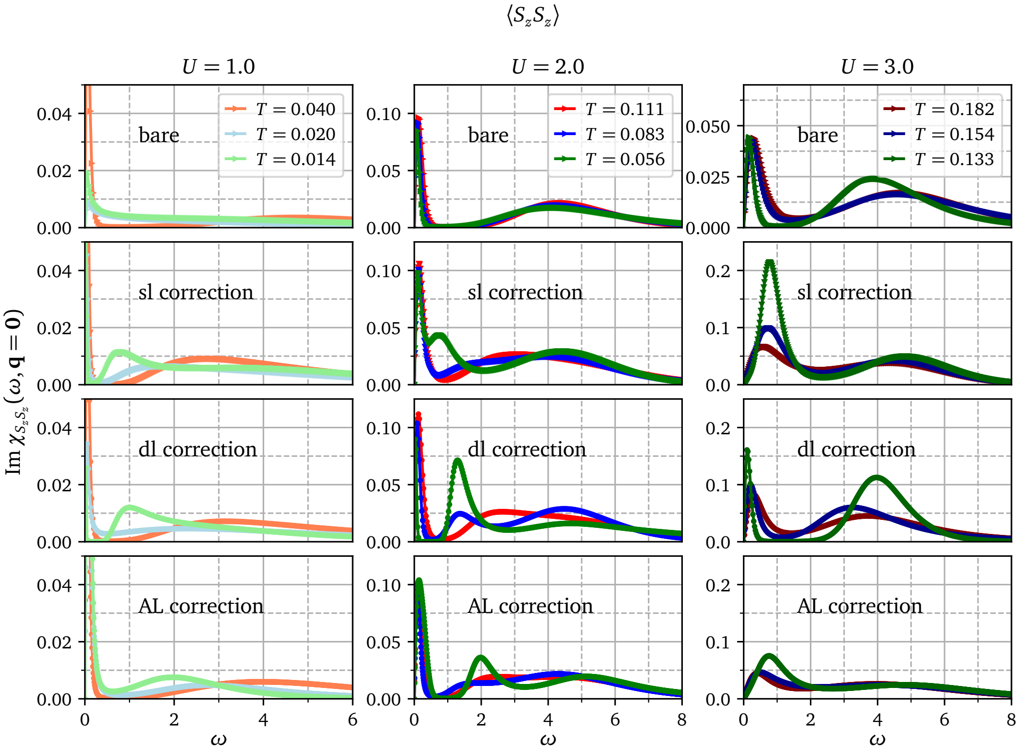

Figure 6.6: 1D magnetic susceptibility for $U = 1$ (first column), $U = 2$ (second column) and $U = 3$ (third column) obtained using DMFT+IPT and (for the ladder corrections) appropriately renormalized interactions. First row: bare response. Second row: bare response plus single-ladder vertex corrections. Third row: bare response plus single-ladder and double-ladder vertex corrections. Fourth row: bare response plus single-ladder and AL vertex corrections. The temperatures considered for the different interactions are shown in the legends.

the edges of the bandwidth. For that reason, the π-ton appears as an "in-gap" peak in the optical conductivity. For $U \lesssim 2$, the π-ton broadens the Drude peak, while at $U = 3$, due to strong cancellations between the bare bubble and π-ton vertex corrections, it suppresses the Drude peak. At higher temperatures, the π-ton contribution shifts to higher energies until it merges with the high-energy spectral weight of the bare bubble. To sum up, the single-ladder vertex corrections lead to a broadening of the Drude peak and a red-shift of the edge of the high-energy spectral weight. These results coming from the RPA-π-ton post-processing procedure are qualitatively consistent with the results published in Refs. [66, 150]. In Refs. [66, 150], similar broadenings of the Drude peak, in-gap peaks, and shifts of the gap edge were reported for a set of different models related to the Hubbard model.

Moving down to the third row of Fig. 6.5, from top, the double-ladder vertex corrections are added to the optical conductivity illustrated on the second row. Including the double-ladder diagrams in the vertex corrections broadens the peak associated with the in-gap state (π-ton) and suppresses the hump at $\omega \simeq 4$ associated with the 1D density of states, especially for $U = 1$ and $U = 2$. For the same interaction values, the π-ton peak is also slightly shifted towards higher energy. While the peak is broadened for $U = 1$, it is not much affected in the case of $U = 2$. Overall, the addition of a second vertical ladder has little qualitative effect on the π-ton for $U \leq 2$. A complete different story applies for $U = 3$ when the double-ladder vertex corrections are added, since they induce significant changes in the spectra. For instance, the in-gap π-ton peak vanishes, either absorbed in the hump at $\omega \simeq 4$ or *transformed* into the Drude peak that reappears. These striking changes when passing from $U = 2$ to $U = 3$ signal a breakdown of the RPA-ladder post-processing approach. This breakdown would be due to an increasing importance of other types of diagrams neglected hitherto, and the need for separate U^{ren} for the different types of corrections considered.

Finally, the last row of Fig. 6.5 illustrates the effect of the AL vertex corrections on the optical conductivity. This class of diagrams corresponds to the double-ladder diagrams rotated by $\pi/2$. These diagrams are clearly more significant than the double-ladder corrections. Nonetheless, a spectral feature below half the bandwidth ($\omega < W/2 = 2$) is still observed when approaching the phase boundary for $U = 1$ and $U = 2$, as is the case for the single-ladder vertex corrections (second row from top). The two main effects of the AL-diagrams are an additional broadening and enhancement of the Drude peak, and a shift of the π-ton feature to higher energies.

The results for the magnetic susceptibility, shown in Fig. 6.6, are comparable to the longitudinal optical conductivity discussed until now. The broadening of the “Drude peak” with increasing U is still happening in the bare bubble contribution, and the Hubbard satellites cause high-energy spectral weight to appear. The single-ladder π-ton vertex corrections yield an enhancement of the Drude feature at $U = 1$, a broadening at $U = 2$ and a suppression of the Drude peak at $U = 3$, while characteristic in-gap peaks appear near T_N around $\omega = 0.8$. The π-ton peaks are less prominent in the spin-spin response than in the optical conductivity.

The third row of Fig. 6.6, from top, illustrates the effect of the double-ladder vertex corrections for the three values of U considered. As in the case of the optical response, this additional set of diagrams does not significantly alter the main signature of the π-ton for $U = 1$ and $U = 2$: the π-ton peak is slightly pushed up in the in-gap region and its amplitude is not much affected. Although, major changes come about at $U = 3$ where the π-ton feature again disappears as a result of the double-ladder corrections. Its spectral weight either merges with the hump produced by the 1D density of states or with the Drude feature.

The last row of Fig. 6.6 displays the effect of the AL-type vertex corrections on the magnetic susceptibility. There are once again many similarities with the optical conductivity results, such as the peak associated with the π-ton that is flattened and shifted to higher energies, while the Drude feature increases and becomes wider. The π-ton peak’s location shifts more or less to the same energy as in the optical conductivity (bottom panel of Fig. 6.5).

Up to this point, solely 1D vertex corrections of various sorts have been considered. As a proof of principle and to verify that the vertex corrections have qualitatively similar effects on the susceptibility spectra, the single-ladder vertex corrections, which qualitatively drive the spectral modifications according to Figs. 6.5 and 6.6, represent the only class of corrections that is computed in

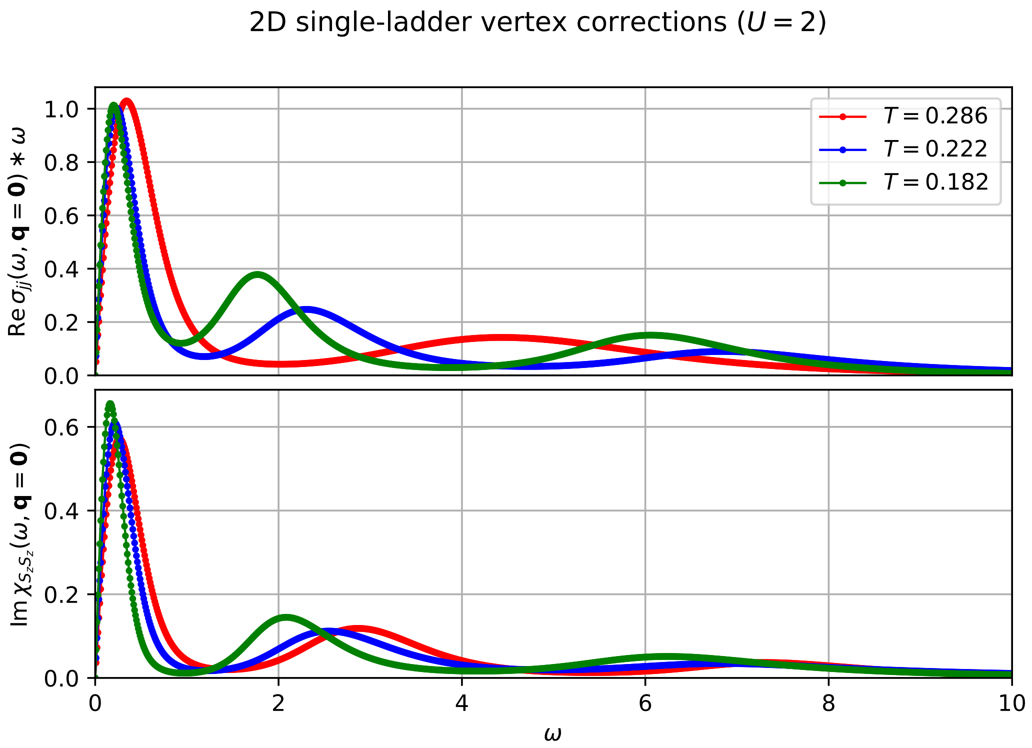

Figure 6.7: Longitudinal optical conductivity (top panel) and spin-spin response (bottom panel) in the 2D single-band Hubbard model at half-filling for $U = 2$. Only the single-ladder vertex corrections are shown for three distinct temperatures, in addition to the bare response. The temperatures are pointed out by the green dots figuring along the vertical grey line in Fig. 6.4. Top panel: imaginary part of the current-current correlation function for $T = 0.286, 0.222, 0.182$. Lower panel: imaginary part of the spin-spin response for the same temperatures as for optical conductivity.

2D. The 2D results are shown in Fig. 6.7. The observations fall in line with the 1D case: as the phase boundary is advanced towards by cooling down the temperature, an in-gap spectral peak grows just below $\omega = 2$. In 2D, the Drude peak is amplified greatly and the higher energy spectral features becomes wider while positioned at energies larger than in 1D. Hence, the RPA-type post-processing method does not really depend on dimension; only a rescaling in energy of the 1D spectral features happens. Henceforth, due to the facts that the double-ladder diagrams have little qualitative effects for $U \leq 2$ in 1D, namely the slight broadening and small red-shift of the π-ton peak, and that the single-ladder corrections have similar consequences in 2D, the π-ton vertex corrections will be studied out of equilibrium in Section 7.1 in 1D only considering the single-ladder diagrams (see Fig. 4.5).

Let's try now to understand in more details the origin of the π-ton that shows up in the responses evaluated so far. In general, the π-ton peak appears in the energy range $\omega \in [0.2, W/2]$, dubbed the "in-gap" region previously (*cf.* Figs. 6.5 and 6.6). To see why the π-ton constantly emerges within this energy window for $U = 1$ and 2 (in 1D), the numerator and denominator of Eq. (4.22) are split up for further analysis. The focus is concentrated on Eq. (4.22) since for weak interactions, Eq. (4.25) and (4.28) both yield a relatively small correction to the peak location. Performing the analytical continuation to the real-frequency of χ_d in the denominator of Eq. (4.22), one obtains

$$\chi_d^{\sigma,-\sigma}(\omega,\tilde{\mathbf{k}}-\bar{\mathbf{k}}) = U\int_{-\pi}^{\pi}\frac{\mathrm{d}^D k}{(2\pi)^D}\iint_{-\infty}^{\infty}\mathrm{d}\omega'\mathrm{d}\omega'' \times \mathcal{A}^{R,\sigma}_{\mathbf{k}+\tilde{\mathbf{k}}-\bar{\mathbf{k}}}(\omega')\mathcal{A}^{R,-\sigma}_{\mathbf{k}}(\omega'')\frac{n_F(\omega')-n_F(\omega'')}{\omega+i\eta-(\omega'-\omega'')}, \tag{6.1}$$

where $\mathcal{A}^R_{\mathbf{k}}(\omega) = -\frac{1}{\pi}\mathrm{Im}\,\mathcal{G}^R(\mathbf{k},\omega)$ is the retarded spectral function, n_F is the thermodynamic Fermi-Dirac distribution, and $\eta \to 0^+$. As mentioned before, the π-ton-type vertex corrections come mainly from momenta differences $\tilde{\mathbf{k}}-\bar{\mathbf{k}} = (\pi,\cdots,\pi) \equiv \mathbf{k}_\pi$. Therefore, the output of Eq. (6.8) heavily depends on the momentum differences between the particle-hole pairs that scatter off each other. Furthermore, not all $(\tilde{\mathbf{k}},\bar{\mathbf{k}})$-tuples leading to $\mathbf{k}_\pi$ give comparable contributions when the numerator and the denominator are considered altogether in Eq. (4.22). The reason is that the $\mathbf{k}$-dependent spectral weight of the interacting lattice Green's function varies substantially with momentum. In 1D, the retarded spectral functions $\mathcal{A}^R_{\mathbf{k}}$ exhibit a sharp peak near $\omega = 0$ for momentum

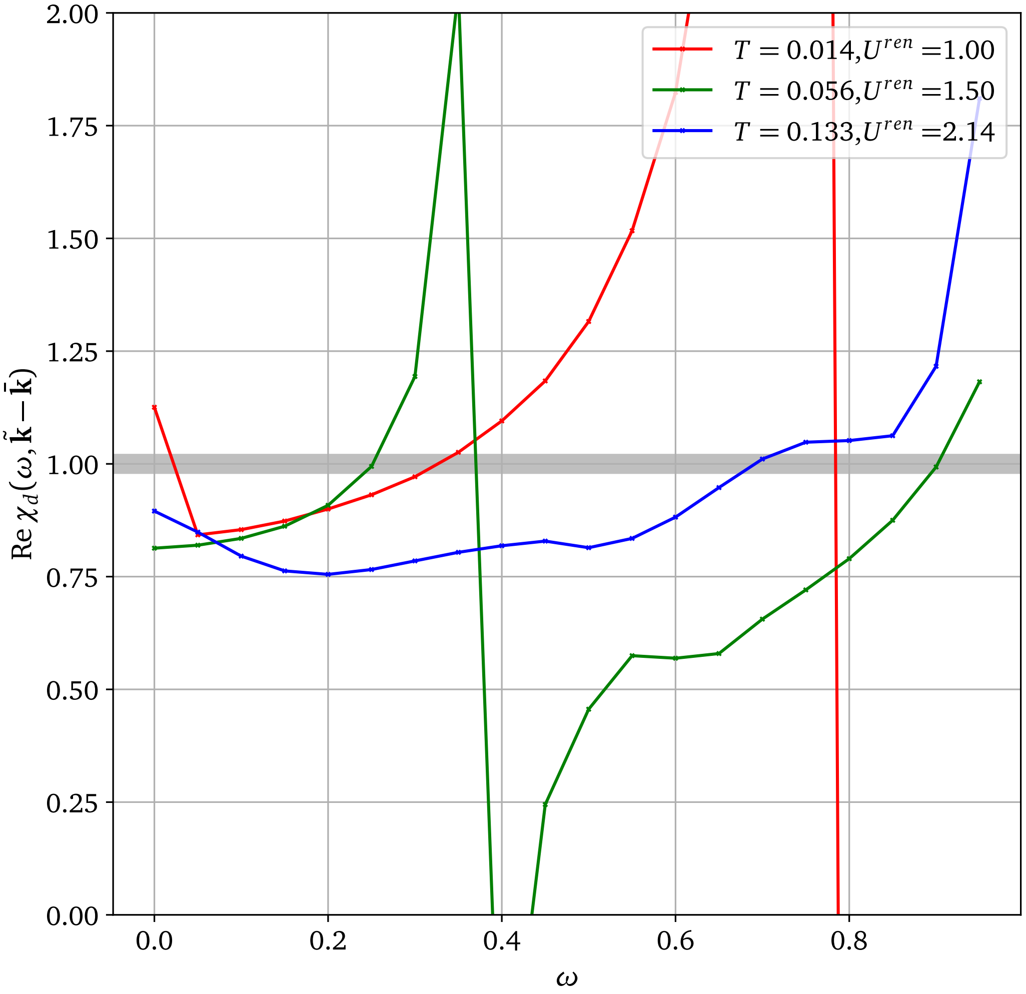

Figure 6.8: Real part of Eq. (6.1) as a function of energy ω. The energies at which the real part approaches 1 correspond to the peaks observed near $\omega \simeq 0$ and $\omega \in [0.4, 0.9]$ in Figs. 6.5 and 6.6.

values around $\mathbf{k} = \pm\frac{\pi}{2}$ (around the Fermi surface), while the spectra broaden as $\mathbf{k}$ approaches 0 or π, these momenta corresponding to peaks positioned near $\omega = \pm 2$. This would mean that the numerator of Eqs. (4.22) and (4.25) yields the largest values for tuples $(\tilde{\mathbf{k}} \simeq \pm\frac{\pi}{2}, \bar{\mathbf{k}} \simeq \mp\frac{\pi}{2})$, whose difference gives $\mathbf{k}_\pi$. On the other hand, as illustrated in Fig. 6.8 for all interaction values, the real part of Eq. (6.1) approaches 1 in the energy range $\omega \in [0.4, 0.9]$, since one pole lies within that energy bracket. This energy range matches well the peak position of $\mathcal{A}^R_{\mathbf{k}}$ near $\mathbf{k} = \pm\frac{\pi}{2}$, so that the corresponding poles get picked up and amplified by the numerator and show up as peaks in the responses. Moreover, as shown in Fig. 6.8, for the interaction value $U = 1$ ($U^{\text{ren}} = 1$), a second pole sits quite close to $\omega = 0$ causing a rise in the responses near $\omega = 0$ (*cf.* Figs. 6.5 and 6.6). This would be the origin of the observed broadening of the Drude peak.

Complementarily, one can study the characteristic energy scales of the π-ton contributions to the 1D responses by calculating directly the spectrum of the vertex function "$\square$" appearing in Eq. (4.30). In Fig. 6.9, the reducible single-ladder vertex "$\square$" is plotted for the three momentum differences $|\tilde{\mathbf{k}} - \bar{\mathbf{k}}| \in \{0, \frac{\pi}{2}, \pi\}$ (red-shaded lines). These spectra are not computed using any kind of Maximum Entropy algorithm [25], but rather Fourier transforming the real-time function $\square(t, t')$ obtained from equilibrium calculations carried out on the KB contour. In Fig. 6.9, both the imaginary parts of the charge and spin susceptibilities for the indicated momenta are plotted to illustrate the effect of multiplying the four Green's functions in Eq. (4.31) and adding bare velocity factors (see below Eq. (4.17)) at the vertices when computing the optical conductivity. The responses $\text{Im}\chi_{\text{sl},j_ij_i}$ (green shades) and $\text{Im}\chi_{\text{sl},s_zs_z}$ (blue shades) represent the π-ton contribution (4.31) associated with the $(\tilde{\mathbf{k}}, \bar{\mathbf{k}})$-tuples whose difference corresponds to $\Delta\mathbf{k} = |\tilde{\mathbf{k}} - \bar{\mathbf{k}}| \in \{0, \frac{\pi}{2}, \pi\}$, namely

A detailed description of the important algorithmic steps featuring in nonequilibrium Green's function calculations on the KB contour is given in Ref. [114]. The same structure is used here in the code.

$$\frac{1}{N_{\mathbf{k}}} \sum_{|\tilde{\mathbf{k}} - \bar{\mathbf{k}}| = \Delta\mathbf{k}} \chi_{\text{sl}}(\tilde{\mathbf{k}}, \bar{\mathbf{k}}, \mathbf{q} = \mathbf{0}; \omega).$$

The spin-spin single-ladder vertex corrections $\chi^{\mathbf{q}}_{\text{sl},s_zs_z}$ are equal to Eq. (4.31) with a global factor of -1 and without the velocity factors.

First of all, by comparing both Figs. 6.8 and 6.9, one can identify that the poles in the single-ladder vertex shown in Fig. 6.9 are reflected in the vertex function spectra $\square(\Delta\mathbf{k} = \pi)$ within the same energy range. To recall, in Fig. 6.8, only the poles of Eq. (6.1) at wave vector difference $\Delta\mathbf{k} = \pi$ are plotted. Although, as Fig. 6.9 shows, the momentum-dependence of $\square$ is more complicated and another prominent peak appears around $\omega \simeq 2$ originating from $\Delta\mathbf{k} = \frac{\pi}{2}$. This feature is suppressed once the four Green's functions are multiplied to the ladder, as defined in Eq. (4.29), and this is independent of the presence/absence of the bare velocity factors. On the contrary, the tiny contributions of $\square(\Delta\mathbf{k} = \mathbf{0})$ to the single-ladder corrections get enhanced by the multiplication with these Green's function, especially for $\text{Im}\chi_{\text{sl},jj}$. However, as the name suggests, the dominant contributions to the π-ton come from $|\tilde{\mathbf{k}} - \bar{\mathbf{k}}| = \mathbf{k}_\pi$. In the single-band nearest-neighbor Hubbard model, the Fermi momenta are $\mathbf{k}_F = \pm\frac{\pi}{2}$. These coincide with the largest values of the velocities and are separated by a momentum shift π, partly explaining why $\text{Im}\chi_{\text{sl},j_ij_i}$ is larger than $\text{Im}\chi_{\text{sl},s_zs_z}$. In the nonequilibrium RPA-type post-processing calculations presented in Section 7.1, the time

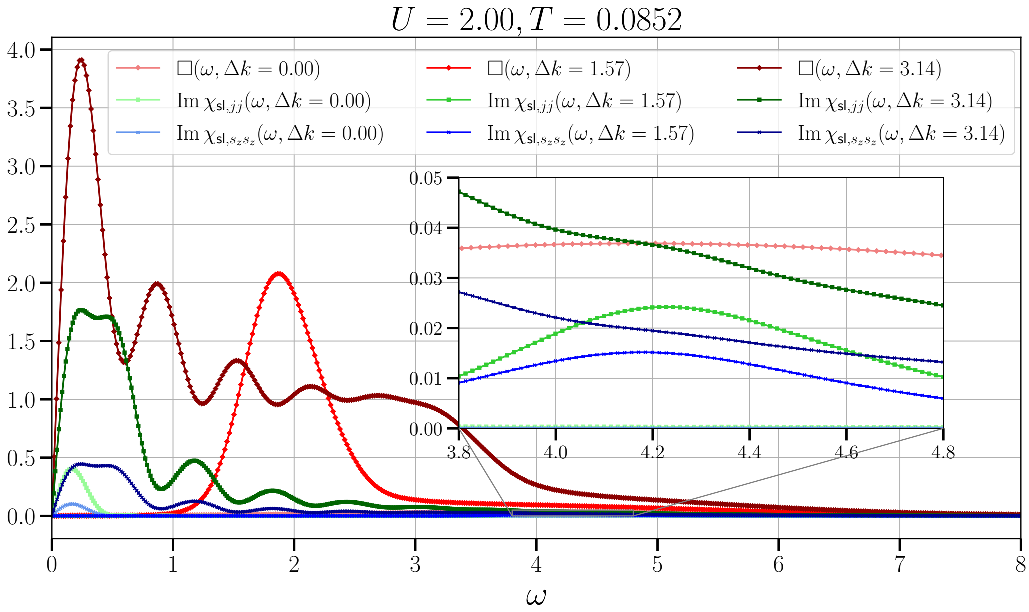

Figure 6.9: Analysis of different contributions to the π-ton spectrum in 1D. The different shades of red show the momentum dependence of the single-ladder vertex spectrum. Light, intermediate and dark colored lines show the contributions from momentum tuples with $\Delta\mathbf{k} = |\tilde{\mathbf{k}} - \bar{\mathbf{k}}| = 0, \frac{\pi}{2}$, and π, respectively. The shades of green show the momentum dependence of $\mathrm{Im}\chi_{\mathrm{sl},j_i j_i}$, whereas the different shades of blue show that of $\mathrm{Im}\chi_{\mathrm{sl},s_z s_z}$ (vertex corrections only).

traces of the conductivity will be investigated at $\omega = 0.35$, 1.0 and 3.9 (see black dashed lines in Fig. 6.10) based off the important spectral features characterizing $\mathrm{Im}\chi_{\mathrm{sl},j_i j_i}(\omega, \Delta\mathbf{k} = \pi)$ (dark green spectrum in Fig. 6.9), making sure to include the hump that appears near $\omega \simeq 1$.

To make sure that the features in the responses calculated using Maximum Entropy (Fig. 6.5) are reproduced using the real-time evolution technique [114], the equilibrium optical conductivity $\omega * \mathrm{Re}\sigma_{jj}(\mathbf{q} = \mathbf{0}, \omega) = \mathrm{Im}\chi_{j_i j_i \mathbf{q}=\mathbf{0}}(\omega)$ is plotted in Fig. 6.10 at $U = 2$ for different temperatures. Blue-shaded lines show the bubble contribution and red-shaded lines the π-ton contribution. Since the optical conductivity is multiplied by ω, the Drude peak is cut off so as to emphasize on the spectral weight distribution at higher energies, just like done in previous figures. With increasing temperature, the Drude peak shrinks but broadens, which leads to a significant increase in the bubble contribution at low frequencies, as seen in Fig. 6.10. The broad peak in the bubble contribution near $\omega = 3.9$ can be associated with excitations between the peaks in the density of states (see Fig. 7.4). The spectrum obtained from the π-ton contribution shows a nontrivial temperature dependence at low frequencies, but the main characteristic feature is a peak near $\omega = 0.4$, which grows as one approaches the AFM phase boundary at low temperatures. At high temperatures, this peak switches from positive to negative, which implies that the π-ton narrows (broadens) the Drude feature at high (low) T. The black dotted curve in Fig. 6.10 shows the π-ton spectrum calculated using bare IPT Green's functions at $U = 2$ and $T = 0.08$.[2] This exam-

---

[2] The spectrum has been divided by half for presentation.

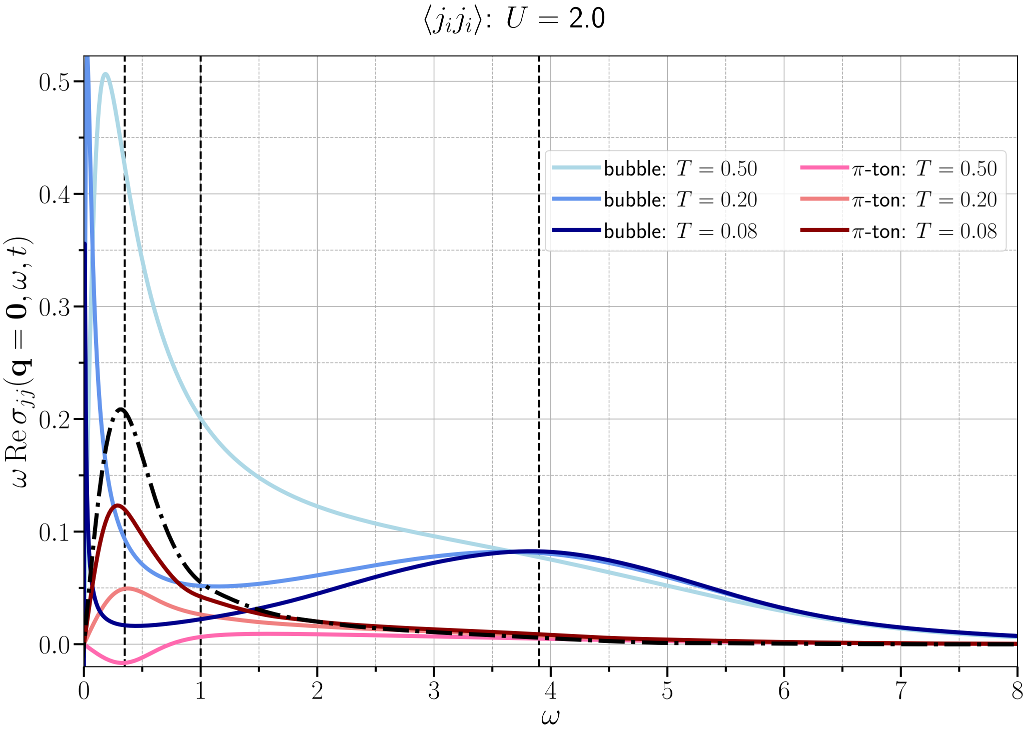

Figure 6.10: Longitudinal optical conductivities separated into the bubble (blue shades) and the π-ton (red shades) contributions in equilibrium for different temperatures and $U = 2$. (The $U = 1$ results show the same qualitative trend, although the temperature scales are lower.) The vertical dotted lines indicate the energies for which we compute the time evolution of the spectral weight. The black dotted line portrays the π-ton at $U = 2$ and $T = 0.08$ using bare IPT instead of bold IPT.

ple shows that both bare and bold IPT capture the key aspects associated with the RPA-type π-ton vertex corrections.

To resolve the low-frequency behavior of the susceptibilities in Fig. 6.10, a very large time window is needed since that resolution is inversely proportional to the time window. The bubble spectra were obtained by extrapolating the equilibrium data to long times with an exponential fit. As for the π-ton contribution, non-monotonic oscillations persist to much longer times and its decay can't be extrapolated confidently, so the Fourier transformation relied on a time window $\Delta t = 17$, implying that there is more smearing at the low frequencies in this case.

In summary, near the AFM boundary, the equilibrium optical conductivity (including vertex corrections) is composed of (i) a low-energy Drude peak, which depending on the temperature range can be enhanced or narrowed by the π-ton-type vertex corrections, and (ii) a broad high-energy hump near $\omega = 3.9$, originating mainly from the bubble diagram and related to peaks in the single-particle density of states. These general features and trends are consistent with the π-ton related modifications of the conductivity reported in Refs. [66, 150]. To capture nonlocal electronic correlations without selecting *a priori* the relevant classes of diagrams that renormalize the vertices, one would need to resort to Diagrammatic Quantum Monte Carlo methods [101, 142], extensions to DMFT [82, 103, 107, 133], or the Parquet summation of diagrams [73, 74], which are unbiased numerical techniques that allow in principle to check the relevance of different classes of diagrams.

6.1.3 *Comparison to DMRG*

DMFT does not capture properly the low-dimensional 1D physics of the Hubbard model, so for that reason the DMFT+IPT results of the previous section are compared to Density Matrix Renormalization Group (DMRG) [112, 120, 149] at $T = 0$ for the 1D Hubbard model. As opposed to DMFT, DMRG captures physics specific to 1D such as spin-charge separation [65] and it treats more accurately nonlocal correlations. Even though it is not expected that DMFT susceptibilities, which are representative of finite-temperature higher dimensional systems [91, 94], agree well with the zero-temperature DMRG results, the π-ton related features identified in the previous subsection are sought after in the DMRG spectra.

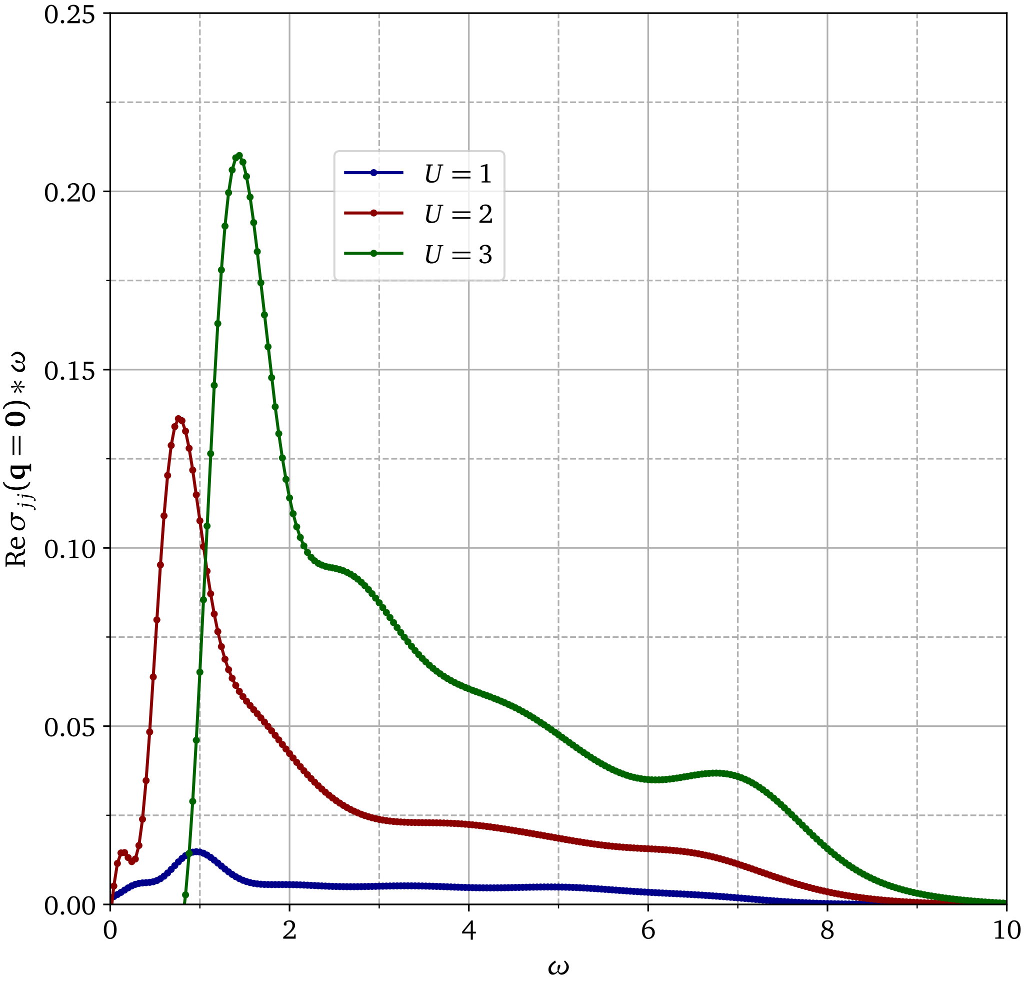

Figure 6.11: Longitudinal optical conductivity for $U = 1,2,3$ and $T = 0$ obtained using DMRG.

In Figs. 6.11 and 6.12, respectively, the DMRG results [120] for both the current and magnetic responses are shown using the same values of the interaction

U as in Section 6.1.2. The spectral weight located in the energy range $2 \lesssim \omega \lesssim 7$ is related to structures in the 1D density of states, essentially captured at the level of the bare bubble in the diagrammatic calculation (*cf.* top row of Figs. 6.5 and 6.6). Like observed in Section 6.1.2, the spin susceptibility in DMRG has lower spectral weight amplitude compared to the optical conductivity, consistent with the bare bubble calculations (Figs. 6.5 and 6.6). This difference in spectral amplitudes can be attributed to the factors $\frac{1}{2}$ in the spin vertices coming from the Pauli matrices, as well as the fact that the velocities at the vertices entering the optical conductivity – corresponding to the derivative of the bare electronic dispersion with respect to momentum – are proportional to a sinusoidal function weighted by $(2t)^2$, with maxima at $\mathbf{k} = \pm\frac{\pi}{2}$ coinciding with the momenta for which the spectral weight of the interacting Green's function is large, *i.e.* where the self-energy only results in weak broadening.

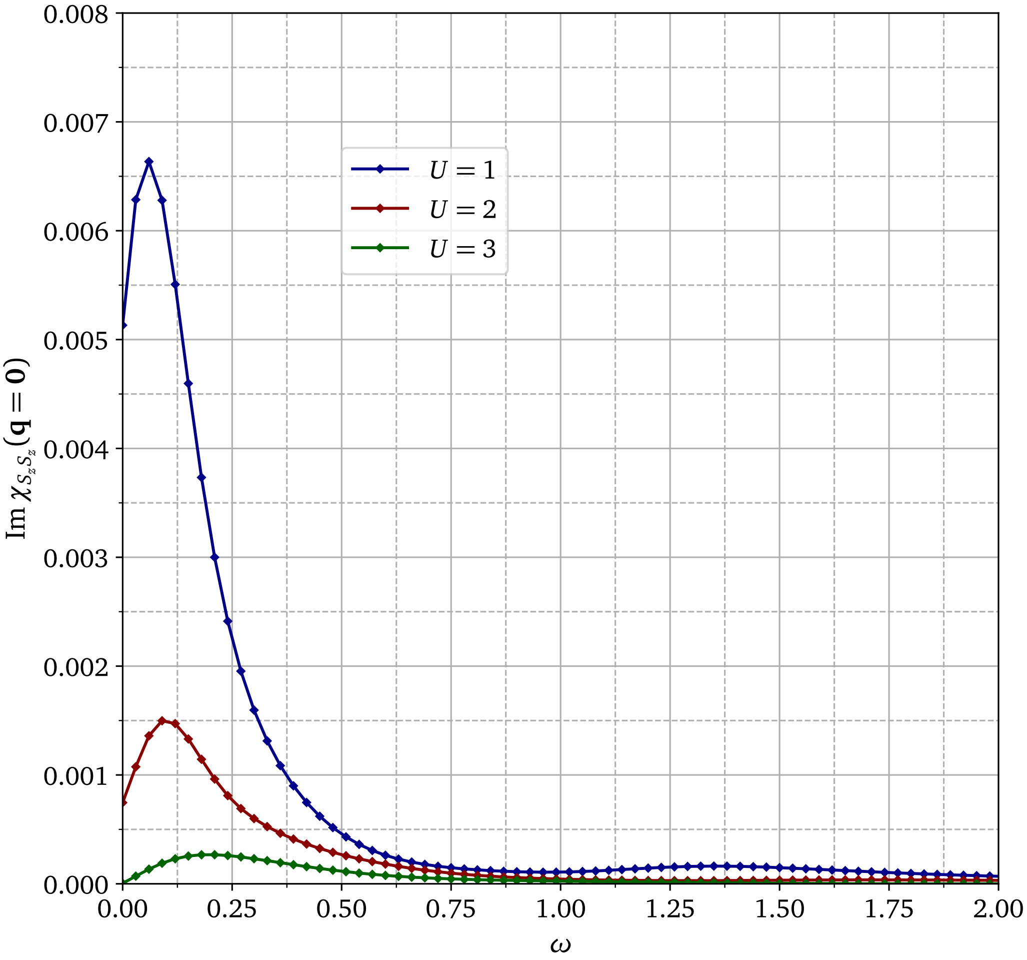

Figure 6.12: Magnetic susceptibility for $U = 1,2,3$ and $T = 0$ obtained using DMRG.

The low-energy peak in $\mathrm{Im}\chi_{S_zS_z}$ looks similar to the broadened "Drude" feature found in the DMFT+IPT spectra with single-ladder and double-ladder corrections. However, the amplitude of the magnetic response is much weaker than that obtained in DMFT and the trend as a function of interaction is opposite: in DMFT the optical conductivity and magnetic susceptibility follow qualitatively similar trends, but in DMRG the spin-spin correlation function decreases with increasing U. The latter can be explained by the fact that, in 1D, the exchange coupling J (same J as in Eq. (3.7)) is proportional to $J \propto t\sqrt{1-\mathrm{const}(U/t)}$ in the weak U regime, which connects to $J = 4t^2/U$ in the strong U regime. Hence, the spin exchange coupling J decreases with increasing U. Moreover, the low energy effective theory describes an independent sum of charge and spin degrees of freedom, which is known as the spin-charge separation. As a consequence, for any $U > 0$ at $T = 0$, the charge sector is in the Mott-gapped phase, and the spin sector is described by the Heisenberg model.

A prominent peak appears at low frequencies ($\omega \approx 0.2 - 1.2$) in the optical conductivity. This peak moves up in frequency and increases in amplitude with increasing U, a behavior qualitatively similar to the π-ton peak identified in the diagrammatic analysis at approximately the same energies (Fig. 6.5). While one might thus expect a significant π-ton contribution, this peak in the DMRG solution is mainly originating from charge excitations across the Mott gap [48]. As mentioned, one peculiarity of the half-filled 1D case is that it is Mott insulating at zero temperature for any $U > 0$. The absence of a gap in the $U = 1$ and 2 spectra is due to broadening. Hence, even if a π-ton feature exists in the energy range suggested by the ladder calculations, it is dominated by the Mott gap feature in 1D. At $U = 3$, the DMFT results for both the magnetic and optical responses show that the single-ladder vertex corrections almost completely suppress the Drude peak at $\omega = 0$ (it remains present when considering the double-ladder vertex corrections). This suppression is not observed in DMRG in the case of the magnetic response. The qualitative difference between the spin and charge responses in DMRG may be attributed to specificities of the zero-temperature 1D physics of the Hubbard model.

Contrary to the DMFT results, the magnetic and charge degrees of freedom are completely independent (spin-charge separation) in 1D according to the DMRG results. The low-energy structure of the magnetic excitation spectra in the Hubbard model is always the same as that in the Heisenberg model in 1D, and the excitations created are gapless spinons. In higher dimensions, in contrast, the magnetic and charge degrees of freedom cannot be easily separated, even more so in strongly interacting systems, and the magnetic excitation structure differs substantially from that of the Heisenberg model. At $T = 0$, gapless magnons should exist because of the AFM order, while other collective spin excitations may exist above T_N. In 1D, as the temperature is increased, the spin and charge sectors become less asymmetric [65] (less decoupled) and the spectrum of the spin correlation function is expected to resemble more the charge and/or optical conductivity. It would thus be interesting to eventually perform a comparison of the optical conductivity between the diagrammatic results of the previous section and $T > 0$ DMRG results in 1D, especially since the DMRG optical conductivity features a Drude peak at elevated temperatures [65, 116].

The spinons are fractionalized quasiparticles carrying no charge, only the spin.

6.2 TPSC AND VARIANTS

As shown in Section 5.2.10, four major variants to the original formulation of TPSC [152] have been considered and detailed in this thesis. All the four methods were implemented in the C/C++ programming languages and import functionalities from the NESSi library [114]. For the calculations to succeed within one week runtime and with as little memory usage as possible, MPI parallelization is unavoidable and sophisticated memory management across processors is crucial. The codes are available upon request under this link.

First, depending on the model Hamiltonian chosen, TPSC makes use of a second-level approximation to the nonlocal self-energy that is *lifted off* a first-level approximation based off a Luttinger-Ward functional (5.25). That second-level approximation was derived in Section 5.2.3 and leads to Eq. (5.63) for the Hubbard model. To the exception of the original formulation of TPSC (OG TPSC), an extra sum-rule (5.71) that relates the first-level (right-hand side of Eq. (5.71), determined via Eq. (5.54)) and second-level (left-hand side of Eq. (5.71)) double occupancies comes in to stabilize the nonequilibrium solutions after the parameter quenches/ramps – this will be discussed in further details in Section 7.2.1.

Second, TPSC+GG is closely related to TPSC, although it is the fully self-consistent version of it owing to the fact that the single-particle Green's function $\mathcal{G}^{(1)}$ dressed with $\Sigma^{(1)}$ (5.70) is now inserted back into the noninteracting susceptibility (5.65) to repeat the algorithm laid out in Section 5.2.4, until desired convergence is reached. TPSC+GG is much more heavy than TPSC, although it offers more stable results at longer times on the real-time axis $\mathcal{C} \in \mathcal{C}_1 \oplus \mathcal{C}_2$.

Computationally speaking, note that the cheapest method among TPSC and its variants is TPSC, especially at higher U, lower T and in higher dimensions. The scaling is however nonlinear.

Third, DMFT+TPSC (see Section 5.2.9) is an extension to DMFT introduced in Section 3.2 in which the nonlocal degrees of freedom are emulated by the TPSC nonlocal self-energy. This method replaces the local TPSC fluctuations by the DMFT one and it allows the spin and charge degrees of freedom in the lattice environment to have feedback in the local impurity correlations. Using the 3$^{\text{rd}}$-order IPT impurity solver detailed in Section 3.2.1.3, one can also dope the impurity in electrons and holes, just like it is possible for TPSC and TPSC+GG.

Fourth and last, DMFT+TPSCα branches off DMFT+TPSC and includes an extra sum-rule (5.105) that ensures "D consistency", as described in Section 5.2.10. Hence, this method possesses all the attributes of DMFT+TPSC, with the extra feature that D^{imp} (5.99) and $D^{\text{TPSC},(1)}$ (5.104) are equal; this in turn implies that the thermalized temperatures of the impurity and lattice subspaces are equal. This method however is unstable when changing model parameters across time, thus it will only be discussed in equilibrium.

The results of the aforementioned methods will be presented in the roughly same order they have just been skimmed over. Note that all the results in this section make use of the KB contour (Fig. 2.1), hence the Matsubara solution is bootstrapped [114] onto the real-time horizontal axes and no analytical continuation [25, 143] is needed: a forward Fourier transform like that of Eq. (2.67) suffices to extract out the spectral function on the energy domain.

6.2.1 *TPSC and TPSC+GG*

To start with, on several occasions, benchmarks against equilibrium results available in the literature are provided. Moreover, some complementary equilibrium results in 3*D* will be shown, both for TPSC and TPSC+GG, for different band dispersion relations and dopings. In this section, on several occasions, the physical units are renormalized by the bandwidth W to enable direct comparisons between 2D and 3D results. Half-filling is the most challenging filling within the single-band nearest-neighbor Hubbard model [89, 152].

6.2.1.1 *2D*

In 2D, the dispersion relation $\epsilon(\mathbf{k})$ (5.66) contains both nearest- and next-nearest-neighbor hopping terms, denoted respectively t_{hop} and t'_{hop}:

$$\epsilon(\mathbf{k}) = -2t_{\text{hop}}\left(\cos k_x + \cos k_y\right) - 2t'_{\text{hop}}\left(\cos\left(k_x + k_y\right) + \cos\left(k_x - k_y\right)\right) \qquad (6.2)$$

In some cases, only the nearest-neighbor hopping will be considered, whereas in other situations, both t_{hop} and t'_{hop} are nonzero.

To recall, the time is represented in units of the inverse of the lattice nearest-neighbor hopping energy t_{hop}.

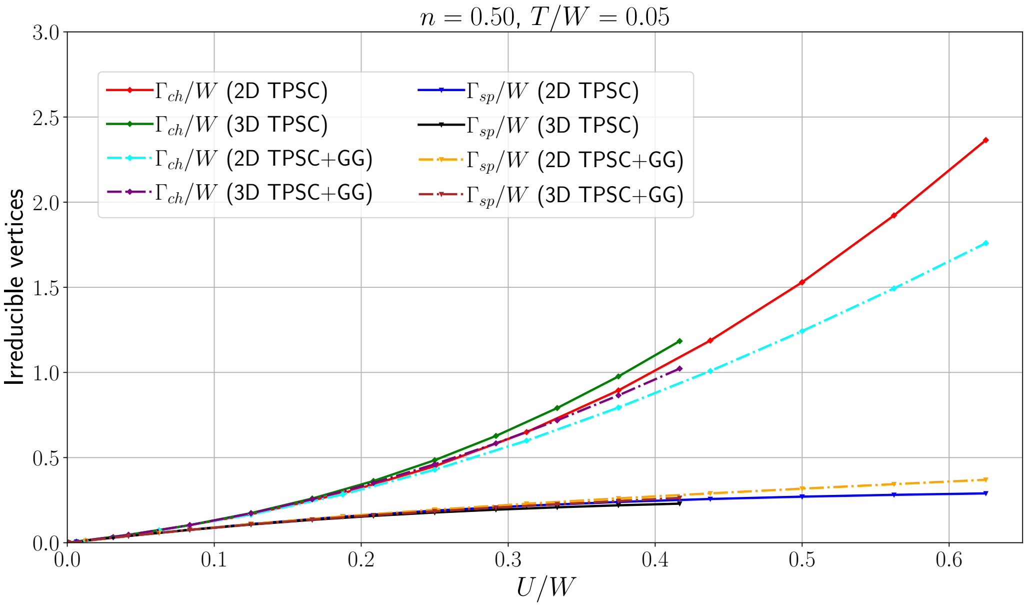

Figure 6.13: Bandwidth-normalized spin and charge irreducible vertices as a function of normalized bare interaction for the nearest-neighbor square (2D) and cubic (3D) lattices for TPSC (bold lines) and TPSC+GG (dotted lines). The *dimensionless* temperature is $T/W = 0.05$ and the spin-density per site is $n = 0.5$.

At equilibrium, the charge and spin irreducible vertices are constant in time, since the bare Coulomb interaction or lattice hopping parameter are unchanged – in fact all different observables and parameters remain constant throughout the time propagation along the real-time axis. In Fig. 6.13, the charge Γ^{ch} and spin Γ^{sp} irreducible vertices are illustrated for various values of *dimensionless* bare Coulomb interaction U/W at half-filling ($n = 0.5$) and *dimensionless* temperature $T/W = 0.05$ for both the nearest-neighbor square lattice Hubbard model and the nearest-neighbor cubic lattice Hubbard model.

The half-filled case turns out to be the most challenging doping value for TPSC and its variants, since the spin correlations build up at the highest temperatures throughout the doping range. At low interaction values $U/W \lesssim 0.1$, the irreducible vertices roughly overlap with the normalized bare interaction U/W and the trend is therefore linear in U/W for both $\Gamma^{\text{sp/ch}}/W$. Then, in the vicinity of $U/W \simeq 0.2$, the spin and charge vertices start drifting away from each other at an increasing rate: in 3D, the rate of deviation is larger than in $2D$ and this is valid for both TPSC and TPSC+GG. The spin irreducible vertex obtained in TPSC+GG is constantly larger than that obtained within TPSC, whereas it is the reverse situation when looking at the charge irreducible vertex: Γ^{ch}/W from TPSC+GG is constantly smaller than that calculated using TPSC. The Figure 6.13 also shows that the spin irreducible vertex saturates at higher values of U/W, due to the Kanamori-Brueckner screening [63]. This screening implies that the crossover temperature into the renormalized classical regime T_x saturates with increasing U [152], as can be seen from Fig. 6.14, which shows the static spin susceptibility of the two-dimensional model for increasing U/W at $\mathbf{k} = (\pi,\pi)$ – the upturns become closer in temperature when U/W becomes larger. The crossover temperature T_x marks the region below which the anti-

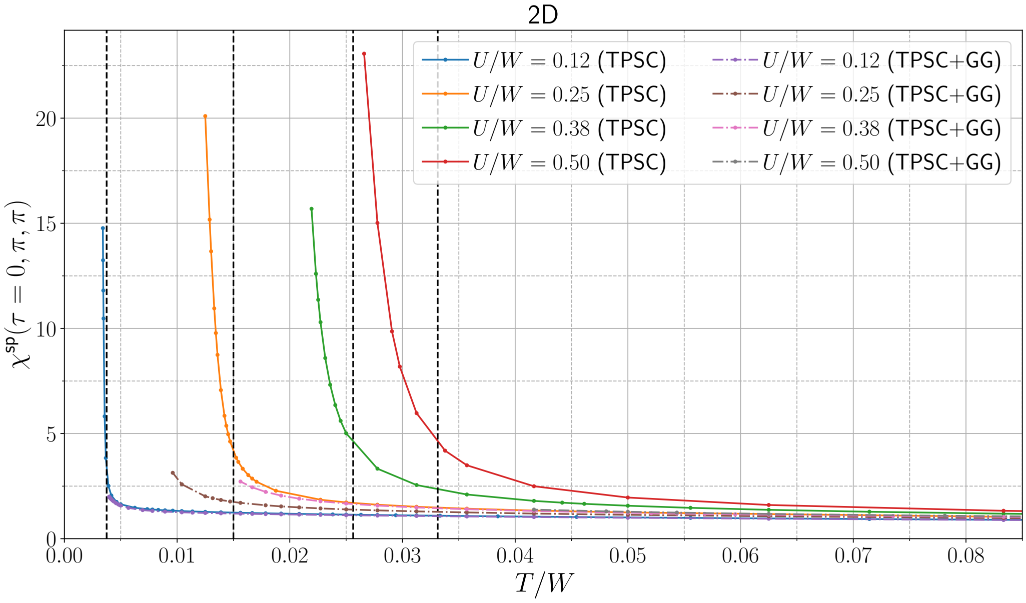

Figure 6.14: Static spin susceptibility of the 2D model at momentum $\mathbf{k} = (\pi,\pi)$ as a function of temperature for interactions $U = 1,2,3$ and 4. The filling per spin is $n = 0.5$. The data points for TPSC+GG at $U = 4$ are not shown since the solution becomes unstable at high temperature ($T \approx 0.3$). The red curve can be compared with Fig. 3 of Ref. [144]. The interactions appearing in the legend are normalized by the bandwidth W to facilitate the comparison across dimensions; they are thus made *dimensionless*. The y-axis is upper-bounded to avoid squashing the data.

ferromagnetic correlation length ξ_{sp} becomes larger than the de Broglie wave length, and it corresponds to the temperature where the static spin susceptibility starts shooting up, as illustrated in Fig. 6.14 for various values of the interaction. Sticking to Fig. 6.14, as the normalized bare interaction decreases, TPSC+GG diverts away from the TPSC results at lower temperatures. Also, the TPSC+GG results do not show a steep shooting-up of the static spin susceptibility at lower temperature, like for TPSC, which is related to the observation that the precursor AFM bands do not show up in the single-particle spectra at the same T_x as the one extracted from TPSC. The vertical black lines indicate the temperature where the vertices deviate from their linear temperature trend in Fig. 6.17. This temperature would mark the whereabouts of T_x (normalized by W).

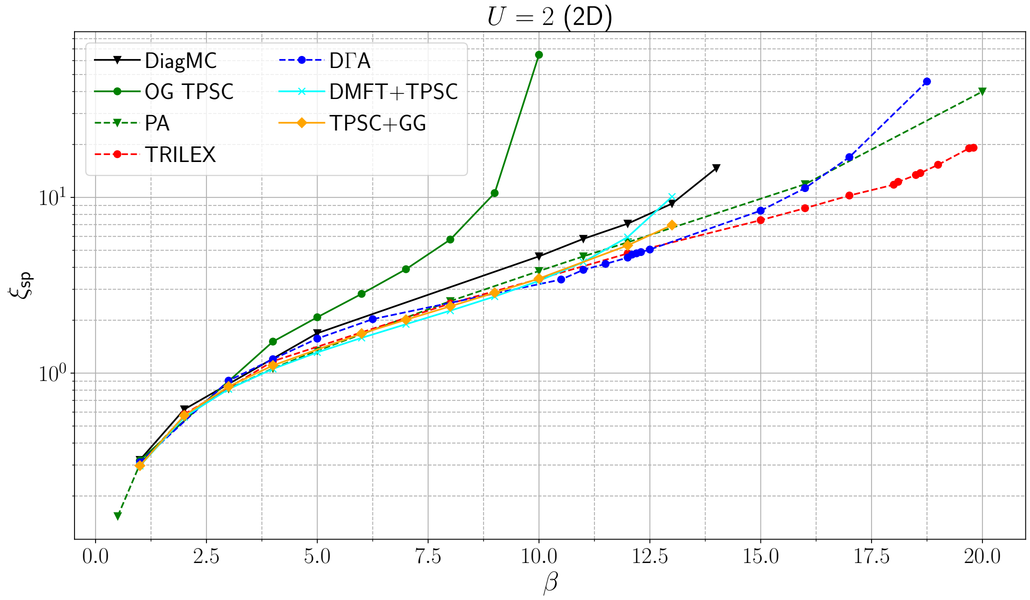

Figure 6.15: ξ_{sp} as a function of $1/T$ for $U = 2$ in the 2D half-filled nearest-neighbor Hubbard model. The y-axis uses a logarithmic scale. The methods compared are "OG TPSC" (green circles, called TPSC in Refs. [89, 110]), TPSC+GG (orange diamonds), DMFT+TPSC (cyan crosses), DΓA (blue circles), DiagMC (black triangles), TRILEX (red circles) and PA (green triangles). The data calculated using TRILEX, DiagMC, OG TPSC, DΓA and PA were taken from Ref. [110]. The 3^{rd}-order IPT impurity solver is used for DMFT+TPSC (see Section 3.2.1.3).

A different way to "quantify" the growth of the spin correlations is to directly compute the antiferromagnetic correlation length ξ_{sp} as a function of inverse temperature. In Fig. 6.15, ξ_{sp} is plotted for the half-filled 2D square lattice Hubbard model at constant interaction $U = 2$. Several methods are compared against each other, namely OG TPSC, TPSC+GG, DMFT+TPSC, DΓA [133], the Diagrammatic Monte Carlo method (DiagMC) [72, 100], TRILEX [11, 12] and the Parquet Approximation (PA) [33, 34]. The correlation length ξ_{sp} is extracted from the Ornstein-Zernicke fit of the momentum-dependent static spin susceptibility $\chi^{\mathrm{sp}}_{\mathbf{q}-\mathbf{Q}}(iq_n = 0)$ in the vicinity of the AFM scattering wave vector $\mathbf{Q}$:

$$\chi^{\mathrm{sp}}_{\mathbf{q}-\mathbf{Q}}(iq_n = 0) \approx \frac{A}{(\mathbf{q}-\mathbf{Q})^2 + \xi_{\mathrm{sp}}^{-2}},$$

where $\mathbf{Q} = \mathbf{k}_\pi$ ($\mathbf{k}_\pi = (\pi, \pi)$ in 2D) at half-filling and A is some weight of the order of 1. It is clear from Fig. 6.15, that the original formulation of TPSC (OG TPSC) overestimates the growth of spin correlations as the temperature is decreased – T_x would lie at a much higher temperature than that calculated using the remaining more accurate methods. On the other hand, all remaining methods cluster around each other for most of the temperature range considered, *i.e.* up to $\beta \simeq 12$. In particular, both TPSC+GG and DMFT+TPSC follow very closely the ξ_{sp} results obtained from TRILEX, PA and DΓA. Thus, TPSC+GG and DMFT+TPSC both correct the overestimation of the spin correlations of

OG TPSC and this will be reflected later on in the antinodal self-energy at the Fermi surface, where TPSC+GG and DMFT+TPSC agree quite well with DiagMC, especially in the case of TPSC+GG.

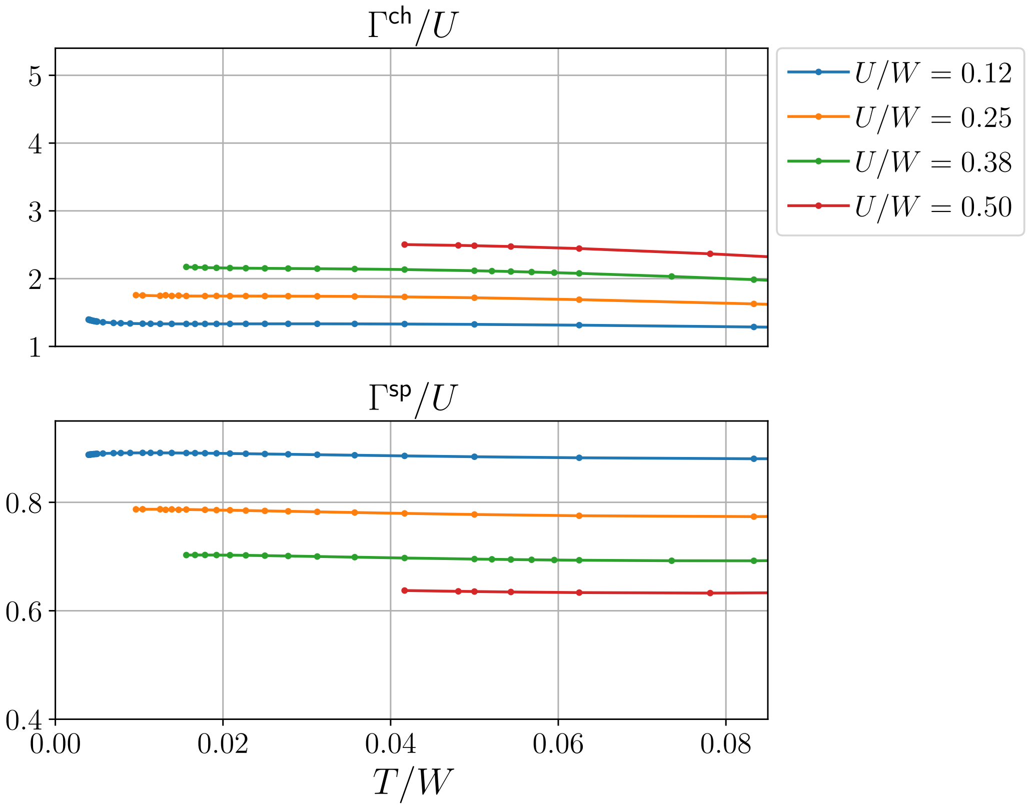

Figure 6.16: Γ^{ch} (top panel) and Γ^{sp} (bottom panel) as a function of T/W for $U = \{1,2,3\}$ in the 2D half-filled nearest-neighbor Hubbard model. The values of the vertices are normalized by U for compactness reasons and were obtained using TPSC+GG.

In Fig. 6.13, the irreducible vertices are sketched out for fixed $T/W = 0.05$ as a function of the interaction U/W using TPSC and TPSC+GG. Now, taking a different perspective, the temperature dependency look-up of the vertices for $U = \{1,2,3\}$ is shown in Figs. 6.16 for TPSC+GG and 6.17 for TPSC. Both Figs. 6.16 and 6.17 use the same y-axis range to ease comparisons. The vertices are normalized by U. In the top (bottom) panel is displayed Γ^{ch} (Γ^{sp}) versus temperature. In TPSC, Γ^{ch} grows substantially when T_x is approached, especially when U is larger. Moreover, the pace of the growth is enhanced when entering the renormalized classical regime. To a lesser extent, Γ^{sp} also increases as T_x is neared, before saturating and flexing down when setting foot in the renormalized classical regime, as opposed to Γ^{ch}. Hence, not only would Γ^{sp} and Γ^{ch} deflect from each other when U increases – Figs. 6.14 and 6.16 back this up, especially in the case of TPSC –, but they deflect as well when decreasing the temperature, particularly in the renormalized classical regime. Hence, overall, when the vertices are calculated within TPSC, the same qualitative observations are drawn, despite the fact that the growth and deflections of the vertices would be even greater, in particular close to T_x. This falls in line with the weaker overshooting of the static spin susceptibility observed in Fig. 6.14 for TPSC+GG when compared to TPSC.

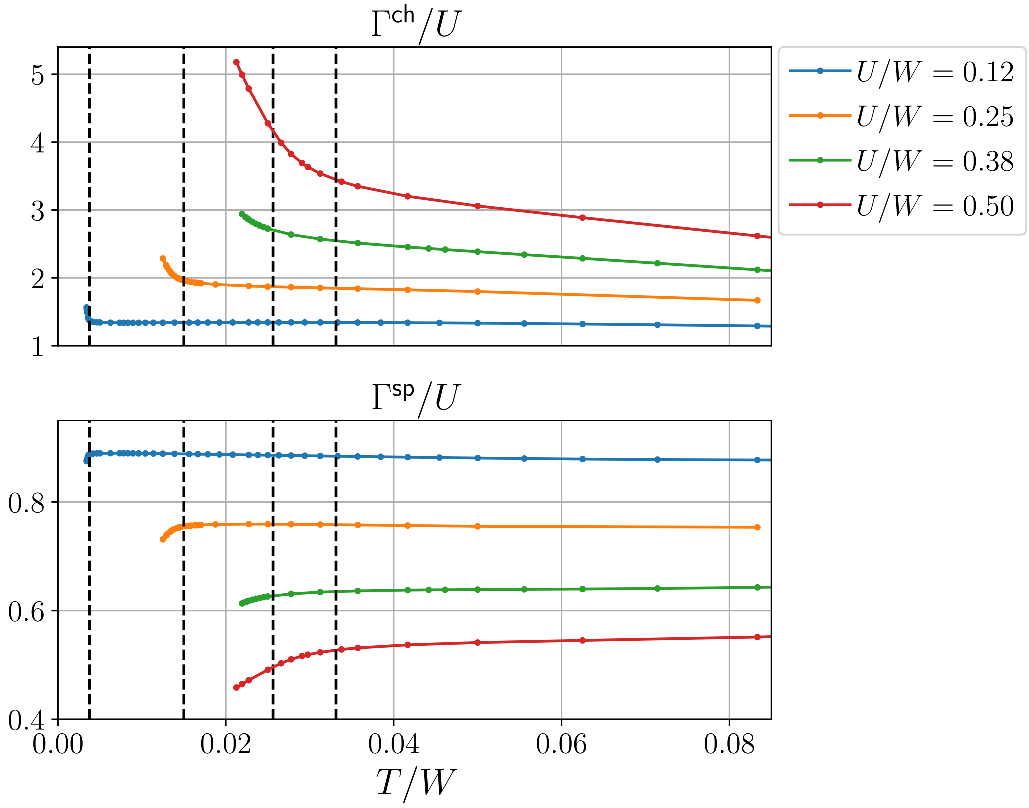

Figure 6.17: Γ^{ch} (top panel) and Γ^{sp} (bottom panel) as a function of T/W for $U = \{1,2,3\}$ in the 2D half-filled nearest-neighbor Hubbard model. The values of the vertices are normalized by U and were obtained using TPSC. The black vertical lines correspond to those drawn in Fig. 6.14.

The growth of the spin correlations as the temperature is dropped has a clear signature in the TPSC double occupancy. In Fig. 6.18, the double occupancies D calculated from the TPSC local ansatz (5.54) are illustrated as a function temperature for the same set of interactions as in Fig. 6.14, for both TPSC (green color shades) and TPSC+GG (brown color shades). In TPSC, the double occupancy depletes rapidly as one approaches the renormalized classical regime due to the enhanced spin correlations that renormalize the quasiparticle weight, until the Fermi-liquid picture breaks down. This sharp drop in D is associated with the increase in the TPSC charge irreducible vertex observed in Fig. 6.16 at low temperatures. TPSC+GG however does not show such decrease of D as a function of temperature, but rather a slight increase (like for DMFT+TPSC shown further down). This in turn explains why no sharp overshooting of the TPSC+GG irreducible vertices is seen in Fig. 6.14. As will be seen later on (Fig. 6.36), getting rid of the TPSC ansatz binding the double occupancy and spin irreducible vertex by using the double occupancy provided by DMFT will allow one to dive in deeper in temperature, before coming across some similar weaker downturning in D. Similar results to Fig. 6.18 have been reported in Ref. [89] (see Fig. 2).

In the renormalized classical regime, the growth of the spin fluctuations leads to a precursor of an AFM gap, as can be seen in the top panel of Fig. 6.19

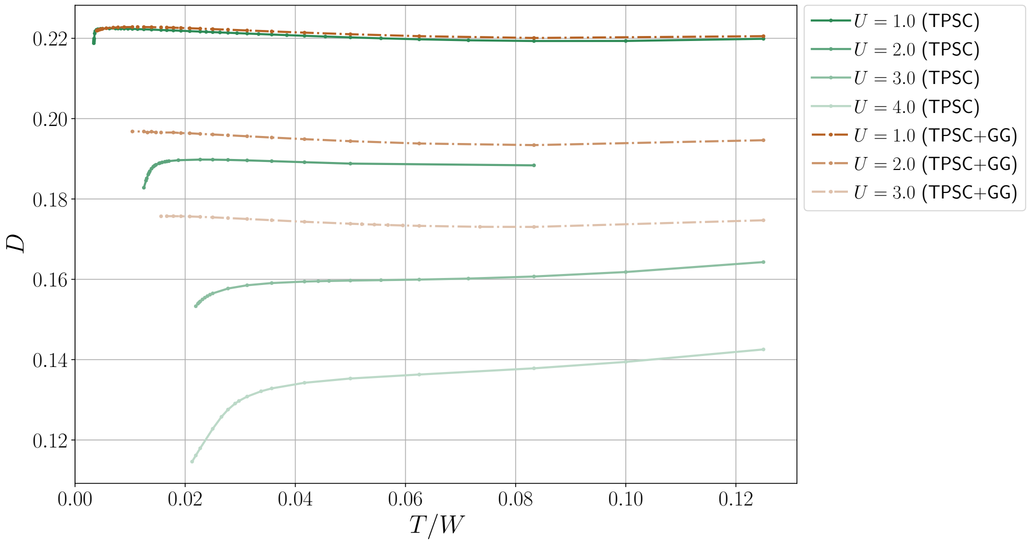

Figure 6.18: TPSC (bold lines) and TPSC+GG (dotted lines) double occupancy extracted from the local ansatz (5.54) as a function of bandwidth-normalized temperature for various U. The 2D half-filled nearest-neighbor Hubbard model was used.

from the splitting of the spectral weight about $\omega = 0$. The spin fluctuations destroy the Fermi-liquid quasiparticles above the zero-temperature phase transition in 2D (TPSC fulfils the Mermin-Wagner theorem) [152]. To observe the AFM pseudo-gap in the spectral function near the Fermi level, one needs to dress the nonlocal Green's function with the TPSC self-energy (5.70). In the bottom panel of Fig. 6.19, the Matsubara component of the dressed Green's function for the filling of $n = 0.4375$ is shown at the Fermi surface ($\mathbf{k}_F = (0, \pi)$). The results of the lower panel of Fig. 6.19 can be compared with Ref. [145] (left panel of Fig. 1), whereas the top panel can be compared with Ref. [152] (Fig. 9).

A great asset to TPSC lies in the fact that it captures nonlocal correlations, essential when approaching phase transitions and crossovers. The reciprocal-space dependence of the self-energy over the original Brillouin zone allows one to nail down ordering mechanisms that can build up at different momenta $\mathbf{k}$. To better grasp the reciprocal structure of the spin and charge susceptibilities, the *lesser* spectra of the charge (top panels) and spin (bottom panels) susceptibilities for $U = 1$ (left panels) and $U = 3$ (right panels) is plotted in Fig. 6.20 at equilibrium for TPSC. To clarify on how the spectra $\chi^{\text{ch/sp}}$ are calculated, a given time window Δt was used in the forward Fourier transform (2.67) and the results depend on the frequency resolution used ($\Delta\omega \equiv 2\pi/\Delta t$) – this should however change only very slightly the results, if recognizable. The same information is displayed in Fig. 6.21 for TPSC+GG. In the top right corner of the top panels of Fig. 6.20 are drawn triangles that represent the wedge of the irreducible Brillouin zone of the square lattice. Walking across the triangle in the direction of the arrows corresponds to the momentum figuring on the y-axis of the panels from top to bottom, with $\mathbf{k} = (0,0)$ the starting point (in green). At $U = 3$, the difference between the charge and spin spectra is more obvious than at $U = 1$: the charge susceptibility features an excitation gap away from $\mathbf{k} = (0,0)$, while the spin response is marked by predominant weight around

The code used to calculate the irreducible Brillouin zone was written in the Julia programming language and it is inspired from Ref. [61].

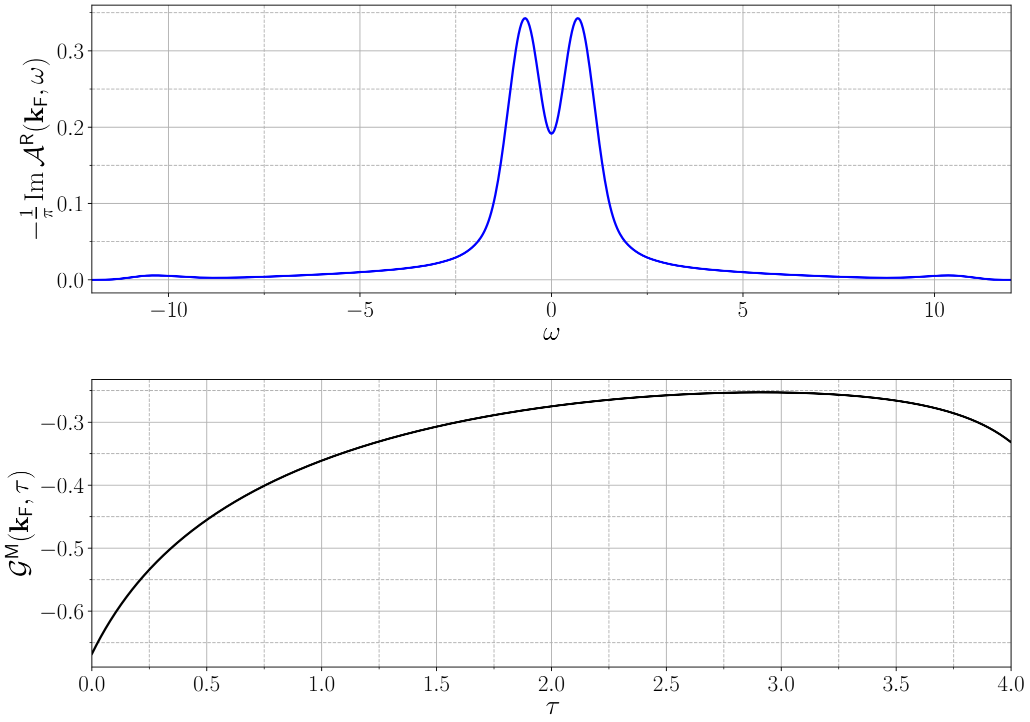

Figure 6.19: Top panel: TPSC electronic spectral density of the 2D model for spin-density $n = 0.5$ and the Fermi surface momentum $\mathbf{k}_F = (0, \pi)$. The bare interaction is $U = 4$ and the inverse temperature $\beta = 5.88$ ($T = 0.17$). Bottom panel: TPSC Matsubara Green's function for $n = 0.4375$ for the 2D model and the Fermi surface momentum $\mathbf{k}_{\mathrm{F}} = (0, \pi)$. The bare interaction is $U = 4$ and the inverse temperature $\beta = 4$. These results can be compared with Fig. 9 in Ref. [152] (top panel) and the left panel of Fig. 1 in Ref. [145] (bottom panel). Since the calculations are implemented on the Kadanoff-Baym contour, spectral functions can be calculated directly by Fourier transformation, *i.e.* without analytical continuation.

$\omega \simeq 0$ in the vicinity of $\mathbf{k} = (\pi, \pi)$. At $U = 1$, the charge and spin susceptibilities look more alike and this is explained by the fact that by decreasing the Hubbard interaction, both the spin and charge response functions approach the Lindhard function (5.65) for the square lattice [31]. In Fig. 6.21, the spin and charge *lesser* spectra are shown keeping the same layout as Fig. 6.20. The spectra calculated from TPSC+GG is remarkably smeared out when compared to these obtained from TPSC, especially in the case where $U = 3$. Moreover, the intensity of the spectra is diminished in TPSC+GG due to its smearing. For the rest, the same observations can be made with TPSC and TPSC+GG. In both the TPSC and TPSC+GG calculations, the spectra of the *lesser* spin and charge susceptibilities roughly span over the bandwidth $W = 8t^{\mathrm{hop}}$, with the largest extent at $\mathbf{k} = (\pi, \pi)$. However, in general, the spin-spin excitation spectra covers a larger energy window with sizeable amplitude compared to the charge susceptibility.

Not only the charge χ^{ch} and spin χ^{sp} susceptibilities (5.64) are defined over the full original Brillouin zone, but so are the second-level self-energy and interacting single-particle Green's function by extension due the facts that $\Sigma^{(1)}$ (5.70) depends on $\chi^{\mathrm{ch/sp}}$ and $\mathcal{G}^{(1)}$ depends on $\Sigma^{(1)}$. In Fig. 6.22 are shown, using

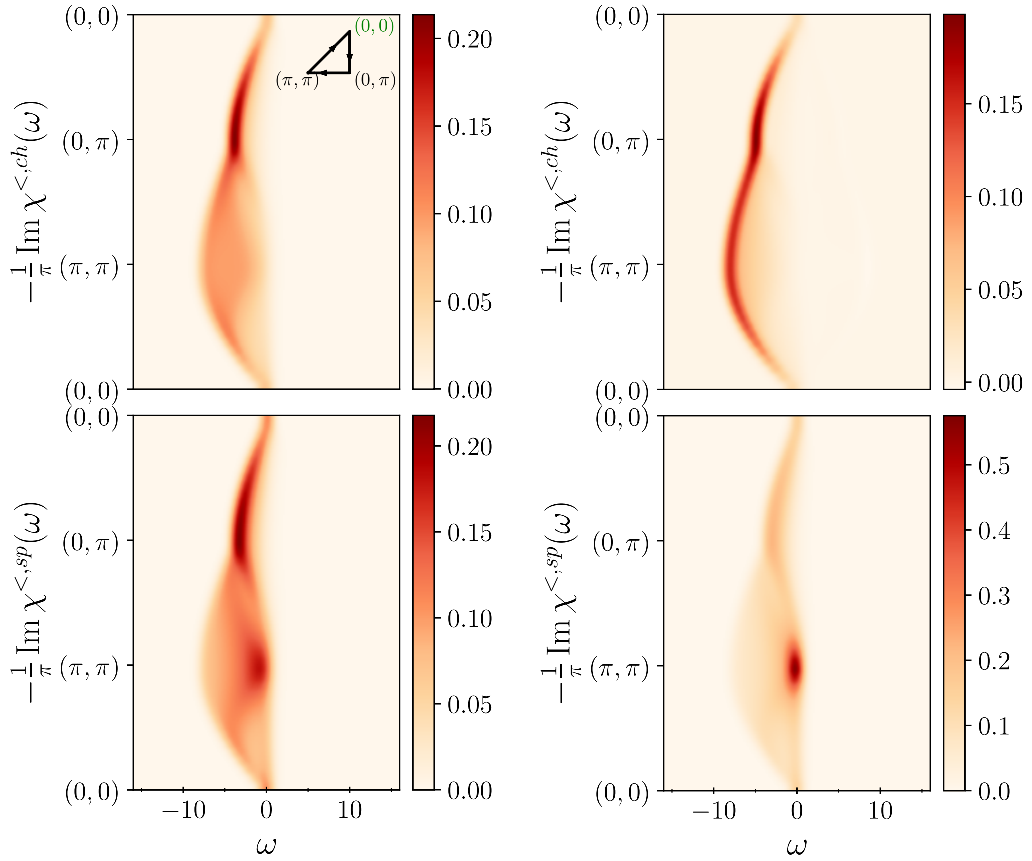

Figure 6.20: The imaginary parts of the *lesser* component of the charge (top panels) and spin (bottom panels) susceptibilities, obtained using TPSC in 2D. The left (right) panels show the equilibrium spectra for $U = 1$ ($U = 3$). The inverse temperature is $\beta = 3$. The time window used for the Fourier transform is $\Delta t = 5$.

TPSC, the second-level self-energy $\Sigma^{\text{TPSC},(1)}$ (top panels) and the Green's function $\mathcal{G}^{(1)}[\Sigma^{(1)}]$ (5.66) (bottom panels) along the wedge of the irreducible Brillouin zone for $U = 1$ (left panels) and $U = 3$ (right panels). Again, the square lattice Hubbard model at half-filling is used. For the two interactions U, the self-energy shows a predominant clustering of the spectra in the vicinity of the AFM wave vector $\mathbf{k}_\pi = (\pi, \pi)$, although this is more visible for $U = 3$. At $\mathbf{k}_\pi$, the self-energy features significant weighing for an energy window of about the bandwidth W, which is the largest among all the $\mathbf{k}$-points. Notice that the overall amplitude of $\Sigma^{(1)}$ grows substantially at $U = 3$ when compared to $U = 1$. Now moving on to the $\mathbf{k}$ description of the single-particle Green's function $\mathcal{G}^{(1)}$, one can immediately notice a spectral gap between $\mathbf{k} = (0, \pi)$ and $\mathbf{k} = (\pi/2, \pi/2)$ because these momenta lie at the Fermi surface. The amplitude of the spectral weight is clearly reduced and spread out in energy when the local interaction U is increased. Additionally, the effect of the intensified interaction makes the spectra stretch out further along $\mathbf{k}$ into the excitation gap.

Notice that the colorscale changes on every colormap panel.

The Figure 6.22 can also be produced using TPSC+GG; this is what is done in Fig. 6.23. Both TPSC and TPSC+GG display essentially the same features

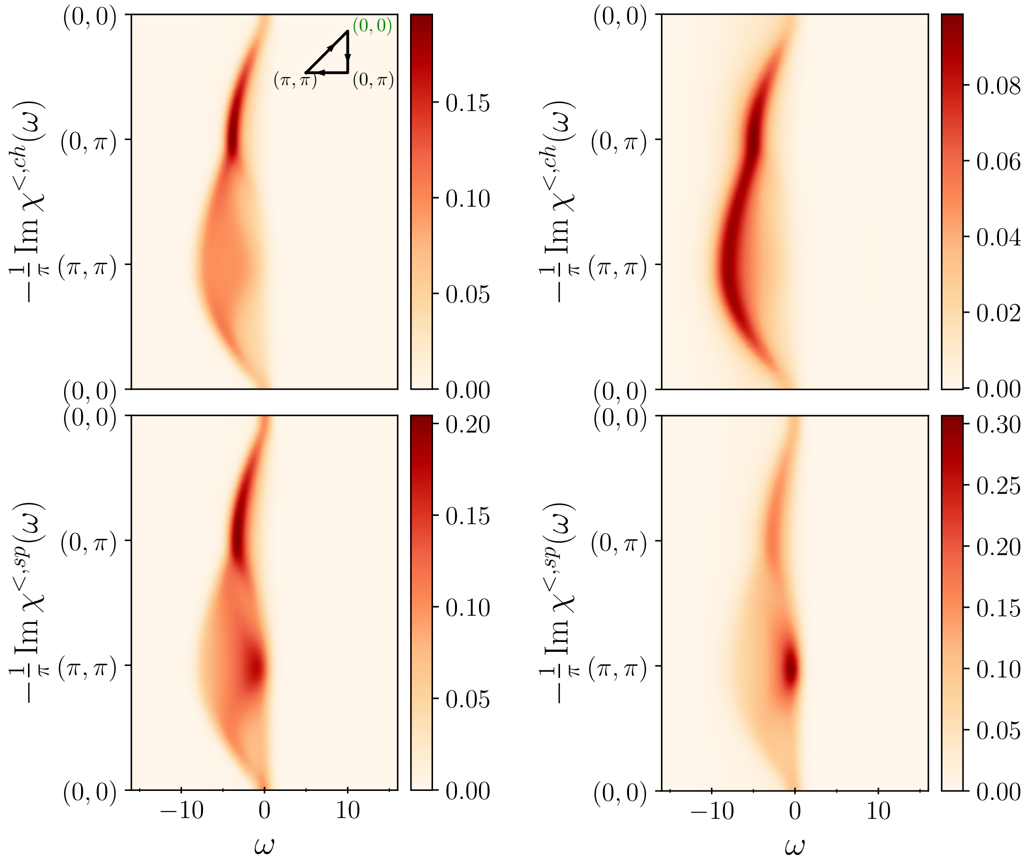

Figure 6.21: Idem to Fig. 6.20 for TPSC+GG.

through $\Sigma^{(1)}$ and $\mathcal{G}^{(1)}$. Especially, at low interactions ($U=1$), TPSC and TPSC+GG give very similar self-energies and single-particle Green's functions on all aspects. Although, for larger $U \simeq W/2$, the TPSC+GG self-energy is much more spread out over the energy and momentum axes and the features start melting away. Nevertheless, the spectral weight remains clustered around $\mathbf{k}_{\pi}$. On the other hand, the Green's functions at $U=3$ for both TPSC and TPSC+GG are quantitatively very similar.

Let's now shift the focus to the effects of electron/hole doping and the turning-on of t'_{hop} on the spin and charge correlations. Incidentally, changing the electron densities and band structures affects the chemical potential μ. In Fig. 6.24, the equilibrium spectra difference for various quantities between the densities $n=1$ and $n=1.15$ is shown for the nearest-neighbor Hubbard model. The chemical potential μ is normalized with the Hartree self-energy, such that half-filling ($n=1$) corresponds to $\mu=0$ and $n=1.15$ corresponds to $\mu \simeq 0.377$. The temperature is $T=0.33$ ($\beta=3$) and $U=3$. Denoting the spectrum of the quantity in question $Q(n)$, the spectral difference on the y-axes reads $\Delta Q \triangleq Q(n=1.0) - Q(n=1.15)$. Hence, all the panels composing Fig. 6.24 illustrate the evolution of the spectra upon decreasing the electronic chemical potential μ (doping in holes). Like explained previously, the $\mathbf{k}$ points are placed on the triangle enclosing the irreducible Brillouin zone following the arrows. The colormap is normalized such that the white color corresponds to zero difference, with blue representing spectral removal and red spectral addi-

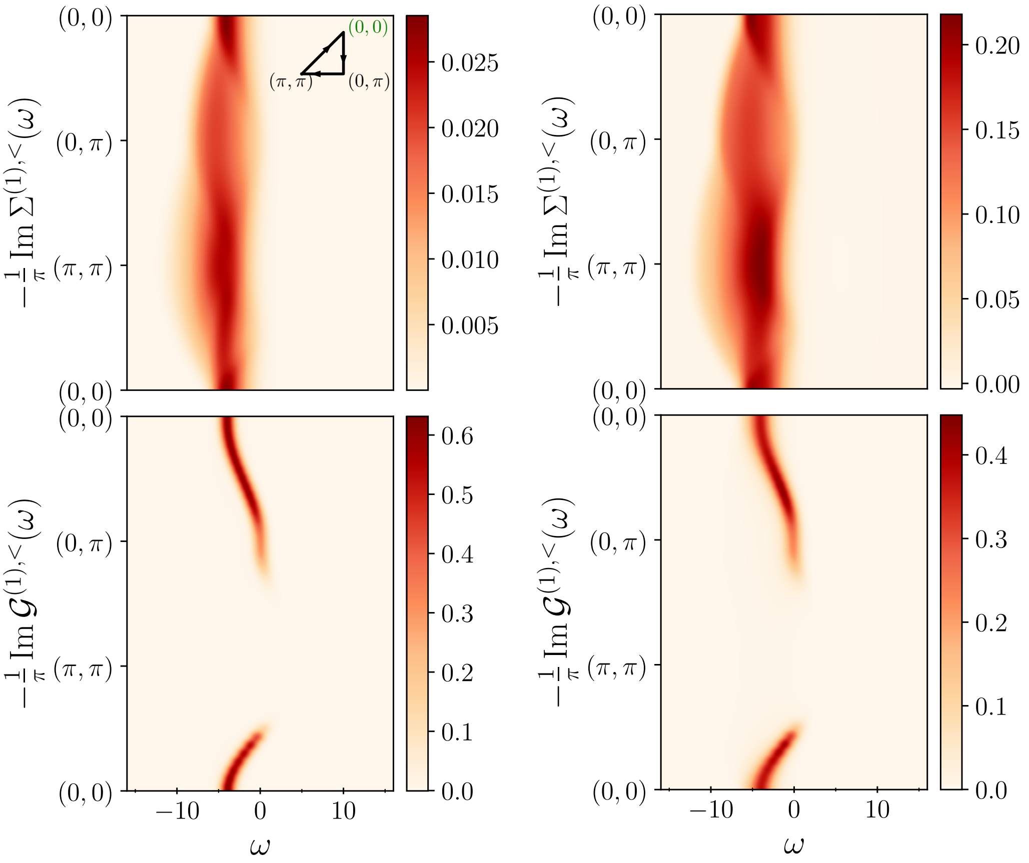

Figure 6.22: The imaginary parts of the *lesser* component of the second-level self-energy (top panels) and Green's function (bottom panels), obtained using TPSC. The left (right) panels show the equilibrium spectra for $U = 1$ ($U = 3$). The inverse temperature is $\beta = 3$. The time window used for the Fourier transform is $\Delta t = 5$.

tion. The top left panel displays the difference $\Delta\chi^{\text{ch}}$ and it shows that passing from $\chi^{\text{ch}}(n = 1.15)$ to $\chi^{\text{ch}}(n = 1)$ makes the spectra move to higher energies. At the density $n = 1.15$, the double occupancy is increased since more electrons lie under the Fermi surface and therefore, because of the on-site interaction U, the charge excitations are pushed up to higher energies in absolute values. Moving on to the bottom left panel illustrating the passage from $\chi^{\text{sp}}(n = 1.15)$ to $\chi^{\text{sp}}(n = 1)$, one can see that the spin-spin correlations are enhanced in the vicinity of $\mathbf{k} = (\pi, \pi)$. This makes sense, since the Néel temperature is larger at half-filling for any fixed interaction within the single-band Hubbard model and therefore the AFM correlations build up at larger temperatures. Next, turning to the self-energy exposed on the top right panel, reducing the electronic density increases the single-particle scattering at low energy (absolute value) around $\mathbf{k}_\pi$: this falls in line with the enhancement of the spin susceptibility around the AFM wave vector. Finally, in the bottom right panel, the Green's function shows a shift of the Fermi surface because μ decreases from $n = 1.15$ to $n = 1$. As a result, less electronic momenta lie underneath the Fermi surface. The same observations would apply had the TPSC+GG results been shown instead.

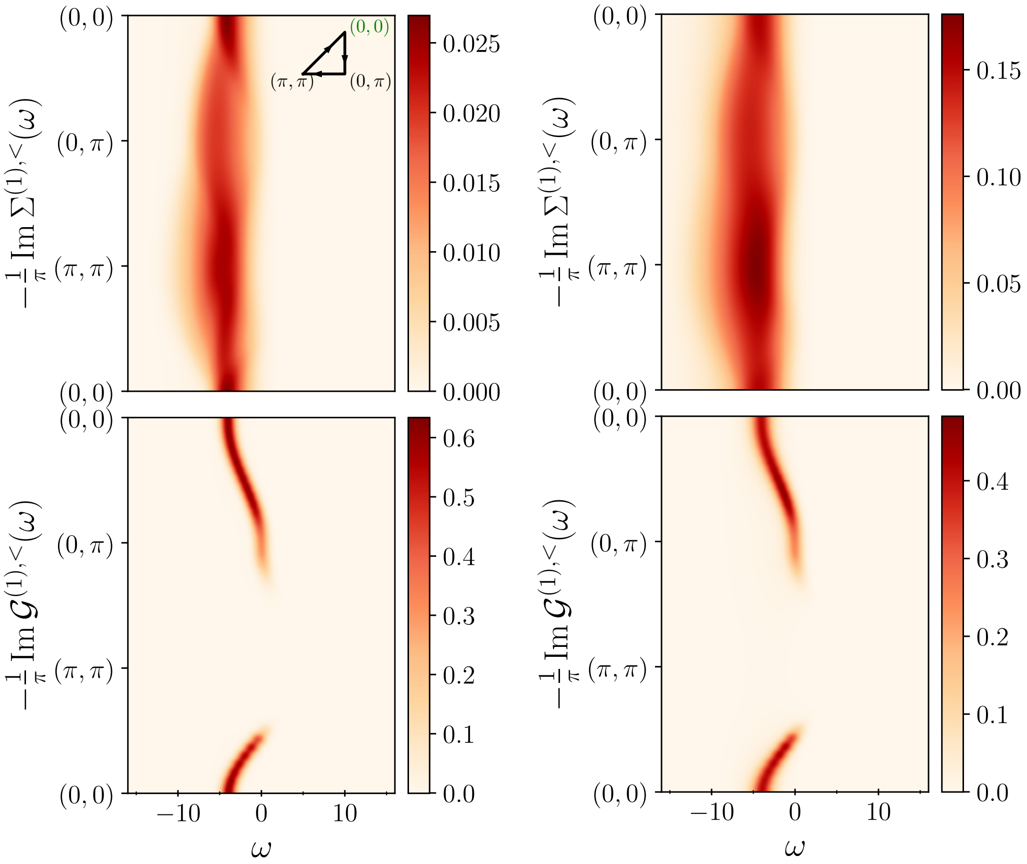

Figure 6.23: Idem to Fig. 6.22 making use of TPSC+GG.

To follow up on Fig. 6.24, the equivalent is shown in Fig. 6.25 using TPSC by fixing the density to $n = 1.15$, but varying the next-nearest-neighbor hopping t'_{hop} defined in Eq. (6.2) from $t'_{\text{hop}} = -0.275 t_{\text{hop}}$ to $t'_{\text{hop}} = 0$. When the nearest-neighbor hopping is normalized to 1 ($t_{\text{hop}} = 1$), the band structure crossing the Fermi level matches the tight-binding calculations of the electron-doped superconducting cuprates $\text{Nd}_{2-x}\text{Ce}_x\text{CuO}_4$ (NCCO) [76]. In the case presented in Fig. 6.25, even though the density is fixed, the chemical potential changes since the topology of the band structure does – the chemical potential becomes $\mu \simeq -0.077$ in the case where $n = 1.15$ and $t'_{\text{hop}} = -0.275 t_{\text{hop}}$, so it increases when passing from $t'_{\text{hop}} = -0.275 t_{\text{hop}}$ to $t'_{\text{hop}} = 0$. Looking first at the charge susceptibility in the top left panel, one can observe qualitatively the same behavior as that of the top left panel of Fig. 6.24. For the NCCO band structure, the van Hove singularity lies under the Fermi surface making the density of states sharper at around $\omega \simeq -1.01$. This would explain why charge excitations appear at larger absolute values in energies. Turning to the spin fluctuations in the bottom left panel, it features an increased spin response at $\omega \simeq 0$ for many $\mathbf{k}$ points, but especially for $\mathbf{k}_\pi$. This comes around because there is a better AFM nesting on the Fermi surface in the case where there is only the nearest-neighbor hopping term taking part in the dispersion relation. Then, concerning the self-energy, the very many features that move around hinders the analysis. Although, the fact that the difference in the spectra accounts for the disappearance of the van Hove singularity around $\omega \simeq -1.01$ would explain why

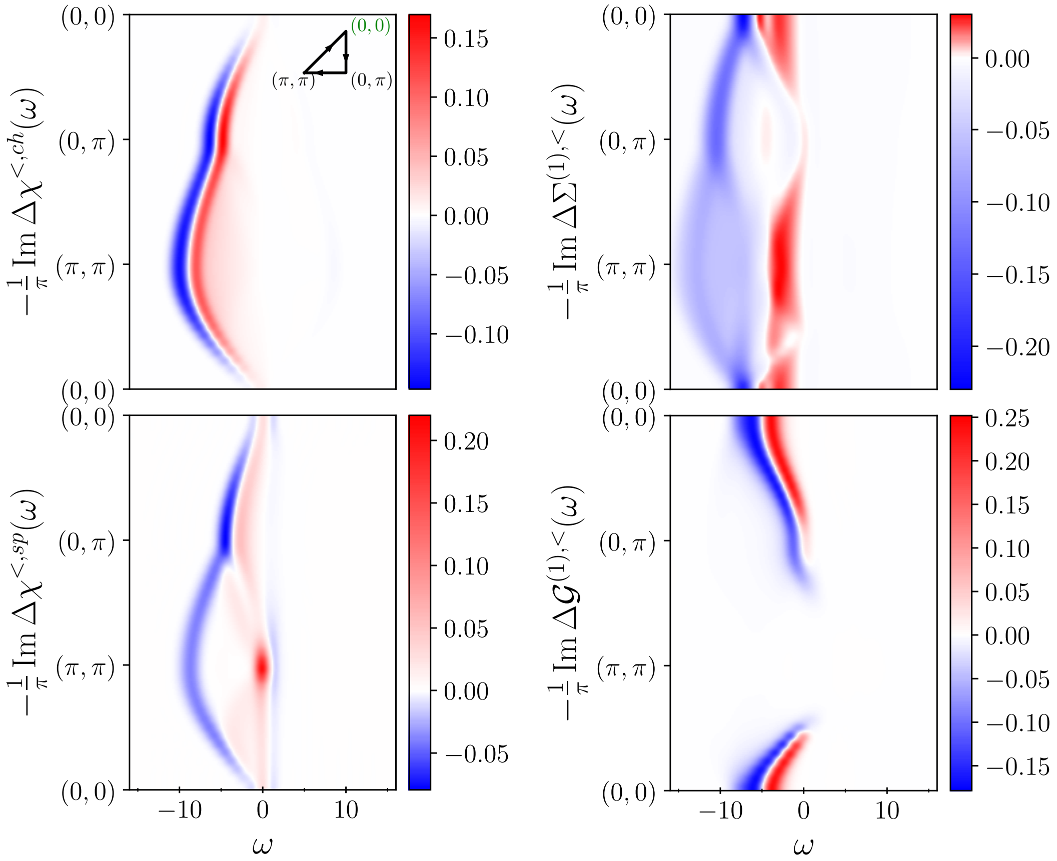

Figure 6.24: Spectra difference of various quantities Q between $Q(n=1)$ and $Q(n=1.15)$ at $T=0.33$ and $U=3$ in the nearest-neighbor Hubbard model calculated within TPSC. The *lesser* component is shown. The charge susceptibility is shown in the top left panel, the spin susceptibility in the bottom left panel, the second-level TPSC in the top right panel and the single-particle Green's function $\mathcal{G}^{(1)}$ in the bottom right panel. The time window $\Delta t=5$.

the spectra just below $\omega \simeq 0$ is reduced for all $\mathbf{k}$ points. Let's finish with the Green's function spectra shown in the bottom right panel. The band structure below the Fermi level is flattened out in NCCO and this explains why the blue areas cover less energies (it is more filiform).

To carry on with the equilibrium comparisons and understand how the different methods considered in this thesis capture the correlations, the first Matsubara frequencies of the self-energy at the antinode $\Sigma^{(1)}(\mathbf{k}=(0,\pi);i\omega_n)$ (see Eq. (2.37)) are illustrated in Fig. 6.26 for the original TPSC formulation (OG TPSC), TPSC, TPSC+GG, DMFT+TPSC, DMFT+TPSCα and DiagMC. The temperature used is $T=0.33$ ($\beta=3$) and the model used is the square lattice Hubbard model. The exact same equilibrium comparison involving the same set of methods is illustrated in Fig. 6.27 with the sole difference that the temperature is now $T=0.1$ ($\beta=10$). To remind oneself, OG TPSC does not fulfil the sum-rule relating the first- and second-level TPSC approximations (5.71). Comparing the results of Figs. 6.26 and 6.27 with the "TPSC" (which means "OG TPSC" in our notation) panel in Fig. 10 of Ref. [110], one can notice that TPSC+GG (green curves) improves the self-energy substantially by almost overlapping completely with the numerically exact stochastic DiagMC method

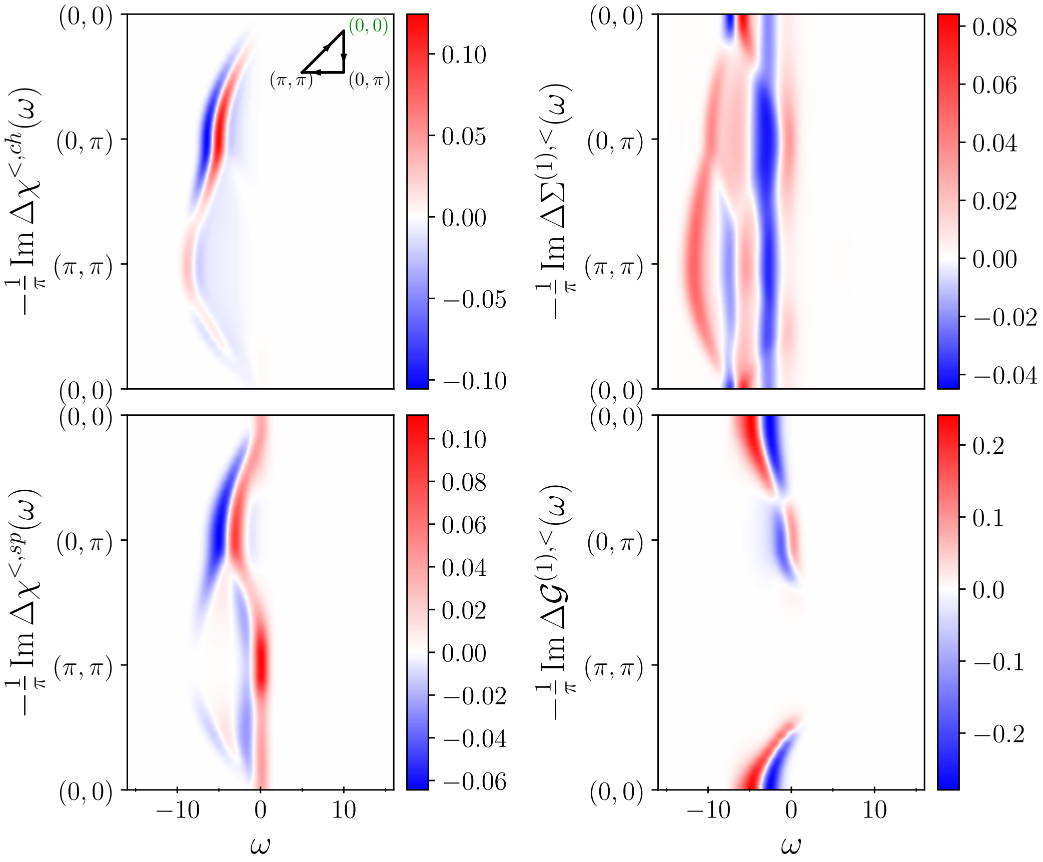

Figure 6.25: Spectra difference of various quantities Q between $Q(t'_{\text{hop}} = 0)$ and $Q(t'_{\text{hop}} = -0.275)$ at $T = 0.33$ and $U = 3$ in the Hubbard model calculated within TPSC. The *lesser* component is shown once again. The quantities are placed in the same way as in Fig. 6.24. The time window $\Delta t = 5$.

(black curves). Both DMFT+TPSC (orange curves) and DMFT+TPSCα (blue curves) come in great agreement at $T = 0.33$ with TPSC+GG and DiagMC. In fact, the DMFT+TPSC and DMFT+TPSCα antinodal self-energies follow very closely that of TPSC+GG except for the very last Matsubara frequency: the system would be more metallic in the DMFT+TPSC schemes. The TPSC (red curves) self-energy is shifted down by a constant proportional to α (see Eq. (5.70)) with respect to that of the OG TPSC (cyan curves). Even though TPSC worsens the antinodal self-energy results, since TPSC+GG also uses the parameter α and agrees very well with DiagMC, the lack of self-consistency seems to be the problem. At lower temperatures like $T = 0.1$ shown in Fig. 6.27, TPSC+GG seems to win out over all the other methods. Nonetheless, DMFT+TPSC and DMFT+TPSCα follow qualitatively the trend of the self-energy results produced by TPSC+GG and DiagMC, whereas it is not the case for both TPSC and OG TPSC which bend in opposite directions at lower Matsubara frequencies. As will be seen in Section 7.2, even though TPSC+GG seems to win on this matter based off Figs. 6.26 and 6.27, it is not the case out of equilibrium when evaluating local quantities such as the impurity double occupancy (5.99) – the same goes for the comparison between OG TPSC and TPSC. Furthermore, the DMFT+TPSC schemes and TPSC+GG allow one to access lower temperature

The one-time function α is most of the time of the order of 1, except in sharp and large interaction ramps.

results alleviating the convergence problems creeping up in TPSC and OG TPSC in the vicinity of T_x (crossover temperature of the renormalized classical regime). The temperature behavior of DMFT+TPSC will be broached in Section 6.2.2. It is worth mentioning that the non-self-consistent TPSC+DMFT scheme introduced in Ref. [89] matches well the DiagMC data, although less accurately than TPSC+GG.

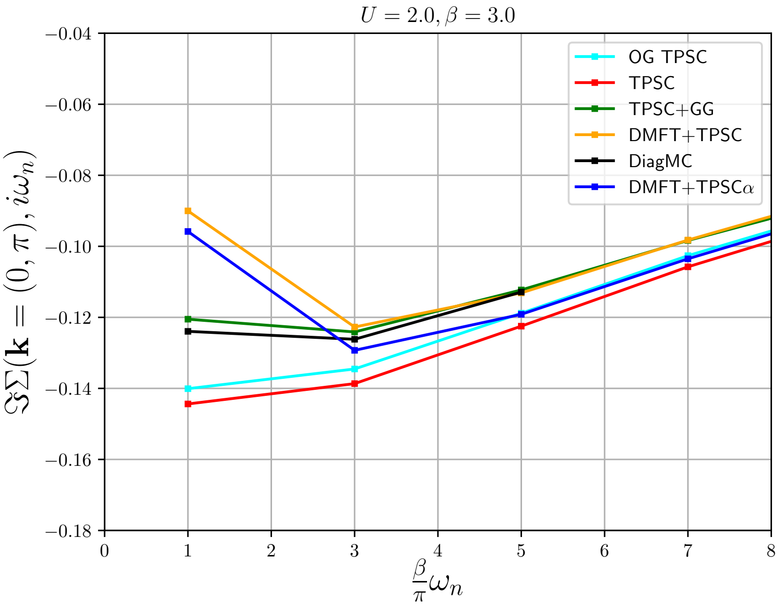

Figure 6.26: Imaginary part of the Matsubara self-energy at the antinode ($\mathbf{k} = (0, \pi)$) for various methods (listed out in the legend) at $T = 0.33$ ($\beta = 3$) and $U = 2$ in the half-filled Hubbard model. The first several Matsubara frequencies are shown. This figure can be compared with the "TPSC" – which corresponds to OG TPSC in this thesis – panel in Fig. 10 of Ref. [110].

6.2.1.2 *3D*

In this section, TPSC and TPSC+GG are employed to solve 3D systems. The cubic lattice Hubbard model will be of main interest (unless mentioned otherwise), although the code has been implemented so as to deal with other band dispersions, namely the face-centered cubic, body-centered cubic and tetragonal unit-cells. In the case of the simple cubic unit-cell, the bandwidth $W = 12t^{\text{hop}}$. This consequently means that a wider range of interaction values U will lead to converged results (in TPSC+GG), and that for same U, as long as $U \leq 4$, the 3D results will stretch out to lower temperatures than in the 2D case before hitting T_x. The modified cubic lattice dispersion relation of concern reads

The energy reference is still the nearest-neighbor hopping term in the 3D case: the interaction and bandwidth are normalized to t^{hop}.

$$\epsilon(\mathbf{k}) = -2t^{\text{hop}}\left(\cos k_x + \cos k_y\right) - 2t_z^{\text{hop}}(t)\cos k_z, \tag{6.3}$$

where t_z^{hop} is the time-dependent out-of-plane lattice hopping energy sticking out in 3^{rd} dimension.

In Fig. 6.28, the α parameter relating the second- and first-level TPSC self-energy approximations via the sum-rule exposed in Eq. (5.71) is shown for

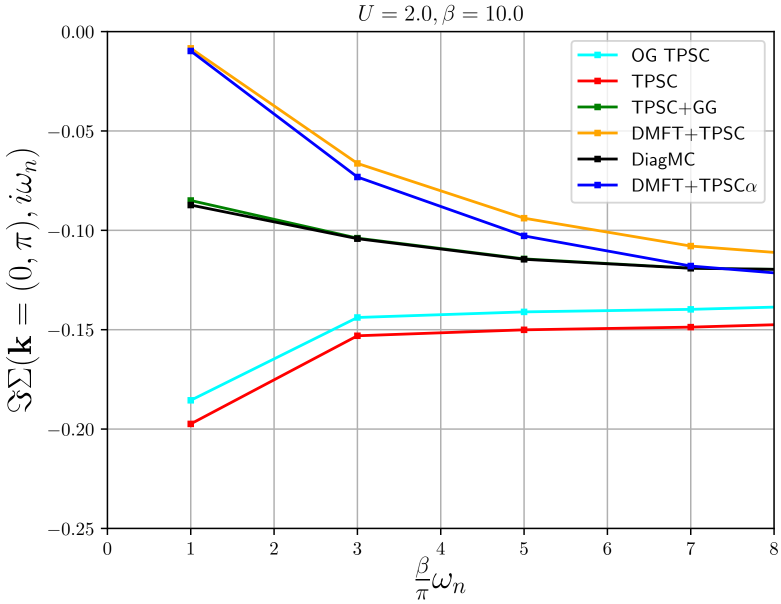

Figure 6.27: Imaginary part of the Matsubara self-energy at the antinode ($\mathbf{k} = (0, \pi)$) for various methods (listed out in the legend) at $T = 0.1$ ($\beta = 10$) and $U = 2$ in the half-filled Hubbard model. This figure can also be partly found in Fig. 10 of Ref. [110].

different U values as a function of normalized temperature. The vertical lines identify the normalized temperatures at which the spin vertices start shooting up in Fig. 6.32. For all interactions, the α parameter stays constant for a wide range of T/W until it starts shooting up. This further renormalization of the vertices $\Gamma^{\text{sp/ch}}$ comes about when the static spin susceptibility starts shooting up as well (see Fig. 6.29). The values of this renormalization are always modestly larger than 1, meaning that the original TPSC formulation (OG TPSC), which does not enforce Eq. (5.71), underestimates the amplitude of the interactions by some constant factor (in equilibrium). Note that in the nonequilibrium setting, this α-factor will acquire some nontrivial time-dependence that improves the conservation rules, nonthermal properties and the overall stability of the method.

The 3D irreducible vertices Γ^{sp}/W and Γ^{ch}/W are compared with those of the 2D square lattice system in Fig. 6.13 as a function of U/W. To follow up on Fig. 6.14, the static spin susceptibility is traced out as a function of T/W in Fig. 6.29 at the highest symmetric point in the cubic lattice reciprocal space, *i.e.* $\mathbf{k}_\pi = (\pi, \pi, \pi)$, for both TPSC and TPSC+GG. In Fig. 6.29, the 3D case corresponds to half-filling for the cubic lattice nearest-neighbor Hubbard model. Even though the AFM nesting of the scattering wave vector is better in the 2D Hubbard model because of the diamond-shaped AFM Brillouin zone [118], the 3D cubic lattice does capture in a very similar fashion the spin correlations; in fact, as will be seen in Fig. 6.30, these spin-spin excitations tightly cluster around $\mathbf{k}_\pi$ in 3D and smear out less than in 2D. Moreover, in 3D, the spin correlations seem to be captured in greater amount at low temperatures for TPSC+GG: the upturns are quite similar to those appearing in the TPSC results.

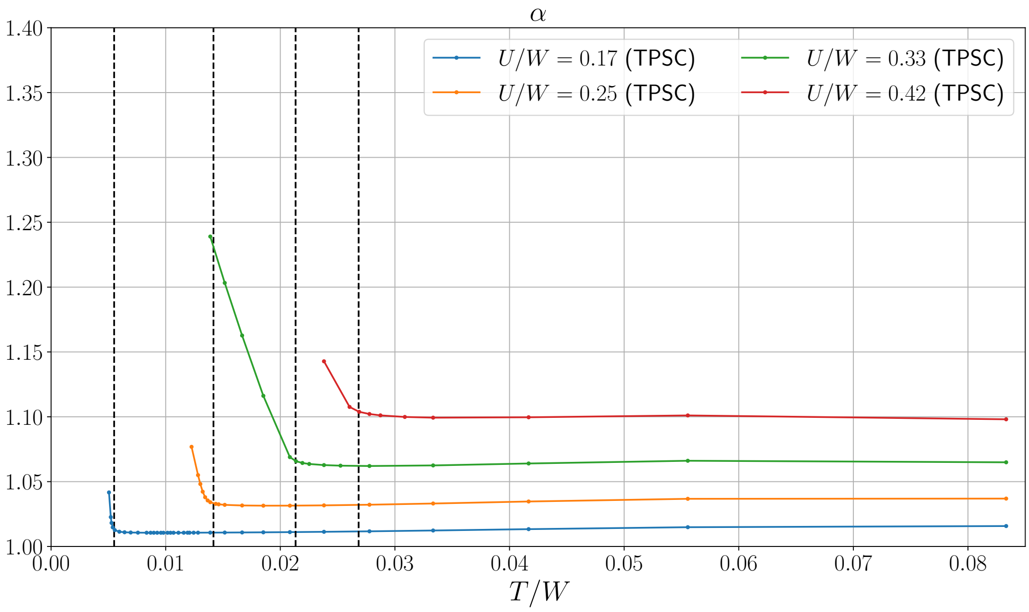

Figure 6.28: Dynamical renormalization parameter of the irreducible vertices α (5.70) as a function of normalized temperature for different interactions. The results are for the 3D single-band half-filled nearest-neighbor Hubbard model. The vertical lines mark the downturn of Γ^{sp} in Fig. 6.32.

In Fig. 6.30, the **k**-defined susceptibilities $\chi^{\mathrm{sp/ch}}$ (left panels), as well as the single-particle spectra (right panels), are shown for $U = 3$ and $T = 0.2$. The excitation spectra of the charge susceptibility (top left panel) span over a wider energy window as compared to the 2D scenario, because the wider 3D bandwidth permits density-density interactions at larger absolute energy values – even more so when the interaction in cranked up. The charge susceptibility excitation spectra appears also more smeared out than, for instance, that shown in Fig. 6.21 in the top right panel. At lower temperatures, Γ^{ch} grows larger and $T = 0.2$ ($T/W \simeq 0.017$) sits close to the renormalized classical regime where Γ^{ch} and Γ^{sp} are split further apart; this phenomenon was discussed in the context of Fig. 6.16 for the 2D model and this applies to the 3D scenario. Turning to the spin-spin correlation function in the bottom left panel of Fig. 6.30, the excitation profile is strikingly focalized around $\mathbf{k}_\pi$, overshadowing the contributions from other momenta (*cf.* Fig. 6.21, lower right panel). This difference lies mainly in the fact that the temperature $T = 0.2$ at $U = 3$ ($T/W \simeq 0.017$ at $U/W = 0.25$) in 3D is located closer to the upturn in the spin static susceptibility (Fig. 6.29) than it is the case for $T = 0.33$ at $U = 3$ ($T/W = 0.04125$ at $U/W = 0.375$) in 2D (Fig. 6.14).

Then, looking at the second-level TPSC self-energy in the top right panel of Fig. 6.30, one can see a clear dominating self-energy contribution at $\mathbf{k}_\pi$ which boosts the AFM spin correlations in χ^{sp}, like what was observed in 2D (Fig. 6.23). The cut at $k_z = \pi$ in the reciprocal space features a large gap in the single-particle spectra because at that momentum, a disk-shaped hole pocket makes up the Fermi surface centered at the Γ-point[3] and it has a large radius, therefore it does not contain a large amount of momenta below the Fermi level.

---

[3] The Γ-point is the highest symmetry point in reciprocal space.

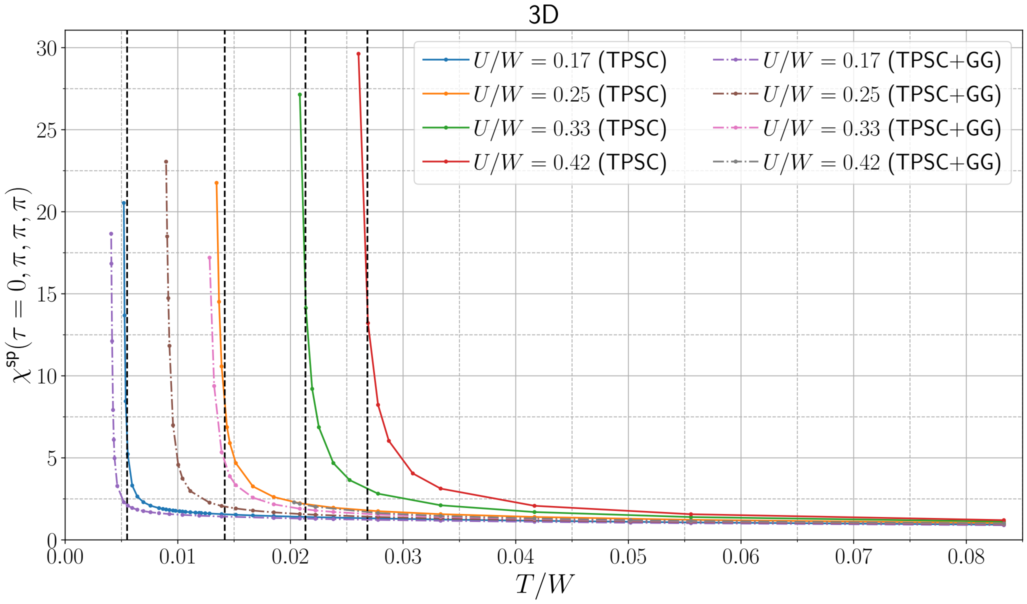

Figure 6.29: Static spin susceptibility of the 3D model at momentum $\mathbf{k}_\pi = (\pi, \pi, \pi)$ as a function of normalized temperature for interactions $U = 2, 3, 4$ and 5 using both TPSC (bold lines) and TPSC+GG (dotted lines). The filling per spin is $n = 0.5$. The interactions strengths in the legend are normalized by the bandwidth W. The vertical lines are identical as in Fig. 6.28.

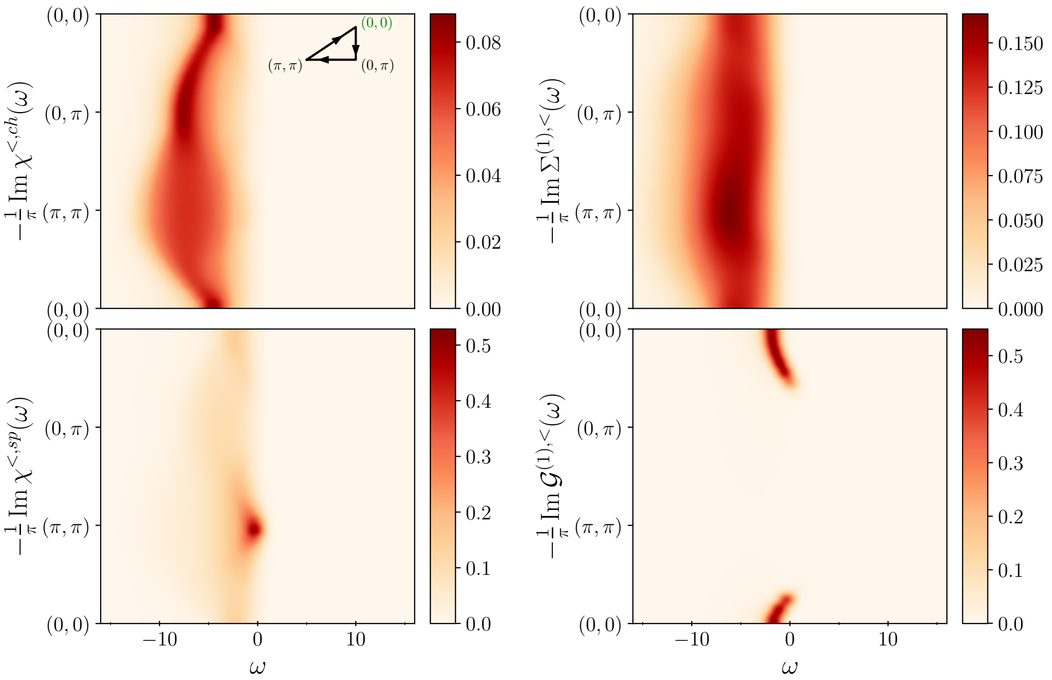

Figure 6.30: Left panels: *lesser* charge (top panel) and spin (bottom panel) susceptibilities. Right panels: second-level TPSC self-energy (top panel) and single-particle Green's function ($\mathcal{G}^{(1)}$) (5.66) spectra (bottom panel). The calculations were performed using TPSC+GG at half-filling for the cubic lattice at $T = 0.2$ and $U = 3$. The wedge of the irreducible Brillouin zone cuts along $k_z = \pi$; the path runs along within that plane. The time window employed for the Fourier transforms is $\Delta t = 5$.

Remember that since TPSC and variants make use of the spin rotational symmetry in its derivation, only the growth of spin correlations can be picked up, but not the spontaneous symmetry-breaking.

As underlined by Fig. 6.13, both the charge and spin vertices drift at a larger pace from each other with respect to U in 3D. In Fig. 6.31, the temperature dependence of the vertices calculated with TPSC+GG for various interaction strengths is plotted, so as to directly compare with Fig. 6.16 showing the same quantities in 2D. It is noticeable that the vertices display a distinct temperature dependence in 3D: in the charge channel, the charge vertex admits a maximum halfway through temperature ($T/W \approx 0.0417$) while the 2D charge vertex increases nonstop with decreasing T/W. Nevertheless, the temperature dependency of Γ^{sp} is quite similar to that in 2D. For TPSC+GG, at lower temperatures in the vicinity of (normalized) T_x, a hint of an upturn appears in Γ^{ch}, while in the case of TPSC (Fig. 6.32) a much more pronounced upturn in Γ^{ch} appears. On the other hand, Γ^{sp} indicates a sharp downturn close to the renormalized classical regime meaning that Γ^{ch} and Γ^{sp} split further apart since the double occupancy extracted from the ansatz (5.54) gets suppressed in that region, especially in the case of TPSC (Fig. 6.32). Notice the fact that the static spin susceptibility at $\mathbf{k}_\pi$ computed in 3D using TPSC+GG shoots up at lower temperature (see Fig. 6.29) while Γ^{ch} and Γ^{sp} at low T (top panel of Fig. 6.31) behave relatively steadily. However, as will be seen further down below, the vertices display significant changes in TPSC in the temperature range where $\chi^{\text{sp}}(\tau = 0, \mathbf{k}_\pi)$ shoots up in Fig. 6.29. The black vertical lines mark the temperature regime where the irreducible vertices drift apart from each other, entering the classical renormalized regime.

In Fig. 6.32, the temperature dependence of the vertices is also plotted for TPSC using the same model parameters as those used in Fig. 6.31, and the same scale on the y-axis to facilitate comparisons. One can compare how correlations build up when the renormalized classical regime is approached in the two methods (TPSC and TPSC+GG). Strikingly, in the case of TPSC, both Γ^{ch} and Γ^{sp} are mirror reflexions to each other about the temperature axis. Looking back at Fig. 6.31, in the charge channel, the charge vertex exhibits a maximum around $T \approx 0.5$, while it is not the case for TPSC (Fig. 6.32). The latter would be related to the fact that the upturn occurs at significantly higher T in TPSC than in TPSC+GG. The sudden decrease of Γ^{sp} at the lowest T (bottom panel of Figs. 6.31 and 6.32) coincides with the sharp upturn at lower temperature of the static spin susceptibility presented in Fig. 6.29, as can be assessed from the position of the black vertical lines. The decrease in Γ^{sp} stems from the decrease of the double occupancy via Eq. (5.54), which in turn implies a growth in the charge scattering Γ^{ch}. In 3D, as seen in Fig. 6.29, the shooting-up of the static spin susceptibility at $\mathbf{k}_\pi$ at low temperature in TPSC+GG does not coincide with an upturn of Γ^{ch}, like is the case for TPSC (*cf.* Figs. 6.32 and 6.29). To recall, TPSC and its variants make use of the spin rotational symmetry in the derivation, thus only the growth of spin correlations can be picked up and no spontaneous symmetry-breaking can occur. Overall, the 3D temperature dependence of Γ^{sp} is quite similar to that in 2D for TPSC (*cf.* Fig. 6.17).

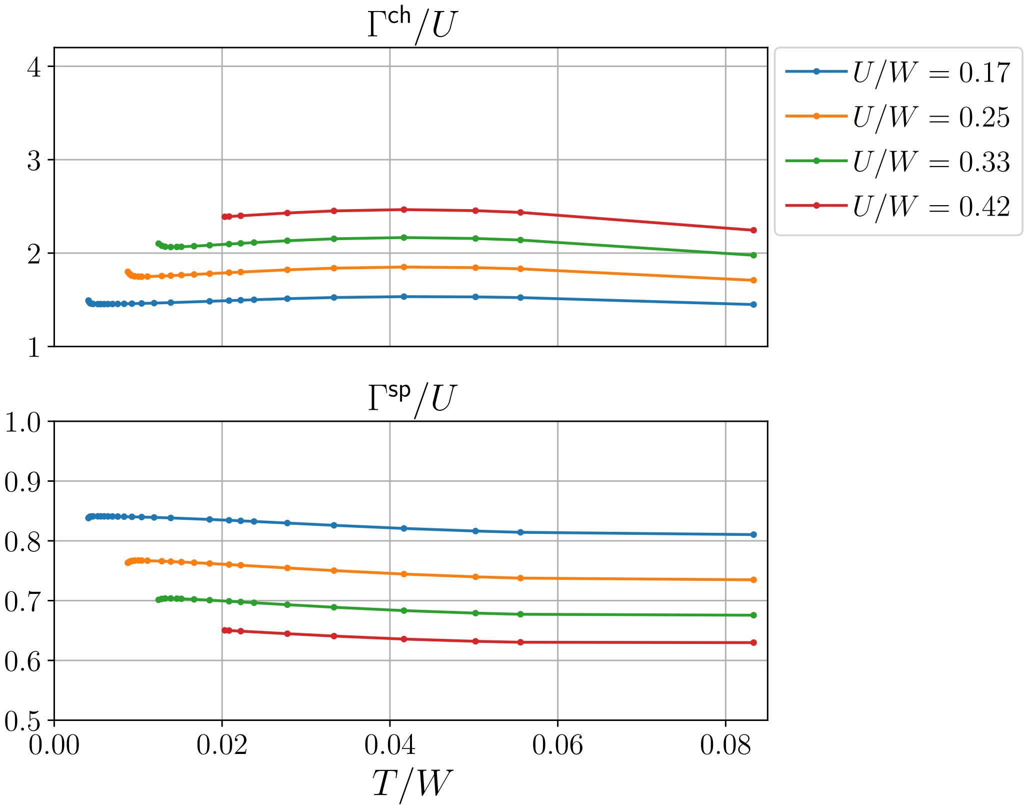

Figure 6.31: Γ^{ch} (top panel) and Γ^{sp} (bottom panel) as a function of T/W for $U = \{2,3,4,5\}$ in the 3D half-filled nearest-neighbor Hubbard model. The values of the vertices are normalized by U for presentation reasons and were obtained using TPSC+GG.

6.2.2 *DMFT+TPSC*

DMFT+TPSC was introduced in Section 5.2.9 and it makes use of the nonlocal TPSC second-level self-energy (5.63) to account for the feedback of the nonlocal correlations on the DMFT impurity. In many aspects, DMFT+TPSC resembles to GW+DMFT [22, 96], although in this case, the second-level TPSC self-energy is not derivable from a Luttinger-Ward functional ensuring a conserving approximation. This DMFT+TPSC scheme replaces the local correlations of the TPSC self-energy assumption with the DMFT ones (see Eq. (5.101)). Hence, when subtracting out the local TPSC self-energy component like in Eq. (5.101), the energy conservation is not guaranteed. As will be touched on later in this section, some internal accuracy checks will enable one to judge the parameter range within which DMFT+TPSC is reliable. The energy conservation issue should be weak for a wide range of weak-coupling results and that would hinge on the fact that Eq. (5.70) reduces to the second-order IPT lattice self-energy (5.67) for small U, and a definite Luttinger-Ward functional exists for $\Sigma^{(2)}$. The scheme exposed in Section 5.2.9 should not be mixed up with those introduced in Refs. [89, 155] which do not add the local correlations in a self-consistent manner. The self-consistency of this DMFT+TPSC scheme improves the stability of the calculations along the KB contour in a similar way as TPSC+GG improves it compared

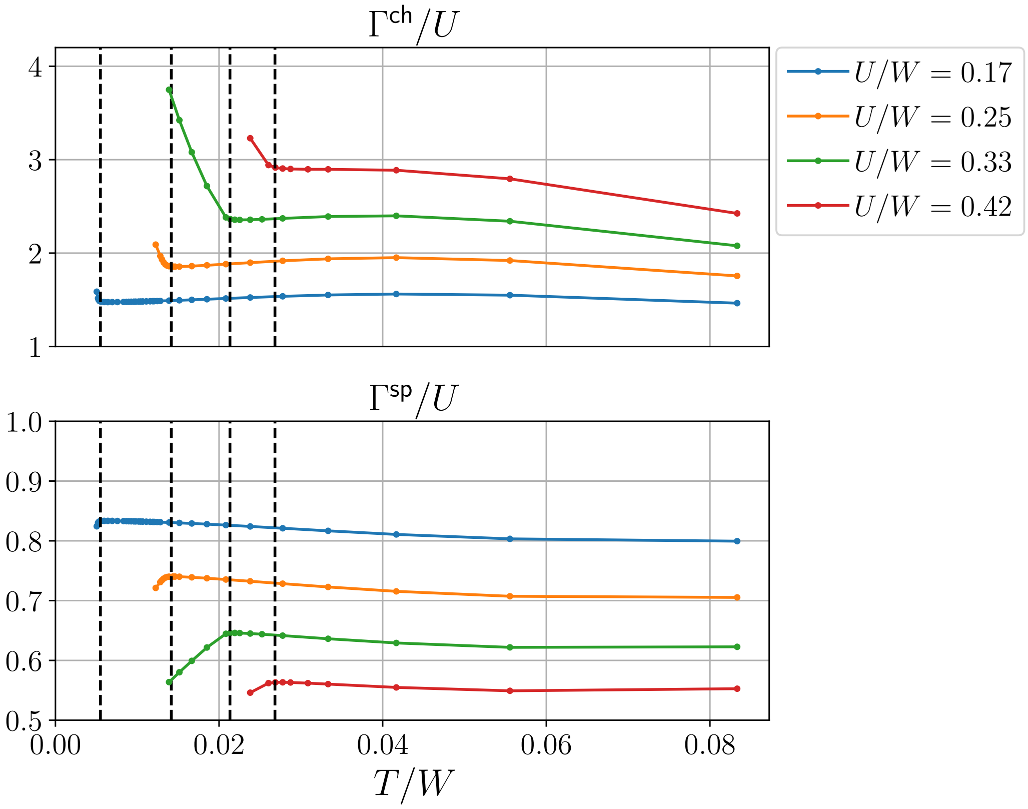

Figure 6.32: Γ^{ch} (top panel) and Γ^{sp} (bottom panel) as a function of T for $U = \{2,3,4,5\}$ in the 3D half-filled nearest-neighbor Hubbard model. The values of the vertices are normalized by U and were obtained using TPSC. The vertical lines are the same as in Fig. 6.29.

to TPSC (see Section 7.2.1). In the following, direct comparisons will be made with the results discussed in Section 6.2.1 for the 2D and 3D cases.

The local two-particle irreducible spin and charge vertices can be computed as well in DMFT+TPSC. Throughout this thesis, weak-coupling IPT impurity solvers (see Section 3.2.1.3) are used to simulate the local impurity interactions. At half-filling, the second-order IPT self-energy is used as impurity solver whereas away from half-filling the third-order self-energy expansion diagrams constitute the DMFT self-energy. In Fig. 6.33, like in Fig. 6.13, the irreducible vertices are plotted as a function of the normalized bare interaction parameter U/W. Comparing both Figs. 6.33 and 6.13, one can clearly identify many qualitative similarities. Γ^{ch}/W and Γ^{sp}/W drift apart with the increase of U/W and this is even more pronounced in the 3D case when compared to 2D. In DMFT+TPSC, both Γ^{ch}/W and Γ^{sp}/W have larger values than TPSC or TPSC+GG for equal U/W. Moreover, because IPT is reliable only at weak-coupling $U \lesssim W/2$, the range of interactions shown is limited to $U/W = 0.5$.

The bandwidth of the square lattice is $W = 8t^{hop}$.

Similarly to Figs. 6.16 (2D) and 6.31 (3D) in the case of TPSC+GG, the irreducible vertices Γ^{ch} (top panel) and Γ^{sp} (bottom panel) are plotted in Fig. 6.34 as a function of the temperature for $U = \{1,2,3,4\}$ in 2D (blue-shaded colors) and $U = \{2,3,4,5\}$ in 3D (red-shaded colors). The square (cubic) lattice half-filled nearest-neighbor Hubbard model using DMFT+TPSC is opted for in 2D (3D). The vertices are divided by U for compactness. Contrary to the TPSC+GG

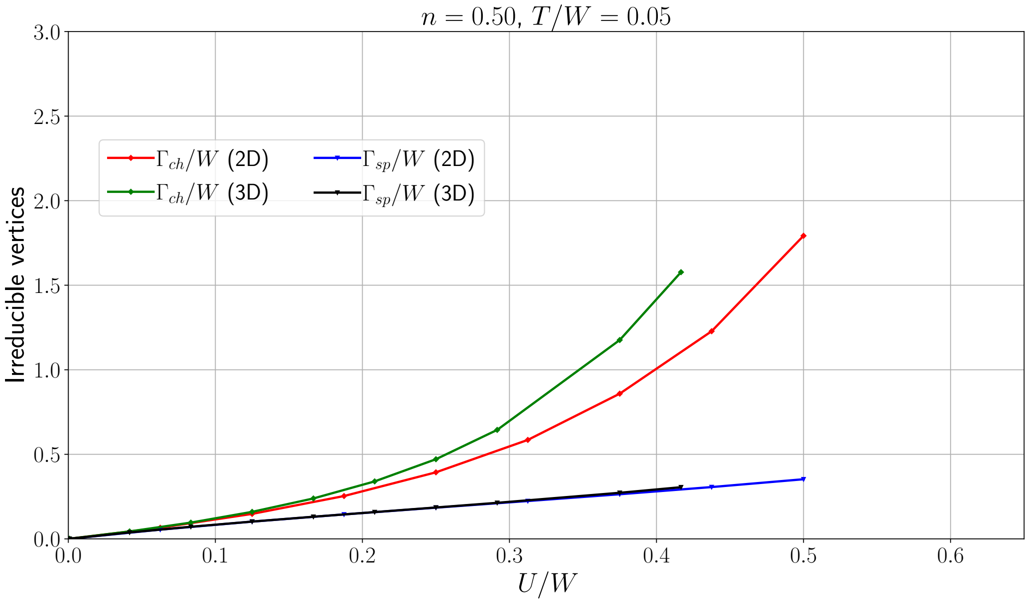

Figure 6.33: Bandwidth-normalized spin and charge irreducible vertices as a function of normalized bare interaction for the nearest-neighbor square (2D) and cubic (3D) lattices within DMFT+TPSC. The normalized inverse temperature is $\beta = 0.3125$ and the spin-density per site is $n = 0.5$.

temperature dependence of Γ^{ch} (Fig. 6.31), there is a decreasing trend in T/W that describes Γ^{ch} in all dimensions in DMFT+TPSC; it decreases until it hits the whereabouts of T_x, where it remains more or less flat (some hint of an upturn appears for TPSC+GG in that temperature regime). On the other hand, Γ^{sp} decreases quite drastically for most temperatures in DMFT+TPSC and this downfall is accelerated – especially in 2D – in the renormalized classical regime, unlike for TPSC+GG. Despite the fact that Γ^{sp} flexes down in the renormalized classical regime, the overall temperature dependence of the vertices is a bit more flattened out in 3D at constant interaction. The temperature dependence of the vertices seems to be more affected by the dimensionality than their dependence in U from looking at Γ^{sp} in Fig. 6.33 at higher temperature ($T/W = 0.05$). Looking at the spin irreducible vertex of Fig. 6.34 (bottom panel), it is quite clear that the spread between successive Γ^{sp} computed at different U becomes larger as T lowers. The spread between successive Γ^{sp} also grows when U increases, meaning that the Kanamori-Brueckner screening [63] of the spin-spin interactions would saturate earlier on as a function of U at temperatures close enough to T_x. In the charge channel, the separation between different Γ^{ch} computed at different values of U widens when the temperature is raised, in opposition with Γ^{sp}.

To make sure that DMFT+TPSC does capture the growth of the AFM correlations when decreasing the temperature at various interactions, the equivalent of Fig. 6.14 is plotted within DMFT+TPSC in Fig. 6.35 for 2D (blue-shaded colors) and 3D (red-shaded colors). The same qualitative behavior of the static spin response is observed in DMFT+TPSC: as the impurity interaction increases, the upturn in the static spin susceptibility is pushed down at lower temperatures. Furthermore, the separation between the upturns increases as U/W

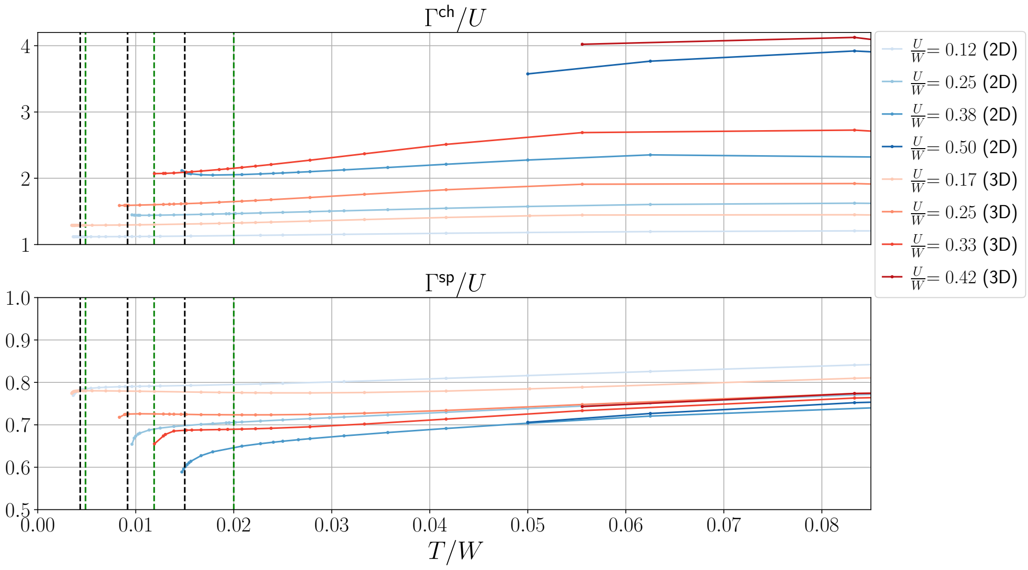

Figure 6.34: Γ^{ch} (top panel) and Γ^{sp} (bottom panel) as a function of T/W for $U = \{1,2,3,4\}$ and $U = \{2,3,4,5\}$ in the 2D and 3D half-filled nearest-neighbor Hubbard model, respectively. The values of the vertices are normalized by U and were obtained using DMFT+TPSC. At $U/W = 0.5$, due to numerical difficulties to converge the solution at low temperatures, only few points are included. The black (green) vertical lines pin down the temperatures where Γ^{sp} deviates from a linear behavior in 3D (2D).

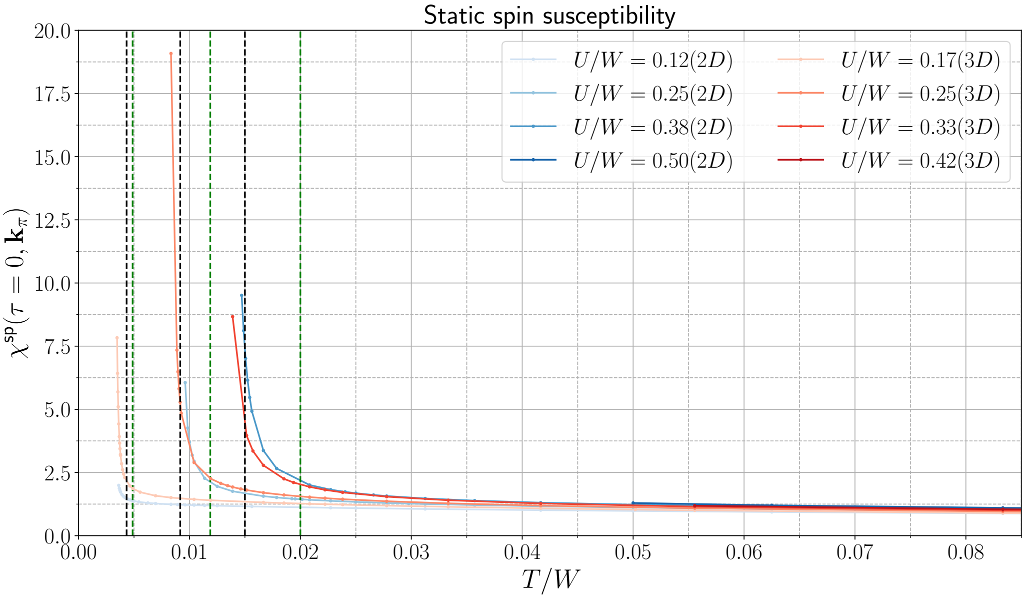

Figure 6.35: Static spin susceptibility of the 2D (3D) model at momentum $\mathbf{k}_\pi = (\pi,\pi)$ ($\mathbf{k}_\pi = (\pi,\pi,\pi)$) and half-filling as a function of normalized temperature for interactions $U = \{1,2,3,4\}$ ($U = \{2,3,4,5\}$) for DMFT+TPSC. The black and green vertical lines bear the same meaning and values as in Fig. 6.34.

is decreased and this is corroborated by TPSC and TPSC+GG. Similarly to TPSC+GG, the upturns at equal U/W kick in at lower temperatures when compared to TPSC, although DMFT+TPSC seems to pick up *more* spin correlations in 2D than TPSC+GG. Quite interestingly, even if the temperature dependence of the vertices differs substantially between TPSC+GG and DMFT+TPSC, the static spin susceptibility in Fig. 6.35 shows that the Fermi-liquid quasiparticles start breaking down at almost the same (normalized) temperatures for all interactions considered in 3D. TPSC+GG and DMFT+TPSC would therefore portray a similar crossover temperature T_x as a function of U/W.

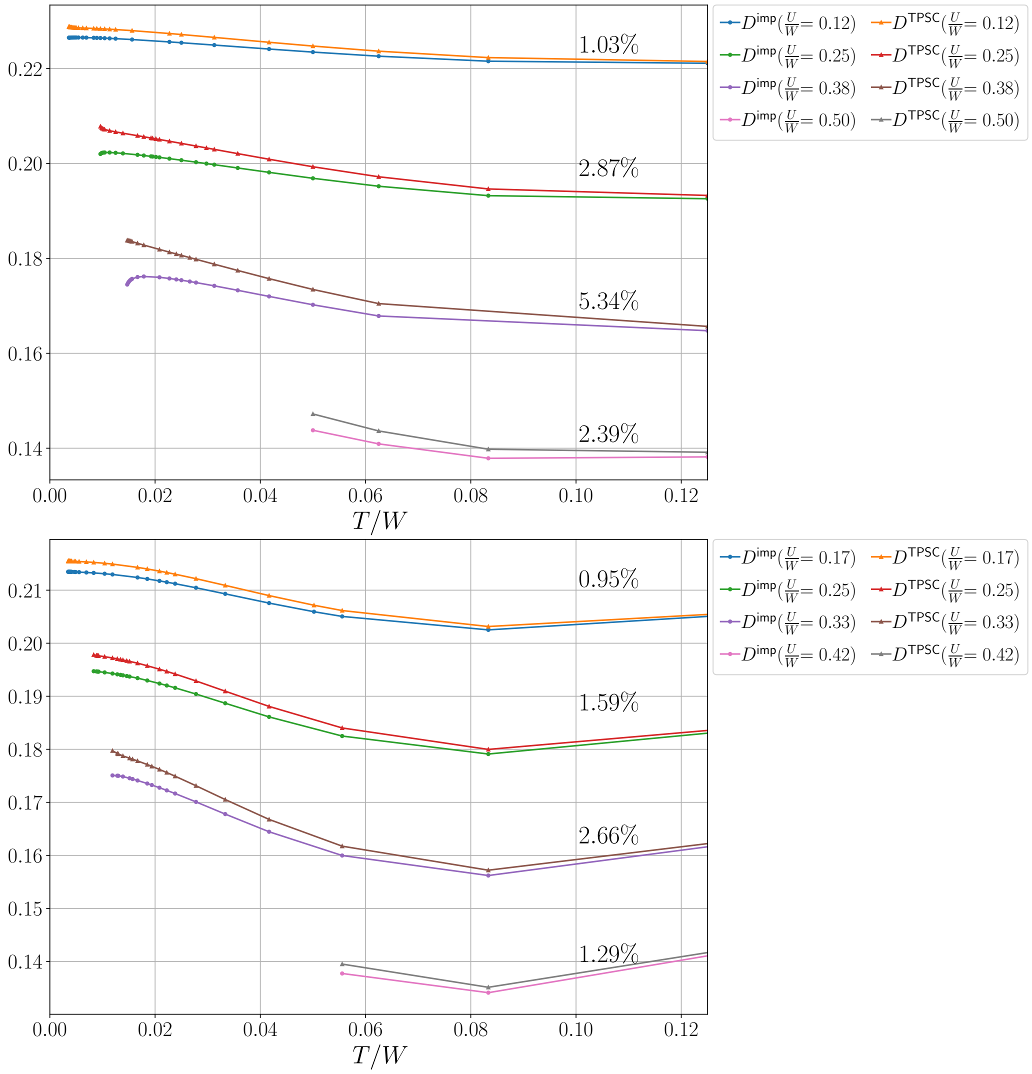

Figure 6.36: Double occupancies D^{imp} (5.99) and D^{TPSC} (5.104) as a function of normalized temperature for several interactions U/W in the 2D (top panel) and 3D (bottom panel) nearest-neighbor Hubbard model. The annotated percentages denote the largest absolute variation relative to D^{imp}.

In DMFT+TPSC, there are auxiliary Green's functions defined on the Anderson impurity embodying the local correlations, *i.e.* $\mathcal{G}^{\mathrm{imp}}$, Σ^{imp}, and Green's functions defined on the lattice representing the nonlocal correlations, *i.e.* $\mathcal{G}^{\mathrm{TPSC}}$, Σ^{imp}. Normally, if DMFT+TPSC was consistent at the double occupancy level (D-consistent according to Table 5.1), then the double occupancy calculated on the impurity D^{imp} (5.99) would equal that on the lattice D^{TPSC} (5.104). For that reason, these two ways to compute the double occupancies are shown in Fig. 6.36 for the 2D and 3D single-band nearest-neighbor Hubbard model, respectively located in the top and bottom panel. The lower the temperature gets and the larger the interaction is, the larger the deviation between D^{imp} and D^{TPSC} becomes in all dimensions considered. The largest values for each interaction is displayed in absolute relative percentage with respect to D^{imp}. Overall, the deviations are quite small; they are caped below 6% in 2D and below 3% in 3D. Rising the dimensionality alleviates the diversion of both D^{imp} and D^{TPSC} (at same U/W). Note that at higher T/W, the double occupancy goes back up in accordance with the fact that the double occupancy at infinite temperature at half-filling reaches 0.25, irrespective of U/W.

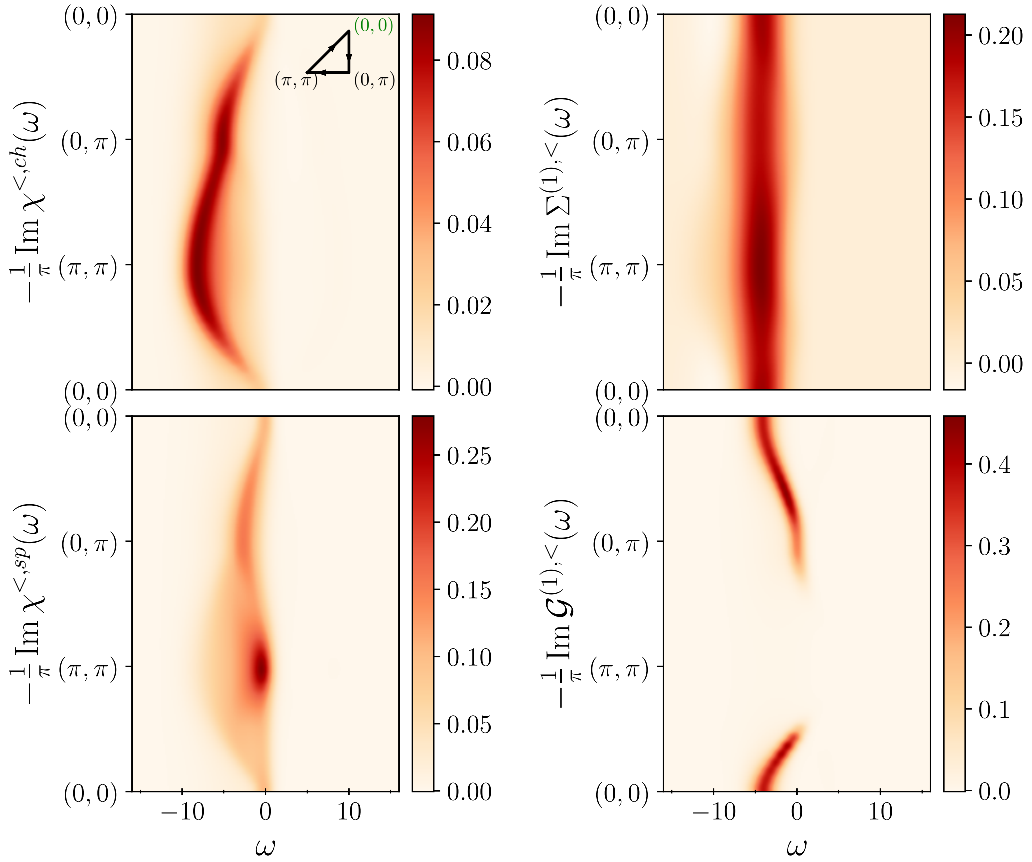

Figure 6.37: Left panels: *lesser* charge (top panel) and spin (bottom panel) susceptibilities. Right panels: second-level TPSC self-energy (top panel) and single-particle Green's function spectra (bottom panel). The calculations were performed using DMFT+TPSC at half-filling for the square lattice model at $T = 0.33$ and $U = 3$. The time window employed for the Fourier transforms is $\Delta t = 5$.

The differences between DMFT+TPSC and TPSC+GG in the two- and single-particle nonlocal spectra are quite small. To check out what those differences are, the DMFT+TPSC nonlocal quantities are computed at $U = 3$ and $T = 0.33$ for the nearest-neighbor 2D Hubbard model. Thus, in Fig. 6.37 are shown the susceptibilities in the left panels (top panel for χ^{ch} and bottom panel for χ^{sp}) and the single-particle quantities on the right ones (top panel for $\Sigma^{\text{TPSC},(1)}$ and bottom panel for $\mathcal{G}^{(1)}$). The data on the left panels of Fig. 6.37 can be compared with the TPSC+GG susceptibilities illustrated in Fig. 6.21 (right panels) and Fig. 6.23 for the TPSC+GG single-particle quantities (right panels) – the same set of parameters was used in TPSC+GG.

Starting with the susceptibilities, TPSC+GG and DMFT+TPSC both render very similar $\mathbf{k}$-defined spectra on all regards. The spectral excitation amplitudes are almost quantitatively equal across all the $\mathbf{k}$-points in the plots and the profiles are pretty much identical. The biggest difference between TPSC+GG and DMFT+TPSC comes about in the nonlocal self-energies: the self-energy in the top right panel of Fig. 6.37 looks narrower for several $\mathbf{k}$-points than the TPSC+GG self-energy displayed in the top right panel of Fig. 6.23. The excitation spectra seem to also be distributed differently across the path walked along in the irreducible Brillouin zone: more spectral weight is gathered around $\mathbf{k}_{\pi}$ and the neighboring $\mathbf{k}$-points in DMFT+TPSC, whereas the spectral weight at $\mathbf{k}_{\pi}$ stands out more from the rest in TPSC+GG. These differences however seem to not affect too much the single-particle spectral weight, because they could be confused with one another in TPSC+GG and DMFT+TPSC.

7

NONEQUILIBRIUM RESULTS

The nonequilibrium counterpart of the results discussed in Chapter 6 for both the RPA-type post-processing scheme (Section 6.1), and TPSC and its variants (Section 6.2.1), are presented in this section. In particular, as far as the RPA-type post-processing scheme is concerned, the electronic interaction will be changed in Section 7.1 in the vicinity of the DMFT magnetic phase boundary to check how the π-ton vertex corrections build up in the longitudinal optical conductivity. Then, in Section 7.2, the 2D and 3D nearest-neighbor single-band Hubbard model will be studied by ramping the interaction and lattice hopping energy. TPSC, TPSC+GG and DMFT+TPSC are compared and discussed, flashing out their main advantages and disadvantages.

7.1 POST-PROCESSING DMFT

In Section 6.1, the effect of ladder-type vertex corrections introduced in Chapter 4 on the thermodynamic ($\mathbf{q} = \mathbf{0}$) optical and magnetic response of the half-filled Hubbard model was studied. It was revealed that the single-ladder vertex corrections can capture the key signatures of the π-ton, as it was identified in Ref. [66]. These vertex corrections become increasingly relevant as one approaches a magnetically ordered phase with ordering wave vector $\mathbf{k}_\pi$, as in the single-band Hubbard model near the AFM phase boundary. The vertex corrections were considered within the RPA-type post-processing DMFT method proposed in Ref. [120]. This method constructs the vertices out of interacting Green's functions obtained from a DMFT simulation using the bare interaction U, which are then inputted in the ladder diagrams ($\square$-terms) making up the vertices, whose interaction terms U are renormalized $U \to U^{\text{ren}}$ so as to match the DMFT AFM phase boundary (see Fig. 6.3). According to the results published in Refs. [66, 119, 120, 150], this RPA-type post-processing method would pick up the relevant features attributed to the π-ton at weak coupling, thereby allowing the inclusion of relevant fluctuations into the $\mathbf{q} = \mathbf{0}$ responses measured with DMFT. These features related to the π-ton at weak U are the broadening of the Drude peak and the appearance of a characteristic "in-gap" feature in the optical and spin response. However, as pointed out in Section 6.1.2, the calculation of the RPA-π-tons in the intermediate coupling and Mott regimes suffer from inconsistencies, where the corresponding vertex correction is larger in the high temperature region than close to the AFM phase boundary (if the diagrams are evaluated with the more reliable NCA Green's functions in that regime). The breakdown of this RPA-type method is seen at $U = 3$, where the Drude peak is suppressed and the in-gap feature shifts up in energy, merging with the higher energy spectral weight. Furthermore, it was shown in Section 6.1.3 that DMFT is dubious in 1D by comparing it to DMRG, but the π-ton results obtained in 1D from the post-processing DMFT method can carry over to 2D (see Fig. 6.7) and higher dimensions. In 1D, there is the presence of a Mott gap at $T = 0$ in the half-filled Hubbard model for any finite $U > 0$, and the spin and charge responses are very asymmetric.

In this section, the results of a nonequilibrium treatment of the single-ladder vertex corrections (4.30) in the longitudinal optical conductivity for the weakly interacting half-filled one-band Hubbard model Eq. (3.9) are shown. The calculations take place in 1D using the RPA-type post-processing DMFT technique with the Green's functions obtained with nonequilibrium IPT in the PM state (see Section 3.2.1.1). The calculations are restricted to $U \lesssim W/2$, since this is the regime of parameters where the post-processing method can be expected to give sensible results [120] (see Section 6.1.2). There exist two alternative schemes[1] based on the second-order self-energy, namely $\Sigma^{(2)}[\mathcal{G}^0]$ (bare IPT) or $\Sigma^{(2)}[\mathcal{G}]$ (bold IPT). As explained under the paragraph called "Asymptotic limits of the Hubbard model self-energy" in Section 3.2.1.3, bare IPT can capture the Mott physics whereas it is not the case for the bold IPT. On the other hand, if the self-energy is expressed as a product of dressed Green's functions, it conserves the total energy at all times following a U-quench or U-ramp, whereas the implementation with the bare Green's function $\mathcal{G}^0$ does not conserve energy at longer times, as illustrated in Figs. 7.1 and 7.2. The latter comes down to the fact that bold IPT is derived from a well-defined interacting Luttinger-Ward functional [80]. In Figures 7.1 and 7.2, the change in the kinetic energy

$$E_{\mathrm{k}}(t) = \frac{-i}{N_{\mathbf{k}}}\sum_{\mathbf{k}}\epsilon_{\mathbf{k}}\mathcal{G}^{<}_{\mathbf{k}}(t,t), \tag{7.1}$$

in the potential energy

$$E_{\mathrm{p}}(t) = \frac{-i}{N_k}\sum_{\mathbf{k}}\int_{\mathcal{C}}\mathrm{d}z\,[\Sigma_{\mathbf{k}}(t,z)\mathcal{G}_{\mathbf{k}}(z,t)]^{<}, \tag{7.2}$$

and in the total energy $E_{\mathrm{tot}}(t) = E_{\mathrm{k}}(t) + E_{\mathrm{p}}(t)$ are plotted for a U-ramp going from $U = 1.5$ to $U = 2$ (Fig. 7.1) and from $U = 1.5$ to $U = 1$ (Fig. 7.2). The bars over the energies $\bar{E}$ in Fig. 7.1 mean that the respective energies have been subtracted with their value at initial time $\bar{E} \equiv E(t) - E(t = 0)$. In both up and down U-quenches, for short times, the deviations in the parameter regime considered are rather small between bare and bold IPT, although they grow as time progresses. For that reason, the conserving bold IPT scheme will be considered in the following calculations. Nonetheless, the down U-quench whose energies are presented in Fig. 7.2 display a weaker deviation of the bare IPT results from the bold ones: energy conservation would be violated to a lesser extent when using bare IPT in a down U-quench when starting out with the same interaction strength.

IPT is a good weak coupling ($U \lesssim W/2$) impurity solver, with $W = 4t^{hop}$ in 1D.

For consistency between the DMFT and the post-processing two-particle vertex calculations, one needs to use renormalized interactions U^{ren} in the latter. To recall, the renormalized interaction U^{ren} in the π-ton ladder (4.30) is defined such that the divergence of the ladder contribution matches the DMFT Néel temperature T_N at equilibrium. The renormalized interactions U^{ren} were

---

[1] See discussion below Eq. (3.26).

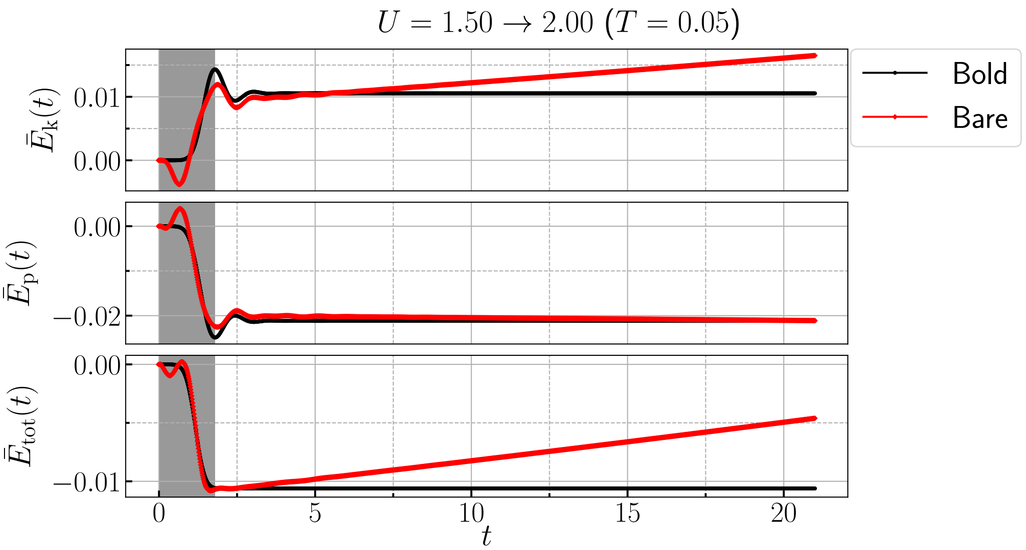

Figure 7.1: Energies as a function of time for an interaction ramp from $U = 1.5$ to 2.0 and initial temperature $T = 0.05$. Upper panel: change in the kinetic energy $\bar{E}_k$. Middle panel: change in the potential energy $\bar{E}_p(t)$. Lower panel: change in the total energy $\bar{E}_{tot}$. The black curves show the results for bold IPT, which conserves energy after the ramp, and the red curves show the results for bare IPT. A time step $dt = 0.015$ is used on the real axis and 1200 imaginary time points on the Matsubara axis to ensure the stability of the solution at longer times. The shaded area indicates the duration of the interaction ramp.

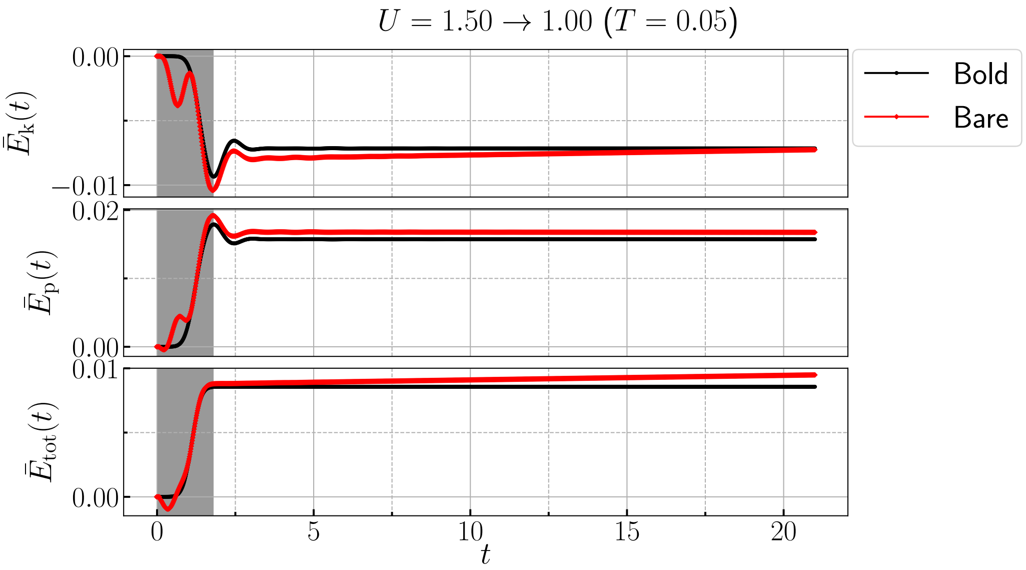

Figure 7.2: Energies as a function of time for an interaction ramp from $U = 1.5$ to 1.0 and initial temperature $T = 0.05$. The plot has the same layout as in Fig. 7.1 and the same discretization of the KB contour was employed. The U-ramp used in this case corresponds to the mirror reflexion along the x-axis of that of Fig. 7.1.

determined in Ref. [120] and they are $U^{\text{ren}} = 1.33$ for $U = 2$, $U^{\text{ren}} = 1.10$ for $U = 1.5$ and $U^{\text{ren}} = U$ for $U = 1$. Up to some rescaling, the shape of the ramp profile used for the renormalized interaction is the same as that used for the bare interaction.

The interaction range is narrowed down to $U \in [1,2]$, since in that regime bare and bold IPT lead to similar self-energies and the Néel temperature is not too low, therefore allowing to stay close to the AFM phase boundary and still have a stable time propagation with a reasonably large time step. The time propagation needs to be stable in order to access long enough times for a meaningful Fourier analysis and not accumulate errors across the propagation. In that interaction range, the RPA-type post-processing calculations are sufficiently reliable because the local irreducible vertices in both the charge and spin channels do not differ much from each other and are close to the bare interaction value [152] (see for instance Fig. 6.13 in Section 6.2.1.1).

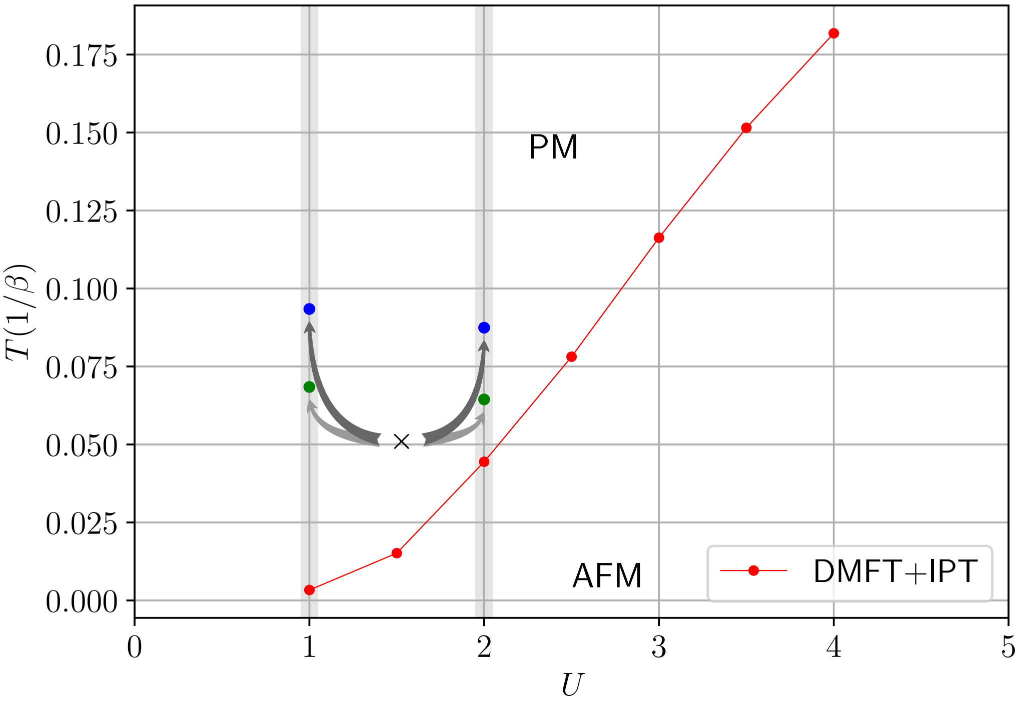

Figure 7.3: Sketch of the interaction ramps and quenches discussed in the present section. The green dots (blue dots) show the temperatures of the thermalized systems after the U-ramps (U-quenches), while the red line shows the DMFT+IPT AFM phase boundary taken from Ref. [119]. The black cross represents the initial state ($U = 1.5, T = 0.05$).

To be specific, (i) a ramp and quench up from $U = 1.5$ to $U = 2$ and (ii) a ramp and quench down from $U = 1.5$ to $U = 1$, both starting at $T = 0.05$ will be considered – the black cross and arrows in Fig. 7.3 illustrate the ramps/quenches in question. The interaction ramp ΔU is described by the *error* function

An expression similar to Eq. (7.3) is used to describe the ramps in lattice hopping parameters.

$$\Delta U(t) = \pm \left(\frac{U_\mathrm{f} - U_\mathrm{i}}{2} \right) \mathrm{erf}(\gamma t + \delta) + \left(\frac{U_\mathrm{f} + U_\mathrm{i}}{2} \right), \tag{7.3}$$

where U_i corresponds to the initial interaction value and U_f to the final one, γ tweaks the steepness of the inflection of the curve and δ controls the onset of the ramp. A global minus sign appears in Eq. (7.3) in the case of a down ramp ($U_f < U_i$). When the interaction is ramped/quenched up or down, energy is injected into the system and the temperature T_{therm} after thermalization gets higher than in the initial state. It is important to point out that the asymptotic behavior (in ramp duration) of the excitation energy depends on the ramp protocol, on whether the ramp brings the system across a phase transition, as well as on the equilibrium state from which the ramp is applied, *i.e.* if it is a gapped system or not [35].

The temperature of the thermalized state T_{therm} is determined by computing the total energy $E_+ = E_{\text{tot}}(\tau_+)$, which is conserved after the ramp ($t \geq \tau_+$) when using the bold IPT solver, and then searching for the temperature of the equilibrium system with the post-ramp U and $E_{\text{tot}} = E_+$. The steps to get this thermalized temperature are detailed in Appendix I showing an example for TPSC. For the ramp (quench) up, the thermalized temperature yields $T_{\text{therm}} = 0.0616$ ($T_{\text{therm}} = 0.0852$) and for the ramp (quench) down $T_{\text{therm}} = 0.0664$ ($T_{\text{therm}} = 0.0909$). The two ramps (quenches) are sketched in Fig. 7.3 together with the AFM phase boundary in the (U,T) plane. The black cross indicates the initial state of the system and the final thermalized states are pinned down by the green dots (blue dots) in the case of the ramp (quench).

7.1.1 *Single-particle spectrum*

Because the RPA-type post-processing method to treat two-particle vertex corrections hinges on the assumption that the single-particle properties, such as the density of states, influences a lot the two-particle properties – even more so than the other way around –, the density of states is plotted in Fig. 7.4 for a U-quench from $U = 1.5$ to $U = 2$. The vertex corrections to the optical conductivity (4.31) would then depend substantially on the single-particle DMFT propagator $\mathcal{G}$, which enters the calculation of the RPA-type ladder vertex. In Fig. 7.4, the local single-particle spectral function is shown for various times during and after the interaction ramp from $U = 1.5$ to 2 (see inset). The spectral weight is calculated using the forward Fourier transform (2.66), allowing to access very early times as opposed to the time-averaged Fourier transformation which builds off a Wigner transformation [6].

In Fig. 7.4, one can notice sharp density of states in the vicinity of $\omega \simeq \pm 1.6$ corresponding to the van Hove singularities that would appear at $\omega = \pm 2$ in the noninteracting density of states; the interactions broaden and shift those two peaks in energy. Furthermore, some amount of spectral weight is transferred to higher energies (*e.g.* $2.2 \lesssim \omega \lesssim 6$) when increasing U. These features can be interpreted as satellites of the main peaks ($\omega \simeq \pm 1.6$) that are split off by an energy $\sim U$. The upper satellite corresponds to an electron insertion plus creation of a short-lived “doublon-holon” pair. The density of states thermalizes rapidly so that no significant evolution in the spectral weight can be observed after $t = 2$, and the spectra coincide with those of the thermalized system.

7.1.2 *Optical conductivity*

The $\mathbf{q} = \mathbf{0}$ optical conductivity is investigated by applying interaction ramps and quenches in the vicinity of the AFM phase boundary (see Fig. 7.3). One

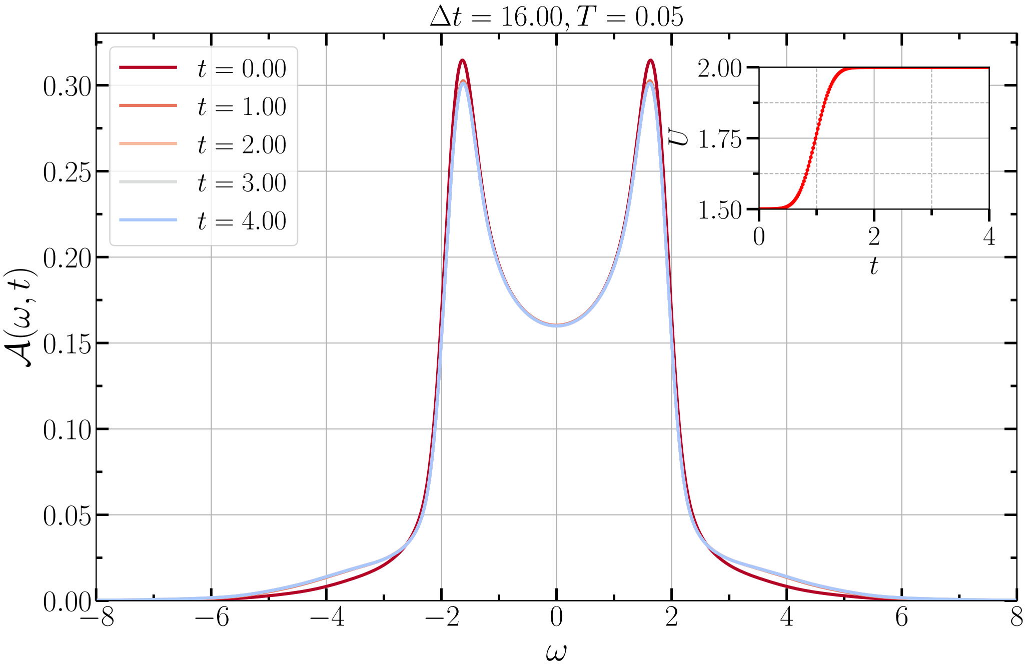

Figure 7.4: Illustration of the time-dependent single-particle spectral function during and after the up ramp. The inset shows the profile of the interaction ramp. The inverse temperature of the initial state is $\beta = 20$ and the Fourier window is $\Delta t = 16$.

of the goals is to evaluate how the bubble and π-ton contributions to the conductivity evolve in time after the interaction changes and how they thermalize. To characterize the time evolution of the bubble and π-ton contributions, the spectrum is measured at different times during and after the up and down ramps in Figs. 7.5 and 7.6, respectively. The bubble contribution to the optical conductivity is plotted in blueish and the π-ton contribution in reddish. The (dotted-)dashed black line indicates the π-ton (bubble) spectrum in the initial equilibrium state ($U = 1.5$, $T = 0.05$). Like in Section 6.1.2, the imaginary part of the current-current correlation function $\omega \mathrm{Re}\sigma_{jj}(\omega; \mathbf{q} = \mathbf{0}) = \mathrm{Im}\chi_{jj;\mathbf{q}=\mathbf{0}}(\omega)$ is plotted to cut the Drude peak off at low frequencies and see better the high-energy features. In both Figs. 7.5 and 7.6, a time window $\Delta t = 7$ is used for the forward Fourier transformation.

The first time (light color) sits close to the beginning of the interaction ramp, while the remaining curves (darker colors) track the evolution after the ramp. The high-energy feature in the bubble conductivity associated with excitations between the van Hove singularities in the density of states (Fig. 7.4) shows a rapid relaxation after the ramp. To the contrary, the features appearing at lower frequencies, such as the prominent π-ton feature near $\omega \approx 0.4$, relax more slowly without exhibiting the oscillations that appear at short times in the low-energy bubble contribution. Ramping up the interaction brings the system closer to the AFM phase boundary and it therefore amplifies the π-ton contribution with the peak at $\omega \approx 0.4$ becoming larger. The π-ton peak builds up rather slowly compared to the timescale at which the changes occur in the bubble contribution.

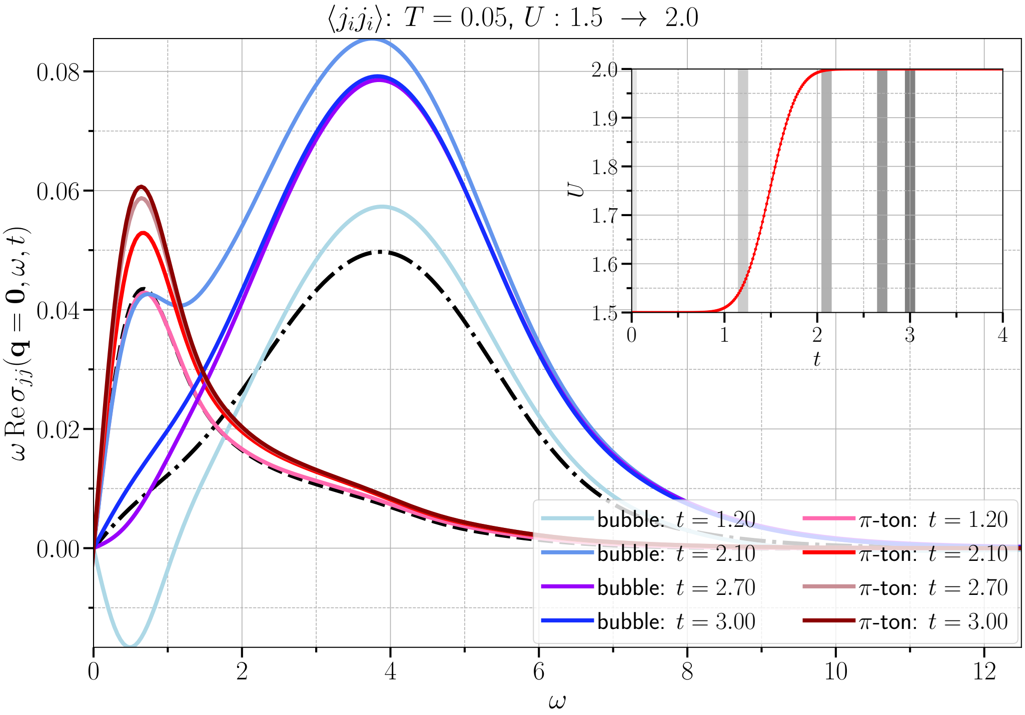

Figure 7.5: Real-time snapshots of the bubble contribution to the optical conductivity (blue) and the RPA π-ton vertex corrections (red) during and after the up ramp. The ramp shape is shown in the inset plot and the grey lines indicate the measurement times. The (dotted-)dashed black line shows the (bubble) π-ton contribution in the initial equilibrium state.

In Fig. 7.6, the bubble and π-ton contributions to the optical conductivity spectra are illustrated when ramping down the interaction ($U = 1.5 \rightarrow U = 1$). The bubble contribution displays similar early-time oscillations in the Drude component and a qualitatively similar relaxation behavior with more damped relaxation of the spectral features at higher energies. Ramping down the interaction clearly brings the system farther away from the AFM phase boundary (Fig. 7.3) and this melts away the π-ton feature at $\omega \simeq 0.4$, which decreases at a faster rate than that at which it builds up when ramping up the interaction. While the π-ton spectral peak melts away, it shifts at the same time slightly in energy – more so than in the up quench.

As pointed out in Fig. 6.10, some energies corresponding to different spectral features will be traced in time to analyze the relaxation behavior. These three characteristic energies are $\omega = 0.35$ (Drude feature), $\omega = 1$ (intermediate-energy feature) and $\omega = 3.9$ (high-energy feature). The bubble contribution is plotted in the left panels of Fig. 7.7 for the ramp up, ramp down, quench up and quench down (from top to bottom). The right panels show the same arrangements for the π-ton contribution. The values of the spectral features in the thermalized state, obtained by calculating the total energy after the ramp/quench, are indicated by grey horizontal lines: these values of the spectra should be converged to upon thermalization of the system. The bubble results shown in Fig. 7.7 clearly reveal a large amplitude single harmonic oscillation of the Drude peak during (after) the ramps (quenches). At higher energy cuts, the oscillations are more damped but very similar. Once these initial oscillations have fizzled out,

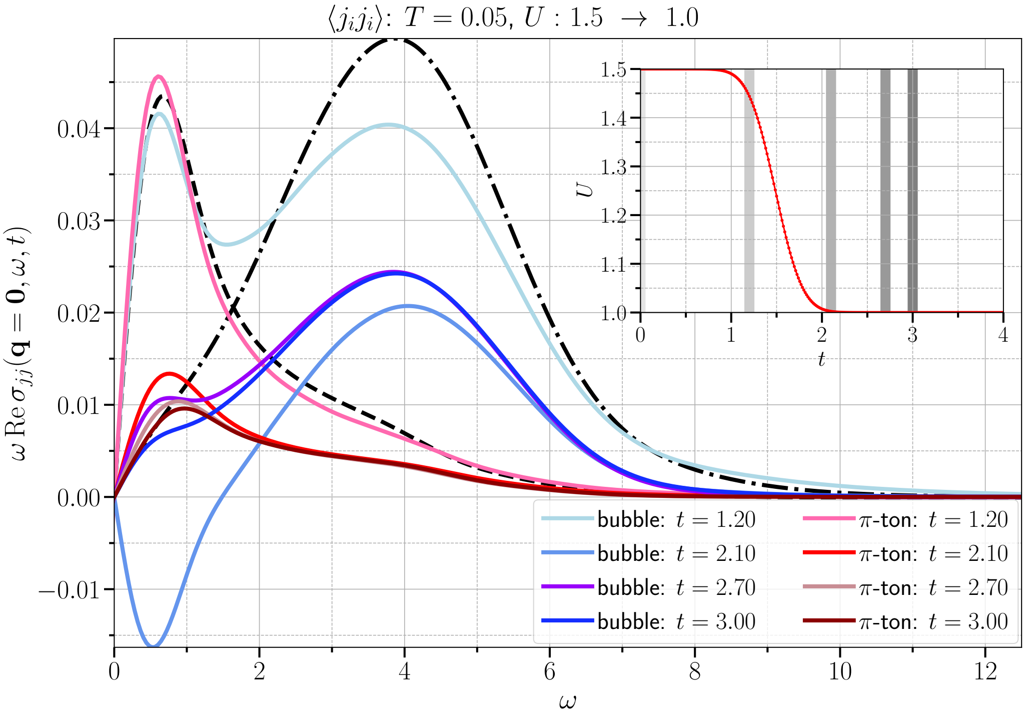

Figure 7.6: Real-time snapshots of the bubble contribution to the optical conductivity (blue) and the RPA π-ton vertex corrections (red) during and after the down ramp. The ramp shapes are shown in the inset plot and it corresponds to a mirror reflexion of the up-ramp along the x-axis. The grey lines indicate the measurement times which are the same as in Fig. 7.5. The black lines are the same as in Fig. 7.5 (same initial equilibrium state).

the bubble contribution to the conductivity rapidly relaxes to the thermalized result for all energy cuts.

Still focusing on the bubble contribution, it is interesting to see that the initial response of the Drude feature to the ramp goes in the opposite direction. This initial decrease of the Drude peak happens quite early on and can be spotted in Figs. 7.5 and 7.6 for time $t = 1.2$. However, because this short-time behavior does not show up in the case of the quenches, it thus appears to be related to the details of the U-ramp spectrum. Because the time window used in the Fourier transformation is much smaller ($\Delta t = 7$) than that used in Fig. 6.10 ($\Delta t = 500$) to compute the bubble spectral contributions, it is difficult to elaborate upon the relative changes of the Drude weight at low energies. Recall that the bubble spectra in Fig. 6.10 are equilibrium spectra and can therefore easily be extrapolated after time differences $t - t' \simeq 10$. It is not the case for the bubble spectra out of equilibrium shown in Fig. 7.7.

Let's now turn the focus to the changes induced in the π-ton contributions to the optical conductivity ensuing a U-ramp and U-quench. As for the bubble contribution, the studied energy slices of the RPA-type π-ton contribution sit at $\omega = 0.35$, 1 and 3.9. The high-energy structure of the π-ton at $\omega = 3.9$ approaches, on a timescale comparable to the bubble contribution, the thermal value quickly after the ramp or quench. This is completely different for the intermediate-energy and Drude features which exhibit a delayed thermalization, overshooting the thermal reference values by a significant amount, espe-

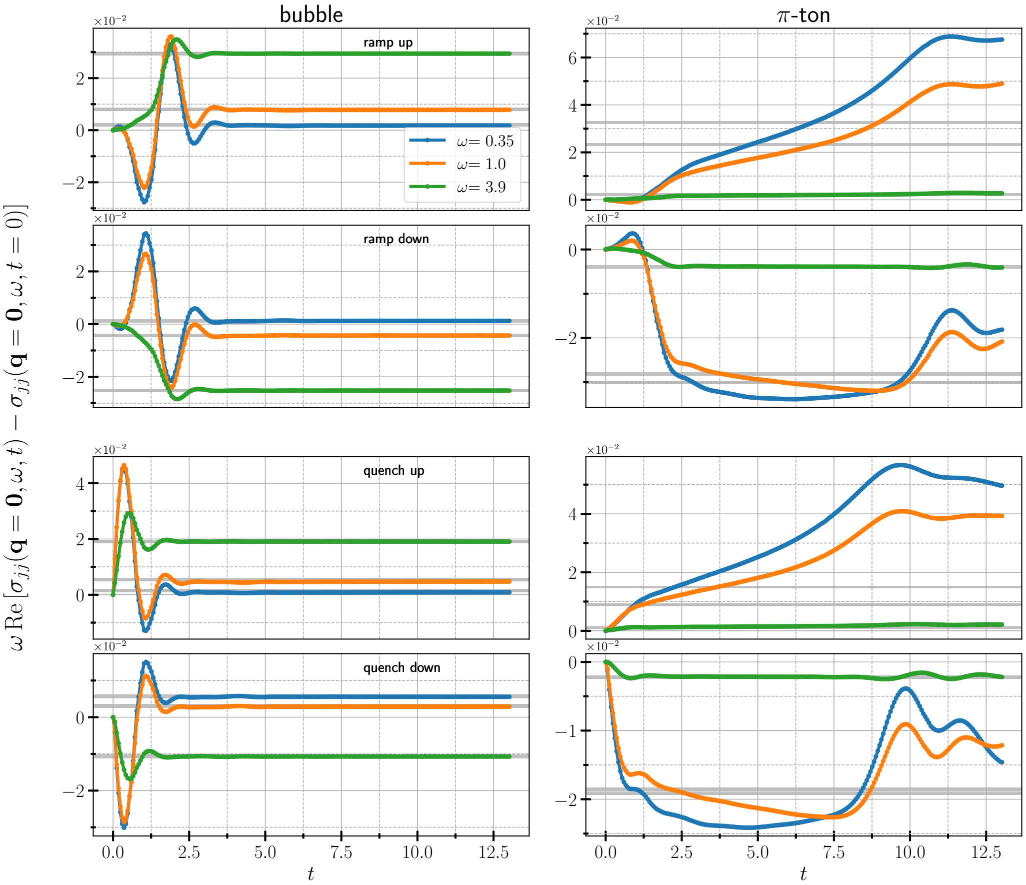

Figure 7.7: Time-dependent change in the bubble (left column) and π-ton (right panel) contributions to $\omega \mathrm{Re}\sigma_{jj}(\mathbf{q}=\mathbf{0},\omega,t)$ at $\omega = 0.35$ (blue), 1.0 (orange) and 3.9 (green). The two upper rows of panels show the results for the ramps: upper (lower) panel for the ramp up (down). Likewise, the two lower rows of panels show the results for the quenches. The horizontal grey lines indicate the values reached in the thermalized state after the ramp. For a better visualization of the change in conductivity, the values at $t = 0$ are subtracted. Just like for Fig. 7.5, a time window $\Delta t = 7$ was used at all times t.

cially when quenching/ramping the interaction up. The initial response to the U-ramps of the π-ton, although less pronounced, looks qualitatively similar to that of the bubble contribution: a transient change of the spectral weight goes in the opposite direction from the modification expected in the thermalized state (see Fig. 6.10).

The long-lasting overshooting of the π-ton contribution over the thermal reference values in Fig. 7.7 would constitute the prethermalization phase. This behavior will be studied in more details further down below by looking at the nonthermal distribution function. Indeed, as reported in Refs. [36, 92], the energy distribution function is known to exhibit a prethermalization plateau at low energies after quenches in the weak-couplig regime, and this would reflect in the optical conductivity since it is related to the kinetic energy via the sum rule (E.7). As a consequence, this would mean that the occupation (*lesser* spectral function) and nonequilibrium distribution functions remain nonthermal for a long period of time after the quench/ramp, in contrast with the spectral function which thermalizes fast (Fig. 7.4). Moreover, the thermalization of the momentum-resolved nonthermal distribution function depends strongly on how close to the Fermi level the momentum lies; in this case $\mathbf{k}_F \approx \frac{\pi}{2}$. Hence, because the bare velocities $v_i(\mathbf{k}) = \partial_{k_i}\epsilon(\mathbf{k})$ give the largest absolute values near the Fermi level and that the poles of the single-ladder vertex dominate for momentum differences equal to $\mathbf{k}_\pi$, the RPA-type π-ton vertex corrections to the optical conductivity depend strongly on the occupied density of states near the Fermi level.

The leading oscillation frequencies ω_{osc} that shape the bubble signals in Fig. 7.7 (left panels) can be extracted by carrying out Fourier transformations on the time traces shown. The quantity ω_{osc} represents the dominant oscillation frequencies induced by the interaction perturbations. To remove from the bubble signals the residual spectral weight coming from the ramp, the signal is subtracted by a smooth function proportional to the ramp profile. In Fig. 7.8, the norms of the Fourier transforms of the bubble time traces are shown and solid lines are associated to the harmonics ω_{osc} after the U-ramps whereas the dashed lines are associated with the U-quenches. The upper (lower) panel of Fig. 7.8 sets out the bubble oscillation spectra for the up (down) ramp/quench at $\omega = 0.35$ (red), 1.0 (orange) and 3.9 (blue). The time-traces are convolved with a wide gaussian envelope function so as to pull down the tail of the Fourier transformed function to zero. For the lower energies looked at – $\omega = 0.35$ (Drude component) and 1.0 (intermediate-energy peak) – the oscillations share a dominant harmonic which is independent of the direction of the ramp/quench whose peak is centered at $\omega_{\text{osc}} \approx 3.2$: it roughly matches the energy separation between the peaks in the density of states (see Fig. 7.4). The broadness of this peak is caused by the damping of the time traces after the first oscillation. From inspecting the time traces in Fig. 7.7, the amplitude of the oscillations is a bit smaller but a bit broader for the quench (dashed lines) than for the ramps (solid lines). At higher energy $\omega = 3.9$, the damping is stronger and the thermalization faster. At this energy cut, the oscillation frequency in the time traces is described by two humps centred around $\omega \simeq 1.5$ and $\omega \simeq 5$, revealed after the subtraction of the smooth background in the form of the ramp shape. These robust peaks may correspond to fluctuations between the density of states' peaks and the Hubbard side-bands visible in Fig. 7.4, especially at $U = 2$. Also, for $\omega = 3.9$, the amplitude of the oscillations is larger for the quench than for the ramp.

In the case of the π-ton time traces shown in Fig. 7.7 (right panels), no pronounced oscillations give rise to harmonics ω_{osc} that would stand out. The lack of oscillations followed by some damping would be related to the prethermalization behavior, especially at $\omega = 0.35$ and 1.0, and in the case of the up ramp/quench. Note that the prethermalization phenomenon is whittled down at larger temperatures (not shown). The thermalization of the π-ton vertex corrections to the optical conductivity occurs on timescales that are longer than the accessible simulation times and to be able to describe the thermalization processes, one would need to resort to numerical schemes that reduce the computational cost such as memory truncation techniques [113, 125], compact representation basis to store nonequilibrium Green's functions [67] and/or methods

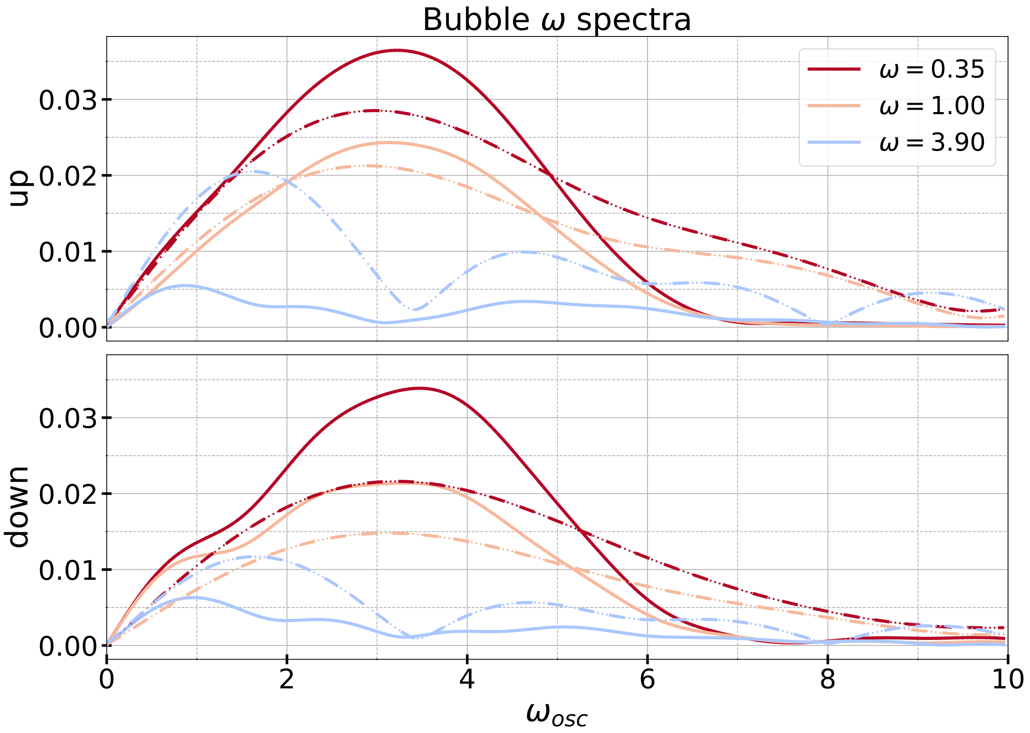

Figure 7.8: Spectral decompositions of the time traces (see Fig. 7.7) of the bubble contribution $\omega \mathrm{Re}\sigma_{jj}(\mathbf{q}=\mathbf{0},\omega,t)$ at the indicated energies. The plotted lines show the norms of the Fourier transformations, after subtracting a background proportional to the ramp shape. In the case of the quenches, the mean was subtracted. Dashed (solid) lines are for interaction ramps (quenches).

that extrapolate the time-diagonal of nonequilibrium Green's functions on the time plane [141].

As mentioned on several occasions, the RPA-type post-processing DMFT treatment of the vertex corrections makes use of the nonequilibrium DMFT Green's functions. The vertex corrections should consequently depend on the single-particle density of states (Fig. 7.4). To investigate in more details the origin of the prethermalization behavior, the time evolution of the different components of the *lesser* – related to the particle occupation – and retarded components of $\mathcal{G}$ are calculated. Now, as shown in Fig. 7.4, the retarded spectral component $\mathcal{A}^R$ (2.39) thermalizes fast, inferring that the prethermalized state must be primarily due to nonthermal properties of the *lesser* spectral function $\mathcal{A}^<$ (2.28). The nonequilibrium distribution function can be determined from the knowledge of $\mathcal{A}^R$ and $\mathcal{A}^<$ as

$$n_{\mathbf{k}}(\omega,t) = \frac{\mathcal{A}^<_{\mathbf{k}}(\omega,t)}{\mathcal{A}^R_{\mathbf{k}}(\omega,t)}, \tag{7.4}$$

and its calculation allows one to establish how fast the system reaches the momentum-independent thermalized Fermi distribution function n_F. To get the spectra, the forward-in-time Fourier transformation (2.30) is employed with a large cut-off in time. Because the real-time functions $\mathcal{G}^{<,R}_{\mathbf{k}}(t,t')$ for fixed time t have predictable tails which can be fitted by the function $\alpha e^{-t'/\beta}\cos(\varepsilon t' + \delta)$, large time windows can be used prior to Fourier transforming to access finer

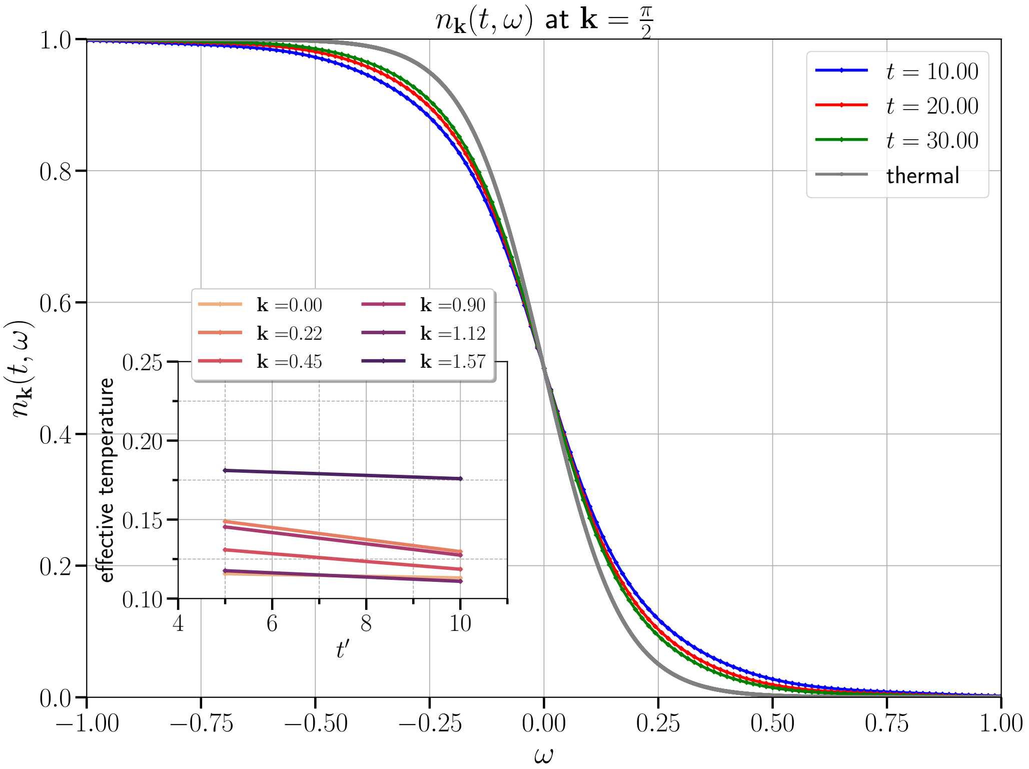

Figure 7.9: In the main plot, the grey curve depicts the Fermi distribution function for the thermalized state after the quench from $U = 1.5$ to $U = 2$ at $T = 0.05$. The other curves illustrate the non-equilibrium distributions $n_{\mathbf{k}}(t,\omega)$ at $\mathbf{k} = \frac{\pi}{2}$ (Fermi level) and for $t = \{10,20,30\}$. An exponential function was used to extrapolate the tails of both $\mathcal{A}^{<}(t,t+\Delta t')$ and $\mathcal{A}^{R}(t,t+\Delta t')$. A time window $\Delta t' = 4000$ was used in the Fourier transformation. In the inset plot, the time traces of the effective temperatures Eq. (7.5) of the $\mathbf{k}$-dependent distribution functions are plotted.

resolution in the spectra. The nonthermal distribution functions might not be of the form of the Fermi-Dirac distribution function and they therefore can't be fitted. To overcome this difficulty and still achieve to assign a nonthermal temperature to the system, one can define an effective inverse temperature $\beta_{\text{eff}} = 1/T_{\text{eff}}$ from the derivative of $n_{\mathbf{k}}(t,\omega)$ at $\omega = 0$ as

$$\beta_{\text{eff}} \equiv -4\frac{\partial n_{\mathbf{k}}(t,\omega)}{\partial\omega}\bigg|_{\omega=0}. \tag{7.5}$$

In Fig. 7.9, the nonthermal distribution functions $n_{\mathbf{k}}(t,\omega)$ for $\mathbf{k} = \frac{\pi}{2}$ (Fermi level) at times $t = 10$, 20 and 30, for the ramp from $U = 1.5$ to $U = 2$ at initial temperature $T = 0.05$, are plotted. The Fermi distribution function evaluated at the thermalized temperature $T_{\text{therm}} = 0.0852$ is also shown in grey. One can notice that even at time $t = 30$, the distribution function is nonthermal and this has been reported in previous studies where an interaction quench in the weak coupling regime led to nonthermal stationary distributions at the Fermi level [70, 88, 92]. On the other hand, when the momenta differ from $\mathbf{k} = \pm\frac{\pi}{2}$, the relaxation rate of the distribution towards the thermalized one is faster, as can be seen in the inset plot of Fig. 7.9 plotting the effective temperature extracted from the slope of $n_{\mathbf{k}}$ at $\omega = 0$ (Eq. (7.5)). The inset plot shows that the

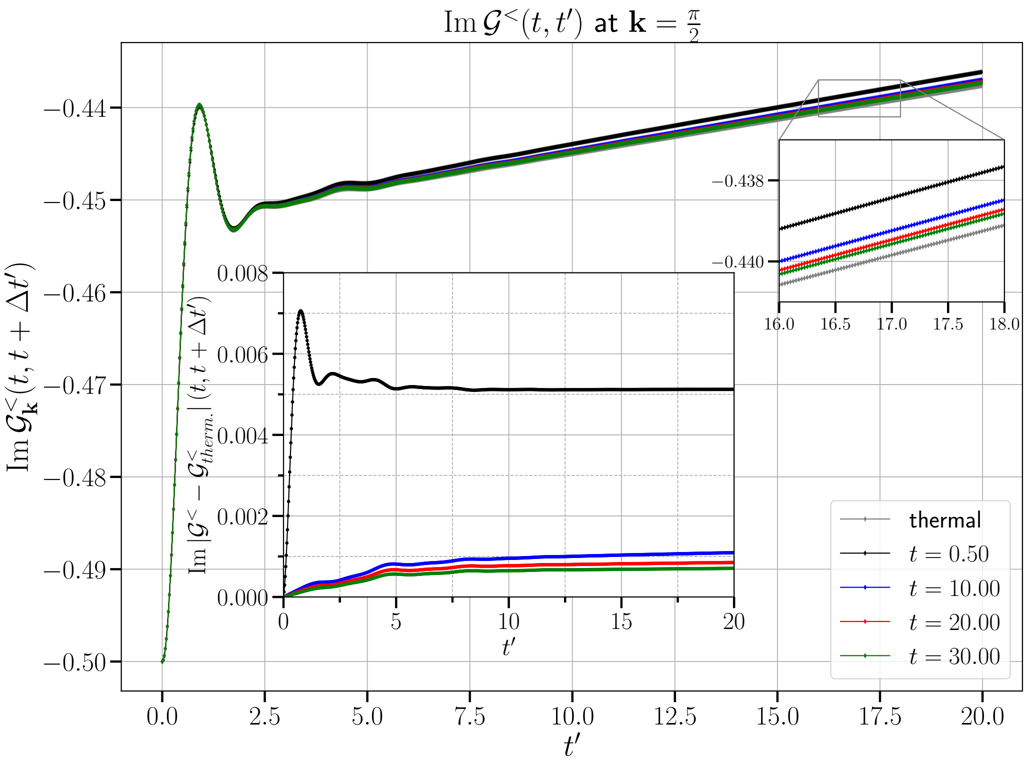

Figure 7.10: In the main plot, the time evolution of the lesser component of the dressed Green's function for the Fermi momentum $\mathbf{k}=\frac{\pi}{2}$ is plotted for the same quench. The inset shows the difference between the time traces of the quenched system and the thermalized system ($T=0.085$ and $U=2.0$).

effective temperature for various **k**-points are significantly different from each other for times $t \lesssim 10$ and that they converge to the thermal temperature on a timescale of $\mathcal{O}(10)$, except for $\mathbf{k}=\pm\frac{\pi}{2}$. This **k**-dependent relaxation of the distributions on a timescale of $\mathcal{O}(10)$ might be causing the upturn/downturn in the π-ton spectra in Fig. 7.7 (right panels). Hence, the slow relaxation of the distribution at the Fermi level, which is expected from Fermi liquid theory, dramatically slows down the thermalization of the RPA-type π-ton vertex corrections. In the case of a down ramp, because the heating effect is stronger, the distribution functions thermalize faster compared to the quench up and the prethermalization phenomenon is less prominent.

Alternatively, the prethermalization can be detected directly in the time dependence of the Green's functions' Keldysh components. In Fig. 7.10 the *lesser* spectral function $\mathrm{Im}\mathcal{G}^{<}(t,t+\Delta t')$ for $0 \leq \Delta t' \leq 20$ is plotted. The same interaction ramp is used as in Fig. 7.9, *i.e.* from $U=1.5$ to $U=2$, and the initial temperature is also $T=0.05$. The inset shows the difference of the various time traces to the thermal result, namely $\mathrm{Im}\mathcal{G}^{<}_{\text{therm}}(t,t+\Delta t')$ at $T_{\text{therm}}=0.0852$ and constant interaction $U=2$. These real-time comparisons confirm the slow relaxation of the distribution function to its thermal value, and consequently of the π-ton vertex corrections. This would mean that the ladder-type vertex corrections, which are prominent near the AFM phase boundary, be it the single- and double-ladder vertex corrections, would have a large effect on the nonthermal optical properties in weakly-correlated Hubbard systems. The prethermalization phenomena dominates the slow relaxation of the conductivity after an interaction perturbation.

7.2 TPSC AND VARIANTS

The nonequilibrium TPSC method and its variants will be applied to interaction ramps as well as lattice hopping ramps. In particular, the interaction ramps will be carried out in the 2D and 3D single-band Hubbard model. In this thesis, the lattice hopping quenches will be mainly focused on the transition from a 2D nearest-neighbor square lattice system to a 3D cubic nearest-neighbor system, and vice-versa. Note that the lattice hopping and interaction are not quenched simultaneously, as it would be hard to disentangle the effects from one another. In Section 7.2.1, the nonequilibrium results obtained from using TPSC and TPSC+GG are presented whereas in Section 7.2.2 those obtained from DMFT+TPSC are shown. The section about TPSC and TPSC+GG is organized like the equilibrium results of Section 6.2, in that the 2D and 3D results are mostly separated out.

7.2.1 *TPSC and TPSC+GG*

In the first place, both nonequilibrium TPSC and TPSC+GG are applied to the half-filled – unless mentioned otherwise – 2D Hubbard model (3.9) to study the nonthermal dynamics induced by interaction ramps. Then, the 3D results are tackled, trying to understand the effect of dimensionality on single- and two-particle nonthermal dynamics.

7.2.1.1 *2D*

The effect of the interaction ramp profile on the nonthermal dynamics and the thermalization of the local two-particle quantities $\Gamma^{\mathrm{sp}}(t)$, $\Gamma^{\mathrm{ch}}(t)$, as well as the double occupation $D(t) = \langle n_{\uparrow}(t)n_{\downarrow}(t)\rangle$, is studied in Fig. 7.11, after ramps from $U = 1$ to $U = 3$ with initial temperature $T = 0.33$ using TPSC+GG. The bare interaction ramps for both the slow and fast ramps are indicated by the black dot-dashed and dotted lines, respectively, having rescaled the profile for better comparison.

For the fast ramp, the dynamics of $\Gamma^{\mathrm{sp}}(t)$ and $\Gamma^{\mathrm{ch}}(t)$ seem to decouple – more than for the slow ramp – over the timescale t^{hop}. Furthermore, $\Gamma^{\mathrm{sp}}(t)$ reacts very quickly to the change in U – the spin vertex grows on the timescale set by the ramp –, although the growth of Γ^{ch} is delayed. The fast response and relaxation after the ramp of Γ^{sp} can both be explained from Eq. 5.54: the right-hand side is proportional to $U(t)$, while the denominator is constant and $D(t)$ changes only marginally in time, *i.e.* in the bracket of $10-20\%$ change. In the bottom panel of Fig. 7.11, the double occupation continues to decrease up to $t \approx 1.8$ after the fast ramp, thereby producing the overshooting of Γ^{sp}. Past $t \approx 2$, the double occupation $D(t)$ is thermalized such as Γ^{sp}, because both reach a constant value. In the charge channel, the small change of the double occupation after the ramp still produces, via Eqs. (5.68) and (5.64), a persistent increase of Γ^{ch}. All the local

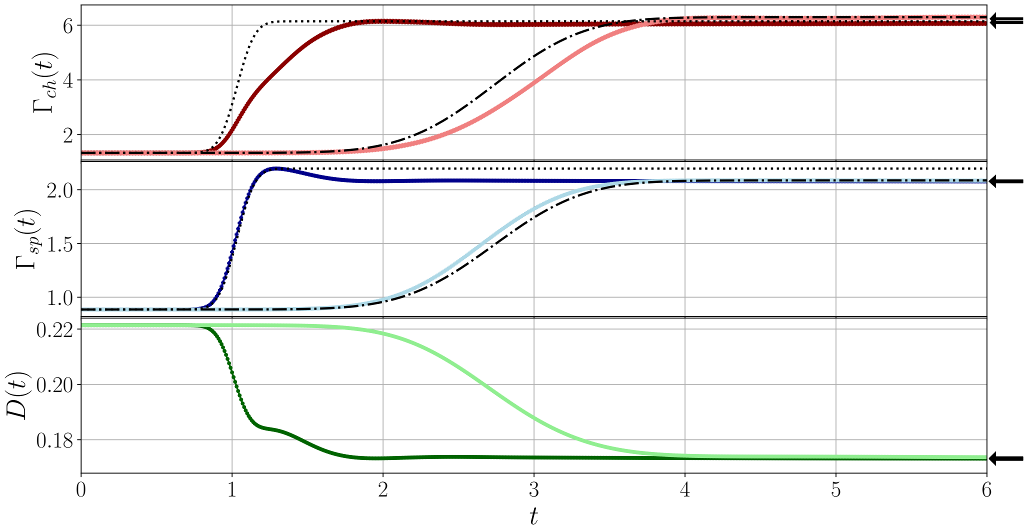

Figure 7.11: Dynamics after interaction ramps from $U = 1$ to $U = 3$ using TPSC+GG. The dotted and dash-dotted lines show the ramp profiles in arbitrary units. The quantities plotted in light (dark) colors correspond to the slow (fast) ramp. Top panel: charge irreducible vertex $\Gamma^{\text{ch}}(t)$. Middle panel: spin irreducible vertex $\Gamma^{\text{sp}}(t)$. Bottom panel: Double occupancy $D(t)$. The arrows on the right indicate the thermalized values for the slow and fast ramps calculated from E_{tot} after the ramp. The ramp shapes are described by Eq. (7.3).

quantities reach a plateau at large enough t whose value depends only slightly on the ramp profile: this relates to the fact that the inverse temperatures β_{th} of the thermalized systems do not differ much after the fast and slow ramps, namely $\beta_{\text{th}} = 1.7$ and $\beta_{\text{th}} = 2.1$, respectively. Only a slight difference in the thermalized values can be observed in Γ^{ch} (top panel of Fig. 7.11), probably due to a stronger temperature dependence of Γ^{ch} (see, *e.g.* Fig. 6.16).

Like discussed at the beginning of Section 7.1, the interaction ramps inject some energy ΔE into the system making the temperature of the thermalized state higher than that of the initial state. As explained in Appendix I, the inverse thermalized temperature β_{th} can be computed from the total energy of the system calculated after the ramp, where the total energy is given by the sum $E_{\text{tot}}(t) = E_k(t) + E_p(t)$, with the kinetic energy $E_k(t)$ given by Eq. (7.1) and the potential energy $E_p(t)$ given by Eq. (7.2). To remind oneself, $\epsilon_{\mathbf{k}}$ appearing in $E_k(t)$ corresponds to the square lattice nearest-neighbor dispersion relation (6.2). In TPSC and TPSC+GG, since $E_{\text{tot}}(t)$ is conserved after the ramp to a good approximation, this enables one to find β_{therm} by searching for the β of the thermal system with the post-ramp U and energy $E_{\text{tot}}(0) + \Delta E$. In Fig. 7.11, the black arrows indicate the thermalized values for the two ramps, but they are indistinguishable for the fast and slow ramp at that temperature for all quantities except Γ^{ch}. The fact that the thermal reference data agree well with the long-time values is a clear indication that TPSC+GG captures the relatively fast thermalization of local quantities after the ramps.

By ramping down the interaction to small U, the susceptibilities become more alike approaching the Lindhard function [31].

Through TPSC and TPSC+GG, the **k**-resolved time evolution of the spin and charge susceptibilities' spectra can be accessed, as shown in Fig. 7.12 for TPSC+GG and Fig. 7.13 for TPSC. On the y-axis, a similar notation to Figs. 6.24

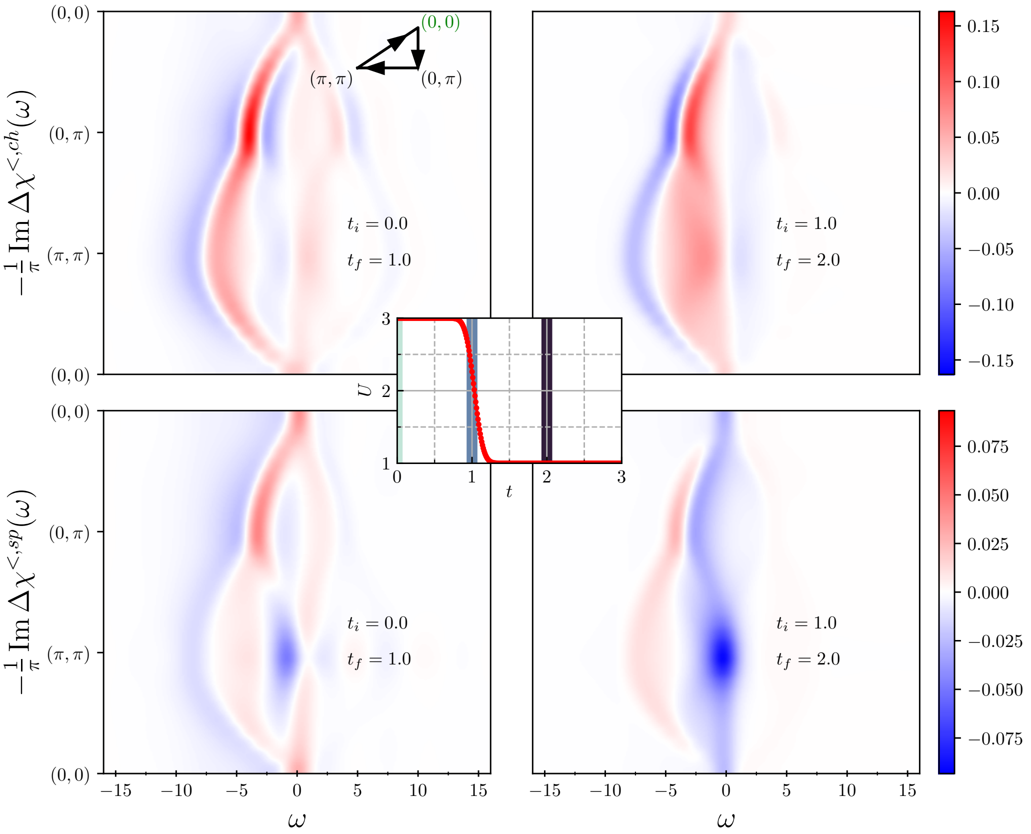

Figure 7.12: Top (Bottom) panels: Difference spectra of the lesser component of the charge (spin) susceptibility after the interaction ramp shown in the inset, using TPSC+GG. The inset black triangle illustrates the path in reciprocal space along which the spectra are displayed. The times t_i and t_f used in the calculation of the difference spectra are annotated in each panel. The time window used in the Fourier transformation is $\Delta t = 5$. Each row of panels uses the same colorscale.

and 6.25 is employed, to the exception that now $\Delta Q(t_f,t_i;\omega) \triangleq Q(t_f;\omega) - Q(t_i;\omega)$, with Q some arbitrary contour-time object. In this particular case, the spectral time differences that are plotted show the imaginary parts of the *lesser* components of the charge (top panels) and spin (bottom panels) susceptibilities. The middle inset plot of Fig. 7.12 shows the profile of the interaction ramp from $U = 3$ to $U = 1$, with its inflection point coinciding with $t = 1$. The initial temperature is $T = 0.33$. The interaction ramp corresponds to the upside-down version of the fast one used in Fig. 7.11. The panels on the left-hand side show $\Delta Q(t_f = 1, t_i = 0; \omega)$, while the right-hand side panels show later-time differences $\Delta Q(t_f = 2, t_i = 1; \omega)$. On the top panels of Fig. 7.12, $\Delta\chi^{\mathrm{ch}}$ displays some shift of the dispersive features that results from the reduced broadening of the density of states with smaller U. Interestingly, the charge spectral excitations have nonzero weight near $\omega \simeq 0$ during the ramp, with maximum intensity around $\mathbf{k}_\pi = (\pi,\pi)$, indicating the appearance of transient low-energy charge excitations. Moreover, a two-peak structure with inverted weight pops up around $\mathbf{k} = (0,\pi)$.

The colorbar is symmetric with respect to 0, having it largest absolute single value setting both the negative and positive scales.

The bottom panels of Fig. 7.12 show the time evolution of the spin excitations throughout the ramp from $U = 3$ to 1. It clearly shows a depletion of the

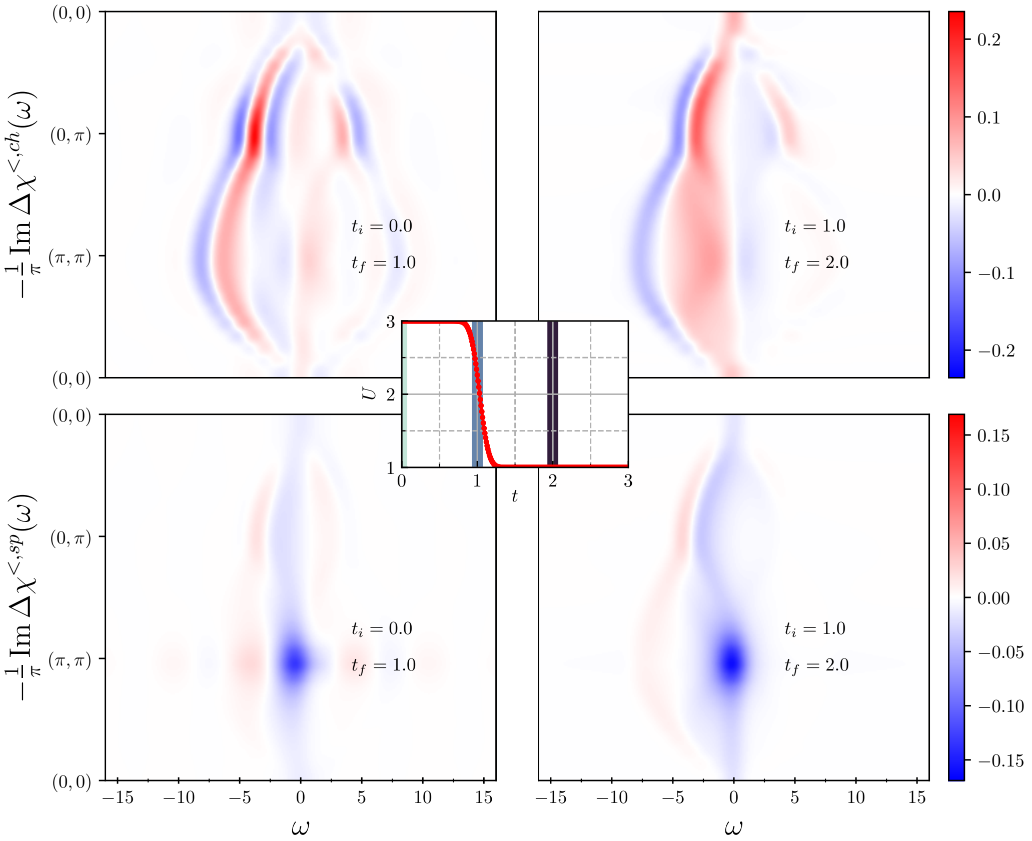

Figure 7.13: Difference spectra analogous to Fig. 7.12, but calculated with TPSC. The corresponding initial and final times t_i and t_f are indicated in each panel. Top (Bottom) panels: The spectral difference of the *lesser* charge (spin) susceptibility after the interaction ramp shown in the inset (the vertical bars indicate the times t_i and t_f). The inset black triangle illustrates the path in reciprocal space along which the spectra are displayed, with the green coordinates corresponding to the initial **k**-point. The time window used for the Fourier transformation is $\Delta t = 5$. Each row of panels uses the same colorscale.

spin excitations around $\mathbf{k}_\pi$, where the spectral weight is strongly reduced. This reduction of the spectral weight at the AFM wave vector is expected since the combined effect of the reduced U and the heating suppresses the antiferromagnetic correlations; one effectively moves away from the renormalized classical regime. The larger spectral change is observed in the second half of the ramp for the two susceptibilities.

The **k**-defined spectral difference shown in Fig. 7.12 can be compared to that computed with TPSC, which does not insert the single-particle interacting Green's functions (5.66) back into the noninteracting two-particle Green's function (5.65) iteratively. In Fig. 7.13, the difference spectra of the TPSC *lesser* component of the charge (top panel) and spin (bottom panel) susceptibilities are shown for the same interaction ramp as in Fig. 7.12 (see middle inset plots). The initial inverse temperature is also $\beta = 3$. The main difference between TPSC and TPSC+GG turns out to be in the colorscale between the bottom panel of Fig. 7.13 and the bottom panel of Fig. 7.12; TPSC shows a larger decrease of the $\mathbf{k}_\pi$ spin excitations when compared to TPSC+GG. These differences arise due to the fact that TPSC overestimates the spin correlation growth. The TPSC and TPSC+GG charge spectra give out similar results for the charge susceptibility (top panels).

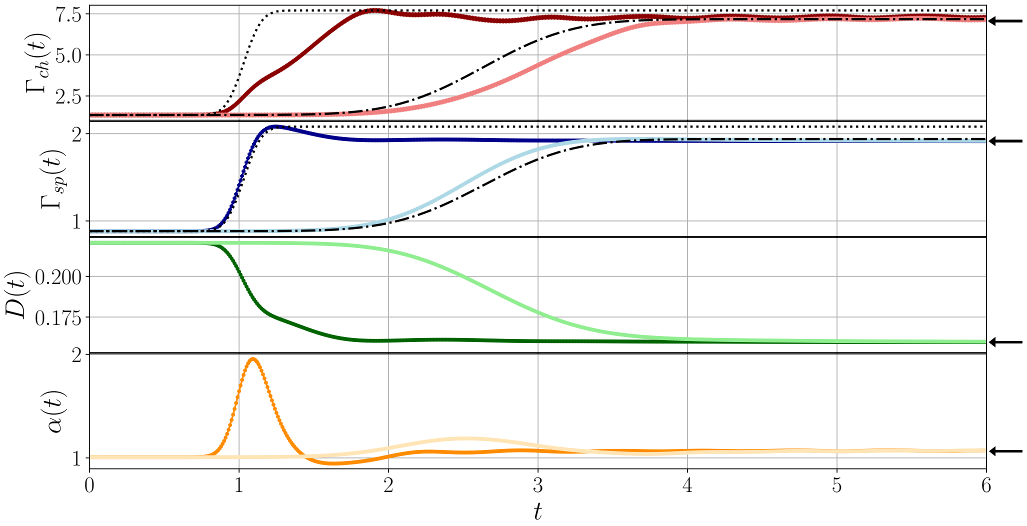

Figure 7.14: Results analogous to Fig. 7.11 using TPSC. The quantities plotted in light colors are associated with the smooth interaction ramp and those in dark colors with the sharp interaction ramp. The dotted lines represent the interaction ramps in arbitrary units. Top panel: charge irreducible vertex Γ^{ch}. Second panel: spin irreducible vertex Γ^{sp}. Third panel: Double occupancy $D(t)$. Bottom panel: α parameter enforcing the sum-rule Eq. (5.71). The thermal values for the two different ramps are almost indistinguishable.

Likewise, the local quantities computed with TPSC can be traced out across time, as is done in Fig. 7.14, where the irreducible vertices, the double occupancy and the parameter α are illustrated for different ramp profiles. The initial temperature is $T = 0.33$ and the thermal temperatures for the slow (fast) ramp is $\beta_{\text{therm}} = 2.83$ ($\beta_{\text{therm}} = 2.71$). The same ramp profile as those in Fig. 7.11 are used. The steeper ramp therefore heats up more the system than the slower one, as is the case for TPSC+GG. The heating effect ensuing the interaction ramp is less strong than for TPSC+GG, where the thermal temperatures are significantly higher. Like for TPSC+GG (Fig. 7.11), the charge vertex approaches the thermal value later than the spin vertex and the transient evolution of the charge vertex does not follow the ramp profile. Furthermore, since the thermalized temperatures after the slow and fast ramps do not differ as much as in TPSC+GG, the thermalized Γ^{ch}'s almost coincide in TPSC. Noticeably, some oscillations emerge in the charge vertex after the ramp, but not in the spin vertex. These oscillations carry a dominant frequency harmonic of $\omega_{\text{osc}} \simeq \frac{2\pi}{W}$, where $W = 8t^{\text{hop}}$ is the square lattice bandwidth. These oscillations persist when changing some tuneable parameters such as the time step, Matsubara grid and $\mathbf{k}$ grid discretization. Once again, the thermal values expected for the different quantities after the slow and fast ramps are pointed by the black arrows, which can be hardly distinguished between the two ramps. These reference data are calculated from the total energy after the ramp. The TPSC results of the vertices Γ_{ch} and Γ_{sp} thermalize at values which are farther apart from each other as compared to the TPSC+GG (Fig. 7.11).

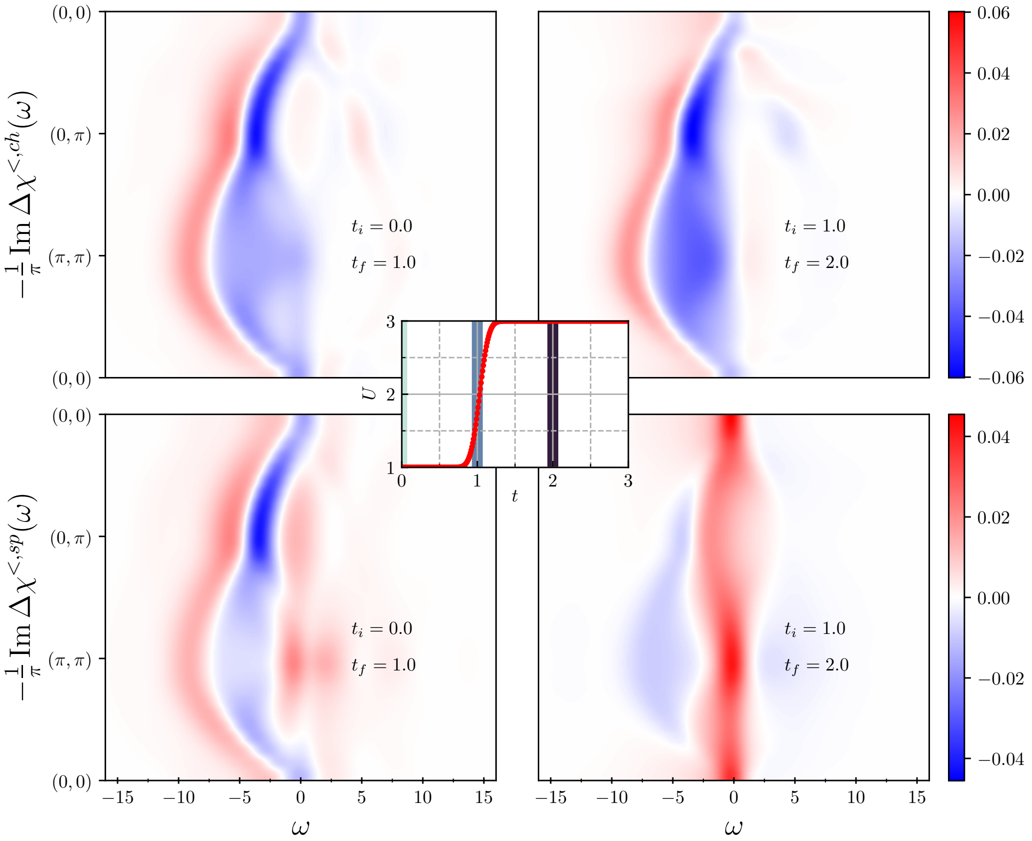

Figure 7.15: Top (Bottom) panels: Difference spectra of the TPSC+GG lesser component of the charge (spin) susceptibility after the interaction ramp from $U = 1$ to $U = 3$ shown in the inset. The time window employed in the Fourier transformation is $\Delta t = 5$. Each row of panels uses the same colorscale.

So far, only the down interaction ramps have been touched on. In Fig. 7.15, the **k**-resolved time differences of the *lesser* spectral weight of the spin (bottom panels) and charge (top panels) susceptibilities calculated within TPSC+GG are plotted for a ramp from $U = 1$ to $U = 3$. The initial temperature inputted in the simulations is $T = 0.33$. This ramp profile is the mirror equivalent along the real-time axis of the down ramp previously employed. Using the same figure layout as Fig. 7.12, the middle inset panel illustrates the up interaction ramp with the vertical colored bars indicating the times involved in $\Delta Q(t_f, t_i; \omega)$. Looking first at the charge response, differently from Fig. 7.12, the up ramp clears out the nonthermal low-energy charges excitations that emerge from the charge scrambling during the down interaction ramp. Dismissing the latter, Fig. 7.15 looks rather like the negative contrast of Fig. 7.12 as far as the charge spectra are concerned: part of the charge spectral weight is shifted to higher absolute energy because of the enhanced broadening caused by the interactions. For the spin spectral time differences, since the up ramp brings the system closer to the renormalized classical regime, $\Delta\chi^{\text{sp},<}(t_f, t_i; \mathbf{k}_\pi)$ is positive portraying an increase in the AFM spin-spin correlations. The stronger heating in the up ramp makes it so that the spectral increase of $\Delta\chi^{\text{sp},<}(t_f, t_i; \mathbf{k}_\pi)$ does not compensate the loss observed in Fig. 7.12, since a higher temperature means weaker spin correlations at $\mathbf{k}_\pi$.

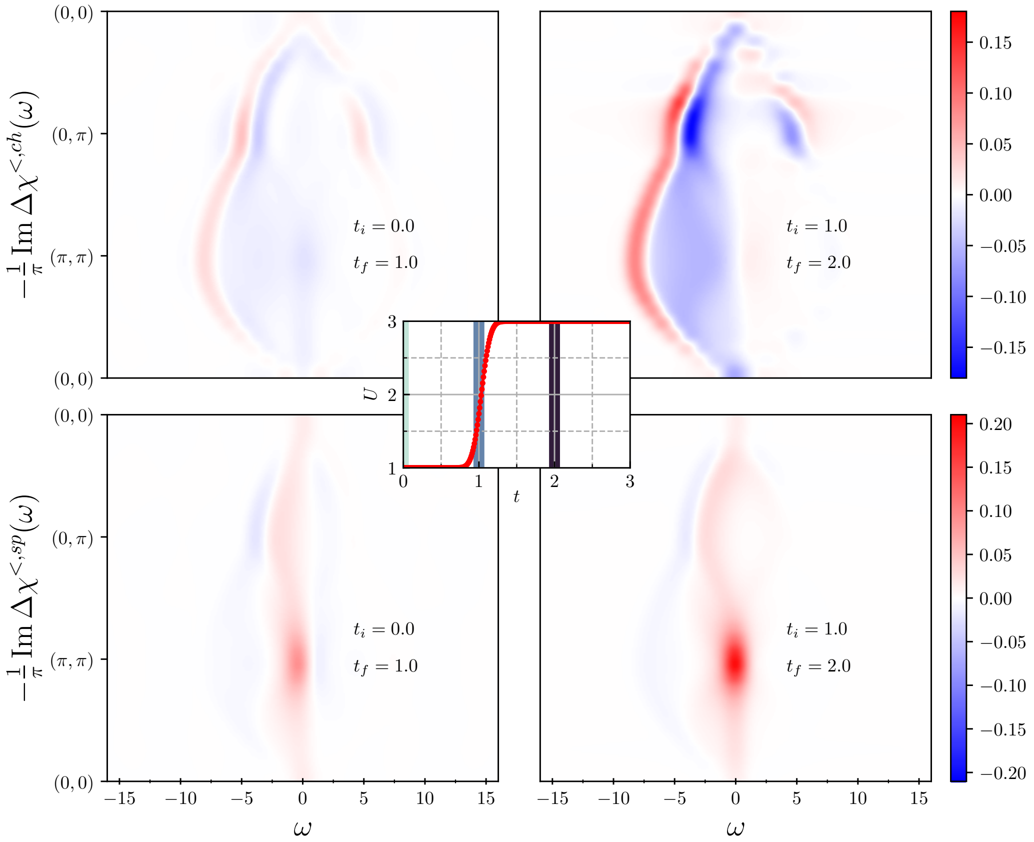

Figure 7.16: Top (Bottom) panels: Difference spectra of the TPSC lesser component of the charge (spin) susceptibility after the interaction ramp from $U = 1$ to $U = 3$ shown in the inset. The time window employed in the Fourier transformation is $\Delta t = 5$. Each row of panels uses the same colorscale.

Fig. 7.16 shows the TPSC results for the spin and charge susceptibilities for the same up ramp as in Fig. 7.15 and same initial temperature. Among the differences that stand out between the TPSC and TPSC+GG results are the changes in the spectra in TPSC that are substantially larger than in TPSC+GG (about 4 times larger) – even more so than for the down ramp (2 times larger in Fig. 7.13). Also, the time differences for the first and second half of the ramp are more similar in TPSC+GG for the two responses as opposed to TPSC, in which case the first time differences (left panels) show weaker spectral amplitudes. In both TPSC and TPSC+GG, the transient charge excitations near $\omega \simeq 0$ show up during the down ramp, not during the up ramp.

There are many ways to read out the momentum dependent time evolution of the responses, each of which enables one to emphasize on some characteristics of the data. One way adopted so far has been to look at the time differences of the spectra. A different stance would be to follow up the time evolution of the full susceptibility spectra, like shown in Fig. 7.17, where the *lesser* component of the spin susceptibility (left panels) and of the charge susceptibility (right panels) after an interaction ramp, obtained with TPSC+GG, are shown at momentum $\mathbf{k}_{\pi}$. The upper (lower) row of panels plot the spectra for an upward (downward) interaction ramp, as shown in the inset plots. The colors of the vertical bars in the inset plots associate with those of the spectra. For $U = 3$ and $T = 0.33$,

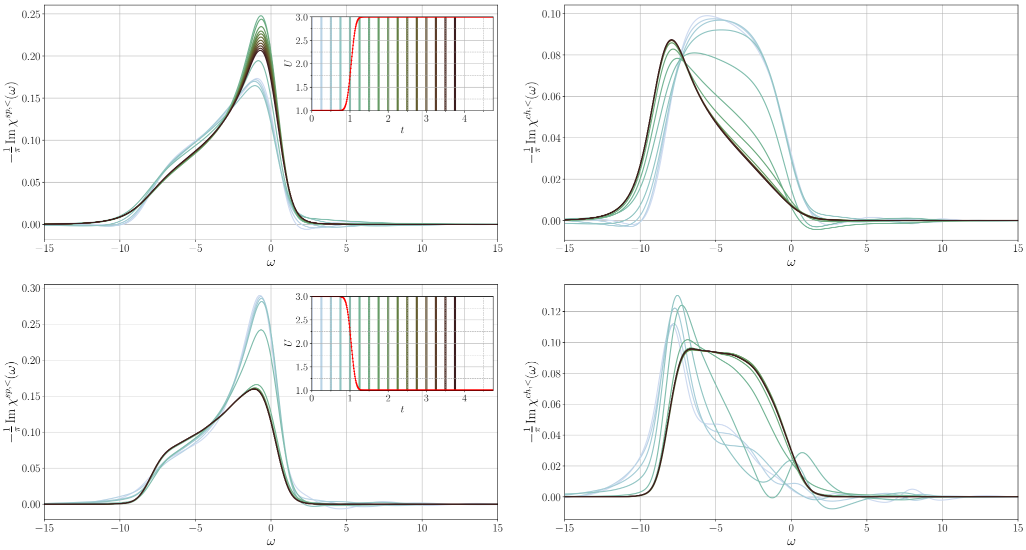

Figure 7.17: The imaginary parts of the *lesser* component of the spin (left panels) and charge (right panels) susceptibilities for momentum $\mathbf{k}_{\pi}$. The top (bottom) panels display the evolution of the susceptibilities upon ramping the interaction up (down). The initial temperature is $T = 0.33$. The insets show the profiles of the interaction ramps with the vertical bars representing the times for which the spectra are calculated. The time window for the Fourier transformation is $\Delta t = 5$.

the system is close to the renormalized classical regime, as can be seen from glancing at Fig. 6.14 [152]. Focalising at momentum $\mathbf{k}_{\pi}$ in Fig. 7.12, the same trends can be observed in Fig. 7.17 (bottom panels) from a different perspective: the dispersive nature of the charge excitation spectra is renormalized in the same way and the spin correlations are depleted at $\mathbf{k}_{\pi}$. The same exercise can be done for the up ramp with Fig. 7.15 and the top panels of Fig. 7.17, both datasets corroborating each other.

In the same spirit to what was done in Section 7.1.2 when studying the π-ton vertex corrections, nonthermal effective temperatures can be drawn out from the one- and two-particle quantities $\mathcal{G}$, χ^{ch}, and χ^{sp}. For that purpose, similar to Eq. (7.5), a frequency and momentum dependent inverse temperature $\beta_{\mathbf{k}}(t,\omega)$ measured at time t is introduced by the formula [24, 121]

$$\beta_{\mathbf{k}}(t,\omega) = \frac{1}{\omega}\ln\left[\mp\frac{\mathcal{A}^{R}_{\mathbf{k}}(t,\omega)}{\mathcal{A}^{<}_{\mathbf{k}}(t,\omega)} \pm 1\right], \tag{7.6}$$

which boils down to the inverse temperature of the system in equilibrium. In Eq. (7.5), the effective temperature was determined computing the slope of the distribution function at the inflection point, whereas now, Eq. (7.6) is more complete in that it bestows a frequency dependence to the effective nonthermal temperature. In Eq. (7.6), the upper (lower) sign holds for bosonic (fermionic) quantities. If the quantities $\mathcal{G}$, χ^{ch} and χ^{sp} are grouped under Λ, then $\mathcal{A}^{R}_{\mathbf{k}}(t,\omega) = -\frac{1}{\pi}\,\mathrm{Im}\,\Lambda^{R}_{\mathbf{k}}(t,\omega)$ (*cf.* Eq. (2.31)) stands for the spectral function, computed with the retarded component, while $\mathcal{A}^{<}_{\mathbf{k}}(t,\omega) = \frac{1}{2\pi}\,\mathrm{Im}\,\Lambda^{<}_{\mathbf{k}}(t,\omega)$ (*cf.* Eq. (2.28)) [5].

In Fig. 7.18, the nonthermal inverse temperature $\beta_{\mathbf{k}}(t,\omega)$ is plotted for $\mathbf{k} = (0,\pi)$ (left panels) and $\mathbf{k} = (\frac{\pi}{2},\frac{\pi}{2})$ (right panels) before the interaction ramp

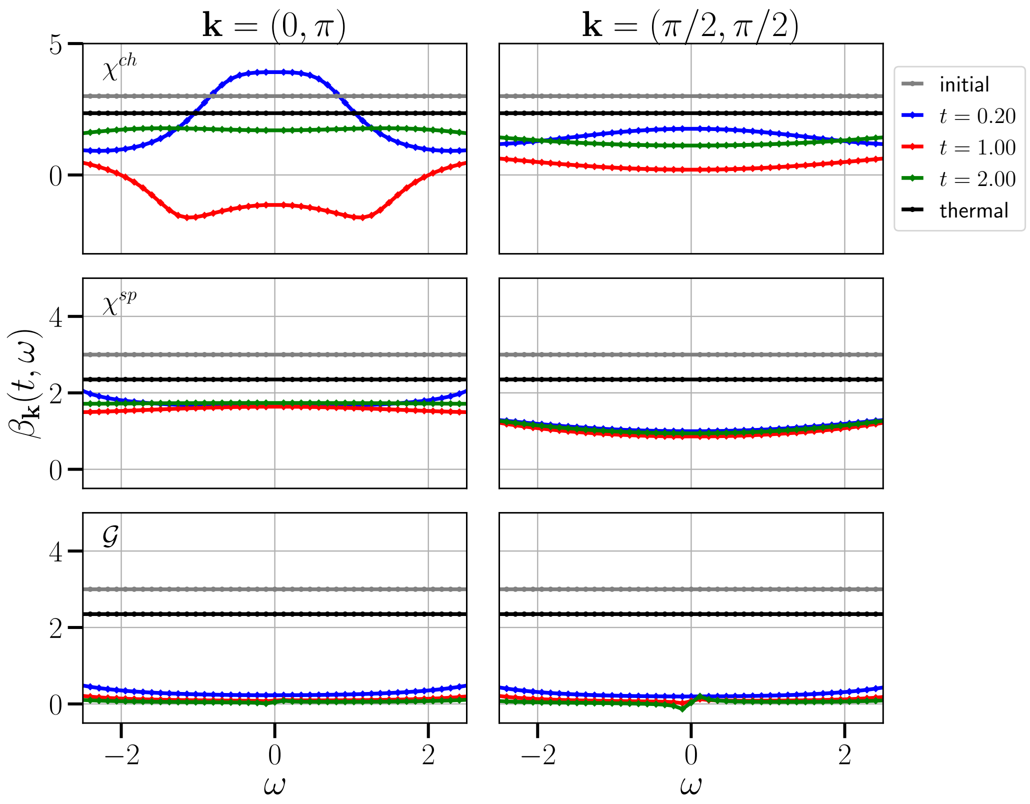

Figure 7.18: Effective inverse temperatures $\beta_{\mathbf{k}}(t,\omega)$ for the Fermi momenta $\mathbf{k} = (0,\pi)$ (left panels) and $\mathbf{k} = (\frac{\pi}{2}, \frac{\pi}{2})$ (see Eq. (7.6)). The gray curve plots the initial $\beta = 3$, the blue curve $\beta_{\mathbf{k}}(t = 0.2,\omega)$, the red curve $\beta_{\mathbf{k}}(t = 1,\omega)$, the green curve $\beta_{\mathbf{k}}(t = 2,\omega)$, and the black curve the thermalized value $\beta_{\text{th}} = 2.35$. The top panels show the effective inverse temperature extracted from χ^{ch}, the middle panels for χ^{sp} and the bottom panels for $\mathcal{G}$.

A negative temperature can be associated with an inverted population of the states: more high energy states are populated than the lower energy states.

($t = 0$ and $t = 0.2$), during the ramp ($t = 1$), after the ramp ($t = 2$) and in the thermalized state. These momenta lie at the Fermi level as depicted by the colormaps of the single-particle spectra of Section 6.2.1.1. The interaction ramp profile is the same as the one illustrated in Fig. 7.12 in the inset plot. Interestingly, for the two Fermi momenta, one finds that while a nonequilibrium temperature can be defined by Eq. (7.6), in the sense that $\beta_{\mathbf{k}}(t,\omega)$ varies slowly with ω near $\omega = 0$, all the three quantities exhibit different nonequilibrium temperatures and different relaxations towards the thermal value. For $\mathbf{k} = (0,\pi)$, the charge susceptibility displays a negative effective temperature in the middle of the interaction ramp ($t = 1$) around $\omega = 0$, which is related to the short-lived transient charge excitations with inverted weight near $\omega \simeq 0$ seen in Fig. 7.12. For $\mathbf{k} = (\frac{\pi}{2}, \frac{\pi}{2})$, the charge susceptibility does not yield negative effective β for the times considered, although the result for $t = 1$ corresponds to a high effective temperature and displays a significant ω-dependence. At $t = 1$ and later, for both Fermi momenta, the charge susceptibility effective temperature becomes almost ω-independent and slowly approaches the thermal value. The spin susceptibility shows a positive $\beta_{\mathbf{k}}(t,\omega)$ for all intermediate times ($t = 0.2, 1, 2$) and an even slower relaxation. At $t = 2$, the charge and spin susceptibilities yield comparable inverse temperatures for given $\mathbf{k}$, but the results differ between the two momenta. The $\beta_{\mathbf{k}=(\frac{\pi}{2},\frac{\pi}{2})}(t,\omega)$ and $\beta_{\mathbf{k}=(0,\pi)}(t,\omega)$ extracted from the one-body Green's function correspond to very high effective temperatures, which increase up to $t=2$. The slow thermalization of $\mathcal{G}_{\mathbf{k}}$ near the Fermi level in weakly correlated systems is expected and has already been discussed in Refs. [92, 119].

7.2.1.2 *3D*

In the 3D case, interaction ramps as well as lattice hopping ramps are used to validate the performance of TPSC and TPSC+GG in dimensions larger than 2. The cubic lattice will be the main unit-cell studied, although like mentioned earlier, the C++ code[2] can handle more 3D unit-cells. For that purpose, as a first scenario looked into, the quench will be of dimensional nature, that is to say, a lattice hopping ramp in the direction perpendicular to the plane t_z^{hop} will be applied. Hence, in Fig. 7.19, a dimensional ramp from the square lattice ($t_z^{\text{hop}}=0$ in Eq. (6.3)) to a cubic lattice ($t_z^{\text{hop}}=1$ in Eq. (6.3)) is calculated at constant interaction $U=2.5$ and initial temperature $T=0.2$ for both TPSC (solid lines) and TPSC+GG (dashed lines). The top panel of Fig. 7.19 shows a decreasing Γ^{ch} when the dimension is increased. This makes sense, since the double occupancy (second last panel) increases with the ratio W/U increasing – recall that moving from 2D to 3D, the bandwidth passes from $8t^{\text{hop}}$ (square lattice) to $12t^{\text{hop}}$ (cubic lattice) –, meaning that the effective charge vertex is reduced. On the other hand, the spin irreducible vertex Γ^{sp} varies in the opposite direction, due to the fact that the double occupancy D increases and both Γ^{sp} and D are related via the ansatz (5.54). This is exactly what is observed in the second panel from top of Fig. 7.19. As a last panel, the renormalizing parameter α is plotted as a function of time (see Eq. (5.71)). In the case of TPSC, this quantity however takes more time to thermalize, since its description (Eq. (5.71)) is strongly affected by the **k**-dependent thermalization of the (convolved) single-particle quantities. Overall, TPSC admits larger variations of the quantities with faster thermalization compared to TPSC+GG.

Thus, quenching from 2D to 3D brings closer the spin and charge vertices, as already depicted by Fig. 6.13. Therefore, the deviation of $\Gamma^{\text{sp/ch}}$ with respect to U seems to hinge strongly on the ratio W/U. As a side note, this assessment would in consequence mean that the RPA-type post-processing method to treat the two-particle vertex corrections (Section 6.1) would be more reliable in 3D for a wider range of interactions and temperatures.

By construction, nonequilibrium TPSC and its variants rely to a much larger extent on the conservation of the potential energy E_{p} than on the kinetic energy E_{k}. This hinges on the fact that the local irreducible vertices are strongly dependent on the double occupancy D (see for instance Eqs. (5.54), (5.68) or (5.71)). Hence, when the total energy deviates after the ramp, which happens for too large and/or too fast ramps, especially for TPSC following a lattice hopping ramp like depicted in Fig. 7.20, it is caused by E_{k} in virtually all cases – it is similar to bare IPT which is the impurity solver used in DMFT+TPSC (see Figs. 7.1 and 7.2). Therefore, as long as E_{p} is stable after the ramps, which is the case in most situations, the TPSC quantities such as $\Gamma^{\text{sp/ch}}$ and D will

---

[2] The code can obtained upon request.

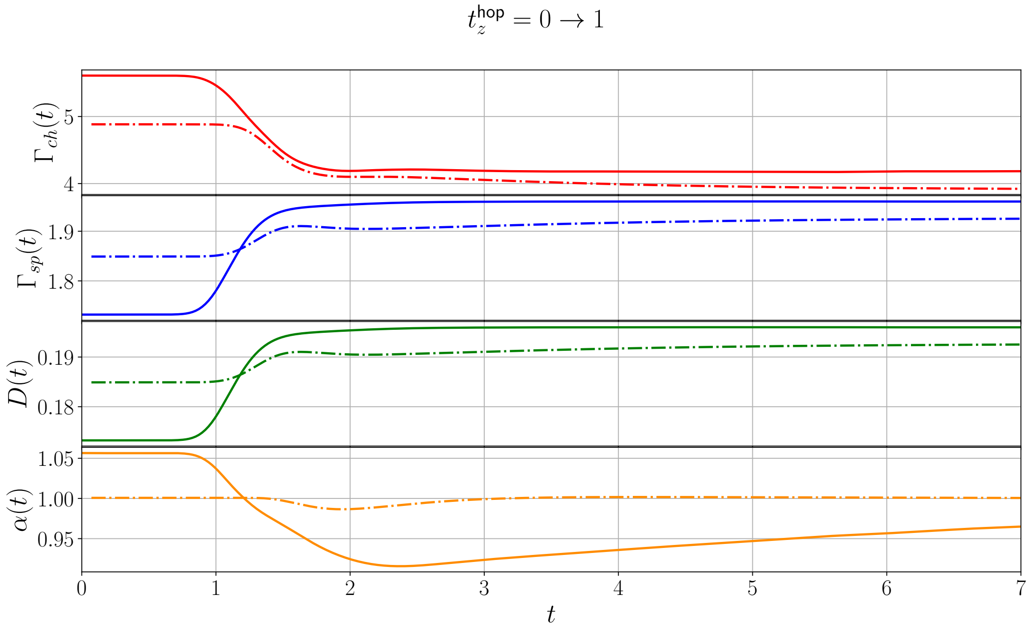

Figure 7.19: Local TPSC (solid lines) and TPSC+GG (dashed lines) quantities in a dimensional ramp from a square lattice to a cubic translating into a ramp from $t_z^{\text{hop}} = 0$ to $t_z^{\text{hop}} = 1$ in the dispersion relation (6.3). The initial temperature is $T = 0.2$ and the constant interaction is $U = 2.5$. The charge irreducible vertex (top panel), spin irreducible vertex (second panel from top), D^{imp} (third panel from top) and α (bottom panel) are plotted for a time window of $\Delta t = 7$.

stabilize at some value. One particularly useful observation is that even if E_{k} drifts, thermalized temperatures can be assigned within TPSC frameworks by matching the post-ramp values of the local quantities ($\Gamma^{\text{sp/ch}}$ and D) with those calculated at equilibrium for the same post-ramp value: the T_{therm} values thereby extracted for each local quantities are almost exactly the same[3], *i.e.* $T_{\text{therm}}(\Gamma^{\text{ch}}) = T_{\text{therm}}(\Gamma^{\text{sp}}) = T_{\text{therm}}(D)$. When calculating the thermalized temperature of the system after the t_z^{hop} ramp in Fig. 7.19, one finds that the variation from the initial temperature ($T = 0.2$) is negligible in TPSC. Hence, the thermalized values of the local quantities depicted in Fig. 7.19 are those, at equilibrium, of a cubic lattice at $U = 2.5$ and $T_{\text{therm}} \simeq 0.204$. On the other hand, the thermalized temperature calculated from TPSC+GG would be much higher, that is $T_{\text{therm}} \simeq 1.06$. The way the thermalized temperature is computed after a lattice hopping ramp is the same as the one explained for U-ramps (Eq. (7.3)), with the exception that equilibrium results are calculated with the post-ramp t_z^{hop} (U is fixed).

The system heats up much more in TPSC+GG as well when ramping the interaction, compared to TPSC (see Section 7.2.1.1).

Next, the spectral time evolution of the spin and charge susceptibilities is studied across the dimensional ramp in Fig. 7.21. The spectral evolution is tracked down at momentum $\mathbf{k}_\pi = (\pi, \pi, \pi)$. In the top panel, the spin susceptibility shows that the peak at $\omega \simeq 0$ melts down when going to third dimension: the spins scatter less at momentum $\mathbf{k}_\pi$. Also, the energy domain of spin spectral excitations is stretched out to larger absolute energies since the bandwidth is increased. Like in 2D (Section 7.2.1.1), the spin spectral weight tends to thermalize slower than the charge excitation spectra. In the bottom panel, the charge spectral weight features also an increase of its energy domain. Apart from the broadening it is subject to, the spectral peak is also shifted up in energy when going to 3D: this would be because the bandwidth becomes substantially wider, *i.e.* the ratio W/U is increased (see Fig. 7.20).

---

[3] This is however not the case in DMFT+TPSC.

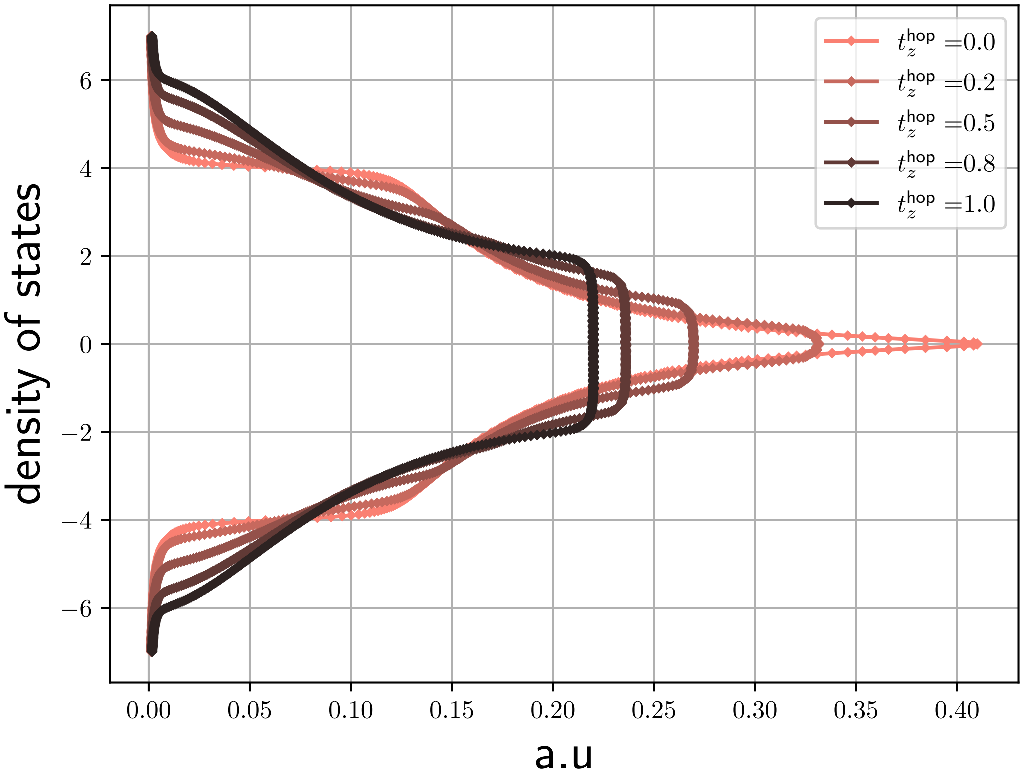

Figure 7.20: Evolution of the local electronic density of states when passing from a 2D square lattice to a 3D cubic lattice at half-filling. The equation describing this evolution is Eq. (6.3), with t_z^{hop} the perpendicular lattice hopping being changed.

The spectral time-cuts shown in Fig. 7.21 are taken out of the full **k**-dependent spectral evolution of the spin and charge susceptibilities displayed in Fig. 7.22. The inset plot of Fig. 7.22 illustrates the ramp profile of t_z^{hop}, with the vertical bars matching the spectral time cuts sharing the same color. In the top panel of Fig. 7.22, the spin *lesser* spectral weight at $\mathbf{k}_\pi$ shows an important reduction of the peak at $\omega \simeq 0$ associated with the AFM ordering when going to 3D from 2D. In addition, the excitation spectra stretch out to larger absolute frequencies in relation with the enlarged bandwidth W. The enlargement of W in 3D can also be observed in the charge spectral weight displayed in the bottom panel of Fig. 7.22, where the charge excitation spectra that peaked around $\omega \simeq -8$ is redistributed across roughly the same energy window $\omega \in [-13,2]$ as the spin spectral weights.

In Fig. 7.22, the full **k**-defined spectral time difference is drawn for the charge susceptibility in the top panels and the spin susceptibility at the bottom. The y-axis folds back onto the inset wedge of the irreducible Brillouin zone (black triangle) in the sense the arrows point to. The black triangle lies within the recip-

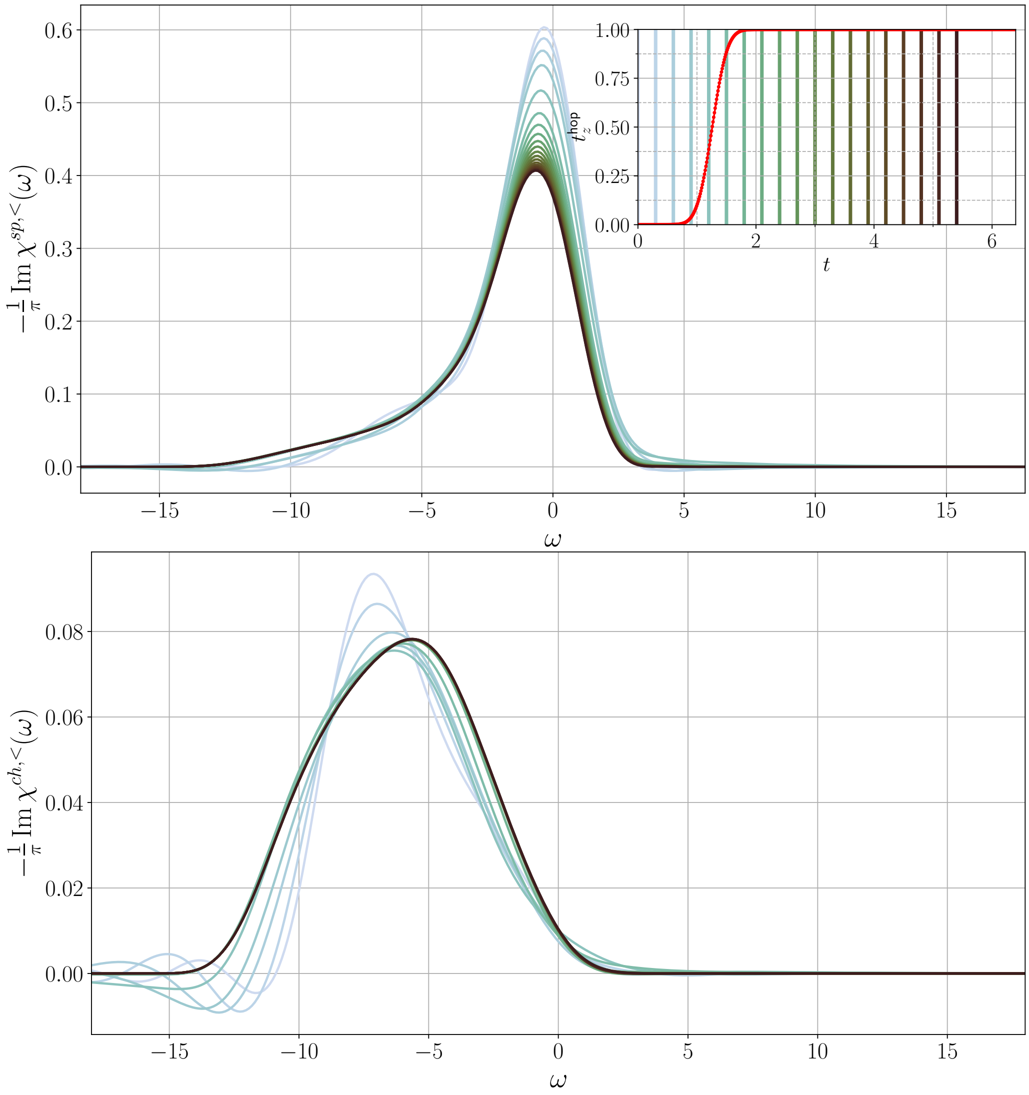

Figure 7.21: The imaginary parts of the *lesser* component of the spin (top panel) and charge (bottom panel) susceptibilities for momentum $\mathbf{k}_\pi$ using TPSC. The initial temperature is $T = 0.2$ and interaction $U = 2.5$. The inset shows the profile of the perpendicular hopping ramps t_z^{hop} with the vertical bars representing the times at which the spectra are calculated. The time window for the Fourier transformation is $\Delta t = 2.5$.

rocal plane $k_z = \pi$. On the left-hand side of Fig. 7.22, the difference $\Delta\chi(t_f, t_i; \omega)$ is plotted for $t_i = 0$ and $t_f = 1.2$, whilst $t_i = 1.2$ and $t_f = 2.4$ on the right-hand side. The inset plot traces the perpendicular hopping ramp with the vertical bars indicating the time snapshots t_i and t_f. Firstly, one striking feature standing out is the unevenness between the left and right panels; much of the change happens in the first half part of the ramp, while almost nothing happens in the second half of the ramp. This can be partly explained by the fact that these spectra are computed using a forward Fourier transform (2.67) that employs a time window Δt that is larger than the duration of the ramp; these transforms take into account the state after the ramp, even at early times. Since the relative weight of the ripples appearing at $|\omega| \gtrsim 15$ varies a lot with the time window

Δt used in the forward Fourier transform, these are artefacts of the Fourier transformation that can be diminished. In the case of the charge susceptibility, the excitations are redistributed to larger absolute energies. Regarding the spin excitation spectra, a wide array of $\mathbf{k}$-points loose spectral weight around $\omega \simeq 0$, especially in the vicinity of $\mathbf{k}_{\pi}$, as seen in the bottom panels of Fig. 7.21. The ripples showing up in Fig. 7.22 at large absolute frequencies ($|\omega| \gtrsim 15$) are artefacts that get slightly enhanced when increasing the time window Δt in the forward Fourier transform; for that reason, $\Delta t = 2.5$ for all time difference colormaps plotting dimensional crossover ramps. Those artefacts can be spotted in the lower left corner of the bottom panel of Fig. 7.21.

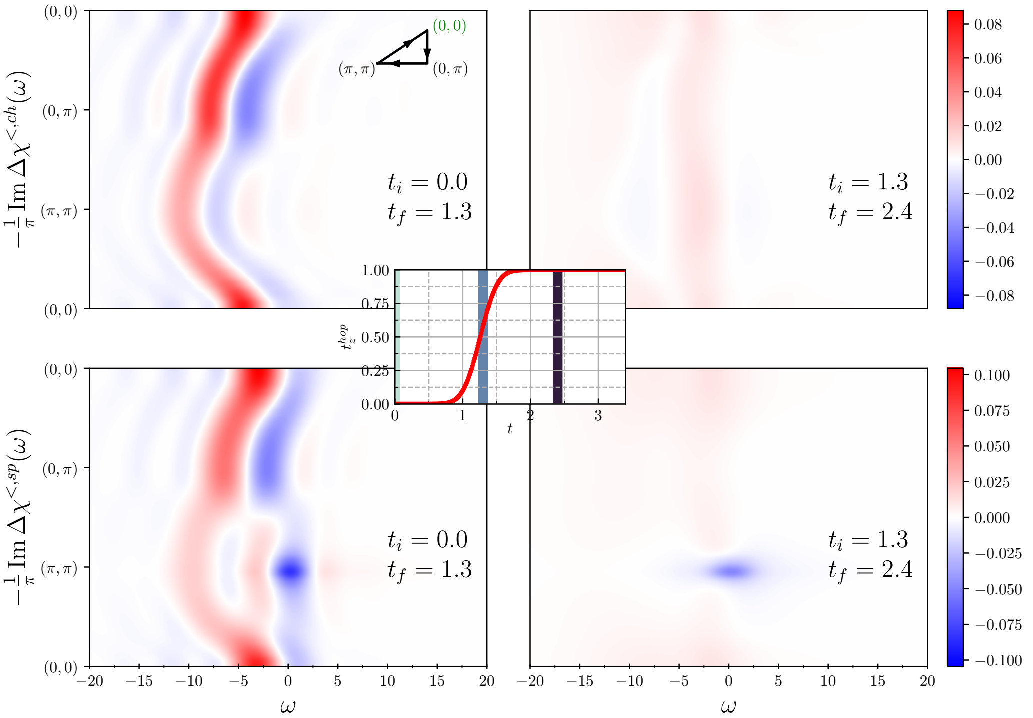

Figure 7.22: Top (Bottom) panels: Difference spectra of the lesser component of the charge (spin) susceptibility after the interaction ramp shown in the inset. The inset black triangle illustrates the path in reciprocal space along which the spectra are displayed, within the plane cut $k_z = \pi$. The times t_i and t_f used in the calculation of the difference spectra are annotated in each panel. The time window used in the Fourier transformation is $\Delta t = 2.5$. Each row of panels uses the same colorscale. The method used here is TPSC.

Finally, an interaction ramp using TPSC+GG in 3D is done from $U = 4$ to $U = 2$ to check out if there are similarities with what was observed in 2D interaction ramps, as shown in Fig. 7.12. The Figure 7.23 illustrates the *lesser* component spectral difference $\Delta\chi(t_f, t_i; \omega)$ for $t_i = 0$ and $t_f = 1.2$ on the left-hand side, and for $t_i = 1.2$ and $t_f = 2.4$ on the right-hand side. The top panels show the charge susceptibility whereas the bottom ones show the spin susceptibility. Again, the middle inset plot shows the interaction ramp profile. The triangle inset, which displays the $\mathbf{k}$-point layout along the y-axis in the direction of the arrows starting from the green coordinate, lies in the $k_z = \pi$ plane. From inspecting the charge susceptibility spectral differences, one can notice the appearance of transient low-energy charge excitations for most $\mathbf{k}$-points, like was reported in the 2D case (see Fig. 7.12) [121]. Turning to the spin spectral difference, one can see once again salient similarities: a spectral reduction at $\mathbf{k}_\pi = (\pi, \pi, \pi)$ dominates the picture because, on top of the heating phenomenon, the decrease in U pushes the system farther away from the 3D renormalized classical regime in the (T, U)-plane.

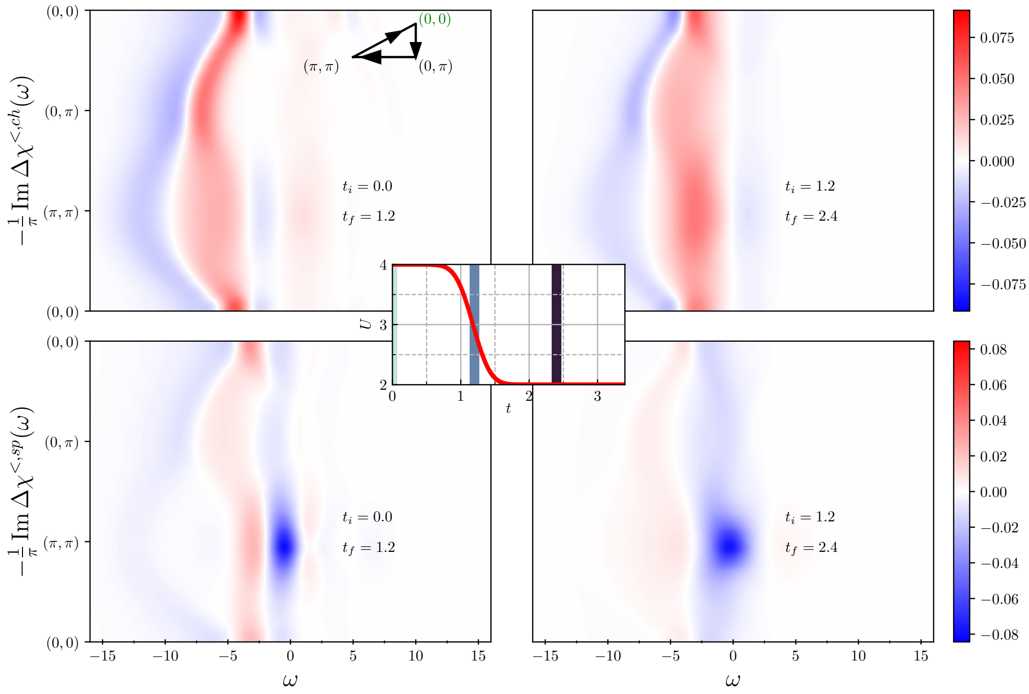

Figure 7.23: Top (Bottom) panels: Difference spectra of the TPSC+GG lesser component of the charge (spin) susceptibility after the interaction ramp from $U = 4$ to $U = 2$ shown in the inset. The time window employed in the Fourier transformation is $\Delta t = 5$. The 3D cubic lattice model is used and the initial temperature is $T = 0.33$. Each row of panels uses the same colorscale.

7.2.2 *DMFT+TPSC*

In this section, several results are presented of the self-consistent DMFT+TPSC and DMFT+TPSCα methods introduced in Section 5.2.9. Just like for the nonequilibrium TPSC and TPSC+GG, the quantity ramped in 2D is the interaction, whereas in 3D both the interaction parameter and the lattice hopping term are ramped in time. The strengths of the DMFT+TPSC schemes in systems out of equilibrium will be mainly discussed in the beginning.

In Section 6.2.1.1, it was shown by comparing to DiagMC (Figs. 6.26 and 6.27) that the equilibrium self-energy at the antinodal point of the Fermi surface calculated with TPSC+GG and DMFT+TPSC was improved substantially, especially at higher temperatures in the case of DMFT+TPSC. One could therefore naively argue that TPSC+GG would be superior to all other methods at computing the nonlocal electronic correlations out of equilibrium. This is however not the case, as will be shown further down. It will be shown that DMFT+TPSC surpasses the array of methods introduced in this thesis when it comes to nonthermal transient correlations.

Let's start off by comparing the local electronic double occupancy following an interaction ramp from $U = 0 \to 1$ and one from $U = 1 \to 2$ in the 2D nearest-neighbor Hubbard model. The goal is to compare the nonthermal dynamics captured by various methods that are reliable at weak coupling. For that purpose, the lattice second-order method[4] $\Sigma^{(2)}$ [135], DMFT+IPT with second-order IPT as impurity solver (see Eq. (3.26)), the original formulation of TPSC (OG TPSC), DMFT+TPSC and TPSC+GG are tested one against the other. To put it as a reminder, OG TPSC does not enforce the sum-rule (5.71) introducing some time-dependent parameter α that evens out the double occupancy calculated from the TPSC ansatz Eq. (5.54) and that computed from the trace over lattice TPSC quantities (5.104) (the double occupancy from the ansatz (5.54) is the reference value). Because both DMFT+IPT and $\Sigma^{(2)}$ are reliable at weak coupling, the data from these two methods will be benchmarked upon.

In Fig. 7.24 are shown the double occupancies calculated from lattice quantities as a function of time across the interaction ramp $U = 0 \to 1$ (top panel) and the one $U = 1 \to 2$ (bottom panel). For the single-orbital model, the double occupancy shown in Fig. 7.24 is generically computed via

$$\langle \hat{n}_{-\sigma}(z)\hat{n}_{\sigma}(z)\rangle = \frac{-i}{2U(z)} \mathrm{Tr}\left[\Sigma_{\mathbf{k}} * \mathcal{G}_{\mathbf{k}}[\Sigma_{\mathbf{k}}]\right]^{<}(z,z). \tag{7.7}$$

For the different methods compared, the self-energy $\Sigma_{\mathbf{k}}$ and lattice Green's function $\mathcal{G}_{\mathbf{k}}$ represent different expressions (see Table. 5.1). Indeed, in the case of lattice IPT, $\Sigma_{\mathbf{k}}$ becomes $\Sigma^{(2)}_{\mathbf{k}}$ (5.67) and the lattice Dyson equation to be solved is Eq. (5.66) with its respective self-energy expression. For DMFT+IPT, $\Sigma_{\mathbf{k}} \to \Sigma^{(2)}_{\mathrm{imp}}$ (Eq. (3.26)) with Eq. (3.14) representing the lattice Dyson equation. As for OG TPSC, $\Sigma_{\mathbf{k}} \to \Sigma^{(1),\mathrm{TPSC}}_{\mathbf{k}}$ (Eq. (5.63)) with $\mathcal{G}_{\mathbf{k}}$ determined from Eq. (5.66). In the case of TPSC+GG, $\Sigma_{\mathbf{k}} \to \Sigma^{(1),\mathrm{TPSC}}_{\mathbf{k}}$ (Eq. (5.70)) with $\mathcal{G}_{\mathbf{k}}$ determined from Eq. (5.66). Finally, for DMFT+TPSC, $\Sigma_{\mathbf{k}}$ is defined in Eq. (5.101) and $\mathcal{G}_{\mathbf{k}}$ in Eq. (5.102).

Looking back at Fig. 7.24, the double occupancies D traced out by DMFT+IPT and $\Sigma^{(2)}$ follow each other very tightly, both featuring a dip right after the bare interaction ramp, succeeded by a fast thermalization for the two ramps. Out of all the methods and for the two ramps, solely OG TPSC fails to reproduce the qualitative transient behavior of this local quantity: it shows a sudden increase of the double occupancy at the beginning of the interaction ramp with no dip at the end. Furthermore, the thermalized value of D calculated from OG TPSC differs quite a lot from the other methods, in particular for the ramp $U = 1 \to 2$. The unphysical behavior of D could also be related to the approximation of the Bethe-Salpeter (5.69) that is used out of equilibrium. DMFT+TPSC agrees very well at all times with the results of DMFT+IPT and lattice IPT $\Sigma^{(2)}$, especially for the interaction ramp $U = 0 \to 1$ (*cf.* top and bottom panels of Fig. 7.24). One way to correct the transient anomalies of OG TPSC is to resort to the sum-rule (5.71) in determining the second-level approximation (5.70): this is nothing else than TPSC – TPSC+GG if there is self-consistency. Doing so, the double occupancy does not show a transient dubious increase at the start of the up-ramp and there is only one double occupancy, since that obtained from

---

[4] Check out Eq. (5.67).

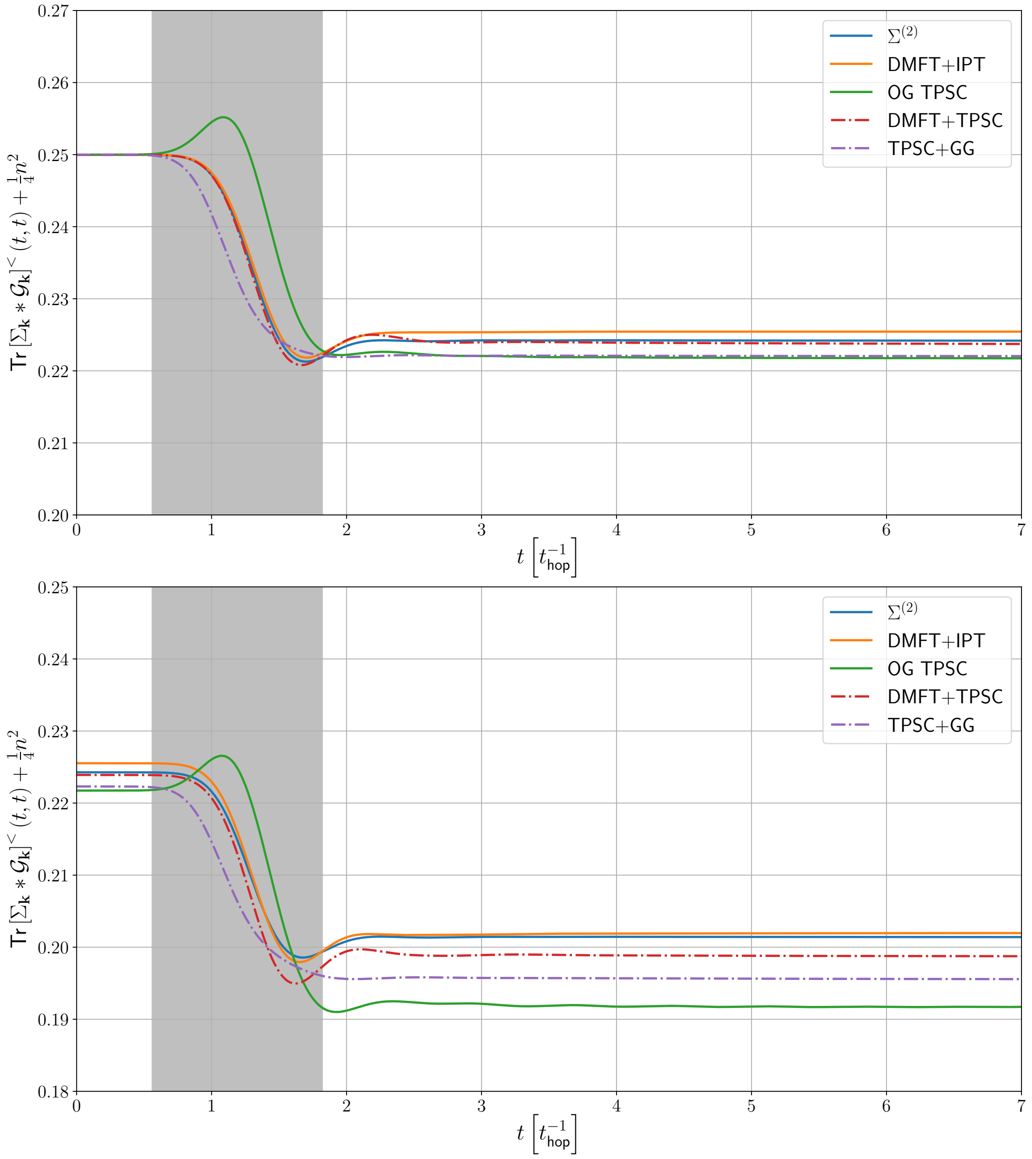

Figure 7.24: Lattice-defined double occupancies calculated from Eq. (7.7) for lattice IPT, DMFT+IPT, OG TPSC, DMFT+TPSC and TPSC+GG. The interaction ramp travels from $U = 0$ to $U = 1$ (top panel) and from $U = 1$ to $U = 2$ (bottom panel) at initial inverse temperature $\beta = 5$. The grey shading indicates the time window over which the interaction changes. The model used is the 2D nearest-neighbor single-band Hubbard model (3.9).

the ansatz is explicitly equal to that calculated from the lattice quantities (left-hand side of Eq. (7.7)). This correction is shown in Fig. 7.25 along with the same results for $\Sigma^{(2)}$ and DMFT+IPT as in Fig. 7.24. DMFT+TPSC differs from Fig. 7.24 in that the double occupancy illustrated in Fig. 7.25 is taken from the impurity quantities (5.99). Again, the top panel of Fig. 7.25 displays the ramp $U = 0 \to 1$ while the bottom panel shows the ramp $U = 1 \to 2$. However, the result changes slightly when using D^{imp} in DMFT+TPSC, since, as demonstrated in Section 6.2.2, DMFT+TPSC approximately accounts for the double-counting of the self-energy diagrams (see Fig. 6.36). In DMFT+TPSC, the change between D^{imp} (Fig. 7.25) and D^{TPSC} (Fig. 7.24) widens when the interaction is increased.

In fact, the difference between the DMFT+TPSC data of Figs. 7.24 and 7.25 for the ramp $U = 0 \to 1$ is very small, *i.e.* of about 1%, while that of the ramp from $U = 1 \to 2$ is about 4%.

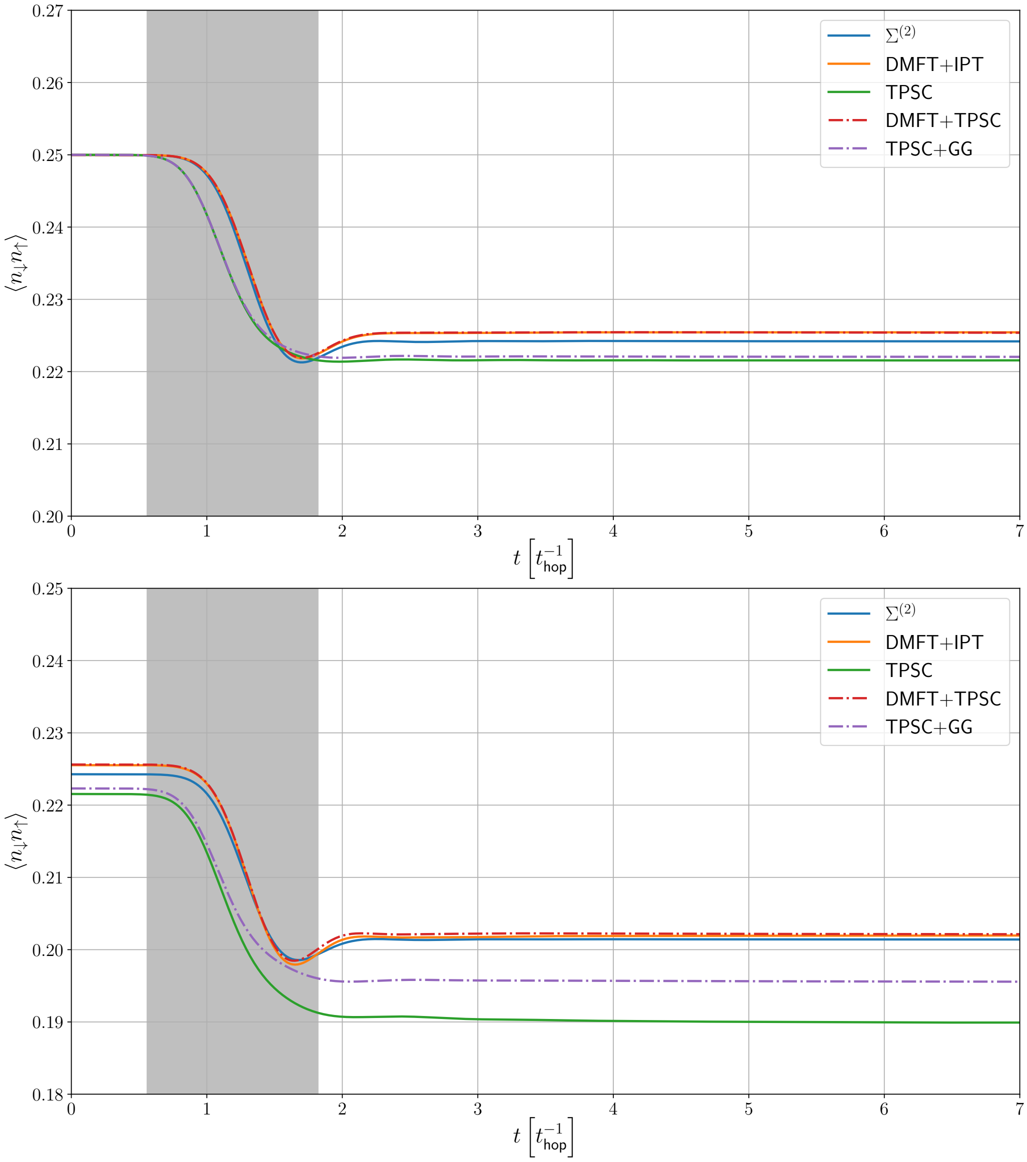

Figure 7.25: Double occupancies calculated using the impurity quantities (5.99) in the case of DMFT+TPSC. In the case of TPSC, the double occupancy taken from Eq. (5.54) is shown. Nothing changes for lattice IPT, lattice $\Sigma^{(2)}$ and TPSC+GG. The same model and parameters as in Fig. 7.24 are employed and the top panel illustrates the ramp $U = 0 \to 1$ and the bottom panel shows $U = 1 \to 2$. Once more, the grey shading indicates the time range over which U changes.

Let's now look at a particular interaction quench going from $U = 1$ to $U = 3$ corresponding to the same ramp profile as the slow one of Fig. 7.11. The initial temperature is $T = 0.33$ at half-filling in 2D. In Fig. 7.26, the local irreducible vertices Γ^{ch} (top panel) and Γ^{sp} (second panel from top), the impurity double occupancy D^{imp} (third panel from top) and lattice double occupancy D^{TPSC} (bottom panel) are displayed over a time window of $\Delta t = 8$. After the ramp, Γ^{ch} thermalizes to 6.10 and Γ^{sp} to 2.06 in DMFT+TPSC (dashed lines). These values reached upon thermalization in DMFT+TPSC are very close to these of TPSC+GG (solid lines), which are $\Gamma^{\mathrm{ch}} \simeq 6.01$ and $\Gamma^{\mathrm{sp}} \simeq 2.05$. The same goes for the local double occupancies, which is calculated from Eq. (5.54) in TPSC+GG and from Eq. (5.99) in DMFT+TPSC: for TPSC+GG, the value plateaued at is $D = 0.172$ and it is $D^{\mathrm{imp}} = 0.177$ for DMFT+TPSC (green curves). In DMFT+TPSC, the thermalized value of the double occupancy obtained from the lattice D^{TPSC} (Eq. (5.104)) reads 0.174 (orange curve), which is quite close to that of TPSC+GG. In Fig. 7.26, the double occupancies D^{TPSC} and D^{imp} overlap almost perfectly on top of each other for the two schemes. Moreover, given that the interaction ramp used in Fig. 7.26 is slower than that used in Figs. 7.24 and 7.25, no transient dips in the double occupancies are observed: the curves reach almost instantaneously their thermalized value after the interaction ramp is over. Notice that the charge vertex Γ^{ch} (top panel of Fig. 7.26) is delayed compared to the spin Γ^{sp} (second top panel of Fig. 7.26) in attaining its thermalized value, as was reported in the case of TPSC (Fig. 7.14) and TPSC+GG (Fig. 7.11), which contrary to DMFT+TPSC make use of the ansatz (5.54) binding explicitly D and Γ^{sp}.

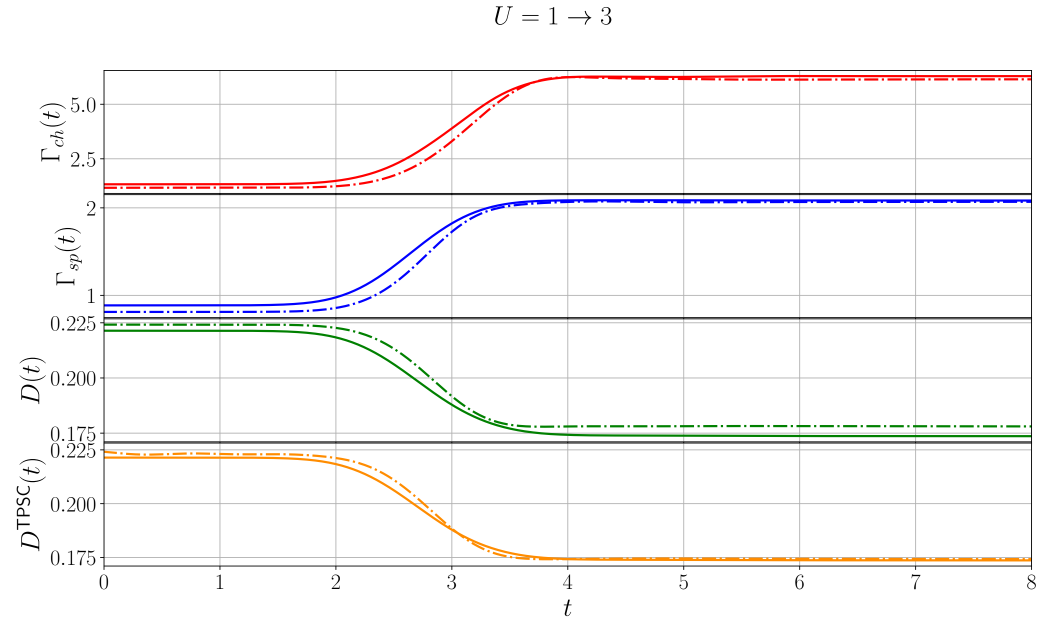

Figure 7.26: Local DMFT+TPSC (dashed lines) and TPSC+GG (solid lines) quantities in the 2D single-band nearest-neighbor Hubbard model for the ramp $U = 1$ to $U = 3$ at initial temperature $T = 0.33$. The charge irreducible vertex (top panel), spin irreducible vertex (second panel from top), D^{imp} (third panel from top) and D^{TPSC} (bottom panel) are plotted for a time window of $\Delta t = 8$.

To confirm that DMFT+TPSC gives sensible results for all **k**-points, time differences in the **k**-defined susceptibility spectra are calculated with DMFT+TPSC and compared with TPSC+GG and TPSC. For that matter, an up-ramp in interaction is utilized to compare all the methods in question. That ramp is shown in Fig. 7.27 as inset plot for DMFT+TPSC. In fact, the ramp shown in Fig. 7.27 corresponds to the same as the one used in Fig. 7.26 and it is slower than the ones used in Figs. 7.15 (TPSC+GG) and 7.16 (TPSC). The spectral time differences $\Delta\chi^{\mathrm{ch/sp},<}(t_f,t_i;\mathbf{k})$ involve times $t_i = 0$ and $t_f = 4$ in the left panels of Fig. 7.27, and times $t_i = 4$ and $t_f = 8$ in the right panels of Fig. 7.27. The fact that the interaction ramp spans over a longer time window in Fig. 7.27 seems to symmetrize the time difference $\Delta\chi^{\mathrm{ch/sp},<}(t_f = 4, t_i = 0;\mathbf{k})$ (left panel) and $\Delta\chi^{\mathrm{ch/sp},<}(t_f = 8, t_i = 4;\mathbf{k})$ (right panel) – they look more similar than the left and right panels of Figs. 7.15 and 7.16 where a faster ramp is utilized. The latter would be an indication that the forward Fourier transform mainly causes this asymmetry in the time differences. Aside from this, the same aspects are picked up by DMFT+TPSC, namely the growth of spin correlations when increasing the interaction and the redistribution of the charge excitation spectra at larger absolute energies due to the enhancement of the correlations.

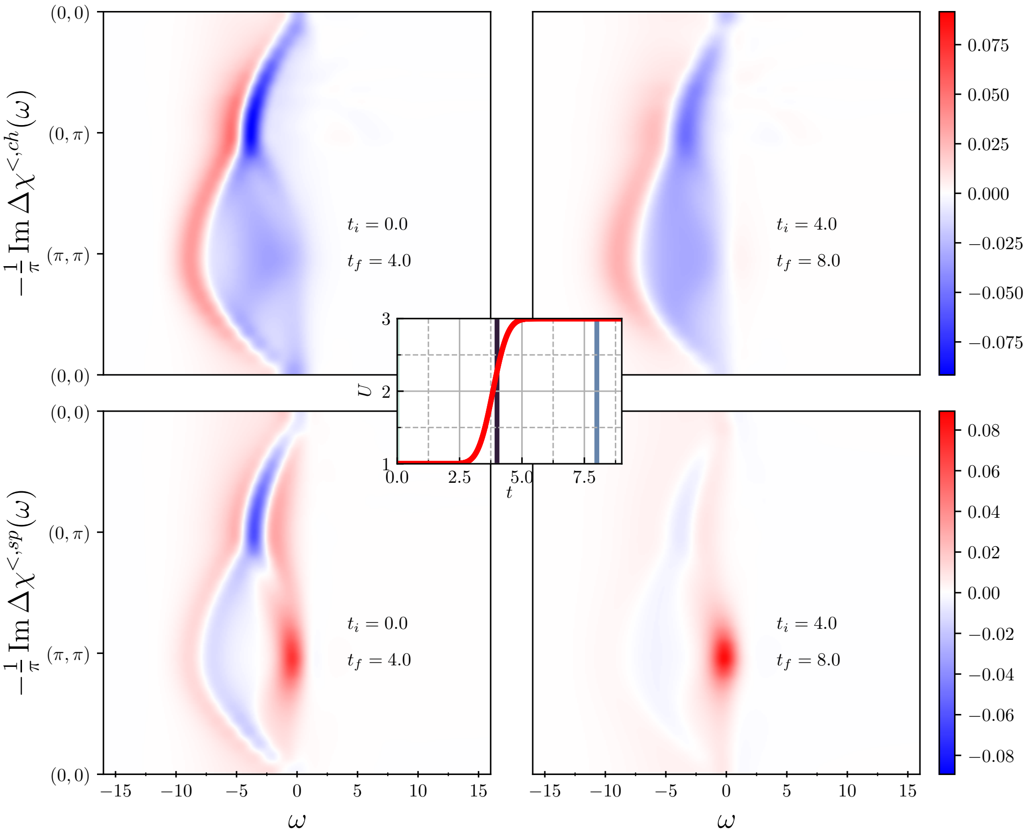

Figure 7.27: Top (Bottom) panels: Difference spectra of the TPSC lesser component of the charge (spin) susceptibility after the interaction ramp from $U = 1$ to $U = 3$ shown in the inset. The initial temperature is $T = 0.33$. The time window employed in the Fourier transformation is $\Delta t = 5$. Each row of panels uses the same colorscale.

The main caveat regarding DMFT+TPSC as currently formulated, *i.e.* without some parameter enforcing the equivalence of D^{TPSC} (Eq. (5.104)) and D^{imp} (Eq. (5.99)), is that there is no unambiguous way to determine a thermalized temperature. Thus, an inverse temperature of $\beta_{\mathrm{therm}} \simeq 2.43$ is obtained on the impurity whereas one of $\beta_{\mathrm{therm}} \simeq 3.52$ is obtained on the lattice. Therefore, the impurity would be hotter than the lattice following the quench in Fig. 7.26. Another problem is that none of these T_{therm} match with the values reached once they stabilize. Hence, neither of the T_{therm} on the lattice nor on the impurity lead to the "thermalized" values[5] of the vertices and double occupancies had the values been calculated with the post-ramp U at T_{therm}. However, as will be seen next when ramping in dimensionality (from 2D to 3D), this difference in temperatures between the impurity and the lattice unfolds interesting observations in the local quantities. This discrepancy between D^{TPSC} (Eq. (5.104)) and D^{imp} (Eq. (5.99)) could in principle be cured by calling in a *renormalizing* parameter α like in Eq. (5.105). This additional constraint leads to DMFT+TPSCα introduced at the end of Section 5.2.9, which is however unstable out of equilibrium. The discrepancy between the lattice and impurity quantities could also mean that the impurity should be seen as some auxiliary object, just like the hybridization function Δ introduced in Section 3.2, and consider the lattice quantities to be the physical ones.

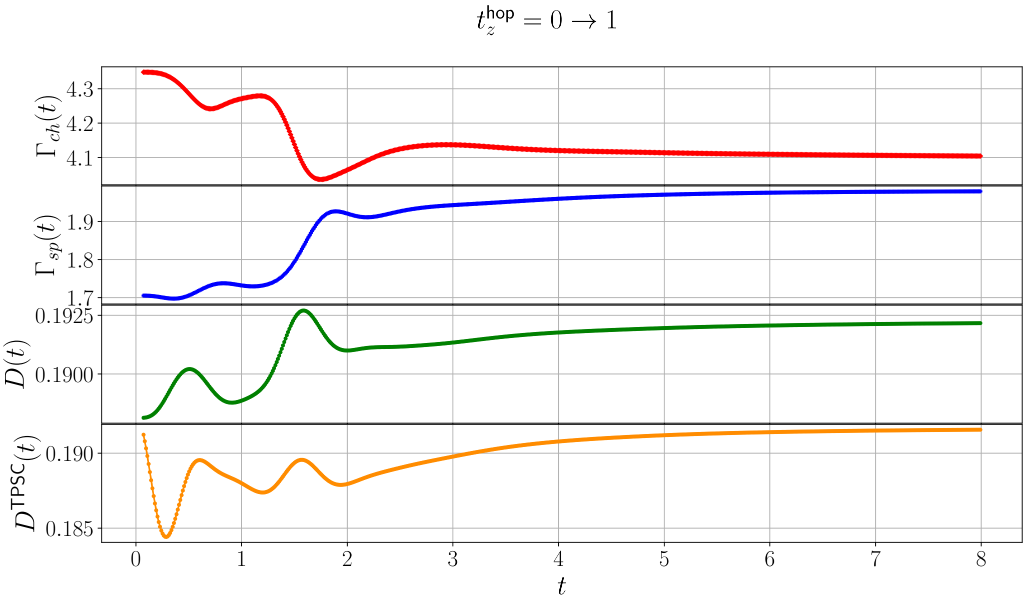

Figure 7.28: Local DMFT+TPSC quantities in the dimensional ramp from $t_z^{\text{hop}} = 0$ to $t_z^{\text{hop}} = 1$ in the single-band nearest-neighbor Hubbard model for $U = 2.5$ at initial temperature $T = 0.2$. The charge irreducible vertex (top panel), spin irreducible vertex (second panel from top), D^{imp} (third panel from top) and D^{TPSC} (bottom panel) are plotted for a time window of $\Delta t = 8$.

Then, the same lattice hopping ramp as the one applied in Fig. 7.19 in TPSC is carried out in DMFT+TPSC. This ramp takes off from $t_z^{\text{hop}} = 0$ (2D square lattice) to $t_z^{\text{hop}} = 1$ (3D cubic lattice). The initial temperature is also $T = 0.2$, the interaction is fixed at $U = 2.5$ and the filling is $n = 1$ (half-filling). In Fig. 7.28 are shown Γ^{ch} (top panel), Γ^{sp} (second top panel), the impurity double occupancy (second-to-bottom panel) and the lattice double occupancy (bottom panel). The overall trend follows that of Fig. 7.19, in that Γ^{ch} falls down and Γ^{sp} goes up when the dimensionality is increased from 2D to 3D. As a consequence, in response to the decrease in charge scattering, the double occupancies rise, although significantly less than what is observed in TPSC (Fig. 7.19). The main qualitative difference that pops up in DMFT+TPSC that are absent in all other methods for this particular set-up, are the transient humps – one located at $t \simeq 0.7$ and the other at $t \simeq 1.7$ – showing up across all the local quantities in Fig. 7.28. These humps seem to slow down the onset of the thermalization. As shown in the inset plot of Fig. 7.29, the lattice hopping ramp stops at about the same time that the second hump appears. Each hollow feature in the charge vertex, corresponding to a sudden decrease of the charge interactions, correlate with a hump in Γ^{sp} as well as in the double occupancies.

---

[5] In principle, in strict terms, the system would never really themalize, since T_{therm} does not associate with the post-ramp stabilized values of the physical quantities.

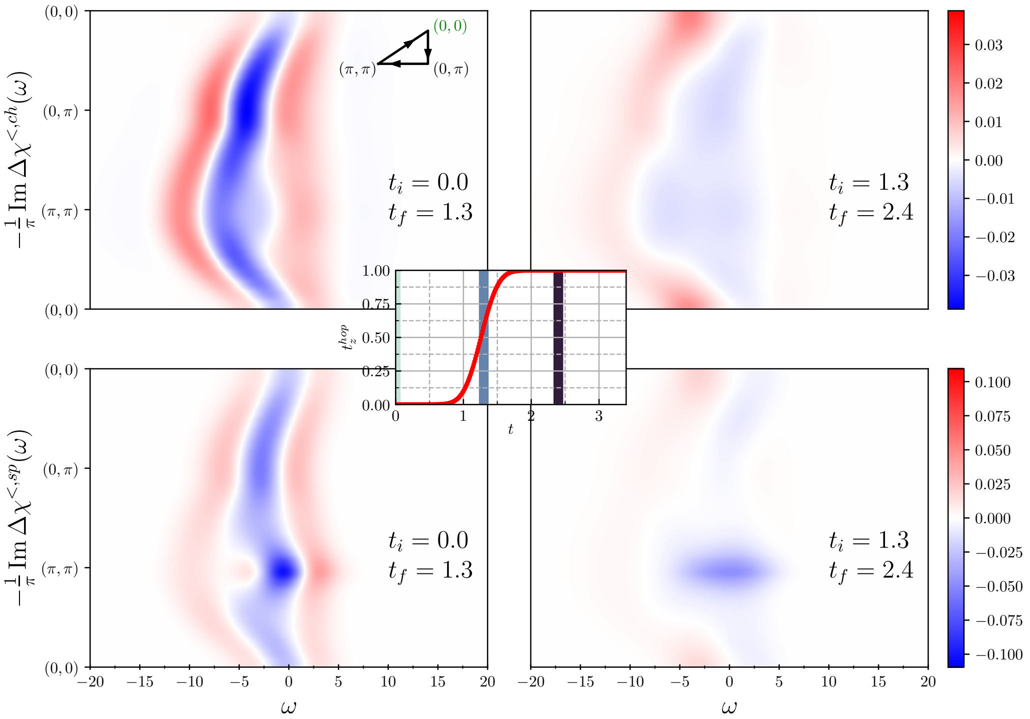

Figure 7.29: Top (Bottom) panels: Difference spectra of the DMFT+TPSC lesser component of the charge (spin) susceptibility after the perpendicular lattice hopping ramp from $t_z^{\text{hop}} = 0$ to $t_z^{\text{hop}} = 1$ shown in the inset. The time window employed in the Fourier transformation is $\Delta t = 2.5$. Each row of panels uses the same colorscale.

It was shown in Section 7.1 that the RPA-type π-ton vertex corrections, in conjunction with the slow relaxation of the electronic occupation near the Fermi level, drove the prethermalization phase following the interaction ramps. In both TPSC and TPSC+GG, even though the local vertices thermalize rather fast (within a few inverse t^{hop}), the $\mathbf{k}$-defined susceptibilities associated with their respective vertex (charge and spin) take much longer to thermalize as can be deduced from the nonthermal temperatures shown in Fig. 7.18. In DMFT+TPSC, based off Fig. 7.28, one can clearly notice that the thermalization of the local vertices and double occupancies is delayed compared to TPSC and TPSC+GG. Thereof, it looks like the continuous feedback between the lattice degrees of freedom and impurity degrees of freedom is related to the slow-down of the thermalization, since all the quantities change well past the end of the ramp at $t \simeq 1.7$, even if the total energy is constant (not shown).

Finally, in complement to the local quantities plotted across the dimensional ramp (Fig. 7.28), the spectral time differences $\Delta\chi^{\mathrm{ch/sp},<}(t_f,t_i;\mathbf{k})$ of the *lesser* charge susceptibility (top panels) and spin susceptibility (bottom panels) are shown for times $t_i = 0$ and $t_f = 1.3$ in the left panels of Fig. 7.29, and for times $t_i = 1.3$ and $t_f = 2.4$ in the right panels. Just like was illustrated by Fig. 7.22 for TPSC, a significant asymmetry appears with the early times contributing to most of the changes happening during the lattice hopping ramp. The results from DMFT+TPSC display less ripples in the spectra than TPSC at higher absolute frequencies, especially for the charge susceptibility. As for TPSC (Fig. 7.22), the spin-spin correlations in the vicinity of $\mathbf{k}_{\pi}$ get reduced drastically when going to 3D, since at fixed U, the crossover temperature T_x gets pulled down (*cf.* Fig. 6.35); the heating effect is yet another factor reducing the spectral weight at $\mathbf{k}_{\pi}$.

Part V

CONCLUSION

8 CONCLUSION

Correlated many-body numerical methods treating nonlocal vertex corrections have been investigated in this thesis in order to carry them over to nonequilibrium set-ups. The nonequilibrium methods that have been proposed, namely the RPA post-processing DMFT method (Chapter 4), TPSC and TPSC+GG (Section 5.2), and DMFT+TPSC and DMFT+TPSCα (Section 5.2.9), turn out to be relatively cheap computationally speaking, considering the fact that nonlocal nonequilibrium correlations are technically (and conceptually) hard to access. Each of these methods performs well at weak coupling in Hubbard-like Hamiltonian models (Section 3.1) in 2D and 3D for a wide range of temperatures and chemical dopings.

As a first method investigated, the RPA-type post-processing DMFT method to compute two-particle vertex corrections (Chapter 4) was tested in the single-band half-filled Hubbard model after an interaction ramp or quench, by computing the nonlocal longitudinal optical conductivity and magnetic response. Ladder vertex corrections of the RPA π-ton type were investigated in Section 6.1 at equilibrium and in Section 7.1 out of equilibrium. In agreement with previous studies related to the π-ton [18, 66, 120, 151], the relevant spectral features, like that of a sharp spectral feature that emerges at low energy in the optical conductivity when approaching the AFM phase boundary, were captured by this method in equilibrium systems under the condition that $U \lesssim \text{bandwidth}/2$. In Section 7.1, it was shown that the single-ladder vertex corrections increased upon quenching or ramping the interaction U if it brings the system closer to the AFM phase in (U, T)-plane [119]. The up and down quenches or ramps resulted in different dynamics of the π-ton, having the upward trends enhancing the π-ton-related spectral features and the downward ones reducing them. This is due to the effects of heating and the U-dependence of the AFM phase boundary. Furthermore, it was shown in Section 7.1.2 that ladder-type vertex corrections, which are prominent near the AFM phase boundary (or some other ordering instability with wave-vector $\mathbf{k}_\pi$), have a significant effect on the optical properties in nonthermal, weakly-correlated Hubbard systems. In particular, prethermalization phenomena in these vertex corrections dominate the slow relaxation of the conductivity after a quench or other perturbation. Since this RPA-type DMFT post-processing method depends on the profile of the local density of states, it was established that the observed prethermalization phenomenon is primarily due to the slow relaxation of the nonthermal distribution function happening close to the Fermi level, as was previously reported for weakly interacting systems [92].

A rather different class of methods – to the count of 4 – have also been studied to tackle nonlocal correlations in 2D and 3D at equilibrium (Section 6.2) and out of equilibrium (Section 7.2), namely TPSC and its variants introduced in Chapter 5. Among these variants, two of them have been directly derived from the original TPSC formulation, *i.e.* the so-called TPSC and TPSC+GG approaches in Section 5.2. TPSC differs from the original formulation [152] in that it enforces an extra sum-rule necessary to stabilize the thermalized states in nonequilibrium set-ups and render physically reasonable transient dynamics. TPSC+GG is the TPSC counterpart that fulfils this sum-rule iteratively. In equilibrium, these approximate methods yield remarkably accurate results in the intermediate-correlation regime [110, 121] and they satisfy the Mermin-Wagner theorem [152]. Moreover, TPSC+GG fits very well the results from DiagMC [110] and it would thereby correctly capture the growth of spin correlations when approaching the renormalized classical regime. In nonequilibrium studies (Section 7.2.1), the Hubbard model interaction and lattice hopping term have been ramped in 2D and 3D. In Section 7.2.1, it was reported that fast perturbations induce qualitatively different nonthermal dynamics in the spin and charge channels, but the local vertices and double occupation thermalize within a few inverse hopping times [121]. The nonequilibrium implementation of TPSC and TPSC+GG on the KB contour turns out to capture interesting nonthermal transient phenomena, such as low-energy charge excitations corresponding to a negative effective temperature in the charge sector, and $\mathbf{k}$-dependent and frequency-dependent effective temperatures extracted from the charge and spin susceptibilities and single-particle Green's function. However, to push the simulations to larger times and study the thermalization processes, the implementation requires the usage of memory truncation techniques [113, 125, 154] and compact basis representations [67] to access the long-time dynamics.

In an attempt to better capture the local correlations, TPSC has been combined with DMFT to get rid of some assumptions that TPSC and TPSC+GG use, namely the local irreducible spin vertex ansatz of Section 5.2.2. This method introduced in Section 5.2.9 self-consistently introduces the local DMFT correlation into the lattice TPSC self-energy. This method is made self-consistent since it improves the conservation of energy, hence the determination of thermalized temperature. However, on the basis that DMFT+TPSC does not possess a Luttinger-Ward functional from which it is derived – it only resembles the Luttinger-ward functional of second-order IPT at weak-coupling – the "thermalized" temperatures reached might differ on the impurity and lattice subspaces. The latter is mainly due to the fact that the impurity double occupancy strays away from the lattice one when decreasing temperature. The temperature differences between the impurity and the lattice demonstrates that this scheme is not internally consistent. The results drawn out of this self-consistent DMFT+TPSC scheme agree well with those reported in Ref. [89] using a non-self-consistent version. A way to cure this double occupancy discrepancy is to once again introduce a one-time parameter that forces the lattice and impurity double occupancy to match, in the same spirit as TPSC+GG: this modified method is coined DMFT+TPSCα and suffers from instabilities in nonequilibrium set-ups.

On the basis that single-band TPSC can be extended to deal with multi-orbital Hund's metals [155, 156] (Section 5.2.7) and extended-Hubbard [32] model systems, its generalizations indicate that TPSC (and DMFT+TPSC) could be combined with time-dependent Density Functional Theory input [20, 108] so as to provide a promising and computationally tractable path towards realistic simulations of photoexcited correlated materials. Moreover, extensions of nonequilibrium TPSC which account for nonperturbative local correlations from DMFT [75, 89, 155] should capture strong correlation effects and could provide access to nascent Mott physics.

Part VI

APPENDICE

A

LANGRETH RULES

The Langreth rules for the convolution (2.18) and the products (2.19) are derived for the *lesser* Keldysh component. Both the retarded (2.20) and advanced (2.21) components will pop up naturally across the derivation.

To start out, the *lesser* Keldysh component is defined on the real-time branches exclusively, meaning that Eq. (2.18) becomes

$$C^<(t,t') = \int_{\mathcal{C}} \mathrm{d}z \; A(t,z)B(z,t'), \tag{A.1}$$

where the contour functions A and B are defined in Eq. (2.15). The next step is to unpack the contour-defined functions according to Eq. (2.15)

$$\begin{aligned} C^<(t,t') = \int_{\mathcal{C}} \mathrm{d}z \; &\Big[A^\delta(t)\delta(t,z) + A^>(t,z)\Theta(t,z) + A^<(t,z)\Theta(z,t)\Big] \\ &\times \Big[B^\delta(t)\delta(z,t') + B^>(z,t')\Theta(z,t') + B^<(z,t')\Theta(t',z)\Big]. \end{aligned} \tag{A.2}$$

By definition, Eq. (A.2) is defined only if $t' > t$, and when writing $C^<(t,t)$, it actually means $C^<(t,t^+)$, with t^+ infinitesimally later than t. $C^<$ can be discontinuous when $t = t'$. Hence, in Eq. (A.2), the term with $A^\delta B^\delta$ vanishes. Also, in Eq. (A.2), the terms multiplied by $\Theta(t,t')$ disappear. Therefore, when expanding, there remains

$$\begin{aligned} C^<(t,t') &= A^\delta(t)B^<(t,t') + A^<(t,t')B^\delta(t') + \int_{\mathcal{C}} \mathrm{d}z \; A^>(t,z)B^<(z,t')\Theta(t,z)\Theta(t',z) \\ &+ \int_{\mathcal{C}} \mathrm{d}z \; A^<(t,z)B^>(z,t')\Theta(z,t)\Theta(z,t') + \int_{\mathcal{C}} \mathrm{d}z \; A^<(t,z)B^<(z,t')\Theta(z,t)\Theta(t',z). \end{aligned} \tag{A.3}$$

The first integrated term in Eq. (A.3) gives

$$\int_{t_0}^{t} \mathrm{d}\bar{t} \; A^>(t,\bar{t})B^<(\bar{t},t'). \tag{A.4}$$

The second integrated term gives

$$\int_{t'}^{t_0} \mathrm{d}\bar{t} \; A^<(t,\bar{t})B^>(\bar{t},t') - i\int_{0}^{\beta} \mathrm{d}\bar{\tau} \; A^<(t,\bar{\tau})B^>(\bar{\tau},t'). \tag{A.5}$$

The last integrated term gives

$$\int_{t}^{t'} \mathrm{d}\bar{t} \; A^<(t,\bar{t})B^<(\bar{t},t') = \int_{t}^{t_0} \mathrm{d}\bar{t} \; A^<(t,\bar{t})B^<(\bar{t},t') + \int_{t_0}^{t'} \mathrm{d}\bar{t} \; A^<(t,\bar{t})B^<(\bar{t},t'). \tag{A.6}$$

By gathering up Eqs. (A.4), (A.5) and (A.6) back into Eq. (A.3), one obtains

$$\begin{aligned}C^{<}(t,t') &= A^{\delta}(t)B^{<}(t,t') + A^{<}(t,t')B^{\delta}(t') - i\int_0^{\beta} \mathrm{d}\bar{\tau}\; A^{\rceil}(t,\bar{\tau})B^{\lceil}(\bar{\tau},t') \\ &+ \int_{t_0}^{t} \mathrm{d}\bar{t}\; [A^{>}(t,\bar{t}) - A^{<}(t,\bar{t})]\, B^{<}(\bar{t},t') + \int_{t_0}^{t'} \mathrm{d}\bar{t}\; A^{<}(t,\bar{t}) \left[B^{<}(\bar{t},t') - B^{>}(\bar{t},t')\right], \end{aligned} \tag{A.7}$$

where the definitions of the left-mixing and right-mixing components, were used as stated in Table 2.1. In Eq. (A.7), by using the definitions of the advanced (Eq. (2.21)) and retarded (Eq. (2.20)) Keldysh components, one can simplify to finally get

$$\begin{aligned}C^{<}(t,t') = \int_{t_0}^{t} \mathrm{d}\bar{t}\; A^{R}(t,\bar{t})B^{<}(\bar{t},t') + \int_{t_0}^{t'} \mathrm{d}\bar{t}\; A^{<}(t,\bar{t})B^{A}(\bar{t},t') \\ - i\int_0^{\beta} \mathrm{d}\bar{\tau}\; A^{\rceil}(t,\bar{\tau})B^{\lceil}(\bar{\tau},t'). \end{aligned} \tag{A.8}$$

Regarding the products (2.19), it is more straightforward to work out their expression from Eq. (2.15). Although, these products do not preserve the structure of the contour-defined functions (2.15), unless the one-time terms are zeroed, *i.e.* $A^{\delta} = B^{\delta} = 0$. It is easy to see that

$$\begin{aligned}&C^{<(>)}(t,t') \\ &= \left[A^{<}(t,t')\Theta(t',t) + A^{>}(t,t')\Theta(t,t')\right] \left[B^{<}(t',t)\Theta(t,t') + B^{>}(t',t)\Theta(t',t)\right] \\ &= A^{<(>)}(t,t')B^{>(<)}(t',t), \end{aligned} \tag{A.9}$$

and that

$$\begin{aligned}&C^{<(>)}(t,t') \\ &= \left[A^{<}(t,t')\Theta(t',t) + A^{>}(t,t')\Theta(t,t')\right] \left[B^{<}(t,t')\Theta(t',t) + B^{>}(t,t')\Theta(t,t')\right] \\ &= A^{<(>)}(t,t')B^{<(>)}(t',t). \end{aligned} \tag{A.10}$$

B

GAUSSIAN INTEGRALS

Let's consider a general one-variable Grassmann function of the form (2.84)

$$f(\eta_i;\{\eta\}) = 1 + \eta_i \lambda(\{\eta\}),$$

where λ is a multivariable Grassmann function. If one carries out the change of variable

$$\eta_i \to \eta_i' \Omega(\{\eta\}) + \Xi(\{\eta\}) = \Omega(\{\eta\})\eta_i' + \Xi(\{\eta\}), \tag{B.1}$$

where both Ω and Ξ are Grassmann functions of the new set of Grassmann generators, then Ω is an even function of η' and Ξ an odd to conserve the parity. This means that Ω commutes with η_i, as shown in Eq. (B.1). Since the derivative and integral behave the *same* (see Eq. (2.85)), one can easily verify that the following holds

$$\int \mathrm{d}\eta_i \; f(\eta_i;\{\eta\}) = \Omega^{-1}(\{\eta\}) \int \mathrm{d}\eta_i' f(\eta_i'\Omega(\{\eta\}) + \Xi(\{\eta\});\{\eta\}). \tag{B.2}$$

It turns out from Eq. (B.1) that

$$\left(\frac{\partial \eta_i}{\partial \eta_i'}\right)^{-1} = \Omega^{-1}(\{\eta\}). \tag{B.3}$$

Therefore, Eq. (B.2) can be written as

$$\int \mathrm{d}\eta_i \; f(\eta_i;\{\eta\}) = \left(\frac{\partial \eta_i}{\partial \eta_i'}\right)^{-1} \int \mathrm{d}\eta_i' f(\eta_i(\eta_i');\{\eta\}). \tag{B.4}$$

The partial derivative in Eq. (B.3) is called the Jacobian. The variable change result (B.4) can also be carried over to simultaneous change of multiple variables

$$\int \prod_{i=1}^{n} \mathrm{d}\eta_i^* \mathrm{d}\eta_i \; f(\{\eta,\eta^*\}) = \underbrace{\left(\frac{\partial\{\eta,\eta^*\}}{\partial\{\eta',\eta'^*\}}\right)^{-1}}_{\equiv J} \int \prod_{i=1}^{n} \mathrm{d}\eta_i'^* \mathrm{d}\eta_i' f(\{\eta',\eta'^*\}). \tag{B.5}$$

The Jacobian was denoted J in Eq. (B.5). The transformation relating the arrays of generators $\eta_i^{(*)}$ and $\eta_i'^{(*)}$ is

$$\eta_i^{(*)} \to M_{ij}\eta_j'^{(*)}, \tag{B.6}$$

where M is a symmetric unitary matrix. For simplicity, Eq. (B.5) is worked out using only the set $\{\eta\}$: dismissing the conjugate set doesn't change the outcome. With the multiple variable change (B.6) applied to Eq. (B.5), one obtains

$$\begin{aligned}
&J\int\prod_{i=1}^{n}\mathrm{d}\eta_i'^{*}\mathrm{d}\eta_i' f(\{\eta',\eta'^{*}\})\\
&=J\int \mathrm{d}\eta_1'\cdots\mathrm{d}\eta_n'\prod_{i=1}^{n}\left(\sum_j M_{ij}\eta_j'\right)\\
&=J\int \mathrm{d}\eta_1'\cdots\mathrm{d}\eta_n'\sum_{\{P\}}\prod_{i=1}^{n}\left(M_{iP(i)}\eta'_{P(i)}\right),
\end{aligned}\tag{B.7}$$

where the set $\{P\}$ represents the set of $n!$ permutations of indices that lead to non-zero terms. Eq. (B.7) can be further developed

$$\begin{aligned}
&J\sum_{\{P\}}\prod_{i=1}^{n}M_{iP(i)}(-1)^{P}\int \mathrm{d}\eta_1'\cdots\mathrm{d}\eta_n'\eta_1'\cdots\eta_n'\\
&=J\det[M]\,(-1)^{n}.
\end{aligned}\tag{B.8}$$

Eq. (B.8) implies that the Jacobian $J=\det[M]^{-1}$, since the left-hand side of Eq. (B.5) gives $(-1)^{n}$. The exponent P in Eq. (B.8) represents the signature of the permutation.

Finally, evaluating a Gaussian integral using Grassmann algebra is rather easy. Once the integrand has been made diagonal in Grassmann fields, the Gaussian integral reads

$$\int\prod_{i=1}^{n}\mathrm{d}\xi_i^{*}\mathrm{d}\xi_i e^{-\sum_{i,j}\xi_i^{*}a_{i,j}\xi_j},\tag{B.9}$$

where $a_{i,j}=a_i\delta_{i,j}$, *i.e.* a is a diagonal matrix. Eq. (B.9) gives

$$\int\prod_{i=1}^{n}\mathrm{d}\xi_i^{*}\mathrm{d}\xi_i\,(1-\xi_i^{*}a_i\xi_i)=\prod_{i=1}^{n}a_i=\det[a].\tag{B.10}$$

The determinant of H appearing in Eq. (2.103) is a result of Eq. (B.10), since the matrix H is diagonal.

C

WEAK-COUPLING SELF-ENERGY EXPANSION

The weak-coupling self-energy expansion starts off from the general physical ($\phi \to 0$) self-energy expression (2.59), whose Fock term vanishes in the Hubbard model. Substituting the first-order term describing the susceptibility (2.46) into (2.59), one gets

$$\begin{aligned}\Sigma_{\sigma,\sigma'}(z_1,z_2) &= -iU(z_1)\mathcal{G}_{-\sigma}(z_1,z_1^+)\delta^{\mathcal{C}}(z_1,z_2)\delta_{\sigma,\sigma'}\\ &+ U(z_1)\mathcal{G}_{\sigma,\bar{\sigma}_3}(z_1,\bar{z}_3)\Gamma_{\bar{\sigma}_3\sigma';\bar{\sigma}_4\bar{\sigma}_5}(\bar{z}_3,z_2,\bar{z}_4,\bar{z}_5)\left[-i\mathcal{G}_{\bar{\sigma}_4,-\sigma}(\bar{z}_4,z_1^+)\mathcal{G}_{-\sigma,\bar{\sigma}_5}(z_1,\bar{z}_5)\right]. \quad \text{(C.1)}\end{aligned}$$

Note that most general expression relating to the self-energy is boldified, in that the propagators are dressed themselves with the self-energy according to the Dyson's equation (2.44). To recall, the assumptions of the local Hubbard interaction (*cf.* Eq. (3.6)) transform the interaction term appearing in Eq. (2.59) into

$$V^{\sigma_\gamma,\sigma_\delta}_{\sigma_\epsilon,\sigma_\zeta}(z_1,z_2,z_3,z_4) \to U(z_1)\delta_{\sigma_\epsilon,\sigma_\zeta}\delta_{\sigma_\gamma,\sigma_\delta}\delta_{\sigma_\epsilon,-\sigma_\gamma}\delta^{\mathcal{C}}(z_1,z_2)\delta^{\mathcal{C}}(z_1,z_3)\delta^{\mathcal{C}}(z_1,z_4).$$

Hence, the bubble term featuring in χ contains spins with opposite projections $-\sigma$, owing to the Pauli principle.

Recalling that the vertex function showing up in Eq. (C.1) is defined as

$$\Gamma_{\sigma_3\sigma';\sigma_4\sigma_5}(z_3,z_2,z_4,z_5) = -\frac{\delta\Sigma_{\sigma_3,\sigma'}(z_3,z_2)}{\delta\mathcal{G}_{\sigma_4,\sigma_5}(z_4,z_5)}, \quad \text{(C.2)}$$

it is easy to work out $\Sigma^{(2)}$, as defined in Eq. (3.26), by selecting the Hartree term in Eq. (C.1) as the differentiated self-energy component in Eq. (C.2). Doing so and using the first-order term in the Dyson's equation (2.44), Eq. (C.1) becomes

$$\begin{aligned}&\Sigma^{(2)}_{\sigma,\sigma'}(z_1,z_2) =\\ &U(z_1)\mathcal{G}^0_{\sigma,\bar{\sigma}_3}(z_1,\bar{z}_3)\left[iU(\bar{z}_3)\delta^{\mathcal{C}}(\bar{z}_3,\bar{z}_4)\delta^{\mathcal{C}}(\bar{z}_3^+,\bar{z}_5)\delta^{\mathcal{C}}(\bar{z}_3,z_2)\delta_{\bar{\sigma}_3,\sigma'}\delta_{-\bar{\sigma}_3,\bar{\sigma}_4}\delta_{-\bar{\sigma}_3,\bar{\sigma}_5}\right]\\ &\times\left[-i\mathcal{G}^0_{\bar{\sigma}_4,-\sigma}(\bar{z}_4,z_1^+)\mathcal{G}^0_{-\sigma,\bar{\sigma}_5}(z_1,\bar{z}_5)\right]. \quad \text{(C.3)}\end{aligned}$$

Since σ' needs to be equal to σ to be nonzero, Eq. (C.3) clearly gives Eq. (3.26).

Next, to determine the second-order Hartree term $\Sigma^{(2)}_H$ (3.25), it involves the usage of the Dyson's equation to expand out the boldified propagator, whereby the Hartree term constitutes the self-energy (second term in the $\mathcal{G}$ expansion):

$$\mathcal{G}^{(2)}_{-\sigma}(z_1,z_1^+) = \mathcal{G}^0_{-\sigma,\bar{\sigma}}(z_1,\bar{z}_2)\left[-iU(\bar{z}_2)\mathcal{G}^0_{-\bar{\sigma}}(\bar{z}_2,\bar{z}_2^+)\delta_{\bar{\sigma},\bar{\sigma}'}\delta^{\mathcal{C}}(\bar{z}_2,\bar{z}_3)\right]\mathcal{G}^0_{\bar{\sigma}',-\sigma}(\bar{z}_3,z_1^+). \quad \text{(C.4)}$$

Reinserting the Green's function expansion term (C.4) into the Hartree term of Eq. (C.1), one stumbles upon the $\Sigma^{(2)}_H$ term

$$\begin{aligned}&\Sigma^{(2)}_{H,\sigma,\sigma'}(z_1,z_2) = \\ &-iU(z_1)\left[\mathcal{G}^0_{-\sigma}(z_1,\bar{z}_2)\left[-iU(\bar{z}_2)\mathcal{G}^0_{\sigma}(\bar{z}_2,\bar{z}_2^+)\delta^{\mathcal{C}}(\bar{z}_2,\bar{z}_3)\right]\mathcal{G}^0_{-\sigma}(\bar{z}_3,z_1^+)\right]\delta^{\mathcal{C}}(z_1,z_2)\delta_{\sigma,\sigma'}.\end{aligned} \tag{C.5}$$

Moving on to the 3rd-order diagrams, the first set of diagrams, comprised of two elements, uses the 2nd-order diagram (C.3) in the vertex calculation (C.2). Carrying out the functional derivatives and changing all propagators with $\mathcal{G}^0$, one gets

$$\begin{aligned}&\Gamma_{\sigma_3\sigma';\sigma_4\sigma_5}(z_3,z_2,z_4,z_5) = \\ &-U(z_3)U(z_2)\mathcal{G}^0_{-\sigma_3}(z_2,z_3)\mathcal{G}^0_{-\sigma_3}(z_3,z_2^+)\delta_{\sigma_3,\sigma_4}\delta_{\sigma_3,\sigma_5}\delta_{\sigma_3,\sigma'}\delta^{\mathcal{C}}(z_3,z_4)\delta^{\mathcal{C}}(z_2,z_5) \\ &-U(z_3)U(z_2)\mathcal{G}^0_{\sigma_3}(z_3,z_2)\mathcal{G}^0_{-\sigma_3}(z_3,z_2^+)\delta_{-\sigma_3,\sigma_4}\delta_{-\sigma_3,\sigma_5}\delta_{\sigma_3,\sigma'}\delta^{\mathcal{C}}(z_2,z_4)\delta^{\mathcal{C}}(z_3^+,z_5) \\ &-U(z_3)U(z_2)\mathcal{G}^0_{\sigma_3}(z_3,z_2)\mathcal{G}^0_{-\sigma_3}(z_2,z_3^+)\delta_{-\sigma_3,\sigma_4}\delta_{-\sigma_3,\sigma_5}\delta_{\sigma_3,\sigma'}\delta^{\mathcal{C}}(z_3,z_4)\delta^{\mathcal{C}}(z_2,z_5).\end{aligned} \tag{C.6}$$

The first term of Eq. (C.6) cancels out because σ_4 and σ_5 cannot have the same spin projection as σ', only its opposite. Otherwise, the first-order bubble term appearing in the susceptibility vanishes (see Eq. (C.1)). Substituting the third term featuring in Eq. (C.6) into the self-energy expression (C.1) leads to the self-energy Σ^{3a} (3.30)

$$\begin{aligned}&\Sigma^{3a}_{\sigma,\sigma'}(z_1,z_2) = \\ &iU(z_1)\mathcal{G}_{\sigma,\bar{\sigma}_3}(z_1,\bar{z}_3)\Big[U(\bar{z}_3)U(z_2)\mathcal{G}^0_{\sigma_3}(\bar{z}_3,z_2)\mathcal{G}^0_{-\bar{\sigma}_3}(z_2,\bar{z}_3^+) \\ &\times\delta_{-\bar{\sigma}_3,\bar{\sigma}_4}\delta_{-\bar{\sigma}_3,\bar{\sigma}_5}\delta_{\bar{\sigma}_3,\sigma'}\delta^{\mathcal{C}}(\bar{z}_3,\bar{z}_4)\delta^{\mathcal{C}}(z_2,\bar{z}_5)\Big]\left[\mathcal{G}_{\bar{\sigma}_4,-\sigma}(\bar{z}_4,z_1^+)\mathcal{G}_{-\sigma,\bar{\sigma}_5}(z_1,\bar{z}_5)\right],\end{aligned} \tag{C.7}$$

while the second term of Eq. (C.6) into Eq. (C.1) gives the self-energy Σ^{3b} (3.31)

$$\begin{aligned}&\Sigma^{3b}_{\sigma,\sigma'}(z_1,z_2) = \\ &iU(z_1)\mathcal{G}_{\sigma,\bar{\sigma}_3}(z_1,\bar{z}_3)\Big[U(\bar{z}_3)U(z_2)\mathcal{G}^0_{\bar{\sigma}_3}(\bar{z}_3,z_2)\mathcal{G}^0_{-\bar{\sigma}_3}(\bar{z}_3,z_2^+) \\ &\delta_{-\bar{\sigma}_3,\bar{\sigma}_4}\delta_{-\bar{\sigma}_3,\bar{\sigma}_5}\delta_{\bar{\sigma}_3,\sigma'}\delta^{\mathcal{C}}(z_2,\bar{z}_4)\delta^{\mathcal{C}}(\bar{z}_3^+,\bar{z}_5)\Big]\left[\mathcal{G}_{\bar{\sigma}_4,-\sigma}(\bar{z}_4,z_1^+)\mathcal{G}_{-\sigma,\bar{\sigma}_5}(z_1,\bar{z}_5)\right].\end{aligned} \tag{C.8}$$

The second set of 3rd-order self-energy diagrams is generated by substituting the second term of the expanded boldified Green's function (C.4) into each interacting Green's function making up the second-order self-energy diagram. This produces 3 different diagrams, whose expressions are

$$\begin{aligned}&\Sigma^{3c}_{\sigma,\sigma'}(z_1,z_2) = \\ &U(z_1)U(z_2)\Big[\mathcal{G}^0_{\sigma,\bar{\sigma}}(z_1,\bar{z}_1)\left[-iU(\bar{z}_1)\mathcal{G}^0_{-\bar{\sigma}}(\bar{z}_1,\bar{z}_1^+)\delta^{\mathcal{C}}(\bar{z}_1,\bar{z}_2)\delta_{\bar{\sigma},\bar{\sigma}'}\right] \\ &\times\mathcal{G}^0_{\bar{\sigma}',\sigma}(\bar{z}_2,z_2)\Big]\mathcal{G}^0_{-\sigma}(z_2,z_1^+)\mathcal{G}^0_{-\sigma}(z_1,z_2^+),\end{aligned} \tag{C.9}$$

corresponding to Eq. (3.32),

$$\begin{aligned}
&\Sigma^{3d}_{\sigma,\sigma'}(z_1,z_2) = \\
&U(z_1)U(z_2)\mathcal{G}^0_{\sigma}(z_1,z_2)\Big[\mathcal{G}^0_{-\sigma,\bar{\sigma}}(z_2,\bar{z}_1)\Big[-iU(\bar{z}_1)\mathcal{G}^0_{\bar{\sigma}}(\bar{z}_1,\bar{z}_1^+)\delta^{\mathcal{C}}(\bar{z}_1,\bar{z}_2)\delta_{\bar{\sigma},\bar{\sigma}'}\Big] \\
&\times \mathcal{G}^0_{\bar{\sigma}',-\sigma}(\bar{z}_2,z_1^+)\Big]\mathcal{G}^0_{-\sigma}(z_1,z_2^+),
\end{aligned} \tag{C.10}$$

corresponding to Eq. (3.33), and

$$\begin{aligned}
&\Sigma^{3e}_{\sigma,\sigma'}(z_1,z_2) = \\
&U(z_1)U(z_2)\mathcal{G}^0_{\sigma}(z_1,z_2)\mathcal{G}^0_{-\sigma}(z_2,z_1^+)\Big[\mathcal{G}^0_{-\sigma,\bar{\sigma}}(z_1,\bar{z}_1)\Big[-iU(\bar{z}_1)\mathcal{G}^0_{\bar{\sigma}}(\bar{z}_1,\bar{z}_1^+)\delta^{\mathcal{C}}(\bar{z}_1,\bar{z}_2)\delta_{\bar{\sigma},\bar{\sigma}'}\Big] \\
&\times \mathcal{G}^0_{\bar{\sigma}',-\sigma}(\bar{z}_2,z_2^+)\Big],
\end{aligned} \tag{C.11}$$

corresponding to Eq. (3.34).

Next, turning to the 3rd-order Hartree self-energy diagrams, the top Green's function of $\Sigma^{(2)}_H$ (C.5) is split up by a Hartree self-energy insertion

$$\begin{aligned}
&\Sigma^{3a}_{H,\sigma,\sigma'}(z_1,z_2) = \\
&-iU(z_1)\mathcal{G}^0_{-\sigma}(z_1,\bar{z}_2)\Big[-iU(\bar{z}_2)\mathcal{G}^0_{\sigma,\bar{\sigma}}(\bar{z}_2,\bar{z}_3)\Big[-iU(\bar{z}_3)\mathcal{G}^0_{-\bar{\sigma}}(\bar{z}_3,\bar{z}_3^+)\delta^{\mathcal{C}}(\bar{z}_3,\bar{z}_4)\delta_{\bar{\sigma},\bar{\sigma}'}\Big] \\
&\times \mathcal{G}^0_{\bar{\sigma}',\sigma}(\bar{z}_4,\bar{z}_2^+)\delta^{\mathcal{C}}(\bar{z}_2,\bar{z}_3)\Big]\mathcal{G}^0_{-\sigma}(\bar{z}_3,z_1^+)\delta^{\mathcal{C}}(z_1,z_2)\delta_{\sigma,\sigma'}
\end{aligned} \tag{C.12}$$

and this simplifies down to Σ^{3a}_H laid out in Eq. (3.27). The next 3rd-order Hartree diagram is obtained by expanding the Dyson's equation up to third order. The third-order term reads

$$\begin{aligned}
\mathcal{G}^{(3)}_{-\sigma}(z_1,z_1^+) &= \mathcal{G}^0_{-\sigma,\bar{\sigma}}(z_1,\bar{z}_2)\Big[-iU(\bar{z}_2)\mathcal{G}^0_{-\bar{\sigma}}(\bar{z}_2,\bar{z}_2^+)\delta_{\bar{\sigma},\bar{\sigma}'}\delta^{\mathcal{C}}(\bar{z}_2,\bar{z}_3)\Big]\mathcal{G}^0_{\bar{\sigma}',\bar{\sigma}''}(\bar{z}_3,\bar{z}_4) \\
&\times \Big[-iU(\bar{z}_4)\mathcal{G}^0_{-\bar{\sigma}''}(\bar{z}_4,\bar{z}_4^+)\delta_{\bar{\sigma}'',\bar{\sigma}'''}\delta^{\mathcal{C}}(\bar{z}_4,\bar{z}_5)\Big]\mathcal{G}^0_{\bar{\sigma}''',-\sigma}(\bar{z}_5,z_1^+).
\end{aligned} \tag{C.13}$$

Replacing the Green's function in the Hartree diagram of Eq. (C.1) by $\mathcal{G}^{(3)}$ (Eq. (C.13)), one obtains Σ^{3b} as described by Eq. (3.28)

$$\begin{aligned}
&\Sigma^{3b}_{H,\sigma,\sigma'}(z_1,z_2) = \\
&-iU(z_1)\mathcal{G}^0_{-\sigma,\bar{\sigma}}(z_1,\bar{z}_2)\Big[-iU(\bar{z}_2)\mathcal{G}^0_{-\bar{\sigma}}(\bar{z}_2,\bar{z}_2^+)\delta_{\bar{\sigma},\bar{\sigma}'}\delta^{\mathcal{C}}(\bar{z}_2,\bar{z}_3)\Big]\mathcal{G}^0_{\bar{\sigma}',\bar{\sigma}''}(\bar{z}_3,\bar{z}_4) \\
&\times \Big[-iU(\bar{z}_4)\mathcal{G}^0_{-\bar{\sigma}''}(\bar{z}_4,\bar{z}_4^+)\delta_{\bar{\sigma}'',\bar{\sigma}'''}\delta^{\mathcal{C}}(\bar{z}_4,\bar{z}_5)\Big]\mathcal{G}^0_{\bar{\sigma}''',-\sigma}(\bar{z}_5,z_1^+)\delta^{\mathcal{C}}(z_1,z_2)\delta_{\sigma,\sigma'}.
\end{aligned} \tag{C.14}$$

For Eq. (C.14) to be nonzero, since the off-diagonal spin component of the Green's function is zero within the Hubbard model, it is easy to deduce that $\bar{\sigma} = \bar{\sigma}' = \bar{\sigma}'' = \bar{\sigma}''' = -\sigma$.

Finally, the very last 3rd-order Hartree self-energy diagram comes from the insertion of the 2nd-order self-energy diagram (3.26) into the second term of the Dyson's equation expansion

$$\begin{aligned}
&\mathcal{G}^{(2)'}_{-\sigma}(z_1,z_1^+) = \\
&\mathcal{G}^0_{-\sigma,\bar{\sigma}}(z_1,\bar{z}_2)\left[U(\bar{z}_2)\mathcal{G}^0_{\bar{\sigma}}(\bar{z}_2,\bar{z}_3)U(\bar{z}_3)\mathcal{G}^0_{-\bar{\sigma}}(\bar{z}_3,\bar{z}_2^+)\mathcal{G}^0_{-\bar{\sigma}}(\bar{z}_2,\bar{z}_3^+)\right]\mathcal{G}^0_{\bar{\sigma},-\sigma}(\bar{z}_3,z_1^+).
\end{aligned} \tag{C.15}$$

Plugging $\mathcal{G}^{(2)'}$ from (C.15) into the Hartree term of Eq. (C.1), one gets Σ^{3c}_{H} (3.29)

$$\begin{aligned}&\Sigma^{3c}_{H,\sigma,\sigma'}(z_1,z_2) = \\ &- iU(z_1)\mathcal{G}^0_{-\sigma,\bar{\sigma}}(z_1,\bar{z}_2)\left[U(\bar{z}_2)\mathcal{G}^0_{\bar{\sigma}}(\bar{z}_2,\bar{z}_3)U(\bar{z}_3)\mathcal{G}^0_{-\bar{\sigma}}(\bar{z}_3,\bar{z}_2^+)\mathcal{G}^0_{-\bar{\sigma}}(\bar{z}_2,\bar{z}_3^+)\right] \\ &\times \mathcal{G}^0_{\bar{\sigma},-\sigma}(\bar{z}_3,z_1^+)\delta^{\mathcal{C}}(z_1,z_2)\delta_{\sigma,\sigma'}. \end{aligned} \tag{C.16}$$

All of the self-energy diagrams set out in Appendix C will be used to solve the AIM in DMFT.

D

CAUCHY INTEGRAL

In this section, integrals in the complex frequency plane that come around often, of the form

$$I(\omega,t) = \int_{-\infty}^{\infty} \mathrm{d}\omega' \, \frac{F(\omega',t)e^{i(\omega+i\eta)0^+}}{\omega' - \omega \pm i\eta}, \tag{D.1}$$

with $\eta \to 0^+$, are investigated. These are integrals like that of Eq. (2.30) and their solution determines the form of the retarded (*advanced*) spectral functions (2.31). In the case where the complex pole is located in the lower half-plane ($\omega' - \omega + i\eta$ in the denominator), the time-dependent function $F(\omega',t)$ is assumed to be analytic in the entire upper half-plane. On the other hand, when the complex pole sits in the upper half-plane ($\omega' - \omega - i\eta$ in the denominator), the function is assumed to be analytic in the lower half-plane. This property is crucial to be able to carry out the contour integral in the complex plane and make use of the Jordan's lemma when portions of the contour are pushed out to infinity.

The advanced Green's function $\mathcal{G}^A$ is analytic in the lower half-plane.

To deal with Eq. (D.1), the integral domain is extended out into the complex frequency plane, such that it becomes

$$I(\omega,t) = \left[\int_{-\infty}^{\epsilon} + \int_{\gamma} + \int_{\epsilon}^{\infty} + \int_{\Gamma}\right] \mathrm{d}\omega' \, \frac{F(\omega',t)e^{i(\omega+i\eta)0^+}}{\omega' - \omega \pm i\eta}, \tag{D.2}$$

with γ representing the contour with radius ϵ circling around the pole in the (lower) upper half-plane (counter)clockwise and Γ the contour stretched out to infinity in the (upper) lower half-plane. The upper bound contour integral along Γ vanishes since F is holomorphic in the half-plane not containing the complex pole and the absolute value of the integrand decreases at least as $\frac{1}{R}$ when $R \to \infty$[1]. Indeed, the latter can be clearly seen if the variable change $\omega - \omega' \pm i\eta \equiv Re^{\pm i\theta}$ is performed:

$$\begin{aligned} I_\Gamma(\omega',t) &= \lim_{R\to\infty} iR \int_0^{\pi} e^{i\theta}\mathrm{d}\theta \, \frac{F(\omega',t)e^{i(\omega'+Re^{i\theta})0^+}}{Re^{i\theta}} \\ &= \lim_{R\to\infty} iF(\omega',t) \int_0^{\pi} \mathrm{d}\theta \, e^{i(\omega'+R(\cos\theta+i\sin\theta))0^+}. \end{aligned} \tag{D.3}$$

The absolute value of the integral (D.3) reads

$$\begin{aligned} \left|I_\Gamma(\omega',t)\right| &= \lim_{R\to\infty} \left|F(\omega',t)\right| \int_0^{\pi} \mathrm{d}\theta \, e^{-R\sin\theta 0^+} \\ &= 2\lim_{R\to\infty} \left|F(\omega',t)\right| \int_0^{\frac{\pi}{2}} \mathrm{d}\theta \, e^{-R\sin\theta 0^+}. \end{aligned} \tag{D.4}$$

Since within the domain of integration $\sin\theta \geq \frac{2\theta}{\pi}$, this means that

---

[1] This is a consequence of Jordan's lemma.

$$\begin{aligned}\left|I_\Gamma(\omega',t)\right| &\leq 2\lim_{R\to\infty}\left|F(\omega',t)\right|\int_0^{\frac{\pi}{2}}\mathrm{d}\theta\; e^{-2R\theta 0^+/\pi}\\ &= \lim_{R\to\infty}\frac{\pi}{R0^+}\left|F(\omega',t)\right|\left[1-e^{-R0^+}\right]\to 0,\end{aligned}\tag{D.5}$$

because the absolute value of F is bounded at infinity.

Next, the two integrals along the real frequency axis in Eq. (D.2) can be merged to make up the principal part of the integral P. Since on the real axis no convergence factor is needed, it can be dropped such that one obtains for the principal part

$$\begin{aligned}&P\int_{-\infty}^{\infty}\mathrm{d}\omega'\frac{F(\omega',t)}{\omega'-\omega}\\ &=\left[\int_{-\infty}^{\epsilon}+\int_{\epsilon}^{\infty}\right]\mathrm{d}\omega'\;\frac{F(\omega',t)}{\omega'-\omega}.\end{aligned}\tag{D.6}$$

Finally, the contour integral remaining along the infinitesimal contour γ can be evaluated exactly; this will be done in the case where the pole lie in the lower half-plane. But first, one needs to evaluate the Laurent expansion of a complex-valued holomorphic function around z_0 ($z \in \mathbb{C}$):

Note that if the function F were to not be holomorphic, the summation index would run from $n = -\infty$ to $n = \infty$.

$$F(z,t) = F(z_0,t) + \sum_{n=1}^{\infty} a_n(z_0,t)(z-z_0)^n,\tag{D.7}$$

with complex coefficients a_n. Clearly, from Eq. (D.7), a holomorphic complex function does not feature any pole (hence no residues), therefore the terms from $n = -\infty$ to $n = -1$ vanish. Just like the other components of the contour integral, the variable substitution $\omega - \omega' \pm i\eta \equiv \epsilon e^{i\theta}$ is carried out such that

$$\begin{aligned}I_\gamma(\omega,t) &= i\epsilon\int_\pi^0\mathrm{d}\theta\; e^{i\theta}\frac{F(\omega-\epsilon e^{i\theta},t)}{\epsilon e^{i\theta}}\\ &= i\int_\pi^0\mathrm{d}\theta\; F(\omega,t) - i\sum_{n=1}^{\infty}\int_\pi^0\mathrm{d}\theta\; a_n(z_0,t)\epsilon^n e^{in\theta}\\ &= -i\pi F(\omega,t).\end{aligned}\tag{D.8}$$

Overall, the total contour integral $I(\omega,t)$ has two contributions from Eqs. (D.6) and (D.8), adding up to

$$I(\omega,t) = P\int_{-\infty}^{\infty}\mathrm{d}\omega'\frac{F(\omega',t)}{\omega'-\omega} - i\pi F(\omega,t).\tag{D.9}$$

The relation (D.9) is also known as the Cauchy relation. This relation is invoked every time one computes a spectral function. Note that the last term in relation (D.9) would feature a "+" instead if the contour γ had run counterclockwise, *i.e* in the case of an *advanced* Green's function. From Eq. (D.9), it becomes obvious how spectral functions like F are calculated

$$-\frac{1}{\pi}\mathrm{Im}I(\omega,t) = F(\omega,t).\tag{D.10}$$

E

OPTICAL CONDUCTIVITY

In this section, the formula of the longitudinal optical conductivity is derived. The expression stem from the linear response treatment of the continuity equation associated with the electric charge conservation

$$\frac{\partial \rho(\mathbf{r},t)}{\partial t} + \nabla \cdot \mathbf{j}(\mathbf{r},t) = 0, \tag{E.1}$$

where $\mathbf{j}$ is the current density, and ρ is the charge density. When transforming Eq. (E.1) to Fourier space, one gets

$$-\omega \rho(\mathbf{q},\omega) + \mathbf{q} \cdot \mathbf{j}(\mathbf{q},\omega) = 0. \tag{E.2}$$

The two-particle spectral function $\chi''_{\rho\rho}$ corresponding to the charge density observable is, within the linear response theory framework,

$$\chi''_{\rho\rho}(\mathbf{q},\omega) = \frac{1}{N}\langle[\hat{\rho}(\mathbf{q},\omega),\hat{\rho}(-\mathbf{q},-\omega)]\rangle_{\hat{\mathcal{H}}_0}, \tag{E.3}$$

where $\hat{\mathcal{H}}_0$ is the noninteracting Hamiltonian and N is the **k**-space grid, such that according to Eq. (E.2), the current-current two-body spectral function reads

$$\chi''_{j_i j_i}(q_i,\omega) = \frac{\omega^2}{q_i^2}\chi''_{\rho\rho}(q_i,\omega), \tag{E.4}$$

where the index i denotes the Cartesian axes. The spectral representation of the current-current correlation function $\chi_{j_i j_i}$ is

$$\chi_{j_i j_i}(q_i,\omega) = \int \frac{\mathrm{d}\omega'}{\pi}\frac{\chi''_{j_i j_i}(q_i,\omega')}{\omega' - \omega - i\eta}. \tag{E.5}$$

With these ingredients one can derive an expression for the real part of the longitudinal electric conductivity, denoted $\mathrm{Re}\,\sigma_{ii}(q_i,\omega)$. According to Eq. (E.4),

$$\begin{aligned}
\int \frac{\mathrm{d}\omega}{\pi}\frac{\chi''_{j_i j_i}(q_i,\omega)}{\omega} &= \frac{1}{q_i^2}\int \frac{\mathrm{d}\omega}{\pi}\omega\chi''_{\rho\rho}(q_i,\omega) \\
&= \left[\frac{2i}{q_i^2}\frac{\partial}{\partial t}\int \frac{\mathrm{d}\omega}{2\pi}e^{-i\omega t}\chi''_{\rho\rho}(q_i,\omega)\right]\Bigg|_{t=0} \\
&= \frac{1}{Nq_i^2}\left\langle\left[i\frac{\partial}{\partial t}\hat{\rho}(q_i,t),\hat{\rho}(-q_i,0)\right]\Bigg|_{t=0}\right\rangle_{\hat{\mathcal{H}}_0} \\
&= \frac{1}{Nq_i^2}\left\langle\left[[\hat{\rho}(q_i),\hat{\mathcal{H}}]\,(t),\hat{\rho}(-q_i,0)\right]\Bigg|_{t=0}\right\rangle_{\hat{\mathcal{H}}_0},
\end{aligned} \tag{E.6}$$

where $\hat{\mathcal{H}}$ is the Hubbard Hamiltonian Eq. (3.9). The last expression of Eq. (E.6) relates directly to the first moment of the density correlation function. Evaluating the commutators and taking the limit $q_i \to 0$, one gets

$$\int \frac{\mathrm{d}\omega}{\pi} \frac{\chi''_{j_i j_i}(q_i,\omega)}{\omega} = \frac{1}{q_i^2 N} \sum_{\mathbf{k},\sigma} \frac{\partial^2 \epsilon_{\mathbf{k},\sigma}}{\partial k_i^2} \langle \hat{n}_{\mathbf{k},\sigma} \rangle_{\mathcal{H}} \equiv -\langle \hat{j}_{i,d} \rangle, \tag{E.7}$$

where $\epsilon_{\mathbf{k},\sigma}$ is the dispersion relation in D dimensions and σ is the spin. Eq. (E.7) will serve as a sum rule to verify if the longitudinal optical conductivity obeys conservation laws, namely $\mathrm{Re}\chi_{j_i j_i}(iq_n = 0) = \sum_\sigma \int\cdots\int_{-\pi}^{\pi} \mathrm{d}^D k \frac{\partial^2 \epsilon(\mathbf{k})}{\partial k_i} \langle n_{\mathbf{k},\sigma} \rangle$. Equation (E.7) represents the diamagnetic contribution $\hat{j}_{i,d}$ to the current fluctuations $\delta\langle \hat{j}_i(\omega) \rangle$ (when multiplying the expression by (-1)), that is

$$\delta\langle \hat{j}_i(\omega) \rangle = \left[\langle \hat{j}_{i,d} \rangle + \chi_{j_i j_i}(\omega) \right] A_i(\omega). \tag{E.8}$$

Hence, given that without scalar potential, the electric field obeys $E_i(t) = -\frac{\partial A_i(t)}{\partial t}$, the longitudinal conductivity reads

$$\sigma_{ii}(q_i,\omega) = \frac{\langle \hat{j}_{i,d} \rangle + \chi_{j_i j_i}(\omega)}{i(\omega + i\eta)}, \tag{E.9}$$

owing to the relation linking the current fluctuations to the electric field in linear response theory: $\delta\langle j_i(\omega) \rangle = \sigma_{ii}(\omega) E_i(\omega)$. Now using Eqs. (E.5) and (E.7), one aims at extracting the real part of the longitudinal conductivity:

$$\begin{aligned}
&\sigma_{ii}(q_i,\omega) = \\
&\frac{1}{i(\omega+i\eta)} \left[\int \frac{\mathrm{d}\omega'}{\pi} \frac{\chi''_{j_i j_i}(q_i,\omega')}{\omega' - \omega - i\eta} - \int \frac{\mathrm{d}\omega'}{\pi} \frac{\chi''_{j_i j_i}(q_i,\omega')}{\omega'} \right] \\
&= \frac{1}{i(\omega+i\eta)} \int \frac{\mathrm{d}\omega'}{\pi} \frac{(\omega+i\eta)\chi''_{j_i j_i}(q_i,\omega')}{\omega'(\omega' - \omega - i\eta)} \\
&= \frac{1}{i} \int \frac{\mathrm{d}\omega'}{\pi} \frac{\chi''_{j_i j_i}(q_i,\omega')}{\omega'(\omega' - \omega - i\eta)} \\
&\implies \mathrm{Re}\sigma_{ii}(q_i,\omega) = \frac{\chi''_{j_i j_i}(q_i,\omega)}{\omega}.
\end{aligned} \tag{E.10}$$

F

RECIPROCAL-SPACE LADDER-TYPE VERTEX CORRECTIONS

In this section, the Fourier transforms of the quantities introduced in Chapter 4 are carried out. Let's first break down Eq. (4.17) into even and odd components in the following way

$$\begin{aligned}
&\chi^{(\text{even})/(\text{odd})}_{\sigma\sigma'}(1,1^+;2^+,2)\\
&= -\sum_{\tilde{\sigma}''} \mathcal{G}_{\sigma}(1,\bar{4})\Box_{\sigma\tilde{\sigma}''}(\bar{4}-\bar{3})\delta(\bar{4}-\bar{5})\delta(\bar{3}-\bar{6})\mathcal{G}_{\sigma}(\bar{3},1^+)\blacktriangleright^{(\text{odd})/(\text{even})}_{\tilde{\sigma}''\sigma'}(\bar{5},\bar{6},2)\\
&= -\sum_{\tilde{\sigma}''} \mathcal{G}_{\sigma}(1,\bar{4})\Box_{\sigma\tilde{\sigma}''}(\bar{4}-\bar{3})\mathcal{G}_{\sigma}(\bar{3},1^+)\blacktriangleright^{(\text{odd})/(\text{even})}_{\tilde{\sigma}''\sigma'}(\bar{4},\bar{3},2). \qquad (\text{F.1})
\end{aligned}$$

Note that this very equation needs to be considered in its entirety, *i.e* one cannot remove the ladder (□) appearing in Eq. (F.1) to simplify the equations before Fourier transforming, because then the left-hand side of the diagram would not be consistent – two consecutive Green's functions must be separated by a ladder (□) in the opposite direction and removing that ladder (□) would break that requirement. The equation for the general susceptibility is stripped down to the bare minimum considering the symmetries of the ladders. Indeed, for the each of the ladder's expression, one has the correspondence

$$\frac{\delta\Sigma_{\sigma}(4,5)}{\delta\mathcal{G}_{\sigma'}(6,7)} \to \Box_{\sigma\sigma'}(4-5)\delta(4-6)\delta(5-7)\delta_{\sigma',-\sigma} \qquad (\text{F.2})$$

and $\frac{\delta\mathcal{G}}{\delta\phi}^{(\text{odd})/(\text{even})}$ is represented by a filled black triangle with three entries ($\blacktriangleright^{(\text{odd})/(\text{even})}$). There remains now to Fourier transform Eq. (F.1), which will result in

$$\begin{aligned}
&\chi^{(\text{even})/(\text{odd})}_{\sigma,\sigma'}(q)\\
&= -\frac{1}{(V\beta)^3}\sum_{\tilde{\sigma}''}\sum_{\tilde{k},q'}\mathcal{G}_{\sigma}(\tilde{k})\mathcal{G}_{\sigma}(\tilde{k}+q)\Box_{\sigma\tilde{\sigma}''}(q')\blacktriangleright^{(\text{odd}/\text{even})}_{\tilde{\sigma}''\sigma'}(\tilde{k}+q-q',q'-\tilde{k},-q).
\end{aligned}$$
$$(\text{F.3})$$

Let's first compute the Fourier transformation of the ladder term (□) (F.2):

$$\begin{aligned}
&\int \mathrm{d}(4-5)e^{iq'(4-5)}\Box^{\sigma\sigma'}(4-5) = U\delta_{\sigma',-\sigma}\int \mathrm{d}(4-5)e^{iq'(4-5)}\delta(4-5)-\\
&U\delta_{\sigma',-\sigma}\int \mathrm{d}(4-5)\mathrm{d}11\; e^{iq'(4-5)}\mathcal{G}_{\sigma}(4,11)\mathcal{G}_{\sigma'}(11,4)\Box_{\sigma\sigma'}(11-5)\\
&\Leftrightarrow\\
&\Box_{\sigma\sigma'}(q') = U\delta_{\sigma',-\sigma} - \frac{U\delta_{\sigma',-\sigma}}{V\beta}\sum_{k}\mathcal{G}_{\sigma}(k)\mathcal{G}_{\sigma'}(k-q')\Box_{\sigma\sigma'}(q')\\
&\Leftrightarrow\\
&\Box_{\sigma\sigma'}(q') = \frac{U\delta_{\sigma',-\sigma}}{1+\frac{U}{V\beta}\sum_{k}\mathcal{G}_{\sigma}(k)\mathcal{G}_{\sigma'}(k-q')}. \qquad (\text{F.4})
\end{aligned}$$

The result of Eq. (F.4) will have to be substituted into the proper slots when the Fourier expressions for the even and odd susceptibilities (F.1) will be calculated.

F.1 ODD NUMBER OF LADDERS $\chi^{(\mathrm{ODD})}$

To compute $\blacktriangleright^{(\mathrm{even})}_{\sigma''\sigma'}$ appearing in Eq. (F.3), one has to consider the following integral-differential equation

$$\frac{\delta\mathcal{G}^{(\mathrm{even})}_{\sigma}(1,3)}{\delta\phi_{\sigma'}(2^+,2)} = \mathcal{G}_\sigma(1,2^+)\mathcal{G}_\sigma(2,3)\delta_{\sigma,\sigma'} +$$

$$\sum_{\sigma'',\sigma'''}\mathcal{G}_\sigma(1,\bar{4})\mathcal{G}_\sigma(\bar{\bar{5}},3)\frac{\delta\Sigma_\sigma(\bar{4},\bar{\bar{5}})}{\delta\mathcal{G}_{\sigma''}(\bar{6},\bar{\bar{7}})}\mathcal{G}_{\sigma''}(\bar{6},\bar{10})\mathcal{G}_{\sigma''}(\bar{11},\bar{\bar{7}})\frac{\delta\Sigma_{\sigma''}(\bar{10},\bar{11})}{\delta\mathcal{G}_{\sigma'''}(\bar{\bar{8}},\bar{\bar{9}})}\frac{\delta\mathcal{G}^{(\mathrm{even})}_{\sigma'''}(\bar{\bar{8}},\bar{\bar{9}})}{\delta\phi_{\sigma'}(2^+,2)}, \tag{F.5}$$

which in terms of the shapes, using the proper symmetries, becomes

$$\begin{aligned}
&\blacktriangleright^{(\mathrm{even})}_{\sigma\sigma'}(1,3,2) = \mathcal{G}_\sigma(1,2^+)\mathcal{G}_\sigma(2,3)\delta_{\sigma,\sigma'}\\
&+\sum_{\sigma'',\sigma'''}\mathcal{G}_\sigma(1,\bar{4})\mathcal{G}_\sigma(\bar{\bar{5}},3)\Box_{\sigma\sigma''}(\bar{4}-\bar{\bar{5}})\delta(\bar{4}-\bar{6})\delta(\bar{\bar{5}}-\bar{\bar{7}})\\
&\times\mathcal{G}_{\sigma''}(\bar{6},\bar{10})\mathcal{G}_{\sigma''}(\bar{11},\bar{\bar{7}})\Box^{\sigma''\sigma'''}(\bar{10}-\bar{11})\delta(\bar{\bar{9}}-\bar{11})\delta(\bar{\bar{8}}-\bar{10})\blacktriangleright^{(\mathrm{even})}_{\sigma'''\sigma'}(\bar{\bar{8}},\bar{\bar{9}},2)\\
&=\mathcal{G}_\sigma(1,2^+)\mathcal{G}_\sigma(2,3)\delta_{\sigma,\sigma'}+\sum_{\sigma'',\sigma'''}\mathcal{G}_\sigma(1,\bar{6})\mathcal{G}_\sigma(\bar{\bar{7}},3)\Box_{\sigma\sigma''}(\bar{6}-\bar{\bar{7}})\mathcal{G}_{\sigma''}(\bar{6},\bar{10})\mathcal{G}_{\sigma''}(\bar{11},\bar{\bar{7}})\\
&\times\Box_{\sigma''\sigma'''}(\bar{10}-\bar{11})\blacktriangleright^{(\mathrm{even})}_{\sigma'''\sigma'}(\bar{10},\bar{11},2).
\end{aligned}\tag{F.6}$$

The Fourier transformation of Eq. (F.6) is then computed:

$$\begin{aligned}
&\int \mathrm{d}1\mathrm{d}2\mathrm{d}3\; e^{ik1}e^{i\check{q}2}e^{ik'3}\;\blacktriangleright^{(\mathrm{even})}_{\sigma\sigma'}(1,3,2) = \blacktriangleright^{(\mathrm{even})}_{\sigma\sigma'}(k,k',\check{q})\\
&= V\beta\mathcal{G}_\sigma(k)\mathcal{G}_\sigma(k+\check{q})\delta_{\sigma,\sigma'}\delta_{k'+k+\check{q},0}+\\
&\frac{1}{(V\beta)^2}\sum_{\sigma'',\sigma'''}\sum_{q'',q'''}\mathcal{G}_\sigma(k)\mathcal{G}_\sigma(-k')\Box_{\sigma\sigma''}(q'')\mathcal{G}_{\sigma''}(k-q'')\mathcal{G}_{\sigma''}(-k'-q'')\Box_{\sigma''\sigma'''}(q''')\\
&\times\blacktriangleright^{(\mathrm{even})}_{\sigma'''\sigma'}(k-q''-q''',k'+q''+q''',\check{q})\\
\Leftrightarrow\\
&\sum_{\sigma'''}\frac{1}{(V\beta)^2}\sum_{k'',k'''}\Bigg[\delta_{k,k''}\delta_{k',k'''}\delta_{\sigma,\sigma'''}-\sum_{q'',q'''}\frac{\delta_{k-q''-q''',k''}\delta_{k'+q''+q''',k'''}}{(V\beta)^2}\sum_{\sigma''}\mathcal{G}_\sigma(k)\mathcal{G}_\sigma(-k')\\
&\times\Box_{\sigma\sigma''}(q'')\mathcal{G}_{\sigma''}(k-q'')\mathcal{G}_{\sigma''}(-k'-q'')\Box_{\sigma''\sigma'''}(q''')\Bigg]\blacktriangleright^{(\mathrm{even})}_{\sigma'''\sigma'}(k'',k''',\check{q})\\
&= V\beta\mathcal{G}_\sigma(k)\mathcal{G}_\sigma(k+\check{q})\delta_{\sigma,\sigma'}\delta_{k'+k+\check{q},0}.
\end{aligned}\tag{F.7}$$

To isolate $\blacktriangleright^{(\mathrm{even})}$, one needs to invert the matrix on the left-hand side of Eq. (F.7) and this is the same procedure as if it were the real-space expression (equally valid). This procedure requires extra care and it will be done very gradually. If the matrix to invert is renamed Λ, one has

$$\begin{aligned}
&\sum_{\sigma'''}\frac{1}{(V\beta)^2}\sum_{k'',k'''}\Lambda_{\sigma\sigma'''}(k,k',\check{q};k'',k''',\check{q})\blacktriangleright^{(\mathrm{even})}_{\sigma'''\sigma'}(k'',k''',\check{q})\\
&= V\beta\mathcal{G}_\sigma(k)\mathcal{G}_\sigma(k+\check{q})\delta_{\sigma,\sigma'}\delta_{k'+k+\check{q},0}.
\end{aligned}\tag{F.8}$$

Then, to isolate $\blacktriangleright^{(\text{even})}$ in Eq. (F.8), one supposes the existence of an inverse of Λ such that

$$\begin{aligned}
&\sum_{\sigma''',\tilde{\sigma}} \frac{1}{(V\beta)^4} \sum_{\substack{\bar{k},\bar{k}' \\ k'',k'''}} \Lambda_{\sigma\tilde{\sigma}}(k,k',q;\bar{k},\bar{k}',\check{q})^{-1} \Lambda_{\tilde{\sigma}\sigma'''}(\bar{k},\bar{k}',\check{q};k'',k''',\check{q}) \blacktriangleright^{(\text{even})}_{\sigma'''\sigma'} (k'',k''',\check{q}) \\
&= V\beta \sum_{\tilde{\sigma}} \frac{1}{(V\beta)^2} \sum_{\bar{k},\bar{k}'} \Lambda_{\sigma\tilde{\sigma}}(k,k',\check{q};\bar{k},\bar{k}',\check{q})^{-1} \mathcal{G}_{\tilde{\sigma}}(\bar{k}) \mathcal{G}_{\tilde{\sigma}}(\bar{k}+\check{q}) \delta_{\tilde{\sigma},\sigma'} \delta_{\bar{k}'+\bar{k}+\check{q},0} \\
&= \blacktriangleright^{(\text{even})}_{\sigma\sigma'} (k,k',\check{q}).
\end{aligned} \tag{F.9}$$

If one enacts the Kronecker delta in Eq. (F.9), one gets

$$\blacktriangleright^{(\text{even})}_{\sigma\sigma'} (k,k',\check{q}) = \sum_{\bar{k}} \Lambda_{\sigma\sigma'}(k,k',\check{q};\bar{k},-\bar{k}-\check{q},\check{q})^{-1} \mathcal{G}_{\sigma'}(\bar{k}) \mathcal{G}_{\sigma'}(\bar{k}+\check{q}). \tag{F.10}$$

Now, according to Eq. (F.3), one needs to substitute $k \to \tilde{k}+q-q'$, $k' \to q'-\tilde{k}$ and $\check{q} \to -q$ in $\blacktriangleright^{(\text{even})}$ of Eq. (F.10):

$$\begin{aligned}
&\blacktriangleright^{(\text{even})}_{\sigma\sigma'} (\tilde{k}+q-q',q'-\tilde{k},-q) \\
&= \sum_{\bar{k}} \Lambda_{\sigma\sigma'}(\tilde{k}+q-q',q'-\tilde{k},-q;\bar{k},q-\bar{k},-q)^{-1} \mathcal{G}_{\sigma'}(\bar{k}) \mathcal{G}_{\sigma'}(\bar{k}-q).
\end{aligned} \tag{F.11}$$

For a fixed value of q Eq. (F.11) would effectively read something like

$$\begin{aligned}
&\blacktriangleright^{(\text{even})}_{\sigma\sigma',q} (\tilde{k}-q') = \sum_{\bar{k}} \Lambda^{q}_{\sigma\sigma'}(\tilde{k}-q',\bar{k})^{-1} \mathcal{G}_{\sigma'}(\bar{k}) \mathcal{G}^{q}_{\sigma'}(\bar{k}) \\
&\Leftrightarrow \\
&\blacktriangleright^{(\text{even})}_{\sigma\sigma',q} (i\tilde{k}_n - iq'_n,\tilde{\mathbf{k}}-\mathbf{q}') = \sum_{\bar{k}} \Lambda^{q}_{\sigma\sigma'}(i\tilde{k}_n - iq'_n,\tilde{\mathbf{k}}-\mathbf{q}',i\bar{k}_n,\bar{\mathbf{k}})^{-1} \\
&\qquad \times \mathcal{G}_{\sigma'}(i\bar{k}_n,\bar{\mathbf{k}}) \mathcal{G}^{q}_{\sigma'}(i\bar{k}_n,\bar{\mathbf{k}}).
\end{aligned} \tag{F.12}$$

If one restricts furthermore to fixed values of momentum, one would need to invert a matrix in the Matsubara frequency space

$$\blacktriangleright^{(\text{even})}_{\sigma\sigma',q,\tilde{\mathbf{k}}-\mathbf{q}'} (i\tilde{k}_n - iq'_n) = \sum_{\bar{\mathbf{k}}} \Lambda^{q,\tilde{\mathbf{k}}-\mathbf{q}',\bar{\mathbf{k}}}_{\sigma\sigma'}(i\tilde{k}_n - iq'_n,i\bar{k}_n)^{-1} \mathcal{G}^{\bar{\mathbf{k}}}_{\sigma'}(i\bar{k}_n) \mathcal{G}^{q,\bar{\mathbf{k}}}_{\sigma'}(i\bar{k}_n), \tag{F.13}$$

and that matrix would be

$$\begin{aligned}
&\Lambda^{q,\tilde{\mathbf{k}}-\mathbf{q}',\bar{\mathbf{k}}}_{\sigma\sigma'}(i\tilde{k}_n - iq'_n,i\bar{k}_n)^{-1} = \Bigg[\delta^{\tilde{\mathbf{k}}+\mathbf{q}-\mathbf{q}',\bar{\mathbf{k}}}_{i\tilde{k}_n+iq_n-iq'_n,i\bar{k}_n} \delta_{\sigma,\sigma'} - \frac{1}{V\beta} \sum_{\sigma''} \sum_{q''} \mathcal{G}^{q,\tilde{\mathbf{k}}-\mathbf{q}'}_{\sigma}(i\tilde{k}_n - iq'_n) \\
&\times \mathcal{G}^{\tilde{\mathbf{k}}-\mathbf{q}'}_{\sigma}(i\tilde{k}_n - iq'_n) \Box_{\sigma\sigma''}(iq''_n,\mathbf{q}'') \mathcal{G}^{q,\tilde{\mathbf{k}}-\mathbf{q}'}_{\sigma''}(i\tilde{k}_n - iq'_n,iq''_n,\mathbf{q}'') \mathcal{G}^{\tilde{\mathbf{k}}-\mathbf{q}'}_{\sigma''}(i\tilde{k}_n - iq'_n,iq''_n,\mathbf{q}'') \\
&\times \Box^{q,\tilde{\mathbf{k}}-\mathbf{q}',\bar{\mathbf{k}}}_{\sigma''\sigma'}(i\tilde{k}_n - iq'_n,iq''_n,i\bar{k}_n) \Bigg]^{-1}.
\end{aligned} \tag{F.14}$$

Every variable that is fixed adds a for-loop layer. The different objects would be precomputed. Eq. (F.14) would read, if the matrix form was not emphasised,

$$\begin{aligned}&\Lambda_{\sigma\sigma'}(\tilde{k}-q',\bar{k},q')^{-1}\\&=\Bigg[\delta_{\tilde{k}+q-q',\bar{k}}\delta_{\sigma,\sigma'}-\frac{1}{V\beta}\sum_{\sigma''}\sum_{q''}\mathcal{G}_{\sigma}(\tilde{k}+q-q')\mathcal{G}_{\sigma}(\tilde{k}-q')\Box_{\sigma\sigma''}(q'')\\&\times\mathcal{G}_{\sigma''}(\tilde{k}+q-q'-q'')\mathcal{G}_{\sigma''}(\tilde{k}-q'-q'')\Box_{\sigma''\sigma'}(\tilde{k}+q-q'-q''-\bar{k})\Bigg]^{-1}.\end{aligned}\tag{F.15}$$

Then, Eq. (F.13) would be multiplied to Eq. (F.3).

F.2 EVEN NUMBER OF LADDERS $\chi^{(\mathrm{EVEN})}$

Moving on to compute $\blacktriangleright^{(\mathrm{odd})}_{\sigma''\sigma'}$ appearing in Eq. (F.3), one has to consider the following integral-differential equation

$$\begin{aligned}&\frac{\delta\mathcal{G}^{(\mathrm{odd})}_{\sigma}(1,3)}{\delta\phi_{\sigma'}(2^+,2)}=\sum_{\sigma''}\mathcal{G}_{\sigma}(1,\bar{4})\mathcal{G}_{\sigma}(\bar{5},3)\frac{\delta\Sigma_{\sigma}(\bar{4},\bar{5})}{\delta\mathcal{G}_{\sigma''}(\bar{6},\bar{7})}\mathcal{G}_{\sigma''}(\bar{6},2^+)\mathcal{G}_{\sigma''}(2,\bar{7})\delta_{\sigma'',\sigma'}+\\&\sum_{\sigma'',\sigma'''}\mathcal{G}_{\sigma}(1,\bar{4})\mathcal{G}_{\sigma}(\bar{5},3)\frac{\delta\Sigma_{\sigma}(\bar{4},\bar{5})}{\delta\mathcal{G}_{\sigma''}(\bar{6},\bar{7})}\mathcal{G}_{\sigma''}(\bar{6},\bar{10})\mathcal{G}_{\sigma''}(\bar{11},\bar{7})\frac{\delta\Sigma_{\sigma''}(\bar{10},\bar{11})}{\delta\mathcal{G}_{\sigma'''}(\bar{8},\bar{9})}\frac{\delta\mathcal{G}^{(\mathrm{odd})}_{\sigma'''}(\bar{8},\bar{9})}{\delta\phi_{\sigma'}(2^+,2)},\end{aligned}$$

which in terms of the shapes, using the proper symmetries, reads

$$\begin{aligned}&\blacktriangleright^{(\mathrm{odd})}_{\sigma\sigma'}(1,3,2)=\mathcal{G}_{\sigma}(1,\bar{6})\mathcal{G}_{\sigma}(\bar{7},3)\Box_{\sigma\sigma'}(\bar{6}-\bar{7})\mathcal{G}_{\sigma'}(\bar{6},2^+)\mathcal{G}_{\sigma'}(2,\bar{7})+\\&\sum_{\sigma'',\sigma'''}\mathcal{G}_{\sigma}(1,\bar{6})\mathcal{G}_{\sigma}(\bar{7},3)\Box_{\sigma\sigma''}(\bar{6}-\bar{7})\mathcal{G}_{\sigma''}(\bar{6},\bar{10})\mathcal{G}_{\sigma''}(\bar{11},\bar{7})\Box_{\sigma''\sigma'''}(\bar{10}-\bar{11})\\&\times\blacktriangleright^{(\mathrm{odd})}_{\sigma'''\sigma'}(\bar{10},\bar{11},2).\end{aligned}\tag{F.16}$$

The Fourier transformation of Eq. (F.16) is then computed:

$$\begin{aligned}&\int\mathrm{d}1\mathrm{d}2\mathrm{d}3\;e^{ik1}e^{i\check{q}2}e^{ik'3}\;\blacktriangleright^{(\mathrm{odd})}_{\sigma\sigma'}(1,3,2)=\blacktriangleright^{(\mathrm{odd})}_{\sigma\sigma'}(k,k',\check{q})\\&=\sum_{\bar{q}}\mathcal{G}_{\sigma}(k)\mathcal{G}_{\sigma}(k+\check{q})\Box_{\sigma\sigma'}(\bar{q})\mathcal{G}_{\sigma'}(k-\bar{q})\mathcal{G}_{\sigma'}(k+\check{q}-\bar{q})\delta_{k'+k+\check{q},0}+\\&\frac{1}{(V\beta)^2}\sum_{\sigma'',\sigma'''}\sum_{q'',q'''}\mathcal{G}_{\sigma}(k)\mathcal{G}_{\sigma}(-k')\Box_{\sigma\sigma''}(q'')\mathcal{G}_{\sigma''}(k-q'')\mathcal{G}_{\sigma''}(-k'-q'')\Box_{\sigma''\sigma'''}(q''')\\&\times\blacktriangleright^{(\mathrm{odd})}_{\sigma'''\sigma'}(k-q''-q''',k'+q''+q''',\check{q})\\&\Leftrightarrow\\&\sum_{\sigma'''}\frac{1}{(V\beta)^2}\sum_{k'',k'''}\Bigg[\delta_{k,k''}\delta_{k',k'''}\delta_{\sigma,\sigma'''}-\sum_{q'',q'''}\frac{\delta_{k-q''-q''',k''}\delta_{k'+q''+q''',k'''}}{(V\beta)^2}\sum_{\sigma''}\mathcal{G}_{\sigma}(k)\mathcal{G}_{\sigma}(-k')\\&\times\Box_{\sigma\sigma''}(q'')\mathcal{G}_{\sigma''}(k-q'')\mathcal{G}_{\sigma''}(-k'-q'')\Box_{\sigma''\sigma'''}(q''')\Bigg]\blacktriangleright^{(\mathrm{odd})}_{\sigma'''\sigma'}(k'',k''',\check{q})\\&=\sum_{\bar{q}}\mathcal{G}_{\sigma}(k)\mathcal{G}_{\sigma}(k+\check{q})\Box_{\sigma\sigma'}(\bar{q})\mathcal{G}_{\sigma'}(k-\bar{q})\mathcal{G}_{\sigma'}(k+\check{q}-\bar{q})\delta_{k'+k+\check{q},0}.\end{aligned}\tag{F.17}$$

To invert the equation (F.17) and isolate $\blacktriangleright^{(\mathrm{odd})}$, the same trick as that in Eq. (F.8) is used:

$$
\begin{aligned}
&\blacktriangleright^{(\mathrm{odd})}_{\sigma\sigma'}(k,k',\check{q}) \\
&= \sum_{\tilde{\sigma}} \frac{1}{(V\beta)^2} \sum_{\bar{k},\bar{k}',\bar{q}} \mathcal{G}_{\tilde{\sigma}}(\bar{k})\mathcal{G}_{\tilde{\sigma}}(\bar{k}+\check{q})\Box_{\tilde{\sigma},\sigma'}(\bar{q})\mathcal{G}_{\sigma'}(\bar{k}-\bar{q})\mathcal{G}_{\sigma'}(\bar{k}+\check{q}-\bar{q})\delta_{\bar{k}'+\bar{k}+\check{q},0}\Bigg[\delta_{k,\bar{k}}\delta_{k',\bar{k}'}\delta_{\sigma,\tilde{\sigma}} - \\
&\sum_{q'',q'''} \frac{\delta_{\bar{k},k-q''-q'''}\delta_{\bar{k}',k'+q''+q'''}}{(V\beta)^2} \sum_{\sigma''} \mathcal{G}_{\sigma}(k)\mathcal{G}_{\sigma}(-k')\Box_{\sigma\sigma''}(q'')\mathcal{G}_{\sigma''}(k-q'')\mathcal{G}_{\sigma''}(-k'-q'')\Box_{\sigma''\tilde{\sigma}}(q''')\Bigg]^{-1} \\
&= \sum_{\tilde{\sigma}} \frac{1}{V\beta} \sum_{\bar{k},\bar{q}} \mathcal{G}_{\tilde{\sigma}}(\bar{k})\mathcal{G}_{\tilde{\sigma}}(\bar{k}+\check{q})\Box_{\tilde{\sigma},\sigma'}(\bar{q})\mathcal{G}_{\sigma'}(\bar{k}-\bar{q})\mathcal{G}_{\sigma'}(\bar{k}+\check{q}-\bar{q})\Bigg[\delta_{k,\bar{k}}\delta_{k',-\bar{k}-\check{q}}\delta_{\sigma,\tilde{\sigma}} - \\
&\sum_{q''} \frac{\delta_{k'+k+\check{q},0}}{V\beta} \sum_{\sigma''} \mathcal{G}_{\sigma}(k)\mathcal{G}_{\sigma}(-k')\Box_{\sigma\sigma''}(q'')\mathcal{G}_{\sigma''}(k-q'')\mathcal{G}_{\sigma''}(-k'-q'')\Box_{\sigma''\tilde{\sigma}}(k-q''-\bar{k})\Bigg]^{-1}.
\end{aligned}
\tag{F.18}
$$

The equation (F.3) is once again called in, but this time to calculate the even contribution to the ladder-of-ladders, with the help of Eq. (F.18),

$$
\begin{aligned}
&\chi^{(\mathrm{even})}_{\sigma\sigma'}(q) = -\frac{1}{(V\beta)^3} \sum_{\tilde{\sigma}''} \sum_{\tilde{k},q'} \mathcal{G}_{\sigma}(\tilde{k})\mathcal{G}_{\sigma}(\tilde{k}+q)\Box_{\sigma\tilde{\sigma}''}(q') \blacktriangleright^{(\mathrm{odd})}_{\tilde{\sigma}''\sigma'}(\tilde{k}+q-q',q'-\tilde{k},-q) \\
&= -\frac{1}{(V\beta)^4} \sum_{\tilde{\sigma}'',\tilde{\sigma}} \sum_{\substack{\tilde{k},q' \\ \bar{k},\bar{q}}} \mathcal{G}_{\sigma}(\tilde{k})\mathcal{G}_{\sigma}(\tilde{k}+q)\Box_{\sigma\tilde{\sigma}''}(q')\mathcal{G}_{\tilde{\sigma}}(\bar{k})\mathcal{G}_{\tilde{\sigma}}(\bar{k}-q)\Box_{\tilde{\sigma},\sigma'}(\bar{q})\mathcal{G}_{\sigma'}(\bar{k}-\bar{q})\mathcal{G}_{\sigma'}(\bar{k}-q-\bar{q}) \\
&\times \Bigg[\delta_{\tilde{k}+q-q',\bar{k}}\delta_{q'-\tilde{k},-\bar{k}+q}\delta_{\tilde{\sigma}'',\tilde{\sigma}} - \frac{1}{V\beta}\sum_{\sigma''}\sum_{q''} \mathcal{G}_{\tilde{\sigma}''}(\tilde{k}+q-q')\mathcal{G}_{\tilde{\sigma}''}(\tilde{k}-q')\Box_{\tilde{\sigma}''\sigma''}(q'') \\
&\times \mathcal{G}_{\sigma''}(\tilde{k}+q-q'-q'')\mathcal{G}_{\sigma''}(\tilde{k}-q'-q'')\Box_{\sigma''\tilde{\sigma}}(\tilde{k}+q-q'-q''-\bar{k})\Bigg]^{-1}.
\end{aligned}
\tag{F.19}
$$

The following substitutions have been made in Eq. (F.19): $k \to \tilde{k}+q-q'$, $k' \to q'-\tilde{k}$ and $\check{q} \to -q$ in $\blacktriangleright^{(\mathrm{even})}$, again. In Eq. (F.19), the spins become $\tilde{\sigma}'' \to -\sigma$, $\sigma'' \to \sigma$, $\tilde{\sigma} \to -\sigma$ and $\sigma' \to \sigma$. To summarise, Eqs. (F.15) and (F.19) make up for the odd and even corrections, respectively.

F.3 AL DIAGRAM

The task here is to compute the Aslamazov-Larkin diagram $\chi^{\sigma\sigma'}_{\mathrm{AL}}$ shown in Fig. 4.7. The diagram Fig. 4.7 can be written down in real-space in the following form:

$$
\begin{aligned}
\chi^{\sigma\sigma'}_{\mathrm{AL}}(1,1^+;2^+,2) = \sum_{\sigma''} &\mathcal{G}_{\sigma}(1,\bar{12})\mathcal{G}_{\sigma}(\bar{11},1^+)\frac{\delta\Sigma_{\sigma}(\bar{13},\bar{12})}{\delta\mathcal{G}_{\sigma''}(\bar{17},\bar{15})} \\
&\times \mathcal{G}_{\sigma''}(\bar{18},\bar{17})\mathcal{G}_{\sigma''}(\bar{15},\bar{16})\frac{\delta\Sigma_{\sigma''}(\bar{11},\bar{14})}{\delta\mathcal{G}_{\sigma'}(\bar{16},\bar{18})}\mathcal{G}_{\sigma'}(\bar{13},2^+)\mathcal{G}_{\sigma'}(2,\bar{14}),
\end{aligned}
\tag{F.20}
$$

from which the vertex function can be isolated, giving Eq. (4.27), illustrated diagrammatically in Fig. 4.8. To recall, the integral-differential equation that describes the vertical ladders in real-space reads

$$\begin{aligned}\frac{\delta\Sigma_{\sigma}(1,3)}{\delta\mathcal{G}_{\sigma'}(4,5)} &= U\delta_{\sigma',-\sigma}\delta(4-5)\delta(1-3)\delta(1-4)\\ &\quad - U\delta_{\sigma',-\sigma}\delta(1-4)\mathcal{G}_{\sigma}(\bar{7},1)\frac{\delta\Sigma_{\sigma}(\bar{7},3)}{\delta\mathcal{G}_{\sigma'}(\bar{8},5)}\mathcal{G}_{\sigma'}(4,\bar{8}).\end{aligned} \tag{F.21}$$

Considering the Hubbard model and its symmetries, the □ representing the vertical ladder can be narrowed down to the expression shown in Eq. (F.2). Doing so, the AL vertex corrections read

$$\begin{aligned}&\chi^{\sigma\sigma'}_{\mathrm{AL}}(1,1^+;2^+,2) =\\ &\quad \mathcal{G}_{\sigma}(1,1\bar{2})\mathcal{G}_{\sigma}(1\bar{1},1^+)\Box_{\sigma-\sigma}(1\bar{2}-1\bar{3})\delta(1\bar{3}-1\bar{7})\delta(1\bar{2}-1\bar{5})\mathcal{G}_{-\sigma}(1\bar{8},1\bar{7})\mathcal{G}_{-\sigma}(1\bar{5},1\bar{6})\\ &\times \Box_{-\sigma\sigma}(1\bar{4}-1\bar{1})\delta_{\sigma',\sigma}\delta(1\bar{1}-1\bar{6})\delta(1\bar{4}-1\bar{8})\mathcal{G}_{\sigma'}(1\bar{3},2^+)\mathcal{G}_{\sigma'}(2,1\bar{4})\\ &= \mathcal{G}_{\sigma}(1,1\bar{2})\mathcal{G}_{\sigma}(1\bar{6},1^+)\Box_{\sigma-\sigma}(1\bar{2}-1\bar{3})\mathcal{G}_{-\sigma}(1\bar{8},1\bar{3})\mathcal{G}_{-\sigma}(1\bar{2},1\bar{6})\Box_{-\sigma\sigma}(1\bar{8}-1\bar{6})\\ &\times \delta_{\sigma',\sigma}\mathcal{G}_{\sigma'}(1\bar{3},2^+)\mathcal{G}_{\sigma'}(2,1\bar{8}).\end{aligned} \tag{F.22}$$

Fourier transforming Eq. (F.22), one gets easily

$$\begin{aligned}\chi^{\sigma\sigma'}_{\mathrm{AL}}(q) &= \frac{1}{(V\beta)^3}\sum_{\substack{\tilde{k},\bar{k}\\ q'}}\mathcal{G}_{\sigma}(\tilde{k})\mathcal{G}_{\sigma}(\tilde{k}-q)\Box_{\sigma-\sigma}(q')\mathcal{G}_{-\sigma}(\bar{k}-q')\mathcal{G}_{-\sigma}(\tilde{k}-q')\\ &\times \Box_{-\sigma\sigma}(q'-q)\mathcal{G}_{\sigma'}(\bar{k})\mathcal{G}_{\sigma'}(\bar{k}-q)\delta_{\sigma',\sigma}.\end{aligned} \tag{F.23}$$

Eq. (F.23) corresponds to Fig. 4.7.

G

KELDYSH DECOMPOSITION OF THE π-TON VERTEX CORRECTION

As discussed in Fig. 4.2, there exists a total of 9 contributions to the *lesser* and *greater* susceptibilities. Those contributions are set out in this section and need to be computed separately across the whole simulation, at each time steps. The Langreth rules introduced in Section 2.2.1 give the tools to work out all of those contributions. Each of the contributions is broken down into separate paragraphs in what follows. Some color coding is also used to identify the contour-time variables more easily.

BOTH $\bar{z}$ AND $\bar{z}'$ LYING ON $\mathcal{C}_1$ To start off, the decomposition is done by setting the times integrated over on the upper branch $\mathcal{C}_1$ of the Kadanoff-Baym contour. Fig. G.1 shows the contour for calculating $\chi^{>}_{\mathrm{sl}}(z,z')$ with $\bar{z} \succ \bar{z}'$.

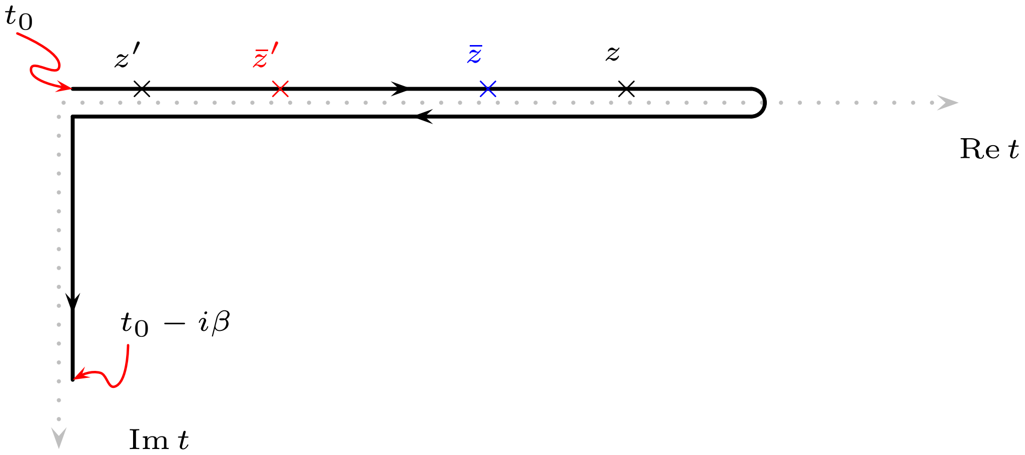

Figure G.1: Kadanoff-Baym contour for $\chi^{>}_{\mathrm{sl}}$ with $\bar{z} \succ \bar{z}'$, $\bar{z} \in \mathcal{C}_1$ and $\bar{z}' \in \mathcal{C}_1$.

The *greater* part of this configuration translates mathematically into Eq. (G.1):

$$\begin{aligned}
\chi^{>,\sigma-\sigma}_{\mathrm{sl}}(\mathbf{q};z,z') = &-\int_{-\pi}^{\pi}\frac{\mathrm{d}^D\tilde{k}}{(2\pi)^D}\int_{-\pi}^{\pi}\frac{\mathrm{d}^D\bar{k}}{(2\pi)^D}\int_{t_0}^{z}\mathrm{d}\bar{z}\int_{t_0}^{z}\mathrm{d}\bar{z}'\times \\
&\mathcal{G}^{>,\sigma}_{\tilde{\mathbf{k}}}(z,\bar{z})\theta^{\mathcal{C}}(z,\bar{z})\mathcal{G}^{<,\sigma}_{\tilde{\mathbf{k}}-\mathbf{q}}(\bar{z}',z)\theta^{\mathcal{C}}(z,\bar{z}')\left[\Box^{>,\sigma-\sigma}_{\tilde{\mathbf{k}}-\bar{\mathbf{k}}}(\bar{z},\bar{z}')\theta^{\mathcal{C}}(\bar{z},\bar{z}')+\Box^{<,\sigma-\sigma}_{\tilde{\mathbf{k}}-\bar{\mathbf{k}}}(\bar{z},\bar{z}')\theta^{\mathcal{C}}(\bar{z}',\bar{z})\right] \\
&\times\left[\mathcal{G}^{>,-\sigma}_{\bar{\mathbf{k}}}(\bar{z},z')\theta^{\mathcal{C}}(\bar{z},z')+\mathcal{G}^{<,-\sigma}_{\bar{\mathbf{k}}}(\bar{z},z')\theta^{\mathcal{C}}(z',\bar{z})\right]\left[\mathcal{G}^{<,-\sigma}_{\bar{\mathbf{k}}-\mathbf{q}}(z',\bar{z}')\theta^{\mathcal{C}}(\bar{z}',z')\right. \\
&\left.\quad+\mathcal{G}^{>,-\sigma}_{\bar{\mathbf{k}}-\mathbf{q}}(z',\bar{z}')\theta^{\mathcal{C}}(z',\bar{z}')\right]\theta^{\mathcal{C}}(z,z'). \qquad \text{(G.1)}
\end{aligned}$$

Now, the case of the *lesser* part $\chi^{<}_{\mathrm{sl}}(z,z')$ with $z' \prec z$ on $\mathcal{C}_1$ is dealt with, meaning that z would swap with z' in Fig. G.1. This leads to the following expression

$$\begin{aligned}
&\chi_{\text{sl}}^{<,\sigma-\sigma}(\mathbf{q};z,z') = -\int_{-\pi}^{\pi}\frac{\mathrm{d}^D\tilde{k}}{(2\pi)^D}\int_{-\pi}^{\pi}\frac{\mathrm{d}^D\bar{k}}{(2\pi)^D}\int_{t_0}^{z}\mathrm{d}\bar{z}\int_{t_0}^{z}\mathrm{d}\bar{z}'\times \\
&\mathcal{G}_{\tilde{\mathbf{k}}}^{>,\sigma}(z,\bar{z})\theta^{\mathcal{C}}(z,\bar{z})\mathcal{G}_{\tilde{\mathbf{k}}-\mathbf{q}}^{<,\sigma}(\bar{z}',z)\theta^{\mathcal{C}}(z,\bar{z}')\left[\Box_{\tilde{\mathbf{k}}-\bar{\mathbf{k}}}^{>,\sigma-\sigma}(\bar{z},\bar{z}')\theta^{\mathcal{C}}(\bar{z},\bar{z}')+\Box_{\tilde{\mathbf{k}}-\bar{\mathbf{k}}}^{<,\sigma-\sigma}(\bar{z},\bar{z}')\theta^{\mathcal{C}}(\bar{z}',\bar{z})\right] \\
&\qquad\times\mathcal{G}_{\bar{\mathbf{k}}}^{<,-\sigma}(\bar{z},z')\theta^{\mathcal{C}}(z',\bar{z})\mathcal{G}_{\bar{\mathbf{k}}-\mathbf{q}}^{>,-\sigma}(z',\bar{z}')\theta^{\mathcal{C}}(z',\bar{z}')\theta^{\mathcal{C}}(z',z).
\end{aligned}\tag{G.2}$$

The retarded component is defined as $\chi^R \equiv \chi^> - \chi^<$.

$\bar{z} \in \mathcal{C}_1$ AND $\bar{z}' \in \mathcal{C}_2$ To continue, the configuration where $\bar{z}$ remains on $\mathcal{C}_1$ with $\bar{z}'$ shifting down to $\mathcal{C}_2$ is considered. In that case, this necessary implies that $\bar{z} \prec \bar{z}'$. The expression for the *greater* component of the single-ladder vertex correction on the contour is

$$\begin{aligned}
&\chi_{\text{sl}}^{>,\sigma-\sigma}(\mathbf{q};z,z') = -\int_{-\pi}^{\pi}\frac{\mathrm{d}^D\tilde{k}}{(2\pi)^D}\int_{-\pi}^{\pi}\frac{\mathrm{d}^D\bar{k}}{(2\pi)^D}\int_{t_0}^{z}\mathrm{d}\bar{z}\int_{z}^{t_0}\mathrm{d}\bar{z}'\times \\
&\mathcal{G}_{\tilde{\mathbf{k}}}^{>,\sigma}(z,\bar{z})\theta^{\mathcal{C}}(z,\bar{z})\mathcal{G}_{\tilde{\mathbf{k}}-\mathbf{q}}^{>,\sigma}(\bar{z}',z)\theta^{\mathcal{C}}(\bar{z}',z)\Box_{\tilde{\mathbf{k}}-\bar{\mathbf{k}}}^{<,\sigma-\sigma}(\bar{z},\bar{z}')\theta^{\mathcal{C}}(\bar{z}',\bar{z}) \\
&\times\left[\mathcal{G}_{\bar{\mathbf{k}}}^{<,-\sigma}(\bar{z},z')\theta^{\mathcal{C}}(z',\bar{z})+\mathcal{G}_{\bar{\mathbf{k}}}^{>,-\sigma}(\bar{z},z')\theta^{\mathcal{C}}(\bar{z},z')\right]\mathcal{G}_{\bar{\mathbf{k}}-\mathbf{q}}^{<,-\sigma}(z',\bar{z}')\theta^{\mathcal{C}}(\bar{z}',z')\theta^{\mathcal{C}}(z,z'),
\end{aligned}\tag{G.3}$$

whilst the *lesser* component reads

$$\begin{aligned}
&\chi_{\text{sl}}^{<,\sigma-\sigma}(\mathbf{q};z,z') = -\int_{-\pi}^{\pi}\frac{\mathrm{d}^D\tilde{k}}{(2\pi)^D}\int_{-\pi}^{\pi}\frac{\mathrm{d}^D\bar{k}}{(2\pi)^D}\int_{t_0}^{z}\mathrm{d}\bar{z}\int_{z}^{t_0}\mathrm{d}\bar{z}'\times \\
&\mathcal{G}_{\tilde{\mathbf{k}}}^{>,\sigma}(z,\bar{z})\theta^{\mathcal{C}}(z,\bar{z})\mathcal{G}_{\tilde{\mathbf{k}}-\mathbf{q}}^{>,\sigma}(\bar{z}',z)\theta^{\mathcal{C}}(\bar{z}',z)\Box_{\tilde{\mathbf{k}}-\bar{\mathbf{k}}}^{<,\sigma-\sigma}(\bar{z},\bar{z}')\theta^{\mathcal{C}}(\bar{z}',\bar{z})\mathcal{G}_{\bar{\mathbf{k}}}^{<,-\sigma}(\bar{z},z')\theta^{\mathcal{C}}(z',\bar{z}) \\
&\times\left[\mathcal{G}_{\bar{\mathbf{k}}-\mathbf{q}}^{<,-\sigma}(z',\bar{z}')\theta^{\mathcal{C}}(\bar{z}',z')+\mathcal{G}_{\bar{\mathbf{k}}-\mathbf{q}}^{>,-\sigma}(z',\bar{z}')\theta^{\mathcal{C}}(z',\bar{z}')\right]\theta^{\mathcal{C}}(z',z).
\end{aligned}\tag{G.4}$$

In Eq. (G.4), the first term in $[\cdots]$ concerns configurations where $\bar{z}'$ is located further to the left on the $\mathcal{C}_2$ branch as compared to z' whereas the second term concerns the opposite situation. Again, $\chi^R \equiv \chi^> - \chi^<$.

$\bar{z} \in \mathcal{C}_1$ AND $\bar{z}' \in \mathcal{C}_3$ Next, the configuration where $\bar{z}$ remains on $\mathcal{C}_1$ with $\bar{z}'$ now shifting onto $\mathcal{C}_3$ is considered. In that case, it necessarily implies that $\bar{z} \prec \bar{z}'$. The expression for the *greater* part of the single-ladder vertex correction on the contour is

$$\begin{aligned}
&\chi_{\text{sl}}^{>,\sigma-\sigma}(\mathbf{q};z,z') = -\int_{-\pi}^{\pi}\frac{\mathrm{d}^D\tilde{k}}{(2\pi)^D}\int_{-\pi}^{\pi}\frac{\mathrm{d}^D\bar{k}}{(2\pi)^D}\int_{t_0}^{z}\mathrm{d}\bar{z}\int_{t_0}^{t_0-i\beta}\mathrm{d}\bar{z}'\times \\
&\mathcal{G}_{\tilde{\mathbf{k}}}^{>,\sigma}(z,\bar{z})\theta^{\mathcal{C}}(z,\bar{z})\mathcal{G}_{\tilde{\mathbf{k}}-\mathbf{q}}^{\neg,\sigma}(\bar{z}',z)\Box_{\tilde{\mathbf{k}}-\bar{\mathbf{k}}}^{\neg,\sigma-\sigma}(\bar{z},\bar{z}') \\
&\times\left[\mathcal{G}_{\bar{\mathbf{k}}}^{<,-\sigma}(\bar{z},z')\theta^{\mathcal{C}}(z',\bar{z})+\mathcal{G}_{\bar{\mathbf{k}}}^{>,-\sigma}(\bar{z},z')\theta^{\mathcal{C}}(\bar{z},z')\right]\mathcal{G}_{\bar{\mathbf{k}}-\mathbf{q}}^{\neg,-\sigma}(z',\bar{z}')\theta^{\mathcal{C}}(z,z').
\end{aligned}\tag{G.5}$$

The *lesser* part in this case reads

$$\begin{aligned}
&\chi_{\text{sl}}^{<,\sigma-\sigma}(\mathbf{q};z,z') = -\int_{-\pi}^{\pi}\frac{\mathrm{d}^D\tilde{k}}{(2\pi)^D}\int_{-\pi}^{\pi}\frac{\mathrm{d}^D\bar{k}}{(2\pi)^D}\int_{t_0}^{z}\mathrm{d}\bar{z}\int_{t_0}^{t_0-i\beta}\mathrm{d}\bar{z}' \\
&\times\mathcal{G}_{\tilde{\mathbf{k}}}^{>,\sigma}(z,\bar{z})\theta^{\mathcal{C}}(z,\bar{z})\mathcal{G}_{\tilde{\mathbf{k}}-\mathbf{q}}^{\neg,\sigma}(\bar{z}',z)\Box_{\tilde{\mathbf{k}}-\bar{\mathbf{k}}}^{\neg,\sigma-\sigma}(\bar{z},\bar{z}')\mathcal{G}_{\bar{\mathbf{k}}}^{<,-\sigma}(\bar{z},z')\theta^{\mathcal{C}}(z',\bar{z})\mathcal{G}_{\bar{\mathbf{k}}-\mathbf{q}}^{\neg,-\sigma}(z',\bar{z}')\theta^{\mathcal{C}}(z',z).
\end{aligned}\tag{G.6}$$

Subtracting Eq. (G.6) from Eq. (G.5) leads to the retarded part of the single-ladder vertex corrections.

$\bar{z} \in \mathcal{C}_2$ AND $\bar{z}' \in \mathcal{C}_1$ Then, the configuration where $\bar{z}$ gets on $\mathcal{C}_2$ while $\bar{z}'$ is on $\mathcal{C}_1$ is considered. In that case, this necessarily implies that $\bar{z} \succ \bar{z}'$. The expression for the *greater* of the single-ladder vertex correction on the contour is

$$\begin{aligned}
&\chi_{\text{sl}}^{>,\sigma-\sigma}(\mathbf{q};z,z') = -\int_{-\pi}^{\pi}\frac{\mathrm{d}^D\tilde{k}}{(2\pi)^D}\int_{-\pi}^{\pi}\frac{\mathrm{d}^D\bar{k}}{(2\pi)^D}\int_{z}^{t_0}\mathrm{d}\bar{z}\int_{t_0}^{z}\mathrm{d}\bar{z}'\times\\
&\mathcal{G}_{\tilde{\mathbf{k}}}^{<,\sigma}(z,\bar{z})\theta^{\mathcal{C}}(\bar{z},z)\mathcal{G}_{\tilde{\mathbf{k}}-\mathbf{q}}^{<,\sigma}(\bar{z}',z)\theta^{\mathcal{C}}(z,\bar{z}')\Box_{\tilde{\mathbf{k}}-\bar{\mathbf{k}}}^{>,\sigma-\sigma}(\bar{z},\bar{z}')\theta^{\mathcal{C}}(\bar{z},\bar{z}')\mathcal{G}_{\bar{\mathbf{k}}}^{>,-\sigma}(\bar{z},z')\theta^{\mathcal{C}}(\bar{z},z')\\
&\times\left[\mathcal{G}_{\bar{\mathbf{k}}-\mathbf{q}}^{<,-\sigma}(z',\bar{z}')\theta^{\mathcal{C}}(\bar{z}',z')+\mathcal{G}_{\bar{\mathbf{k}}-\mathbf{q}}^{>,-\sigma}(z',\bar{z}')\theta^{\mathcal{C}}(z',\bar{z}')\right]\theta^{\mathcal{C}}(z,z').
\end{aligned}\tag{G.7}$$

On the other hand, the *lesser* part reads

$$\begin{aligned}
&\chi_{\text{sl}}^{<,\sigma-\sigma}(\mathbf{q};z,z') = -\int_{-\pi}^{\pi}\frac{\mathrm{d}^D\tilde{k}}{(2\pi)^D}\int_{-\pi}^{\pi}\frac{\mathrm{d}^D\bar{k}}{(2\pi)^D}\int_{z}^{t_0}\mathrm{d}\bar{z}\int_{t_0}^{z}\mathrm{d}\bar{z}'\\
&\times\mathcal{G}_{\tilde{\mathbf{k}}}^{<,\sigma}(z,\bar{z})\theta^{\mathcal{C}}(\bar{z},z)\mathcal{G}_{\tilde{\mathbf{k}}-\mathbf{q}}^{<,\sigma}(\bar{z}',z)\theta^{\mathcal{C}}(z,\bar{z}')\Box_{\tilde{\mathbf{k}}-\bar{\mathbf{k}}}^{>,\sigma-\sigma}(\bar{z},\bar{z}')\theta^{\mathcal{C}}(\bar{z},\bar{z}')\\
&\times\left[\mathcal{G}_{\bar{\mathbf{k}}}^{>,-\sigma}(\bar{z},z')\theta^{\mathcal{C}}(\bar{z},z')+\mathcal{G}_{\bar{\mathbf{k}}}^{<,-\sigma}(\bar{z},z')\theta^{\mathcal{C}}(z',\bar{z})\right]\mathcal{G}_{\bar{\mathbf{k}}-\mathbf{q}}^{>,-\sigma}(z',\bar{z}')\theta^{\mathcal{C}}(z',\bar{z}')\theta^{\mathcal{C}}(z',z).
\end{aligned}\tag{G.8}$$

BOTH $\bar{z}$ AND $\bar{z}'$ LYING ON $\mathcal{C}_2$ Then, the times located on the lower branch $\mathcal{C}_2$ of the Kadanoff-Baym contour are integrated over. Fig. G.2 shows the contour for calculating $\chi_{\text{sl}}^{>}(z,z')$ with $\bar{z} \succ \bar{z}'$.

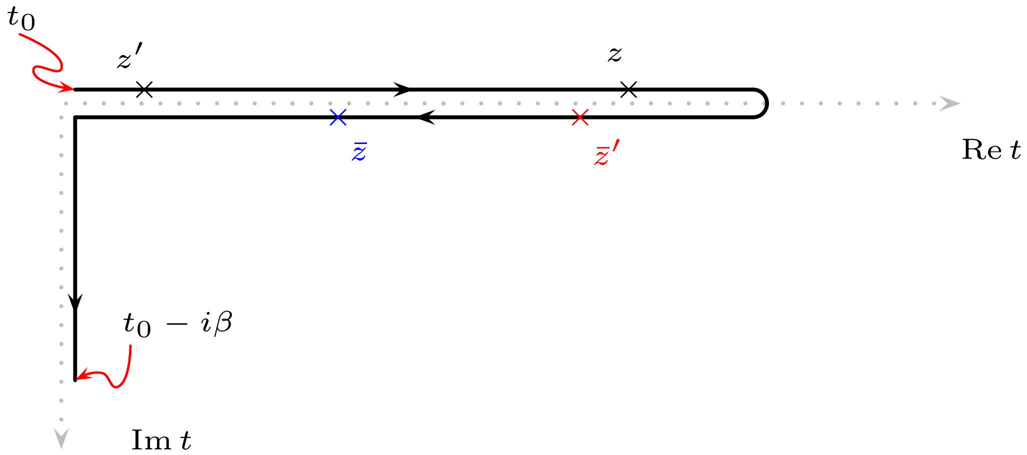

Figure G.2: Kadanoff-Baym contour for $\chi_{\text{sl}}^{>}$ with $\bar{z} \succ \bar{z}'$, $\bar{z} \in \mathcal{C}_2$ and $\bar{z}' \in \mathcal{C}_2$.

The *greater* component translates mathematically into Eq. (G.9):

$$\begin{aligned}
&\chi_{\text{sl}}^{>,\sigma-\sigma}(\mathbf{q};z,z') = -\int_{-\pi}^{\pi}\frac{\mathrm{d}^D\tilde{k}}{(2\pi)^D}\int_{-\pi}^{\pi}\frac{\mathrm{d}^D\bar{k}}{(2\pi)^D}\int_{z}^{t_0}\mathrm{d}\bar{z}\int_{z}^{t_0}\mathrm{d}\bar{z}'\\
&\times\mathcal{G}_{\tilde{\mathbf{k}}}^{<,\sigma}(z,\bar{z})\theta^{\mathcal{C}}(\bar{z},z)\mathcal{G}_{\tilde{\mathbf{k}}-\mathbf{q}}^{>,\sigma}(\bar{z}',z)\theta^{\mathcal{C}}(\bar{z}',z)\\
&\times\left[\Box_{\tilde{\mathbf{k}}-\bar{\mathbf{k}}}^{>,\sigma-\sigma}(\bar{z},\bar{z}')\theta^{\mathcal{C}}(\bar{z},\bar{z}')+\Box_{\tilde{\mathbf{k}}-\bar{\mathbf{k}}}^{<,\sigma-\sigma}(\bar{z},\bar{z}')\theta^{\mathcal{C}}(\bar{z}',\bar{z})\right]\\
&\times\mathcal{G}_{\bar{\mathbf{k}}}^{>,-\sigma}(\bar{z},z')\theta^{\mathcal{C}}(\bar{z},z')\mathcal{G}_{\bar{\mathbf{k}}-\mathbf{q}}^{<,-\sigma}(z',\bar{z}')\theta^{\mathcal{C}}(\bar{z}',z')\theta^{\mathcal{C}}(z,z').
\end{aligned}\tag{G.9}$$

Next we have to deal with the case of $\chi_{\text{sl}}^{<}(z,z')$ with $z \prec z'$, meaning that z would swap with z' in Fig. G.2. This leads to the following expression

$$\begin{aligned}
&\chi_{\mathrm{sl}}^{<,\sigma-\sigma}(\mathbf{q};z,z') = -\int_{-\pi}^{\pi}\frac{\mathrm{d}^D\tilde{k}}{(2\pi)^D}\int_{-\pi}^{\pi}\frac{\mathrm{d}^D\bar{k}}{(2\pi)^D}\int_{z}^{t_0}\mathrm{d}\bar{z}\int_{z}^{t_0}\mathrm{d}\bar{z}'\times\\
&\mathcal{G}_{\tilde{\mathbf{k}}}^{<,\sigma}(z,\bar{z})\theta^{\mathcal{C}}(\bar{z},z)\mathcal{G}_{\tilde{\mathbf{k}}-\mathbf{q}}^{>,\sigma}(\bar{z}',z)\theta^{\mathcal{C}}(\bar{z}',z)\left[\Box_{\tilde{\mathbf{k}}-\bar{\mathbf{k}}}^{>,\sigma-\sigma}(\bar{z},\bar{z}')\theta^{\mathcal{C}}(\bar{z},\bar{z}')+\Box_{\tilde{\mathbf{k}}-\bar{\mathbf{k}}}^{<,\sigma-\sigma}(\bar{z},\bar{z}')\theta^{\mathcal{C}}(\bar{z}',\bar{z})\right]\\
&\times\left[\mathcal{G}_{\bar{\mathbf{k}}}^{>,-\sigma}(\bar{z},z')\theta^{\mathcal{C}}(\bar{z},z')+\mathcal{G}_{\bar{\mathbf{k}}}^{<,-\sigma}(\bar{z},z')\theta^{\mathcal{C}}(z',\bar{z})\right]\\
&\times\left[\mathcal{G}_{\bar{\mathbf{k}}-\mathbf{q}}^{>,-\sigma}(z',\bar{z}')\theta^{\mathcal{C}}(z',\bar{z}')+\mathcal{G}_{\bar{\mathbf{k}}-\mathbf{q}}^{<,-\sigma}(z',\bar{z}')\theta^{\mathcal{C}}(\bar{z}',z')\right]\theta^{\mathcal{C}}(z',z).
\end{aligned}\tag{G.10}$$

$\bar{z}\in\mathcal{C}_2$ AND $\bar{z}'\in\mathcal{C}_3$ Then there is the configuration where $\bar{z}$ remains on $\mathcal{C}_2$ with $\bar{z}'$ now shifting to $\mathcal{C}_3$. In that case, this necessarily implies that $\bar{z}\prec\bar{z}'$. The expression for the *greater* component of the single-ladder vertex correction on the contour is given by Eq. (G.11):

$$\begin{aligned}
&\chi_{\mathrm{sl}}^{>,\sigma-\sigma}(\mathbf{q};z,z') = -\int_{-\pi}^{\pi}\frac{\mathrm{d}^D\tilde{k}}{(2\pi)^D}\int_{-\pi}^{\pi}\frac{\mathrm{d}^D\bar{k}}{(2\pi)^D}\int_{z}^{t_0}\mathrm{d}\bar{z}\int_{t_0}^{t_0-i\beta}\mathrm{d}\bar{z}'\times\\
&\mathcal{G}_{\tilde{\mathbf{k}}}^{<,\sigma}(z,\bar{z})\theta^{\mathcal{C}}(\bar{z},z)\mathcal{G}_{\tilde{\mathbf{k}}-\mathbf{q}}^{\lceil,\sigma}(\bar{z}',z)\Box_{\tilde{\mathbf{k}}-\bar{\mathbf{k}}}^{\rceil,\sigma-\sigma}(\bar{z},\bar{z}')\mathcal{G}_{\bar{\mathbf{k}}}^{>,-\sigma}(\bar{z},z')\theta^{\mathcal{C}}(\bar{z},z')\mathcal{G}_{\bar{\mathbf{k}}-\mathbf{q}}^{\rceil,-\sigma}(z',\bar{z}')\theta^{\mathcal{C}}(z,z')
\end{aligned}\tag{G.11}$$

and that of the *lesser* component is

$$\begin{aligned}
&\chi_{\mathrm{sl}}^{<,\sigma-\sigma}(\mathbf{q};z,z') = -\int_{-\pi}^{\pi}\frac{\mathrm{d}^D\tilde{k}}{(2\pi)^D}\int_{-\pi}^{\pi}\frac{\mathrm{d}^D\bar{k}}{(2\pi)^D}\int_{z}^{t_0}\mathrm{d}\bar{z}\int_{t_0}^{t_0-i\beta}\mathrm{d}\bar{z}'\times\\
&\mathcal{G}_{\tilde{\mathbf{k}}}^{<,\sigma}(z,\bar{z})\theta^{\mathcal{C}}(\bar{z},z)\mathcal{G}_{\tilde{\mathbf{k}}-\mathbf{q}}^{\lceil,\sigma}(\bar{z}',z)\Box_{\tilde{\mathbf{k}}-\bar{\mathbf{k}}}^{\rceil,\sigma-\sigma}(\bar{z},\bar{z}')\left[\mathcal{G}_{\bar{\mathbf{k}}}^{<,-\sigma}(\bar{z},z')\theta^{\mathcal{C}}(z',\bar{z})+\mathcal{G}_{\bar{\mathbf{k}}}^{>,-\sigma}(\bar{z},z')\theta^{\mathcal{C}}(\bar{z},z')\right]\\
&\times\mathcal{G}_{\bar{\mathbf{k}}-\mathbf{q}}^{\rceil,-\sigma}(z',\bar{z}')\theta^{\mathcal{C}}(z',z).
\end{aligned}\tag{G.12}$$

$\bar{z}\in\mathcal{C}_3$ AND $\bar{z}'\in\mathcal{C}_1$ Then there is the configuration where $\bar{z}$ gets on $\mathcal{C}_3$ with $\bar{z}'$ sitting on $\mathcal{C}_1$. In that case, this necessarily implies that $\bar{z}\succ\bar{z}'$. The expression for the *greater* part of the single-ladder vertex correction on the contour is given by Eq. (G.13):

$$\begin{aligned}
&\chi_{\mathrm{sl}}^{>,\sigma-\sigma}(\mathbf{q};z,z') = -\int_{-\pi}^{\pi}\frac{\mathrm{d}^D\tilde{k}}{(2\pi)^D}\int_{-\pi}^{\pi}\frac{\mathrm{d}^D\bar{k}}{(2\pi)^D}\int_{t_0}^{t_0-i\beta}\mathrm{d}\bar{z}\int_{t_0}^{z}\mathrm{d}\bar{z}'\mathcal{G}_{\tilde{\mathbf{k}}}^{\rceil,\sigma}(z,\bar{z})\mathcal{G}_{\tilde{\mathbf{k}}-\mathbf{q}}^{<,\sigma}(\bar{z}',z)\\
&\times\theta^{\mathcal{C}}(z,\bar{z}')\Box_{\tilde{\mathbf{k}}-\bar{\mathbf{k}}}^{\lceil,\sigma-\sigma}(\bar{z},\bar{z}')\mathcal{G}_{\bar{\mathbf{k}}}^{\lceil,-\sigma}(\bar{z},z')\mathcal{G}_{\bar{\mathbf{k}}-\mathbf{q}}^{<,-\sigma}(z',\bar{z}')\theta^{\mathcal{C}}(\bar{z}',z')\theta^{\mathcal{C}}(z,z'),
\end{aligned}\tag{G.13}$$

whilst that of the *lesser* component reads

$$\begin{aligned}
&\chi_{\mathrm{sl}}^{<,\sigma-\sigma}(\mathbf{q};z,z') = -\int_{-\pi}^{\pi}\frac{\mathrm{d}^D\tilde{k}}{(2\pi)^D}\int_{-\pi}^{\pi}\frac{\mathrm{d}^D\bar{k}}{(2\pi)^D}\int_{t_0}^{t_0-i\beta}\mathrm{d}\bar{z}\int_{t_0}^{z}\mathrm{d}\bar{z}'\mathcal{G}_{\tilde{\mathbf{k}}}^{\rceil,\sigma}(z,\bar{z})\mathcal{G}_{\tilde{\mathbf{k}}-\mathbf{q}}^{<,\sigma}(\bar{z}',z)\\
&\theta^{\mathcal{C}}(z,\bar{z}')\Box_{\tilde{\mathbf{k}}-\bar{\mathbf{k}}}^{\lceil,\sigma-\sigma}(\bar{z},\bar{z}')\mathcal{G}_{\bar{\mathbf{k}}}^{\lceil,-\sigma}(\bar{z},z')\Big[\mathcal{G}_{\bar{\mathbf{k}}-\mathbf{q}}^{<,-\sigma}(z',\bar{z}')\theta^{\mathcal{C}}(\bar{z}',z')\\
&\qquad+\mathcal{G}_{\bar{\mathbf{k}}-\mathbf{q}}^{>,-\sigma}(z',\bar{z}')\theta^{\mathcal{C}}(z',\bar{z}')\Big]\theta^{\mathcal{C}}(z',z).
\end{aligned}\tag{G.14}$$

$\bar{z}\in\mathcal{C}_3$ AND $\bar{z}'\in\mathcal{C}_2$ Then, as second last, there is the configuration where $\bar{z}$ is still on $\mathcal{C}_3$ but with $\bar{z}'$ sitting on $\mathcal{C}_2$. In that case, this necessarily implies that $\bar{z}\succ\bar{z}'$. The expression for the *greater* part of the single-ladder vertex correction on the contour is given by Eq. (G.15):

$$\chi_{\mathrm{sl}}^{>,\sigma-\sigma}(\mathbf{q};z,z') = -\int_{-\pi}^{\pi}\frac{\mathrm{d}^D\tilde{k}}{(2\pi)^D}\int_{-\pi}^{\pi}\frac{\mathrm{d}^D\bar{k}}{(2\pi)^D}\int_{t_0}^{t_0-i\beta}\mathrm{d}\bar{z}\int_{z}^{t_0}\mathrm{d}\bar{z}'\mathcal{G}_{\tilde{\mathbf{k}}}^{\neg,\sigma}(z,\bar{z})\mathcal{G}_{\tilde{\mathbf{k}}-\mathbf{q}}^{>,\sigma}(\bar{z}',z)$$
$$\times\,\theta^{\mathcal{C}}(\bar{z}',z)\Box_{\tilde{\mathbf{k}}-\bar{\mathbf{k}}}^{\ulcorner,\sigma-\sigma}(\bar{z},\bar{z}')\mathcal{G}_{\bar{\mathbf{k}}}^{\ulcorner,-\sigma}(\bar{z},z')\mathcal{G}_{\bar{\mathbf{k}}-\mathbf{q}}^{<,-\sigma}(z',\bar{z}')\theta^{\mathcal{C}}(\bar{z}',z')\theta^{\mathcal{C}}(z,z'), \tag{G.15}$$

whilst that of the *lesser* part is

$$\chi_{\mathrm{sl}}^{<,\sigma-\sigma}(\mathbf{q};z,z') = -\int_{-\pi}^{\pi}\frac{\mathrm{d}^D\tilde{k}}{(2\pi)^D}\int_{-\pi}^{\pi}\frac{\mathrm{d}^D\bar{k}}{(2\pi)^D}\int_{t_0}^{t_0-i\beta}\mathrm{d}\bar{z}\int_{z}^{t_0}\mathrm{d}\bar{z}'\mathcal{G}_{\tilde{\mathbf{k}}}^{\neg,\sigma}(z,\bar{z})\mathcal{G}_{\tilde{\mathbf{k}}-\mathbf{q}}^{>,\sigma}(\bar{z}',z)$$
$$\times\,\theta^{\mathcal{C}}(\bar{z}',z)\Box_{\tilde{\mathbf{k}}-\bar{\mathbf{k}}}^{\ulcorner,\sigma-\sigma}(\bar{z},\bar{z}')\mathcal{G}_{\bar{\mathbf{k}}}^{\ulcorner,-\sigma}(\bar{z},z')\Big[\mathcal{G}_{\bar{\mathbf{k}}-\mathbf{q}}^{<,-\sigma}(z',\bar{z}')\theta^{\mathcal{C}}(\bar{z}',z')$$
$$+\,\mathcal{G}_{\bar{\mathbf{k}}-\mathbf{q}}^{>,-\sigma}(z',\bar{z}')\theta^{\mathcal{C}}(z',\bar{z}')\Big]\theta^{\mathcal{C}}(z',z), \tag{G.16}$$

BOTH $\bar{z}$ AND $\bar{z}'$ LYING ON $\mathcal{C}_3$ At last, but not least, there is the configuration where both $\bar{z}$ and $\bar{z}'$ are on $\mathcal{C}_3$. In that case, there is translation invariance and only the imaginary time difference matters. The expression for the single-ladder vertex correction on the contour is given by Eq. (G.17):

$$\chi_{\mathrm{sl}}^{>,\sigma-\sigma}(\mathbf{q};z,z') = -\int_{-\pi}^{\pi}\frac{\mathrm{d}^D\tilde{k}}{(2\pi)^D}\int_{-\pi}^{\pi}\frac{\mathrm{d}^D\bar{k}}{(2\pi)^D}\int_{t_0}^{t_0-i\beta}\mathrm{d}\bar{z}\int_{t_0}^{t_0-i\beta}\mathrm{d}\bar{z}'\mathcal{G}_{\tilde{\mathbf{k}}}^{\neg,\sigma}(z,\bar{z})\mathcal{G}_{\tilde{\mathbf{k}}-\mathbf{q}}^{\ulcorner,\sigma}(\bar{z}',z)$$
$$\times\,\Box_{\tilde{\mathbf{k}}-\bar{\mathbf{k}}}^{M,\sigma-\sigma}(\bar{z}-\bar{z}')\mathcal{G}_{\bar{\mathbf{k}}}^{\ulcorner,-\sigma}(\bar{z},z')\mathcal{G}_{\bar{\mathbf{k}}-\mathbf{q}}^{\neg,-\sigma}(z',\bar{z}'). \tag{G.17}$$

The last 9 sub-integrals that make up the single-ladder vertex corrections have been laid out from Eq. (G.1) to (G.17).

H

NONEQUILIBRIUM APPROXIMATION TO THE TPSC IRREDUCIBLE VERTICES

In this section, the approximation introduced in the Bethe-Salpeter equations (5.64) so as to satisfy the two-particle sum-rules (5.68) on the real-time axis is motivated. To start out, the spin/charge susceptibility is decomposed into Keldysh components by making use of the Langreth rules introduced in Section 2.2.1. Since the local sum-rules (5.68) involve *lesser* components[1], the equation (2.22) is used for the Bethe-Salpeter equations (5.64)

$$\begin{aligned}\chi_{\mathbf{q}}^{\mathrm{sp/ch},<(>)}(t,t') &= \int_{t_0}^{t} \mathrm{d}\bar{t}\; \chi_{\mathbf{q}}^{0,R}(t,\bar{t})\Gamma^{\mathrm{sp/ch}}(\bar{t})\chi_{\mathbf{q}}^{\mathrm{sp/ch},<(>)}(\bar{t},t')\\ &+ \int_{t_0}^{t'} \mathrm{d}\bar{t}\; \chi_{\mathbf{q}}^{0,<(>)}(t,\bar{t})\Gamma^{\mathrm{sp/ch}}(\bar{t})\chi_{\mathbf{q}}^{\mathrm{sp/ch},A}(\bar{t},t')\\ &- i\int_{0}^{\beta} \mathrm{d}\bar{\tau}\; \chi_{\mathbf{q}}^{0,\urcorner}(t,\bar{\tau})\Gamma^{\mathrm{sp/ch}}(0^{-})\chi_{\mathbf{q}}^{\mathrm{sp/ch},\ulcorner}(\bar{\tau},t').\end{aligned} \tag{H.1}$$

Because the vertices are local in time, i.e one-time objects, they are not endowed with Keldysh components and do not contain memory kernels per se.

In the last term of Eq. (H.1), the fact that the irreducible vertices are constants on the imaginary-time contour branch $\mathcal{C}_3$ (Fig. 2.1) was put to use, *i.e.* $\Gamma^{\mathrm{sp/ch}}(\tau) \to \Gamma^{\mathrm{sp/ch}}(0^{-})$. Note that the general contour-time arguments z have been traded off for real-time variables t because the *lesser* (*greater*) are exclusively defined on the real-time branches $\mathcal{C}_1 \oplus \mathcal{C}_2$. Now, the local-time two-particle sum-rules apply at equal time, namely when $t = t'$ in Eq. (H.1). These sum-rules are fulfilled at each time steps by varying the local vertices $\Gamma^{\mathrm{sp/ch}}$ at latest time t. This transforms Eq. (H.1) into

$$\begin{aligned}\chi_{\mathbf{q}}^{\mathrm{sp/ch},<(>)}(t,t) &= \int_{t_0}^{t} \mathrm{d}\bar{t}\; \chi_{\mathbf{q}}^{0,R}(t,\bar{t})\Gamma^{\mathrm{sp/ch}}(\bar{t})\chi_{\mathbf{q}}^{\mathrm{sp/ch},<(>)}(\bar{t},t)\\ &+ \int_{t_0}^{t} \mathrm{d}\bar{t}\; \chi_{\mathbf{q}}^{0,<(>)}(t,\bar{t})\Gamma^{\mathrm{sp/ch}}(\bar{t})\chi_{\mathbf{q}}^{\mathrm{sp/ch},A}(\bar{t},t).\end{aligned} \tag{H.2}$$

In Eq. (H.2), the last term was dropped out since it only involves the vertices on the vertical branch $\mathcal{C}_3$ and it does not contribute to the time-dependent sum-rule at time t. As mentioned, only the vertices at latest time t are changed such as to modify the local sum-rules. Thus, let's replace in Eq. (H.2) the dummy variable $\bar{t}$ integrated over by t:

$$\begin{aligned}\chi_{\mathbf{q}}^{\mathrm{sp/ch},<(>)}(t,t) &= \chi_{\mathbf{q}}^{0,R}(t,t)\Gamma^{\mathrm{sp/ch}}(t)\chi_{\mathbf{q}}^{\mathrm{sp/ch},<(>)}(t,t)\\ &+ \chi_{\mathbf{q}}^{0,<(>)}(t,t)\Gamma^{\mathrm{sp/ch}}(t)\chi_{\mathbf{q}}^{\mathrm{sp/ch},A}(t,t).\end{aligned} \tag{H.3}$$

On the basis that the susceptibilities χ are bosonic quantities, their equal-time retarded/advanced Keldysh components give 0 – indeed, this is because

$$\chi_{\mathbf{q}}^{R}(t,t')^{*} = \chi_{\mathbf{q}}^{A}(t',t).$$

---

[1] Equivalently, because the susceptibilities are bosonic contour-time objects, the *greater* component could also be used in the sum-rules (5.68) ($\chi^{<}(t,t) = \chi^{>}(t,t)$).

Therefore, the two terms of Eq. (H.2) drop out as well. It is now clear that using the form of the Bethe-Salpeter equations laid out in Eq. (5.64) leads to a numerically ill-conditioned problem that precludes one from satisfying the sum-rules (5.68) at each time step across the real-time branches. Hence, the trick to get around this difficulty is to multiply the first two terms of Eq. (H.1) by $\Gamma^{\mathrm{sp/ch}}(t)$, just like it is the case on the Matsubara branch (last term of Eq. (H.1)), instead of integrating over it in between of χ^0 and $\chi^{\mathrm{sp/ch}}$. This way, the vertices affect directly the local-time *lesser* (*greater*) Keldysh component of the susceptibilities, necessary to solve the time-dependent local sum-rules.

I

TEMPERATURE OF A THERMALIZED STATE

Here, the way the thermal state is attributed a temperature is discussed and detailed using TPSC (Section 5.2) and DMFT+TPSC (Section 5.2.9) as examples. Note that the DMFT+TPSC shown does not use any α parameter enforcing that D^{imp} (5.99) be equal to D^{TPSC} (5.104). The deviation between D^{imp} and D^{TPSC} have been plotted in Section 6.2.2 in 2D and 3D (Fig. 6.36). Albeit these variations be relatively small, this will pose some ill-defined temperature in the thermalized state wherein the lattice and impurity will have slightly different temperatures, due to the fact that the lattice potential energy will differ slightly from that of the impurity. This problem is overcome in TPSC and TPSC+GG because of the α parameter employed in the sum-rule (5.71). The same can be done for DMFT+TPSC, although no results of this improved DMFT+TPSC method are shown in this thesis, mainly for length concerns.

As previously mentioned in Section 7.1 and Section 7.2, the temperature of the thermalized state is determined by calculating the total energy of the system after the ramp, and then by comparing this total post-ramp energy with a graph representing the energy of the post-ramp U as a function of temperature T calculated at equilibrium. In the scenario that the lattice hopping term would be ramped instead of U, the total energy would be traced out with respect to T at the given post-ramp lattice hopping value. That total energy is nothing else but the sum of the kinetic energy (7.1) and potential energy (7.2).

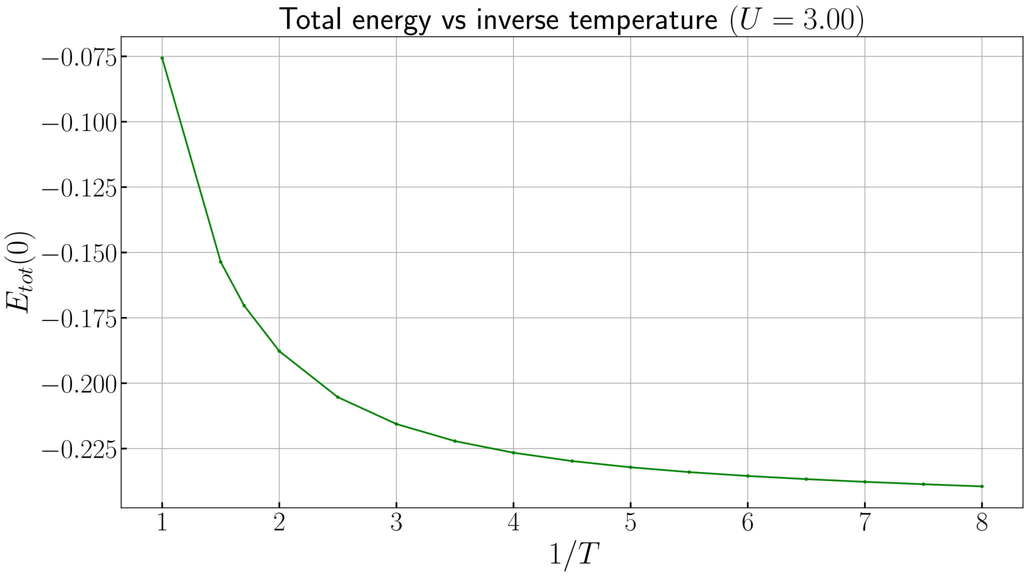

Figure I.1: Total energy calculated in the 2D nearest-neighbor Hubbard model with TPSC+GG at $U = 3$ as a function of inverse temperature.

In Fig. I.1, the total energy (potential plus kinetic) is sketched out as a function of inverse temperature. The shape of the curve resembles to the function $1/T^2$. The plot shows the energy calculated in equilibrium for the post-ramp

U value of Fig. 7.15, for instance. Hence, the figure I.1 allows one to associate a temperature to the thermalized state given that the total energy after the quench is known. In Fig. I.2, the time-dependent kinetic energy (top panel), potential energy (middle panel) and total energy (bottom panel) related to the up-ramp featuring in Fig. 7.15 are shown. In a fully conserving scheme, the total energy should be constant after the ramp, meaning that the drop around $t = 2$ would be a non-conserving feature. Although, this drop is rather small and most importantly, the energy remains constant shortly after the interaction ramp is over. This way, the total energy at later times in Fig. I.2 (bottom panel) gives $E_{\text{tot}} \simeq -0.168$ and it refers to a temperature in Fig. I.1, leading in this particular case to a thermalized temperature of about $T_{\text{therm}} = 1.7$. Then, a TPSC+GG calculation at equilibrium with the T_{therm} found for the post-ramp $U = 3$ is run. The various quantities extracted out of this calculation correspond to the thermalized values displayed in Fig. 7.11 (fast ramp) indicated by the arrows.

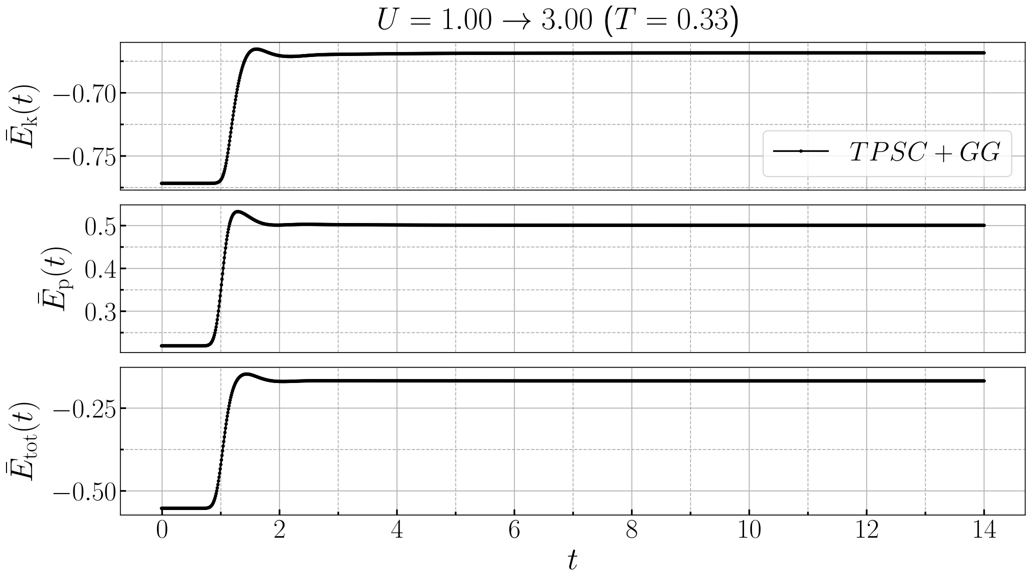

Figure I.2: Time-dependent energies calculated in the 2D nearest-neighbor Hubbard model with TPSC+GG for the up-ramp used in Fig. 7.15. Top panel: kinetic energy calculated from Eq. 7.1. Middle panel: potential energy calculated from Eq. 7.2. Bottom panel: Total energy calculated from the addition of $E_{\text{p}} + E_{\text{k}}$.

Similarly to TPSC and TPSC+GG, DMFT+TPSC uses the total energy of the thermalized state to extract the thermalized temperature out of the relation of the post-ramp U total energy versus (inverse) temperature. Although, in this case, if no extra α parameter enforces that $D^{\text{imp}} = D^{\text{TPSC}}$ at each iteration, the total energies of the full lattice and of the impurity will differ from each other, resulting in a different thermalized temperature in the two sub-systems.

BIBLIOGRAPHY

[1] S. Allen and A.-M. S. Tremblay. "Nonperturbative approach to the attractive Hubbard model." In: *Phys. Rev. B* 64 (7 2001), p. 075115. DOI: 10.1103/PhysRevB.64.075115. URL: https://link.aps.org/doi/10.1103/PhysRevB.64.075115.

[2] P. W. Anderson. "Localized Magnetic States in Metals." In: *Phys. Rev.* 124 (1 1961), pp. 41–53. DOI: 10.1103/PhysRev.124.41. URL: https://link.aps.org/doi/10.1103/PhysRev.124.41.

[3] P. W. Anderson. "The resonating valence bond state in La_2CuO_4 and superconductivity." In: *Science* 235 (1987), pp. 1196 –8.

[4] K. Andres, J. E. Graebner, and H. R. Ott. "$4f$-Virtual-Bound-State Formation in $CeAl_3$ at Low Temperatures." In: *Phys. Rev. Lett.* 35 (26 1975), pp. 1779–1782. DOI: 10.1103/PhysRevLett.35.1779. URL: https://link.aps.org/doi/10.1103/PhysRevLett.35.1779.

[5] Hideo Aoki, Naoto Tsuji, Martin Eckstein, Marcus Kollar, Takashi Oka, and Philipp Werner. "Nonequilibrium dynamical mean-field theory and its applications." In: *Reviews of Modern Physics* 86.2 (June 2014), pp. 779–837. DOI: 10.1103/RevModPhys.86.779.

[6] Hideo Aoki, Naoto Tsuji, Martin Eckstein, Marcus Kollar, Takashi Oka, and Philipp Werner. "Nonequilibrium dynamical mean-field theory and its applications." In: *Rev. Mod. Phys.* 86 (2 2014), pp. 779–837. DOI: 10.1103/RevModPhys.86.779. URL: https://link.aps.org/doi/10.1103/RevModPhys.86.779.

[7] N. P. Armitage, P. Fournier, and R. L. Greene. "Progress and perspectives on electron-doped cuprates." In: *Rev. Mod. Phys.* 82 (3 2010), pp. 2421–2487. DOI: 10.1103/RevModPhys.82.2421. URL: https://link.aps.org/doi/10.1103/RevModPhys.82.2421.

[8] F Aryasetiawan and O Gunnarsson. "The GW method." In: *Reports on Progress in Physics* 61.3 (1998), p. 237. DOI: 10.1088/0034-4885/61/3/002.

[9] L. G. Aslamazov and A. Larkin. "Effect of Fluctuations on the Properties of a Superconductor Above the Critical Temperature." In: *Sov. Phys. Solid State* 10 (1968), p. 875.

[10] R D Averitt and A J Taylor. "Ultrafast optical and far-infrared quasiparticle dynamics in correlated electron materials." In: 14.50 (2002), R1357. DOI: 10.1088/0953-8984/14/50/203. URL: https://dx.doi.org/10.1088/0953-8984/14/50/203.

[11] Thomas Ayral and Olivier Parcollet. "Mott physics and spin fluctuations: A unified framework." In: *Phys. Rev. B* 92 (11 2015), p. 115109. DOI: 10.1103/PhysRevB.92.115109. URL: https://link.aps.org/doi/10.1103/PhysRevB.92.115109.

[12] Thomas Ayral and Olivier Parcollet. “Mott physics and spin fluctuations: A functional viewpoint.” In: *Phys. Rev. B* 93 (23 2016), p. 235124. DOI: `10.1103/PhysRevB.93.235124`. URL: `https://link.aps.org/doi/10.1103/PhysRevB.93.235124`.

[13] D. N. Basov and T. Timusk. “Electrodynamics of high-T_c superconductors.” In: *Rev. Mod. Phys.* 77 (2 2005), pp. 721–779. DOI: `10.1103/RevModPhys.77.721`. URL: `https://link.aps.org/doi/10.1103/RevModPhys.77.721`.

[14] Denitsa R. Baykusheva et al. “Ultrafast Renormalization of the On-Site Coulomb Repulsion in a Cuprate Superconductor.” In: *Phys. Rev. X* 12 (1 2022), p. 011013. DOI: `10.1103/PhysRevX.12.011013`. URL: `https://link.aps.org/doi/10.1103/PhysRevX.12.011013`.

[15] Samuel Beaulieu et al. “Ultrafast dynamical Lifshitz transition.” In: *Science Advances* 7.17 (2021), eabd9275. DOI: `10.1126/sciadv.abd9275`. URL: `https://www.science.org/doi/abs/10.1126/sciadv.abd9275`.

[16] E. Beaurepaire, J.-C. Merle, A. Daunois, and J.-Y. Bigot. “Ultrafast Spin Dynamics in Ferromagnetic Nickel.” In: *Phys. Rev. Lett.* 76 (22 1996), pp. 4250–4253. DOI: `10.1103/PhysRevLett.76.4250`. URL: `https://link.aps.org/doi/10.1103/PhysRevLett.76.4250`.

[17] J G Bednorz and K.A. Müller. “Possible High-T$_c$ Superconductivity in the Ba-La-Cu-O System.” In: *Zeitschrift für Physik B* 66 (1986), pp. 189–193.

[18] Dominic Bergeron, Vasyl Hankevych, Bumsoo Kyung, and A.-M. S. Tremblay. “Optical and dc conductivity of the two-dimensional Hubbard model in the pseudogap regime and across the antiferromagnetic quantum critical point including vertex corrections.” In: *Phys. Rev. B* 84 (8 2011), p. 085128. DOI: `10.1103/PhysRevB.84.085128`. URL: `https://link.aps.org/doi/10.1103/PhysRevB.84.085128`.

[19] J. Berges, Sz. Borsányi, and C. Wetterich. “Prethermalization.” In: *Phys. Rev. Lett.* 93 (14 2004), p. 142002. DOI: `10.1103/PhysRevLett.93.142002`. URL: `https://link.aps.org/doi/10.1103/PhysRevLett.93.142002`.

[20] Shinibali Bhattacharyya, Kristofer Björnson, Karim Zantout, Daniel Steffensen, Laura Fanfarillo, Andreas Kreisel, Roser Valentí, Brian M. Andersen, and P. J. Hirschfeld. “Nonlocal correlations in iron pnictides and chalcogenides.” In: *Phys. Rev. B* 102 (3 2020), p. 035109. DOI: `10.1103/PhysRevB.102.035109`. URL: `https://link.aps.org/doi/10.1103/PhysRevB.102.035109`.

[21] N. E. Bickers. “Review of techniques in the large-N expansion for dilute magnetic alloys.” In: *Rev. Mod. Phys.* 59 (4 1987), pp. 845–939. DOI: `10.1103/RevModPhys.59.845`.

[22] S. Biermann, F. Aryasetiawan, and A. Georges. “First-Principles Approach to the Electronic Structure of Strongly Correlated Systems: Combining the GW Approximation and Dynamical Mean-Field Theory.” In: *Phys. Rev. Lett.* 90 (8 2003), p. 086402. DOI: `10.1103/PhysRevLett.90.086402`. URL: `https://link.aps.org/doi/10.1103/PhysRevLett.90.086402`.

[23] K. Binder. "Time-Dependent Ginzburg-Landau Theory of Nonequilibrium Relaxation." In: *Phys. Rev. B* 8 (7 1973), pp. 3423–3438. DOI: 10.1103/PhysRevB.8.3423. URL: https://link.aps.org/doi/10.1103/PhysRevB.8.3423.

[24] Nikolaj Bittner, Denis Golež, Martin Eckstein, and Philipp Werner. "Effects of frustration on the nonequilibrium dynamics of photoexcited lattice systems." In: *Phys. Rev. B* 102 (23 2020), p. 235169. DOI: 10.1103/PhysRevB.102.235169. URL: https://link.aps.org/doi/10.1103/PhysRevB.102.235169.

[25] R. K. Bryan. "Maximum entropy analysis of oversampled data problems." In: *Euro. Biophys. J.* 18.3 (Apr. 1990), pp. 165–174. DOI: 10.1007/BF02427376.

[26] M. Budden et al. "Evidence for metastable photo-induced superconductivity in K3C60." In: *Nature Physics* 17.5 (2021), pp. 611–618. ISSN: 1745-2481. DOI: 10.1038/s41567-020-01148-1. URL: https://doi.org/10.1038/s41567-020-01148-1.

[27] Michele Buzzi, Michael Först, Roman Mankowsky, and Andrea Cavalleri. "Probing dynamics in quantum materials with femtosecond X-rays." In: *Nature Reviews Materials* 3.9 (2018), pp. 299–311. DOI: 10.1038/s41578-018-0024-9.

[28] A. Cantaluppi, M. Buzzi, G. Jotzu, D. Nicoletti, M. Mitrano, D. Pontiroli, M. Riccò, A. Perucchi, P. Di Pietro, and A. Cavalleri. "Pressure tuning of light-induced superconductivity in K3C60." In: *Nature Physics* 14.8 (2018), pp. 837–841. ISSN: 1745-2481. DOI: 10.1038/s41567-018-0134-8.

[29] P. Chalupa, P. Gunacker, T. Schäfer, K. Held, and A. Toschi. "Divergences of the irreducible vertex functions in correlated metallic systems: Insights from the Anderson impurity model." In: *Phys. Rev. B* 97 (24 2018), p. 245136. DOI: 10.1103/PhysRevB.97.245136. URL: https://link.aps.org/doi/10.1103/PhysRevB.97.245136.

[30] Andrea Damascelli, Zahid Hussain, and Zhi-Xun Shen. "Angle-resolved photoemission studies of the cuprate superconductors." In: *Rev. Mod. Phys.* 75 (2 2003), pp. 473–541. DOI: 10.1103/RevModPhys.75.473. URL: https://link.aps.org/doi/10.1103/RevModPhys.75.473.

[31] Vu Hung Dao and Raymond Frésard. "Collective modes in the paramagnetic phase of the Hubbard model." In: *Phys. Rev. B* 95 (16 2017), p. 165127. DOI: 10.1103/PhysRevB.95.165127. URL: https://link.aps.org/doi/10.1103/PhysRevB.95.165127.

[32] B. Davoudi and A.-M. S. Tremblay. "Nearest-neighbor repulsion and competing charge and spin order in the extended Hubbard model." In: *Phys. Rev. B* 74 (3 2006), p. 035113. DOI: 10.1103/PhysRevB.74.035113. URL: https://link.aps.org/doi/10.1103/PhysRevB.74.035113.

[33] Cyrano De Dominicis and Paul C. Martin. "Stationary Entropy Principle and Renormalization in Normal and Superfluid Systems. I. Algebraic Formulation." In: *Journal of Mathematical Physics* 5.1 (1964), pp. 14–30. DOI: 10.1063/1.1704062. URL: https://doi.org/10.1063/1.1704062.

[34] Cyrano De Dominicis and Paul C. Martin. “Stationary Entropy Principle and Renormalization in Normal and Superfluid Systems. II. Diagrammatic Formulation.” In: *Journal of Mathematical Physics* 5.1 (1964), pp. 31–59. DOI: 10.1063/1.1704064. URL: https://doi.org/10.1063/1.1704064.

[35] Martin Eckstein and Marcus Kollar. “Near-adiabatic parameter changes in correlated systems: influence of the ramp protocol on the excitation energy.” In: *New Journal of Physics* 12.5 (2010), p. 055012. DOI: 10.1088/1367-2630/12/5/055012. URL: https://dx.doi.org/10.1088/1367-2630/12/5/055012.

[36] Martin Eckstein, Marcus Kollar, and Philipp Werner. “Thermalization after an Interaction Quench in the Hubbard Model.” In: *Phys. Rev. Lett.* 103 (5 2009), p. 056403. DOI: 10.1103/PhysRevLett.103.056403. URL: https://link.aps.org/doi/10.1103/PhysRevLett.103.056403.

[37] Martin Eckstein and Philipp Werner. “Nonequilibrium dynamical mean-field calculations based on the noncrossing approximation and its generalizations.” In: *Phys. Rev. B* 82.11 (Sept. 2010), p. 115115. DOI: 10.1103/PhysRevB.82.115115. URL: https://link.aps.org/doi/10.1103/PhysRevB.82.115115.

[38] Maximilian Eichberger, Hanjo Schäfer, Marina Krumova, Markus Beyer, Jure Demsar, Helmuth Berger, Gustavo Moriena, Germán Sciaini, and R. J. Dwayne Miller. “Snapshots of cooperative atomic motions in the optical suppression of charge density waves.” In: *Nature* 468.7325 (2010), pp. 799–802. ISSN: 1476-4687. DOI: 10.1038/nature09539.

[39] M. Eisele, T. L. Cocker, M. A. Huber, M. Plankl, L. Viti, D. Ercolani, L. Sorba, M. S. Vitiello, and R. Huber. “Ultrafast multi-terahertz nano-spectroscopy with sub-cycle temporal resolution.” In: *Nature Photonics* 8.11 (2014), pp. 841–845. ISSN: 1749-4893. DOI: 10.1038/nphoton.2014.225.

[40] D. Fausti, R. I. Tobey, N. Dean, S. Kaiser, A. Dienst, M. C. Hoffmann, S. Pyon, T. Takayama, H. Takagi, and A. Cavalleri. “Light-Induced Superconductivity in a Stripe-Ordered Cuprate.” In: *Science* 331.6014 (2011), pp. 189–191. DOI: 10.1126/science.1197294. URL: https://www.science.org/doi/abs/10.1126/science.1197294.

[41] L. Fratino, P. Sémon, G. Sordi, and A.-M. S. Tremblay. “Pseudogap and superconductivity in two-dimensional doped charge-transfer insulators.” In: *Phys. Rev. B* 93 (24 2016), p. 245147. DOI: 10.1103/PhysRevB.93.245147.

[42] J. K. Freericks, V. M. Turkowski, and V. Zlatić. “Nonequilibrium Dynamical Mean-Field Theory.” In: *Phys. Rev. Lett.* 97 (26 2006), p. 266408. DOI: 10.1103/PhysRevLett.97.266408. URL: https://link.aps.org/doi/10.1103/PhysRevLett.97.266408.

[43] Antoine Georges and Gabriel Kotliar. “Hubbard model in infinite dimensions.” In: *Phys. Rev. B* 45 (12 1992), p. 6479. DOI: 10.1103/PhysRevB.45.6479. URL: https://link.aps.org/doi/10.1103/PhysRevB.45.6479.

[44] Antoine Georges, Gabriel Kotliar, Werner Krauth, and Marcelo J. Rozenberg. “Dynamical mean-field theory of strongly correlated fermion systems and the limit of infinite dimensions.” In: *Rev. Mod. Phys.* 68 (1 1996), pp. 13–125. DOI: 10.1103/RevModPhys.68.13. URL: https://link.aps.org/doi/10.1103/RevModPhys.68.13.

[45] Antoine Georges and Werner Krauth. “Numerical solution of the $d = \infty$ Hubbard model: Evidence for a Mott transition.” In: *Phys. Rev. Lett.* 69 (8 1992), pp. 1240–1243. DOI: 10.1103/PhysRevLett.69.1240. URL: https://link.aps.org/doi/10.1103/PhysRevLett.69.1240.

[46] Antoine Georges, Luca de’ Medici, and Jernej Mravlje. “Strong Correlations from Hund’s Coupling.” In: *Annual Review of Condensed Matter Physics* 4.1 (2013), pp. 137–178. DOI: 10.1146/annurev-conmatphys-020911-125045. URL: https://doi.org/10.1146/annurev-conmatphys-020911-125045.

[47] S. Gerber et al. “Femtosecond electron-phonon lock-in by photoemission and x-ray free-electron laser.” In: *Science* 357.6346 (2017), pp. 71–75. DOI: 10.1126/science.aak9946.

[48] Thierry Giamarchi. *Quantum Physics in One Dimension*. Note: see Fig. 7.12(b) of this book. In our data, the gap is not apparent due to the small gap size and the peak broadening, but for much larger U, the spectrum of the optical conductivity is as depicted in this figure. Oxford: Oxford university press, 2004. ISBN: 9780198525004.

[49] Denis Golež, Martin Eckstein, and Philipp Werner. “Multiband nonequilibrium GW + EDMFT formalism for correlated insulators.” In: *Phys. Rev. B* 100 (23 2019), p. 235117. DOI: 10.1103/PhysRevB.100.235117. URL: https://link.aps.org/doi/10.1103/PhysRevB.100.235117.

[50] Denis Golež, Philipp Werner, and Martin Eckstein. “Photoinduced gap closure in an excitonic insulator.” In: *Phys. Rev. B* 94 (3 2016), p. 035121. DOI: 10.1103/PhysRevB.94.035121. URL: https://link.aps.org/doi/10.1103/PhysRevB.94.035121.

[51] C. E. Graves et al. “Nanoscale spin reversal by non-local angular momentum transfer following ultrafast laser excitation in ferrimagnetic GdFeCo.” In: *Nature Materials* 12.4 (2013), pp. 293–298. ISSN: 1476-4660. DOI: 10.1038/nmat3597.

[52] E. Gull and A. J. Millis. “Superconducting and pseudogap effects on the interplane conductivity and Raman scattering cross section in the two-dimensional Hubbard model.” In: *Phys. Rev. B* 88 (7 2013), p. 075127. DOI: 10.1103/PhysRevB.88.075127. URL: https://link.aps.org/doi/10.1103/PhysRevB.88.075127.

[53] E. Gull, P. Werner, O. Parcollet, and M. Troyer. “Continuous-time auxiliary-field Monte Carlo for quantum impurity models.” In: *EPL (Europhysics Letters)* 82.5 (2008), p. 57003. DOI: 10.1209/0295-5075/82/57003. URL: https://doi.org/10.1209/0295-5075/82/57003.

[54] Emanuel Gull, Andrew J. Millis, Alexander I. Lichtenstein, Alexey N. Rubtsov, Matthias Troyer, and Philipp Werner. “Continuous-time Monte Carlo methods for quantum impurity models.” In: *Rev. Mod. Phys.* 83 (2 2011), pp. 349–404. doi: `10.1103/RevModPhys.83.349`. url: `https://link.aps.org/doi/10.1103/RevModPhys.83.349`.

[55] O. Gunnarsson, G. Rohringer, T. Schäfer, G. Sangiovanni, and A. Toschi. “Breakdown of Traditional Many-Body Theories for Correlated Electrons.” In: *Phys. Rev. Lett.* 119 (5 2017), p. 056402. doi: `10.1103/PhysRevLett.119.056402`. url: `https://link.aps.org/doi/10.1103/PhysRevLett.119.056402`.

[56] K. Haule, S. Kirchner, J. Kroha, and P. Wölfle. “Anderson impurity model at finite Coulomb interaction U: Generalized noncrossing approximation.” In: *Phys. Rev. B* 64 (15 2001), p. 155111. doi: `10.1103/PhysRevB.64.155111`.

[57] Shintaro Hoshino and Philipp Werner. “Superconductivity from Emerging Magnetic Moments.” In: *Phys. Rev. Lett.* 115 (24 2015), p. 247001. doi: `10.1103/PhysRevLett.115.247001`. url: `https://link.aps.org/doi/10.1103/PhysRevLett.115.247001`.

[58] J. Hubbard. “Electron correlations in narrow energy bands.” In: *Proc. R. Soc. Lond. A* 276 (1963), pp. 238–257.

[59] M. Jarrell. “Hubbard model in infinite dimensions: A quantum Monte Carlo study.” In: *Phys. Rev. Lett.* 69 (1 1992), pp. 168–171. doi: `10.1103/PhysRevLett.69.168`. url: `https://link.aps.org/doi/10.1103/PhysRevLett.69.168`.

[60] J. D. Jorgensen, B. W. Veal, A. P. Paulikas, L. J. Nowicki, G. W. Crabtree, H. Claus, and W. K. Kwok. “Structural properties of oxygen-deficient $\mathrm{YBa_2Cu_3O_{7-ffi}}$.” In: *Phys. Rev. B* 41 (4 1990), pp. 1863–1877. doi: `10.1103/PhysRevB.41.1863`. url: `https://link.aps.org/doi/10.1103/PhysRevB.41.1863`.

[61] Jeremy J. Jorgensen, John E. Christensen, Tyler J. Jarvis null, and Gus L. W. Hart. “A General Algorithm for Calculating Irreducible Brillouin Zones.” In: *Communications in Computational Physics* 31.2 (2022), 495–515. issn: 1991-7120. doi: `10.4208/cicp.oa-2021-0094`. url: `http://dx.doi.org/10.4208/cicp.OA-2021-0094`.

[62] Henrik Kajueter and Gabriel Kotliar. “New Iterative Perturbation Scheme for Lattice Models with Arbitrary Filling.” In: *Phys. Rev. Lett.* 77 (1 1996), pp. 131–134. doi: `10.1103/PhysRevLett.77.131`. url: `https://link.aps.org/doi/10.1103/PhysRevLett.77.131`.

[63] Junjiro Kanamori. “Electron Correlation and Ferromagnetism of Transition Metals.” In: *Progress of Theoretical Physics* 30.3 (Sept. 1963), pp. 275–289. doi: `10.1143/PTP.30.275`. url: `https://doi.org/10.1143/PTP.30.275`.

[64] Emmanuel Kant. *Critique de la faculté de juger*. Traduction et présentation par Alain Renaut. Flammarion, 2000.

[65] C. Karrasch, D. M. Kennes, and J. E. Moore. “Transport properties of the one-dimensional Hubbard model at finite temperature.” In: *Phys. Rev. B* 90 (15 2014), p. 155104. DOI: `10.1103/PhysRevB.90.155104`. URL: `https://link.aps.org/doi/10.1103/PhysRevB.90.155104`.

[66] A. Kauch, P. Pudleiner, K. Astleithner, P. Thunström, T. Ribic, and K. Held. “Generic Optical Excitations of Correlated Systems: π-tons.” In: *Phys. Rev. Lett.* 124 (4 2020), p. 047401. DOI: `10.1103/PhysRevLett.124.047401`. URL: `https://link.aps.org/doi/10.1103/PhysRevLett.124.047401`.

[67] Jason Kaye and Denis Golež. “Low rank compression in the numerical solution of the nonequilibrium Dyson equation.” In: *SciPost Phys.* 10 (2021), p. 091. DOI: `10.21468/SciPostPhys.10.4.091`. URL: `https://scipost.org/10.21468/SciPostPhys.10.4.091`.

[68] K. W. Kim, A. Pashkin, H. Schäfer, M. Beyer, M. Porer, T. Wolf, C. Bernhard, J. Demsar, R. Huber, and A. Leitenstorfer. “Ultrafast transient generation of spin-density-wave order in the normal state of BaFe2As2 driven by coherent lattice vibrations.” In: *Nature Materials* 11.6 (2012), pp. 497–501. ISSN: 1476-4660. DOI: `10.1038/nmat3294`. URL: `https://doi.org/10.1038/nmat3294`.

[69] Erik Koch, Giorgio Sangiovanni, and Olle Gunnarsson. “Sum rules and bath parametrization for quantum cluster theories.” In: *Phys. Rev. B* 78.11 (Sept. 2008). DOI: `10.1103/PhysRevB.78.115102`.

[70] Corinna Kollath, Andreas M. Läuchli, and Ehud Altman. “Quench Dynamics and Nonequilibrium Phase Diagram of the Bose-Hubbard Model.” In: *Phys. Rev. Lett.* 98 (18 2007), p. 180601. DOI: `10.1103/PhysRevLett.98.180601`.

[71] Gertjan Koster, Lior Klein, Wolter Siemons, Guus Rijnders, J. Steven Dodge, Chang-Beom Eom, Dave H. A. Blank, and Malcolm R. Beasley. “Structure, physical properties, and applications of $SrRuO_3$ thin films.” In: *Rev. Mod. Phys.* 84 (1 2012), pp. 253–298. DOI: `10.1103/RevModPhys.84.253`. URL: `https://link.aps.org/doi/10.1103/RevModPhys.84.253`.

[72] E. Kozik, K. Van Houcke, E. Gull, L. Pollet, N. Prokof’ev, B. Svistunov, and M. Troyer. “Diagrammatic Monte Carlo for correlated fermions.” In: *Europhysics Letters* 90.1 (2010), p. 10004. DOI: `10.1209/0295-5075/90/10004`. URL: `https://dx.doi.org/10.1209/0295-5075/90/10004`.

[73] Friedrich Krien, Anna Kauch, and Karsten Held. “Tiling with triangles: parquet and GWγ methods unified.” In: (2020). arXiv: `2009.12868 [cond-mat.str-el]`.

[74] Friedrich Krien, Angelo Valli, Patrick Chalupa, Massimo Capone, Alexander I. Lichtenstein, and Alessandro Toschi. “Boson Exchange Parquet Solver (for dual fermions).” In: (2020). arXiv: `2008.04184 [cond-mat.str-el]`.

[75] Hiroaki Kusunose. “Influence of Spatial Correlations in Strongly Correlated Electron Systems: Extension to Dynamical Mean Field Approximation.” en. In: *Journal of the Physical Society of Japan* 75.5 (May 2006). ISSN: 0031-9015, 1347-4073. DOI: `10.1143/JPSJ.75.054713`. (Visited on 08/15/2020).

[76] B. Kyung, V. Hankevych, A.-M. Daré, and A.-M. S. Tremblay. "Pseudogap and Spin Fluctuations in the Normal State of the Electron-Doped Cuprates." In: *Phys. Rev. Lett.* 93 (14 2004), p. 147004. DOI: `10.1103/PhysRevLett.93.147004`. URL: `https://link.aps.org/doi/10.1103/PhysRevLett.93.147004`.

[77] Bumsoo Kyung, Jean-Sébastien Landry, and A.-M. S. Tremblay. "Antiferromagnetic fluctuations and d-wave superconductivity in electron-doped high-temperature superconductors." In: *Phys. Rev. B* 68 (17 2003), p. 174502. DOI: `10.1103/PhysRevB.68.174502`. URL: `https://link.aps.org/doi/10.1103/PhysRevB.68.174502`.

[78] Patrick A. Lee and Xiao-Gang Wen. "Unusual Superconducting State of Underdoped Cuprates." In: *Phys. Rev. Lett.* 78 (21 1997), pp. 4111–4114. DOI: `10.1103/PhysRevLett.78.4111`.

[79] M. Ligges et al. "Ultrafast Doublon Dynamics in Photoexcited $1T$-TaS$_2$." In: *Phys. Rev. Lett.* 120 (16 2018), p. 166401. DOI: `10.1103/PhysRevLett.120.166401`. URL: `https://link.aps.org/doi/10.1103/PhysRevLett.120.166401`.

[80] J. M. Luttinger and J. C. Ward. "Ground-State Energy of a Many-Fermion System. II." In: *Phys. Rev.* 118 (5 1960), pp. 1417–1427. DOI: `10.1103/PhysRev.118.1417`. URL: `https://link.aps.org/doi/10.1103/PhysRev.118.1417`.

[81] Thomas Maier, Mark Jarrell, Thomas Pruschke, and Matthias H. Hettler. "Quantum cluster theories." In: *Rev. Mod. Phys.* 77 (3 2005), pp. 1027–1080. DOI: `10.1103/RevModPhys.77.1027`. URL: `https://link.aps.org/doi/10.1103/RevModPhys.77.1027`.

[82] Thomas Maier, Mark Jarrell, Thomas Pruschke, and Matthias H. Hettler. "Quantum cluster theories." In: *Rev. Mod. Phys.* 77 (3 2005), pp. 1027–1080. DOI: `10.1103/RevModPhys.77.1027`.

[83] Kazumi Maki. "Critical Fluctuation of the Order Parameter in a Superconductor. I." In: *Prog. Theor. Phys.* 40.2 (Aug. 1968), pp. 193–200. DOI: `10.1143/PTP.40.193`.

[84] J. Maklar et al. "Nonequilibrium charge-density-wave order beyond the thermal limit." In: *Nature Communications* 12.1 (2021), p. 2499. ISSN: 2041-1723. DOI: `10.1038/s41467-021-22778-w`. URL: `https://doi.org/10.1038/s41467-021-22778-w`.

[85] P. R. Mandal, Tarapada Sarkar, J. S. Higgins, and Richard L. Greene. "Nernst effect in the electron-doped cuprate superconductor La$_{2-x}$Ce$_x$CuO$_4$." In: *Phys. Rev. B* 97 (1 2018), p. 014522. DOI: `10.1103/PhysRevB.97.014522`.

[86] R. Mankowsky et al. "Nonlinear lattice dynamics as a basis for enhanced superconductivity in YBa2Cu3O6.5." In: *Nature* 516.7529 (2014), pp. 71–73. ISSN: 1476-4687. DOI: `10.1038/nature13875`.

[87] Roman Mankowsky, Michael Först, and Andrea Cavalleri. "Non-equilibrium control of complex solids by nonlinear phononics." In: *Reports on Progress in Physics* 79.6 (2016), p. 064503. DOI: `10.1088/0034-4885/79/6/064503`. URL: `https://dx.doi.org/10.1088/0034-4885/79/6/064503`.

[88] S. R. Manmana, S. Wessel, R. M. Noack, and A. Muramatsu. “Strongly Correlated Fermions after a Quantum Quench.” In: *Phys. Rev. Lett.* 98 (21 2007), p. 210405. DOI: 10.1103/PhysRevLett.98.210405.

[89] N. Martin, C. Gauvin-Ndiaye, and A. M. S. Tremblay. *Non-local corrections to dynamical mean-field theory from the two-particle self-consistent method*. 2022. DOI: 10.48550/ARXIV.2211.01919. URL: https://arxiv.org/abs/2211.01919.

[90] Paul C. Martin and Julian Schwinger. “Theory of Many-Particle Systems. I.” In: *Phys. Rev.* 115 (6 1959), pp. 1342–1373. DOI: 10.1103/PhysRev.115.1342. URL: https://link.aps.org/doi/10.1103/PhysRev.115.1342.

[91] Walter Metzner and Dieter Vollhardt. “Correlated Lattice Fermions in $d = \infty$ Dimensions.” In: *Phys. Rev. Lett.* 62 (3 1989), pp. 324–327. DOI: 10.1103/PhysRevLett.62.324. URL: https://link.aps.org/doi/10.1103/PhysRevLett.62.324.

[92] Michael Moeckel and Stefan Kehrein. “Interaction Quench in the Hubbard Model.” In: *Phys. Rev. Lett.* 100 (17 2008), p. 175702. DOI: 10.1103/PhysRevLett.100.175702. URL: https://link.aps.org/doi/10.1103/PhysRevLett.100.175702.

[93] Selene Mor et al. “Ultrafast Electronic Band Gap Control in an Excitonic Insulator.” In: *Phys. Rev. Lett.* 119 (8 2017), p. 086401. DOI: 10.1103/PhysRevLett.119.086401. URL: https://link.aps.org/doi/10.1103/PhysRevLett.119.086401.

[94] E. Müller-Hartmann. In: *Z. Phys.* B74 (1989), p. 507.

[95] John W. Negele and Henri Orland. *Quantum Many-Particle Systems (1st ed.)* CRC Press, Nov. 1998. URL: https://doi.org/10.1201/9780429497926.

[96] F. Nilsson, L. Boehnke, P. Werner, and F. Aryasetiawan. “Multitier self-consistent $GW + \mathrm{EDMFT}$.” In: *Phys. Rev. Materials* 1 (4 2017), p. 043803. DOI: 10.1103/PhysRevMaterials.1.043803. URL: https://link.aps.org/doi/10.1103/PhysRevMaterials.1.043803.

[97] T. F. Nova, A. S. Disa, M. Fechner, and A. Cavalleri. “Metastable ferroelectricity in optically strained $\mathrm{SrTiO_3}$.” In: *Science* 364.6445 (2019), pp. 1075–1079. DOI: 10.1126/science.aaw4911. URL: https://www.science.org/doi/abs/10.1126/science.aaw4911.

[98] L. Perfetti, P. A. Loukakos, M. Lisowski, U. Bovensiepen, H. Eisaki, and M. Wolf. “Ultrafast Electron Relaxation in Superconducting $\mathrm{Bi_2Sr_2CaCu_2O_{8+\delta}}$ by Time-Resolved Photoelectron Spectroscopy.” In: *Phys. Rev. Lett.* 99 (19 2007), p. 197001. DOI: 10.1103/PhysRevLett.99.197001. URL: https://link.aps.org/doi/10.1103/PhysRevLett.99.197001.

[99] Antonio Picano, Francesco Grandi, and Martin Eckstein. *Inhomogeneous disordering at a photo-induced charge density wave transition*. 2021. DOI: 10.48550/ARXIV.2112.15323. URL: https://arxiv.org/abs/2112.15323.

[100] Nikolai V. Prokof’ev and Boris V. Svistunov. “Polaron Problem by Diagrammatic Quantum Monte Carlo.” In: *Phys. Rev. Lett.* 81 (12 1998), pp. 2514–2517. DOI: 10.1103/PhysRevLett.81.2514. URL: https://link.aps.org/doi/10.1103/PhysRevLett.81.2514.

[101] Nikolay Prokof'ev and Boris Svistunov. "Bold Diagrammatic Monte Carlo Technique: When the Sign Problem Is Welcome." In: *Phys. Rev. Lett.* 99 (25 2007), p. 250201. DOI: `10.1103/PhysRevLett.99.250201`. URL: `https://link.aps.org/doi/10.1103/PhysRevLett.99.250201`.

[102] Th. Pruschke, D. L. Cox, and M. Jarrell. "Hubbard model at infinite dimensions: Thermodynamic and transport properties." In: *Phys. Rev. B* 47 (7 1993), pp. 3553–3565. DOI: `10.1103/PhysRevB.47.3553`.

[103] G. Rohringer, H. Hafermann, A. Toschi, A. A. Katanin, A. E. Antipov, M. I. Katsnelson, A. I. Lichtenstein, A. N. Rubtsov, and K. Held. "Diagrammatic routes to nonlocal correlations beyond dynamical mean field theory." In: *Rev. Mod. Phys.* 90 (2 2018), p. 025003. DOI: `10.1103/RevModPhys.90.025003`. URL: `https://link.aps.org/doi/10.1103/RevModPhys.90.025003`.

[104] G. Rohringer, H. Hafermann, A. Toschi, A. A. Katanin, A. E. Antipov, M. I. Katsnelson, A. I. Lichtenstein, A. N. Rubtsov, and K. Held. "Diagrammatic routes to nonlocal correlations beyond dynamical mean field theory." In: *Rev. Mod. Phys.* 90 (2 2018), p. 025003. DOI: `10.1103/RevModPhys.90.025003`. URL: `https://link.aps.org/doi/10.1103/RevModPhys.90.025003`.

[105] M. J. Rozenberg, G. Kotliar, and X. Y. Zhang. "Mott-Hubbard transition in infinite dimensions. II." In: *Phys. Rev. B* 49 (15 1994), pp. 10181–10193. DOI: `10.1103/PhysRevB.49.10181`. URL: `https://link.aps.org/doi/10.1103/PhysRevB.49.10181`.

[106] A. N. Rubtsov, V. V. Savkin, and A. I. Lichtenstein. "Continuous-time quantum Monte Carlo method for fermions." In: *Phys. Rev. B* 72 (3 2005), p. 035122. DOI: `10.1103/PhysRevB.72.035122`. URL: `https://link.aps.org/doi/10.1103/PhysRevB.72.035122`.

[107] A.N. Rubtsov, M.I. Katsnelson, and A.I. Lichtenstein. "Dual boson approach to collective excitations in correlated fermionic systems." In: *Annals of Physics* 327.5 (2012), pp. 1320–1335. ISSN: 0003-4916. DOI: `https://doi.org/10.1016/j.aop.2012.01.002`. URL: `https://www.sciencedirect.com/science/article/pii/S0003491612000164`.

[108] Erich Runge and E. K. U. Gross. "Density-Functional Theory for Time-Dependent Systems." In: *Phys. Rev. Lett.* 52 (12 1984), pp. 997–1000. DOI: `10.1103/PhysRevLett.52.997`. URL: `https://link.aps.org/doi/10.1103/PhysRevLett.52.997`.

[109] Tetsuro Saso. "Investigation of the Two-Particle-Self-Consistent Theory for the Single-Impurity Anderson Model and an Extension to the Case of Strong Correlation." In: *Journal of the Physical Society of Japan* 69.12 (2000), pp. 3912–3916. DOI: `10.1143/JPSJ.69.3912`.

[110] Thomas Schäfer et al. "Tracking the Footprints of Spin Fluctuations: A MultiMethod, MultiMessenger Study of the Two-Dimensional Hubbard Model." In: *Phys. Rev. X* 11 (1 2021), p. 011058. DOI: `10.1103/PhysRevX.11.011058`. URL: `https://link.aps.org/doi/10.1103/PhysRevX.11.011058`.

[111] F. Schmitt et al. "Transient Electronic Structure and Melting of a Charge Density Wave in TbTe<sub>3</sub>." In: *Science* 321.5896 (2008), pp. 1649–1652. DOI: 10.1126/science.1160778.

[112] Ulrich Schollwöck. "The density-matrix renormalization group in the age of matrix product states." In: *Ann. Phys.* 326.1 (2011), pp. 96 –192. ISSN: 0003-4916. DOI: https://doi.org/10.1016/j.aop.2010.09.012. URL: http://www.sciencedirect.com/science/article/pii/S0003491610001752.

[113] Michael Schüler, Martin Eckstein, and Philipp Werner. "Truncating the memory time in nonequilibrium dynamical mean field theory calculations." In: *Phys. Rev. B* 97 (24 2018), p. 245129. DOI: 10.1103/PhysRevB.97.245129. URL: https://link.aps.org/doi/10.1103/PhysRevB.97.245129.

[114] Michael Schüler, Denis Golež, Yuta Murakami, Nikolaj Bittner, Andreas Herrmann, Hugo Strand, Philipp Werner, and Martin Eckstein. "NESSi: The Non-Equilibrium Systems Simulation package." In: *Computer Physics Communications* 257 (2020), p. 107484. ISSN: 0010-4655. DOI: https://doi.org/10.1016/j.cpc.2020.107484. URL: https://www.sciencedirect.com/science/article/pii/S0010465520302277.

[115] Mark S. Senn, Jon P. Wright, and J. Paul Attfield. "Charge order and three-site distortions in the Verwey structure of magnetite." In: *Nature* 481.7380 (2012), pp. 173–176. ISSN: 1476-4687. DOI: 10.1038/nature10704.

[116] B. Sriram Shastry and Bill Sutherland. "Twisted boundary conditions and effective mass in Heisenberg-Ising and Hubbard rings." In: *Phys. Rev. Lett.* 65 (2 1990), pp. 243–246. DOI: 10.1103/PhysRevLett.65.243. URL: https://link.aps.org/doi/10.1103/PhysRevLett.65.243.

[117] O. Simard, C.-D. Hébert, A. Foley, D. Sénéchal, and A.-M. S. Tremblay. "Superfluid stiffness in cuprates: Effect of Mott transition and phase competition." In: *Phys. Rev. B* 100 (9 2019), p. 094506. DOI: 10.1103/PhysRevB.100.094506. URL: https://link.aps.org/doi/10.1103/PhysRevB.100.094506.

[118] Olivier Simard. "Rigidité superfluide et température critique en présence d'une autre phase." Master's thesis. Sherbrooke: Université de Sherbrooke, 2019. URL: http://hdl.handle.net/11143/15039.

[119] Olivier Simard, Martin Eckstein, and Philipp Werner. "Nonequilibrium evolution of the optical conductivity of the weakly interacting Hubbard model: Drude response and π-ton type vertex corrections." In: *Phys. Rev. B* 104 (24 2021), p. 245127. DOI: 10.1103/PhysRevB.104.245127. URL: https://link.aps.org/doi/10.1103/PhysRevB.104.245127.

[120] Olivier Simard, Shintaro Takayoshi, and Philipp Werner. "Diagrammatic study of optical excitations in correlated systems." In: *Phys. Rev. B* 103 (10 2021), p. 104415. DOI: 10.1103/PhysRevB.103.104415. URL: https://link.aps.org/doi/10.1103/PhysRevB.103.104415.

[121] Olivier Simard and Philipp Werner. “Nonequilibrium two-particle self-consistent approach.” In: *Phys. Rev. B* 106 (24 2022), p. L241110. DOI: `10.1103/PhysRevB.106.L241110`. URL: `https://link.aps.org/doi/10.1103/PhysRevB.106.L241110`.

[122] Olivier Simard and Philipp Werner. *Dynamical Mean Field Theory extension to the nonequilibrium Two-Particle Self-Consistent approach*. 2023. arXiv: `2302.14134 [cond-mat.str-el]`.

[123] K. S. Singwi, M. P. Tosi, R. H. Land, and A. Sjölander. “Electron Correlations at Metallic Densities.” In: *Phys. Rev.* 176 (2 1968), pp. 589–599. DOI: `10.1103/PhysRev.176.589`. URL: `https://link.aps.org/doi/10.1103/PhysRev.176.589`.

[124] Baruch Spinoza. *L’Éthique*. Réédition dans la collection Points Essais en 2010. Seuil, 1988.

[125] Christopher Stahl, Nagamalleswararao Dasari, Jiajun Li, Antonio Picano, Philipp Werner, and Martin Eckstein. “Memory truncated Kadanoff-Baym equations.” In: *Phys. Rev. B* 105 (11 2022), p. 115146. DOI: `10.1103/PhysRevB.105.115146`. URL: `https://link.aps.org/doi/10.1103/PhysRevB.105.115146`.

[126] P C E Stamp. “Spin fluctuation theory in condensed quantum systems.” In: *Journal of Physics F: Metal Physics* 15.9 (1985), pp. 1829–1865. DOI: `10.1088/0305-4608/15/9/005`. URL: `https://doi.org/10.1088/0305-4608/15/9/005`.

[127] Gianluca Stefanucci and Robert van Leeuwen. *Nonequilibrium Many-Body Theory of Quantum Systems: A Modern Introduction*. Cambridge: Cambridge University Press, 2013. DOI: `10.1017/CBO9781139023979`.

[128] G. R. Stewart. “Superconductivity in iron compounds.” In: *Rev. Mod. Phys.* 83 (4 2011), pp. 1589–1652. DOI: `10.1103/RevModPhys.83.1589`. URL: `https://link.aps.org/doi/10.1103/RevModPhys.83.1589`.

[129] D. Sénéchal, AM. Tremblay, and C. Bourbonnais. *Theoretical Methods for Strongly Correlated Electrons*. New York: Springer, 2004. DOI: `https://doi.org/10.1007/0-387-21717-7_8`.

[130] Richard S. Thompson. “Microwave, Flux Flow, and Fluctuation Resistance of Dirty Type-II Superconductors.” In: *Phys. Rev. B* 1 (1 1970), pp. 327–333. DOI: `10.1103/PhysRevB.1.327`.

[131] Alberto de la Torre, Dante M. Kennes, Martin Claassen, Simon Gerber, James W. McIver, and Michael A. Sentef. “Colloquium: Nonthermal pathways to ultrafast control in quantum materials.” In: *Rev. Mod. Phys.* 93 (4 2021), p. 041002. DOI: `10.1103/RevModPhys.93.041002`. URL: `https://link.aps.org/doi/10.1103/RevModPhys.93.041002`.

[132] Alberto de la Torre et al. “Decoupling of static and dynamic criticality in a driven Mott insulator.” In: *Communications Physics* 5.1 (2022), p. 35. ISSN: 2399-3650. DOI: `10.1038/s42005-022-00813-6`. URL: `https://doi.org/10.1038/s42005-022-00813-6`.

[133] A. Toschi, A. A. Katanin, and K. Held. "Dynamical vertex approximation: A step beyond dynamical mean-field theory." In: *Phys. Rev. B* 75 (4 2007), p. 045118. DOI: 10.1103/PhysRevB.75.045118. URL: https://link.aps.org/doi/10.1103/PhysRevB.75.045118.

[134] A.-M. S. Tremblay. *Problème à N-corps*. (unpublished). Sherbrooke, Qc, Canada: Lecture notes, 2017. URL: https://www.physique.usherbrooke.ca/tremblay/cours/phy-892/N-corps-2017.pdf.

[135] Naoto Tsuji, Peter Barmettler, Hideo Aoki, and Philipp Werner. "Nonequilibrium dynamical cluster theory." In: *Phys. Rev. B* 90 (7 2014), p. 075117. DOI: 10.1103/PhysRevB.90.075117. URL: https://link.aps.org/doi/10.1103/PhysRevB.90.075117.

[136] Naoto Tsuji, Martin Eckstein, and Philipp Werner. "Nonthermal Antiferromagnetic Order and Nonequilibrium Criticality in the Hubbard Model." In: *Phys. Rev. Lett.* 110 (13 2013), p. 136404. DOI: 10.1103/PhysRevLett.110.136404. URL: https://link.aps.org/doi/10.1103/PhysRevLett.110.136404.

[137] Naoto Tsuji and Philipp Werner. "Nonequilibrium dynamical mean-field theory based on weak-coupling perturbation expansions: Application to dynamical symmetry breaking in the Hubbard model." In: *Phys. Rev. B* 88 (16 2013), p. 165115. DOI: 10.1103/PhysRevB.88.165115. URL: https://link.aps.org/doi/10.1103/PhysRevB.88.165115.

[138] Naoto Tsuji and Philipp Werner. "Nonequilibrium dynamical mean-field theory based on weak-coupling perturbation expansions: Application to dynamical symmetry breaking in the Hubbard model." In: *Phys. Rev. B* 88.16 (Oct. 2013), p. 165115. DOI: 10.1103/PhysRevB.88.165115.

[139] V. M. Turkowski and J. K. Freericks. "Spectral moment sum rules for strongly correlated electrons in time-dependent electric fields." In: *Phys. Rev. B* 73 (7 2006), p. 075108. DOI: 10.1103/PhysRevB.73.075108. URL: https://link.aps.org/doi/10.1103/PhysRevB.73.075108.

[140] S. Uchida, T. Ido, H. Takagi, T. Arima, Y. Tokura, and S. Tajima. "Optical spectra of $La_{2-x}Sr_xCuO_4$: Effect of carrier doping on the electronic structure of the CuO_2 plane." In: *Phys. Rev. B* 43 (10 1991), pp. 7942–7954. DOI: 10.1103/PhysRevB.43.7942. URL: https://link.aps.org/doi/10.1103/PhysRevB.43.7942.

[141] "Using dynamic mode decomposition to predict the dynamics of a two-time non-equilibrium Green's function." In: *Journal of Computational Science* 64 (2022), p. 101843. ISSN: 1877-7503. DOI: https://doi.org/10.1016/j.jocs.2022.101843.

[142] Kris Van Houcke, Evgeny Kozik, N. Prokof'ev, and B. Svistunov. "Diagrammatic Monte Carlo." In: *Phys. Procedia* 6 (2010), pp. 95 –105. ISSN: 1875-3892. DOI: https://doi.org/10.1016/j.phpro.2010.09.034. URL: http://www.sciencedirect.com/science/article/pii/S1875389210006498.

[143] H Vidberg and J. Serene. In: *J. Low Temp. Phys.* 29 (1977), p. 179.

[144] Y. M. Vilk, Liang Chen, and A.-M. S. Tremblay. "Theory of spin and charge fluctuations in the Hubbard model." In: *Phys. Rev. B* 49 (18 1994), pp. 13267–13270. DOI: `10.1103/PhysRevB.49.13267`. URL: `https://link.aps.org/doi/10.1103/PhysRevB.49.13267`.

[145] Y. M Vilk and A.-M. S Tremblay. "Destruction of Fermi-liquid quasiparticles in two dimensions by critical fluctuations." In: *Europhysics Letters (EPL)* 33.2 (1996), pp. 159–164. DOI: `10.1209/epl/i1996-00315-2`. URL: `https://doi.org/10.1209/epl/i1996-00315-2`.

[146] Hai-Hu Wen and Shiliang Li. "Materials and Novel Superconductivity in Iron Pnictide Superconductors." In: *Annual Review of Condensed Matter Physics* 2.1 (2011), pp. 121–140. DOI: `10.1146/annurev-conmatphys-062910-140518`. URL: `https://doi.org/10.1146/annurev-conmatphys-062910-140518`.

[147] F. Werner, O. Parcollet, A. Georges, and S. R. Hassan. "Interaction-Induced Adiabatic Cooling and Antiferromagnetism of Cold Fermions in Optical Lattices." In: *Phys. Rev. Lett.* 95 (5 2005), p. 056401. DOI: `10.1103/PhysRevLett.95.056401`. URL: `https://link.aps.org/doi/10.1103/PhysRevLett.95.056401`.

[148] Philipp Werner, Armin Comanac, Luca de'Medici, Matthias Troyer, and Andrew J. Millis. "Continuous-Time Solver for Quantum Impurity Models." In: *Phys. Rev. Lett.* 97 (7 2006), p. 076405. DOI: `10.1103/PhysRevLett.97.076405`. URL: `https://link.aps.org/doi/10.1103/PhysRevLett.97.076405`.

[149] Steven R. White. "Density matrix formulation for quantum renormalization groups." In: *Phys. Rev. Lett.* 69 (19 1992), pp. 2863–2866. DOI: `10.1103/PhysRevLett.69.2863`. URL: `https://link.aps.org/doi/10.1103/PhysRevLett.69.2863`.

[150] Paul Worm, Clemens Watzenböck, Matthias Pickem, Anna Kauch, and Karsten Held. "Broadening and sharpening of the Drude peak through antiferromagnetic fluctuations." In: *Phys. Rev. B* 104 (11 2021), p. 115153. DOI: `10.1103/PhysRevB.104.115153`. URL: `https://link.aps.org/doi/10.1103/PhysRevB.104.115153`.

[151] Paul Worm, Clemens Watzenböck, Matthias Pickem, Anna Kauch, and Karsten Held. "Broadening and sharpening of the Drude peak through antiferromagnetic fluctuations." In: (2020). arXiv: `2010.15797 [cond-mat.str-el]`.

[152] Y.M. Vilk and A.-M.S. Tremblay. "Non-Perturbative Many-Body Approach to the Hubbard Model and Single-Particle Pseudogap." In: *J. Phys. I France* 7.11 (1997), pp. 1309–1368. DOI: `10.1051/jp1:1997135`. URL: `https://doi.org/10.1051/jp1:1997135`.

[153] L. X. Yang et al. "Ultrafast Modulation of the Chemical Potential in $BaFe_2As_2$ by Coherent Phonons." In: *Phys. Rev. Lett.* 112 (20 2014), p. 207001. DOI: `10.1103/PhysRevLett.112.207001`. URL: `https://link.aps.org/doi/10.1103/PhysRevLett.112.207001`.

[154] Jia Yin, Yang-hao Chan, Felipe da Jornada, Diana Qiu, Steven G. Louie, and Chao Yang. *Using dynamic mode decomposition to predict the dynamics of a two-time non-equilibrium Green's function*. 2022. DOI: 10.48550/ARXIV.2203.14892. URL: https://arxiv.org/abs/2203.14892.

[155] Karim Zantout, Steffen Backes, Aleksandar Razpopov, Dominik Lessnich, and Roser Valenti. *Improved effective vertices in the multi-orbital Two-Particle Self-Consistent method from Dynamical Mean-Field Theory*. 2022. DOI: 10.48550/ARXIV.2211.01400. URL: https://arxiv.org/abs/2211.01400.

[156] Karim Zantout, Steffen Backes, and Roser Valentí. "Two-Particle Self-Consistent Method for the Multi-Orbital Hubbard Model." In: *Annalen der Physik* 533.2 (2021), p. 2000399. DOI: https://doi.org/10.1002/andp.202000399. URL: https://onlinelibrary.wiley.com/doi/abs/10.1002/andp.202000399.

[157] Alfred Zong et al. "Dynamical Slowing-Down in an Ultrafast Photoinduced Phase Transition." In: *Phys. Rev. Lett.* 123 (9 2019), p. 097601. DOI: 10.1103/PhysRevLett.123.097601. URL: https://link.aps.org/doi/10.1103/PhysRevLett.123.097601.

[158] Alfred Zong et al. "Evidence for topological defects in a photoinduced phase transition." In: *Nature Physics* 15.1 (2019), pp. 27–31. ISSN: 1745-2481. DOI: 10.1038/s41567-018-0311-9. URL: https://doi.org/10.1038/s41567-018-0311-9.

[159] Alfred Zong et al. "Role of Equilibrium Fluctuations in Light-Induced Order." In: *Phys. Rev. Lett.* 127 (22 2021), p. 227401. DOI: 10.1103/PhysRevLett.127.227401. URL: https://link.aps.org/doi/10.1103/PhysRevLett.127.227401.